REUSE AND SUSTAINABILITY OF FLOOD DEFENCES

A thesis submitted to Imperial College London in partial fulfilment of the requirements for the degree of Doctor of Philosophy

By

BENJAMIN WEI LI GUO

Geotechnics Section

Department of Civil and Environmental Engineering

Imperial College London

London SW7 2AZ

November 2021

For my parents and sister Adelyn

May you be well and happy always

“知彼知己，勝乃不殆；

知天知地，勝乃可全。”

(“Know the enemy and know yourself, and victory will not be in doubt;

know the Heavens and know the Earth, and victory will be complete.”)

Sun Tzu, The Art of War

DECLARATION OF AUTHORSHIP

I, Benjamin Wei Li GUO, declare that this thesis titled “Reuse and Sustainability of Flood Defence” and all work described within it are wholly my own. Any quotations, or description of work from others are acknowledged and referenced to the source. The work presented in here was done completely while as a candidate for a research degree at Imperial College London.

ABSTRACT

Rainfall has always been an important quantity to measure throughout history due to its importance in predicting floods and droughts. In the present day, such predictions on the severity of flooding events are critical so that appropriate flood defences may be constructed in anticipation of these events to limit any damages. With the increasing concerns of human influenced (anthropogenic) climate change will affect rainfall, there is a growing need to quantify and incorporate these events into the design of flood defences, such as earthfill embankments.

As geotechnical modelling techniques are being developed to assist in the design and upgrading of earth embankments, various failure mechanisms and the behaviour of the soil within an embankment are better understood. However, one concern which arises is that there is an uncertainty on how climate change would affect the performance of these embankments. Therefore, the main purpose of this research is to identify the key failure mechanisms that may occur throughout the embankment's life cycle, taking into account climate change effects, and to develop solutions to these issues.

A site on the Thames estuary was chosen as the setting for this research. Taking into consideration a changing climate, sub-daily rainfall was produced for this site using a combination of stochastic rainfall generators and projected climate variables at the location. Following calibration and validation analyses for the foundation and embankment soils, a complete lifecycle analysis framework was established, using the previously generated rainfall as inputs to the soil-atmosphere boundary. The lifecycle framework was able to inform on both the general long-term performance of the embankment in a changing climate, and the resilience of the embankment to future extreme events. With the detailed lifecycle analysis, various strategies in reusing the embankment by raising it was also explored, to improve the embankment's adaptability to future climate.

ACKNOWLEDGEMENTS

I would like to first thank my supervisors:

Professor Lidija Zdravkovic, for her selfless support, clear guidance and good company throughout this journey. Her company as both a supervisor in College, and as a friend in the pub on Fridays is invaluable and always pleasant. Her comments are always constructive, and pushes me to be a better person to always improve.

Dr. Katerina Tsiampousi, for her advice, patience and kind words in pushing me along this journey and even before then throughout my time at Imperial. Some of the best lessons I learnt are from making the most laughable of mistakes, of which she has the patience to humour me.

Dr. Christian Onof, for his high enthusiasm and insight into the world of rainfall and philosophy. Discussions were always entertaining with him, and often spurred some of their own "spurious-relationship" threads, that could only be stopped because of other commitments.

I would like to thank my sponsors the Engineering and Physical Science Research Council Centre for Doctoral Training in Sustainability Civil Engineering, specifically Professor Chris Cheeseman and Dr. Robert Vollum, without which this research would not have been possible. In addition, I would also like to thank Geotechnical Consulting Group LLP for their role as industrial sponsors to this project.

In the past year of isolation, my appreciation for the past social gatherings with the Geotechnics Section only grows fonder. From beer clubs to the post celebratory drinks after a colloquium, the people in the Section never fails to cheer me up, or help me along home for that matter! For this I would like to personally thank Prof Potts (for his recommendations of ale especially), Dr. David Taborda, Dr. Wenjie Cui and Eli Sailer. I also have a special appreciation to my friends in 430 whom I got to know very well for the past 5 years as they provided great company while I worked on this research. I would like to thank Guilia Ghiadistri, Ken Vinck, Tom Morgan, Tara Sassel and Ding Zhou.

I would also like to thank Cheng Wei Kwang for her support and company, especially so for the past year during the lockdowns.

Finally, I would like to thank my mum and dad, and am grateful for all their guidance and sacrifices that led up to this moment.

TABLE OF CONTENTS

LIST OF FIGURES

LIST OF TABLES

LIST OF ABBREVIATIONS

Ac(n)/AC(n):	Monthly lag-1 Autocorrelation of n hours
AM:	Annual maxima
BBM:	Barcelona Basic Model
BLRP:	Bartlett-Lewis Rectangular Pulse
BLRPR:	Random Parameter BLRP
BLRPRx:	Randomised μ_x Random Parameter BLRP model
CPM:	Convection Permitting Model
CV(n):	Monthly coefficient of variation of n hours
EA:	Environment Agency
ERA5:	European Re-Analysis 5
FoS:	Factor of Safety
GCM:	Global Circulation Model
GLM:	Generalised Linear Model
ICFEP:	Imperial College Finite Element Program
ICG3S:	Imperial College Generalised Small Strain Stiffness
ICL:	Intrinsic compression line
ICSSM:	Imperial College Single Structure Model
IPCC:	Intergovernmental Panel on Climate Change
LC:	Load-Collapse
MCC:	Modified Cam Clay
mODN:	Metres above Ordinance Datum
NWP:	Numerical weather predictor

OCR:	Overconsolidation ratio
PDC:	Principal drying curve
POT:	Peaks-over-threshold
PWC:	Principal wetting curve
Pwet(n):	Monthly percentage wet of n hours
RCM:	Regional Circulation Model
RCP:	Representative concentration pathways
SWR(C):	Soil water retention (curve)
TBR:	Tipping bucket raingauge
UKCP18:	UK Climate Projections 2018

Chapter 1: Introduction

1.1 Background and motivation

Great civilisations have always depended on major rivers, enriched by their flood plains and waters for large scale agriculture or as a convenient mode for trade and transport. This necessitated our drive to control the power of rivers, by both predicting rainfall and flood events, and by controlling the consequences of such events with the construction and management of major riverine infrastructure such as embankments, weirs and canals.

With increasing population densities surrounding rivers, flooding in the modern era causes widespread humanitarian and economic crisis to hundreds of millions of people every year. From 1995 to 2015, floods have affected 2.6 billion people, killed 157000 people, and resulted in $662 million in recorded economic damages worldwide (UNISDR, 2015). In England, there is a strong push in preventing these extreme flood events due to the proximity of major national economic activities around key rivers, such as the Thames, Severn, and Tyne. Long-term infrastructure plans such as the Thames Estuary 2100 Plan are being deployed to ensure that current infrastructure can adapt to future climates.

The situation is further exacerbated by a rapidly changing climate in recent years, driven by global greenhouse emissions in the past century (IPCC, 2013) and leading to intensification of storm events, droughts, and rising sea levels. These atmospheric changes require us to first quantify these climatic changes, and then to re-evaluate the lifecycle, resilience, and adaptation of our existing riverine infrastructure in light of the changes to climatic conditions.

The principal methodology for assessing the long-term resilience of flood embankments is the predictive computational analysis, which needs to combine the geotechnical modelling of an earth embankment as a geotechnical structure exhibiting transient hydro-mechanical behaviour, together with the modelling of changing rainfall patterns as an advanced hydraulic boundary condition to geotechnical modelling. Existing geotechnical modelling approaches of infrastructure slopes and embankments have adopted simpler average annual pore water pressure hydraulic boundary conditions on open surfaces of slopes and embankments, which were justified by moderate seasonal changes of water balance evidenced in the last century (Potts et al., 1990; Vaughan, 1994). Such hydraulic boundary conditions are unable to reproduce embankment failure induced by rainfall or by overtopping. Equally, the existing rainfall models are limited in their ability to reproduce finer temporal rainfall intensity associated with short and intense rainfalls that are increasingly more common.

1.2 Scope and objective of the research

This research presented in this thesis aims to provide answers to some of the current modelling limitations, posed previously, in two parts. Firstly, a stochastic rainfall methodology is developed to derive temporally finer scale rainfall series for the future that takes into account a changing climate, complete with quantifying the increases in frequency and intensity of storms and droughts. This is then followed by the development and analysis of a complete lifecycle of earth embankments, from construction and into the future, including studies into the adaptability and resilience of these embankments to future storm events at key moments of their lifecycle.

Due to the cross-disciplinary nature of the research presented in this thesis, the scope of the research is wide. The objectives of this research may be split into two broad categories, with the first consisting of development, calibration and validation of stochastic and geotechnical numerical models with the use of appropriate case studies. Following all validation exercises, the second category consists of the application of these models and their outputs in a complete numerical lifecycle analysis of earth embankments.

The development, calibration and validation part of this research may be summarised as following:

- Development, calibration, and validation of Bartlett-Lewis Rectangular Pulse (BLRP; Rodriguez-Iturbe et al., 1987, 1988; Kaczmarska et al., 2014) modelling methodologies for the purposes of synthetically generating statistically similar rainfall to the observed rainfall.
- Calibration and validation of Generalised Linear Models (GLMs; Chandler, 2020) with relevant climate variables for predictive rainfall modelling, generating projected future daily rainfall that accounts for a changing climate.
- Development and validation of a downscaling methodology, in conjunction with the previously validated BLRP models, to generate sub-daily future rainfall.

- Calibration and validation of a constitutive model to simulate the soft clay foundations commonly found in the Thames estuary using the Dartford trial embankment as a case study (Marsland and Powell, 1977).
- Calibration and validation of an unsaturated constitutive model to realistically simulate the compacted embankment clay and soil-atmosphere interaction of existing embankments, using the Magnolia Road rail embankment as a case study (Geotechnical Observations, 2013).
- Development and validation of a numerical model for infrastructure embankments and development of methodology for their lifecycle assessment.

These components are then applied to a complete lifecycle analysis of embankments in the second part of this research, with the following objectives:

- Assessing the impact of future weather patterns on both infrastructure and flood embankment behaviour. Emphasis is placed on hydraulic, displacement and stability changes within the embankment.
- Assessing the resilience of both infrastructure and flood embankments to extreme storm events at key moments of their lifecycle.
- Investigating several flood embankment raising strategies to find the most optimal raising methodology.

1.3 Thesis outline

With the motivations and research objectives set out, the following chapters in this thesis explore each objective in detail, with Chapters 2 to 4 focusing on stochastic rainfall modelling using the R programming environment (R Core Team, 2019) and Chapters 5 to 8 on the geotechnical aspects of infrastructure embankments, using the finite element platform ICFEP (Potts and Zdravkovic, 1999).

Chapter 2 first introduces rainfall data from the weather station at Rayleigh, Essex, located in the vicinity of the Magnolia Road rail embankment that serves as a case study in the development of a numerical model for infrastructure embankments. The fundamentals of rainfall statistics to characterise a rainfall series are then presented. The summary statistics and extremes for the Rayleigh rainfall are calculated and assessed, before being used as fitting statistics for the Bartlett-Lewis Rectangular Pulse (BLRP; Rodriguez-Iturbe et al., 1987, 1988;

Kaczmarska et al., 2014) stochastic rainfall models. An investigation into the ability of the BLRP models in simulating statistically similar rainfall to the Rayleigh rainfall is performed, resulting in a validated methodology for calculating and selecting the appropriate summary statistics for the BLRP fitting subsequently in Chapter 4.

Chapter 3 investigates the Generalised Linear model (GLM; Chandler 2020) and its application in simulating future rainfall series using projected future climate. Calibration and validation exercises of the GLM are first presented, followed by the reanalysis of current climate data from ERA5 for implementation of the GLM in identifying the climate variables relevant to rainfall modelling at Rayleigh. Daily rainfall is then generated based upon current climate data and its properties are compared with existing rainfall series. Following from this calibration, the model is used to simulate future daily rainfall series based upon UK climate projection 2018 (UKCP18) data. The results of these simulations are analysed and compared with each other and present rainfall to study the impact of climate change on rainfall at Rayleigh. The daily rainfall simulations from this chapter are used as a precipitation boundary condition input for the embankment lifecycle analyses in Chapter 7 and Chapter 8.

Chapter 4 focuses on downscaling rainfall from daily to sub-hourly time scales using the fractal properties of rainfall statistics. The fractal properties of rain are first explored with a brief literature review. The downscaling methodology is then presented and validated using current Rayleigh rainfall, before being applied to projected daily future rainfall series to obtain a sub-daily future rainfall series affected by climate change. The results are analysed by plotting the evolution of monthly summary statistics and extremes for each decade into the future. An extreme storm event is then chosen based on the results, which is used in studying embankment resilience in Chapter 7.

Chapter 5 presents a literature review of past and present numerical approaches in modelling the coupled soil-atmosphere interactions for infrastructure embankment, in addition to current design guidelines on flood embankments. The chapter then provides an overview of the hydro-mechanical behaviour of unsaturated soils, followed by a review and calibration of the constitutive models and boundary conditions that are used in the numerical modelling of earth embankments in Chapters 7 and 8.

Chapter 6 investigates a trial flood embankment, constructed in the Thames estuary at a site in Dartford in 1970s (Marsland and Powell, 1977). This trial embankment is used as a case study to establish the geotechnical numerical model of typical saturated soft clay foundations that support flood embankments along river banks and coastlines. Particular emphasis is placed on reproducing the strength and stiffness of the soft clay that supports a simple granular embankment in this case. The displacements and pore pressures in the foundation soil have been monitored over a period of time, thus providing field measurements for the validation of the numerical model. A brief background on the embankment layout and location is presented first, followed by the calibration of an extended Cam Clay (MCC) material model, selected as appropriate for simulating the behaviour of soft clay. The numerical analysis of this case study, developed with ICFEP, is then presented and the results compared with field measurements. The developed modelling approach is used in Chapter 8 to represent soft clay foundations in the generic study of flood embankments.

Chapter 7 focuses on establishing the modelling procedure for an embankment body of earthfill infrastructure embankments. The case study of a rail embankment at Magnolia Road, Essex, UK, which was monitored from 2006-2011 (Geotechnical Observations, 2013), is utilised here for the validation of the developed numerical model. Particular emphasis is placed on the realistic modelling of the unsaturated nature of the embankment material and of the seasonal variation of atmospheric conditions (rainfall and evaporation) which affect the hydraulic balance in the embankment body, together with the effect of vegetation that may exist on embankment slopes (transpiration). A brief overview of the embankment history and layout are first presented, followed by the development of the numerical model for this case study with ICFEP. An unsaturated constitutive model for the embankment material was adopted (as calibrated in Chapter 5), together with advanced boundary conditions of precipitation and evapotranspiration to simulate the embankment–vegetation–atmosphere interaction throughout its lifecycle. The results of the analysis are then compared with field measurements taken at the site from 2006-2011 to validate the numerical model. The developed modelling approach for an embankment constructed from compacted clay is used in Chapter 8 for the generic study of earthfill flood embankments. The model is further extended to predict the behaviour of the case study embankment when subjected to a future rainfall series developed in Chapter 3, and storm events developed in Chapter 4.

Chapter 8 combines all the lessons and components learnt from each of the previous chapters to establish a numerical study of the lifecycle of a typical flood embankment in the Thames estuary. A layout of a typical embankment in an estuarine environment is first presented, incorporating the numerical model for the foundation soil validated in Chapter 6, and the numerical model of the embankment fill material validated in Chapter 7. The embankment is then subjected to historical and future rainfall (Chapter 3), in addition to tidal changes, to model the long-term seasonal behaviour of the embankment. In addition, the embankment is subjected to flood and storm events at various points in time of its lifecycle to assess its resilience to extreme events such as overtopping. Finally, a study on raising the embankment in lieu of these conditions is conducted to assess future-proofing options for defending against future flooding events.

Finally, conclusions from this thesis are presented in Chapter 9, with thoughts and recommendations for future research.

Chapter 2: Rainfall Statistics and Stochastic Modelling

2.1 Introduction

As the world is experiencing anthropogenic climate change, there is a clear need to reassess the resilience of existing infrastructure (cut slopes, earth dams, flood embankments) to these environmental changes. Part of the changes will be in the weather and rainfall patterns. In the UK it is projected that summers will experience longer droughts while heavier storms may fall during the winter (Murphy et al., 2018). It is therefore critical to be able to quantify such changes in the weather, in order to assess their likely impact on the lifecycle of both existing and new infrastructure. Consequently, an important step in assessing the infrastructure resilience is the ability to model and predict the future weather patterns.

This chapter discusses the fundamentals in rainfall and storm statistics and introduces stochastic rainfall modelling with emphasis on the Bartlett-Lewis Rectangular Pulse (BLRP) family of models. In the following, the theory behind this modelling methodology is briefly overviewed and then applied in the analyses of rainfall series from the weather station at the town of Rayleigh in Essex, UK, which is located in the vicinity of the rail embankment case study that is the subject of the geotechnical analysis in Chapter 7 of this thesis. Raingauges and rainfall radar monitoring around the town of Rayleigh are introduced and processed to identify and remove outliers, ensuring quality control of the rainfall series. The summary statistics and extreme event statistics of the series are then explored in more detail, characterising the rainfall at the site.

Following the characterisation of the Rayleigh rainfall, the chapter briefly describes the various stochastic rainfall models that were developed during this research. Special emphasis is placed on the Poisson cluster models.

The subsequent section focuses on the Bartlett-Lewis rectangular pulse (BLRP) family of models, starting first with a brief description of three BLRP models which were applied in the study and calibrated using the Rayleigh summary statistics. The results of calibration are discussed and an alternative methodology in calculating summary statistics is proposed and implemented.

The chapter concludes with the main summary points.

2.2 Rainfall series and statistics

2.2.1 Rainfall data series

Essex is the driest region of the UK on average, with average annual rainfall of 520mm compared to the UK annual average of 1200mm (Met Office). Heavy rainfall in Essex usually arrives in two forms: via winter storms blowing in from the North Sea, or via convective storms during the summer months.

The tipping bucket raingauge (TBR) deployed by the Environment Agency is situated approximately 2 km east from the town of Rayleigh, and 3 km west from London Southend Airport. The available rainfall series starts on 25/1/2002 and a cutoff was set on 12/7/2017 (at the time of analysis), with portions of missing data in between, mostly caused by poor maintenance due to its rural location. The tip resolution is 0.2mm and tip times were recorded to the nearest second. By applying a composite cubic spline interpolation and smoothing on the recorded rainfall series, as outlined in Buytaert et al. (2019), aggregated rainfall intensities at coarser time intervals, particularly the 5- and 15-minute resolutions, are obtained.

In addition to the TBR, the Environment Agency monitors and collects rainfall telemetry (radar) data of 15-minute rainfall and these are available at the same site for the period 3/7/2000 to 12/7/2017. The radar rainfall data is more complete, with fewer missing data in between as compared to the tipping bucket series. However, radar rainfall data is known to have significant limitations in terms of accuracy and resolution, and thus would require validation before use (Einfalt et al., 2004).

A cumulative plot is presented in Figure 2.1, containing both the telemetry series and the 15-minute aggregated tipping bucket series to validate the telemetry data at the site. After taking missing data from both series into account (shaded time range) by only comparing time ranges when both series are available, the figure shows good agreement between both 15-minute series, thus validating the telemetry rainfall series at Rayleigh.

Furthermore, in order to ensure that the telemetry series data quality is good, a daily double mass plot (Figure 2.2) was also produced, using additional daily rainfall data near the site (Rayleigh S WKS, Hullbridge S Wks) for the same period (2000 to 2017) from the British Atmospheric Data Centre (BADC) database. A double mass plot compares the cumulative rainfall values at one measuring station against those from a reference station, the latter being the mean from several neighbouring stations. By a sudden change in the gradient of the curve, such a plot is able to detect any sudden changes in rainfall pattern between the sites (i.e. if there is a large rainfall on one site, but none in the other sites, as discussed in Searcy and Hardison, 1950). Any deviations are then subjected to further investigation to check for the occurrence of localised storm events and deviations that cannot be verified are then removed from the series. The resulting double mass curve plotted in Figure 2.2, shows two instances of the gradient change in the aggregated telemetry data, which were verified to be the heavy storms on 25th August 2013 (BBC, 2013) and on 20th July 2014 (BBC, 2014). No other significant changes to gradient of the aggregated telemetry curve were identified.

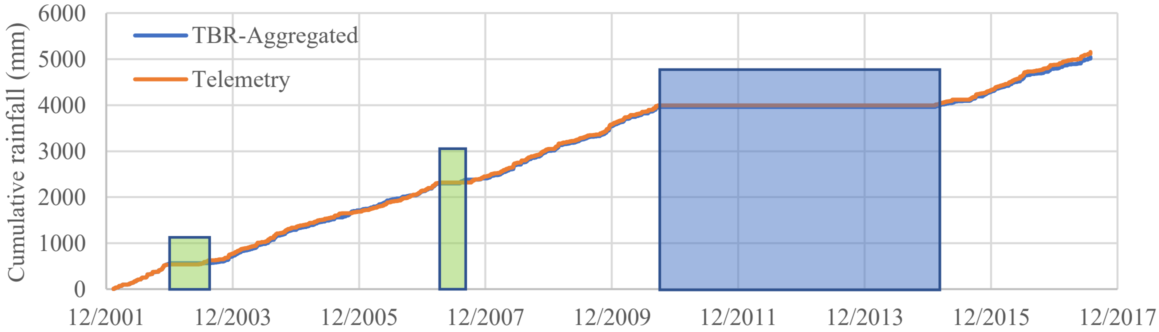

Figure 2.1: Comparison of cumulative rainfall between the TBR 15-minute aggregated series vs telemetry rainfall at Rayleigh. Green highlighted periods indicate missing data for the telemetry series, while blue highlighted periods represent missing data for TBR record.

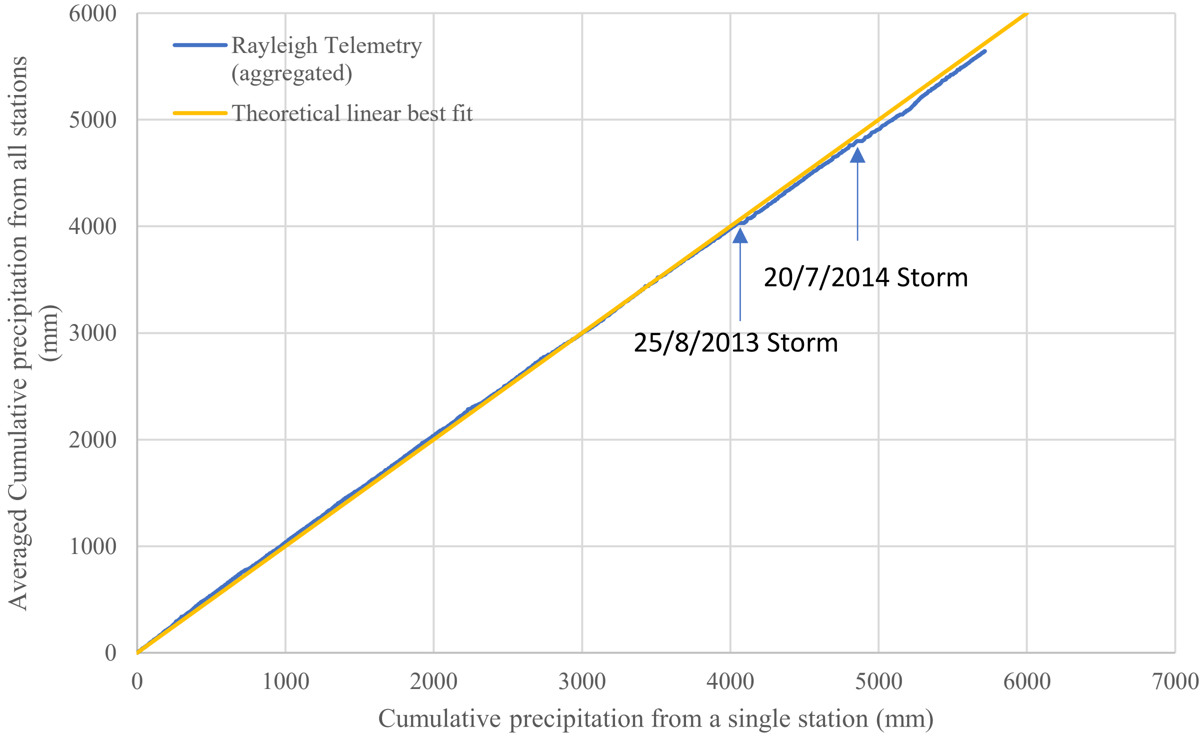

Figure 2.2: Double mass plot of daily rainfall at Rayleigh after quality control.

2.2.2 General rainfall summary statistics

A standard approach in analysing rainfall series is to calculate the monthly summary statistics of the series. The summary statistics for an observed rainfall series consist of the arithmetic mean, unbiased standard deviation, skewness, and auto-correlation. In addition to these univariate properties, the percentage number of wet days for each month is also calculated. As the Rayleigh telemetry rainfall series has a temporal resolution of 15 minutes, the summary statistics for 15 minutes, 1 hour, 6 hours and daily (24 hours) aggregations are calculated for each month so as to provide a more detailed overview of average yearly rainfall behaviour.

The summary statistics for each month of each year is first calculated, before the average of the statistics for a calendar month for all the years is taken. For example, for the Rayleigh rainfall series, the 15-minute summary statistic for each month from July 2000 to July 2017 was first calculated. Then, in order to get the summary statistic for the month of January, the summary statistics for each January from 2001 to 2017 was averaged. Due to the presence of missing data, the averaging process was weighted with percentage of data availability to ensure that months with higher percentage of missing data will have less influence on the final averaged summary statistics.

The summary statistics for each month for the Rayleigh rainfall series can be found in Appendix A1. These were determined using the standard approach, explained below, to calculate the mean, coefficient of variation, skewness, auto-correlation and percentage wet.

Means

The mean rainfall of a month for a given year is defined as:

$$\bar{x}_j = w_j \cdot \frac{\sum_{i=1}^{n_j} x_{i,j}}{n_j} \tag{2.1}$$

where $x_{i,j}$ is the rainfall within the month of j-th year, n_j the number of available data in that month excluding missing data, w_j the missing data weight for that month. The mean monthly rainfall for 1 hour, averaged over all years from 2000 to 2017 at Rayleigh is plotted in Figure 2.3. The mean monthly rainfall of a dataset is the averaged mean monthly rainfall of all years in that dataset.

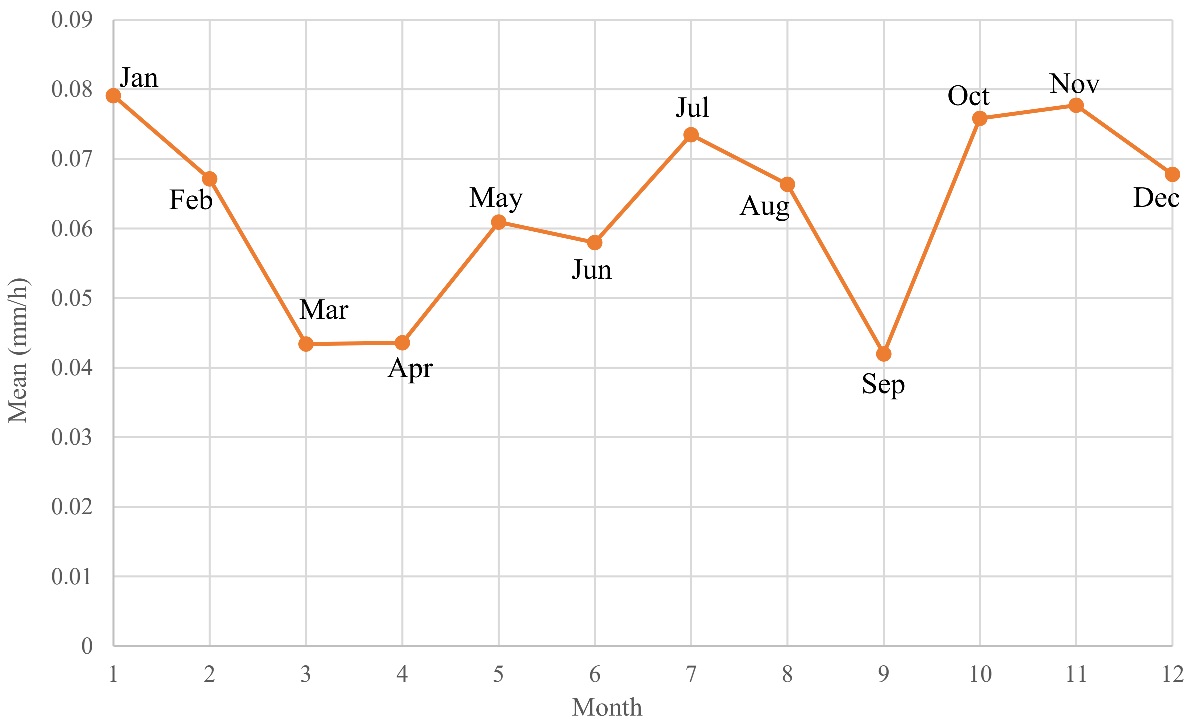

Figure 2.3: Averaged 1h mean rainfall for each month at Rayleigh (Month 1 – January).

As it can be seen in Figure 2.3, most of the annual rainfall occurred during the winter months from October to February, accounting for 68% of the total annual rainfall at the site. However, it should be noted that the months of July and August show an unusually high average rainfall compared to the other summer months of April and September. This was due to the abnormally high rainfall experienced during 2013 and 2014, predominantly caused by high intensity convective rainfall events, which even resulted in local flooding (BBC, 2013; Met Office, 2013). The means for the other time resolutions are not plotted, as mean is a scaling property of rainfall, such that its behaviour at other time resolutions ranging between a few minutes to a few years is scalable with a scaling exponent $D \approx 0.5$ (Hubert et al., 1993). This fractal properties of mean and other summary statistics were explored further in Chapter 4 in downscaling rainfall.

Coefficient of variation

The monthly coefficient of variation of rainfall is defined as the unbiased standard deviation divided by the mean:

$$CV_j = \frac{\sum_i^{n_j}(x_{i,j} - \overline{x_j})^2}{\overline{x_j} \cdot (n_j - 1)} \tag{2.2}$$

where CV_j is the coefficient of variation for a month of j-th year, and $\overline{x_j}$ the mean rainfall for that month of j-th year. Due to the significant differences in mean rainfall across the months from seasonal changes, the coefficient of variation is a more indicative variable when comparing the standard deviation across the months, instead of solely using the standard deviation or variance of the month. Figure 2.4 plots the monthly coefficient of variation for Rayleigh, averaged over all years, applying different temporal resolution: CV0.25 (15 minutes), CV1 (1 hour), CV6 (6 hours) and CV24 (1 day).

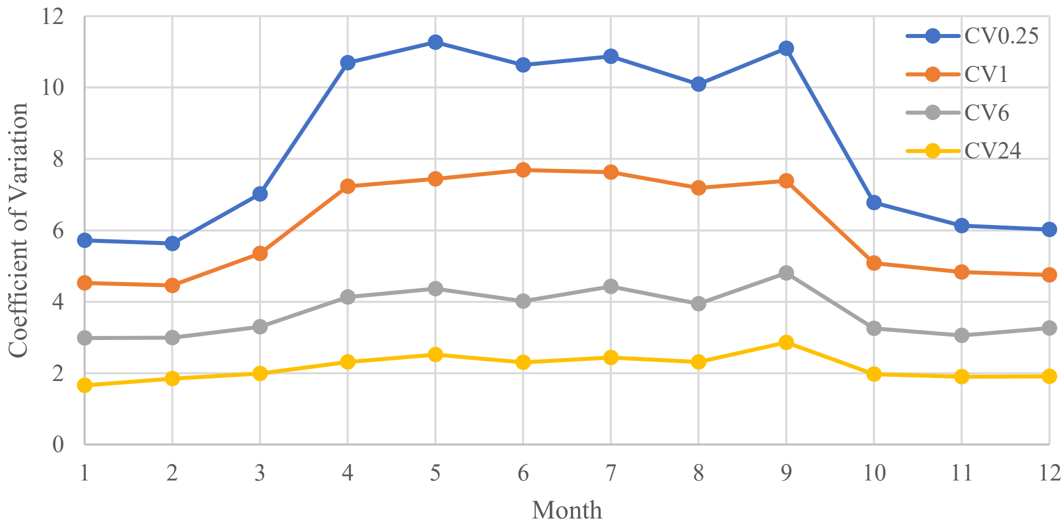

Figure 2.4: Averaged coefficient of variation at different time resolutions for each month at Rayleigh (month 1 – January).

Due to the nature of rainfall in Essex, as discussed in Section 2.2.1, it is anticipated that the CV would be high during the summer months, as a result of the short and intense convective storms generated from the high evapotranspiration throughout the day. Conversely, the CV would be lower during winter as winter storm systems often persist over a longer period of time, with more uniform rainfall intensities. This behaviour is evident in Figure 2.4, with the months from April to September showing a higher CV as compared to the rest of the year. As rainfall is aggregated up to daily values, the rainfall variance reduces as the distinction between short intense 1-hour rainfall and a consistent low intensity rain throughout days becomes negligible with higher temporal resolutions (6 hours and above). Figure 2.4 suggests that using an hourly temporal resolution would be sufficient to highlight these differences in rain intensity between the summer and winter months.

Skewness

The skewness of rainfall is the third standardised moment of rain, defined as:

$$\widetilde{\mu_j} = \frac{\sum_i^{n_j}\left(x_{i,j} - \overline{x_j}\right)^3}{\sigma_j^3 \cdot (n_j - 1)} \tag{2.3}$$

where σ_j is the standard deviation of the month in j-th year. As it is usually more frequent for no rain to occur in a given unit time, rainfall is always positively skewed, as shown in Figure 2.5 for the same temporal resolutions. This behaviour is further exaggerated during the summer when rainfall is infrequent, short and intense, resulting in a higher skewness compared to less intense but much more prolonged rainfall during winter storms. As rainfall is aggregated up to daily values, the skewness, similar to the variance, reduces with higher temporal resolution.

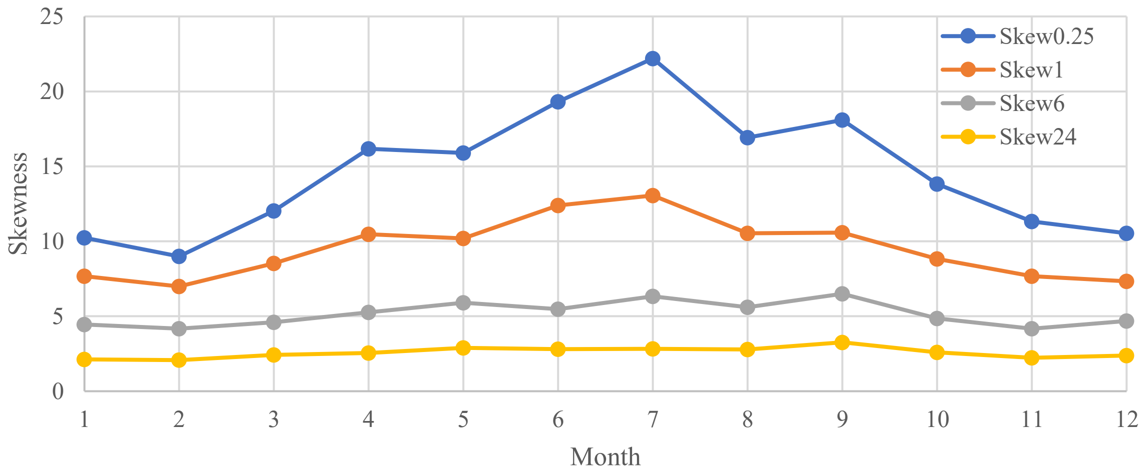

Figure 2.5: Averaged skewness at different time resolutions for each month at Rayleigh (Month 1 – January).

Lag-1 Autocorrelation

The autocorrelation is the degree of correlation of a signal to a delayed copy of the same signal, defined as:

$$R_j(\tau) = \frac{\sum_{i=1}^{n_j-\tau}\left[x_{i+\tau,j} - \overline{x_j}\right]\left[x_{i,j} - \overline{x_j}\right]}{n_j \cdot \sigma_j^2} \tag{2.4}$$

where τ is the time lag. A lag-1 autocorrelation explores the correlation of a rainfall series with itself but shifted (lagged) by 1 time unit, similar to the likelihood of rainfall occurring in the next time unit given that there is rainfall in the current time unit. An autocorrelation of 1 indicates perfect correlation, while a value of -1 indicates perfect anti-correlation; a value close to 0 indicates no correlation is present. Autocorrelation in rainfall for various temporal resolutions and in various weather systems is well documented by Kotz and Neumann (1959) and Rodriguez-Iturbe et al. (1984). In most cases it is expected that rainfall would have good correlation in the fine time scales as there will be continuous rainfall throughout the storm duration, resulting in good lag-1 autocorrelation for time scales shorter than the storm duration. For very short and intense rainfall such as convective rainfall in an arid environment, the lag-1 autocorrelation degradation occurs much quicker in the scale of 5 to 10 minutes (Marra and Morin, 2018), while the lag-1 autocorrelation of winter storms in the UK would degrade over a scale of 30 minutes to hours (Wheater et al., 2000a).

As the Rayleigh rainfall series has 15 minutes as the finest time resolution, with aggregations of hourly, 6 hourly and daily time scales, the lag-1 autocorrelation at these time scales would be able to broadly indicate the general storm durations for each month, as plotted in Figure 2.6. Figure 2.6 shows that the lag-1 autocorrelations indicate good correlations of around 0.5 and 0.4 at 15 minutes (Ac0.25) and 1 hour (Ac1) respectively for most of the year except during the summer in July. Conversely, the Rayleigh rainfall series has poor correlations in the 6 hourly (0.2 for Ac6) and daily time scales (0.1 to 0 for Ac24). In addition, the month of July has poorer correlations for Ac0.25 and Ac1 as compared to the rest of the months, which is suggestive of very short (durations of 1h and less) rainfall during that month.

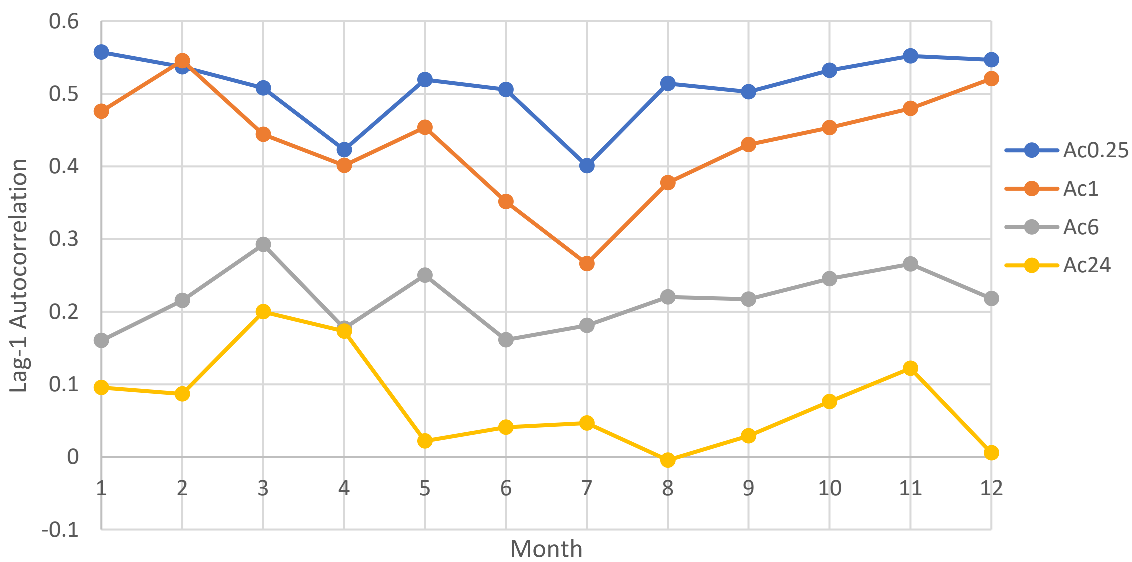

Figure 2.6: Averaged lag-1 autocorrelation at different time resolutions for each month at Rayleigh.

Percentage wet

Another rainfall property commonly calculated in summary rainfall statistics is the percentage of wet times for each month in a rainfall series. It is defined as a percentage of total time in which rain occurred to the total time measured. The average monthly percentage wet for the Rayleigh rainfall series is plotted in Figure 2.7.

The results show a general trend of fewer rainy days and periods during the summer months, while rainfall is more frequent during the winter. With the combination of observations made with the skewness, rainfall at Rayleigh can be described as short and intense during the summer, while winter rains are usually longer and less intense.

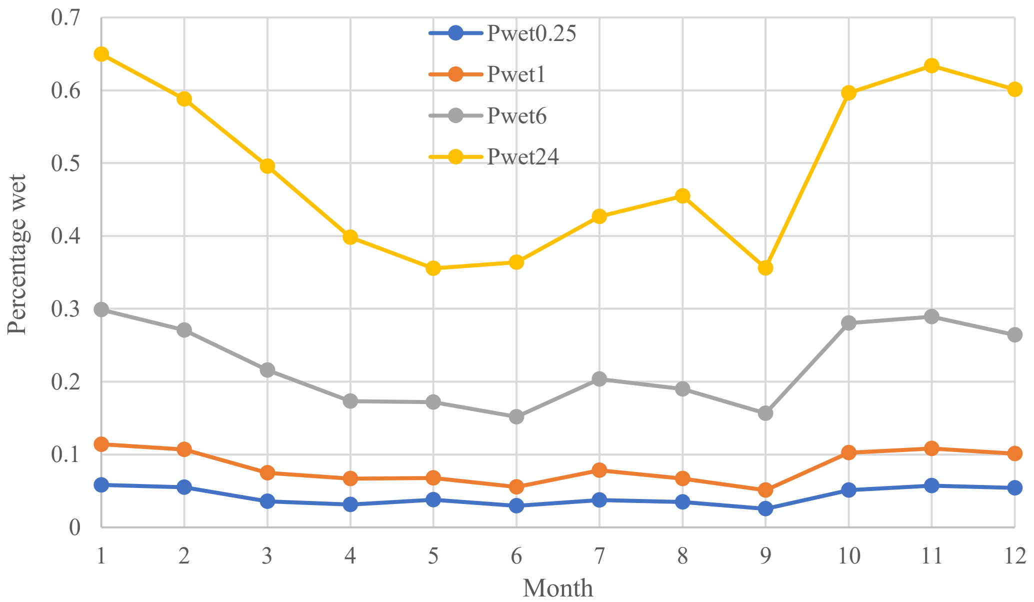

Figure 2.7: Averaged percentage wet at different time resolutions for each month at Rayleigh.

2.2.3 Extreme rainfall statistics and modelling

Summary statistics are useful properties in characterising the general behaviour of the rainfall series. However, they are unable to characterise extreme events of the rainfall series, which is one of the key characteristics for the engineering design of geotechnical infrastructure. Therefore, there is a need for statistical estimation of extreme rainfall in order to adequately design infrastructure to withstand an extreme storm event of a particular return period.

As only the extremes are of importance, a sieving process must first be applied to extract extreme events from a general rainfall series, before further statistical analysis and distribution fitting on those extreme events is performed.

Identification of extreme rainfall

There are two main approaches in identifying extreme rainfall values in a given series: the block maxima method, and the Peak-over-Threshold (POT) approach.

a) *Block maxima method*

The block maxima method first divides a rainfall series into identical temporal blocks (e.g., monthly, annually), before identifying the maximum rainfall event for each block. In order to limit the effects of annual seasonal cycles of rainfall, annual blocks are typically adopted, hence the method is also commonly known as the Annual Maxima (AM) method.

This method is sensitive to the available rainfall series length. The longer the available rainfall series, the more representative of their return periods the identified annual peaks are. It is therefore generally difficult to estimate 50 and 100 year return period events from a short rainfall record of 10 years. Sensitivity studies done by Emmanouil et al. (2020) indicate that the AM method would result in higher biases compared with other methods, including POT, for rainfall records shorter than 10 years. This can be particularly problematic for hourly and sub-hourly rainfall series worldwide due to a scarcity in long and complete records of sub-daily rainfall, as highlighted in the Global Sub-Daily Rainfall project by Lewis et al. (2019). Despite this shortcoming, due to the simplicity and efficiency of the method, AM is still widely adopted globally, as it is significantly easier to implement and obtain design storm rainfall and Intensity-Duration-Frequency (IDF) curves for any given return periods, without needing to perform additional sensitivity checks, as compared to the POT method (Fowler & Kilsby, 2003; Katz et al., 2002; Jaruskova & Hanek, 2006).

b) *Peak-over-Threshold method*

The POT method requires setting of a sufficiently high threshold, u, such that any peaks which occur above that threshold would be considered as an extreme event. The choice of threshold is highly subjective, with multiple valid approaches published in the literature. Langousis et al. (2016) performed a detailed study on the subject of threshold selection and found that the use of graphical methods in assessing the dependence of the Generalised Pareto metrics on threshold level, proposed by Davison & Smith (1990), is an effective method in identifying suitable thresholds. Another suitable method uses a Goodness of Fit test to quantify the deviation between measured data and the fitted distributions for a given threshold (Dupuis, 1999). It should be noted, however, that the graphical method would require visual inspection, making it impractical when a large number of rainfall series are being analysed. In addition, the Goodness of Fit approach would require an iterative procedure to arrive at a suitable threshold, thereby the procedure is limited only by computational speed.

A major benefit of using the POT method is that it does not discard a large proportion of the data as compared to the AM method. Thus the POT method is generally more accurate, compared to the AM method, when the data series is short. Studies by Emmanouil et al. (2020) indicate that for rainfall series of 10 years or less, the POT method would generally yield a less biased result compared to the AM method, for return periods of up to 50 years.

Another variable of importance in the POT method is the minimum distance between peaks. A key assumption in the POT method is that all peaks above the threshold must be representative of an independent event in the series. A good indicator to use in determining a suitable minimum distance in a given series would be to assess the Lag-1 autocorrelation of the series at various timescales. Using the Rayleigh rainfall as an example, the lag-1 autocorrelation plotted in Figure 2.6 indicates that the autocorrelation has decayed sufficiently to near zero at 24 hours to indicate no correlation, hence storms in the Rayleigh series generally would not last for more than a day. Therefore a good minimum distance to adopt for this case would be 2 days between peaks.

Extreme rainfall distribution fitting

Both AM and POT methods will yield different extreme value samples and these must be analysed with different statistical approaches, namely the extreme value (EV) theory, and the extreme excess (EE) theory respectively:

a) *Extreme value (EV) theory*

First described by Fisher and Tippett (1928) and applied to meteorological study by Jenkinson (1955), EV theory states that the cumulative distribution function (CDF) of the maximums of *n* independent copies of a random variable X should converge to the generalised extreme value (GEV) form as given in Equation (2.5):

$$F(x;\ \mu,\sigma,\gamma) = \exp\left[-\left[1+\frac{\gamma(x-\mu)}{\sigma}\right]^{-\frac{1}{\gamma}}\right] \tag{2.5}$$

where μ is the location parameter, $\sigma > 0$ is the scale parameter, and γ the shape parameter. The shape parameter governs the tail or extreme end behaviour of the distribution; if $\gamma > 0$, then the GEV is said to be heavy tailed and is known as the Frechet distribution, while if $\gamma < 0$, then the upper tail is bounded, indicating a Weibull distribution (Gumbel, 1958). Many analyses have been performed indicating that the upper tail should be unbounded when modelling extreme hydrological variables such as rainfall, and that by taking the special case of $\gamma \to 0$ (Gumbel distribution) is sufficient to derive a good fit to the extremes (Smith, 2001; Katz et al., 2002). The Gumbel CDF is given as:

$$F(x;\ \mu,\sigma) = \exp\left[-\exp\left[-\frac{x-\mu}{\sigma}\right]\right] \tag{2.6}$$

where two approaches are used in fitting these GEV distributions to the annual maxima values: the L-moments fit, or the maximum likelihood fitting. While the L-moments fit is the most common fitting approach used due to its simplicity and good performance for small samples (Hosking, 1990), it is unable to incorporate covariates. The maximum likelihood method is able to incorporate covariates, however it would require an iterative procedure to arrive at the parameter estimates.

Gumbel plots are typically used in presenting the behaviour of the extreme values, and how well the distributions fit the extremes. By transforming the horizontal axis to the Gumbel reduce variate of $-\ln\left(-\ln\left(1-\frac{1}{T}\right)\right)$, where T is the return period in years, the Gumbel distribution will present as a linear plot, with the Frechet distribution increasing exponentially unbounded and the Weibull distribution tending towards a bound.

b) Extreme excess (EE) theory

While EV theory deals with the distribution of selecting the maximums from n independent blocks, extreme excess theory suggests that the CDF of excesses of a random variable *X* above threshold u would converge to the generalized Pareto (GP) form expressed in Equation (2.7) (Leadbetter et al., 1983):

$$F(y) = P[X - u \leq y | X > u] = 1 - \left(1 + \xi \frac{y}{a_u}\right)^{-1/\xi} \quad (2.7)$$

where ξ is the shape parameter, a_u the scale parameter, and $Y = X - u$ is the excesses of random variable X. If $\xi = 0$, Equation (2.7) will reduce to the exponential form of $F(y) = 1 - exp(-y/a_u)$. If $\xi > 0$, then it would indicate that the distribution is heavy tailed, similar to the Frechet distribution in GEV, whereas if $\xi < 0$, the distribution will have a finite upper bound, similar to the Weibull distribution.

Extreme value analysis and modelling of Rayleigh rainfall

Due to the simplicity in the annual maxima approach and fitting of the GEV distributions, it was decided for the Rayleigh rainfall that all extreme value analyses will be conducted using the AM/GEV approach. While research has demonstrated that the POT method and subsequent GP distribution fitting if properly implemented are overall more robust as compared to AM and GEV fitting due to it using a larger proportion of the dataset (Vicente-Serrano & Begueria-Portugues, 2003; Caires, 2009)), the former approach is not practical when applied to a large number of rainfall series, as determining the threshold for each fit is not trivial (Langousis et al., 2016).

Figure 2.8 shows the 15-minute AM extremes determined at Rayleigh, plotted on a Gumbel plot and fitted to a Gumbel and Frechet distributions. The Gringorten plotting position rule (Gringorten, 1963) was used in plotting the annual maximums onto the Gumbel plot. From the graph it is clear that the Frechet distribution (unbounded) fits the data better than the Gumbel distribution, suggesting that the data is tail heavy for having larger storms for a given return period.

The fitted Frechet distribution forms the basic extreme value analysis for this site by giving the expected 15-minute storm rainfall for any return period. However, the main weakness of this basic extreme value distribution fitting is that it only provides information on the peak of the storm at given time resolutions. It does not provide any information on the antecedent conditions before the storms, nor on the duration or profile of the storm. These important storm properties can be obtained from a stochastic model instead, which is explored subsequently.

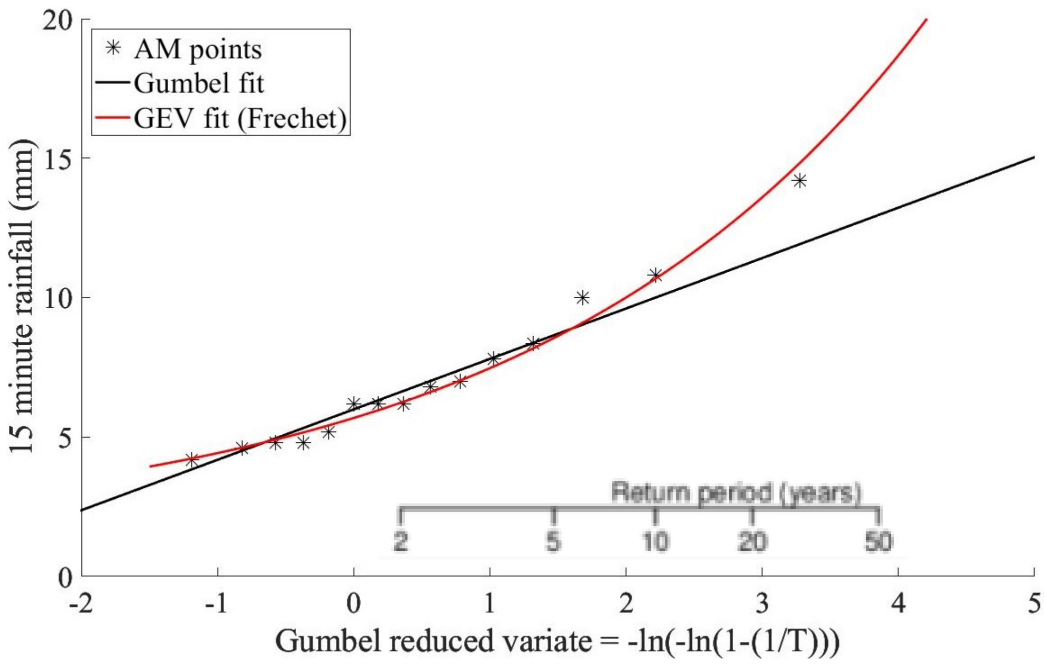

Figure 2.8: Gumbel plot of annual maximums at Rayleigh, fitted to a Gumbel and Frechet distribution.

2.3 Rainfall modelling and stochastic rainfall models

As mentioned in Section 2.2.3, an extreme value distribution is only able to provide information on expected maximum storm rainfall for a given return period, or in other words a design storm. No further information is provided, particularly on the storm antecedent conditions, and historic cycles of prolonged rainfall or droughts, which can significantly affect the structural stability of flood embankments. In addition, many existing rainfall series are often either incomplete or too coarse temporally, thus making it difficult to use the series as it is. These problems can be solved by the use of a rainfall model to simulate a synthetic rainfall series that shares similar statistical properties to the actual series at the site.

Rainfall modelling and simulation may be categorised into two general approaches: physical-based models which consist of partial differential equations of meteorological physics, and stochastic-based models which establish statistical relationships to weather variables.

Physical-based models are typically used in weather forecasting algorithms, which calculate the evolution of weather for a given set of initial conditions and specified boundary conditions. Two common examples of these models would be the numerical weather predictors (NWPs) and global circulation models (GCMs). NWPs, such as the UK Met Office Global and Regional

Ensemble Prediction System (Bowler et al., 2008), typically consist of a three-dimensional grid of the globe and, using real-time meteorological inputs, are able to produce weather forecasts, typically from 5 to 14 days into the future. Nested higher resolution regional models are then used to further decrease the temporal resolution and to predict convective rainfall (Hagelin et al., 2017).

GCMs on the other hand, while structurally similar to NWPs, are used in calculating the evolution of climate variables into the far future, typically tens to hundreds of years. Consequently, their grid and temporal resolutions are typically coarser than NWPs to reduce the computational demand in solving the equations. To obtain regional climate projections, finer resolution nested Regional Circulation Models (RCMs) are used. As their grid resolutions are typically in the range of 12km x 12km, they are still too coarse to model convective rainfall. However, recent developments in 2.2km grid RCMs by the UK Met Office and University of Newcastle have enabled the modelling of convection in RCMs, resulting in clearer forecasts of the impacts of climate change on rainfall (Kendon et al., 2014; Kendon et al., 2017).

While physical-based models are very powerful tools for weather predicting, they were not the main focus of this research as such models are extremely computationally expensive to run. Therefore, stochastic rainfall models were adopted as they are significantly simpler to set up, calibrate and simulate. It should be noted here that stochastic models are not weather forecasting algorithms, instead they are used to generate multiple possible weather time-series based upon the established statistical relationships.

Cox and Isham (1994) divide the stochastic rainfall models into two approaches, namely the empirical statistical modelling and intermediate stochastic modelling. Onof et al. (2000) instead suggest three categories: statistical modelling, multiscaling stochastic modelling and stochastic models with simple physical process representation.

2.3.1 Statistical rainfall models

Purely statistical models as discussed in Onof et al. (2000), similar to the empirical statistical modelling in Cox and Isham (1994), consist of fitting statistical distributions to rainfall, in particular to the occurrence of rainfall, and to amount of rainfall given the event of an occurrence of rainfall. Contrary to the stochastic models, a purely statistical model only models the statistical behaviour of rainfall, it does not attempt to represent the physical processes that govern rainfall generation. Moreover, purely statistical models are typically not scalable, meaning that a given statistical model is only effective at modelling rainfall at a particular time scale, typically daily and coarser (Srikanthan and McMahon, 2001).

A commonly employed statistical model used for most time scales would be Markov chains (Gabriel and Neumann, 1962; Feyerherm and Bark, 1967; Haan et al., 1976), where the occurrence is modelled using a Markov model with state transition probabilities between wet and dry states. This was expanded by Thyer and Kuczera (2000) to simulate annual precipitation time-series based on large scale global climatic mechanisms, and also implemented in the daily time scales as reviewed in Srikanthan and McMahon (2001).

Another popular method for generating rainfall via purely statistical means is with the use of Generalised Linear Models (GLM), first introduced by Nelder and Wedderburn (1972) and subsequently applied to rainfall by Coe and Stern (1982). GLMs are an extension of linear regression theory, where an exponential family of distributions are applied to the observations instead of being limited to only Gaussian linear regression. This approach is suitable for rainfall data as rain characteristics are often well represented with exponential family distributions such as the Gamma distribution. A more in depth discussion on GLMs can be found in Chapter 3.

2.3.2 Multiscaling stochastic models

As briefly mentioned in Section 2.2.2, the mean rainfall has a simple scaling property, where the mean scales with respect to time resolution via a power law, with the scaling exponent $D \approx 0.5$ (Hubert et al., 1993). A similar monoscaling behaviour is also observed for percentage wet. This scaling regime is valid for durations between a few minutes to a few years, thus providing a powerful relationship across a large time scale.

However, other summary statistics, such as coefficient of variation and skewness, does not exhibit such monoscaling behaviour, as the shape of the curves does not scale as the time scale changes. This leads to the development of multifractility and multiscaling, in which the scaling is specified by a function instead of a constant exponent, such that the dimension is now a nonlinear and decreasing function of the time scale (Schertzer and Lovejoy, 1987).

Multiscaling stochastic models are typically used in downscaling models, where temporally coarse rainfall is disaggregated into finer time scales. A popular downscaling model called the cascade process, proposed by Schertzer and Lovejoy (1987) utilises the fractal nature of rainfall to downscale rainfall by first dividing a given rainfall volume over two equally sized sub-intervals of half the original time interval. The process is repeated until the desired time resolution is achieved. At each cascade level, the rainfall division is governed by common probability distribution function.

Generally, multiscaling stochastic models are paired with other stochastic-based models to allow the downscaling of any simulated rainfall. Such was the case in Wheater et al. (2005), Segond et al. (2006) and Onof and Arnbjerg-Nielsen (2009), in which a multiscaling model was used to downscale rainfall either post simulation or before, to obtain the necessary parameters for the subsequent stochastic model fitting. This was explored further in Chapter 4, in which the multiscaling behaviour of various summary statistics was used to downscale projected future rainfall.

2.3.3 Stochastic rainfall models

The final class of stochastic-based rainfall models are those that attempt to represent a simple physical process of rainfall. The most common approach in modelling rainfall is to assume independence among arrivals of rain. This eventually leads to using a Poisson distribution to model rain arrivals over a given period of time.

Kavvas and Delleur (1975, 1981) further hypothesised that rainfall occurrences are clustered within storms and formalised the Neyman-Scott cluster model. However, these early Poisson-cluster models only simulated rainfall occurrence and not the amounts. This led to the developments of stochastic rectangular pulse models by Rodriguez-Iturbe et al. (1987), where each rectangular pulse of rainfall has a random depth for intensity and length for duration. The occurrence of each pulse is governed by a Poisson process of arrival.

A more flexible Poisson-process model is the Bartlett-Lewis or Neyman-Scott rectangular pulse models (Rodriguez-Iturbe et al., 1987), in which the pulses of rainfall are clustered within storms that are governed by a Poisson arrival process. Compared to the earlier rectangular pulse model, the clustered model is able to simulate the intermittency of rainfall over longer durations of time, thus lending itself to be more representative to the physical process of storm events and rainfall within the storms.

The Bartlett-Lewis rectangular pulse (BLRP) family of models has been the subject of much research and improvements over 30 years since its development. Koutsoyiannis and Onof

(2001) used the BLRP model as a disaggregation tool from daily to hourly rainfall by performing adjustment procedures of rainfall totals. More recently, Cross (2019) used the BLRP model to model and project future rainfall influenced by climate change by conditioning the model parameters to the mean monthly near surface air temperature.

Due to the flexibility of the BLRP family of models, this research first utilised these models to simulate rainfall at Rayleigh, for the purpose of assessing its effectiveness in reproducing the summary statistics and extremes experienced at the site. The calibrated BLRP model was then used as part of the downscaling exercise, to downscale projected future daily rainfall influenced by climate change.

2.4 Bartlett-Lewis rectangular pulse (BLRP) model

2.4.1 Types of BLRP models

While there are many varieties of the model, only three models have been explored in detail during this research, namely the classical BLRP model, the random parameter BLRP model, and the randomized μ_x random parameter BLRP model. All models were initially implemented in the R programming environment (R Core Team, 2019) by Kaczmarska (2013) and Cross (2019). The code was further developed by the author during the current research to support the analysis of incomplete rainfall series and to allow the option of changing the summary statistics calculation methodology.

Classical BLRP model

The original BLRP model, as described by Rodriguez-Iturbe et al. (1987), requires only 5 parameters to fully describe the rainfall process. This model is illustrated in Figure 2.9.

The start time of a storm, T_s, is governed by a Poisson process characterised by the parameter λ. For each storm that is generated, the termination point of the storm at time T_{ct} is a random variable, exhibiting an exponential distribution of parameter γ. Rectangular cells of rainfall intensity can only occur within storms, and the cell arrival time T_c is again controlled by another Poisson process with β as its mean. Both the length, L, and height, X, of each cell are then controlled by exponential distributions with respective means of η and $\frac{1}{\mu_x}$. In total, the 5 variables that are to be fitted are λ, γ, β, η, and μ_x.

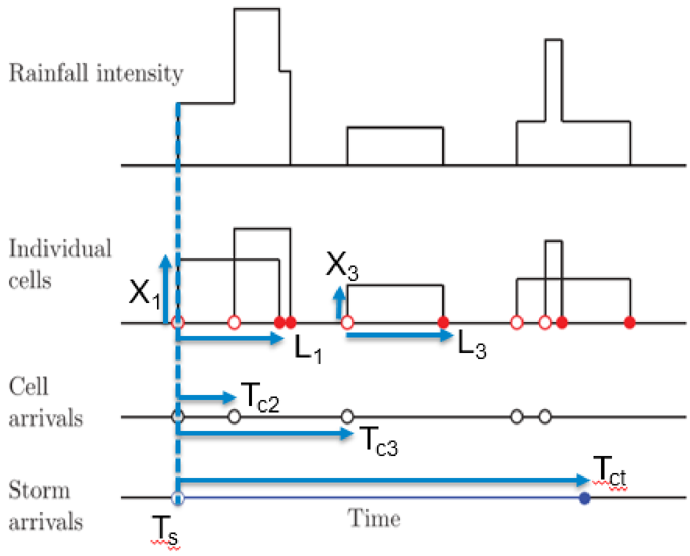

Figure 2.9: Illustration of a single storm with the Bartlett-Lewis rectangular pulse model. Open circles indicate arrival of storm and cells, while solid circles indicate end of cells and storm. Adapted from Kaczmarska et al. (2014).

Random parameter BLRP model (BLRPR)

One of the weaknesses of the original BLRP model is that it does not take into consideration relationships between certain cell or storm properties as it assumes that the random variables are independent from one another. In other words, the cell lengths and depths are not coupled with each other, resulting in unrealistic situations where the model may simulate a long and deep cell. This is highly unlikely to occur in reality as a long cell would be shallow, or a shorter cell would be deeper. Moreover, there is very little variation in cell characteristics between storms. This is contrary to reality, where one can expect convective storm behaviour during the summer, while winter storms are generated by larger scale weather systems, giving it its own profile and behaviour.

These weaknesses were recognised by Rodriguez Iturbe et al. (1988), who proposed to randomize the cell duration parameter η and relate it to other storm characteristics. Instead of adopting a constant η for all storms, η is now varied randomly between storms. By assuming that η values for different storms are independent, η is now gamma-distributed with index α and rate parameter ν.

In addition to the changes to η, the cell arrival rate, β, and storm termination rate, γ, are now reparameterised to $\kappa = \frac{\beta}{\eta}$ and $\phi = \frac{\gamma}{\eta}$ respectively. Instead of keeping the cell arrival rate and storm termination rate constant, it is now the ratio of these parameters to the cell duration parameter that is kept constant. Therefore, when η is high (when cells in a given storm are shorter in duration), the cells would arrive sooner within the storm. As a consequence, the storm is terminated sooner, resulting in a shorter but more intense overall storm event.

As a result of the reparameterisation of the storm properties, it was reported that there was an improvement to the fits for proportion dry (Rodriguez Iturbe et al., 1988; Wheater et al., 2005). However, Kaczmarska et al. (2014) showed that while proportion dry fits were improved with the BLRPR model, the improvement come at the expense of fits to the skewness, in particular overestimating the skewness during the summer at 6- and 24-hour time resolutions.

Randomised μ_x random parameter BLRP model (BLRPRx)

Following from studies on the BLRPR and the Bartlett-Lewis Instantaneous Pulse models, Kaczmarska (2013) found that linking cell duration to intensity would resolve the poor skewness fitting that the BLRPR model suffered from. The new model, called the randomised μ_x random parameter BLRP model, reparameterises the BLRPR model by introducing the ratio $\iota = \mu_x/\eta$, where ι is now kept constant.

In addition, the expressions for $E(X^2)$ and $E(X^3)$ are now expressed in terms of ι. The expressions related to different BLRP models are given in Appendix B.

2.4.2 BLRP model fitting and validation

Three different BLRP models (BLRP, BLRPR, and BLRPRx) were fitted using rainfall summary statistics at the Rayleigh site, derived in Section 2.2.2. As only at most 6 different parameters would require fitting, only 13 summary statistics (1h mean, 0.25/1/6/24 coefficient of variation, 0.25/1/6/24h skewness, and 0.25/1/6/24h lag-1 autocorrelation) were eventually used for the fitting process, as recommended by Cowpertwait et al. (2007). The percentage wet statistic was omitted and used instead in the subsequent validation exercise.

The generalised method of moments is employed for the fitting of the parameters to the summary statistics. The following objective function is set up:

$$S(\theta|T) = \sum_{i=1}^{k} w_i[T_i(y) - \tau_i(\theta)]^2 \tag{2.8}$$

where S is the objective function, T_i is the observed value for each property i, w_i is the weight for each property i, θ is the unknown parameter vector, and $\tau_i(\theta)$ is the vector of expected values for each property under the model. The objective function is then minimized to obtain optimal values for the model parameter θ. The weighting vector w_i is used to establish a hierarchy in fitting summary statistics. It is commonly taken to be the inverse of the covariance matrix of statistics (Hansen 1982), thus summary statistics which are consistent throughout the years (such as the mean) would be prioritised as compared to more varying summary statistics like skewness.

The complete set of fitting equations used in fitting the three models are detailed in Appendix B.

2.4.3 Simulation results and discussion

Initial results

Table 2.1 summarises the parameters obtained from fitting the Rayleigh summary statistics to each of the 3 BLRP models.

Table 2.1: Fitted parameters for the BLRP class of models for Rayleigh summary statistics.

		Jan	Feb	Mar	Apr	May	June	July	Aug	Sep	Oct	Nov	Dec
BLRP	λ	0.0368	0.0301	0.0221	0.0210	0.0167	0.0211	0.0220	0.0204	0.0138	0.0266	0.0284	0.0258
	μ_x	1.47	1.27	1.27	2.55	2.35	3.18	6.24	3.11	2.54	2.08	1.60	1.49
	β	5.80	8.31	2.86	3.47	3.88	3.07	1.62	2.80	5.03	3.02	3.69	6.84
	γ	0.55	0.46	0.28	0.45	0.38	0.59	0.42	0.42	0.48	0.35	0.34	0.45
	η	8.23	11.28	7.48	11.15	8.14	8.00	9.81	7.61	9.76	7.41	7.53	9.41
BLRPR	λ	0.0374	0.0305	0.0223	0.0214	0.0170	0.0214	0.0224	0.0208	0.0141	0.0270	0.0288	0.0262
	μ_x	1.47	1.27	1.27	2.54	2.34	3.18	6.25	3.10	2.54	2.08	1.60	1.49
	α	100	100	100	100	100	100	100	100	100	100	100	100
	$\frac{\alpha}{\nu}$	8.46	11.64	7.64	11.45	8.34	8.27	10.11	7.81	10.06	7.60	7.70	9.69
	κ	0.71	0.74	0.38	0.31	0.48	0.39	0.17	0.37	0.52	0.41	0.49	0.73
	ϕ	0.07	0.04	0.04	0.04	0.05	0.07	0.04	0.06	0.05	0.05	0.04	0.05
BLRPRx	λ	0.0345	0.0290	0.0225	0.0203	0.0159	0.0193	0.0203	0.0206	0.0137	0.0255	0.0284	0.0254
	ι	0.09	0.06	0.07	0.13	0.12	0.13	0.32	0.32	0.12	0.24	0.20	0.10
	α	2.00	2.66	2.00	2.00	2.00	2.00	2.00	2.14	2.49	2.16	3.98	2.84
	$\frac{\alpha}{\nu}$	22.37	55.89	51.98	62.81	57.98	81.06	74.63	10.38	70.60	9.18	8.06	19.59
	κ	0.76	0.36	0.28	0.18	0.28	0.37	0.17	0.50	0.27	0.50	0.52	0.71
	ϕ	0.03	0.01	0.01	0.01	0.01	0.02	0.02	0.06	0.01	0.05	0.04	0.03

Based on Table 2.1, several observations can be made:

- The value of λ for each month remains similar across all three models. This is consistent with the theory that the rate of storm occurrence shouldn't change when a different model is used. λ is also shown to decrease during the summer months, consistent with observations in Essex where there are fewer storms during the summer. The results are also reasonably close to the parameters obtained by Onof (1992) when conducting similar modelling with rainfall series from Elmdon, a village in north-west part of Essex, 65km from Rayleigh.
- Seasonal trends are captured here as higher values of μ_x during the summer months. Combined with a lower β or κ, the results indicate that fewer but deeper cells will be generated per storm, simulating short and intense bursts of rainfall during the summer.
- The BLRPR parameters are very similar to those in the BLRP model despite the reparameterisation of β and γ to κ and ϕ respectively. In addition, the average η for the BLRPR model (represented by $\frac{\alpha}{\nu}$) is also similar to the η in the BLRP model. Therefore, there would be little difference between the BLRP and BLRPR models.
- The BLRPRx cell parameters ($\iota, \alpha, \frac{\alpha}{\nu}$) greatly differ from those in the BLRP and BLRPR models. This results in more frequent but smaller cells for the BLRPRx model.

Using the fitted parameters, 100 rainfall simulations for each BLRP model were carried out and the summary statistics for each simulation calculated. Each simulation will produce a different rainfall series as the random variables are sampled randomly, however the fundamental parameters that govern the probability distribution of each random variable is the same. While the expected summary statistics may be analytically calculated via equations outlined in Appendix B, running 100 simulations would provide an estimate to the degree of variation of each summary statistic, in addition to being able to compare extreme rainfall statistics between the observed and simulated which cannot be derived analytically.

The monthly summary statistics are then plotted together with the observed summary statistics to assess the effectiveness of the model in producing synthetic rainfall that is similar to the observed rainfall. In addition, the annual maxima for each simulation was extracted and plotted together with the observed annual maxima. Figures 2.10a to 2.10r show the summary statistic and extreme value comparison for the BLRP model. Plots for the BLRPR and BLRPRx models are given in Appendix C1 and C2.

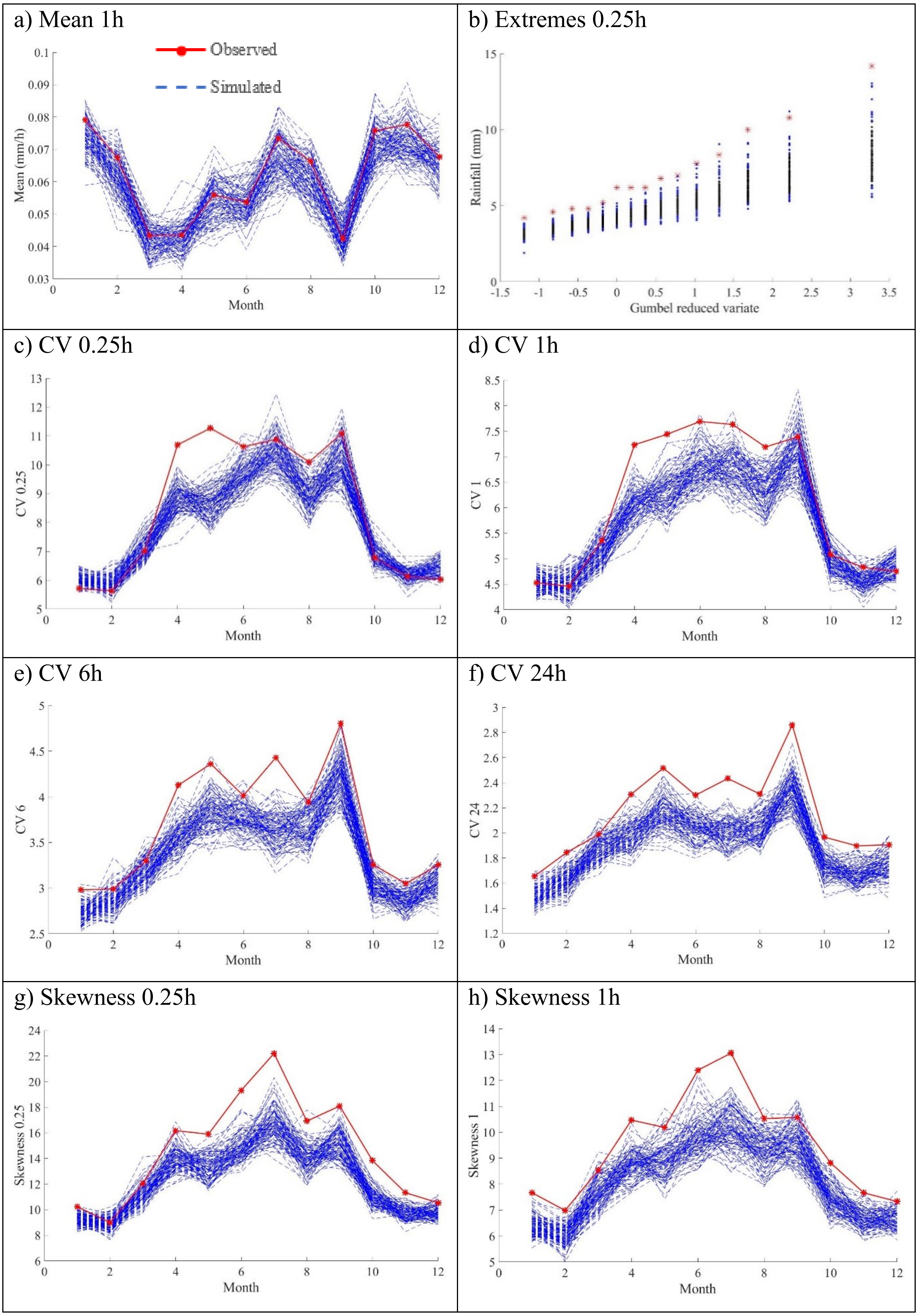

a) Mean 1h
Observed
Simulated
Mean (mm/h)
Month
b) Extremes 0.25h
Rainfall (mm)
Gumbel reduced variate
c) CV 0.25h
CV 0.25
Month
d) CV 1h
CV 1
Month
e) CV 6h
CV 6
Month
f) CV 24h
CV 24
Month
g) Skewness 0.25h
Skewness 0.25
Month
h) Skewness 1h
Skewness 1
Month

i) Skewness 6h

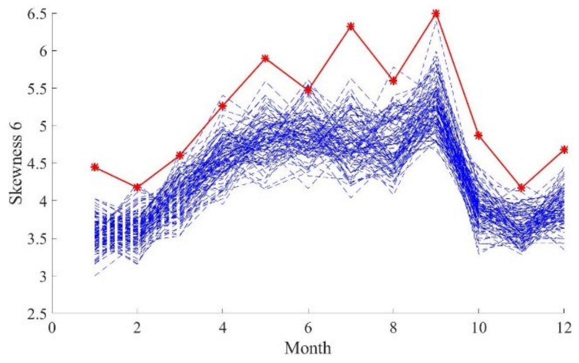

j) Skewness 24h

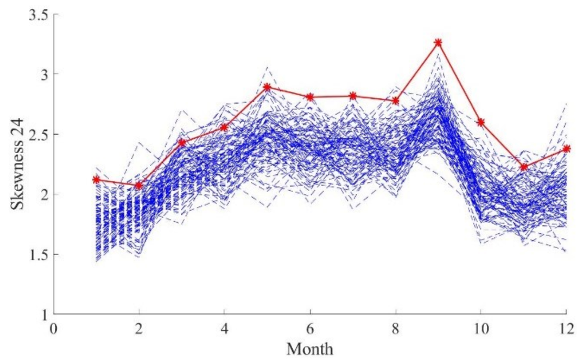

k) AC 0.25h

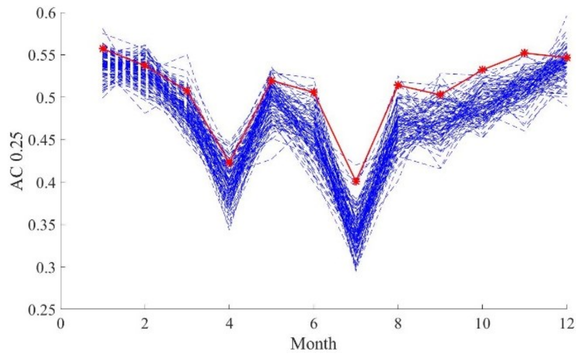

l) AC 1h

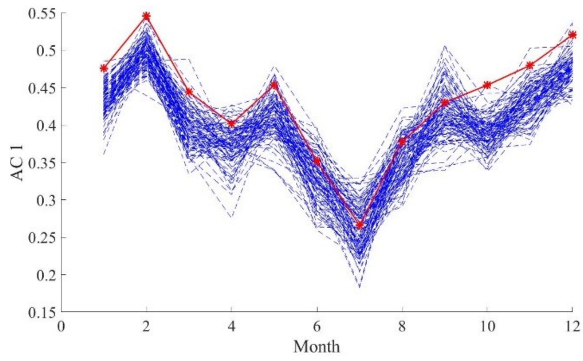

m) AC 6h

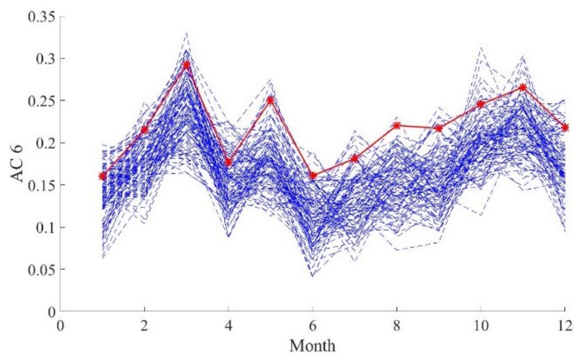

n) AC 24h

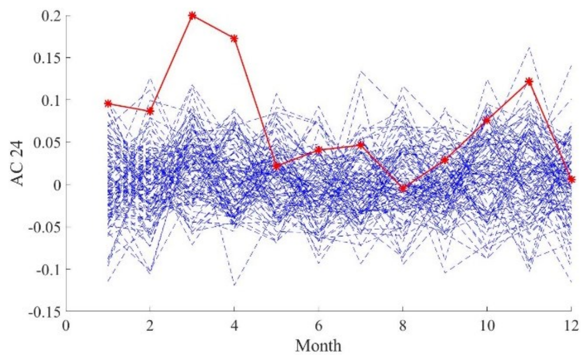

O) Pwet 0.25h

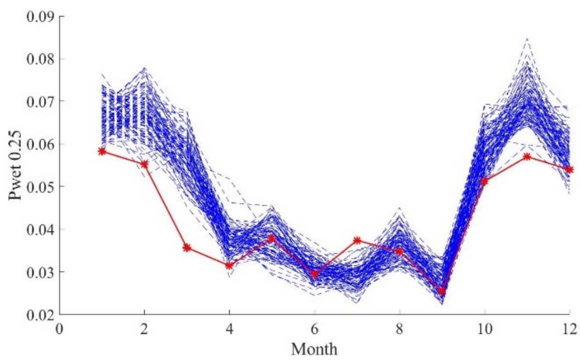

p) Pwet 1h

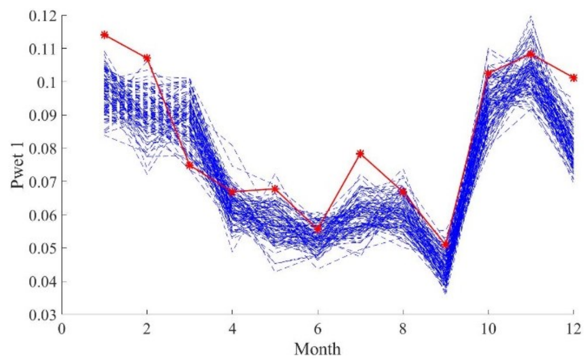

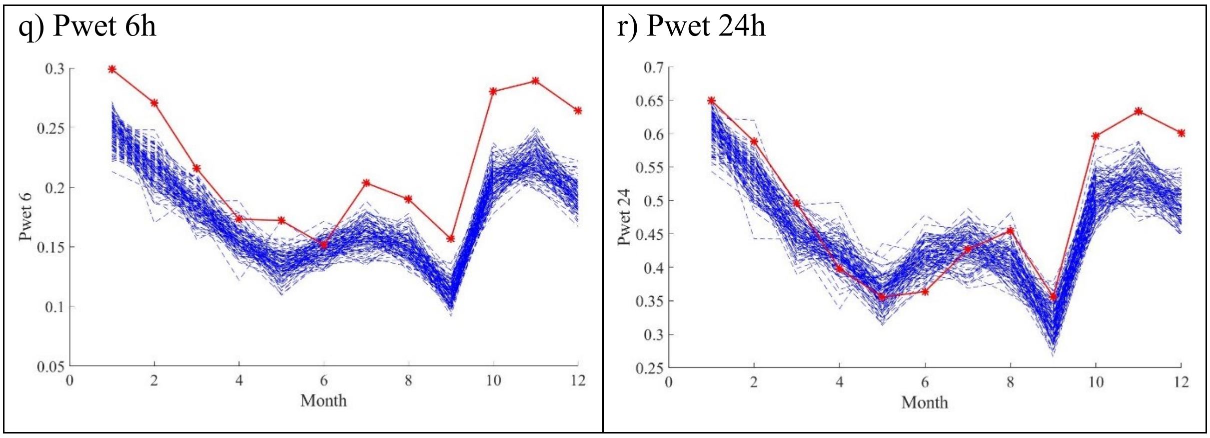

Figure 2.10: Comparison of summary statistics and extremes between BLRP simulated rainfall and measured Rayleigh rainfall. Red is the observed statistic/extreme, while blue the simulated results. (a) Mean 1h. (b) Gumbel plot of annual maxima. (c) – (f) Coefficient of variation for 0.25h, 1h, 6h and 24h. (g) – (j) Skewness for 0.25h, 1h, 6h, and 24h. (k) – (n) Lag-1 autocorrelation for 0.25h, 1h, 6h, and 24h. (o) – (r) Percentage wet for 0.25h, 1h, 6h, 24h.

In general, the mean and lag-1 autocorrelations were very well reproduced by the simulations, while both the coefficient of variation and skewness were slightly underestimated for all time resolutions. The percentage wet was also well reproduced for the fine time scales of 15 minutes and 1h, while the model performed poorly for the daily time resolution. This behaviour was also observed for the remaining two models in this class.

One key weakness of the BLRP class of models, however, is that they tend to underpredict extreme events, which is well documented in the literature (Kaczmarska et al., 2014, Abdellatif et al., 2015). This behaviour is also captured here (Figure 2.10b), showing the classical BLRP model underestimating the extremes experienced at this site (red dots) across all return periods. Only the randomized μ_x model (BLRPRx) has a few simulations which have managed to exceed the extremes at the site for large return periods (Figure 2.11).

Among the 3 models, both the BLRP (Figure 2.10) and BLRPR (Appendix C1) simulations are generally similar to one another, with some slight underestimations in coefficient of variation and skewness, and generally good fits for the rest of the summary statistics. The BLRPRx model on the other hand improves on the fitting for the coefficient of variation and skewness, due to the different cell parameters obtained from the fitting. This is illustrated with comparisons of the 1h CV and 1h skewness fits between the BLRPR and BLRPRx simulations in Figure 2.12.

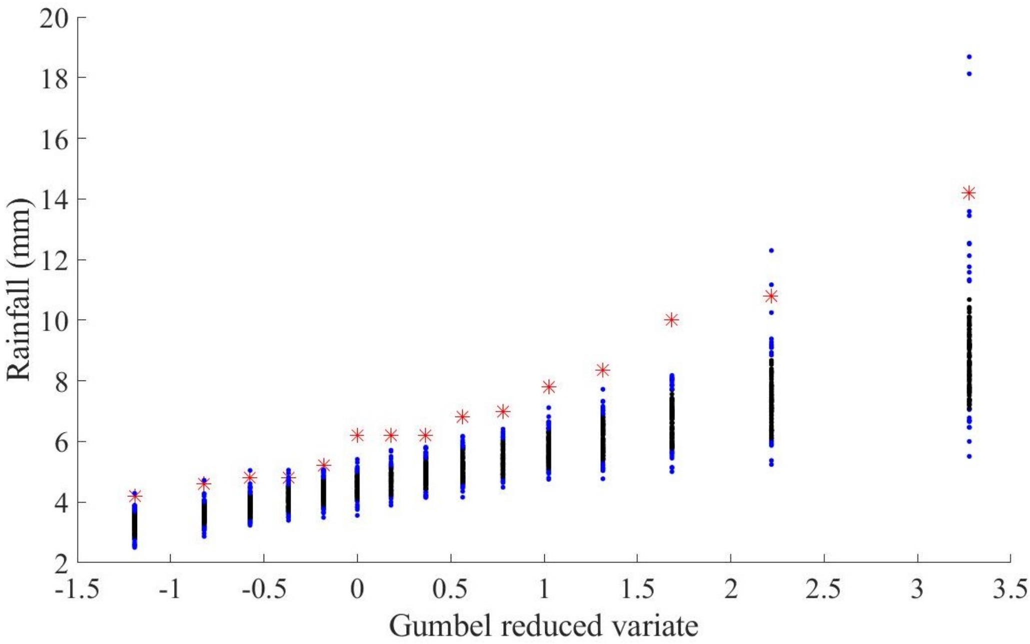

Figure 2.11: Gumbel plot of 15 minute AMs between BLRPRx simulation rainfall (blue) and observed (red).

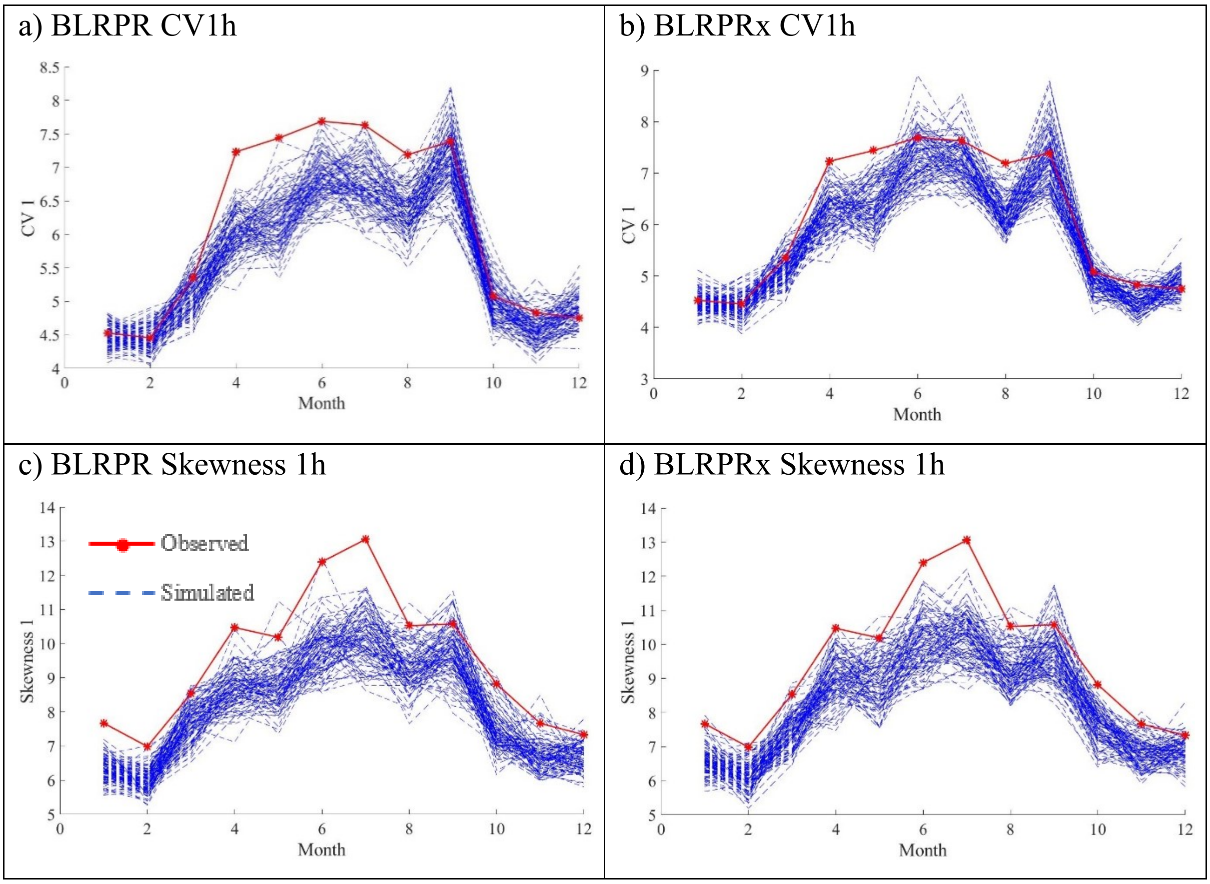

Figure 2.12: Comparison between (a) BLRPR simulated CV1h, (b) BLRPRx simulated CV1h, (c) BLRPR simulated Skewness 1h, and (d) BLRPRx simulated Skewness 1h in blue, against observed CV1h and Skewness 1h in red.

Use of cumulative summary statistics

One of the main reasons for an underestimation of extremes in the initial fitting is the nature of the summary statistics itself. The standard methodology, as outlined in Section 2.2.2, requires calculation of each month's summary statistic, before taking a mean of the summary statistics for a particular month across the years, which is then used in the BLRP fitting procedure. A consequence of this methodology is that skewness tends to be underestimated as the mean of the skewness is used for the fitting, instead of the raw skewness of the data. This would be especially true during the summer, where certain years will have large convective storms, consequently high skewness being averaged with years with no major storms and low skewness.

In order to resolve this problem, a different methodology to compute summary statistics was developed in the current research, known as the Cumulative Method. With this method, similar months across the years (e.g. all Januaries) were first combined together into one large sample of January rainfall data, from which the summary statistics were then computed using that sample.

The cumulative method does not affect the mean and the percentage wet, as both of those statistics are of first order. The impact of this change is on the skewness and coefficient of variation and its significance is shown in Figures 2.13a and 2.13b, respectively, in comparison with a standard approach of determining summary statistics. A complete table of the cumulative summary statistics can be found in Appendix A2.

a)

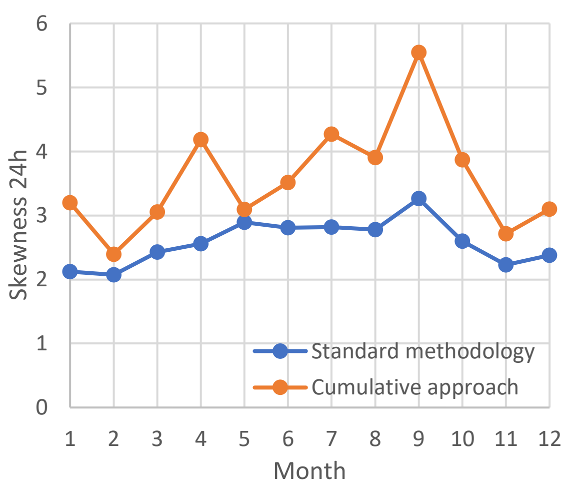

b)

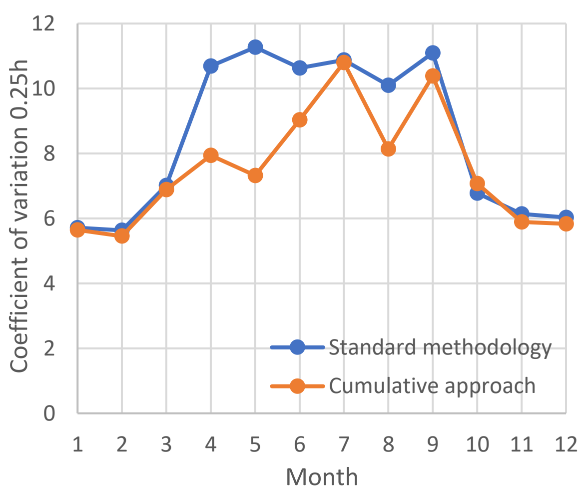

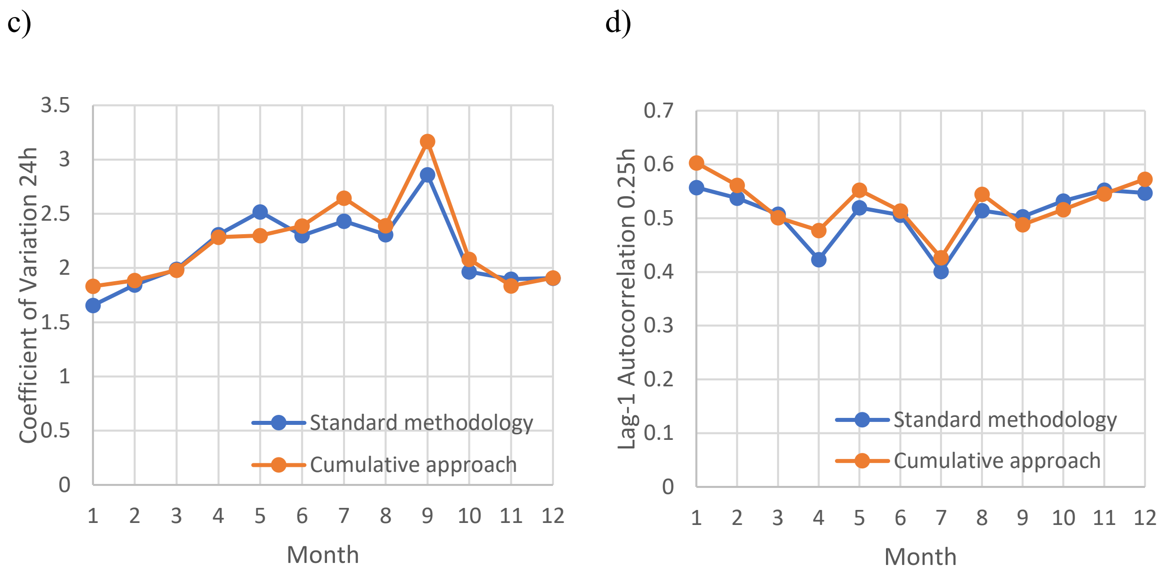

Figure 2.13: Comparison of monthly summary statistics, calculated using the standard methodology and the new cumulative approach. (a) 24h Skewness. (b) 0.25h coefficient of variation.(c) 24h coefficient of variation. (d) 0.25h lag-1 autocorrelation.

By changing the approach in calculating the summary statistics, the new monthly skewness has increased for all time scales in most months, with the 24 hour skewness shown in Figure 2.13 (a). The increases were more significant during the summer months than in winter months, consistent with the hypothesis. Meanwhile, the 0.25 hour coefficient of variation decreased with the new approach during the spring months of April – June (Figure 2.13 (b)). This difference decreased as the time scale increased from 15 minutes to daily, where in the daily plot both approaches gave similar coefficient of variations (Figure 2.13 (c)). The lag-1 autocorrelation meanwhile remained relatively unchanged over all timescales, with the 0.25 hour lag-1 autocorrelation plotted in Figure 2.13 (d).

One weakness of the cumulative method is that it is impossible to compute the variance for each of these summary statistics. Consequently, weighting can be either the same for all statistics, or be adjusted subjectively. A solution to this problem would be to implement a combination of both methods, where the cumulative summary statistics are used for the fitting, while the variances from the standard methodology are used for weighting the summary statistics.

All 3 BLRP models were refitted and the new characteristic parameters are tabulated in Table 2.2.

Table 2.2: Fitted parameters for the BLRP class of models for Rayleigh cumulative approach summary statistics.

		Jan	Feb	Mar	Apr	May	June	July	Aug	Sep	Oct	Nov	Dec
BLRP	λ	0.0241	0.0172	0.0162	0.0071	0.0135	0.0162	0.0151	0.0140	0.0088	0.0170	0.0173	0.0196
	μ_x	1.29	1.20	1.50	1.81	2.36	7.72	9.25	3.25	4.18	1.91	2.39	1.92
	β	0.18	3.38	2.39	1.43	2.58	1.75	0.16	0.01	3.96	0.20	1.99	4.41
	γ	0.07	0.19	0.22	0.08	0.24	0.28	0.10	0.02	0.35	0.07	0.22	0.30
	η	1.49	5.99	7.11	4.87	5.62	17.86	5.07	0.93	9.71	1.71	4.59	9.08
BLRPR	λ	0.0325	0.0242	0.0190	0.0089	0.0150	0.0113	0.0183	0.0167	0.0101	0.0198	0.0264	0.0255
	μ_x	1.56	1.43	1.54	2.37	1.90	2.81	11.00	3.23	4.44	4.68	1.93	1.55
	α	5.17	100.00	8.48	3.61	100.00	10.12	12.64	7.57	5.31	3.56	7.84	5.18
	$\frac{\alpha}{\nu}$	8.49	7.56	8.22	12.24	7.04	5.57	8.14	8.20	18.66	14.56	10.50	10.09
	κ	0.78	0.64	0.25	0.13	0.55	0.15	0.06	0.49	0.40	0.08	0.57	0.58
	ϕ	0.08	0.05	0.03	0.01	0.04	0.02	0.04	0.06	0.03	0.01	0.04	0.04
BLRPRx	λ	0.0197	0.0226	0.0155	0.0053	0.0140	0.0106	0.0167	0.0123	0.0064	0.0123	0.0210	0.0172
	ι	0.20	0.16	0.25	0.55	0.11	0.55	1.80	0.45	0.39	1.31	0.20	0.19
	α	2.00	2.00	2.05	2.00	2.00	2.00	2.00	2.00	2.00	2.00	2.00	2.00
	$\frac{\alpha}{\nu}$	7.85	8.77	6.09	3.88	22.22	4.91	5.31	7.55	11.60	2.14	9.50	7.79
	κ	1.04	0.77	0.26	0.14	0.58	0.23	0.10	0.61	0.42	0.10	0.65	0.76
	ϕ	0.05	0.04	0.03	0.01	0.02	0.03	0.07	0.05	0.03	0.03	0.04	0.04

By comparing Tables 2.1 and 2.2, several observations can be made on the effect that the cumulative approach summary statistic can have on the fitted parameters:

- While the monthly average time between storms, λ, still retained its seasonal trend, it was no longer similar across the models as compared to the standard methodology runs. In addition, the months of April and September both experienced the lowest λ. This is due to the adoption of the new skewness which saw peaks in both April and September (Figure 2.13a). A higher skewness would also result in greater unpredictability, as an indication that there were more extreme rainfall events.
- μ_x still maintained its seasonality, but it was now much higher during the summer as compared to the previous μ_x in Table 2.1, indicating that rainfall would be much more intense during the summer month of July.

Similar to the previous analysis, another 100 simulations per model were generated and their summary statistics compared with the observed values. The plots comparing the summary statistics for the BLRP and BLRPR models can be found in Appendix C3 and C4 respectively. The summary statistic comparisons for the BLRPRx model is given in Figure 2.14.

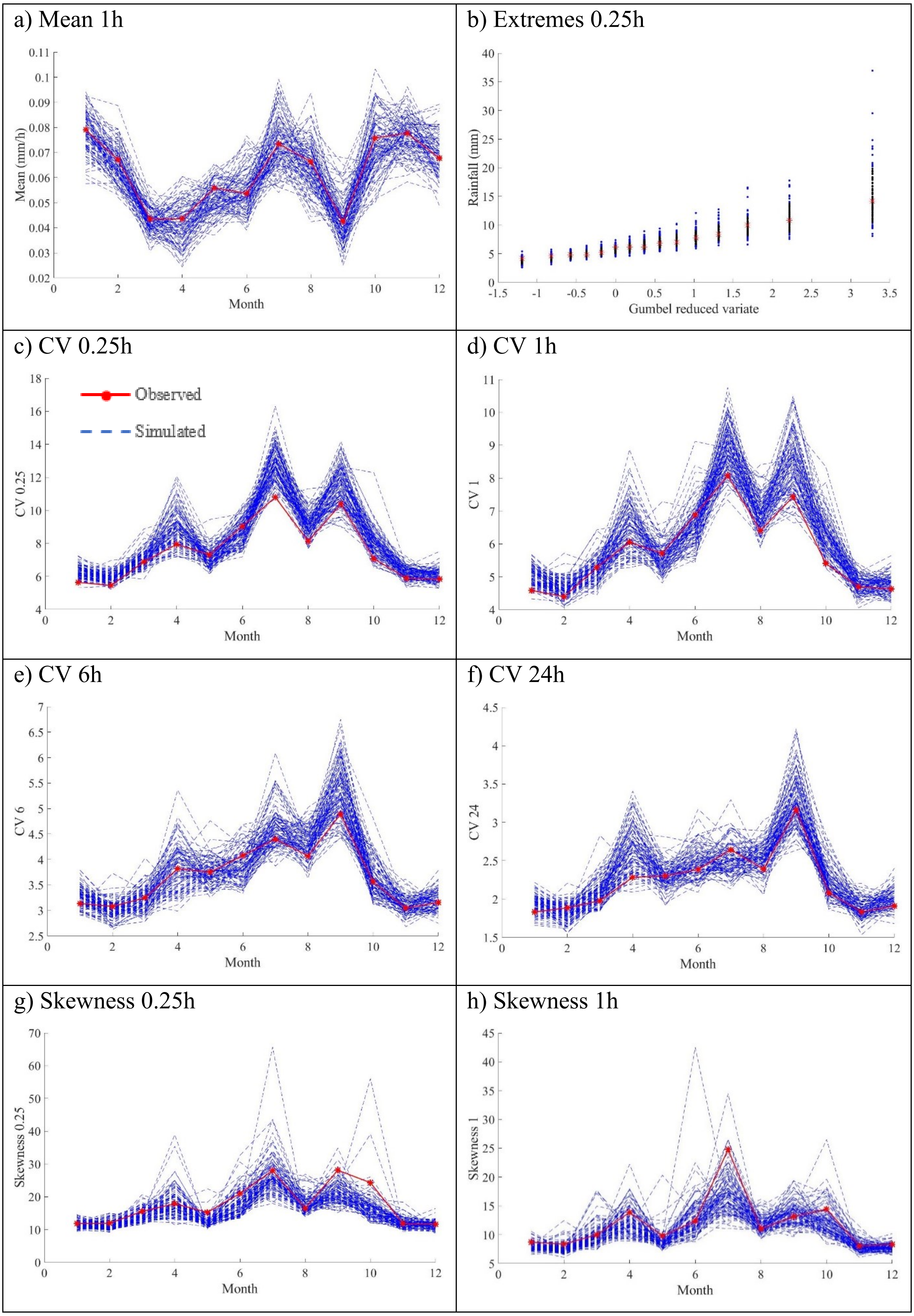
a) Mean 1h
Mean (mm/h)
Month
b) Extremes 0.25h
Rainfall (mm)
Gumbel reduced variate
c) CV 0.25h
Observed
Simulated
CV 0.25
Month
d) CV 1h
CV 1
Month
e) CV 6h
CV 6
Month
f) CV 24h
CV 24
Month
g) Skewness 0.25h
Skewness 0.25
Month
h) Skewness 1h
Skewness 1
Month

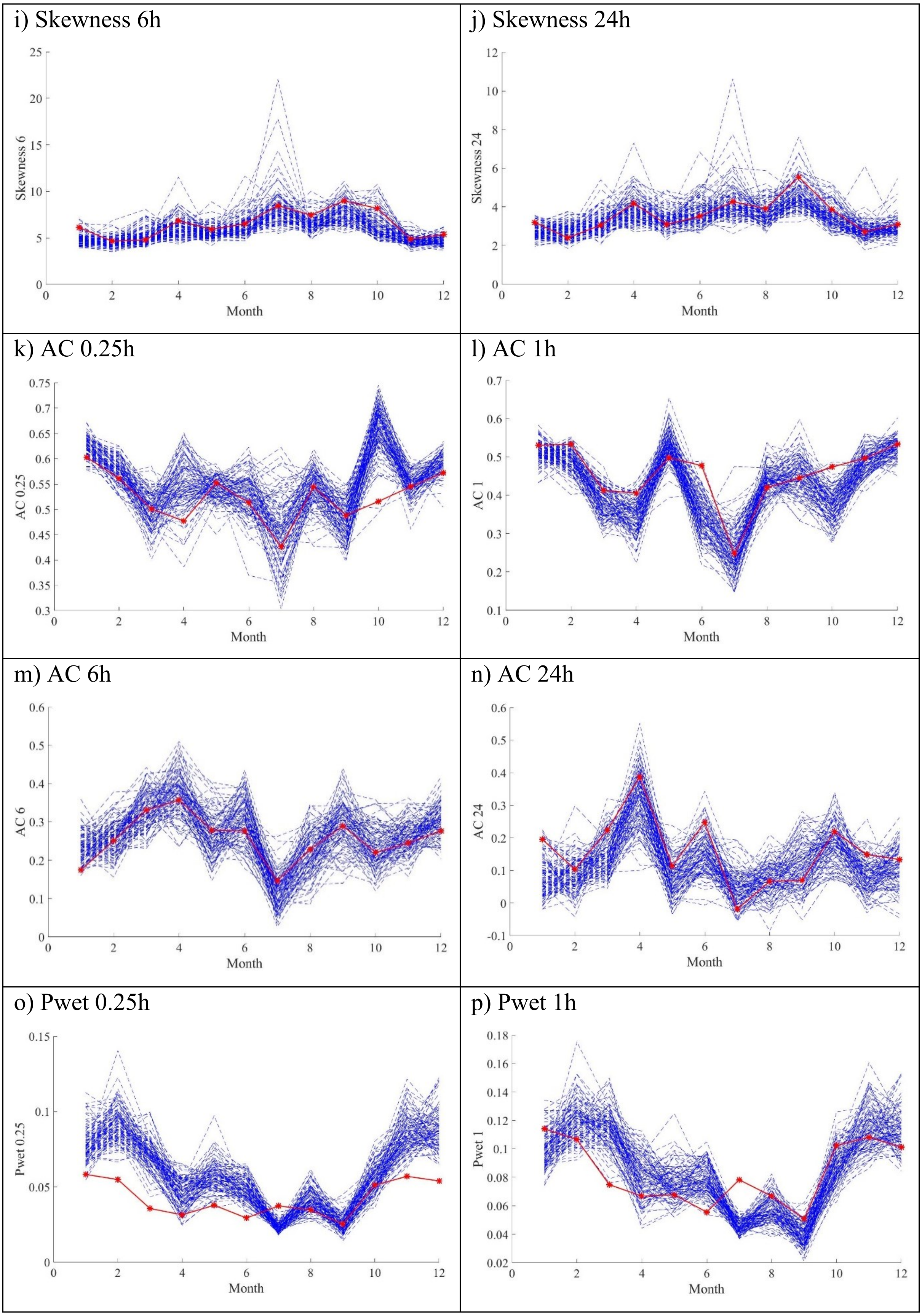
i) Skewness 6h
Skewness 6
Month
j) Skewness 24h
Skewness 24
Month
k) AC 0.25h
AC 0.25
Month
l) AC 1h
AC 1
Month
m) AC 6h
AC 6
Month
n) AC 24h
AC 24
Month
o) Pwet 0.25h
Pwet 0.25
Month
p) Pwet 1h
Pwet 1
Month

q) Pwet 6h

r) Pwet 24h

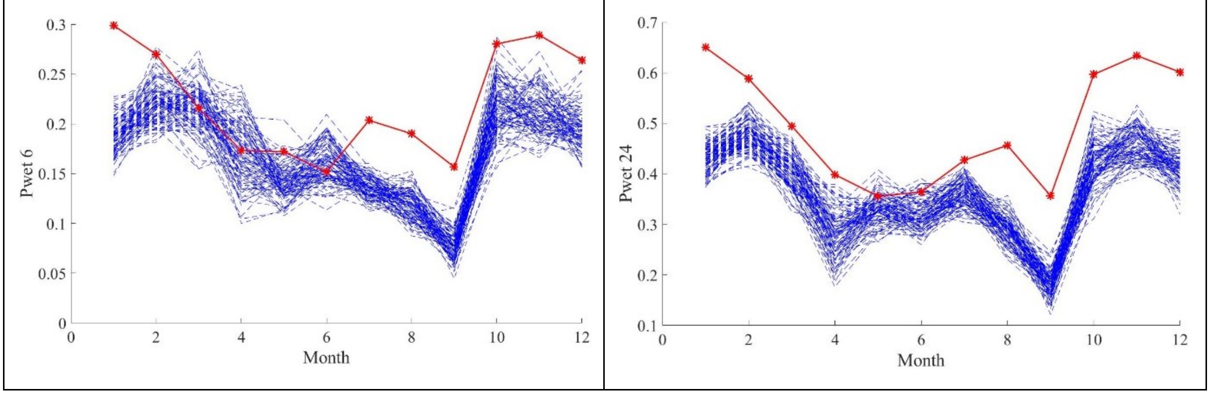

Figure 2.14: Comparison of cumulative summary statistics and extremes between cumulative approach BLRPRx simulated rainfall and measured Rayleigh rainfall. Red is the observed statistic/extreme, while blue the simulated results. (a) Mean 1h. (b) Gumbel plot of annual maxima. (c) – (f) Coefficient of variation for 0.25h, 1h, 6h and 24h. (g) – (j) Skewness for 0.25h, 1h, 6h, and 24h. (k) – (n) Lag-1 autocorrelation for 0.25h, 1h, 6h, and 24h. (o) – (r) Percentage wet for 0.25h, 1h, 6h, 24h.

Based on these calibrations, it was clear that the simulations now fit the observed summary statistics better than the previous simulations, particularly on the skewness and lag-1 autocorrelation. The downside, however, was that the percentage wet did not fit well, especially for the daily percentage wet, where the model underestimated the observed behaviour, especially from the months of August to December and January. It should be noted that while the values were underestimated, the shape of the percentage wet over the year was broadly similar to that observed.

Furthermore, the simulations from all models now simulated very realistic extremes compared to the observed, with the extremes from the BLRP model shown in Figure 2.15. In all cases, the observed annual maximums for all return periods (red dots) were close to the average simulated annual maximums and no longer under-predicted as in the standard methodology.

Comparisons among the 3 BLRP models with the new approach shows little difference between the models, even though it was found that the BLRPRx model fitted the variance and skewness better with the standard methodology. Therefore, when adopting the new approach in summary statistics calculations, all models are equally effective in reproducing rainfall.

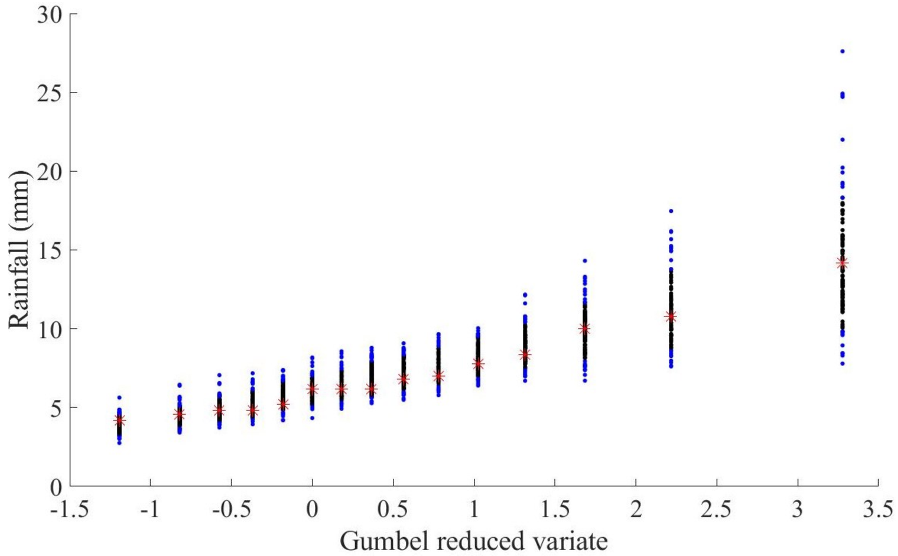

Figure 2.15: Gumbel plot of AMs between BLRP simulation rainfall (blue and black) using the cumulative summary statistics and observed (red).

2.5 Summary remarks

While the field of rainfall monitoring and modelling is significantly developed, there are still many challenges that need to be addressed. The introduction of telemetry rainfall data will certainly help in providing much needed monitoring coverage around rural areas where key infrastructure, such as flood defences, is located. However, care must be taken in handling and validating such data. With the use of double mass plots, errors in the data can be detected and filtered out, before subjected to further analyses.

Missing data is still a very common occurrence in rainfall series, especially so if the site is rural and instruments poorly maintained. Thus a weighting system was implemented to minimise the influence of missing data on monthly summary statistic calculations. This flexibility would allow the BLRP-type model to analyse the hundreds of incomplete rainfall series at various locations, thus not limiting this stochastic model to only specific locations with complete rainfall series.

The simulated BLRP summary statistics fitted well to most of the observed summary statistics, but underestimated the extremes. While some improvements can be seen by using the BLRPRx model compared with the BLRP and BLRPR models, it is still insufficient to overcome the underestimation of the extremes and skewness.

The methodology employed in calculating the summary statistics was reassessed to ensure the sample's skewness is taken directly rather than as the mean of the skewness. The change from standard to cumulative summary statistics proved effective in improving the BLRP fit to the observed extremes for all 3 BLRP models assessed.

Chapter 3: Generalized Linear Modelling of Future Rainfall

3.1 Introduction

In Chapter 2, the rainfall at Rayleigh was characterised and several Bartlett-Lewis Rectangular Pulse (BLRP) models were used in creating a statistically similar rainfall to the one observed at the site. An implicit assumption in that approach was that the monthly rainfall characteristics were assumed to be constant year on year. In other words, the data was stationary and unchanging. As the effects of climate change grow with increased carbon emissions over time, the climate and rainfall are expected to change, thus requiring a rainfall model capable of handling the non-stationarities caused by an evolving climate.

The Generalised Linear Model (GLM) is a purely statistical rainfall model, which develops correlative relationships between rainfall and a combination of its own statistical properties, mathematical functions, or other related climate variables such as temperature and pressure. As the model does not attempt to average rainfall year on year, it does not suffer from the stationarity problems that the BLRP model suffers from. Therefore, it is a suitable model to use to investigate and project future rainfall that is influenced by a constantly changing climate.

The chapter first presents the GLM formulation and implementation in this research. Its mathematical formulation, along with Chandler's implementation in the RGlimClim package is discussed in detail. The GLM model was then calibrated using climate variables from the European Re-Analysis 5 (ERA5) project as predictors, and the aggregated Rayleigh telemetry rainfall series. The GLM fitting timeframe was set to be from 2004 to 2015, due to a combination of large amounts of missing rainfall data for the years 2001 to 2003, especially after aggregation from 15 minutes to daily, and incomplete ERA5 climate data for 2016 and 2017 at the time of this research. Hypothesis testing on each predictor was performed to determine its effectiveness in predicting the occurrence of rainfall on a given day and in predicting the rainfall amount on a given wet day.

Simulations of daily rainfall series of a similar time period as the Rayleigh series were then performed using the calibrated GLM and the ERA5 climate variables. The summary statistics and extremes of the simulations were compared with the observed summary statistics to assess the GLM fitting.

Following from that, the fitted GLM was then applied to climate projections up to the year 2080, available from the UKCP18 project for the Rayleigh site, and future daily rainfall was simulated based on those climate projections. As the UKCP18 analysis simulated the climate from 1980 to 2080, a validation exercise was performed in the years 2004 – 2015 by comparing the simulated summary statistics from the UKCP18 climate projections with those from the ERA5 climate data and with field observations.

Finally, trends in the projected future daily rainfall were explored and discussed in detail. Emphasis was placed on assessing the impact of climate change on the summary statistics of rainfall, in particular on the mean rainfall, percentage wet, and daily extremes. The projected daily rainfall simulations were then used as the atmospheric input for a geotechnical assessment of the lifecycle of infrastructure embankments in Chapters 7 and 8.

3.2 Generalized Linear Model calibration

3.2.1 RGlimClim

The implementation of Generalised Linear Models in this research was performed in the R programming environment (R Core Team, 2019), using the RGlimClim package developed by Chandler (2020), which was initially developed in FORTRAN. Some case studies of the development and application of RGlimClim can be found in Chandler and Wheater (2002), Yan et al. (2005), and Asong et al. (2016).

3.2.2 Model Formulation

Mathematical formulation

Suppose that there is a $n \times 1$ vector of random variables $Y = (Y_1, \ldots, Y_n)'$. Each Y is found to be dependent on k covariates which can be assembled into matrix X with dimensions $n \times k$, such that the (i, j)th element of X is the jth covariate for Y_i. A GLM for Y is a model for the probability distribution to generate Y, based on the covariates X.

A GLM first establishes a linear predictor, η, which is a linear combination of the covariates (predictors):

$$\eta = X\beta \tag{3.1}$$

where β is a $k \times 1$ vector of coefficients for the covariates. The predictors can be treated with a transformation as inputs are limited to only 6 characters in the RGlimClim package. The vector mean $\mu = (\mu_1, \dots, \mu_n)'$ of the distribution of Y is then related to the linear predictor via a non-linear monotonic link function, $g(\mu) = \eta$. The variance of distribution Y, $var(Y_i)$, is then dependent on the mean:

$$var(Y_i) = \phi V(\mu_i) \tag{3.2}$$

where ϕ is the dispersion parameter, typically assumed constant in a GLM; and V is the variance function based on the mean.

While the distribution of Y can take any probability distribution form, only the exponential family of distributions was formulated in the RGlimClim package (Chandler, 2020). This consists of the Bernoulli, Poisson, Normal and Gamma distributions.

For the purposes of modelling rainfall, only the Bernoulli and Gamma distributions were employed in RGlimClim. The GLM implementation of rainfall followed that of Coe and Stern (1982) and Stern and Coe (1984), which consisted of a two-stage approach in modelling rainfall, namely the occurrence and amounts models. This approach was also adopted by Wheater et al. (2000b) in developing stochastic rainfall models for daily UK rainfall to be used in rainfall-runoff models for flood design.

The occurrence model models the probability distribution of the occurrence of rain on a given day at a site using a logistic regression. This can be achieved by fitting the Bernoulli distribution GLM with parameter p, which is the probability of rain. The mean and variance of the distribution are:

$$E(Y_i) = \mu_i = p_i \tag{3.3}$$

$$Var(Y_i) = p_i(1 - p_i) \tag{3.4}$$

This then gives the variance function, $V(\mu_i) = \mu_i(1 - \mu_i)$. As the link function, $g(\mu_i)$, must map from $(0,1) \rightarrow (-\infty, \infty)$, a logit function is used such that

$$g(\mu_i) = (X\beta)_i = \ln\left(\frac{\mu_i}{1 - \mu_i}\right) \tag{3.5}$$

thus linking the vector of factored predictors $X\beta$ to the mean and model parameter p.

The amounts model, on the other hand, models the amount of rainfall on a given wet day. A Gamma distribution GLM, with parameters μ as the mean and ν as the shape parameter, is fitted using the link function:

$$g(\mu_i) = (X\beta)_i = \ln(\mu_i) \tag{3.6}$$

The variance of the distribution is thus $var(Y_i) = \phi V(\mu_i) = \nu\mu_i^2$ with the variance function $V(\mu_i) = \mu_i^2$, and the dispersion term $\phi = \nu$, assumed to be constant for all the gamma distributions.

Model calibration

Both GL models were then fitted (estimation of the coefficient vectors) using the maximum likelihood approach. Fundamentally, the maximum likelihood method is to choose the value of β and, in the case of the Gamma distribution, ϕ, which provide the highest probability to the observations y. Assuming that the observations are independent, such that the density of the distribution of the ith observation, $y_i = f_i(y_i; \beta, \phi)$, then the joint density is a multiplication of all independent densities, which is the likelihood for β for a given y:

$$L(\beta, \phi|y) = f(y; \beta, \phi) = \prod_i^n f_i(y_i; \beta, \phi) \tag{3.7}$$

Therefore, the maximum likelihood estimate of β is the value that maximises the likelihood for β and ϕ for a given y. As products are generally more difficult to work with, the log-likelihood, $ln\ L(\beta, \phi|y) = \sum_i^n f_i(y_i; \beta, \phi)$ is used instead, which is also maximised.

The maximum likelihood method is generally more favourable as compared to other fitting procedures (Cox and Hinkley, 1974). The maximum likelihood estimate will generally have the smallest mean squared error of any estimator in large samples for models based on the exponential family, as used in RGlimClim. In addition, hypothesis testing can be performed based on the likelihood ratio (the ratio of the likelihood from two different estimates), which is the most powerful test for distinguishing between two hypotheses (Neyman-Pearson Lemma; Neyman and Pearson, 1933).

The only disadvantage to the maximum likelihood approach is that it is necessary for the observed probability distribution model to be specified. Thus the effectiveness of the maximum likelihood is only effective if the model distribution is a realistic representation of the observed data. This is the driving reason behind adopting the two-stage modelling approach for rainfall, in which rainfall occurrence and amounts are treated separately. If treated together as one distribution, the observed data will be highly positively skewed with a large number of zero rainfall cases, making model fitting difficult as the exponential family of distributions will have difficulty in matching the observed rainfall.

3.2.3 European Re-Analysis 5 (ERA5) climate data

As climate variables such as temperature, dewpoint temperature, pressure, wind speeds and cloud cover are used as predictors in the GLM, it is essential that good quality climate data is obtained at or near the Rayleigh site discussed in Chapter 2. However, climate measuring stations are far more sparsely spread out as compared to raingauges due to maintenance costs and convenience, resulting in scattered observed climate variable data across the UK.

In order to obtain reasonable climate variables close to the site, reanalysis climate data was utilised in the absence of observed climate data. A reanalysis involves combining individual stations of observed climate variables together with short-range forecasting, to produce a complete global coverage of climate variables over the specified time interval. At the European Centre for Medium Range Weather Forecasts (ECMWF), climate reanalysis was first performed by Bengtsson et al. (1982), producing the First Global Atmospheric Research Program Global Experiment, which reanalysed climate data for 1979 with a grid resolution of 208km. Subsequent reanalyses (ERA-15, Gibson et al., 1999; ERA-40, Uppala et al., 2005; ERA-Interim, Dee et al., 2011) would improve significantly on the grid resolution, period covered, modelling and assimilation capabilities, achieving better correlations with the observed climate data.

The current reanalysis iteration by the ECMWF is the European Reanalysis 5 (ERA5), covering the time period from 1950 to present date with a grid resolution of 31km (Hersbach et al., 2020). Comparisons of climate variables such as wind speeds, irradiance and temperature between ERA5 reanalysis climate outputs and observed climates at several localities, such as in the Arctic (Graham et al., 2019), Antarctic (Tetzner et al., 2019) and Europe (Urraca et al., 2018), indicate good agreements with observed climate variables.

However, there still exist limitations in the use of reanalysis data in any subsequent climatological analysis. Conserving atmospheric water balances has always been an issue with reanalysis (Nigam and Ruiz-Barradas, 2006). Consequently, accuracy in precipitation and evaporation generally suffers, with divergences of up to 2.5 mm/day in ERA-40 over North America. While ERA5 improves on the global water balances from ERA-40 and ERA-Interim, significant differences of 0.58mm/day over the 50°S to 50°N domain still exist (Hersbach et al., 2020). For the period of 1979-2018, global correlations of precipitations between the Global Precipitation Climatology Project and ERA5 are at 77%.

Due to the strengths and limitations of ERA5, the data on surface temperature, dewpoint temperature, surface air pressure, wind speeds and cloud cover was extracted from ERA5 for the grid point nearest to Rayleigh for the GLM fitting. Relative humidity was calculated using the dewpoint temperature and surface temperature based on the Magnus Equation:

$$T_d = \frac{\lambda \cdot \left[ln\left(\frac{RH}{100}\right) + \frac{\beta \cdot T}{\lambda + T} \right]}{\beta - \left[ln\left(\frac{RH}{100}\right) + \frac{\beta \cdot T}{\lambda + T} \right]} \tag{3.8}$$

where T_d is the dewpoint temperature, T the surface temperature, RH the relative humidity, λ and β the Magnus parameters. For the temperature range of -45°C to 60°C, the Magnus parameters are given by $\beta = 17.62$ and $\lambda = 243.12$°C (Sonntag, 1990). Precipitation from ERA5 was not used due to the known limitations of the model, instead, observed field precipitation data, as discussed in Chapter 2, was used.

3.2.4 GLM fitting and refinement

As discussed in 3.2.2, the GLM calibration was separated into two independent models, the occurrence model and the amounts model. As both models are independent, the order in which the models are fitted is inconsequential.

The climate variables were fitted in the order of their relevance to the physical process of rainfall. Surface temperature and pressure are the two most significant variables governing rainfall, followed by wind speeds, relative humidity and cloud cover. This ordering of variables was done to identify and minimise dependencies between the variables used in the fitting. As an example, wind direction and speeds are inherently tied to atmospheric pressure fields, where air moves from regions of high pressure to low pressure. Therefore, surface pressure should be fitted before wind speeds, and if there is a strong dependency behaviour between wind speeds and pressure, it will manifest as a poor improvement in the model when wind speeds are fitted following pressure.

For both occurrence and amounts model, the GLM was first fitted with a constant. For the occurrence model, it involved fitting the Bernoulli distribution to the observations itself to get a constant probability of rainfall, p, while for the amounts model, it was the mean of the Gamma distribution, μ, that was obtained. This first fitting served as the starting point for subsequent fits with the climate variables. The log-likelihood ratio is the increase in log-likelihood from the previous fit, while the likelihood ratio test is the hypothesis test to assess the significance of the log-likelihood ratio, as discussed in 3.2.2.

Occurrence model

Table 3.1 shows the log-likelihood ratio and the p-values of each likelihood ratio test upon the consecutive implementation of each climate variable to the GLM fitting of the occurrence model. If two climate variables were to show significant dependencies and covariate effects, then the consecutive log-likelihood ratio would be small, and the p-value of the likelihood ratio test would approach 1, while if the log-likelihood ratio is large, with a small p-value, there is strong evidence that that variable plays a significant factor to the probability of occurrence of rainfall. Temperature, surface pressure and relative humidity are such variables that play a significant role in rain formation.

Table 3.1: Log-likelihood ratio and the associated likelihood ratio test p-values for fitting each climate variable consecutively to the GL occurrence model.

Climate variable	Log-likelihood ratio to previous fit	Likelihood ratio test (p-value)
Temperature	56.72	$< 2.2 \times 10^{-16}$
Surface pressure	246.81	$< 2.2 \times 10^{-16}$
10m Easterly wind speed	22.79	1.5×10^{-11}
10m Northerly wind speed	3.55	0.0077
Relative humidity	84.03	$< 2.2 \times 10^{-16}$
Cloud cover	0.043	0.77

Some variable dependencies were evident when the 10m Northerly wind variable was added to the GLM, which at that point already had temperature, surface pressure and 10m Easterly wind speed. The resulting log-likelihood ratio of 3.55 and p-value of 0.0077 indicate that it shares a strong covariate effect with another of the previously fitted variables, or it could also be entirely uncorrelated to the occurrence of rainfall.

Upon further investigation, by swapping the order of fitting for the Easterly and Northerly wind speeds and performing the same tests, there was indication of a strong covariate effect between the two wind speeds, which is expected (Yan et al, 2006). Nevertheless, the addition of the 10m Northerly wind speed did improve the model, albeit only marginally (with a p-value of 0.0077, thus a confidence of 99.2%), as compared to the other variables which indicated strong relations to rainfall occurrence.

The final variable fitted to the GLM occurrence model was cloud cover. With a log-likelihood ratio of only 0.043, and a p-value of 0.77, it indicated that this variable either shared a very strong covariate relationship with one of the previous climate variables, or it did not fit the rainfall occurrence well. Consequently, this variable was not included in the GLM occurrence model as it was redundant for that model fitting.

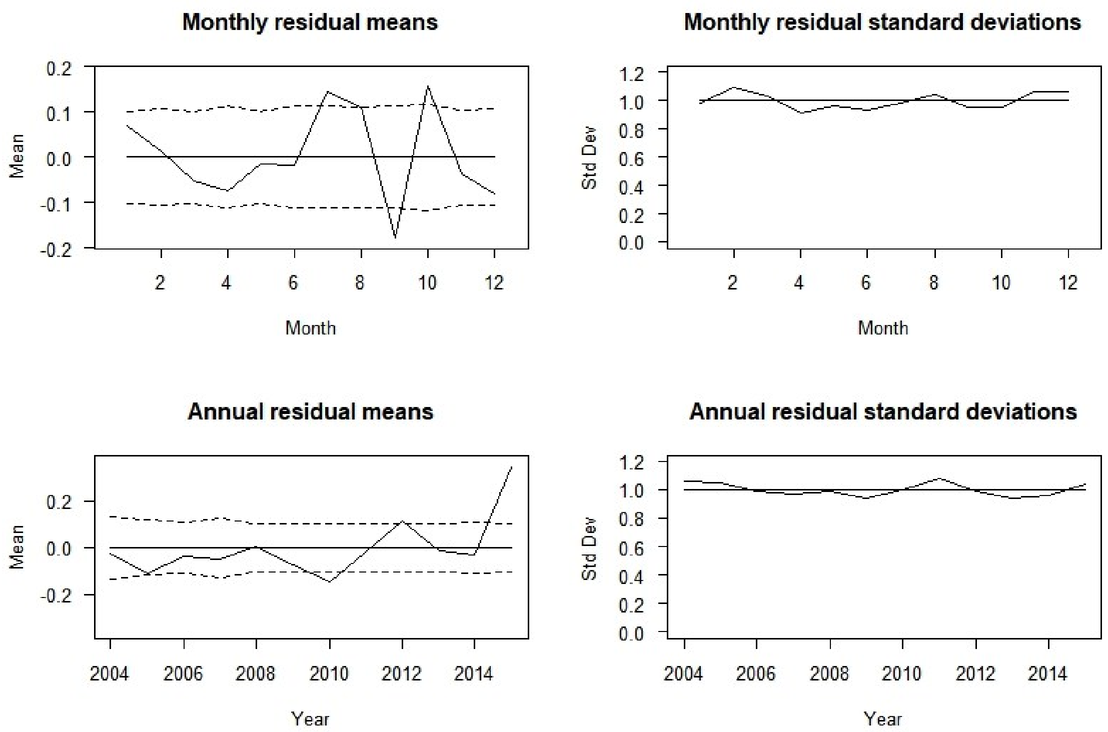

Figure 3.1: Monthly and yearly residual (observed – expected) means and standard deviations for the occurrence GLM following the fitting of all relevant climate variable.

Another approach to assess the goodness of fit of the GLM is to plot the statistics of the residuals between the observed and expected rainfall. Figure 3.1 shows the monthly and yearly means and standard deviations of all residuals, where negative residuals indicate an overprediction by the GLM. While the monthly and yearly mean residuals were generally within the 95% confidence interval, the month of September overpredicted rainfall occurrence, while year 2015 significantly underpredicted rainfall occurrence. The 2015 anomaly can be explained by the exceptional winter of 2015 experienced in the UK, where record persistent rainfall was recorded (McCarthy et al., 2016). In terms of the standard deviations, both monthly and yearly residual standard deviations were relatively well behaved, with small variations about 1.

Amounts model

A similar fitting approach was also adopted for the amounts model, where the GLM was first fitted with a constant, representing the mean of the gamma distribution, before being fitted to temperature, pressure, Easterly and Northerly wind speeds, relative humidity and cloud cover. Table 3.2 tabulates the log-likelihood ratio and the corresponding p-value of the likelihood ratio hypothesis test for each of the fitting stages.

Table 3.2: Log-likelihood ratio and the associated likelihood ratio test p-values for fitting each climate variable consecutively to the GL amounts model.

Climate variable	Dispersion parameter, ϕ	Log-likelihood ratio to previous fit	Likelihood ratio test (p-value)
Temperature	1.5103	20.36	$< 1.8\text{x}10^{-10}$
Surface pressure	1.4887	95.13	$< 2.2\text{x}10^{-16}$
10m Easterly wind speed	1.3908	4.83	0.0019
10m Northerly wind speed	1.386	16.80	$6.8\text{x}10^{-9}$
Relative humidity	1.3693	8.61	$3.3\text{x}10^{-5}$
Cloud cover	1.3609	3.876	0.0054

The amounts model fitting results have some notable similarities and differences to the occurrence model. Similar to the occurrence model, both temperature and surface pressure play a very strong role in determining the amount of rainfall to occur given an occurrence, with very large log-likelihood ratios (two of the largest for this model, at 20.4 and 95.1 respectively) and low p-values for both. This is to be expected as both temperature and pressure are key drivers in controlling the volume of rainfall, with higher temperatures responsible for higher evaporation rates, thus more rainfall (Nkuna and Odiyo, 2016; Chan et al., 2016), and lower pressures responsible for accumulating rainfall over a region (Marsh and Dale, 2002; Golding et al., 2005).

In addition, cloud cover is also found to give poor returns in the fitting (likelihood ratio of 3.88, p-value of 0.0054). While not as poor a fit as in the occurrence model (p-value 0.77), its removal from the GLM fitting wouldn't result in a large difference in the results.

The main difference between the occurrence and amounts model is on the fitting of the two wind speeds. In the occurrence model, by switching the order of the Easterly and Northerly wind speeds, it was determined that both wind speed variables shared a dependency, hence when the second wind speed was fitted to the GLM, it would always produce a low log-likelihood ratio. This was not the case for the amounts model, where the two wind speeds do not share a dependency. The Northerly wind speed had a strong influence on the rainfall amounts (likelihood ratio of 16.8, p-value of 6.8×10^{-9}), while the Easterly wind speed had smaller influence on rain (likelihood ratio of 4.83, p-value of 0.0019). GLM studies by Yan et al. (2002) and Yan et al. (2006) showed that wind speeds would increase around the coastal North Sea regions, supporting the results of the model calibrations.

The mean and standard deviations of the statistical residuals from the amounts GLM are plotted in Figure 3.2. The residuals indicate that rainfall amounts in March and April tended to be overestimated, while rainfall amounts in December might have been underestimated. It should, however, be noted that these were only the amounts of rain generated given a rainy day. If the occurrences of rainy days were underestimated but amounts were overestimated, the effects of both on the mean rainfall might be balanced. This was explored further in the validation exercise.

In addition, the general standard deviations for both monthly and yearly amounts residuals were significantly higher compared to the occurrence residuals in Figure 3.1, with particular peaks occurring in August, September and December, and in years 2013 and 2014. This was due to multiple storm events in 2013 and 2014, both during the summer and winter months (Kendon and McCarthy, 2015). The yearly residual means indicated that the GLM underestimated these storm events.

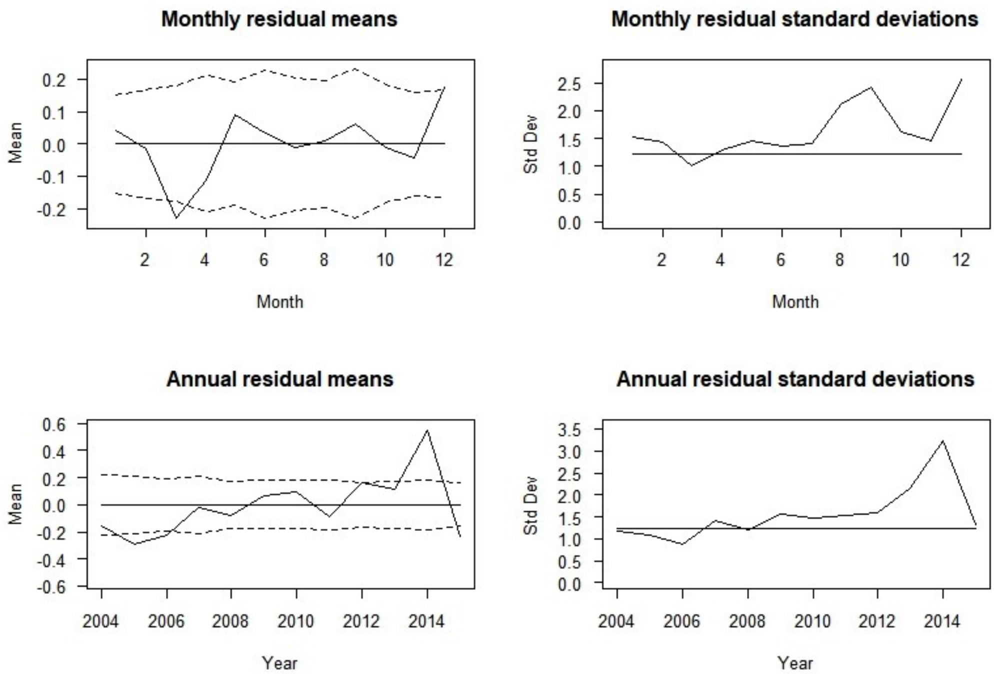

Figure 3.2: Monthly and yearly residual (observed – expected) means and standard deviations for the amounts GLM following the fitting of all relevant climate variable.

3.2.5 GLM simulations and validation

Using the fitted parameters, 100 simulations for each model were carried out and the summary statistics for each simulation calculated. For each simulation, ERA5 climate data for the exact same time period as with the Rayleigh rainfall was used, and the occurrence logistic distribution model was first sampled from to establish whether rainfall will occur on a given day with climate variables for that day. If rainfall is sampled to occur on that day, the amounts gamma distribution is then sampled, given climate variables for that day, to determine the amount of rainfall expected to fall on that day.

The monthly summary statistics were then plotted together with the observed summary statistics to assess the effectiveness of the model in producing synthetic rainfall that would be similar to the observed rainfall. Figure 3.3 shows the monthly summary statistics of the simulations, plotted against the observed summary statistics at Rayleigh (red data). All summary statistics were calculated using the standard approach of taking the means of the monthly summary statistics over the 12 years of data. The cumulative approach was not applied as the summary statistics approach adopted would not have an impact on the comparisons, given that the GLM fitting and simulations do not rely on the summary statistics of the observed rainfall.

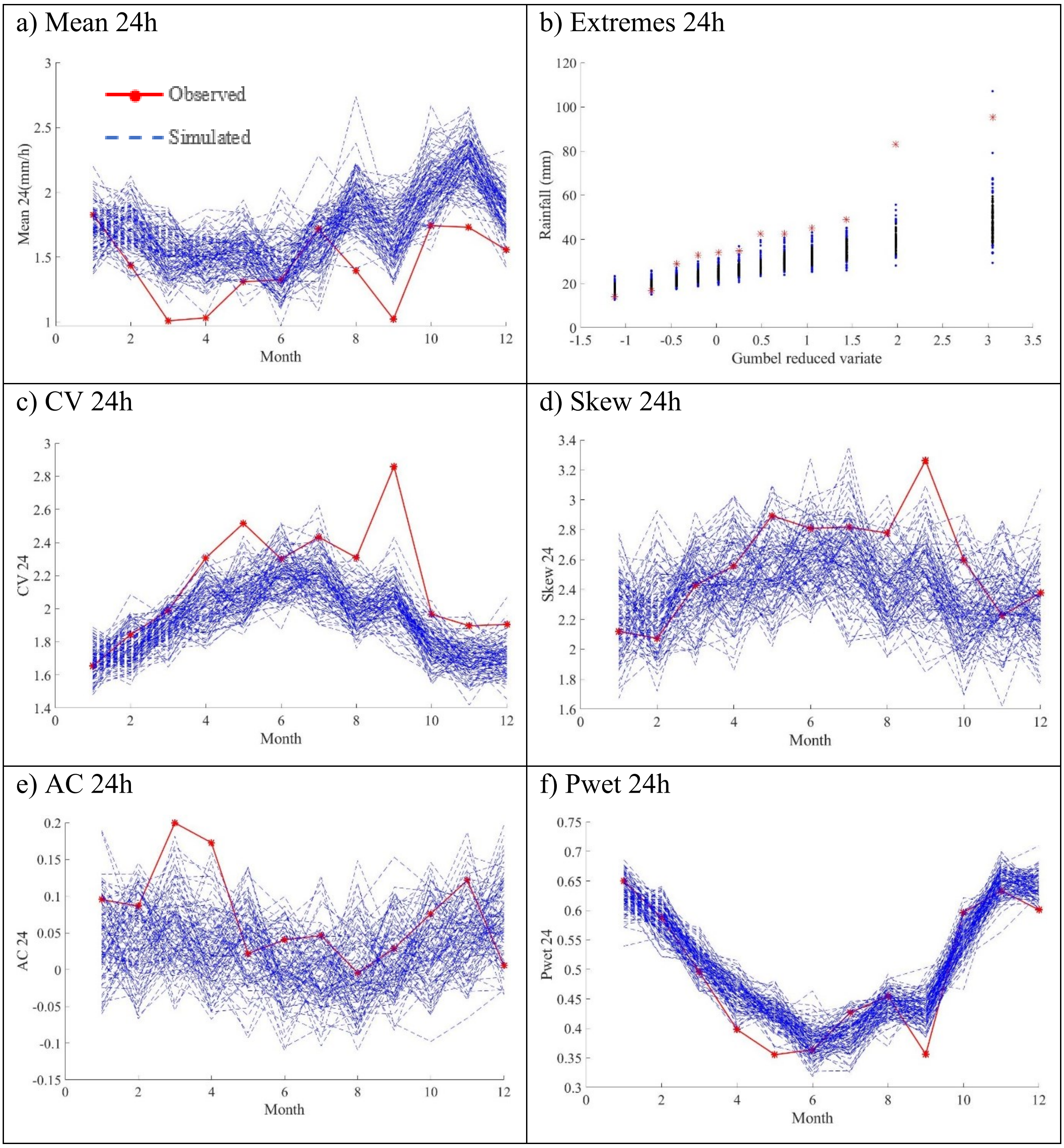

Figure 3.3: Comparisons of monthly summary statistics between 100 GLM daily simulations, using ERA5 climate data, and observed daily rainfall in Rayleigh for 2004-2015. (a) Mean 24h. (b) Gumbel plot of annual maxima. (c) Coefficient of variation for 24h. (d) Skewness for 24h. (e) Lag-1 autocorrelation for 24h. (f) Percentage wet for 24h.

In general, comparisons in Figure 3.3 indicated good agreement between the GLM simulations and the observed summary statistics, in particular for the percentage wet and lag-1 autocorrelation. The mean daily rainfall was generally overestimated, while both the coefficient of variation and skewness were slightly underestimated, especially during the summer. The consequence of lower variability and skewness would indicate that the simulations would not be able to reproduce the extreme events that were documented at the site in the study period. This result was reflected in the Gumbel plot (Figure 3.3(b)), comparing the simulated extremes to the actual extreme events, with nearly all simulations underestimating the extreme events, especially for large return periods.

The accuracy of the occurrence model in reproducing the rainfall was best illustrated in the percentage wet comparison (Figure 3.3(f)), where any overestimations and underestimations of the GLM simulations mirror the mean of the residuals for the occurrence model in Figure 3.1. As the standard deviations were small, there was not much variation among the simulations.

The daily mean rainfall comparison can be viewed as a representation of the combination of both the occurrence and amounts models. The large overestimations, particularly in March, April, September and November can be explained by the negative residual means of either the occurrence or amounts models, or both. For the case of December, as the occurrence model was overestimating, while the amounts model was underestimating, their combined effect resulted in only a small overestimation.

Depending on the GLM methodology and variables used for the fitting, the resulting simulations of higher means and lower extremes were a common occurrence in past analyses. Yang et al. (2005) identified similar results when performing a GLM simulation across Southern England. More recently, GLM simulations undertaken for Portugal showed overestimations for daily rainfalls and incorrect dry spell lengths (Pulquerio et al., 2014).

While the GLM was imperfect in reproducing the observed summary statistics and extremes, it was still able to reasonably reproduce the seasonal changes of the summary statistics. Thus it was judged to be sufficient for it to be used in projecting future rainfall based on the UKCP18 climate projections for the UK.

3.3 Future daily rainfall simulations

3.3.1 UK climate projections and UKCP18

The modelling of global climate change scenarios due to increases in carbon emissions has been undergoing continuous developments since the 1970s (Wigley et al., 1980), with the construction and refinements of various Global Circulation Models (GCMs) of increasing complexity. However, as GCMs are too spatially coarse (with grid sizes of up to 500km by 500km) to inform climate projections on a national level such as the UK, various downscaling methodologies were implemented to derive more applicable regional projections. Hulme and Dessai (2008) outline some of the various strategies that early UK climate projection teams adopted to achieving this goal between the years 1991 and 2002.

The first official UK climate projection was published by the Climate Change Impacts Review Group (CCIRG, 1991) in 1991, commissioned by the Department of the Environment. Their work used pattern scaling to downscale and construct regional projections of temperature and precipitation changes in the UK up to 2050, based on the GCMs published in the First Assessment Report of the Intergovernmental Panel on Climate Change (IPCC, 1990). However, as GCMs then were still highly simplistic, spatially and temporally coarse, only seasonal averages of regional temperature and precipitation based on one GCM climate scenario were produced for the CCIRG91.

The second climate projection for the UK came in 1996, with the conclusion of the CCIRG96 project (CCIRG, 1996). With significant improvements to the base GCM model, significant regional details on projected climate could be gathered. It was in this project that regional patterns of drying in the south and wetting in the north during summer were first projected.

The UK Climate Impacts Programme 1998 (UKCIP98; Hulme and Jenkins, 1998) was the first regional climate projection to consider 4 different climate forcing scenarios up to year 2080. These forcing scenarios range from low to high, based upon 0.5% to 1% per annum growth in greenhouse gas concentrations, with estimated mean global surface warming ranging from 1.5°C to 4.5°C. However, pattern scaling was still needed for regional downscaling and interpolation from the GCM projections.

Regional climate projections have seen a significant improvement with the publication of the fourth generation of UK climate scenarios in UKCIP02 (Hulme et al., 2002). Similar to the UKCIP98, the UKCIP02 also presented 4 different climate scenarios, tied to a different emission profile derived from the IPCC Special Report on Emission Scenarios (Nakicenovic et al., 2000). However, instead of a simple pattern downscaling, regional climate models (RCMs) were employed to model within and between grids of the larger GCM. This produced a significantly finer spatial resolution of 50km grids with daily weather variables.

In the UKCIP02 publication, climate variable uncertainties were purely qualitative as only single estimates of climate projections were provided, in part due to the significant computation costs associated with the RCMs. Improvements to the models and computational speed allowed analyses of multiple models, generating a range of climate projections instead, thus allowing the development of probabilistic climate projections in the UKCP09 project (Jenkins et al., 2010). While climate projections were available at a resolution of 25km grids, a stochastic weather generator was developed in conjunction with the main RCM to further refine the resolution to 5km grids (Jones et al., 2009), with temporal resolutions as fine as hourly. This development enabled the increasing adoption of climate projection in infrastructure design, particularly in water resource management (Christierson et al., 2012) and in the combined storm-sewerage system management (Dale et al., 2015).

The current iteration of UK regional climate projections is the UK Climate Projections 2018 (Lowe et al., 2018). With a spatial resolution of up to 12km, the UKCP18 land projections (Murphy et al., 2018) are able to replace the need for stochastic weather generators in UKCP09. The climate forcing scenarios used now follow the IPCC Representative Concentration Pathways (RCP), outlined in the Fifth Assessment Report (IPCC, 2013), superseding the previous emission scenarios adopted in UKCP09.

The RCPs are defined by their total radiative forcing predicted to occur in the year 2100, thus RCP8.5 would project a radiative forcing of 8.5 W/m^2 in 2100, which is equivalent to 1370ppm of CO_2 (Van Vuuren et al., 2011). In addition, each RCP scenario will have different trajectories before 2100, with each scenario representing the adoption of various climate change mitigation strategies. RCP8.5 assumes that there is no policy change internationally to mitigate greenhouse gas emissions, while RCPs 6 and 4.5 assume that some degree of reduction in emissions are achieved to reach a stable radiative forcing of 6W/m^2 and 4.5W/m^2 in 2100 respectively.

Recent developments into the Convection Permitting Model (CPM) have further allowed the development of sub-daily 2.2km grid projections (Kendon et al., 2019) in UKCP18, as convective storms are now modelled with a finer spatial and temporal resolution. However, there is still much discussion surrounding the validity and accuracy of CPMs at this time (Chen et al., 2020; Kendon et al., 2021), thus CPM projections have not be used for this research.

This research adopted the climate projections from the 12km land projection in the UKCP18 publication. Due to time constraints, only the RCP8.5 climate scenario was investigated, however the methodologies used in this research are applicable to other RCP climate scenario projections.

3.3.2 Validation of UKCP18

To ensure that there are no biases in the use of UKCP18 climate data, validation exercises for the observed time period must be performed as outlined in Fung (2018). Therefore, the summary statistics for the years 2004 to 2015 for each of the 100 simulations were compiled and plotted together with the observed summary statistics at Rayleigh in Figure 3.4. The fits in Figure 3.4 demonstrated that the application of GLM with UKCP18 climate variables underestimated the mean daily rainfall and percentage wet for most of the years, particularly during the summer. Coefficient of variation and skewness on the other hand were well reproduced.

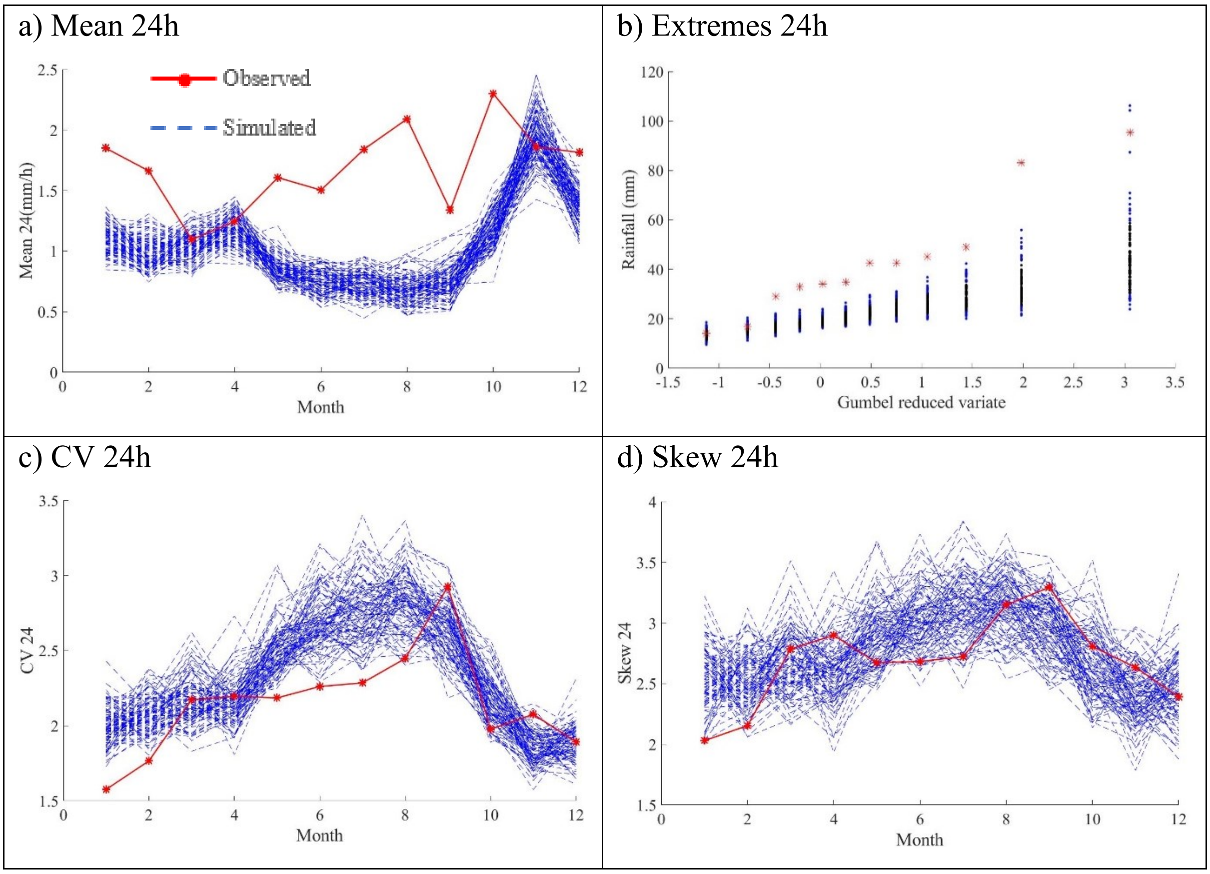

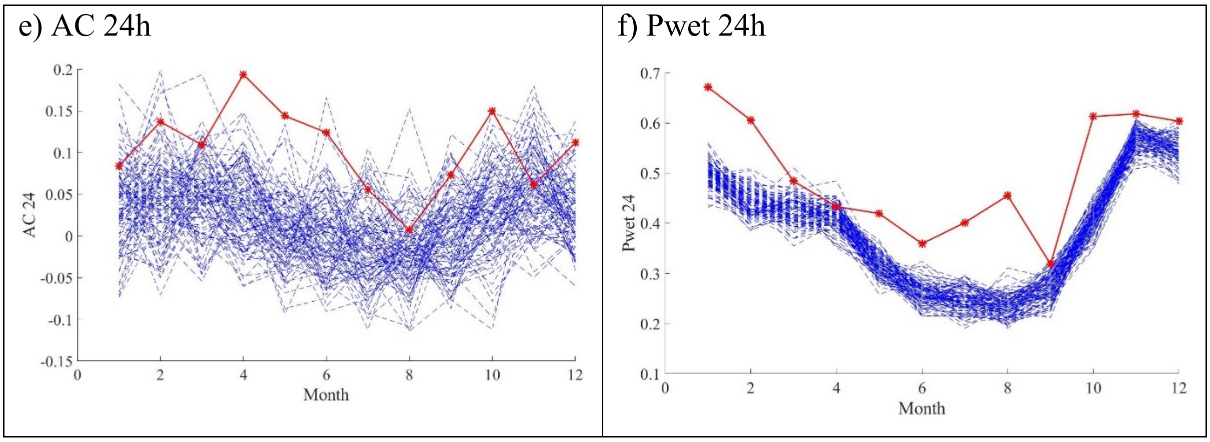

Figure 3.4: Comparisons of monthly summary statistics between 100 GLM daily simulations using UKCP18 climate data and observed daily rainfall in Rayleigh for 2004-2015. (a) Mean 24h. (b) Gumbel plot of annual maxima. (c) Coefficient of variation for 24h. (d) Skewness for 24h. (e) Lag-1 autocorrelation for 24h. (f) Percentage wet for 24h.

While there was a significant gap in mean rainfall during the summer, it was decided that bias correction for the mean was unnecessary in this situation, as both the coefficient of variation and skewness fitted well with the observed data. In addition, the introduction of bias correction has been known to result in some physical inconsistencies and carried their own set of assumptions, most notably the stationarity of biases which was often criticised (Maraun, 2016).

3.3.3 Future rainfall simulations

With the climate model validated in the previous section, 100 future rainfall series based upon the projected climate variables from 1980 to 2080 were then simulated using the fitted GLM. As the UKCP18 RCM runs were performed in decadal intervals before being compiled into a full series (Lowe et al., 2018), decadal monthly rainfall mean, coefficient of variation, skewness, lag-1 autocorrelation, percentage wet, and annual maxima were adopted to assess the impact of climate change on rainfall summary statistics decade on decade. The projected mean daily rainfall per month is plotted in Figure 3.5 with boxplots for each decade from 2020 to 2080, indicating the range, interquartile range and mean for each month and each decade. Similar plots for the other summary statistics can be found in Appendix D.

The long whiskers but relatively short boxes in Figure 3.5 indicate that, while the general spread of the summary statistics is large due to the uncertainties in the GLM methodology and natural variation of the simulations involved, at least 50% of the results are concentrated within a relatively narrow band. As an example, the daily rainfall mean of January for the period 2020-

2030 ranges from 0.8mm/day to 1.6 mm/day. However, 50 simulations are concentrated within 1.2mm/day to 1.4mm/day, with a mean of 1.3mm/day.

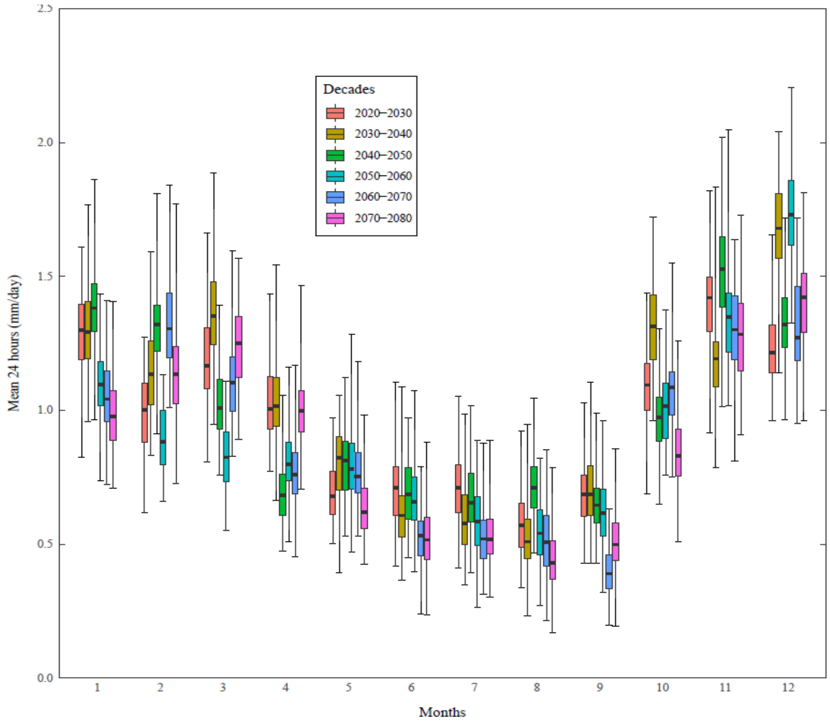

Figure 3.5: Plot of monthly summary statistics for each decade from the GLM-UKCP18 simulations, for the period 2020 – 2080.Each whisker indicates the range, while each box indicates the interquartile range and mean.

While Figure 3.5 does show a trend where summer average rainfall is decreasing, this general behaviour is not so clear in the plot of this type. Therefore, Figure 3.5 was replotted to only include the means and their evolution through time, as the means are centres of the interquartile boxes, hence would serve as a good representative of the behaviour for each month and decade. The same procedure was repeated for the other summary statistics, and the results plotted in Figure 3.6 for each of the ten decades between 1980 and 2080.

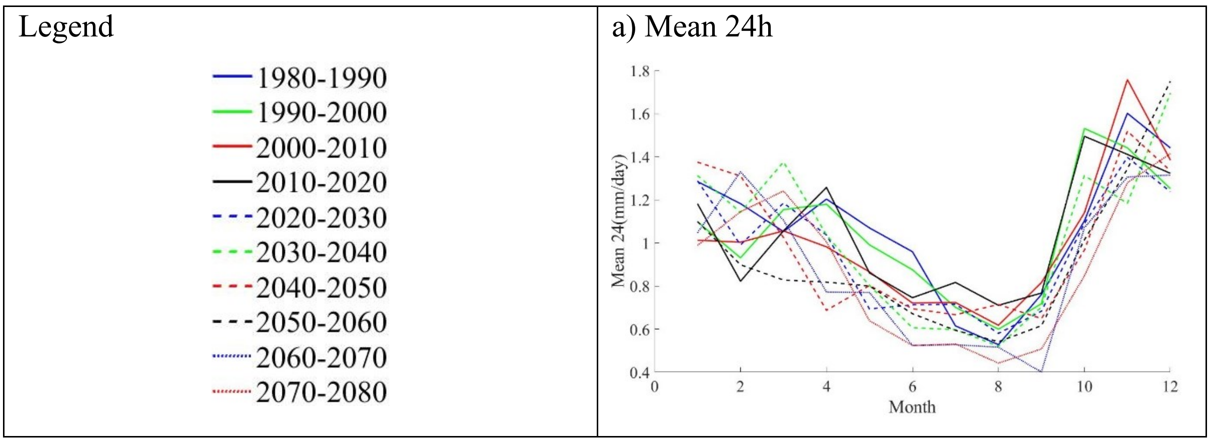

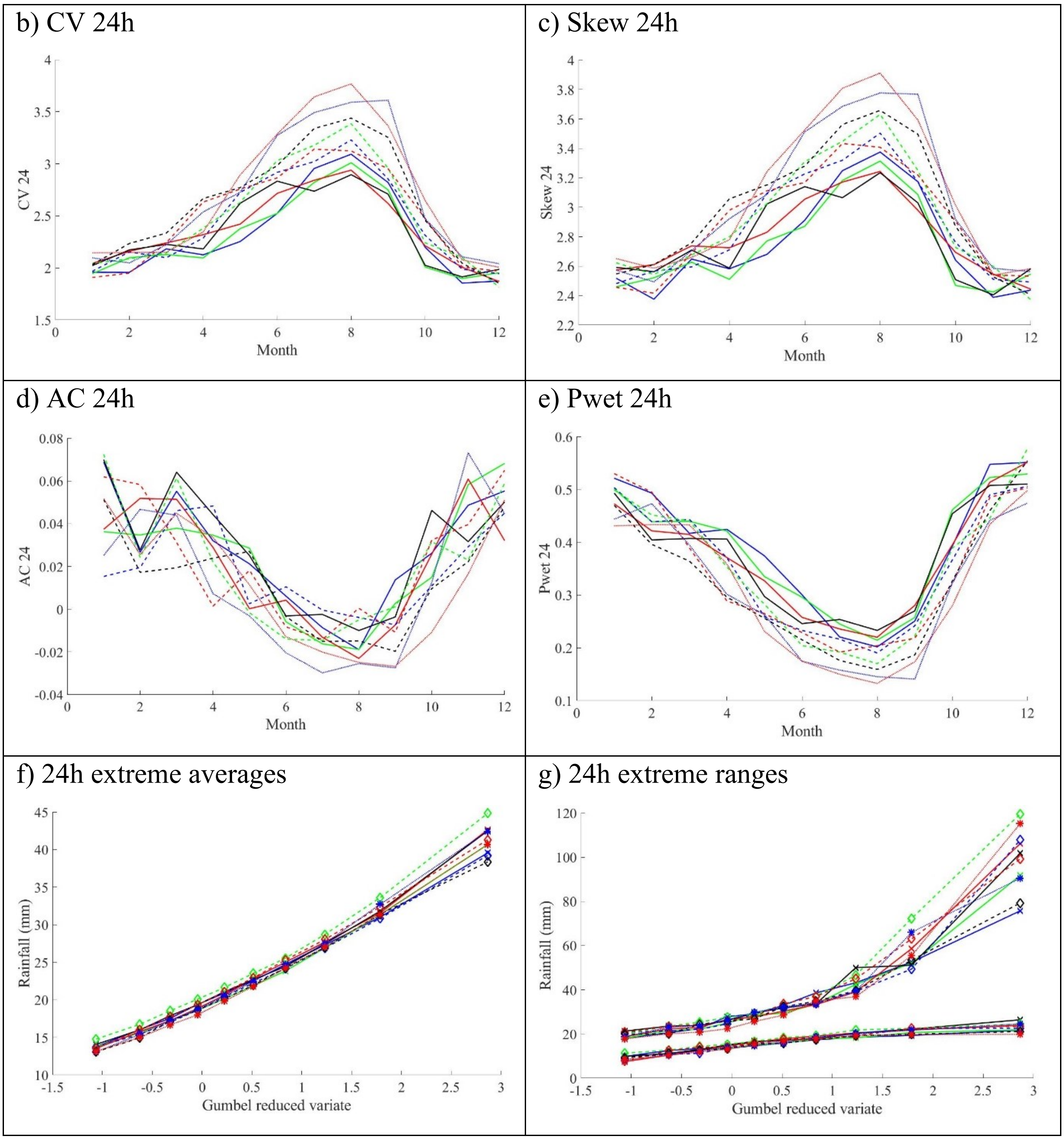

Figure 3.6: Plots of average monthly summary statistics for each decade from 1980 – 2080 for 100 GLM daily simulations using UKCP18 climate data. (a) Mean 24h. (b) (b) Coefficient of variation for 24h. (c) Skewness for 24h. (d) Lag-1 autocorrelation for 24h. (e) Percentage wet for 24h. (f) 24h annual maxima extreme averages. (g) 24h annual maxima extreme range.

The decadal averages of the summary statistics for the projected rainfall now depict a clearer trend caused by the projected climate change at the Rayleigh site. The daily means in Figure 3.6 (a) indicated that average summer rainfall would decrease over the next few decades (0.8mm/day in 2010-2020 to 0.5mm/day in 2070-2080), while winter rainfall averages remained unchanging. This was in response to drier weather conditions in the future, influenced by increases in both temperature and pressures, especially during the summer. This result agreed with UKCP18 probabilistic projections with decreases in mean precipitation of 30% around the region (Murphy et al., 2018).

While there are no discernible trends for winter rainfall averages, the percentage wet decreased slightly by 0.05 in the months of January and December from present rainfall to the 2070-2080 decade, indicating slightly higher storm intensities during the winter in the future. The month of February, however, saw a slight increase in both mean rainfall and percentage wet towards 2080, possibly highlighting a later occurrence of storms during the winter due to a changing climate. This trend was observed by Blöschl et al. (2017) who noted a shift of 8 days per 50 years for winter storms in the North Sea for period 1960 – 2010.

In addition, increases in both skewness and coefficient of variation in the future, indicated in Figures 3.6(b) and 3.6(c), shows a higher variability in rainfall amounts for the future. This is particularly true for the summer months of June, July and August. The increases in skewness and variance indicates that there will be more extreme rainfall during these months.

To investigate the impacts of climate change on extremes, the average annual maxima plot for each decade is first plotted in Figure 3.6(f). While there is some slight movements in average extremes for the very high return periods, this plot does not fully demonstrate the ranges in which the extremes can occur. Thus Figure 3.6(g) plots the maximum and minimum ranges of annual maxima for each decade. This plot now demonstrates very clearly that the maximum range of extreme daily rainfall for the future is noticeably increasing, especially for higher Gumbel reduced variates (return periods). This was expected with higher skewnesses and variances for future rainfall.

3.3.4 Representative monthly projected rainfall series

Due to the intensive computational demands of the geotechnical numerical analysis when analysing the embankment's lifecycle, a representative monthly projected rainfall series was adopted instead of running all 100 different projected future rainfall simulations. While it is recommended to run 3 different representative scenarios representing high rainfall, low rainfall and average rainfall throughout the series, due to time constraints only the average scenario is considered in this thesis.

It was found that the monthly and yearly rainfall of simulation 12 (in red) generally follows the monthly and yearly simulation trends of all 100 simulations (Figures 3.7(a) to 3.7(f)), and is only at the top and bottom extremes of the 100 simulations for only a total of 6 months throughout its entire time series from 2017 – 2080.

a) Monthly rainfall 2017-2029

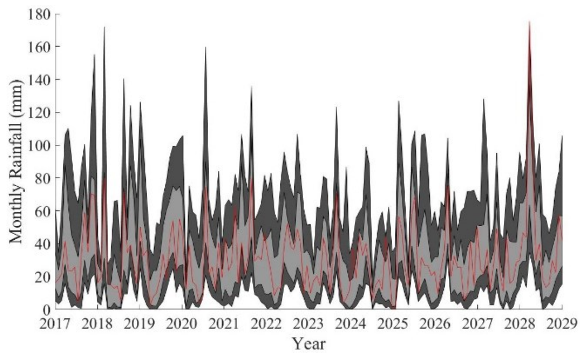

b) Monthly rainfall 2030-2039

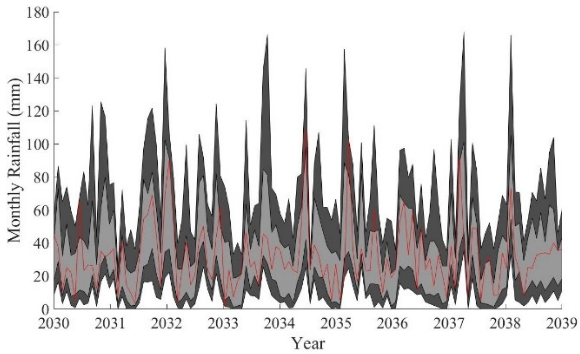

c) Monthly rainfall 2040-2049

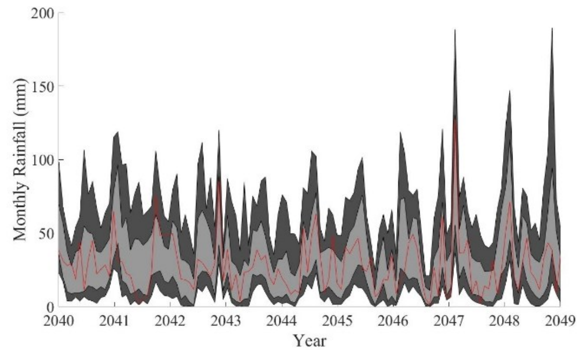

d) Monthly rainfall 2050-2059

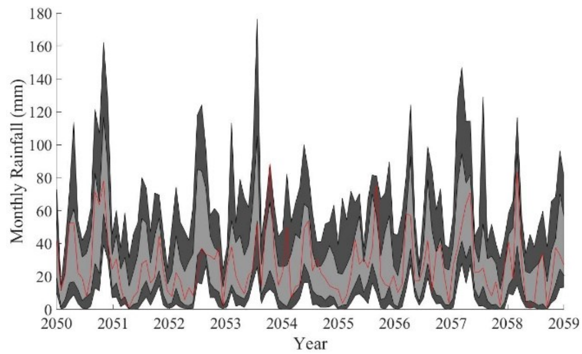

e) Monthly rainfall 2060-2069

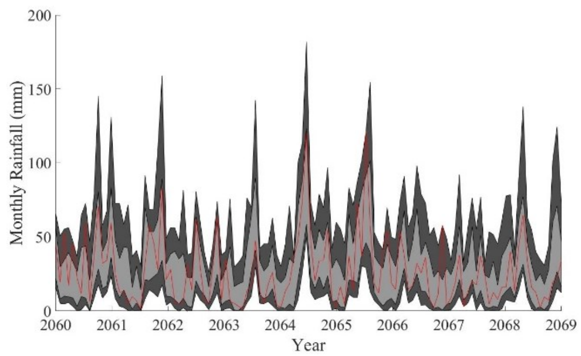

f) Monthly rainfall 2070-2080

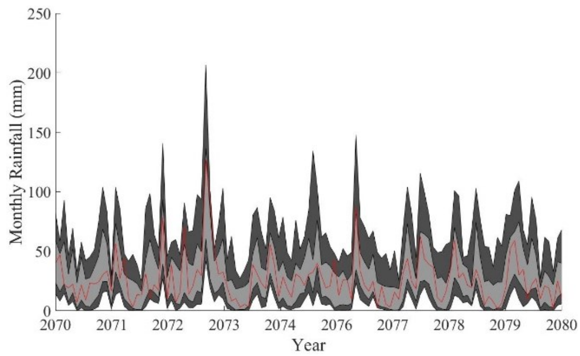

g) Yearly rainfall

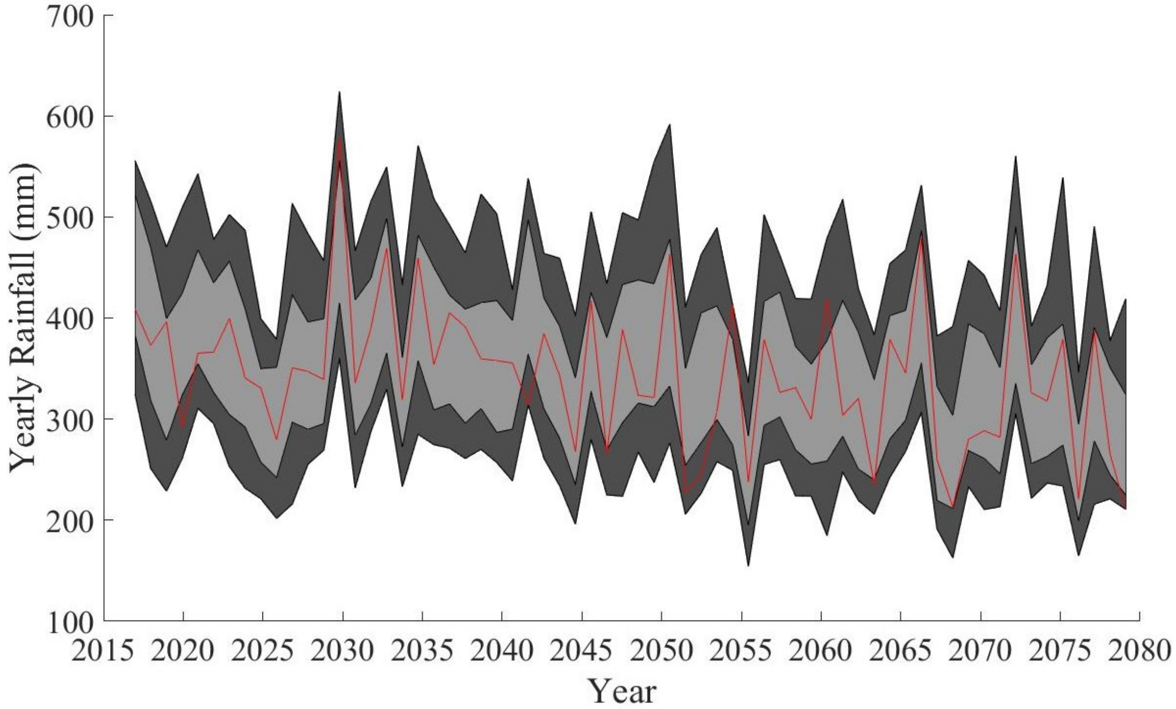

Figure 3.7: Plots of monthly simulated rainfall from years (a) 2017-2029, (b) 2030-2039, (c) 2040-2049, (d) 2050-2059, (e) 2060-2069, (f) 2070-2080 and (g) yearly simulated rainfall for the period 2017 – 2080. The light grey regions represent the middle 80% of the simulated amounts, while the darker grey regions are the top and bottom 10% of simulated amounts for the months and years. Simulation 12 rainfall is plotted in red.

Figure 3.7(g) plots the yearly aggregation instead, further demonstrating that simulation 12 is a suitable representation of the projected rainfall as it is never the lowest nor the highest for each year, and is generally within the middle 80% range of the simulated rainfall. Therefore, simulation 12 was then adopted as the precipitation boundary condition in the lifecycle assessment finite element analyses of the embankments in both Chapters 7 and 8.

3.4 Conclusions

The Generalised Linear Model fitting demonstrated that there exist strong correlations between the occurrence and amount of rainfall with several climate variables, most notably temperature and pressure. Validation exercises with ERA5 showed that while coefficient of variation, skewness and percentage wet were generally well reproduced, the means were overestimated and the extremes were underestimated. This was expected as the GLM model struggled to fit the extreme storm events observed in 2013 and 2014.

With the relationship established, daily projected rainfall that takes into account climate change effects based on the RCP8.5 scenario can be simulated by utilising UKCP18 climate projections, overcoming the stationarity issues inherent in the BLRP approach. Validation of the model with present rainfall showed that while means, percentage wet and extremes were underestimated, coefficient of variation and skewness were well reproduced.

The simulated projected rainfall highlighted the impacts of climate change on rainfall at Rayleigh. Summer rainfall was projected to decrease by as much as 30% by 2080 as compared to present rainfall, while winter storms and rainfall were expected to occur later in February, with higher intensities. Both coefficient of variation and skewness were also expected to increase, increasing the range of extremes that can occur in the future.

Finally, a representative simulated rainfall series (Simulation 12) was selected to be employed in the geotechnical numerical lifecycle analyses in Chapters 7 and 8.

Chapter 4: Rainfall Downscaling

4.1 Introduction

In Chapter 3, the Generalized Linear Model (GLM), applied to the rainfall series from the weather station at the town of Rayleigh in Essex, UK, was shown to be an effective modelling approach in projecting future rainfall under projected future climate parameters that are affected by climate change (RCP 8.5 scenario). As the model was only able to simulate daily rainfall using daily climate inputs, a downscaling process had to be implemented to generate sub-daily rainfall series for future climates.

In Chapter 2, it was briefly discussed that the means of rainfall taken at different time resolutions were related with a scaling property. This fractal properties of rainfall were explored in greater detail and employed in the downscaling of daily rainfall in this chapter.

The chapter first provides a literature review on the fractal properties of rainfall, covering the history and development of the relationship between fractals and rainfall. A downscaling methodology, involving the scaling properties of rainfall summary statistics and the Bartlett Lewis Rectangular Pulse (BLRP) models calibrated in Chapter 2, was then established. The methodology was applied to present daily rainfall measured at the Rayleigh station to assess its effectiveness in downscaling present rainfall, which is then compared with actual sub-daily present rainfall at the same location.

The downscaling process was applied to the projected future daily rainfall from the GLM simulations in Chapter 3, producing future sub-daily rainfall for the Rayleigh site under RCP8.5 conditions. The projected trends of the downscaled rainfall were explored and noted. The range of projected extreme values was also plotted and discussed. Finally, a design storm event of 95mm of rainfall in a day was selected, which was used in Chapter 7 for resilience assessments.

4.2 Scaling and fractal properties of rainfall

4.2.1 Introduction

While the theory of fractals was first developed by Mandelbrot in 1975, the effects of scaling in hydrology were first observed by Hurst while working on water storage and reservoir maintenance. Hurst was the first to develop a statistical method called "rescaled range" (Hurst, 1965), which he started applying not only to his original problem of reservoir storage, but also to other hydrological phenomena such as rainfall. With the establishment of fractal geometry (Mandelbrot, 1975; 1982), the scaling nature of rainfall was extensively studied (Feder, 1988; Falconer, 2004).

Scaling as a concept generally refers to a relation in the property of a structure or object when observed at different scales (Mandelbrot, 1982). The property in question can be anything, from a simple geometric appearance (in which case the scaling is termed self-similarity), or it could refer to a statistical property (in which case the scaling is termed as scale invariance). Within rainfall, scaling is almost always taken as scale invariance (Feder, 1988).

Fundamentally, a property is said to exhibit scaling behaviour when it obeys a power-law relationship:

$$N(s) \propto s^D \tag{4.1}$$

where N(s) is the scaling property, s being the scaling resolution (typically temporal or spatial), and D the scaling power or fractal dimension. One of the fastest methods to check for scaling relationships is to plot $N(s)$ vs s on a log-log plot. If $N(s)$ is scaling over a certain range of scales, it will exhibit a straight line (of gradient D) within that scaling regime. This was demonstrated by Hubert et al. (1993) with point rainfall volume against duration, obtaining a scaling power, $D \approx 0.5$.

Despite disagreements to the use of log-log plots due to their subjectivity and large uncertainties (Tsonis and Elsner, 1995), other methods of detecting scaling do exist, such as with the use of an empirical probability distribution function of rainfall depths (Lovejoy and Mandelbrot, 1985), or with the use of the power spectrum and Fourier transform (Tessier et al., 1993). With the establishment of the scaling behaviour and the scaling regime of a given rainfall series, it is possible to downscale rainfall properties from a coarser to a finer scale.

4.2.2 Downscaling vs disaggregation

The terms downscaling and disaggregation are commonly confused with one another. However, there is a significant difference between the two terms. Disaggregation involves reversing the aggregation of rainfall volume, thus concerning rainfall at every scale. This sets a significant constraint on the model, often at the cost of other important rainfall properties such as variance or extremes (Pui et al., 2012; Lu and Qin, 2014). Popular and frequently employed rainfall disaggregators include the random cascade model, based on the scale-invariance theory of rainfall (Gupta and Waymire, 1993), and the method of fragments (Srikanthan et al., 2006).

In a downscaling model, however, the model is not constrained by conserving rainfall. Instead, a downscaling model can be used to synthetically generate downscaled rainfall which shares similar statistical characteristics to the observed rainfall. Poisson cluster models (Rodriguez-Iturbe et al, 1987; Cowpertwait et al., 2006), such as the Bartlett-Lewis (BLRP) and Nelson-Scott models, are commonly employed stochastic models to generate the synthetic rainfall. Studies by Onof et al. (1996) showed that the BLRP and BLRPR models were able to replicate the scaling behaviour of up to the second order of moment and were unable to reproduce scaling for higher orders.

However, the cluster of Poisson models requires either calibration with a fine resolution rainfall record, or other methods in deriving sub-daily summary statistics, before it can proceed to generate synthetic downscaled rainfall. In the Onof et al. (1996) study, high quality tipping bucket rain gauge data was used for the calibration of the BLRP models. However, this approach was unable to consider non-stationarity and thus was not be suitable for this research. Instead, the scaling relationships of rainfall statistics were used for the downscaling of daily projected future rainfall series.

4.3 Downscaling of present rainfall

4.3.1 Summary statistics scaling

To investigate the suitability of the downscaling methodology discussed in the previous section, the summary statistics of present rainfall (from Rayleigh weather station) at 15 minutes, 30 minutes, 1, 2, 4, 8, 12, 16, 20 hours, and 1, 2, 3, 4 days resolutions were first calculated. A 'linear' extrapolation line in log-log space was then produced by fitting for only the daily (1, 2, 3, and 4 days) time resolutions, reflecting the situation where only daily rainfall is available and is downscaled, with the other sub-daily resolution summary statistics used in assessing the accuracy of the downscaling methodology in deriving sub-daily summary statistics.

The downscaling fits for the monthly means were plotted in Figures 4.1(a) (January – June) and (b) (July – December). The fitting showed good agreement between the extrapolated scaling line and the actual means up to the 15 minutes scale for all months. This was as expected as means exhibit a large scaling regime between a few minutes to a few years (Hubert et al., 1993).

(a)

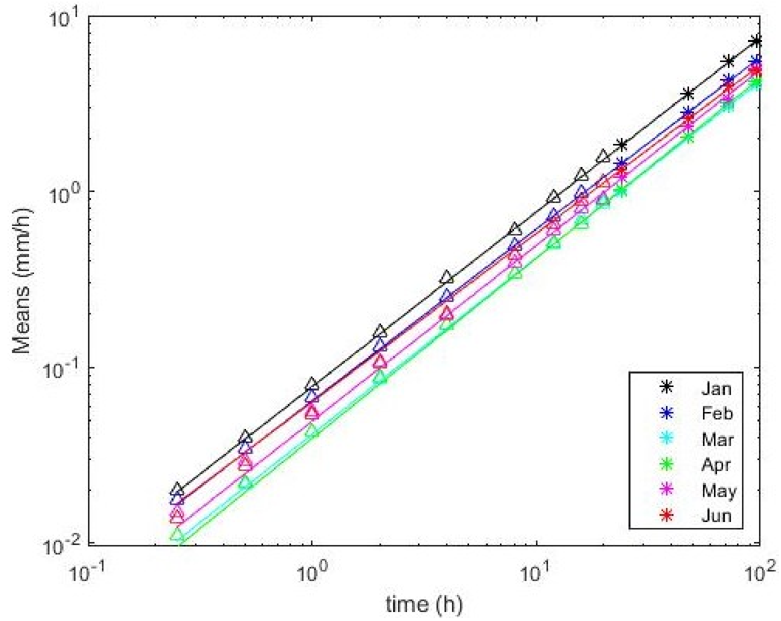

(b)

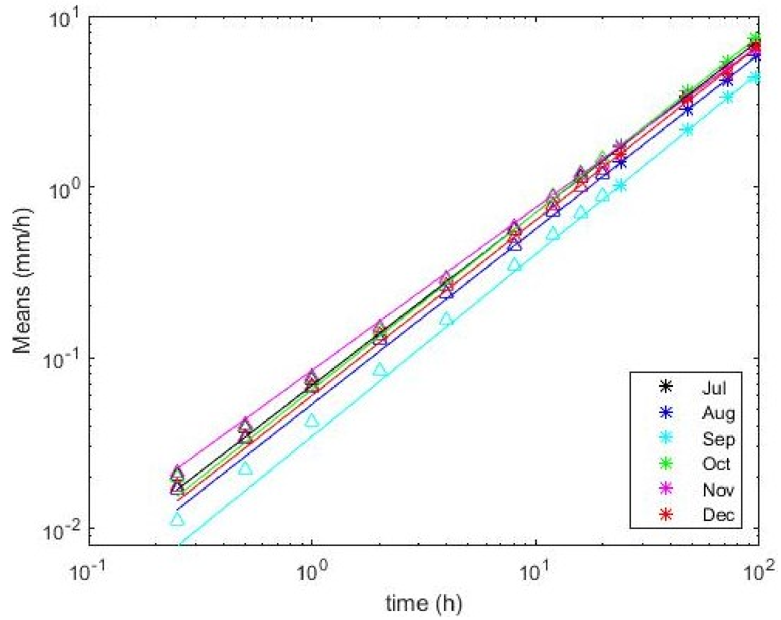

*Figure 4.1: Downscaling of means for the months (a) January to June, and (b) July to December. Triangles are observed sub-daily statistics not used in the fitting, while * are the daily and above (supra-daily) statistics used for the downscaling.*

Nevertheless, it can be seen in Figure 4.1(b) that the fits for July to December generally perform poorer than those in January to June. This may be attributed to more extreme but small storm events during the summer months from July onwards. Two of the strongest storms on record can be found in July and August, as discussed in Chapter 2.

The variance, on the other hand, did not exhibit a similar single scaling regime as did the mean, with the variance having three distinct scaling regimes, from the sub-hourly to weekly time resolutions (Figure 4.2).

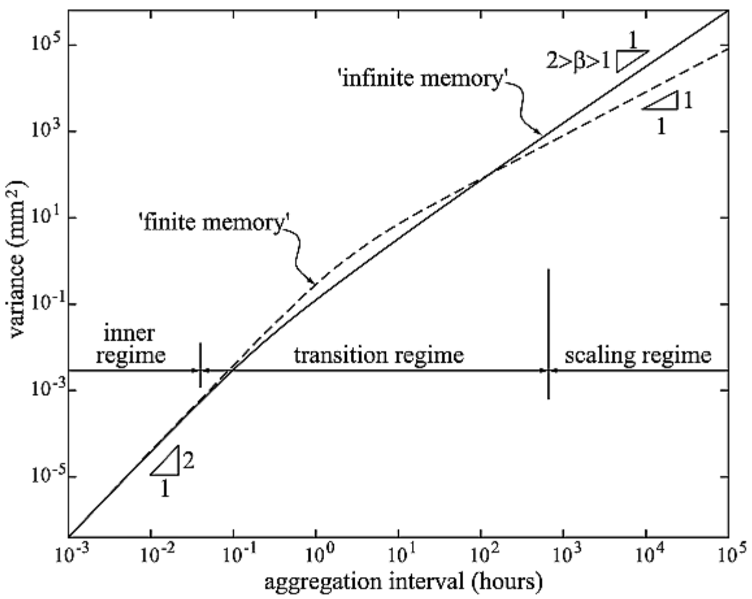

Figure 4.2: The inner, transition and scaling regime of variance across the sub-hourly to weekly aggregation interval (Marani, 2003).

Marani (2003) described the three regimes as follows:

a) An inner regime (sub-hourly and below) in which the variance tends to T^2 as T tends to 0, derived by taking the first 2 terms of the Taylor series of the integration of the autocorrelation function of a stationary instantaneous rainfall intensity series (Vanmarke, 1983).
b) A scaling regime (daily and above) that depends on the memory of the rainfall. Rainfall is said to have finite memory if its autocorrelation function decays rapidly enough such that the autocorrelation tends to 0 when the interval tends to infinity, which is more common during the summer months with shorter, intense rainfall.
c) A transition regime that governs the transition from the inner to scaling regime.

Due to the different behaviour patterns between the inner and scaling regimes, it is not possible to apply a simple linear extrapolation on daily variance, as it would overestimate the variance at the finer time scales. Marani (2003) proposed Equation 4.2, combining the asymptotic behaviour of the variance at both the inner and scaling regimes to achieve a smooth function which transitions from the inner regime to the scaling regime:

$$\sigma^2(T) = 2\sigma_i^2 \frac{\epsilon}{\alpha}\left[\frac{\epsilon}{\alpha}\left(e^{-\frac{\alpha T}{\epsilon}} - 1\right) + T\right] \qquad T \le \epsilon$$

$$\sigma^2(T) = 2\sigma_i^2 \left[\frac{\epsilon^\alpha e^{-\alpha}}{(1-\alpha)(2-\alpha)} T^{2-\alpha} + \frac{\epsilon}{\alpha}\left(1 - \frac{e^{-\alpha}}{1-\alpha}\right) T + \frac{\epsilon^2}{\alpha^2}\left(e^{-\alpha} - 1\right) + 2\frac{\epsilon^2 e^{-\alpha}}{\alpha(2-\alpha)}\right] \qquad T \ge \epsilon \qquad (4.2)$$

where ϵ governs the time interval when the regime changes from the inner to the scaling regime, α is the exponent governing the scaling regime where $\sigma^2(T) \propto T^{2-\alpha}$ and σ_i^2 is the variance of the continuous process of rainfall intensity. This relationship was validated with field data from various climate systems across the world in Marani (2005).

However, as only daily and above resolution variances were available for downscaling in the current study, it was not possible to estimate ϵ, as the transition point would likely exist in the sub-daily time scales, particularly during the summer months (of July, August, September) when the autocorrelation decays rapidly. This was also observed in Marani and Zanetti (2007), who concluded that including external climatic information to informing a suitable estimate of ϵ could help with the downscaling of the variance.

(a)

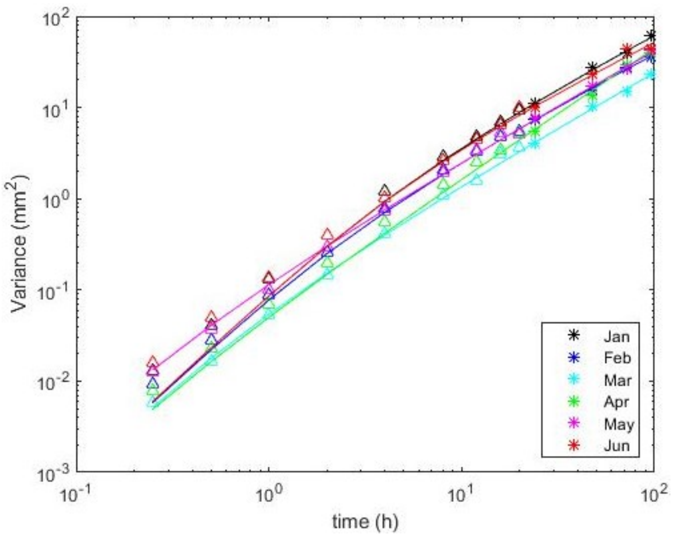

(b)

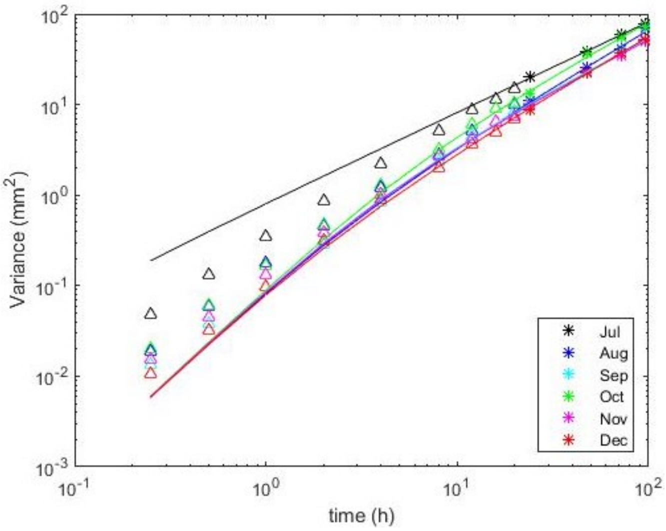

*Figure 4.3: Downscaling of variance using the Marani (2003) expression in Equation 4.2 for the months (a) January to June, and (b) July to December. Triangles are observed sub-daily statistics not used in the fitting, while * are the supra-daily statistics used for the downscaling.*

Therefore, implementation of Equation (4.2) in downscaling daily variance would often lead to an underestimation of fine scale variance, as the transition point is often taken to be larger than it should theoretically be. This is shown in Figures 4.3(a) and (b) for the Rayleigh rainfall.

An alternative solution to downscaling is to downscale the statistical moment, $E(X^n)$, where n is the order of the moment, deriving the variance from the downscaled moment instead of downscaling the variance directly. Described in Gupta and Waymire (1990), it was found that the moments generally behave linearly across the time scale, with the gradients of each order of moment then behaving linearly (simple scaling), or non-linearly (multi-scaling) when plotted vs the order of moment, with rainfall typically exhibiting multi-scaling behaviour. Onof et al. (1996) explored this linear scaling in the second order in greater detail, outlining its suitability in downscaling the variance via the relation:

$$\sigma^2 = E(X^2) - (E(X))^2 \tag{4.3}$$

where $E(X^2)$ is the second order of moment, and $E(X)$ is the first order of moment or the mean.

This downscaling approach was applied to the Rayleigh rainfall, with the resulting extrapolated variance plotted against observed variance in Figures 4.4(a) and (b). This approach showed much better extrapolation results in downscaling the variance from daily to sub-hourly scales, with only the summer months of June and July showing some significant divergence below the hourly scale. Due to the faster implementation of this model and better downscaling results, it was decided to use this approach for downscaling the variance.

(a)

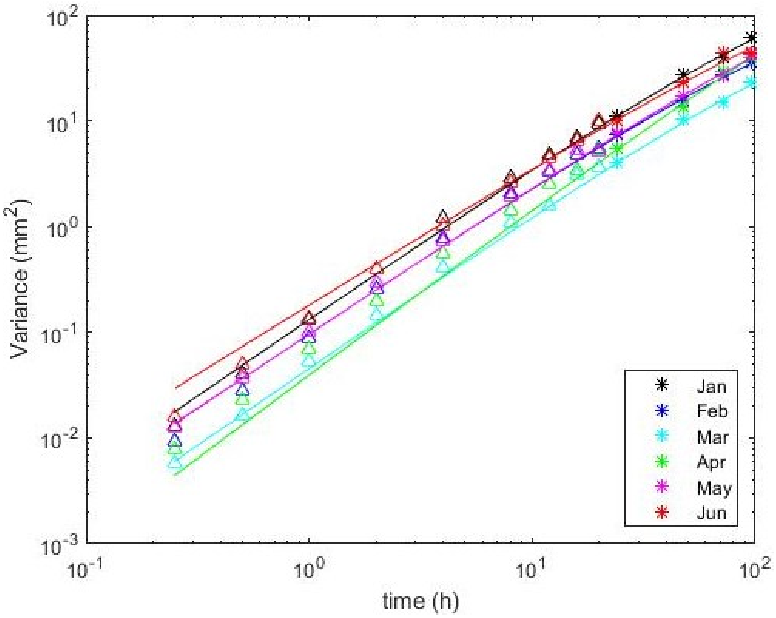

(b)

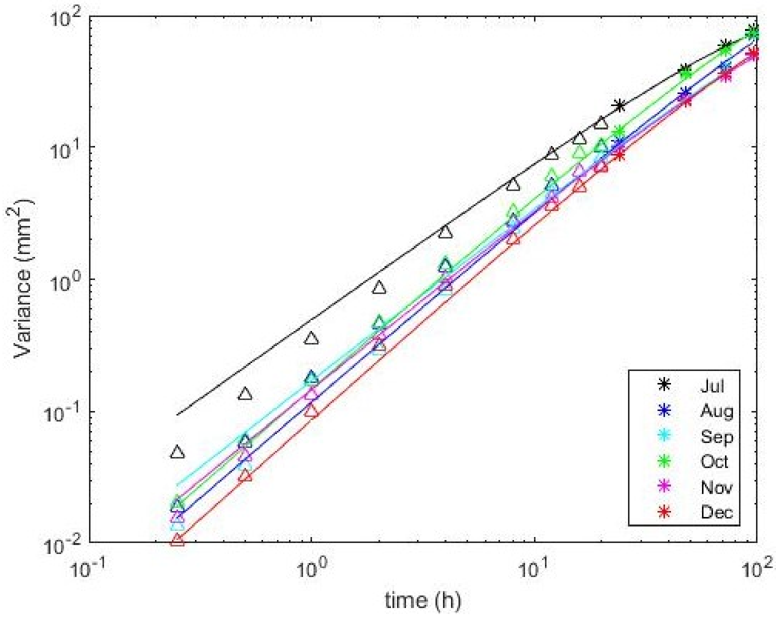

*Figure 4.4: Downscaling of variance using second order moment scaling for the months (a) January to June, and (b) July to December. Triangles are observed sub-daily statistics not used in the fitting, while * are the supra-daily statistics used for the downscaling.*

Not much scaling research has been performed on the skewness of the rainfall, arguably one of the more important statistics as it governs the generation of rainfall extremes in simulations.

This is because of the difficulty and complicated nature in dealing with the third order moments, in addition to the fact that most existing downscaling and disaggregations do not require skewness as an input and only uses variance (Cowpertwait et al., 2002; Marani and Zanetti, 2007; Beuchat et al., 2011). Indeed, this was also true for the BLRP family of models, until skewness and third order fitting were developed by Cowpertwait (1998).

By using the Multivariate Adaptive Regression Splines (MARS; Friedman (1991)) model, Beuchat et al. (2011) was able to downscale the variance, skewness and percentage wet from daily to hourly. However, additional climate information, such as humidity and temperature, was required by the MARS model, which may introduce stationarity issues. Thus, the MARS model was not adopted in this research for the skewness downscaling.

By plotting skewness from Rayleigh rainfall across various time resolution scales in Figures 4.5(a) and (b), it was evident that skewness behaved non-linearly across time scales, similar to variance, indicating that a direct linear fit and extrapolation would not be suitable. Thus, a similar methodology to variance was adopted, where the third statistical moment, $E(X^3)$ was linearly scaled. The skewness was then calculated using Equation 4.4:

$$k = \frac{E(X^3) - 3\mu\sigma^2 - \mu^3}{\sigma^3} \quad (4.4)$$

where σ is the standard deviation, and μ the mean, both of which were downscaled earlier. The downscaled monthly skewness is plotted together with observed skewness in Figures 4.5(a) and (b), indicating good fits for most months for the range of 1 hour and above and slightly overestimating the skewness in the sub-hourly regime.

(a)

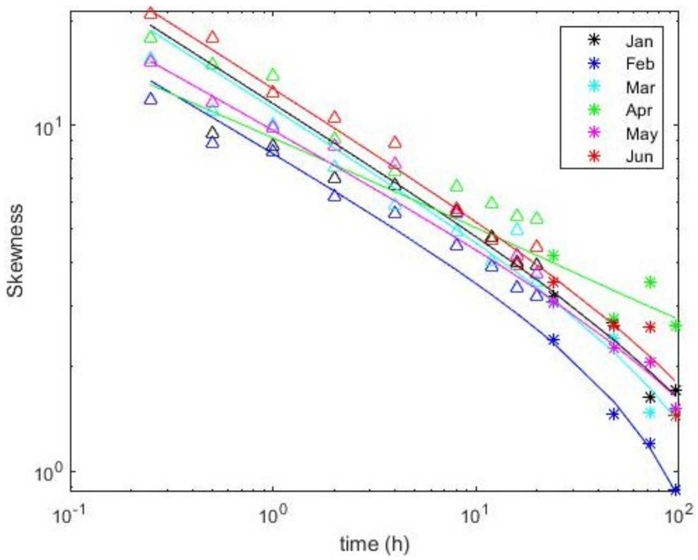

(b)

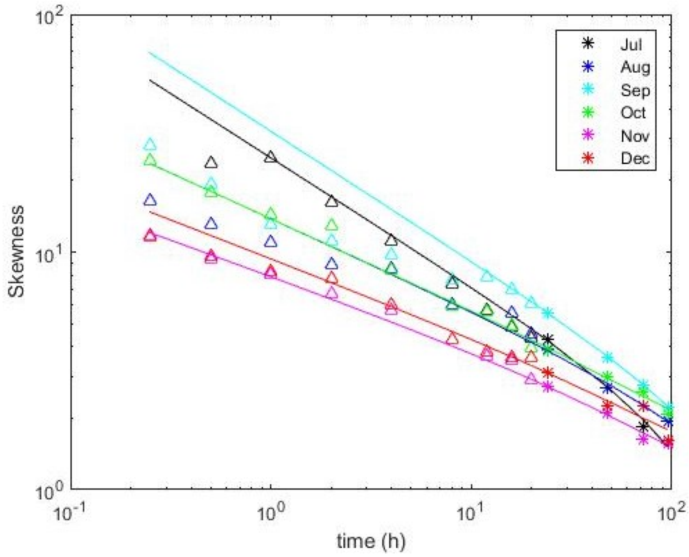

*Figure 4.5: Downscaling of skewness using the third order moments scaling for the months (a) January to June, and (b) July to December. Triangles are observed sub-daily statistics not used in the fitting, while * are the supra-daily statistics used for the downscaling.*

The lag-1 autocorrelation does not scale with time, thus it was excluded from the downscaling process and subsequent BLRP fitting. It was, however, used in assessing the effectiveness of the downscaling approach in reproducing other independent summary statistics, similar to the role that the percentage wet played in Chapter 2.

4.3.2 Downscaling of present rainfall using BLRP

With the downscaled summary statistics for Rayleigh rainfall obtained in Section 4.3.1, a cumulative approach BLRPRx fitting analysis was performed to obtain the Bartlett-Lewis parameters for the downscaled rainfall. Only the BLRPRx model was adopted as it showed the best performance in reproducing rainfall with a similar set of summary statistics in Chapter 2. The fitted parameters for the BLRPRx model can be found in Appendix E.

Subsequently, 50 simulations of rainfall for the observed rainfall time period were performed. The monthly summary statistics and annual maxima extremes for all 50 simulations were plotted and compared against observed summary statistics and extremes in Figure 4.6.

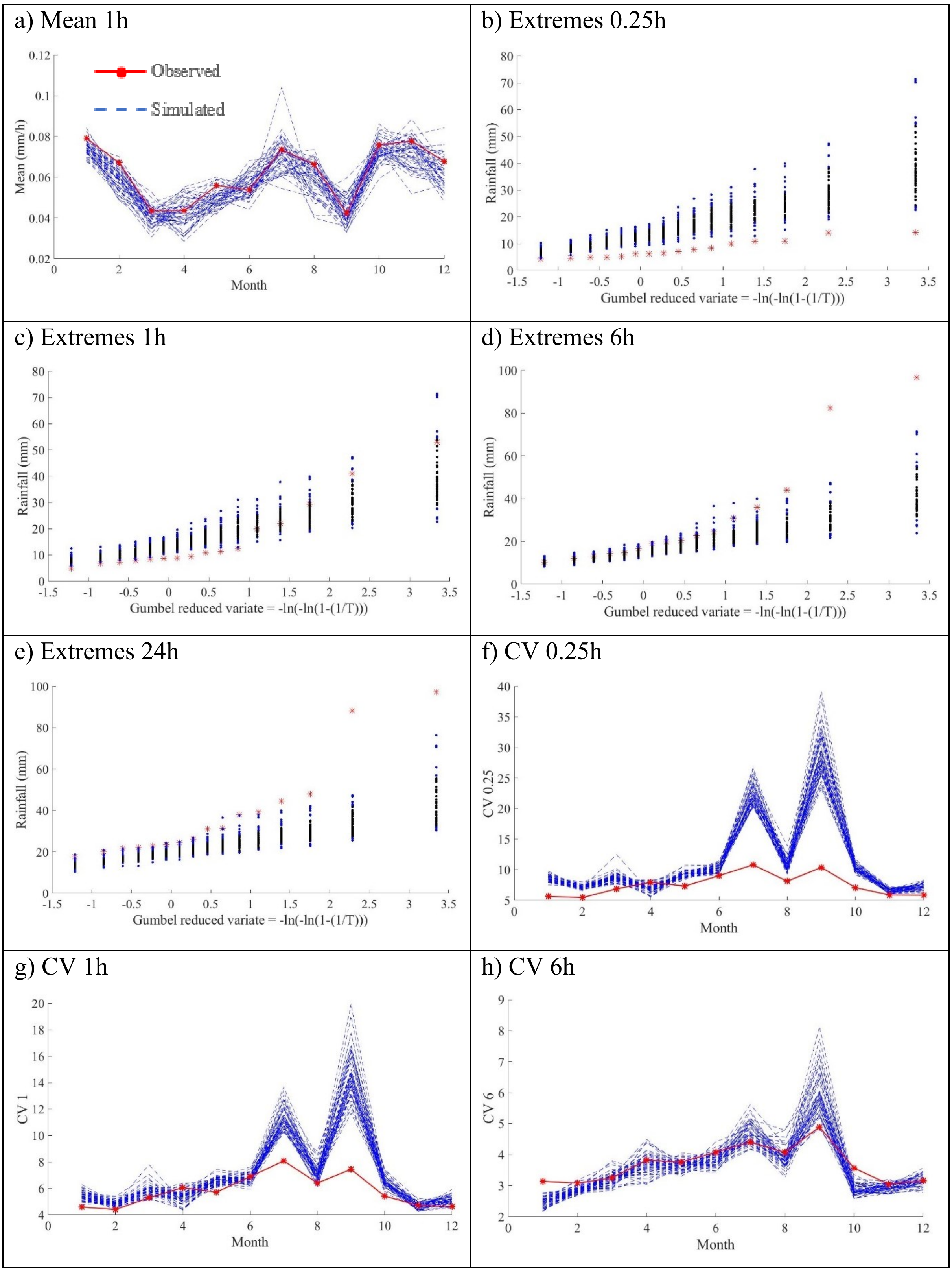
a) Mean 1h
Observed
Simulated
Mean (mm/h)
Month
b) Extremes 0.25h
Rainfall (mm)
Gumbel reduced variate = -ln(-ln(1-(1/T)))
c) Extremes 1h
Rainfall (mm)
Gumbel reduced variate = -ln(-ln(1-(1/T)))
d) Extremes 6h
Rainfall (mm)
Gumbel reduced variate = -ln(-ln(1-(1/T)))
e) Extremes 24h
Rainfall (mm)
Gumbel reduced variate = -ln(-ln(1-(1/T)))
f) CV 0.25h
CV 0.25
Month
g) CV 1h
CV 1
Month
h) CV 6h
CV 6
Month

i) CV 24h

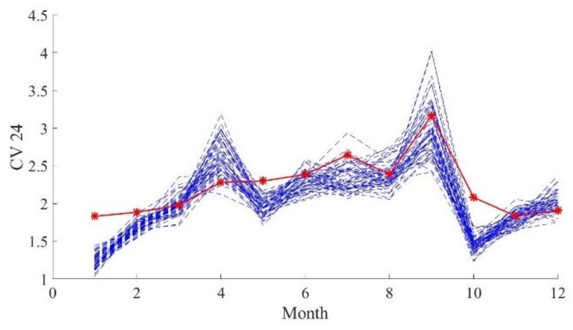

j) Skewness 0.25h

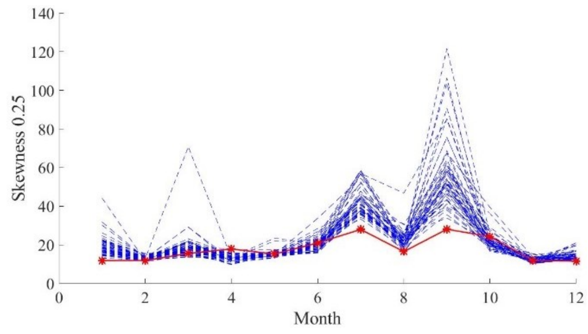

k) Skewness 1h

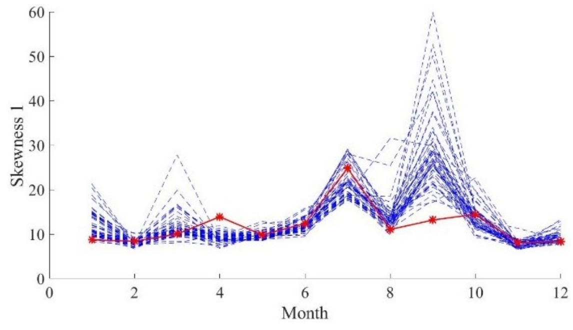

l) Skewness 6h

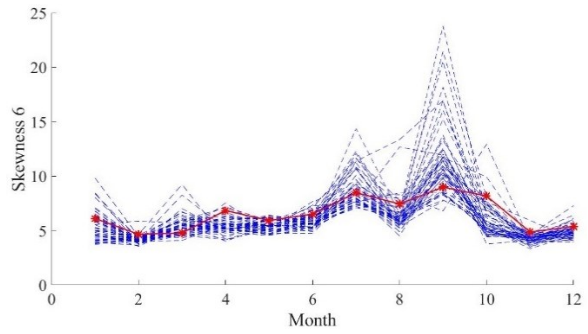

m) Skewness 24h

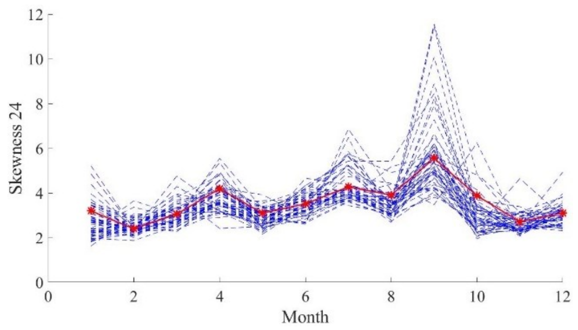

n) AC 0.25h

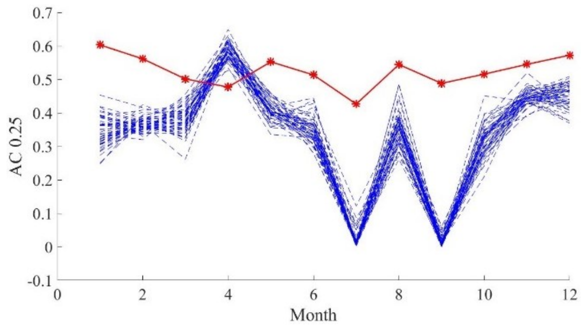

o) AC 1h

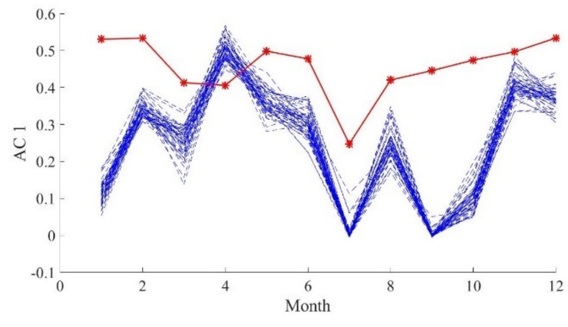

p) AC 6h

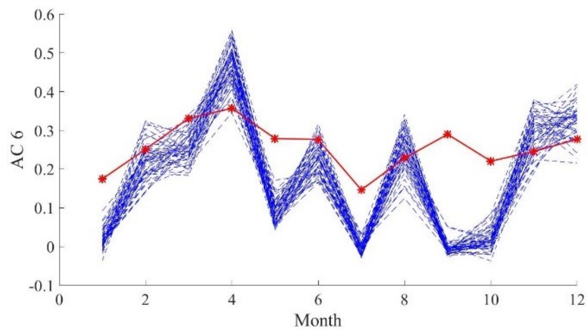

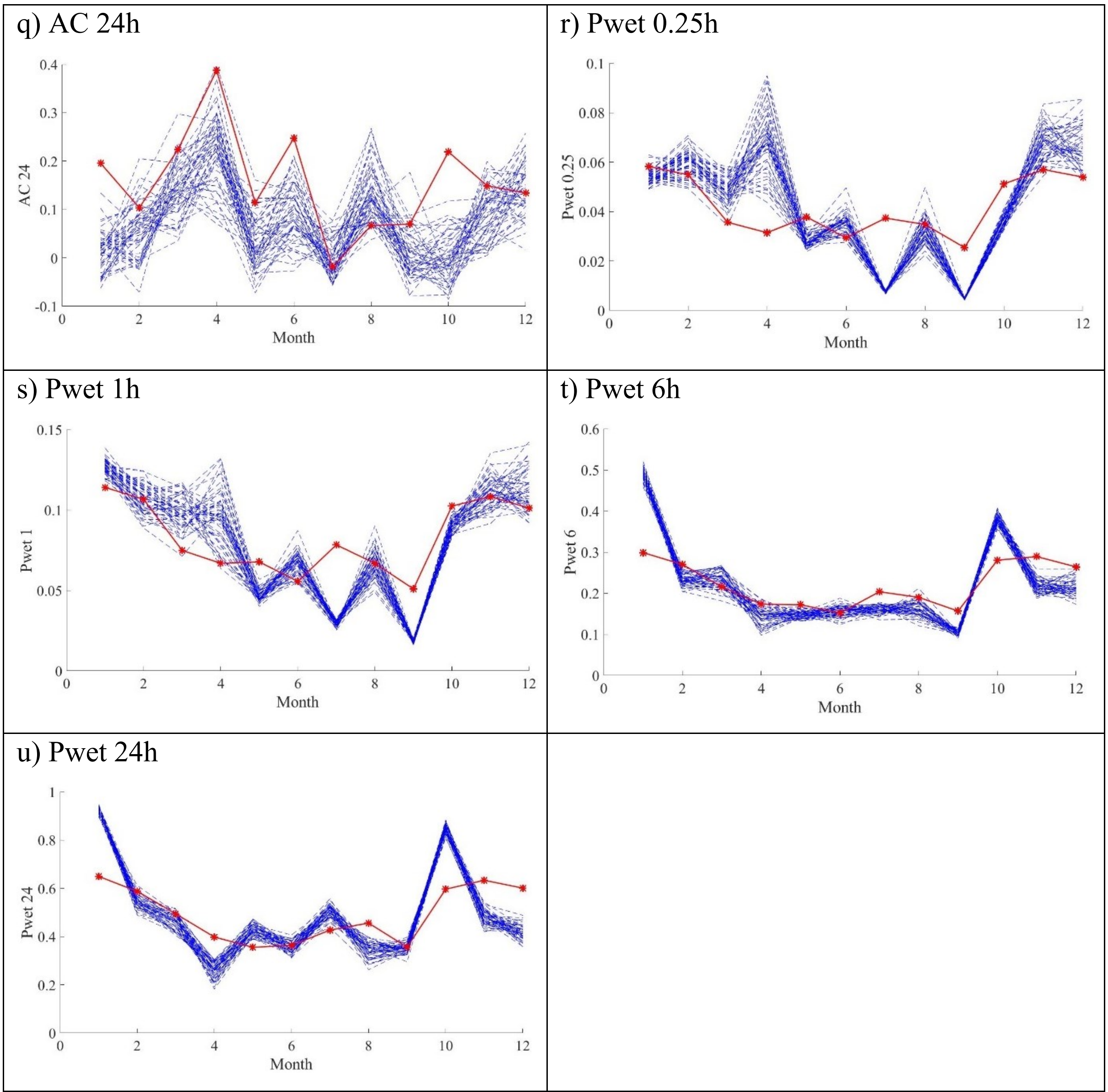

Figure 4.6: Comparison of summary statistics and extremes between the downscaled BLRPRx simulated rainfall and measured Rayleigh rainfall. Red is the observed statistic/extreme, while blue the simulated results. (a) Mean 1h. (b) – (e) Gumbel plot of annual maxima for 0.25h, 1h, 6h and 24h. (f) – (i) Coefficient of variation for 0.25h, 1h, 6h and 24h. (j) – (m) Skewness for 0.25h, 1h, 6h, and 24h. (n) – (q) Lag-1 autocorrelation for 0.25h, 1h, 6h, and 24h. (r) – (u) Percentage wet for 0.25h, 1h, 6h, 24h.

Several observation and inferences on the effectiveness of this downscaling approach may be drawn based on the comparison of observed vs simulated data in Figure 4.6:

- The 24h (daily) summary statistics were generally well reproduced. This was expected as all downscaling fittings used the 24h summary statistic as part of the fitting. Even the 24h extremes (barring the 2 extreme events in 2013 and 2014), while generally slightly underestimated, produced similar results to the calibration analyses performed in Chapter 2.

- The 1h means were well reproduced, which was a good indication that mean downscaling was appropriate. This was expected, following the good fits shown in Figure 4.2.
- The sub-daily coefficient of variance and skewness were generally reproduced well, except for the months of July and September, where both summary statistics were overestimated. This was due to the poor extrapolation and overestimation of the variance and skewness at the sub-daily, especially sub-hourly, scales shown by the Black (July) and Cyan (September) lines in Figures 4.5(b) and 4.6(b) respectively.
- Due to the higher fine scale skewness, both the 15 minute and 1h extremes were overestimated as compared to the observed.
- As both the lag-1 autocorrelation and percentage wet statistics were not used in the BLRPRx fitting, the comparison of these summary statistics represented the effectiveness of the model in reproducing statistics independent from the fitting process. Except for both July and September, the percentage wet values were broadly well reproduced for most time scales and months, while the lag-1 autocorrelation was not well reproduced and was often underestimated.

In general, the downscaling approach, utilising fractal relations of rainfall statistics and the Poisson process BLRPRx model in generating synthetic downscaled rainfall, was shown to be able to reproduce most of the summary statistics of rainfall at timescales from 15 minutes to daily. However, there would always be a possibility of a poor extrapolation of the variance or skewness, resulting in an overestimation of extremes, particularly in the sub-hourly scale. These could be spotted with sudden and large peaks in the variance or skewness, especially in the sub-hourly scales.

4.4 Downscaling of future rainfall

4.4.1 Downscaling UKCP18 GLM simulations

In Chapter 3, a Generalized Linear Model (GLM) was calibrated and used in simulating rainfall at the Rayleigh site using climate data from the UK Climate Projections 2018 (UKCP18; Lowe et al., 2018) for the scenario of RCP8.5. As only daily climate data was available, the simulated rainfall was also at the daily scale. By applying the downscaling methodology outlined in Section 4.3, it was possible to downscale this future rainfall projection to simulate sub-daily rainfall series that consider climate change up to 2080.

To capture all uncertainties from both the GLM and downscaling model, 20 GLM simulations were first chosen at random. A downscaling process and BLRPRx fitting were then performed on each GLM simulation for each decade, generating a set of BLRPRx parameters for each GLM simulation and each decade. Using those unique sets of parameters, twenty 15-minute time resolution simulations using the BLRPRx model were subsequently produced for each GLM simulation for each decade. Thus, there was a total of 400 BLRPRx rainfall simulations at 15-minute time resolution for each decade from 2020 to 2080.

The monthly summary statistics and annual maxima (AM) extreme for each simulation and decade were then calculated and compiled. A box and whisker plots for each monthly summary statistic for each decade from 2020 to 2080 were plotted and presented in Appendix F. Figure 4.7 plots the averages of each monthly summary statistic for each decade derived from the plots in Appendix F, thus allowing for easier assessment of future trends in the projected rainfall.

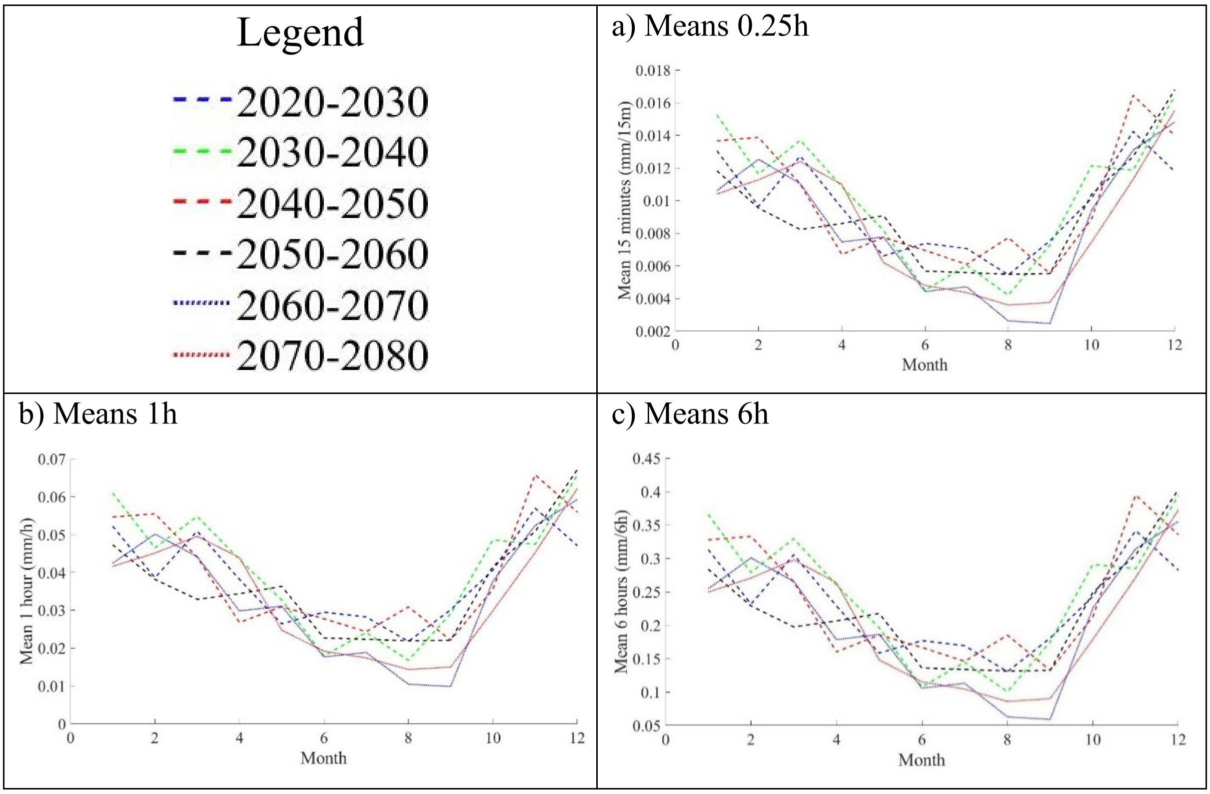

d) Means 24h

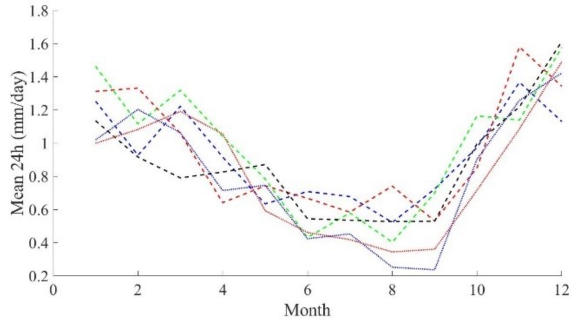

e) CV 0.25h

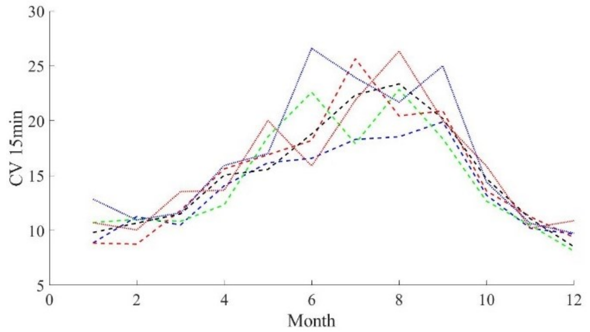

f) CV 1h

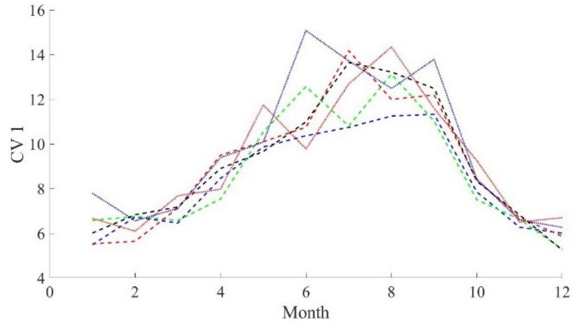

g) CV 6h

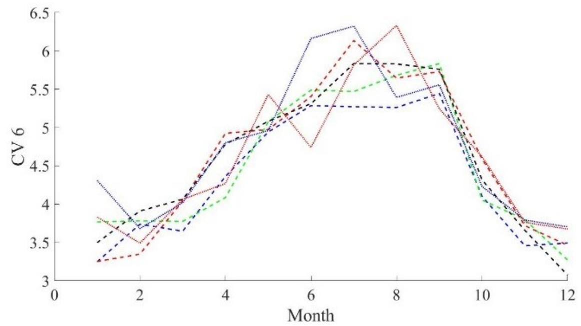

h) CV 24h

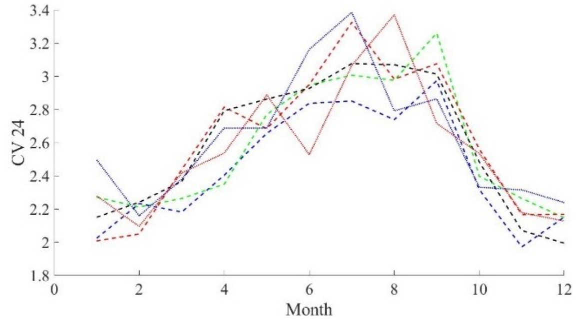

i) Skewness 0.25h

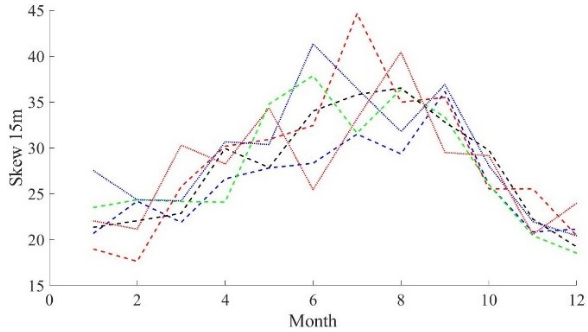

j) Skewness 1h

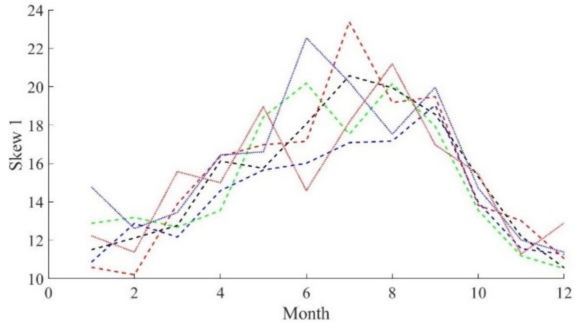

k) Skewness 6h

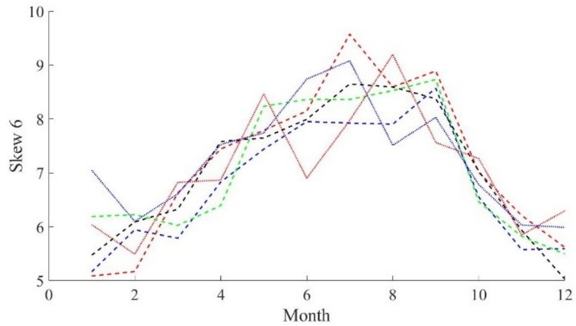

l) Skewness 24h

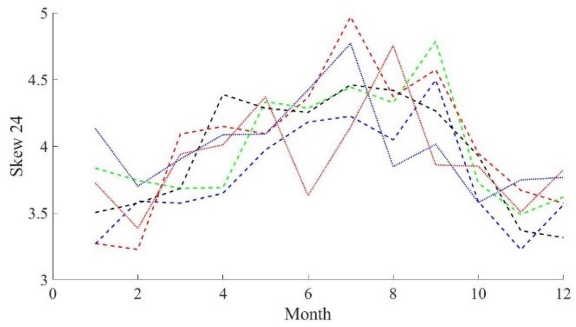

m) AC 0.25h

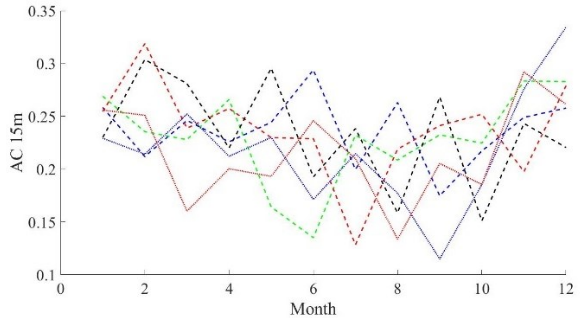

n) AC 1h

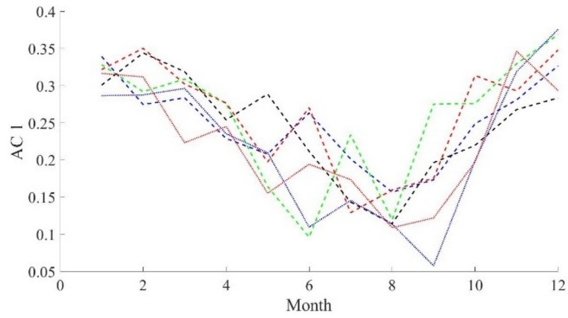

o) AC 6h

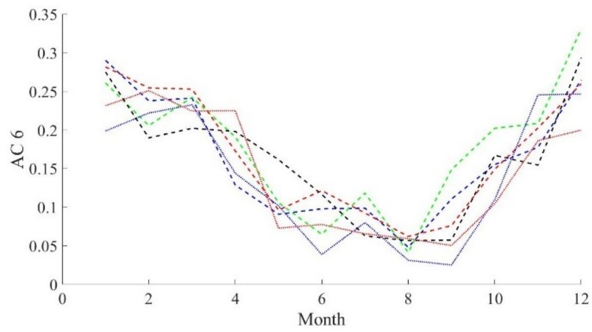

p) AC 24h

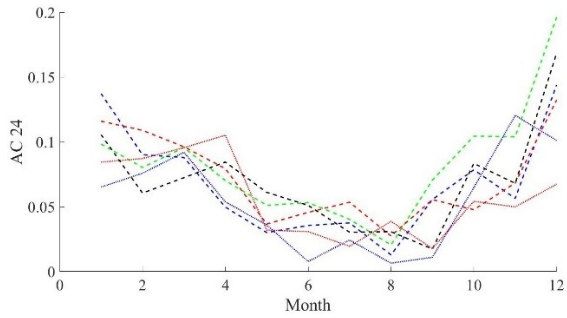

q) Pwet 0.25h

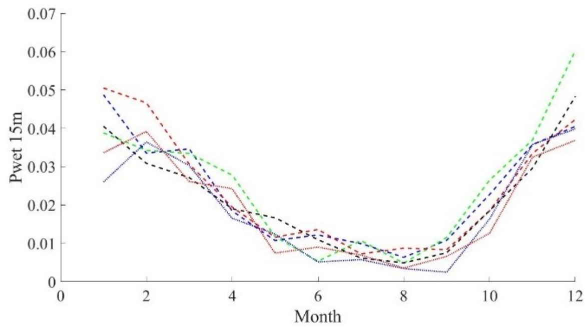

r) Pwet 1h

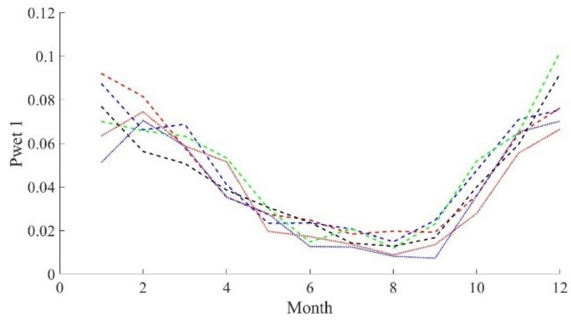

s) Pwet 6h

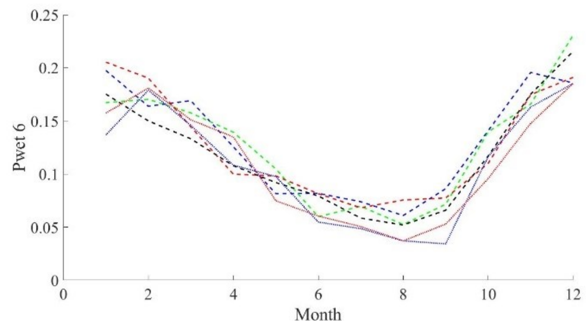

t) Pwet 24h 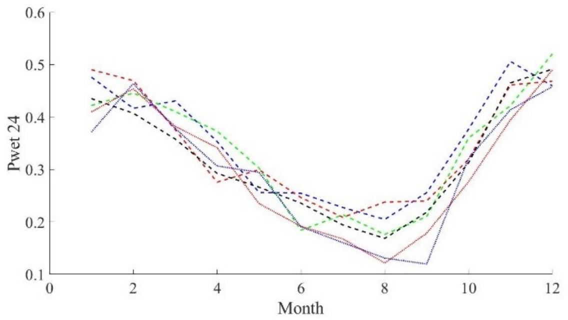	
Figure 4.7: Averaged monthly summary statistics of the projected future rainfall for each decade. (a) – (d) Mean for 0.25h, 1h, 6h and 24h. (e) – (h) Coefficient of variation for 0.25h, 1h, 6h and 24h. (i) – (l) Skewness for 0.25h, 1h, 6h, and 24h. (m) – (p) Lag-1 autocorrelation for 0.25h, 1h, 6h, and 24h. (q) – (t) Percentage wet for 0.25h, 1h, 6h, 24h.	

The means across all time scales (Figure 4.7 (a) – (d)) exhibited a similar trend that showed the climate to get drier from 2060, particularly during the summer months of June to September. In addition, there was a trend of increased rainfall in the future during February and March, indicating later and wetter winters, while summers were also pushed later. A similar trend was observed and discussed for the GLM simulations in Chapter 3.

A similar observation of a drier future climate at Rayleigh location was also seen in the percentage wet for all time scales and months (Figure 4.7 (q) – (t)), with the reduction in wet days which was more prominent during the summer months. This effect was also more prominent in the daily resolution as compared to the sub-hourly scale.

In addition to decadal shifts in means and percentage wet, the coefficient of variation and skewness increased in the future, especially during June and July, and for fine time scales. These changes indicated that more extreme storm events would occur in the future, in part driven by climate change.

4.4.2 Projected extreme rainfall

Apart from the summary statistics, the annual maxima (AM) for each decade and time scale were identified and the maximum and minimum ranges plotted in Figure 4.8. The ranges represent the envelope in which an extreme event can occur for a given return period and decade.

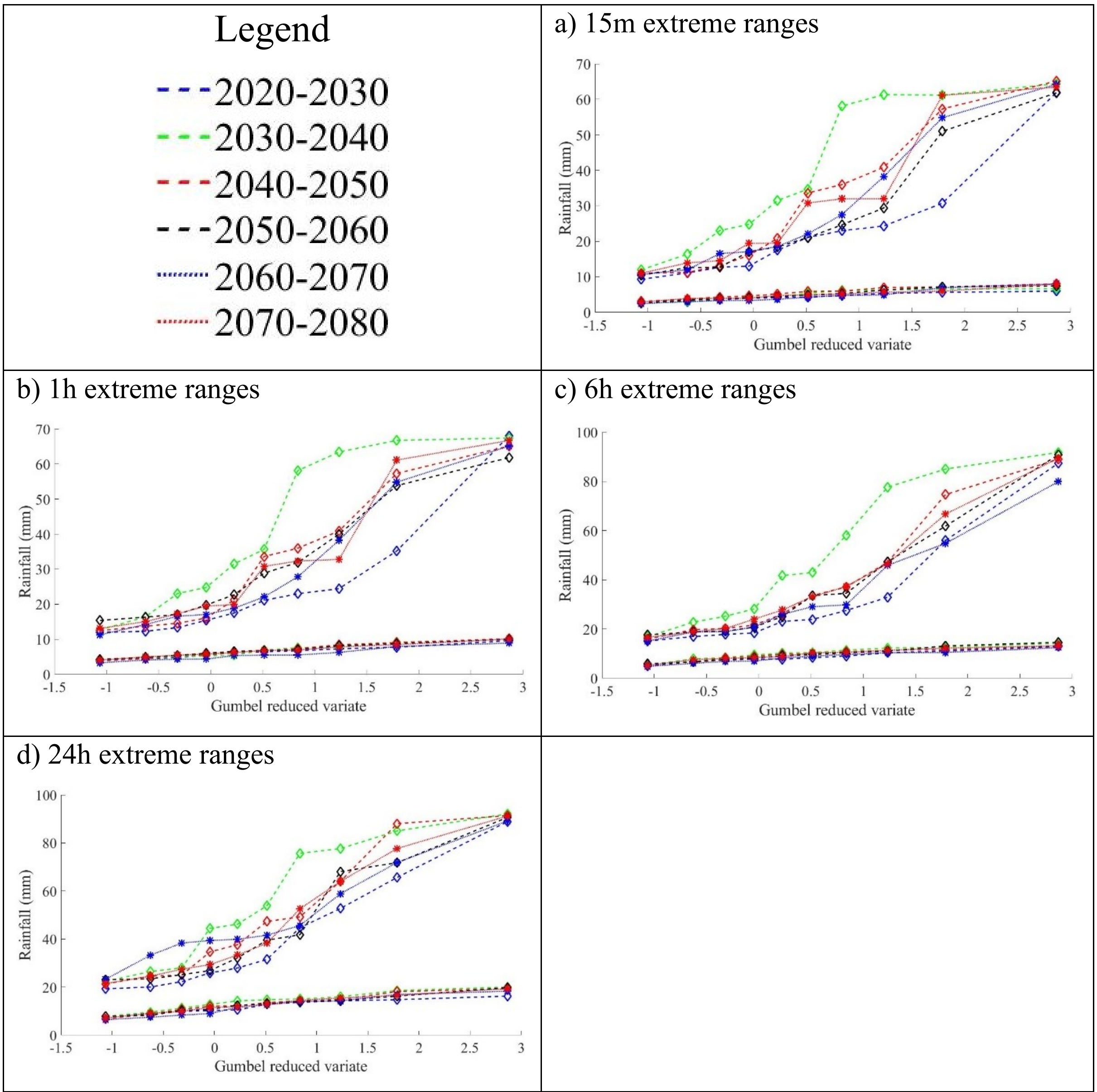

Figure 4.8: Annual maxima extreme maximum and minimum ranges for the projected fine-scale future rainfall at each decade for (a) 15 minutes time scale, (b) 1 hour, (c) 6 hours, and (d) 24 hours time scale.

In all the Gumbel plots for the various time scales, the extremes for the decade 2030 – 2040 seemed most irregular, as they deviated significantly from the general extreme value ranges. This may be caused by poorly downscaling daily coefficient of variation and skewness, resulting in an overestimation of these summary statistics, and consequently, storms in that decade.

By ignoring the 2030-2040 extreme ranges, it could be observed that the extreme envelope was generally pushed higher up for all time resolutions, thus enabling the generation of larger storms in the downscaled BLRPRx simulations. This effect was particularly true for long return period events (i.e. when the Gumbel reduced variate was large).

4.5 Conclusions

This chapter highlighted and briefly explained the use of scaling relations and the BLRPRx stochastic rainfall generator in downscaling daily rainfall to sub-hourly rainfall.

The downscaling approach was demonstrated to be effective at downscaling rainfall summary statistics from daily to hourly, with mixed results in the sub-hourly domain, as variance and skewness tended to be overestimated, thus resulting in an overestimation of extremes in the sub-hourly regime.

When used in downscaling projected future daily rainfall, the effects of climate change were captured in the sub-daily regime as well, with a strong decrease in average rainfall during the summer and wetter late winters during February and March. In addition, the coefficient of variation was found to increase during the summer, particularly for finer temporal scales.

In terms of projected extremes, apart from the decades of 2030-2040, storms were expected to get more intense over the future decades for all time scales and return periods.

Finally, as the maximum daily modelled storm (at 95mm of rainfall) was found to be similar in magnitude with an actual storm experience in Rayleigh, it was decided that a storm of 95mm would be applied as an ideal storm in the resilience study performed for the rail embankment in Chapter 7.

Chapter 5: Earth Embankment Lifecycle Stability and Resilience

5.1 Introduction

Significant advances have been made in the modelling of earth embankment structures over 70 years, from the first use of slope stability tools such as Little and Price (1958), and Morgenstern and Price (1965), to complex numerical models that capture the unsaturated nature of the embankment soil and incorporate soil-atmosphere interaction, with the ultimate aim of assessing and predicting the resilience and stability of the earth embankment throughout its lifecycle. With the rapid changes to our current climate due to anthropogenic global warming, and projections of increasingly extreme climate such as droughts and intense rainfall for the UK (UKCP18), there is a dire need for the evaluation of existing flood embankments in view of their future and for taking active steps now to future-proof these structures.

This chapter first reviews past and present modelling approaches to the unsaturated nature of infrastructure slopes, earth embankments and flood embankments. A discussion on current modelling approaches for flood embankments is also undertaken, with emphasis on the development of the fragility curve concept in flood embankment design.

The basis of unsaturated soil mechanics in the form of unsaturated numerical constitutive models is then introduced and elaborated, with emphasis on the Imperial College Single Structure Model (ICSSM, Georgiadis et al., 2005). The ICSSM was calibrated with experimental data of Monroy (2006), obtained from testing a compacted London clay, which is subsequently used in Chapter 7 and Chapter 8 for the modelling of earthfill embankments. No hydraulic models, in particular the Soil Water Retention Curve (SWRC) and permeability models are presented here as this is explored in greater detail in Chapter 7.

Following from that, soil-atmosphere interaction boundary conditions implemented in the lifecycle analyses in Chapter 7 and Chapter 8 are discussed in detail. The monthly evapotranspiration values are derived, together with other relevant plant parameters, while the mechanism of the precipitation boundary condition is also introduced and quantified.

5.2 Past and present embankment modelling approaches

5.2.1 Infrastructure embankments

Rail earth embankments are a highly sensitive infrastructure to the constant changes in pore-water pressure within its soil. It is known that pore-water pressure plays a direct part in both the serviceability and stability of the soil as it influences the volumetric behaviour of the soil and its effective stress. As a consequence, any significant changes in pore-water pressures either due to seasonal fluctuations, vegetation removal or rain storm events can negatively impact the embankment's serviceability or in extreme cases, its stability. O'Brien (2013) concluded that a majority of serviceability failures of rail embankments in the UK occur during late summer, especially so if heavy vegetation is present. Conversely, ultimate limit state failures such as deep-seated failures tend to occur on sparsely vegetated embankments. Both serviceability and ultimate failures are more prevalent on high plasticity embankment soils.

Greenwood et al. (2004) highlighted the many complex effects vegetation has on embankments, with the main influence being evapotranspiration. In addition, the roots of plants would increase both the effective cohesion and erosion resistance of the soil. If the evapotranspiration demand is high, particularly so during the summer, desiccation cracks may form which would increase the overall permeability of the soil (Wang et al., 2011). On the other hand, if desaturation occurs due to very high evapotranspiration demand, the permeability of the soil decreases (Tsaparas and Toll, 2002).

It is known that the permeability of the soil can significantly influence pore water pressures and stability of an embankment. Nyambayo et al. (2004) showed that slopes with low permeabilities were generally able to retain suctions within the soil throughout winter and thus suffer smaller displacements during the annual shrink-swell cycle overall. In contrast, highly permeable slopes may experience progressive movements after each seasonal cycle, eventually resulting in a progressive failure. Analyses by Ng et al. (2001) further showed the effect of prolonged rainfall in the formation of deep-seated failures in slopes, as well as the influence of permeability in allowing infiltration of rain into the soil.

Due to the complex hydro-mechanical coupling involved in soil-atmosphere interactions, numerical tools such as finite element analysis are necessary for predicting and assessing the resilience of these embankments to both present and future risks. Several modelling strategies are available in the current literature. Analyses done by Tsaparas et al. (2002), Tommasi et al.

(2013) and Cotecchia et al. (2014) employ the Richards' equation (Richards, 1931) for modelling the hydraulic regime within the rigid soil structure, which is then applied as an input in a slope stability analysis to obtain slope safety factors. While this approach provides an uncoupled estimate of the hydraulic behaviour of the embankment, the mechanical behaviour of the soil is uncoupled from the hydraulic regime and soil skeleton deformations due to pore water pressure changes are disregarded.

A different approach to modelling soil-atmosphere interactions would be to employ a coupled hydro-mechanical model. This approach couples the hydraulic and mechanical finite element governing equations and applies a pore pressure boundary condition along an exposed soil surface. The magnitudes of the boundary pore water pressure are prescribed based on the estimated summer and winter pore water pressure profiles, to simulate the seasonal changes (Kovacevic, 1994; Nyambayo et al., 2004; O'Brien et al., 2004). With the developments of advanced hydraulic boundary conditions such as the root water uptake model (Gatmiri and Najari, 2009; Hemmati, 2009; Nyambayo and Potts, 2010) and precipitation (Wilson et al., 1994; Smith, 2003), more realistic and accurate simulations of soil-atmosphere interaction were shown in Briggs et al. (2016), and Tsiampousi et al. (2017) although the latter analysed a cut slope instead.

5.2.2 Flood embankments

Current classical approaches

Being a close relative to infrastructure embankments in nature, the tools for assessing the stability of flood embankments have largely followed infrastructure embankments and slope stability analysis methods with the use of simple limit-equilibrium methods (Swedish wedge methods; slice methods such as Bishop simplified (1955), Janbu simplified (1973), Morgenstern-Price (1965), to name a few), as outlined in the International Levee Handbook (CIRIA, 2013). This is commonly performed by adopting a design flood level and assessing the factor of safety of the embankment slope for that flood level.

However, such simple limit-equilibrium methods should only be used as a first estimate in sizing the embankment due to the many assumptions and highly simplistic soil constitutive models adopted in the calculations, neglecting the partially saturated nature of the embankment soil and constant changes in the pore water pressure regime due to tidal and atmospheric conditions.

In addition to stability analyses, settlement is another important design aspect that must be considered in flood embankments to ensure that the freeboard (the vertical distance between embankment crest and flood design level) is adequate throughout its lifecycle in preventing overtopping. Current design approach utilises Terzaghi's theory of 1-dimensional consolidation to estimate primary consolidation (Skempton and Bjerrum, 1957; Lambe, 1964), while secondary consolidation due to creep both vertically and laterally (Lo, 1961; Barber, 1961; Mesri, 1973) requires empirical methods to estimate settlement.

Finally, other design considerations such as seismic design and both internal and external erosion should also be assessed. However, as the UK is not seismically active, and flood embankment failures in England and Wales are generally caused by either deep seated failures due to construction on soft clays and organic soils, or excessive seepage due to clay desiccation or animal burrows (Dyer, 2004), these design considerations are less critical and thus will not be discussed further in this thesis.

Reliability and fragility calculations

While classical approaches to the geotechnical design of flood embankments rely on both analytical and empirical methods, all design methods are deterministic in nature. That is, for a given set of parameters and loading condition, the design either passes (with a Factor of Safety (FoS) greater than 1), or fails (with FoS < 1) based on a defined standard. Despite the use of partial factors in Eurocode 7 as a means to control the uncertainty of the applied parameters, the conclusions drawn from classical methods are still deterministic in nature.

With the adoption of the source-pathway-receptor-consequence (s-p-r-c) model (Figure 5.1 for flood risk assessments in the UK (ICE, 2001; Sayers et al., 2002; EA, 2002), there is a growing demand to perform these geotechnical assessments in a probabilistic framework, culminating in a reliability analysis where there is a probability of failure for a given loading scenario. The reliability analysis serves as the pathway component in the s-p-r-c model, forming the link between the extreme-value analysis of flood events and the probability of flood extent and depth so that a complete risk and consequence assessment of flooding can be computed.

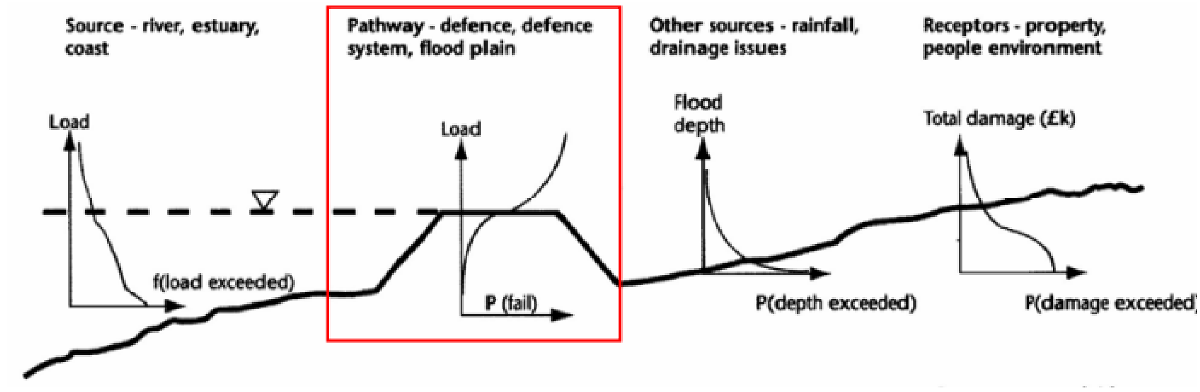

Figure 5.1: Source-pathway-receptor-consequence model for flood risk assessment (Buijs et al., 2007). The reliability analysis component falls under pathway, outlined in red.

The reliability analysis of a flood embankment is typically undertaken based on the concept of fragility (Dawson and Hall, 2002). In Casciati and Faravelli (1991), the fragility of a structure is defined as "*the probability of failure conditional on a specific loading, L*". Failure in this context is defined as the inability of a structure to achieve a given performance target, which can range from exceeding a certain overtopping rate to breach formation, depending on the function of the flood embankment.

The concept of fragility vs the conventional deterministic approaches in flood defence analysis is best illustrated in Figure 5.2. In the conventional approach, the structure is assessed to either pass or fail for any given loading event, that is the probability of failure is either a 0 or 1. The Factor of Safety of the structure is typically given as a ratio of loading at failure to the required design load. When plotted on a probability of failure vs severity of load event plot, the conventional approach produces a step function.

In the probabilistic fragility framework, parameters used in assessing failure are treated as random variables, where each parameter and its variability can be defined with a statistical distribution. A Monte-Carlo analysis is then performed, allowing for all input parameters to be integrated over the total range of possible events to derive the probability of failure at various loading events, producing the fragility curve. This methodology has been successfully applied to overtopping processes (Vrouwenvelder et al., 2001), piping (USACE, 1999), and has been extended to other principal load types in the FLOODsite project (Allsop et al., 2008).

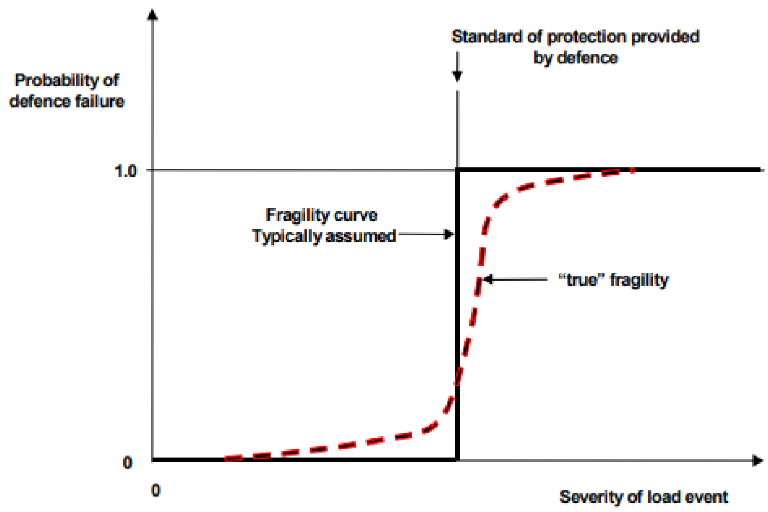

Figure 5.2: Comparison of the fragility approach to the conventional factor of safety method for reliability assessment (Buijs et al., 2007).

Nevertheless, there are still severe limitations to the probabilistic framework. Embankment geometry and ground stratigraphy are often fixed for an analysis, thus a derived fragility curve is only applicable to that given problem geometry, layout, and geology. This renders empirical fragility curves such as those in Shinozuka et al. (2000) unsuitable for other locations and structure geometries.

Furthermore, due to computational demands of the Monte-Carlo analysis, the limit state function that governs failure is often simplified heavily to allow faster computational times. Adopted soil properties and constitutive models are often simple with few parameters, resulting in a higher uncertainty in representation of actual soil behaviour. This can only be resolved with better balancing between the use of more advanced and representative soil constitutive models, with its associated increases in computational demands.

5.3 Unsaturated soil mechanics framework

5.3.1 Stress state variables

In a saturated soil framework, where the pores in the soil skeleton are infilled with water, Terzaghi's (1936) principle of effective stress governs the relationship between effective and total stresses via the pore water pressure. With the partial introduction of air and water into the void space, this relationship is no longer viable, leading to several proposals for the selection of stress variables in what becomes an unsaturated soil.

Bishop (1959) was one of the first to propose an extension on the tension aspect of Terzaghi's principle, with the introduction of air pressure as follows:

$$\sigma' = \sigma_{tot} - u_a + \chi(u_a - u_w) \tag{5.1}$$

where σ' is the effective stress, σ_{tot} the total stress, u_a the air pressure, u_w the pore water pressure, and χ is a function of the degree of saturation, S_r. The parameter χ behaves such that $\chi = 0$ when $S_r = 0$ in dry conditions, and $\chi = 1$ when $S_r = 1$ in fully saturated conditions, simplifying into Terzaghi's effective stress principle. The relationship between χ and S_r in between the two limits is determined experimentally.

One problem with Bishop's extension of the effective stress approach is in its inability to predict the compressibility of unsaturated soils, in particular soil collapse due to wetting when high suctions exist in a soil at high constant mean net stress. This was explored in detail by Jennings and Burland (1962), and Burland (1964, 1965) subsequently concluded that the tension effective stress approach is insufficient to describe the complete mechanical behaviour of unsaturated soils. Hence an alternative representation of stresses in an unsaturated soil assumes two independent stress state variables, with Burland using the net total stress $(\sigma_{tot} - u_a)$ and suction $(u_a - u_w)$.

The use of two or more independent stress state variables continued to gain traction, with Fredlund and Morgenstern (1977) concluding that the complete mechanical behaviour of an unsaturated soil can be described by a minimum of two of the following three variables, $(\sigma_{tot} - u_a)$, $(u_a - u_w)$, and $(\sigma_{tot} - u_w)$.

More recent developments by Jommi (2000), showed that by taking the difference between the total normal stress and the fluid pressure weighted by the degree of saturation, it is possible to define a single stress variable called the average soil skeleton stress. This was well received by Gallipoli et al. (2003) and Wheeler et al. (2003), however both added an additional variable that was a function of suction in order to capture the effects of the menisci within the soil, which the average soil skeleton stress was unable to express. As it was later discovered that the meniscus had a negligible effect on shear strength for compacted clay samples (Tarantino, 2007), using the average soil skeleton stress as the sole stress state variable could be justified if only the macro-pore degree of saturation was taken, instead of the total (micro plus macro porosity), for compacted clays.

Nevertheless, much of the constitutive modelling of unsaturated soils uses net total stress, and suction (Alonso et al., 1990; Cui et al., 1995; Wheeler and Sivakumar, 1995), which are the two most common state variables. This thesis focused on the use of the Imperial College Single Structure Model (ICSSM, Georgiadis, 2003; Georgiadis et al., 2005), which was an extended and modified version of the Barcelona Basic Model (Alonso et al., 1990) and its subsequent modification by Josa et al. (1992).

5.3.2 Modified Cam Clay (MCC), Barcelona Basic Model (BBM) and the Imperial College Single Structure Model (ICSSM)

MCC model

The critical state framework for constitutive modelling was developed through the research of Drucker et al. (1957) and Roscoe et al. (1958), resulting in the Cam Clay constitutive model (Roscoe et al., 1963; Schofield and Wroth, 1968) and the modified Cam Clay constitutive model (Roscoe and Burland, 1968).

Fundamentally, the MCC model consists of the following four elements:

a) A yield function $F(\{\sigma'\},\{k\}) = \left(\frac{J}{p'M_J}\right)^2 - \left(\frac{p'_o}{p'} - 1\right) = 0$ where $\{\sigma'\}$ is the stress state, $\{k\}$ the state parameters, p' the mean effective stress, J the deviatoric stress, M_J the strength parameter, and p'_o the isotropic yield stress and hardening parameter. The MCC yield function represents a surface separating purely elastic from elasto-plastic behaviour, in the shape of an ellipse in the J- p' plane.

b) A plastic potential function $P(\{\sigma'\},\{m\}) = 0$ where $\{m\}$ are state parameters. The plastic potential function calculates the relative magnitudes of the component plastic strains when the current stress state is on the yield surface. The critical state in v- p'-J space is defined with the condition $\frac{\partial P(\{\sigma'\},\{m\})}{\partial p'} = 0$ (leading to the plastic volumetric strain equal to 0 with an increasing shear strains). By assuming associativity, the MCC plastic potential function is assumed to be identical to the MCC yield function in the $p' - J$ plane, but can be non-associated in the deviatoric plane. The incremental plastic strains, $d\varepsilon_i^p$, are determined from the plastic potential function via the flow rule:

$$d\varepsilon_i^p = \Lambda \frac{\partial P(\{\sigma'\},\{m\})}{\partial \sigma_i'} \quad (5.2)$$

where Λ is a scalar multiplier.

c) A hardening or softening rule which governs the magnitude of the plastic strains (see Equation 5.2). For the MCC, this is expressed as:

$$\frac{dp_o'}{p'} = d\varepsilon_v^p \frac{v}{\lambda - \kappa} \quad (5.3)$$

where ε_v^p is the volumetric plastic strain, $v = 1 + e$ the specific volume, λ the coefficient of compressibility along the intrinsic compression line (ICL), and κ the coefficient of compressibility along the swelling lines.

d) Elastic behaviour within the yield surface, where volumetric elastic strains are governed by the swelling lines. For the MCC model, this is expressed as:

$$d\varepsilon_v^e = \frac{\kappa}{v}\frac{dp'}{p'} \quad (5.4)$$

where ε_v^e is the volumetric elastic strains. The elastic shear strains are calculated from the elastic shear modulus, G.

The MCC model was developed upon laboratory tests of reconstituted clay samples (Roscoe and Burland, 1968). Thus, it is reasonably accurate in modelling the behaviour of normally to lightly overconsolidated clays (wet of critical), while it often overestimates peak strength in heavily overconsolidated soils (dry of critical). As such, it was used in the modelling of soft foundation clays in Chapters 6 and 8.

ICSSM

The formulation of the ICSSM implemented in the finite element software ICFEP (Potts and Zdravkovic, 1999), employed to simulate the behaviour of unsaturated behaviour of clay fills in all analyses presented in this thesis, adopts two independent stress variables in the form of matric suction, $s = u_a - u_w$, and net stress, $\bar{\sigma} = \sigma_{tot} - u_a$. The smooth transition from saturated to unsaturated states and vice versa is enabled by introduction of an equivalent suction, $s_{eq} = s - s_{air}$, and equivalent stress, $\sigma = \bar{\sigma} + s_{air}$, where s_{air} is the air entry value of suction for a given soil. The model is generalised in the (J, p, θ, s_{eq}) stress space, where J is generalised deviatoric stress, p is mean equivalent stress and θ is Lode's angle, all representing the invariants of the equivalent stress tensor.

The model adopts two definitions of the isotropic compression line in the $v - \ln p$ plane for $s_{eq} > 0$ kPa. The first is compatible with the BBM formulation (see Figure 5.3(a) and Equation (5.5)), adopting a line with a constant, s_{eq}-dependent, gradient $\lambda(s_{eq})$, that constantly diverges from the fully saturated isotropic line with a gradient $\lambda(0)$ (i.e. $s_{eq} = 0$):

$$v = v_1(s_{eq}) - \lambda(s_{eq}) \cdot \ln(p) \tag{5.5}$$

In the above equation $v_1(s_{eq})$ is the specific volume for the $\lambda(s_{eq})$ line at $p = 1$kPa, while $\lambda(s_{eq})$ is the defined by Alonso et al. (1990) as:

$$\lambda(s_{eq}) = \lambda(0)\left[(1 - r)e^{-\beta s_{eq}} + r\right] \tag{5.6}$$

where r is the soil stiffness parameter and β the stiffness increase parameter.

(a)

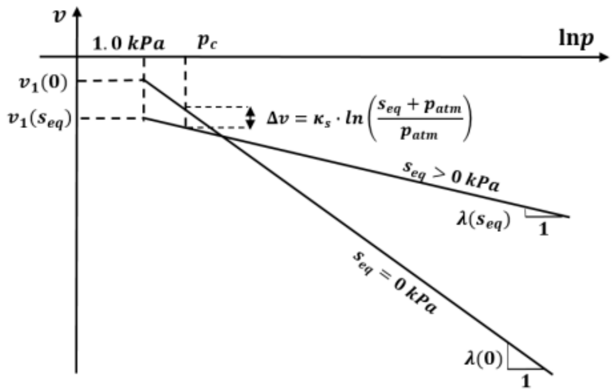

(b)

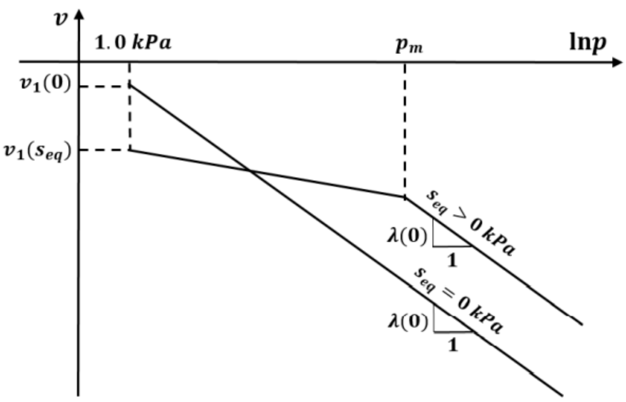

Figure 5.3: (a) Linear unsaturated ICL for the BBM. (b) Bi-linear unsaturated ICL in the ICSSM model (after Georgiadis, 2003; Georgiadis et al., 2005).

In conjunction with this definition of the unsaturated isotropic compression line, the load collapse (LC) curve in the $p - s_{eq}$ plane, which links the equivalent fully saturated yield stress, p_o^*, to the isotropic equivalent yield stress, p_o, at a given suction is given by:

$$p_o = p_c \left(\frac{p_o^*}{p_c}\right)^{\frac{\lambda(0)-\kappa}{\lambda(s_{eq})-\kappa}} \tag{5.7}$$

where p_c is the model parameter for characteristic pressure and κ the coefficient of compressibility for the elastic paths that are independent of suction.

The second option in the ICSSM for defining the unsaturated isotropic compression line has a bi-linear form, as depicted in Figure 5.3(b). It assumes an initial $\lambda(s_{eq})$ gradient (as in Equation (5.6)) until mean equivalent stress p_m, followed by the $\lambda(0)$ gradient subsequently. This option was introduced to reduce the unrealistically high value of the potential wetting-induced collapse at high suctions, which was otherwise implied by the increasing divergence between the $\lambda(s_{eq})$ and $\lambda(0)$ gradient lines in the BBM option. To achieve a constant difference between the two lines, the ratio $\alpha_c = \frac{p_o^*}{p_c}$ is taken as constant for stresses higher than those for which experiments were performed. With this approach the expression for the primary yield surface in the $p - s_{eq}$ plane becomes:

$$p_o = p_o^*(\alpha_c)^{\frac{\lambda(0)-\lambda(s_{eq})}{\lambda(s_{eq})-\kappa}} \tag{5.8}$$

The switch from Equation (5.7) to Equation (5.8) takes place when the two expressions are equal, which defines the magnitude of the confining stress, p_m, at which the switch takes place:

$$p_m = p_c \cdot (\alpha_c)^{\frac{\lambda(0)-\kappa}{\lambda(s_{eq})-\kappa}} \tag{5.9}$$

In the deviatoric plane, the BBM adopts a circular shape for its yield surface, in line with the MCC model. However, a circular yield surface implies that the angle of shearing resistance, ϕ', varies with the Lode's angle, θ, where there can be significant overestimation of ϕ' at other θ values apart from the calibrated value, which is often at triaxial compression ($\theta = -30°$). This pitfall and its implication on numerical analysis of embankments were explored extensively in Grammatikopoulou et al. (2007).

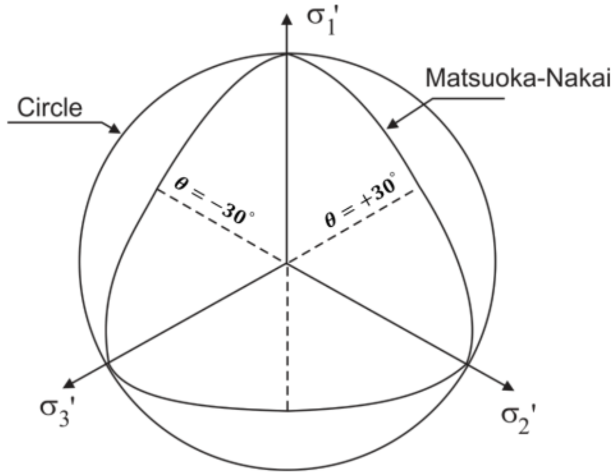

Figure 5.4: Circle (BBM) and Matsuoka-Nakai curve (ICSSM) in the deviatoric plane.

The Matsuoka-Nakai yield surface (Matsuoka and Nakai, 1974; Figure 5.4) on the other hand resolves this issue, as the ϕ' variation with θ closely matches experimental data. The Matsuoka-Nakai failure criterion is expressed as a cubic function:

$$\frac{2}{\sqrt{27}}C_i \cdot \sin(3\theta) \cdot \left(\sqrt{J_{2\eta i}}\right)^3 + (C_i - 3) \cdot \left(\sqrt{J_{2\eta i}}\right)^2 - (C_i - 9) = 0 \tag{5.10}$$

where:

$$C_i = \frac{9 - M_i^2}{\frac{2M_i^3}{27} - \frac{M_i^2}{3} + 1} \tag{5.11}$$

with $i = f$ (for the yield surface criterion), or g (for the plastic potential surface criterion), M_i the gradient of the critical state line in $q - p'$ space corresponding to triaxial compression ($\theta = -30°$) and $J_{2\eta i}$ being the failure value of $J_{2\eta}$, with:

$$J_{2\eta} = \left(\frac{J}{p + f(s_{eq})}\right)^2 \tag{5.12}$$

where $f(s_{eq}) = k \cdot s_{eq}$, with k being the cohesion increase parameter. In the BBM formulation, k is assumed to be a constant, which is only realistic for low values of suction, while in the ICSSM, k is set to vary with the degree of saturation, S_r. With the ICSSM, the cohesion initially increases with suction to a peak, then reduces at large suctions as the degree of saturation tends to a minimum value. As the degree of saturation is calculated from the Soil Water Retention (SWR) model, which is discussed in greater depth in Chapter 7, this parameter provides a direct coupling between mechanical and hydraulic behaviour of unsaturated soils (Tsiampousi, 2011).

Finally, the ICSSM adopts a more versatile primary yield (F_{LC}) and plastic potential (G_{LC}) surfaces, shown in Figure 5.6 in the $J-p$ plane, by implementing the expressions after Lagioia et al. (1996). As only the MCC shape was used in this thesis (Chapters 7 and 8), the complete formulation by Lagioia et al. (1996), as also outlined in Georgiadis (2003), and Ghiadistri (2019), is not be repeated here.

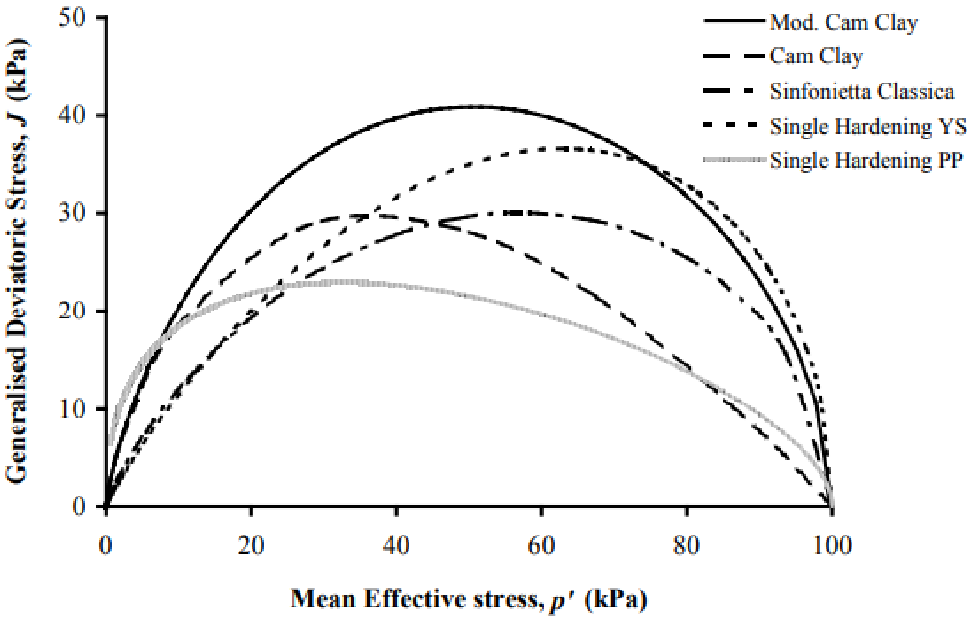

Figure 5.5: The various yield and plastic potential surfaces available using the Lagioia et al. (1996) expression.

There were further developments in the modelling of unsaturated soils, based on the ICSSM, such as the development of a nonlinear Hvorslev surface for highly overconsolidated unsaturated soils (Tsiampousi et al., 2013a; Tsiampousi, 2011), and developments of a double structure model (Ghiadistri, 2019) for compacted clays exhibiting double porosity behaviour. However, these too are not reviewed as only the original ICSSM model was be used in the modelling of all unsaturated soils in this thesis (Chapters 7 and 8).

5.3.3 Calibration of the ICSSM to unsaturated London Clay

The ICSSM was calibrated based on osmotic oedometer testing performed by Monroy (2006) on compacted specimens of weathered London Clay taken from 4m to 6m depths. Before testing, the clay was dried at temperatures of 65ºC, before being mechanically ground and allowed to rehydrate over 3 months. The samples were then compacted to similar initial conditions dry of optimum moisture content.

Two main sets of tests were adopted for the calibration exercise: a set of three free swelling tests, and a set of three confined wetting tests. The tests were presented in Monroy et al. (2010).

Free swelling tests

In each free swelling test, the specimen was wetted under a constant nominal vertical stress of 7kPa to suction values of 0kPa, 120kPa and 430kPa. At equilibrium, each specimen was then loaded and unloaded slowly and continuously at constant suction. Figure 5.6 plots the stress-strain paths of all three free swelling tests.

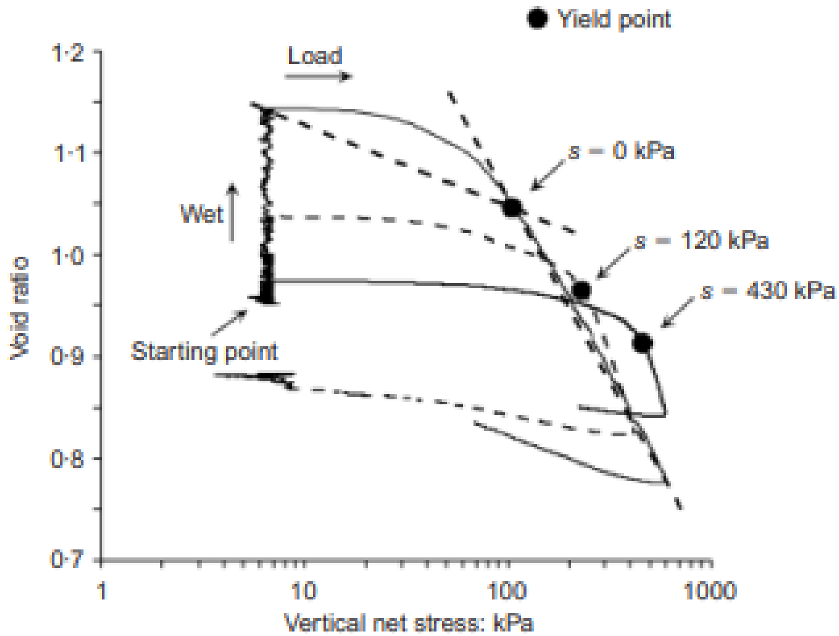

Figure 5.6: Stress-strain paths for the free swelling tests performed on compacted London Clay (Monroy et al., 2010). Solid lines for tests with suction values of 0kPa and 430kPa.

Confined wetting tests

For the confined wetting tests, each sample was first wetted at a constant volume from the same starting condition as the free swelling tests, to suction values of 0kPa, 120kPa, and 405kPa, where the sample was then allowed to equilibrate. After equilibration, each sample was loaded and unloaded at constant suction. Figure 5.7 plots the stress-strain response of each sample from the confined wetting tests.

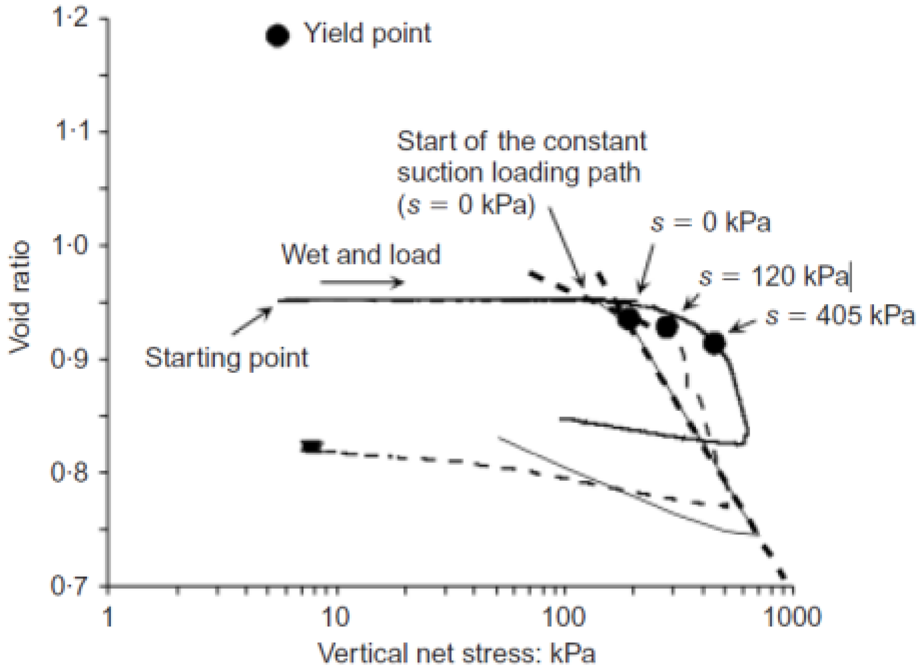

Figure 5.7: Stress-strain paths for the confined wetting tests performed on compacted London Clay (Monroy et al., 2010). Solid lines for tests with suction values of 0kPa and 405kPa.

The yield stress associated with each test was determined by the intersection between the normal compression line and a second line parallel to the swelling line, for a given value of suction, with the start of the load path serving as the start of that second line. The yield points were plotted in Figures 5.6 and 5.7. Monroy et al. (2010) discussed that as the yield lines produced by both sets of tests, when plotted in the $p - s$ plane, were close together, it could be assumed that these yield points would lie on the Load-Collapse (LC) yield curve.

Based on the experimental data presented in Figures 5.6 and 5.7, it was evident that the soil had higher compressibility post-yield and for increasing suction. As previously discussed in Section 5.3.2, this was contrary to the BBM assumption, where compressibility post-yield was assumed to decrease with suction. Consequently, the bi-linear unsaturated ICL of the ICSSM was adopted for the modelling of compacted London clay.

To calibrate the ICSSM, parameters $\lambda(0)$ and κ were first derived from the free swelling tests in Figure 5.6, by identifying the slopes of the stress-strain path before and after yielding. The yield points were then identified and plotted on $p_o - s_{eq}$ plane (Figure 5.8(a)), representing the experimental LC points.

(a)

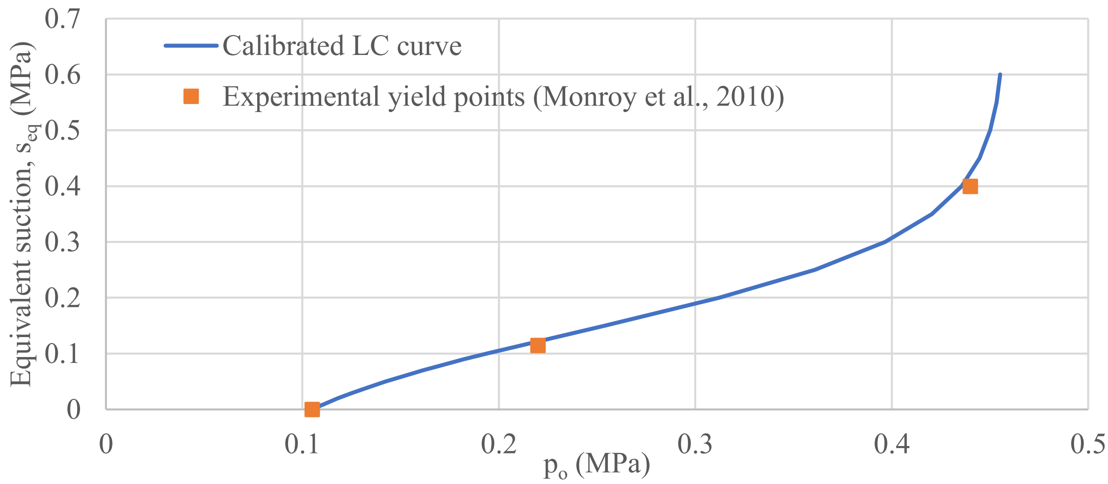

(b)

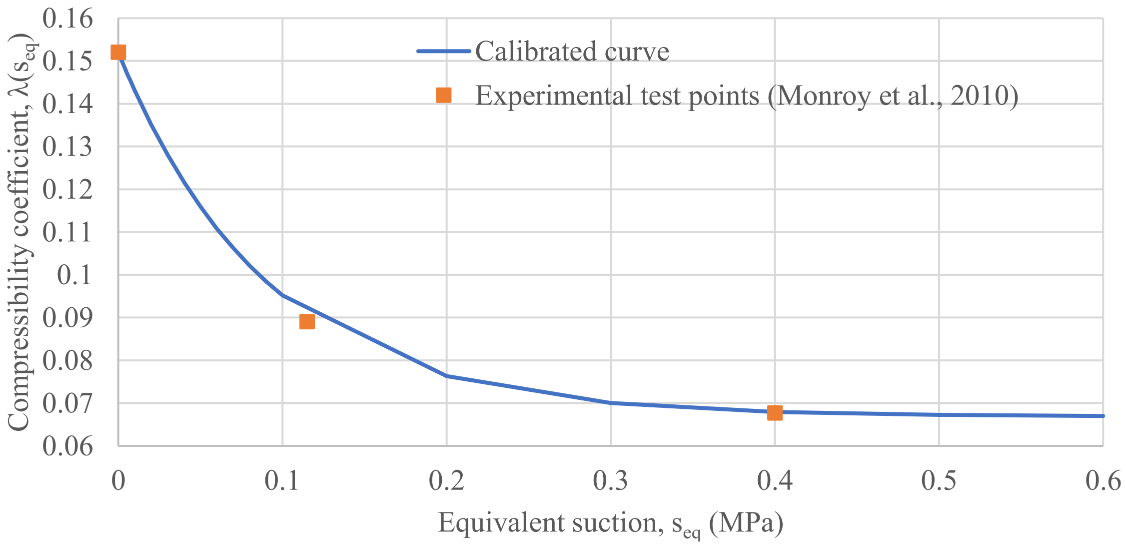

Figure 5.8: Calibration curves against experimental test points for (a) the Load-Collapse curve, and (b) compressibility coefficient vs equivalent suction.

The corresponding values of $\lambda(s_{eq})$ for each test were then calculated by rearranging Equation 5.8 in terms of $\lambda(s_{eq})$:

$$\lambda(s_{eq}) = \kappa + \frac{\lambda(0) - \kappa}{1 + \log_{\alpha_c} \frac{p_m}{p_o^*}} \tag{5.13}$$

where p_m was assumed to be equivalent to the yield point p_o. The test points were then plotted in Figure 5.8(b). Using Equations 5.6 and 5.9, the parameters α_c, r and β were estimated by producing a best fit curve for both Figures 5.8(a) and (b).

To estimate the elastic compressibility coefficient for changes in suction, κ_s, the void ratios at the end of wetting phase from the free swelling tests were plotted against s_{eq}, as shown in Figure 5.9. A line of best fit was then drawn through the points, with the slope of the line giving κ_s.

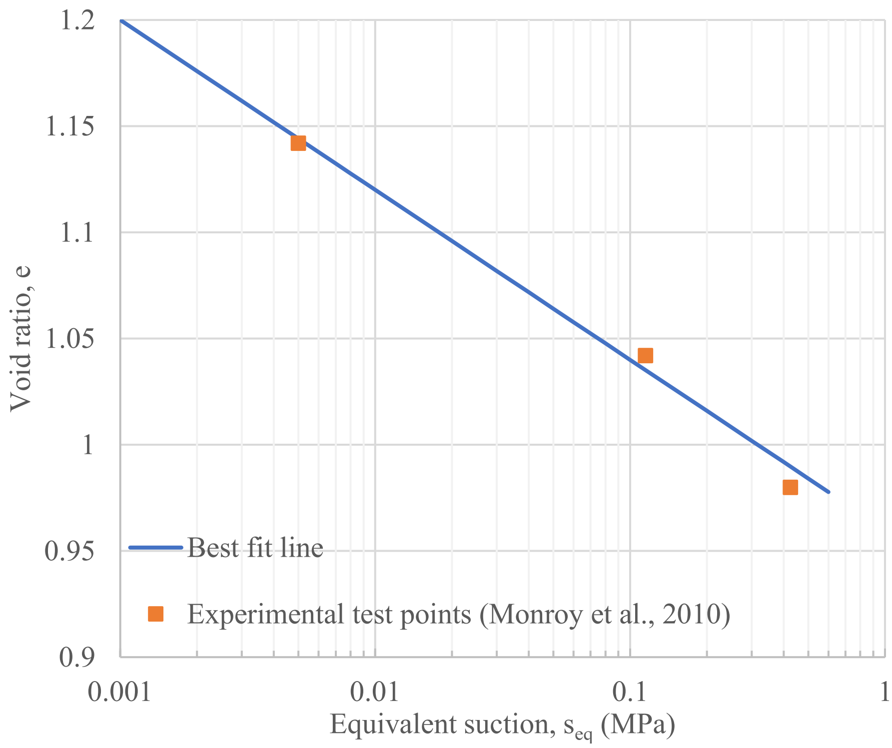

Figure 5.9: Line of best fit for void ratio vs equivalent suction to find κ_s.

The hydraulic properties of compacted London Clay were calibrated based on drying and wetting tests performed by Melgarejo-Corredor (2004) and on a design curve by Croney (1977). This is extensively discussed in Section 7.4.2. The air entry value adopted following from the SWRC calibration was 20kPa. Other parameters such as strength and Poisson ratio were taken from triaxial tests performed by Gasparre (2005), with the MCC shape adopted. The complete list of ICSSM parameters calibrated for the compacted London Clay is presented in Table 5.1.

Table 5.1: Table of parameters for the calibrated ICSSM

Parameter	Calibrated value
Parameters controlling the shape of the yield surface: α_f, μ_f	0.4, 0.9 (MCC shape)
Parameters controlling the plastic potential surface: α_g, μ_g	0.4, 0.9 (MCC shape)
Strength parameters: M_f, M_g	0.85
Characteristic stress ratio: α_c	1.98
Fully saturated compressibility coefficient: $\lambda(0)$	0.152
Elastic compressibility coefficient: κ	0.02
Maximum soil stiffness parameter, r	0.45
Soil stiffness increase parameter: β	0.011 kPa^{-1}
Elastic compressibility coefficient for changes in suction: κ_s	0.05 kPa
Poisson ratio: υ	0.3
Plastic compressibility coefficient for changes in suction: λ_s	0.5
Air-entry value of suction: s_{air}	5 kPa
Yield value of equivalent suction: s_0	10^6
Cohesion increase parameter: k	Dependent on S_r
Atmospheric pressure: p_{atm}	101.3 kPa
Minimum bulk modulus:	10 kPa

Using the above set of ICSSM parameters, a single element axisymmetric numerical analyses were performed with ICFEP, simulating all 6 tests outlined in Monroy et al. (2010). The initial conditions for each simulation, tabulated in Table 5.2, closely followed the initial conditions of the actual samples, reported in Monroy (2006).

Table 5.2: Initial conditions of the London Clay samples before the tests (Monroy, 2006)

Initial Condition	Value
Sample dimensions, D x H	75mm x 30mm
Dry density, ρ_d	1.38 Mg/cm^3
Water content, w	23.6%
Degree of Saturation, S_r	67%
Void ratio, e	0.95
Suction, s	0.99MPa
Vertical stress, σ_v	7kPa

(a)

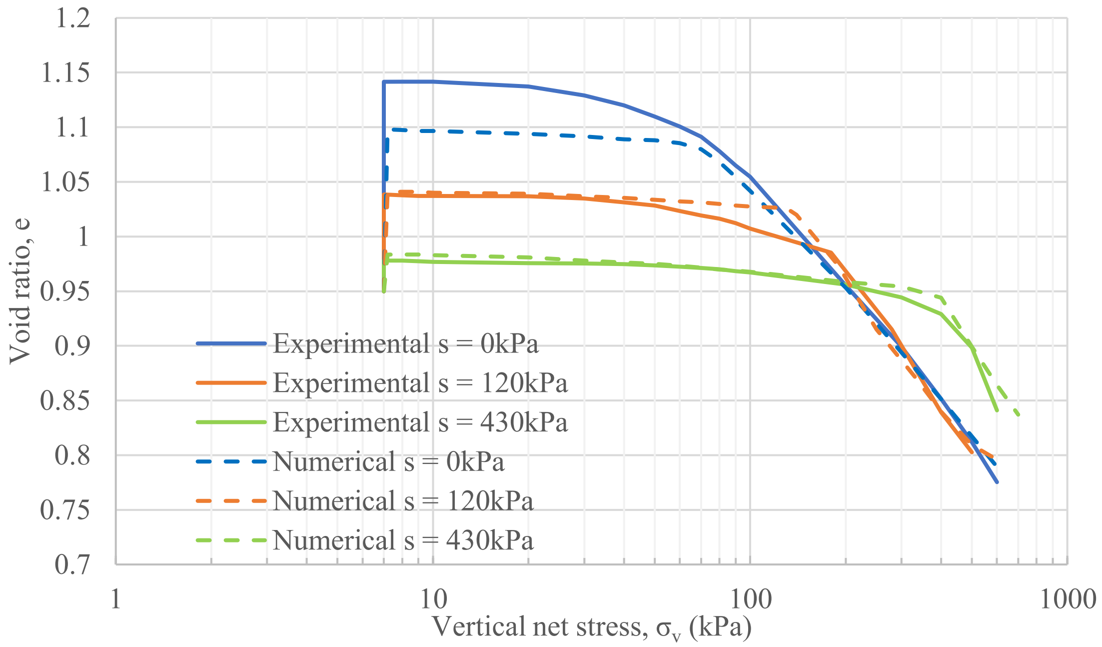

(b)

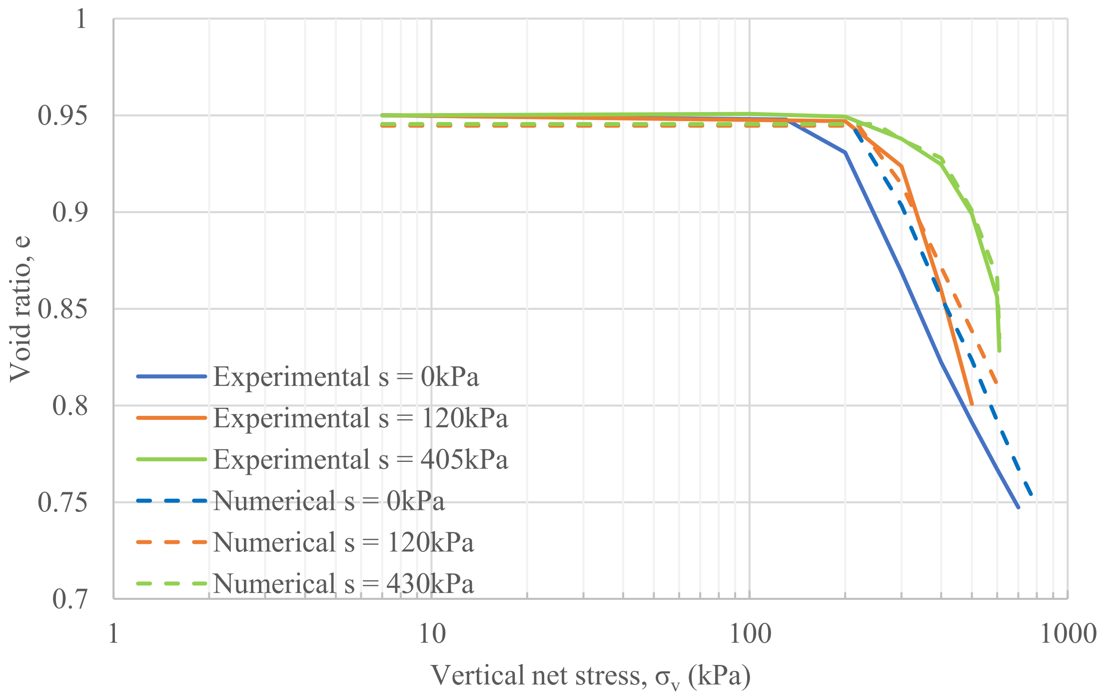

Figure 5.10: Comparison between the ICSSM single element analysis vs experimental tests by Monroy et al. (2010) for (a) the free swelling tests, and (b) the confined wetting tests.

The results of these analyses were presented in Figure 5.10, against the stress-strain paths of Monroy et al. (2010), showing a very close agreement. Slight discrepancy was observed in

Figure 5.10(a) in the mobilisation of the swelling strain for the experiment that simulated full saturation (reaching a zero suction) during the free-swelling path under nominal stress. The model was unable to reproduce the maximum change in the void ratio, however, the yield stress for that experiment and the subsequent compression path were well reproduced. The yield stresses in the initial constant-volume tests were well reproduced, as shown in Figure 5.10(b). Overall, the ICSSM was shown suitable for modelling a compacted unsaturated clay and was then applied in the modelling of compacted clay embankments in Chapter 7 and Chapter 8.

5.4 Soil-atmosphere interaction boundary conditions

To accurately model the soil-atmosphere interaction, specifically water infiltration into the soil from rainfall and removal of water from the soil via evapotranspiration processes, specialised boundary conditions are required.

5.4.1 Evapotranspiration boundary condition

The evapotranspiration boundary condition applied in the soil-atmosphere interaction numerical analyses in Chapter 7 and Chapter 8 was developed and implemented in ICFEP by Nyambayo and Potts (2010). A non-linear root water uptake model (RWUM) was used to simulate the removal of water from the soil by roots.

Fundamentally, a sink term representing the volume of water extracted per unit volume of soil in a unit of time was introduced into the continuity fluid flow equation. By assuming a triangular root water extraction function (Figure 5.11; Prasad, 1988), the maximum water extraction rate in an ideal moisture condition, S_{max}, was defined as:

$$S_{max} = \frac{2 \cdot T_p}{r_{max}} \cdot \left(1 - \frac{r}{r_{max}}\right) \tag{5.14}$$

where T_p is the potential evapotranspiration rate, r the root depth from the ground surface and r_{max} the maximum root depth.

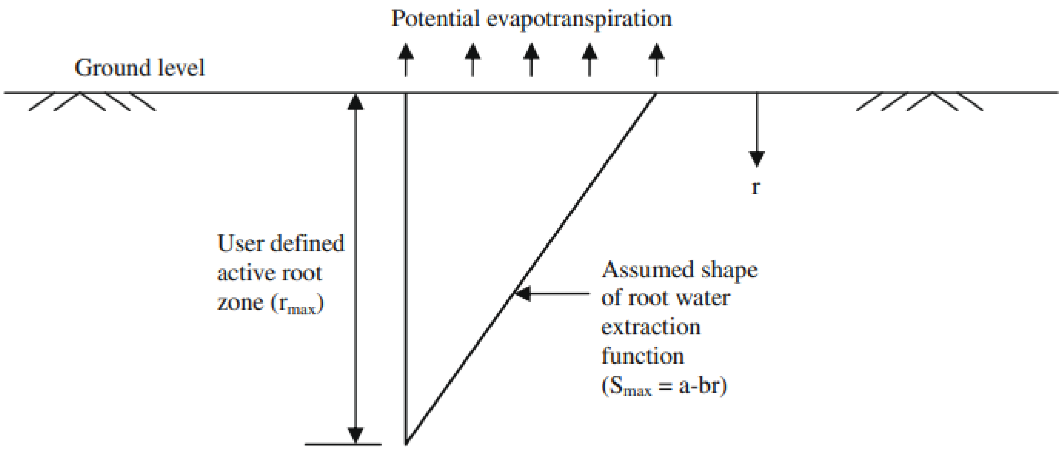

Figure 5.11: The linear root water extraction function within the root zone (Nyambayo and Potts, 2010).

However, soil moisture conditions are not always ideal for plant evapotranspiration. When suctions within the soil are very high, such as during droughts, plants struggle to extract water from the soil, resulting in wilting. On the other hand, when suctions are extremely low, such as in the event of a flood or ponding, evapotranspiration ceases as roots are unable to function due to water-logged conditions (i.e. lack of air or anaerobiosis).

Thus, to simulate more realistic evapotranspiration extraction across a wider range of suction conditions, Feddes et al. (1978) proposed a modification to the sink term such that the actual maximum sink, S_{acc} is given as:

$$S_{acc} = \alpha \cdot S_{max} \tag{5.15}$$

where the parameter α varies with suction as given in Figure 5.12. For suctions below S1 (anaerobiosis point) and above S4 (wilting point) α is assumed equal to zero, while its value is assumed equal to 1 for suctions between S2 and S3, which represent the range for ideal moisture content for maximum plant growth. Suctions S1, S2, S3 and S4, and maximum root depth r_{max} are input parameters and are dependent on plant type. According to Nyambayo and Potts (2010), S1, S2 and S4 are generally taken in the literature to be 0kPa, 5kPa, and 1500kPa respectively. The value of S3 (typically varying from 50kPa to 100kPa) is found to have no significant effect on the actual evapotranspiration rate and was taken as 50kPa, while S1 is typically taken as 0kPa, when the soil is flooded and plants do not evapotranspirate. An S4 value of 1500kPa was first proposed by Richards and Weaver (1943), who defined the soil permanent wilting point as the water content retained in the soil under a matric potential of 1500kPa and it is considered independent of soil grain size and composition. However, it was found in Chapter 7 that having S4=1500kPa produced unrealistically high suction values during the summer, to the extent of 400kPa. Further plant wilting point studies (Wiecheteck et al., 2020; Dexter et al., 2012) showed that there is a difference between biological wilting point and the soil permanent wilting point (of 1500kPa), and that the plant and soil type significantly affects the biological wilting point which should be taken as S4 instead. In Wiecheteck et al. (2020), it was found that in clayey soils the biological wilting point for wheat and barley varies between 370kPa and 18760kPa, with an average close to 900kPa in their study. Thus, it was decided to lower S4 to 750kPa so that more realistic suction ranges due to evapotranspiration were produced. The r_{max} for grass was taken to be 0.1m, while r_{max} for shrubs and trees was 0.5m and 2.0m respectively.

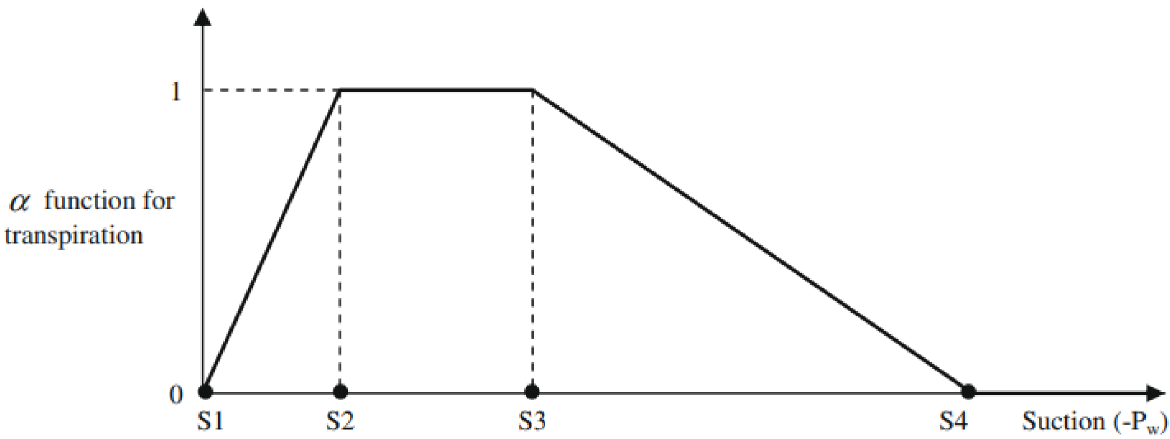

Figure 5.12: Piecewise linear function for the α function against suction.

The potential evapotranspiration rates are governed by plant type and climate conditions such as solar radiation, wind speed and temperature. The reference potential evapotranspiration ET_0 only takes into account climate variables at the site and is independent of plant properties. Penman (1948) introduced a reliable method for calculating reference evapotranspiration rates by combining the energy balance equation at the evaporating surface with equations for vertical steady fluxes for heat and water vapour above the evaporating surface. This was further expanded upon by Monteith (1965), forming the Penman-Monteith equations for determining potential evapotranspiration. The Food and Agriculture Organisation (FAO) further developed and standardised the Penman-Monteith method for all regions and climates (Allen et al, 1998) and introduced correlations that take into account limited and missing climate data for calculating the reference potential evapotranspiration:

$$ET_0 = \frac{0.408\Delta(R_n - G) + \gamma \frac{900}{T + 273} u_2(e_s - e_a)}{\Delta + \gamma(1 + 0.34u_2)} \tag{5.14}$$

where R_n is the net radiation; G the soil heat flux; $(e_s - e_a)$ represents the saturation vapour pressure deficit of the air, with e_s being the saturation vapour pressure and e_a the actual vapour pressure; Δ is the slope of the vapour pressure curve; γ the psychrometric constant; u_2 the wind speed at 2m height, and T the mean daily air temperature at 2m height.

For the Magnolia Road rail embankment site, meteorological data between 2006 and 2011 was obtained from a weather station at Shoeburyness (Met Office, 2012), approximately 10km from the site, and the monthly reference potential evapotranspiration was calculated for the site. It was found that the monthly ET_0 varied significantly throughout the seasons within a year, however the monthly rates did not vary much from year to year (Fig. 5.13). Thus, the average ET_0 for each month was adopted for the analysis in Chapter 7, as tabulated in Table 5.3.

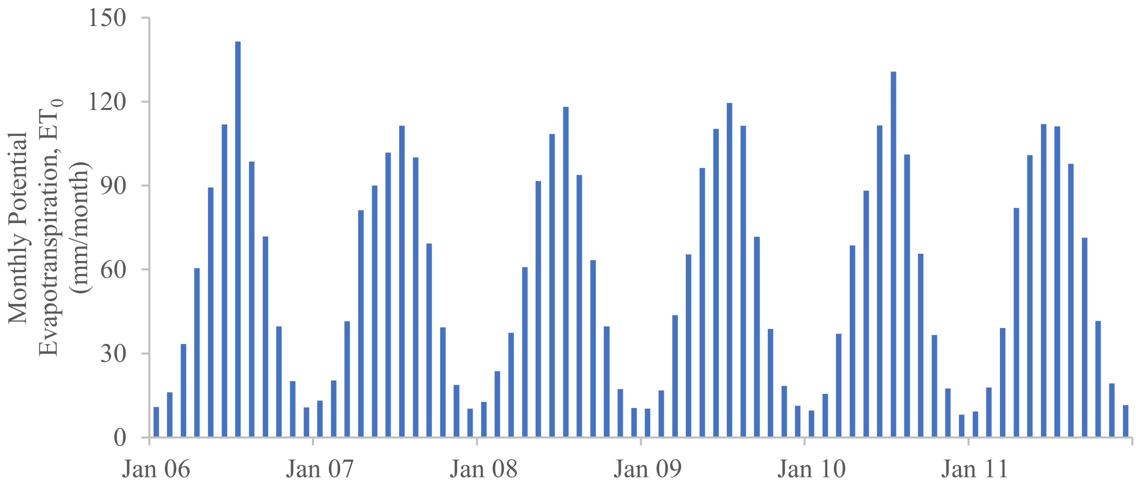

Figure 5.13: Monthly reference potential evapotranspiration, ET_0 at Shoeburyness from 2006 to 2011. Meteorological data provided by Met Office (2012).

Table 5.3: Average monthly reference potential evapotranspiration, ET_0.

Month	Average monthly reference potential evapotranspiration, ET_0 (mm/month)
Jan	10.966
Feb	18.382
Mar	38.731
Apr	69.748
May	92.706
Jun	109.274

Jul	122.089
Aug	100.468
Sep	68.868
Oct	39.306
Nov	18.572
Dec	10.431

An empirical crop coefficient factor (K_c) was then applied to the reference potential evapotranspiration to obtain the crop evapotranspiration (ET_c), which is defined as the evapotranspiration rate of crops growing under optimum agronomical and soil water conditions (Allen et al., 1998). Crop coefficients are highly dependent on the plant type, growth stage, plant height and cover. Meyer et al. (1985) provided monthly K_c values for both warm and cool types of grasses, while Allen et al (1998) provided K_c values for the various growth stages of a variety of agricultural crops. For the analysis in Chapter 7, K_c values for cool grass were adopted for grass vegetation, berries were used as a representative for shrub vegetation, and deciduous fruit trees such as apple trees were used to represent deciduous trees growing on the slopes of the Magnolia Road embankment. The K_c values are summarized in Table 5.4.

Table 5.4: Crop coefficient values for various vegetation types which will be applied in the numerical models in Chapter 7.

Month	cool grass	Berries mix	Trees mix
Jan	0.061	0.305	0.61
Feb	0.064	0.32	0.64
Mar	0.075	0.375	0.75
Apr	0.104	0.4	0.85
May	0.095	0.46	0.95
Jun	0.088	0.525	1.05
Jul	0.094	0.525	1.05
Aug	0.086	0.525	1.05
Sep	0.074	0.45	1.05
Oct	0.075	0.375	0.8
Nov	0.069	0.345	0.69
Dec	0.06	0.3	0.6

5.4.2 Precipitation boundary condition

To simulate realistic infiltration due to rainfall, a precipitation boundary condition was developed and implemented in ICFEP (Smith, 2003; Smith et al., 2008). This boundary condition alternates two different hydraulic conditions on the surface nodes of a finite element mesh, either an infiltration condition with a constant inflow rate, or a constant pore water pressure condition. At the start of every increment for which this boundary condition is active, the numerical solver first compares the pore water pressure at the boundary nodes with the prescribed pore water pressure. If the current pore pressure is more tensile than the prescribed pressure, the infiltration boundary condition is applied at the node. Otherwise, if the current pore pressure is more compressive than the prescribed pressure, the boundary node adopts the fixed pore pressure condition instead and only a portion of the prescribed infiltration is applied. In this situation, ponding has occurred on the surface with a fixed pore pressure, and any excess water build up is considered as run-off and is ignored.

For the analyses in Chapter 7 and Chapter 8, the flow rate was prescribed equal to the rainfall rates, while a fixed value of pore water pressure was prescribed as suction of 10kPa. If the pore water pressure is set to 0kPa, indication is that in very intense rainfall the ground would be fully saturated and any excess water build-up on the surface would be a run-off. However, doing so would remove all suctions within the ground and prevent any evapotranspiration from occurring via the vegetation boundary condition, which would be unrealistic. Therefore, a prescribed pore pressure of 10kPa in tension was applied instead to allow some suctions to be maintained near the surface.

As the analysis in Chapter 7 aimed to simulate the complete lifecycle of the Magnolia Road railway embankment, average monthly rainfall from 1971 to 2000 in Greenwich, London (Met Office, 2012), was taken as the monthly prescribed rainfall throughout the analysis (Figure 5.14). This rainfall resolution was applied to examine the seasonal behaviour and long-term effects of vegetation growth on the embankment. Applying a finer temporal resolution rainfall throughout the embankment lifecycle would be computationally expensive and further discussion and justification of this point is provided in Chapter 7.

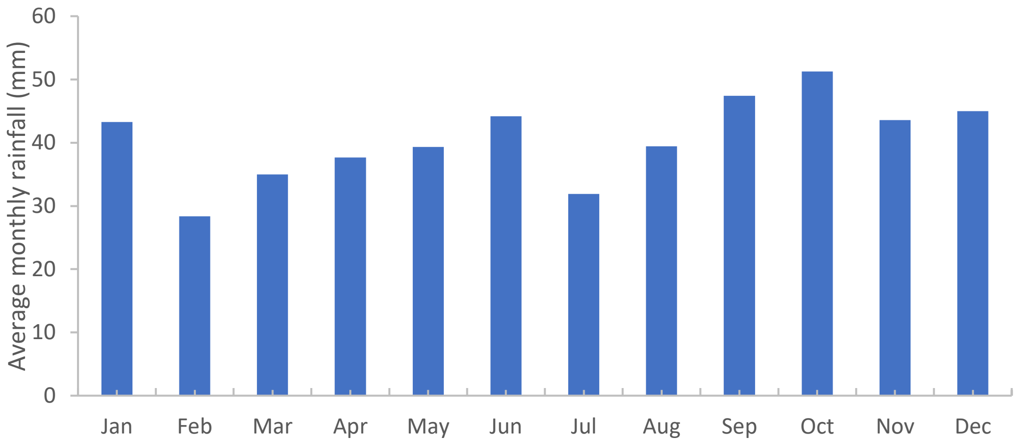

Figure 5.14: Average monthly rainfall in Greenwich, London from 1971 to 2000. Raw rainfall data provided by Met Office (2012).

5.5 Summary

In this chapter past and present geotechnical and reliability analyses of flood embankments and soil-atmosphere interaction were briefly reviewed, highlighting the benefits and drawbacks of different approaches.

The background and formulation of the unsaturated ICSSM constitutive model were summarised for the simulation of initially unsaturated earth embankments constructed from compacted London clay. The model was calibrated using the experimental data from oedometer tests performed on compacted London clay and from triaxial tests performed on intact London clay. The derived model parameters from the input to finite element analyses of earth embankments in Chapter 7 and Chapter 8.

Finally, both vegetation and precipitation boundary conditions, which were employed to model and control soil-atmosphere interaction in the numerical models, were discussed. Emphasis was given on derivation of average monthly potential evapotranspiration and rainfall, both of which were applied as hydraulic boundary conditions in the embankment lifecycle analyses in Chapter 7 and Chapter 8.

Chapter 6: Numerical Modelling of the Foundation Soil Supporting Flood Embankments

6.1 Introduction

One of the key objectives of this research has been the lifecycle assessment of flood embankments through predictive numerical modelling. As this type of structure is usually raised along river banks and coastlines, the foundation soil predominantly constitutes soft clay. This chapter focuses on establishing a realistic and robust numerical model capable of simulating the behaviour of soft clay foundations. For this purpose use was made of the research studies by the Building Research Establishment (BRE) in 1970s and 1980s on soft clay embankments along the river Thames (e.g. Marsland, 1968, 1973, 1974; Marsland and Powell, 1977; Powell and Uglow, 1987), to select a suitable case study for the validation of the developed numerical model.

The North Sea flood of 1953 necessitated many new embankments to be constructed or existing ones to be raised along the River Thames, to prevent another major flood event. However, many of the existing embankments had already been widened and raised before and were showing signs of low stability, manifested by slip failures often occurring on the riverward side (Cooling and Marsland, 1954; Golder and Palmer, 1955; Marsland 1957). It was thought that to raise them by another 1m to 2m would have increased their instability, leading to more slips. Hence, the construction of new embankments was deemed necessary on the virgin marshland. To investigate the viability of using the marshland as a foundation soil, a number of field trial embankments were constructed as part of site investigation. One such embankment was constructed and raised to failure on the site adjacent to Littlebrook power station in Dartford in 1976 (Marsland and Powell, 1977) and was selected as a suitable case study for the development of an appropriate numerical model for the foundation soil.

This chapter introduces the construction of the embankment, available site investigation and characterisation of the ground conditions, as well as the monitoring undertaken during the construction of the trial embankment. The finite element model for the problem is then elaborated, starting with the discretisation of the problem geometry followed by a brief discussion and calibration of the extended Modified Cam Clay model for the foundation soil.

The construction sequence and boundary conditions of the numerical model are then outlined in detail. The results from the numerical model are compared with field monitoring data, primarily in terms of the horizontal displacements, pore water pressures and slip surface generation. Similarities and differences between the numerical results and field observations are noted. Finally, some concluding remarks are provided and the calibrated model for the foundation soil is used for the general flood embankment analysis in Chapter 8.

6.2 Site characteristics, construction and monitoring

6.2.1 Site characteristics

The test site was located adjacent to Littlebrook power station in Dartford, Kent (Figure 6.1), approximately 10m on the riverward side of the existing embankment. The ground level at the site was +3.2m ODN, some 2.5m higher than the marshes on the landward side of the existing embankment. The river level changed twice daily with a mean range of 5.5m due to the tides. As such, the ground level generally remained above water and there was a thin layer of surface crust with vegetation.

Figure 6.1: Satellite view of Dartford, Kent (Google, 2018). The area of research is shown in the red box, with Littlebrook Power Station marked with a red star.

The soil profile consisted of 12m of soft silty-clays and clay-silts, layered with some peat and fine sand laminations, overlaying sand and gravel which in turn rested on a chalk bedrock.

Figure 6.2 (from Marsland and Powell, 1977) depicts profiles of moisture content and saturated density, the latter being broadly uniform with depth, with an average value of around 1500 kg/m^3. The top 3m of the deposit, described as a very soft organic silty clay, had a high moisture content at around 80%, as well as high clay content (50%-60%) and plasticity index (~40%). As the deposit became more silty at depth the moisture content reduced to around 40%, clay content to about 25% and plasticity index to around 20%. Organic content was less than 5% in the top 3m, reducing to around 2% at depth. Two 0.5m thick lenses of peat were identified at 0m and -4m ODN. The ground water level was at 1m below the ground surface.

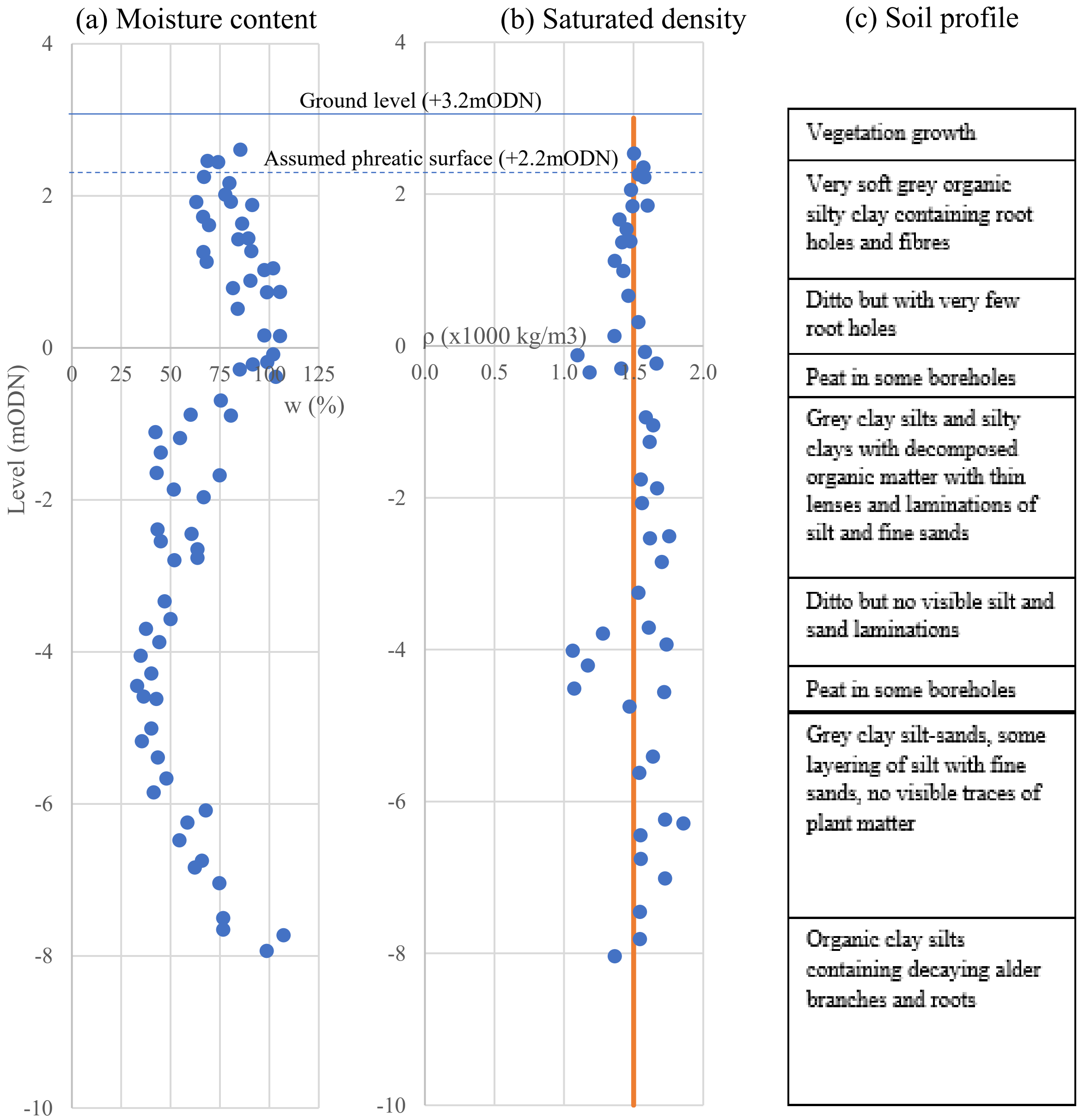

Figure 6.2: (a) Moisture content; (b) bulk unit weight and (c) soil profile of the top 11m of clay at the site (data from Marsland and Powell, 1977).

A programme of undrained triaxial tests was performed on soil specimens taken at frequent depth intervals using a stationary piston sampler, fitted with 1m long, 100mm internal diameter and 2mm thick tubes. Due to the very soft ground, the sampler was pushed down steadily, without using percussive tools, and a low pressure air was fed to the cutting edge of the sampler during extraction to prevent development of high suctions (Marsland and Powell, 1977). This process was thought to retrieve high quality samples, with little disturbance, compared to samples obtained by hand excavations on adjacent sites.

Undrained shear strength

Four types of undrained triaxial compression tests were performed, with measurements of the undrained shear strength, S_u, summarised in Figure 6.3(a). Standard tests, comprising 100mm diameter and 200mm high samples with rough ends, were unconsolidated and conducted as either quick (SQT UU) or slow (SST UU), the latter including the pore water pressure measurement. Tests with lubricated ends were performed as a check of possible sample disturbance, comprising specimens 100mm in diameter and 150mm high. These were slow tests with pore water pressure measurement and either unconsolidated (LEST UU) or consolidated (LEST CU). For latter tests, the vertical effective stress was estimated assuming that the ground water level was 1m below the ground surface, while a value of $K_0 = 0.8$ was used to establish the in-situ horizontal effective stress (Marsland and Powell, 1977). The results from the field vane shear tests were also added in Figure 6.3(a).

Despite the scatter observed among different sets of tests, it was clear that the top 3m of the deposit was consistently much softer in all types of tests performed, compared to the soil at depth. Due to the fluctuating ground water level, it was interpreted for this research that the undrained shear strength in triaxial compression, $S_{u,TC}$, may be taken as higher at the ground surface ($S_{u,TC} =$ 10kPa at +3.2m ODN), reducing to 8kPa at 0m ODN. A subsequent linear increase up to approximately $S_{u,TC} =$ 50kPa at -10m ODN was considered a reasonable approximation of the observed scatter in the data. The final $S_{u,TC}/\sigma_v'$ of approximately 0.27 in normal to slightly overconsolidated clays matches well with the $S_{u,TC}/\sigma_v'$ of other clays with similar plasticity index of 20% (Ladd and Edgers, 1972; Ladd et al., 1977).

In-situ stresses

Figure 6.3(b) plots profiles of the effective overburden stress (taken as effective vertical stress) at the site as given by Marsland and Powell (1977) in grey, the expected effective vertical stress at the site for OCR=1.0 (blue) and of the preconsolidation pressure estimated from oedometer tests, as derived by Marsland and Powell (1977), in orange. The latter profile indicated that the soil from 0m ODN to −3m ODN was approximately normally consolidated, while the rest of it was lightly overconsolidated. From general observations of the local topography Marsland and Powell (1977) further inferred that the top 3m of the site was probably an infill material, deposited at a later date than the clays found in the shallow depths of the neighbouring marshes.

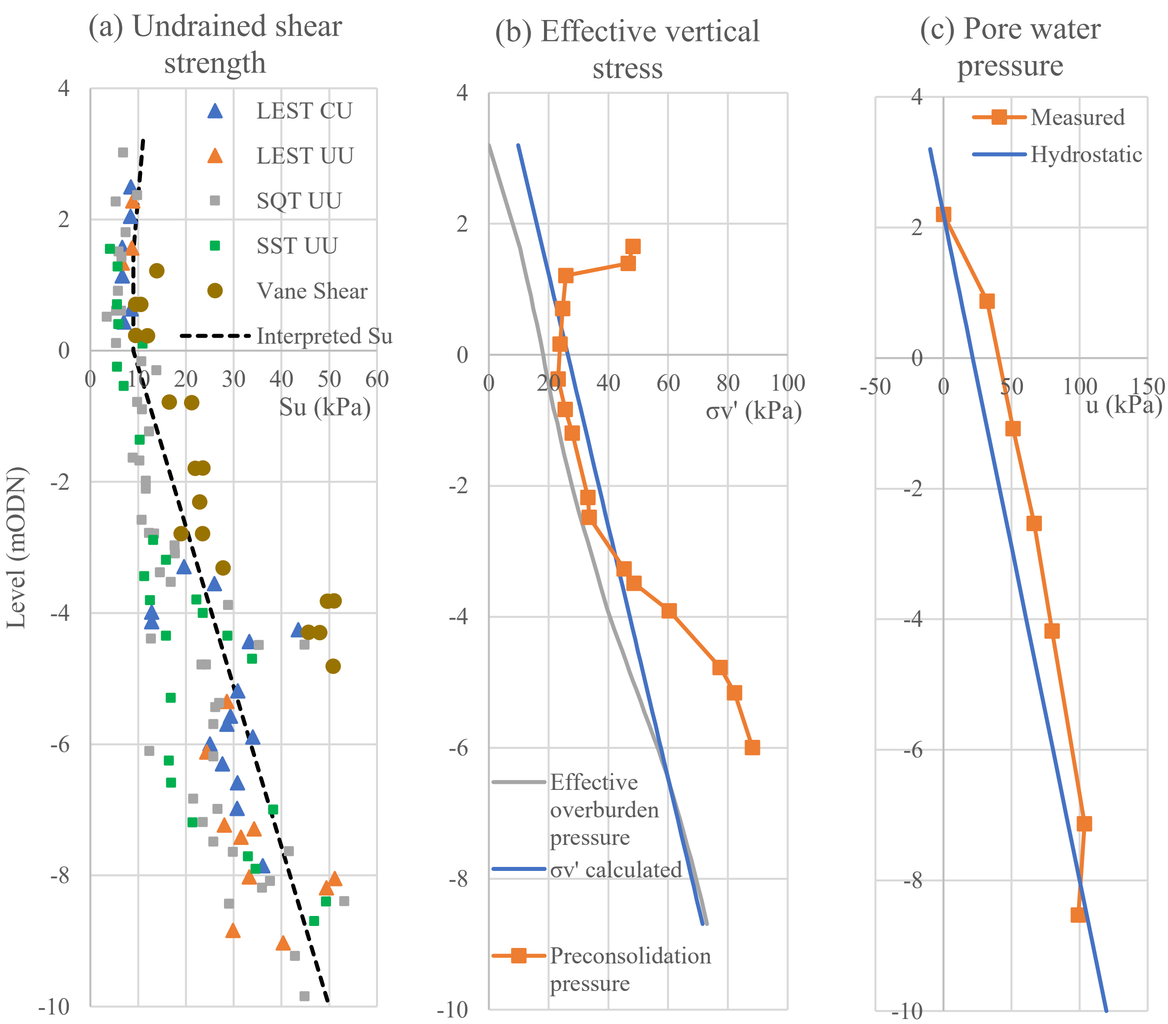

Figure 6.3: (a) Interpreted undrained shear strength profile of the clay in triaxial compression, results are from undrained triaxial tests and vane shear tests. (b) Graph of the effective vertical stress at site and the preconsolidation pressure profile from oedometer tests. (c) Comparison between initial field pore water pressure and an assumed hydrostatic pore pressure profile. Field data from Marsland and Powell (1977).

Figure 6.3(c) shows the pore water pressure profile at the site before construction of the embankment. The pore water pressure values were obtained from piezometers C1 – C6, positioned at up to 12m depth below the embankment (see Figure 6.4 for the location of field instrumentation, Marsland and Powell, 1977). This was plotted alongside a hydrostatic pore water pressure profile with an assumed water table at +2.2m ODN (1m below ground level). The piezometer readings indicated that pore water pressures were higher than hydrostatic up to 10m depth, before reducing to hydrostatic. Given that the site was next to the river Thames and that the high tides would not submerge the site unless during spring, it was considered unrealistic for the pore water pressures to be higher than the assumed hydrostatic profile. Thus, the assumed hydrostatic profile, with the water table at +2.2mODN, was adopted for the numerical modelling of the ground undertaken in this research.

6.2.2 Embankment geometry, construction sequence and monitoring points

The embankment cross-sectional geometry and installed monitoring instrumentation are shown Figure 6.4 (Marsland and Powell, 1977). The embankment was approximately 40m long. The soils on site comprised 2 main types, namely the embankment soil (in blue) consisting of dredged sands and gravels, and the foundation soil consisting of soft clay, silts and peat previously introduced in Section 6.2.1. Ground level was at +3.2mODN, marking the boundary between the two soil layers. Piezometers, inclinometers and magnet extensometres were installed in the foundation soil in 4 vertical sections IB, IC, ID and IE, as shown in the figure. Additional survey targets were positioned on the crest of the berms and on one of the embankment slopes.

While the site was heavily instrumented, Marsland and Powell (1977) reported only a selection of measurements: piezometer readings C1 to C6, horizontal movements at the centre of the berm crest (the exact berm referenced was not clear, this point will be explored further when compared with the numerical results), as well as the inclinometer measurements at IC and ID vertical sections, presented in Section 6.2.3.

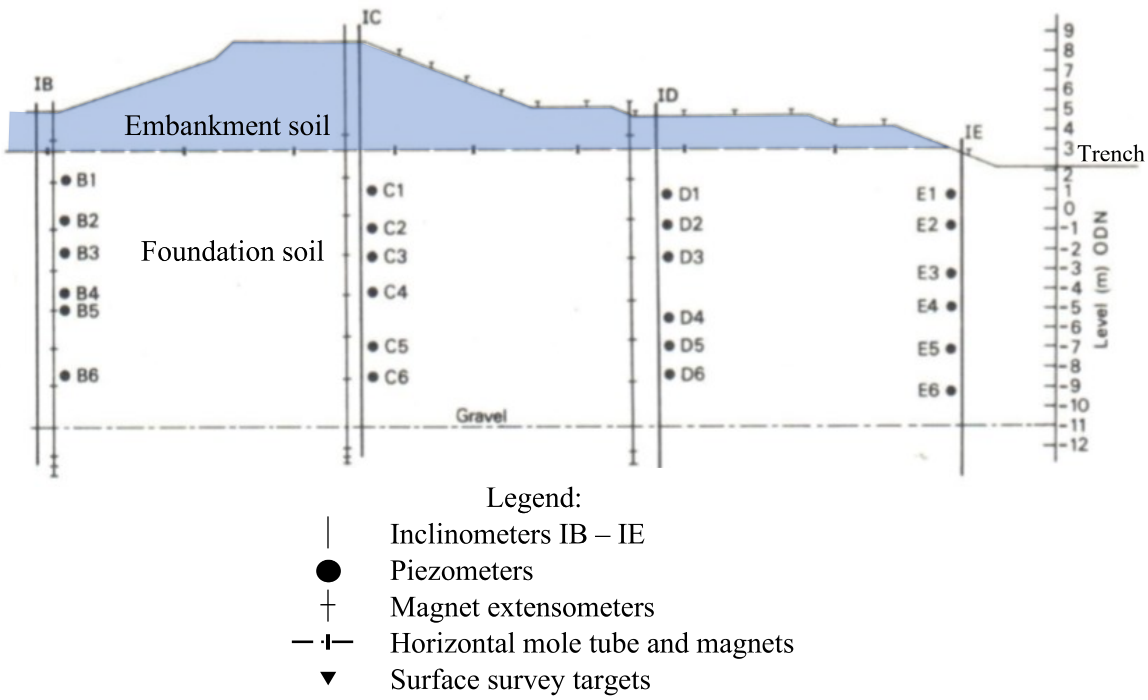

Figure 6.4: Cross-sectional view of the instrumentation employed in measuring the displacements and pore pressures in the foundation soil of the trail embankment (Marsland and Powell, 1977).

.

Construction sequence

The trial embankment was constructed using sandy gravel as fill material and contained several berms, as depicted in the transversal cross-section in Figure 6.4. The construction started after the installation of the monitoring instrumentation was completed and sets of initial measurements were taken. A timeline of the construction sequence is detailed in Table 6.1, together with Figure 6.5 for illustration.

Table 6.1: Construction sequence of the trial embankment, from Marsland and Powell (1977).

Day	**Action**
1 – 30	Excavation of the trench
31 – 45	Construction of 1st phase berm using clay from the trench (up to +4.2mODN)
46 – 60	Construction of sand berm 2 (up to +5.1mODN)
61 – 66	Construction of embankment (up to +5.83mODN)
67 – 69	Construction of embankment (up to +6.17mODN)
70 – 73	Construction of embankment (up to +6.5mODN)
74 – 76	Construction of embankment (up to +6.83mODN)

77 – 78	Construction of embankment (up to +7.17mODN)
79 – 80	Construction of embankment (up to +7.5mODN)
81 – 82	Construction of embankment (up to +7.83mODN)
83 – 87	Filling the trench with water and leaving it full for 5 days
88	Draining the trench
89	Increasing the width of the embankment by 3m
90	Construction of embankment (up to +8.17mODN)
91	Construction of embankment (up to +8.5mODN)

In summary, a 1m deep trench was first excavated at the proposed toe of the embankment, to elevation of +2.2m ODN. The purpose of the trench was to be filled with water, and hence slow down the movement of the embankment (and risk of failure), at times when the field work was unmanned in between construction stages. The clay from the trench was placed into the first berm constructed to elevation of +4.2m ODN. Additional damp sandy gravels obtained from stockpiles was then used to construct the second berm to +5.1m ODN, to create a good working surface for erecting the embankment. Following from this, the trial embankment was constructed in compacted horizontal layers approximately 0.33m thick each.

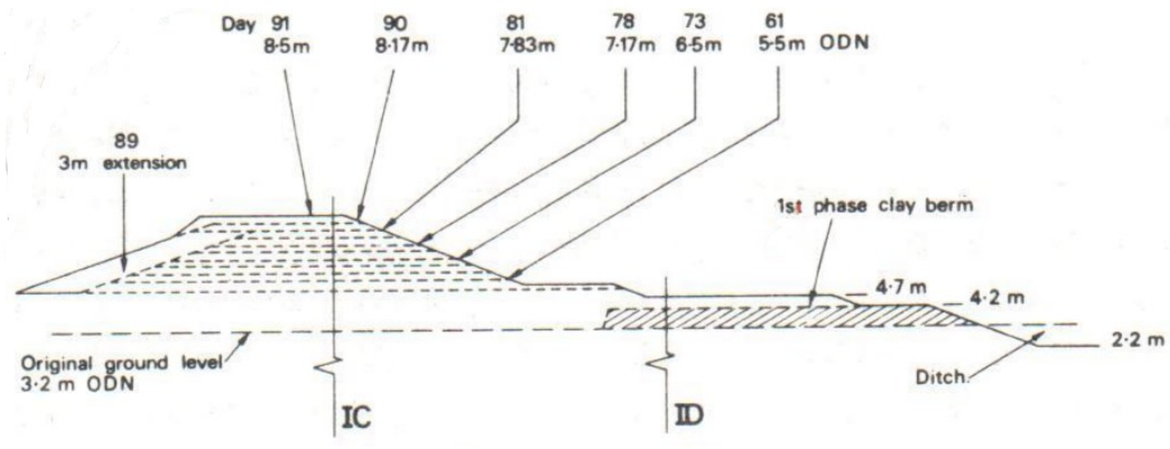

Figure 6.5: Illustration of the construction sequence of the berm and trial embankment (Marsland and Powell, 1977).

Twenty-two days after the construction of the first embankment layer (day 60), the trial embankment had reached +7.83m ODN elevation (day 82). Due to the impending week-long holiday, the trench was filled with water and the site left unmanned for 5 days. After the holidays a considerable increment of horizontal movements (around 40-50mm) was measured by inclinometers IC and ID (see Figure 6.5 for locations) and at the surface target located near the centre of the berm, but the embankment had not yet failed. Thus, the construction was extended to allow further raising and widening of the embankment and the trench was drained beforehand. Over the next 2 days the embankment was raised to an elevation of +8.5m ODN, when it started to fail, mobilising large increments of the horizontal movement. A clear slip surface formed over 10 hours after the last layer was placed. The evolution of the embankment height from the initial ground surface level of +3.2m ODN is plotted against time in Figure 6.6, showing the average construction rate of the embankment of around 0.1m/day (between day 50 and day 90).

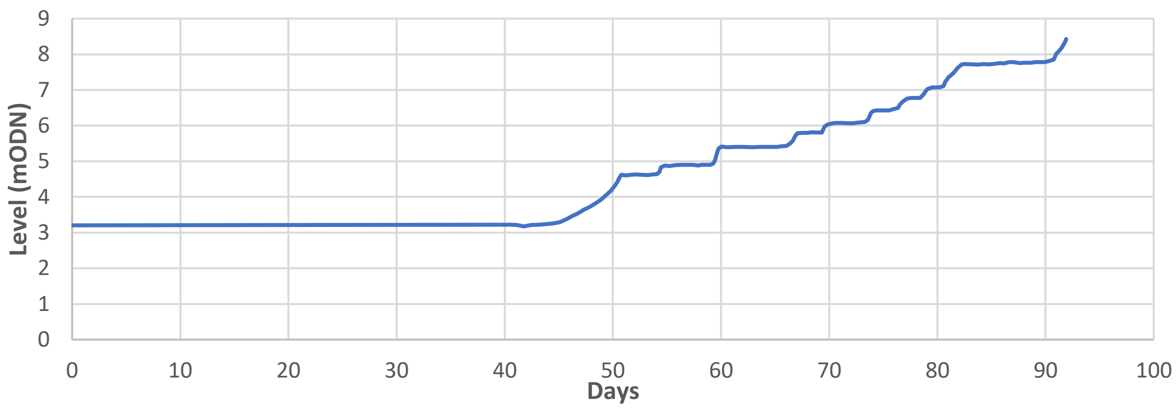

Figure 6.6: Construction profile of the trial embankment.

6.2.3 Field monitoring data

The piezometer data C1 to C6 from underneath the embankment is shown in Figure 6.7, as evolution of pore water pressures with time of construction. In general, the measurements mirrored the construction rate in Figure 6.6, in that pore water pressures rose with the construction steps presented in Table 1. This also indicated that most of the embankment construction could be considered as undrained, as excess pore water pressures were generated and were not dissipating very fast.

However, when the embankment was left without any activity for a week, starting on Day 83, there was a drop of approximately 10kPa of pore water pressure in the shallowest piezometers C1 and C2. This indicated that a certain degree of consolidation in the foundation soil had occurred during the break, which may have provided additional strength to the foundation soil and allowed further embankment raising later on Day 90.

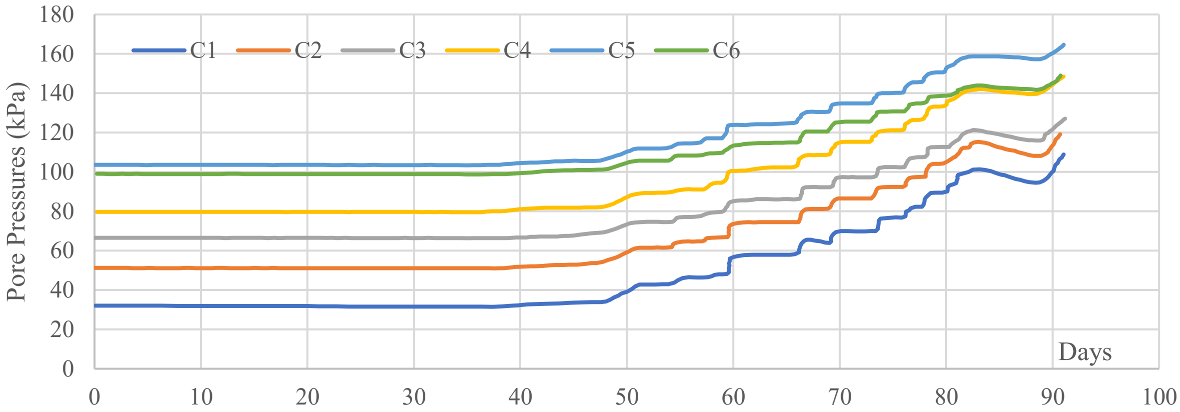

Figure 6.7: Evolution of pore water pressures with construction at piezometer C (data from Marsland and Powell, 1977)

Figure 6.8 shows the evolution of the horizontal movement measured in the centre of the crest of the sand berm, which is why the time axis starts at Day 60, after the construction of this berm was completed. As no further information concerning the location of this horizontal displacement measurement was provided, several potential monitoring points were examined and results from the numerical model at those points were compared with this measurement in Section 6.4.1. In general, the lateral spreading from the embankment toe increased with further layers of construction. By the time the construction was paused (at Day 83), the change in the displacement gradient had become substantial from around Day 78, indicating that the embankment was nearing failure. The pause period, and the trench filled with water, seemed to have allowed for some consolidation / pore water pressure dissipation to take place, which slowed down the lateral spreading. However, the failure was fully realised with the final layer of embankment construction.

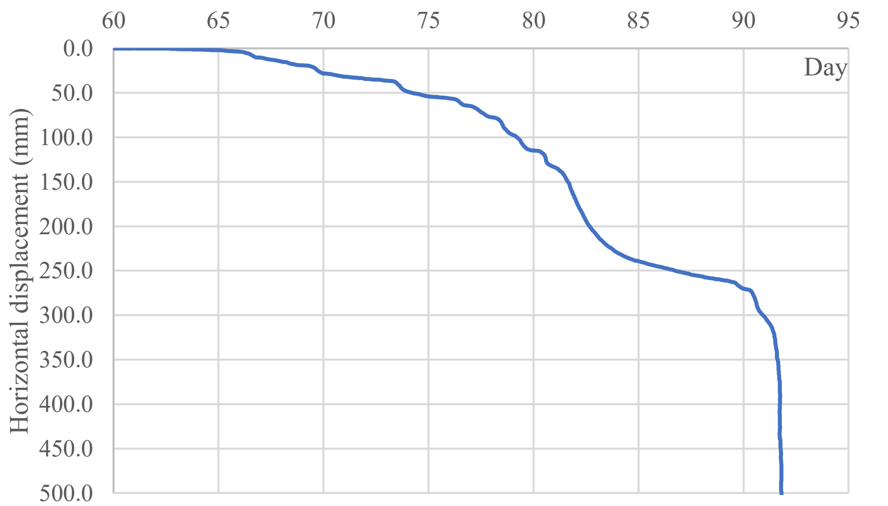

Figure 6.8: Surface horizontal displacements at the centre of the sand berm.

Figures 6.9(a) and 6.9(b) show the results from the inclinometer readings at IC and ID sections (see Figure 6.4) during the construction of the embankment. From the results, which show a significant increment of movements in both sections between Day 90 and Day 91, it is evident that a slip surface was starting to form at around -1.5m ODN at IC section, while a deeper slip surface, at around -3.5m ODN, was forming at ID section, during the last stage of construction before failure. With measurements from inclinometers and breaks in the mole settlement gauges, it was possible to draw out the slip surface that formed at embankment failure, as shown in Figure 6.10.

a)

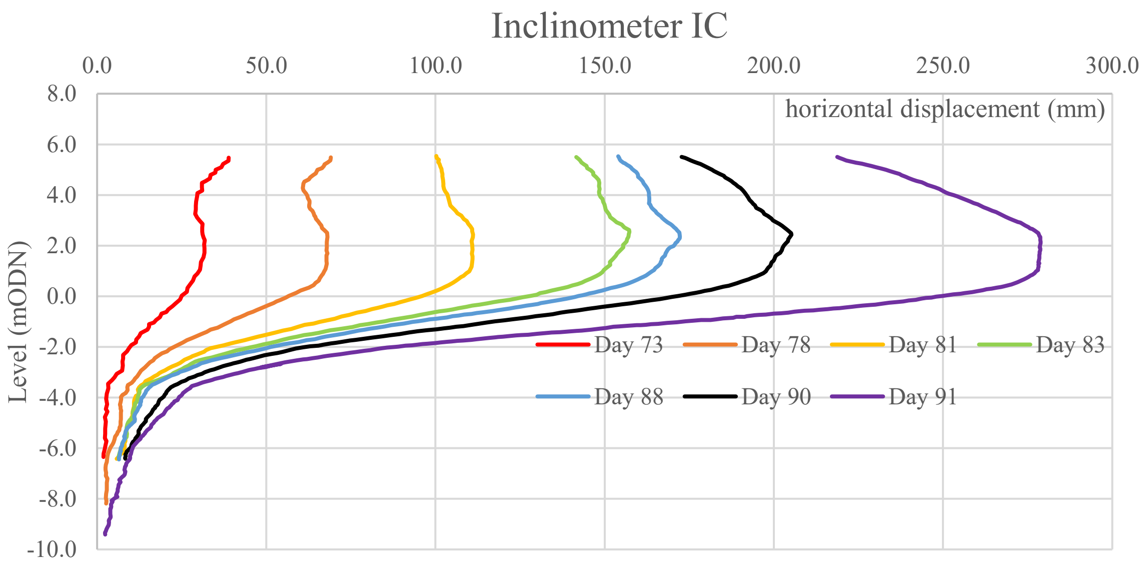

b)

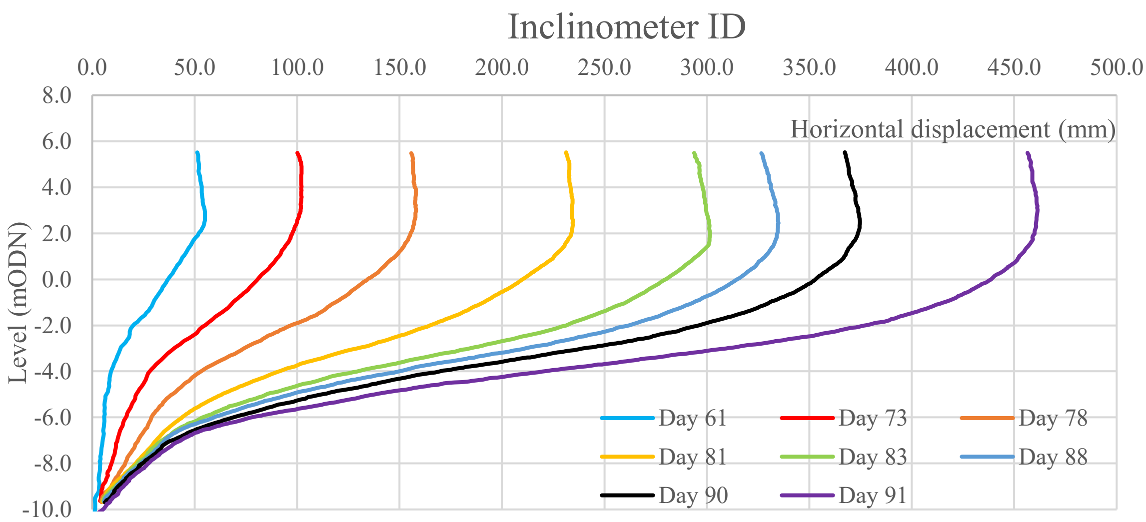

Figure 6.9: Inclinometer (a) IC and (b) ID data during the construction of the embankment.

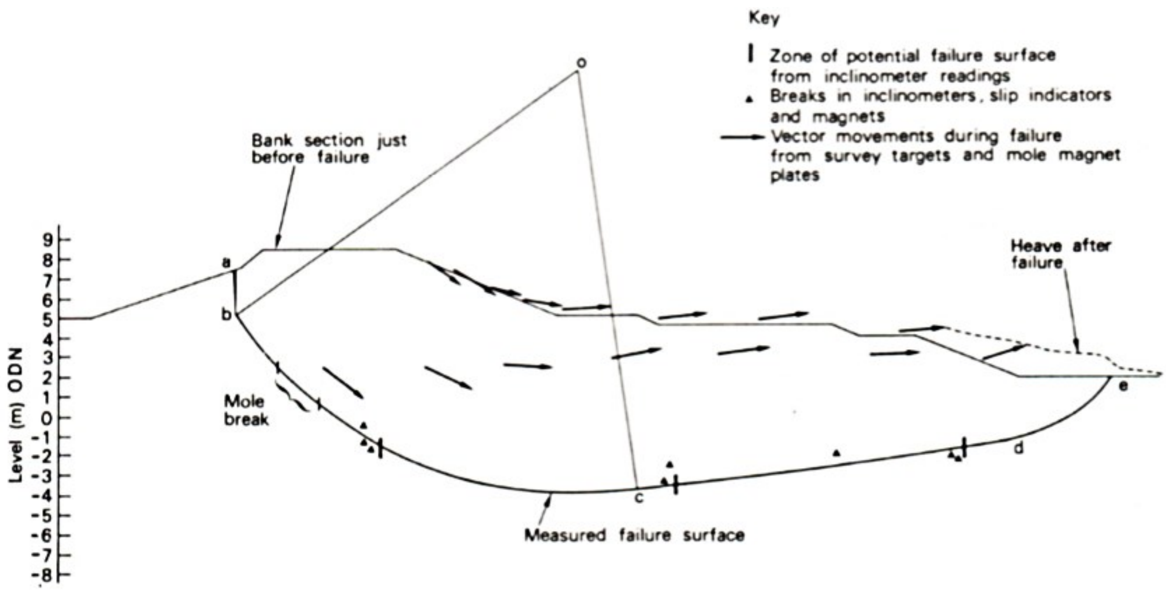

Figure 6.10: Observed slip surface that formed when the embankment failed (Marsland and Powell, 1977).

6.3 Finite element analysis of trial embankment

6.3.1 Introduction

As introduced earlier, the Dartford trial embankment was used as a case study in this research to develop a numerical model for a representative soft-clay foundation. The validity and accuracy of the model would be demonstrated by comparisons between calculated and measured (as introduced in Section 6.2) ground movements and pore water pressures mobilised during the embankment construction. The numerical model was developed with the Imperial College Finite Element Program (ICFEP) (Potts and Zdravkovic, 1999). This involved hydro-mechanically coupled two-dimensional (2D) plane strain finite element (FE) analyses of the trial embankment, applying the construction sequence and timeline of construction as introduced in Section 6.2.

6.3.2 Geometric discretisation and finite element mesh

The FE mesh of the trial embankment is shown in Figure 6.11(a), with the close-up of the embankment detailed in Figure 6.11(b). It comprised eight-noded quadrilateral elements, which have two displacement degrees of freedom at each node and a pore water pressure degree of freedom at corner nodes. The far field vertical boundaries were assumed to be 40 m to the left of the embankment's left toe and 50 m to the right of the berm toe. The base of the mesh was at -10mODN, along the boundary of the clay and gravels.

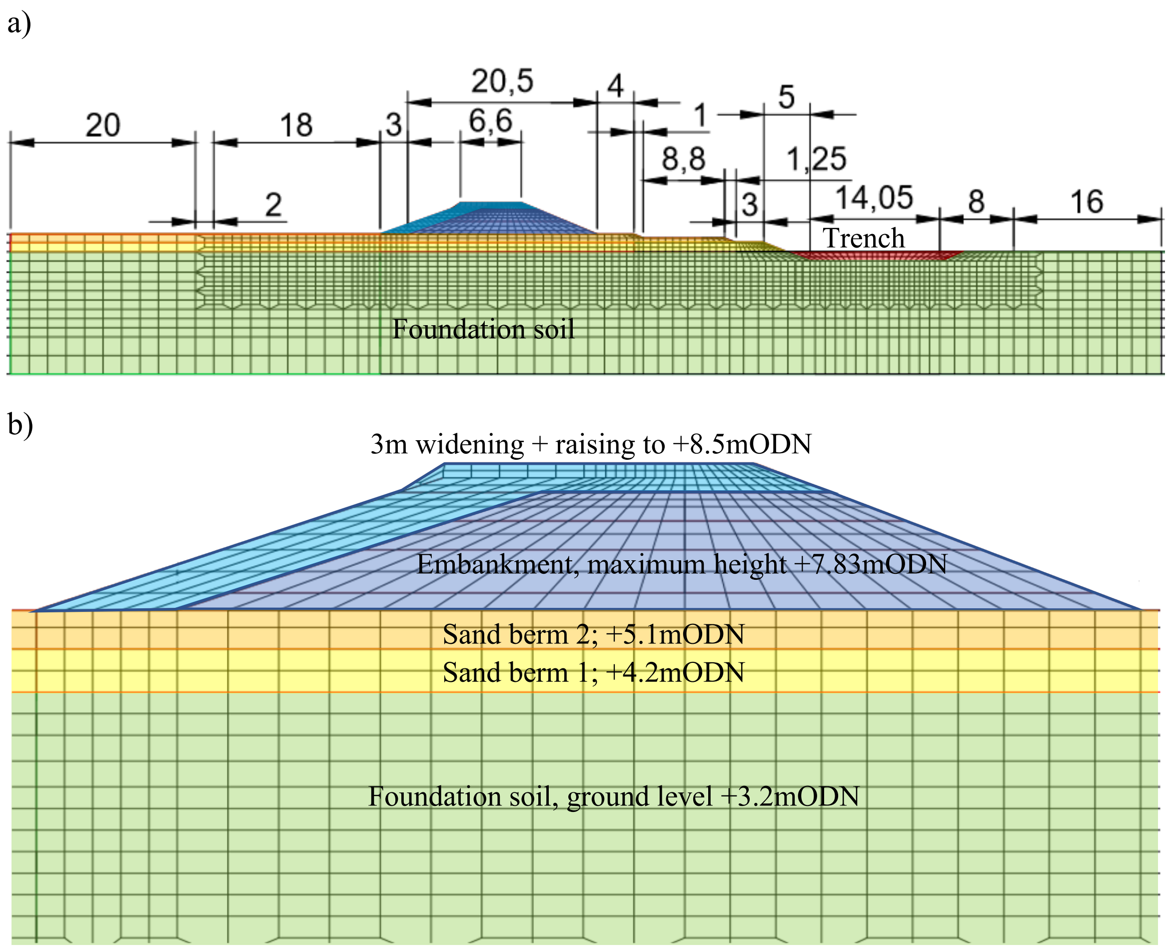

Figure 6.11:(a) Finite element mesh for the complete construction sequence; (b) The trial embankment, including its widening.

6.3.3 Soil constitutive modelling

The numerical model of the embankment construction comprised two soil types, the soft clay foundation and the sandy embankment fill. Based on the site characterisation in Section 6.2, it was considered appropriate to model the soft clay using an extended Modified Cam Clay (MCC) model (Potts and Zdravkovic, 1999; Zdravkovic et al., 2020). No experimental investigation was available to characterise the mechanical behaviour of the fill, hence it was simulated with a simpler linear elastic Mohr-Coulomb model (Potts and Zdravkovic, 1999). This section presents derivation of model parameters.

Extended Modified Cam Clay (MCC) model

The constitutive model for soft clay adopts elements of the original MCC model formulation (Roscoe and Burland, 1968), but is enhanced with (i) a Van Eekelen (1980) generalised shape for the yield and plastic potential surfaces in the deviatoric plane, to account for the effect of the intermediate principal stress on soil strength; and (ii) a nonlinear small strain stiffness overlay model which enables variation of the elastic shear and bulk moduli with mean effective stress and strain level (ICG3S, Taborda & Zdravkovic, 2012; Taborda et al., 2016). The model can also employ a nonlinear Hvorslev-type surface dry of critical (Tsiampousi et al., 2013a), to capture more accurately the undrained strength of stiff clays. As the soft clay behaviour is governed by the shape of the yield surface wet of critical, the overall yield and plastic potential surfaces adopted the original shape of an ellipse in the $p' - J$ plane (Figure 6.12):

$$F(\{\boldsymbol{\sigma}'\},\{k\}) = \left(\frac{J}{p' \cdot g(\theta)}\right)^2 - \left(\frac{p_0'}{p'} - 1\right) = 0 \tag{6.1}$$

where p' is the mean effective stress, J is a generalised deviatoric stress, p_0' is a hardening parameter and $g(\theta)$ is the gradient of the critical state line on the J-p' plane.

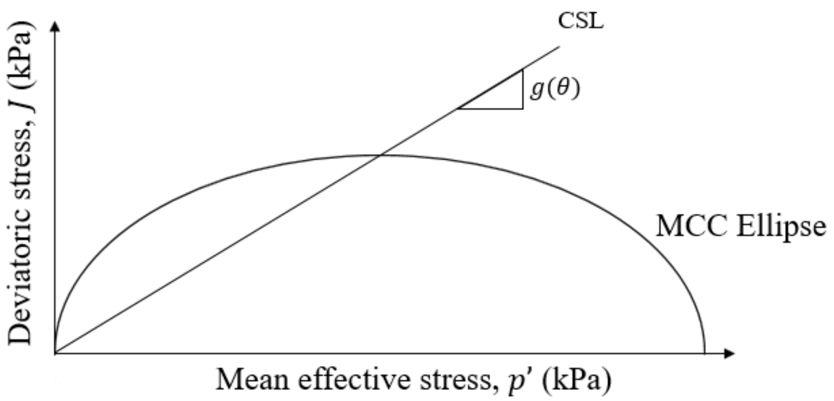

Figure 6.12: MCC elliptical yield surface in the $p' - J$ *plane.*

The $g(\theta)$ gradient is defined by the Van Eekelen (1980) generalised shape of the yield surface in the deviatoric plane:

$$g(\theta) = \frac{X}{(1 + Y \cdot \sin 3\theta)^Z} \tag{6.2}$$

where θ is Lode's angle, and X, Y and Z are model parameters, the combination of which can reproduce, among others, the original circular shape, the Mohr-Coulomb hexagon, the Matsuoka and Nakai (1974), or Lade and Duncan (1975) shapes. The importance of this function is discussed in detail in Potts and Zdravkovic (1999).

The ICG3S model for a nonlinear variation of the tangent shear, G_{tan}, and bulk, K_{tan}, moduli adopts the expressions described in Taborda and Zdravkovic (2012) and Taborda et al. (2016):

$$G_{tan} = G_0 \cdot \left(\frac{p'}{p'_{ref}}\right)^{m_G} \cdot \left(R_{G,min} + \frac{\left(1 - R_{G,min}\right)}{1 + \left(\frac{\left|E_d - E_{d,r}\right|}{n_G \cdot a}\right)^b}\right) \geq G_{min} \tag{6.3}$$

$$K_{tan} = K_0 \cdot \left(\frac{p'}{p'_{ref}}\right)^{m_K} \cdot \left(R_{K,min} + \frac{\left(1 - R_{K,min}\right)}{1 + \left(\frac{\left|\varepsilon_{vol} - \varepsilon_{vol,r}\right|}{n_K \cdot r}\right)^s}\right) \geq K_{min} \tag{6.4}$$

where G_0 is the reference shear modulus, K_0 the reference bulk modulus, G_{min} the minimum shear modulus, K_{min} the minimum bulk modulus, m_G the parameter controlling the nonlinearity between G_{tan} and p' (mean effective stress), m_k the parameter controlling the nonlinearity between K_{tan} and p', a the degradation parameter for G_{tan}, r the degradation parameter for K_{tan}, $R_{g,min}$ the minimum normalized tangent shear modulus, $R_{k,min}$ the minimum normalized tangent bulk modulus, b the parameter controlling the nonlinearity of G_{tan} degradation, s the parameter controlling the nonlinearity of K_{tan} degradation, $n_G = 1$ the shear modulus scaling factor, and $n_K = 1$ the bulk modulus scaling factor.

Extended MCC model calibration

Normal compression parameters

Based on density, moisture content, oedometer and undrained triaxial test data from the specimens of the foundation clay shown in Section 6.2.1, parameters for the extended MCC model were derived. The first of these parameters involved the compressibility of soil, namely the normal compression line parameters λ and N, and the swelling line gradient κ. By taking a mean saturated density of 1500 kg/m^3 and taking the specific gravity (G_s) of the clay to be 2.63

as reported in Marsland and Powell (1977), the void ratio at various depths of the soft clay foundation could be obtained, assuming fully saturated conditions:

$$e = w * G_s \tag{6.5}$$

where e is the void ratio, w the water content and G_s the specific gravity.

The calculated void ratio was plotted against $ln\, p'$, as shown in Figure 6.13, in an attempt to establish a normal consolidation line and estimate parameters λ and N. Recognising the large scatter, a linear regression resulted in line of best fit (blue) with $\lambda = 0.337$ and N = 3.67. However, Figure 6.3(b) indicated that only a small part of the clay layer (from 0mODN to -3mODN) was relatively normally consolidated, with the pre-consolidation pressure being close to the overburden pressure at the site, while it was over-consolidated at other depths. A second line of best fit was therefore fitted only through the points corresponding to normal consolidation (orange), providing a different set of parameters, $\lambda = 0.57$ and N = 4.39, and indicating a higher compressibility compared to the overall line of best fit (blue).

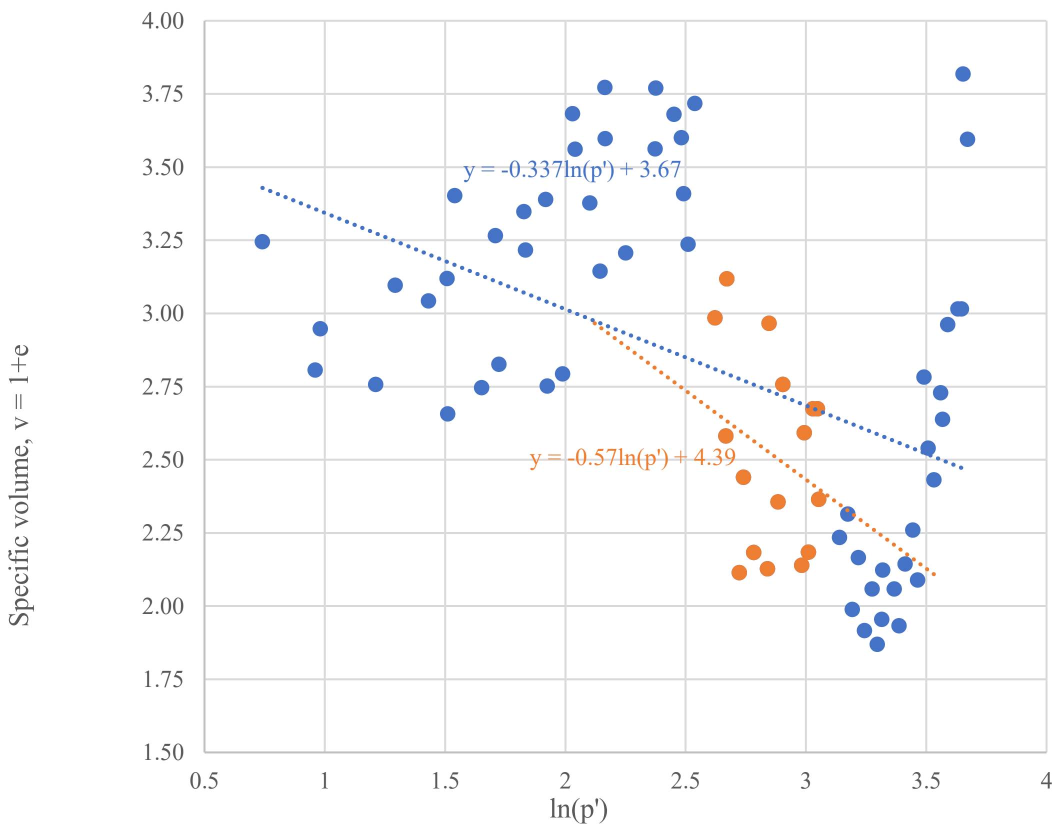

Figure 6.13: Plot of v-ln(p') of the foundation clay. Points in orange represent the data between 0m ODN and -3m ODN, with the orange line of best fit. Points in blue represent all data points, with the blue line of best fit fitting through all points.

As no unloading test data were available, it was not possible to directly estimate the swelling gradient κ. Instead, a κ/λ ratio of 0.1 was assumed, as applicable to clays. Given the approximations applied in this calibration due to the scatter in the field data, a numerical analysis with a column of the foundation soil, initialised with these parameters was performed to check the resulting initial void ratio profile in the simulation against the field void ratio calculated using Equation (6.5). Figure 6.14 indicated a reasonable numerical representation of the field data, especially in between 0mODN and -3mODN, although the numerical void ratio profile was at a lower boundary of the field data.

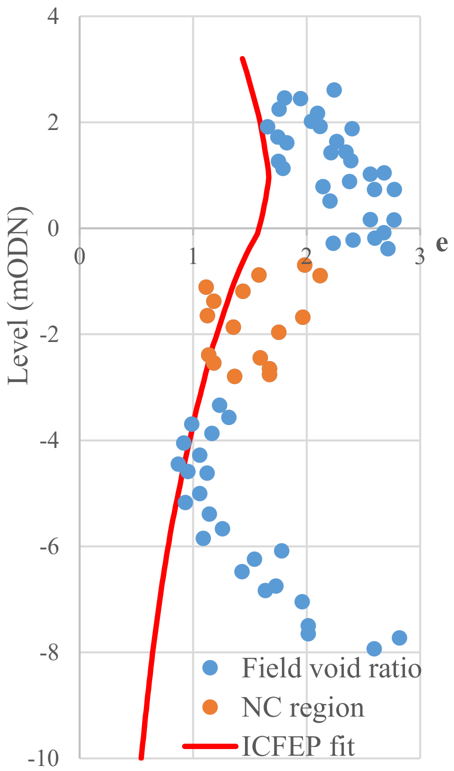

Figure 6.14: Foundation soil void ratio profile plotted with the calibrated extended MCC model in ICFEP.

<u>*Drained shear strength*</u>

Figure 6.15 summarised failure points, in the $p' - q$ plane, in consolidated-undrained and unconsolidated-undrained triaxial compression tests performed on the foundation clay (Marsland, 1986). The scatter in the data was large and a linear regression for a possible failure envelope, passing through all data points and through the stress origin ($p' = q = 0$), indicated a magnitude of the angle of shearing resistance, $\phi' = 31^{o}$. However, a closer inspection of data noted that there was a number of data points at higher p' values that exhibited particularly low mobilised magnitudes of q at failure. Without any explanation found in Marsland (1986),

it was deemed by Marsland and Powell (1977) that those samples had higher organic content. When such points were removed from consideration, the gradient of the failure envelope become higher, resulting in $\phi' = 35^{o}$.

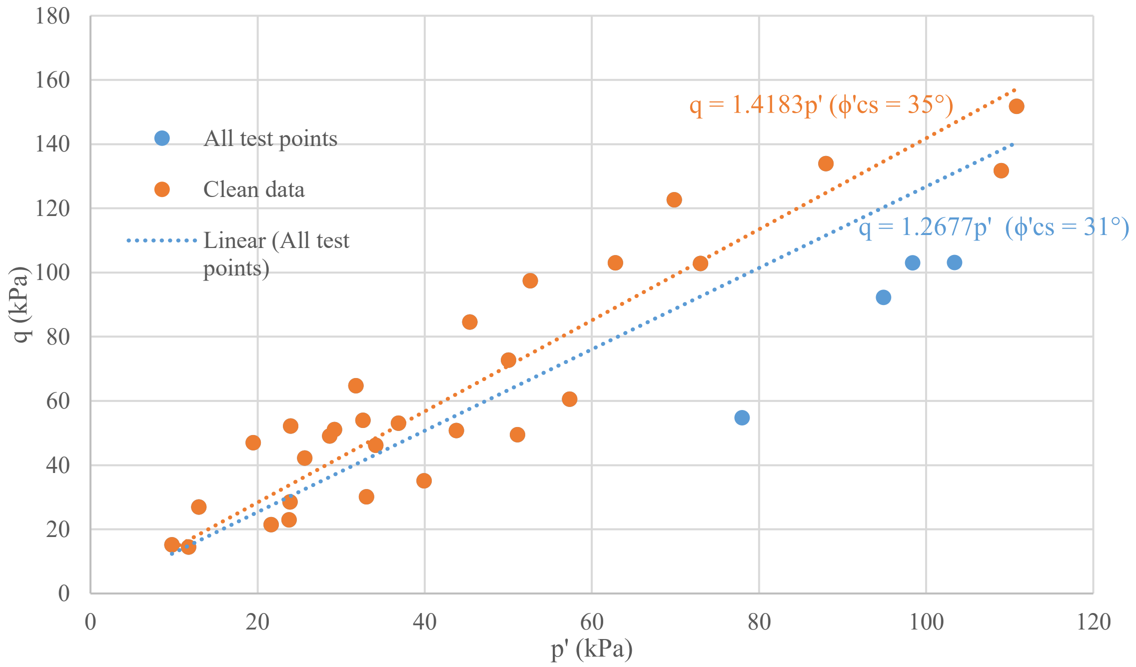

Figure 6.15: $q - p'$ plot of triaxial test results of the foundation soil. The blue line of best fit fits for all data points, while the orange line of best fit is applied only for the orange data points.

<u>Undrained shear strength</u>

Using the MCC model, it is possible to prescribe in the numerical model the initial undrained shear strength, S_u, profile in the foundation soil, as shown by Equation (6.6). This uses the model's input parameters λ, κ and ϕ', the profile of the initial vertical effectives stress, σ_v', and derived profiles of K_0 and OCR to match the experimentally interpreted S_u profile.

$$Su = \sigma'_{vi} g(\theta)\cos(\theta)\frac{(1+2K_O^{NC})}{6}(1+B^2)\left[\frac{2(1+2K_O^{OC})}{(1+2K_O^{NC})OCR(1+B^2)}\right]^{\frac{\kappa}{\lambda}} \qquad (6.6)$$

where $g(\theta) = \frac{\sin(\phi)}{\cos(\theta)+\frac{1}{\sqrt{3}}\sin(\phi)\sin(\theta)}$, $B = \frac{\sqrt{3}(1-K_O^{NC})}{g(\theta)(1+2K_O^{NC})}$, $K_O^{OC} = (1-\sin(\phi)) * OCR^{\sin(\phi)}$

$K_O^{NC} = 1 - \sin(\phi')$, and θ = Lode's angle.

Figure 6.16(a) shows the calibrated numerical undrained shear strength profile in triaxial compression, $S_{u,TXC}$, for which $\theta = -30^{o}$. The profile coincides with that interpreted in

Section 6.2.1 from experimental data. Figures 6.16(b) and (c) compare the numerically derived K_0 and OCR profile, respectively, against those characterised for the site (Marsland and Powell, 1977). In general, there is a reasonable agreement between the calibrated and experimentally interpreted profiles of both the OCR and K_o, albeit slightly underestimated above 0mODN elevation.

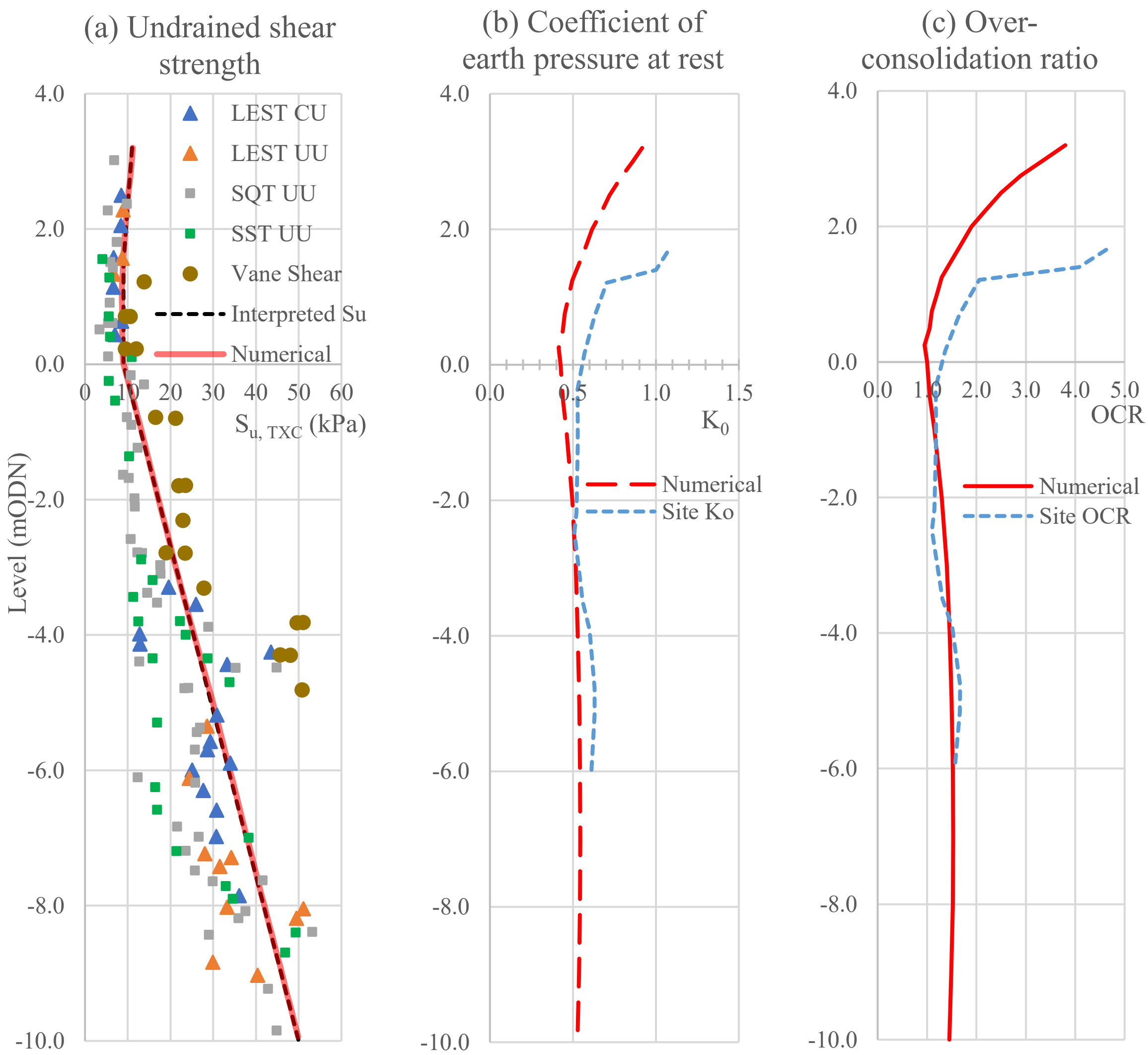

Figure 6.16: Comparison of the calibrated (a) Undrained shear strength in triaxial compression, $S_{u,TXC}$; (b) Coefficient of earth pressure at rest K_0; and (c) Over-consolidation ratio OCR; against experimental data for the foundation soil (Marsland and Powell, 1977).

Shear stiffness

The small strain stiffness data was not available for the foundation soil. It was deemed, however, that this soft clay was similar to the Bothkennar clay and therefore the small strain stiffness properties of Bothkennar clay (Hight et al., 2003) were selected to represent the shear stiffness at the Dartford site. Both sites were situated next to rivers and experienced tides as both were close to their respective estuaries. The clays from both sites exhibited similar properties such as the bulk unit weight of 15 kN/m^3 and specific gravity of 2.63. The undrained shear strength and Ko profiles of both sites were also similar, with both having a thin crust, followed by soft clay that increases in strength linearly with depth.

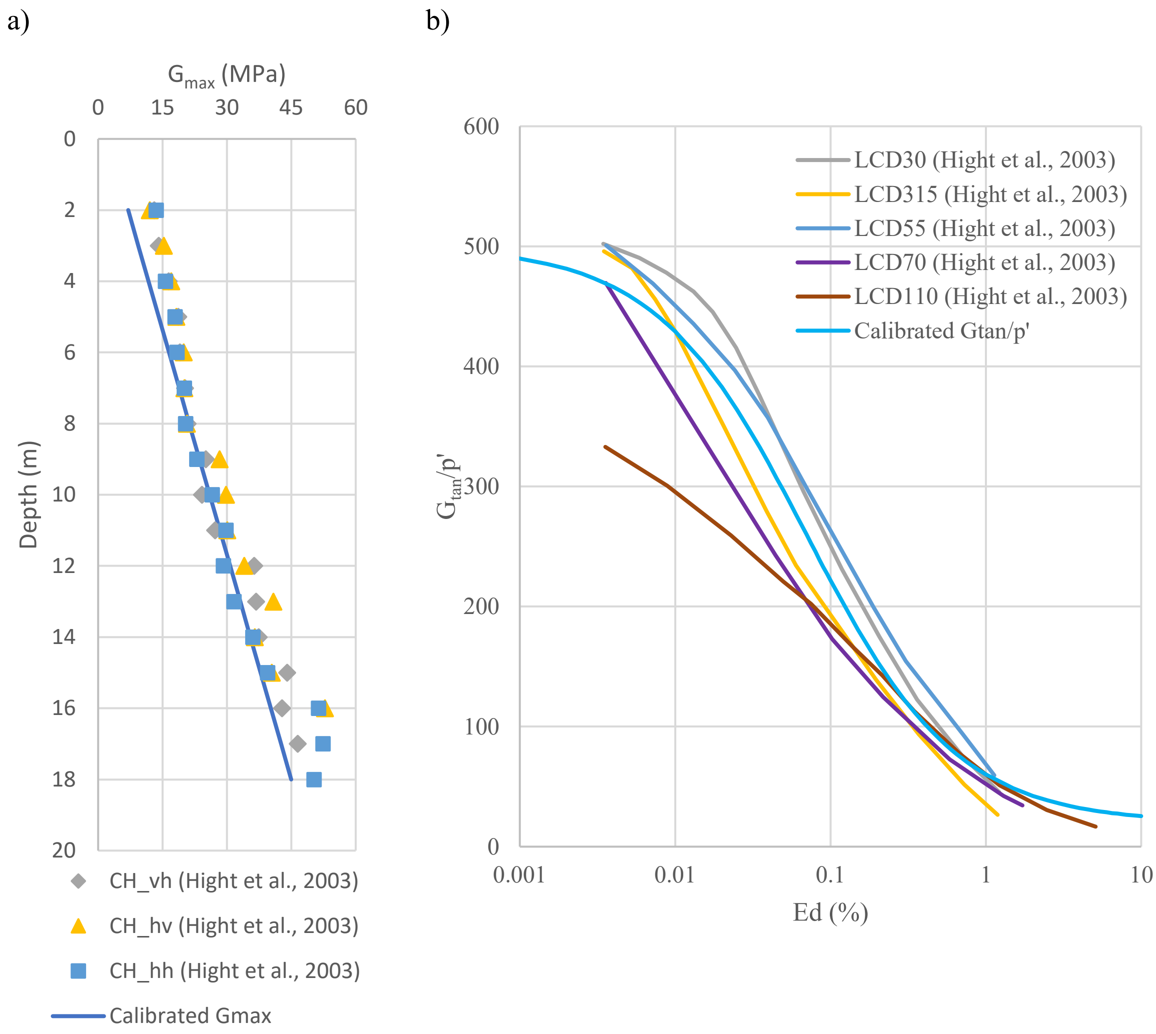

Figure 6.17: (a) Plot of G_{max} vs depth and (b) Plot of normalised G_{tan} vs deviatoric strain for Bothkennar clay (Hight et al., 2003) and the calibrated small strain model.

The experimental data from crosshole geophysics measurements of the elastic shear modulus, G_{max}, at Bothkennar (Hight et al., 2003) are shown in Figure 6.17(a), while the normalised small strain tangent shear modulus (G_{tan}/p') vs the deviatoric strain ($|\mathrm{E}_d$) curves from triaxial shearing in compression are plotted in Figure 6.17(b). The geophysics data indicated negligible elastic shear stiffness anisotropy and therefore the isotropic small strain stiffness model, expressed by Equation 6.3, was employed to represent the tangent shear modulus variation with both depth and strain. The maximum shear stiffness in Equation 6.3 is calculated as:

$$G_{max} = G_0 \left(\frac{p'}{p'_{ref}}\right)^{mG} \tag{6.7}$$

where G_0 is the maximum shear stiffness at a reference mean effective stress, p'_{ref}, and m_G controls the stiffness dependency on the mean effective stress p'. The calibration of the small strain stiffness model followed the procedure outlined in Measham et al. (2014), and the resulting G_{max} profile and the normalised shear stiffness, G_{tan}/p', degradation with strain were shown in Figure 6.17(a) and 6.17(b), respectively. The bulk modulus, K_{tan}, was not calibrated independently using Equation 6.4 due to the lack of any experimental data. The bulk stiffness was calculated from the prescribed shear stiffness.

Table 6.2 summarises the derived input parameters for the MCC model, while Table 6.3 summarises input parameters for the ICG3S small strain stiffness model. An additional parameter necessary for the definition of ground condition in a coupled numerical analysis is permeability. As no permeability measurements were available for the Dartford site, an isotropic permeability was assumed, with the coefficient of permeability, $k = 10^{-8}$ m/s. This was based on the upper bound of permeability measurements at Bothkennar (Nash et al., 1992; Leroueil et al., 1992).

Table 6.2: Input parameters for MCC model representing the foundation soil

Parameter	Value
Gradient of the normal compression line, λ	0.57
Gradient of the swelling compression line, κ	0.057
Angle of shearing resistance, ϕ'	35°
Specific volume of NCL when p'=1, N	4.39
Shear stiffness, G	See Table 6.3

Table 6.3: Input parameters for ICG3S small strain model representing the foundation soil

Parameter	Value
Maximum shear modulus at p'_{ref}, G_0 (MPa)	50
Reference mean effective stress, p'_{ref} (kPa)	100
Exponent controlling variation of G_{max} with p', m_G	1
Normalised minimum shear modulus, $R_{G,min}$	0.04
Basic shear modulus degradation parameter, a	0.07
Basic nonlinearity of shear modulus degradation, b	0.9
Minimum shear modulus, G_{min} (MPa)	2

Embankment fill material

No detailed soil investigations were performed on the dredged sandy gravels that was used as the embankment fill in the trial embankment. Instead, it was assumed in Marsland and Powell (1977) that the material had a cohesion, c', of 10kPa and angle of shearing resistance, ϕ', of 35° in their analysis of the embankment stability which yielded a Factor of Safety of 0.95 at maximum trial embankment height, calculated using the method of slices and the established failure mechanism. As the primary objective of the numerical analysis was to model the foundation soil and its behaviour under a trial embankment, a simple linear-elastic Mohr-Coulomb constitutive model was adopted to simulate the fill behaviour. Table 6.4 tabulates the model parameters for the fill material. As the fill was granular in nature, it was assumed to be a drained material, with the bulk unit weight $\gamma = 20\ \mathrm{kN/m^3}$.

Table 6.4: Model parameters of the Mohr-Coulomb model representing the embankment fill

Parameter	Value
Cohesion, c'	10kPa
Angle of shearing resistance, ϕ'	35°
Angle of dilation, Ψ'	12°
Young's modulus, E	20MPa
Poisson's ration, ν	0.2

6.3.4 Construction sequence

The construction sequence and timeline of the embankment construction in the field was modelled as closely as possible in the numerical model and this process is detailed in Table

6.5. Table 6.6 illustrates the changes to the boundary conditions in the numerical model, at appropriate stages of the analysis. Figure 6.18 shows the modelled construction height of the embankment, plotted against the actual construction height of the embankment, presented earlier in Figure 6.6.

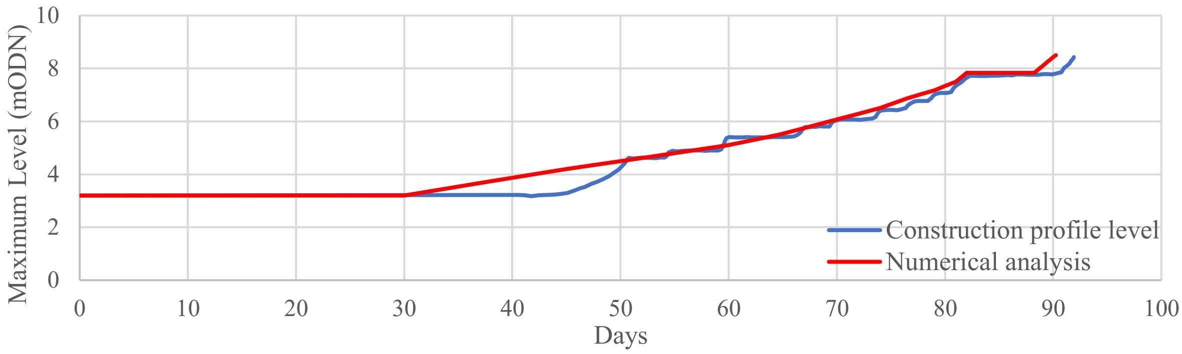

Figure 6.18: Comparison between actual and simulated construction rates.

Table 6.5: Construction sequence adopted in the numerical analysis of the trial embankment, including setting and changing of boundary conditions

Time per increment	Total time (days)	Increments	Steps			Section
		0	Excavate all embankment soil material (material 1) mesh			1
	30	1 - 1000	Prescribe fixed horizontal displacement for sides and base, vertical for base			-
			Prescribe $\Delta u = 0$ for sides and along phreatic surface			19
15		1 - 2	Excavate trench			2
	30	3	Reset elastic hardening parameters for foundation soil after excavation			14
7.5		3 - 4	Construction sand berm 1 (to +4.2mODN)			3
		3 - 1000	Extend left BC for fixed horizontal displacement to include construction section			-
			Set pwp for the entire section: u = 0			3
7.5		5 - 6	Construction sand berm 2 (to +5.1mODN)			4
		5 - 1000	Extend left BC for fixed horizontal displacement to include construction section			-
			Set pwp for the entire section: u = 0			4
2.33	14	7 - 8	Embankment construction:	layer 1	height +5.5mODN	5
2.33		9 - 10		layer 2	+6.0mODN	6
2.33		11 - 12		layer 3	+6.5mODN	7
1.25	5	13 - 14		layer 4	+6.83mODN	8
1.25		15 - 16		layer 5	+7.17mODN	9
1	2	17 - 18		layer 6	+7.35mODN	10
0.25	1	19 - 20		layer 7	+7.55mODN	11
0.25		21 -22		layer 8	+7.83mODN	12
5	6	23 - 25	Filling the trench, setting load:	Right side of trench	0 to 9.81kPa	-
0.5				Base of trench	9.81kPa	-
0.5				Left side of trench	9.81 to 0kPa	-
0.5	1	24 - 25	Extending the embankment width by 3m			13
0.25	0.25	26 - 1000	Draining the trench, setting load:	Right side of trench	0 to -9.81kPa	-
				Base of trench	-9.81kPa	-
				Left side of trench	-9.81 to 0kPa	-
0.25	1	27 - 28	Embankment construction:	layer 9	+8.00mODN	15
0.25		29 - 30		layer 10	+8.17mODN	16
0.25	1	31 - 32		layer 11	+8.32mODN	17
0.25		33 - 34		layer 12	+8.5mODN	18

Table 6.6: Illustration of the changing boundary conditions (mechanical and hydraulic) during the numerical analysis

Inc. Number	Numerical Boundary Conditions
1 – 2	Excavation of the trench 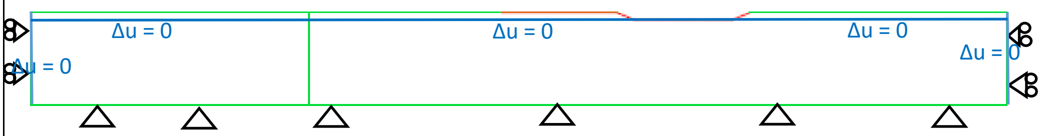
3 – 6	Construction of sand berms 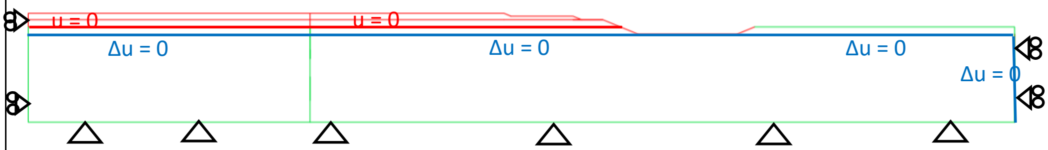
7 – 22	Construction of embankment up to +7.83mODN 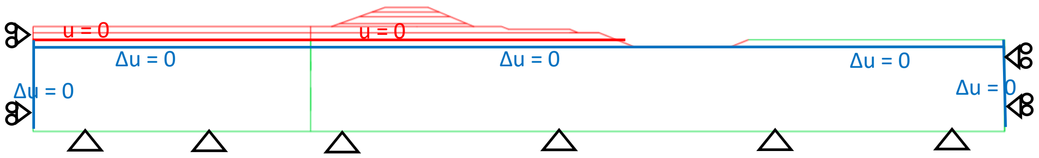
23 – 25	Filling of trench, construction of embankment extension 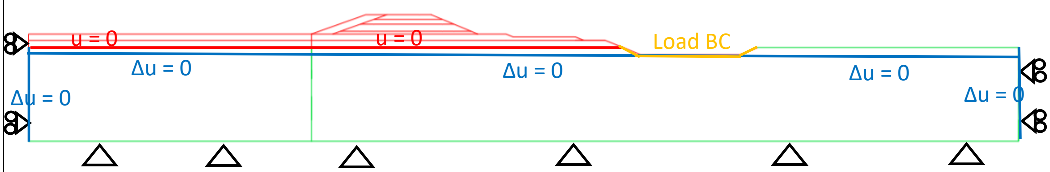
26 – 34	Draining of trench, construction of final layers of embankment up to +8.5mODN 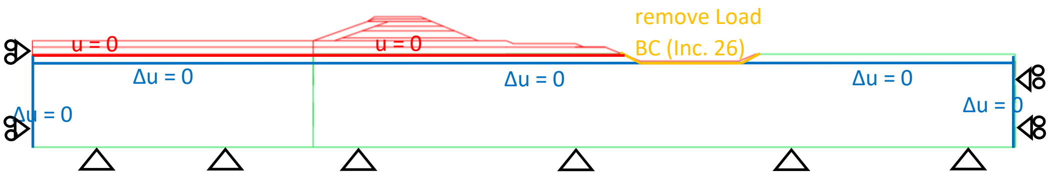

While it was previously mentioned that the bottom boundary of the mesh corresponds to the clay-gravel interface, the gravels beneath the clay are hydraulically linked to the river, and thus exhibit tidal cycling throughout the day. This complicates the bottom boundary considerably, thus it was assumed that the bottom boundary would be impermeable, on the basis that the tidal pore pressures will not cause excess pore pressures within the foundation to dissipate easily.

In addition, due to dessication cracks on the ground surface allowing for faster dissipation of excess pore pressures, the phreatic surface was maintained constant at +2.2mODN (1m below ground level). Additionally, the filling up of the trench with water, as a stabilising effect over the 6-day pause-period in the works, was simplified to applying only a load boundary condition (marked in yellow in Table 6.6) along the excavated boundary, which represented the weight of the water. The accompanying hydraulic boundary condition to simulate the pore water pressure on the excavated boundary was ignored, as it was considered that the water flow from that boundary would be negligible during the short duration of this construction phase.

6.4 Results and discussion

The numerical analysis was able to converge up to increment 28 (Day 90) during the raising of the embankment to +8.17mODN. The subsequent increment started to experience divergence in the solution algorithm, indicated that the embankment was failing.

Three key comparisons between the results of the numerical analysis and field measurements from the trial embankment were selected for presentation: the horizontal displacements at inclinometer locations IC and ID, the slip surface generated at the end of construction, and the pore water pressure evolution throughout the construction of the embankment.

6.4.1 Horizontal displacements

Figures 6.19(a) and (b) compare the measured horizontal displacements in the foundation soil from inclinometers IC and ID, respectively, with those predicted from the numerical model at the same locations and for similar days of embankment construction.

Figure 6.19 demonstrated that the numerical model was capable of reproducing a broadly similar evolution of the horizontal displacement profiles at two locations, predicting similar maximum displacements at final stable stages of both the numerical simulation and field construction. The model, however, predicted a shallower slip surface (at about 0.5m and 1.0m ODN at the two locations, respectively), possibly due to the lower values of the K_0 and OCR profiles calibrated in the numerical model above 0mODN (see Figure 6.16).

Figure 6.20 further compared the horizontal displacement measured on the surface of a right-hand side berm against numerical predictions. As there was no additional information indicating the exact location of this measurement point, the predicted horizontal displacements at three nodal points on the side berms were compared against the measured displacement. The positions of nodes are marked out on the plot of the mesh in Appendix G.

a)

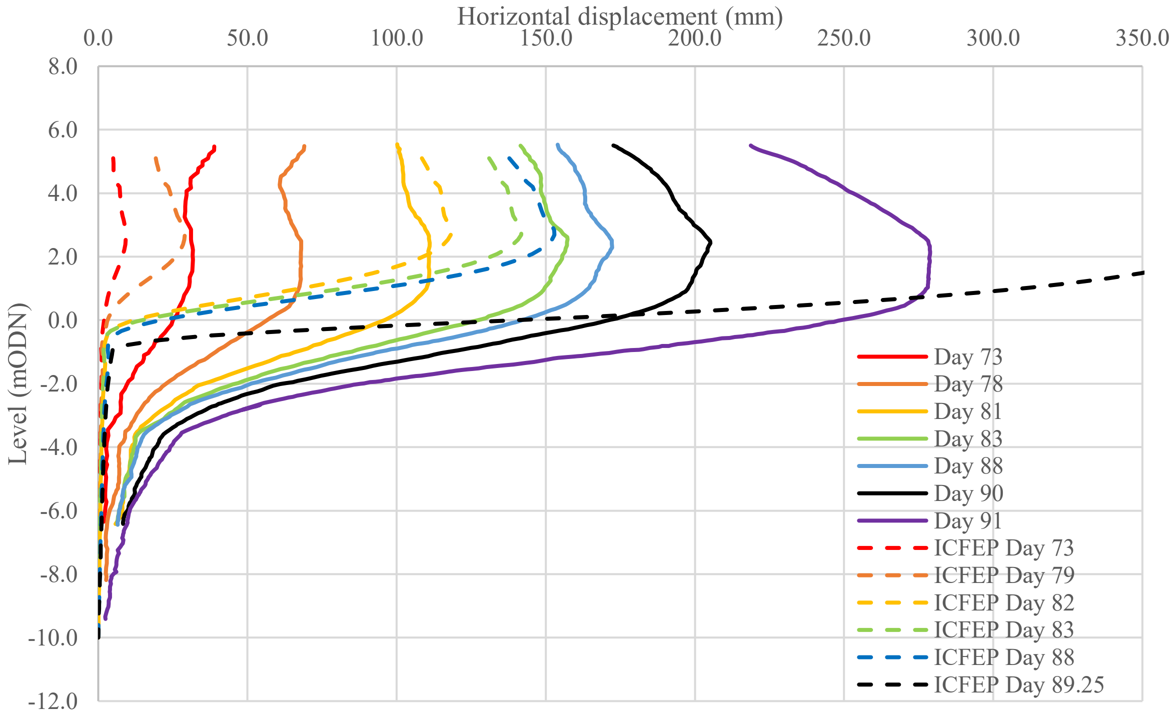

b)

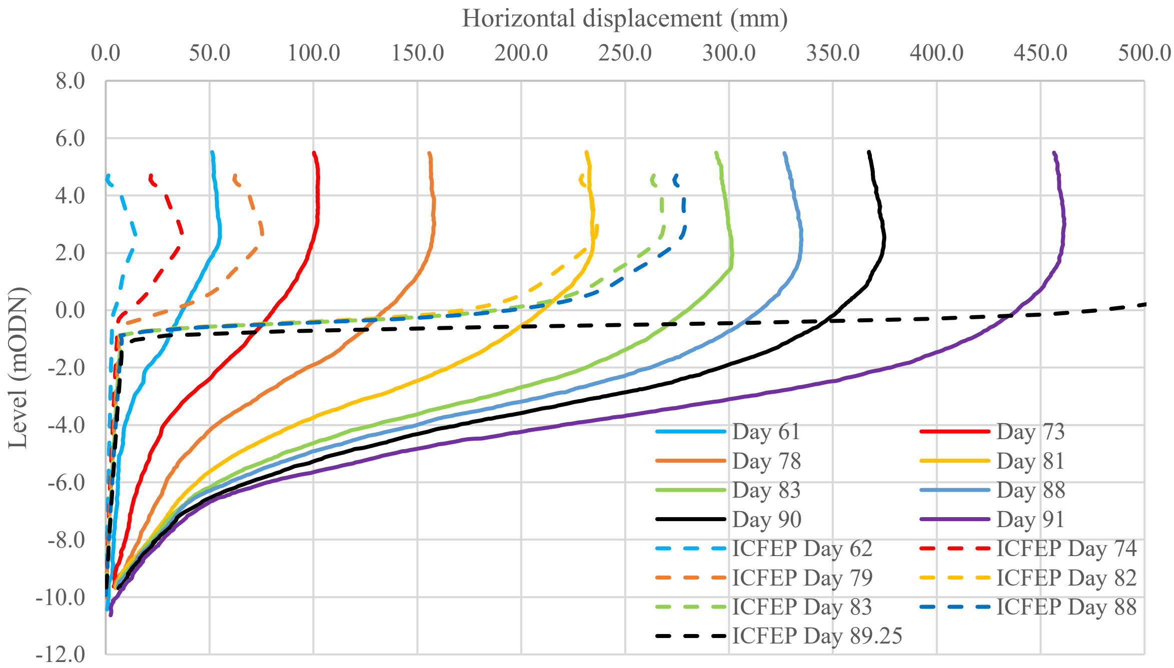

Figure 6.19: Profiles of horizontal displacements at inclinometer location (a) IC and (b) ID (field data from Marsland and Powell, 1977)

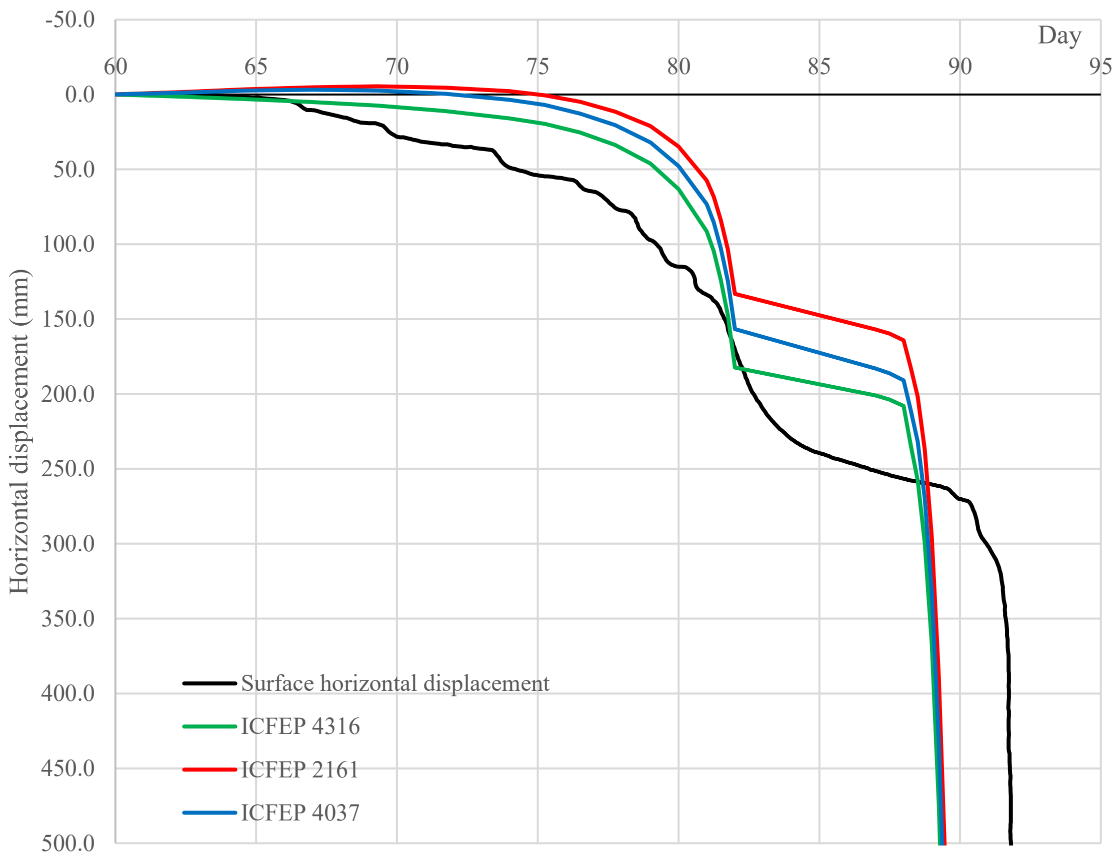

Figure 6.20: Comparison of surface horizontal displacements of field vs several surface nodal points along the centre of berms of the embankment. The exact location of these nodal points can be found in Appendix G; (field data from Marsland and Powell, 1977)

Figure 6.20 showed similar overall agreement between the numerical model and field measurement in the evolution of horizontal displacements on the embankment body (side berm). Although the predicted displacement values were slightly smaller, the numerical model was shown capable of capturing all stages of construction, including temporary stabilisation during the pause-period, followed by ultimate failure at the subsequent construction stage.

6.4.2 Slip surface generation

The inclinometer measurements shown in Figure 6.19, as well as other measuring points in the foundation soil, enabled the mapping of the failure surface mobilised on site, as shown in Figure 6.10 by Marsland and Powell (1977). As discussed above, these measurements documented a deeper failure surface compared to that predicted by the numerical model. However, the vectors of the embankment and ground movements at failure, predicted by the numerical model and shown in Figure 6.21, demonstrated a very good prediction of the lateral extent of the failure surface. The absolute magnitudes of these vectors are not important, as it is that their relative magnitudes showed a clear failure mechanism, with patterns of movements agreeing very well with those indicated in Figure 6.10, including the heave in the trench area.

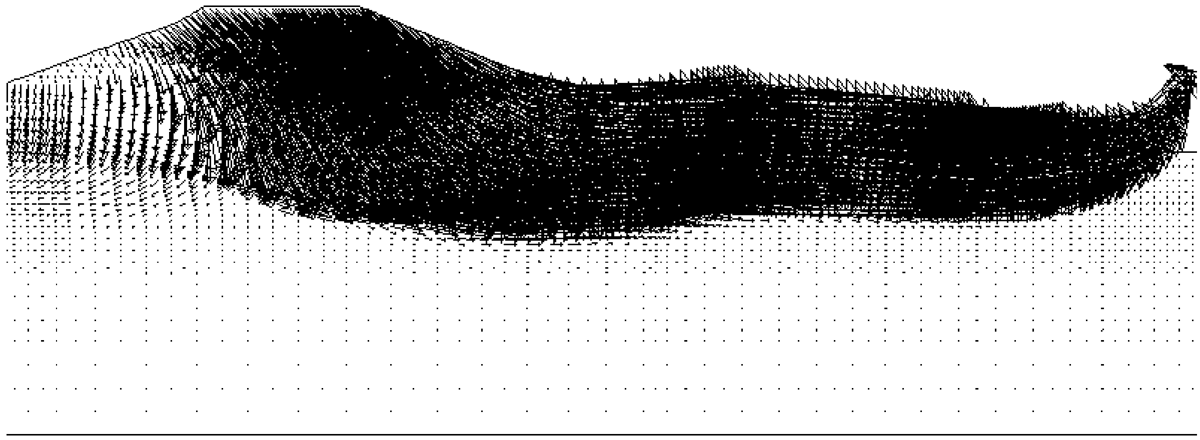

Figure 6.21: Vectors of accumulated construction displacements at failure.

6.4.3 Pore water pressure

The excess pore water pressures generated during embankment construction are presented in Figure 6.22, comparing numerical predictions against measurements. The calculated rate of excess pore water pressure generation mirrored the construction height profile and matched well with field monitoring data along piezometer C. The model also captured very well the dissipation of excess pore water pressure during the pause-period of construction. These agreements verified the assumed isotropic permeability of 10^{-8} m/s for the foundation soil in the numerical model.

The only discrepancy in Figure 6.22 was in the initial pore water pressure values in the ground. As discussed in Section 6.2.1, in relation to the initial pore water pressure profile, the numerical model adopted a hydrostatic distribution of the pore water pressure below the phreatic surface. There were no obvious reasons why the initial pore water pressure profile should have been higher than hydrostatic, as presented in Figure 6.3(c). It is possible, though, that the measured profile in Figure 6.3(c) already incorporated the increase in pore pressures caused by the construction of the sand berms, which was done over the larger extent of the site, as shown in Table 6.6. This would explain the initially lower pore water pressure values in the numerical model in Figure 6.22, which have then reached the respective measured values after the simulated construction of sand berms at around day 50.

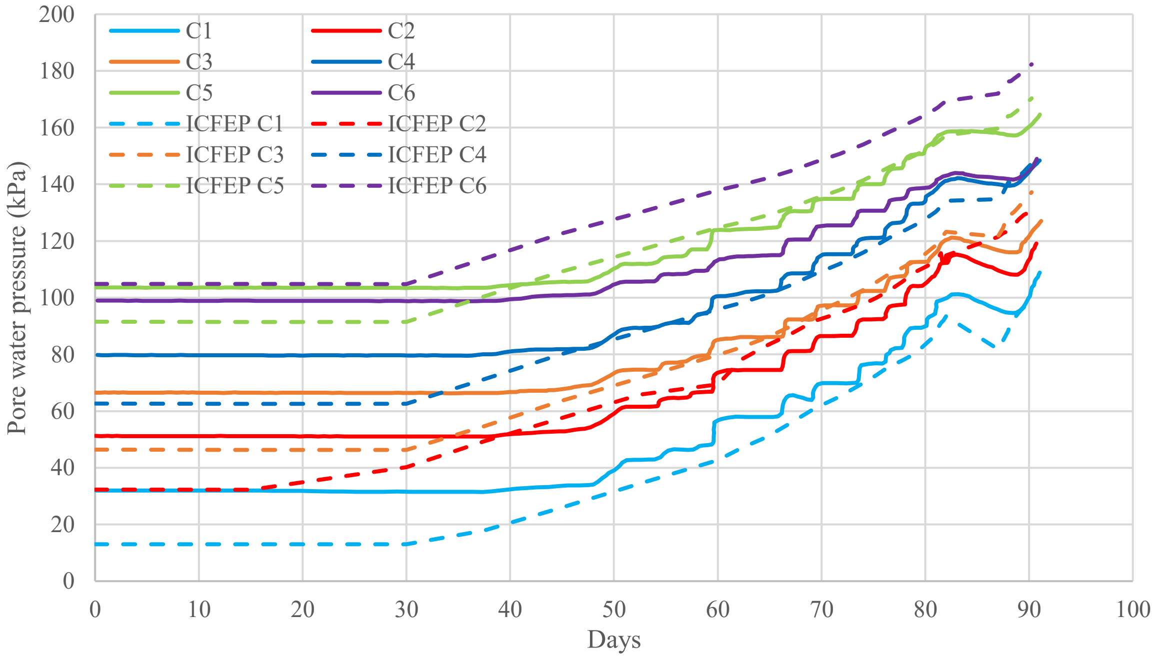

Figure 6.22: Comparison of pore water pressures between Piezometer C and the numerical model.

6.5 Summary

This chapter explored the Dartford trial embankment case study to develop a calibrated constitutive model for the soft clay foundations usually present at similar sites along rivers and estuaries.

As the laboratory and field tests at the site were insufficient to completely calibrate the extended MCC model for the foundation soil, the small strain stiffness characterisation was performed with the data supplemented from the Bothkennar clay investigations (Hight et al., 2003). The assumption of the permeability of the foundation clay was also derived from the Bothkennar data. The trial embankment was then simulated, showing very satisfactory comparisons with field observations in terms of the horizontal displacements, failure surface geometry and pore water pressure generation, thus validating the model for the foundation soil.

The numerical model developed here for the foundation soil at the Thames estuary was adopted in the in subsequent modelling of a typical flood embankment in Chapter 8.

Chapter 7: Numerical Modelling of Infrastructure Embankments

7.1 Introduction

This chapter focuses on developing a realistic and robust numerical modelling procedure of earthfill embankments, which usually support road and rail infrastructure or serve as flood defences. To be able to numerically examine the future performance of existing earthfill embankments, it is necessary to know their current state of stress and pore pressure to initialise the numerical model. This, however, is one of the principal challenges, as most earth embankments are decades old and with an unknown process of initial construction, having also been exposed to annual cycles of seasonal atmospheric conditions (rainfall, drought) as well as vegetation growth and its potential maintenance. Such embankments are also likely to be initially unsaturated, being usually constructed from compacted clay.

The research presented in this chapter has made use of the Magnolia Road rail embankment case study in Essex, UK (Geotechnical Observations, 2013; Chalmers, 2013; Smethurst et al., 2015), for the development and validation of a numerical model of an earthfill embankment. This is an old embankment that was monitored for movements and pore pressures for a period of one year (April 2006 to March 2007) when its slopes were covered with deciduous trees. The trees were then removed from part of the slope in April 2007, as vegetation maintenance, and the monitoring continued for another 4 years. This was therefore an ideal case study that enabled comparison between numerical predictions and field measurements of movements and pore water pressures in the embankment.

The initialisation procedure of the current state of an earthfill embankment is proposed in this chapter. A saturated numerical model of the embankment was first developed with the finite element software ICFEP (Potts & Zdravković, 1999) and the results compared with field measurements (Geotechnical Observations, 2013). The shortcomings of such an approach were evaluated and further development of the numerical model with ICFEP was undertaken, treating the embankment as an unsaturated material. The Imperial College Single Structure Model for unsaturated soils (ICSSM, Georgiadis et al., 2005; Tsiampousi et al., 2013a) discussed in Chapter 5, which is an extension of the Barcelona Basic Model (BBM, Alonso et al., 1990), was employed to simulate the mechanical behaviour of the fill material. Further attention was placed on evaluating and modelling the Soil Water Retention (SWR) behaviour of the fill, as well as its permeability.

The modelling of the embankment's hydro-mechanical behaviour was combined with the application of advanced boundary conditions for the simulation of soil-plant-atmosphere interaction, such as precipitation (Smith, 2003; Smith et al., 2008) and evapotranspiration (Nyambayo & Potts, 2010). The past, current and future atmospheric conditions at the site were obtained from the rainfall records and models developed in Chapter 3 and Chapter 4.

The analyses presented here first explored the effectiveness of a saturated and unsaturated numerical model in reproducing the seasonal behaviour and vegetation removal of a typical earth embankment, constructed from compacted clay. The analyses further investigated appropriate SWR and permeability models in their ability to accurately reproduce the unsaturated response of the embankment, serving as a calibration for field-compacted clay in the embankment body. Having validated the numerical model against the Magnolia Road case study, a complete lifecycle analysis of the rail embankment studied here is presented, with emphasis on the long-term serviceability and resilience of the embankment. The developed numerical approach was then applied in the modelling of flood embankments in Chapter 8.

7.2 Magnolia Road embankment

The Magnolia Road rail embankment is situated in between Hockley and Rochford stations in Essex, UK, along the Shenfield-Southend line (Figure 7.1). The railway was first opened in 1889, after its construction started in the 1880s (Ordnance Survey, 2010). It was built in accordance to standard Victorian-era construction methodologies, where London Clay clods were used as the fill material, loosely dumped on site and with low compaction effort. With time, to maintain the design level of the rail line, the clay fill was topped up with ash and ballast due to the significant embankment settlement. Figure 7.2 (Arup Geotechnics, 2007; Chalmers, 2013; Smethurst et al., 2015), shows the current cross-section through the embankment, with a heterogenous mix of granular and clay fills for the southern slope and relatively uniform layers of clay fills and ash on the northern slope.

The foundation soil is London Clay, with a chalk bedrock assumed to be 69.7m below ground level (Arup Geotechnics, 2007). As the site would have experienced seasonal variations of pore water pressure during the summer and winter throughout its past, the surface layer of the London Clay was considered to be weathered, having different soil properties as compared to the unweathered London Clay. Smethurst et al. (2012) showed that the top 2.5-3m of London Clay was naturally weathered at a cut slope in Newbury, UK. For the Magnolia Road site, it was assumed that the top 3m of London Clay was similarly weathered.

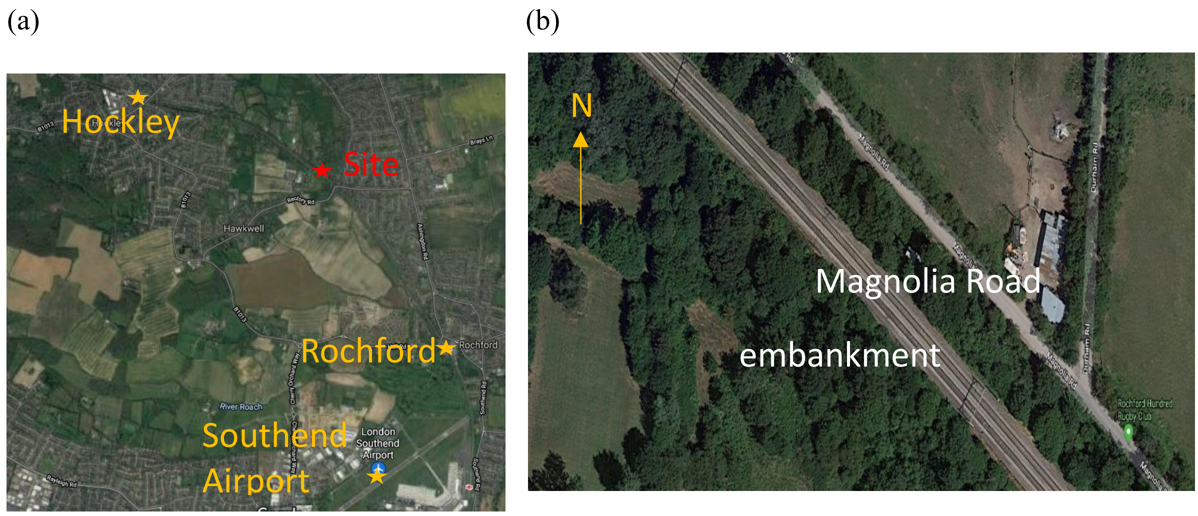

Figure 7.1: (a) Satellite view of the site location in South-East Essex. (b) Close up view of the embankment alongside Magnolia Road (Google, 2021).

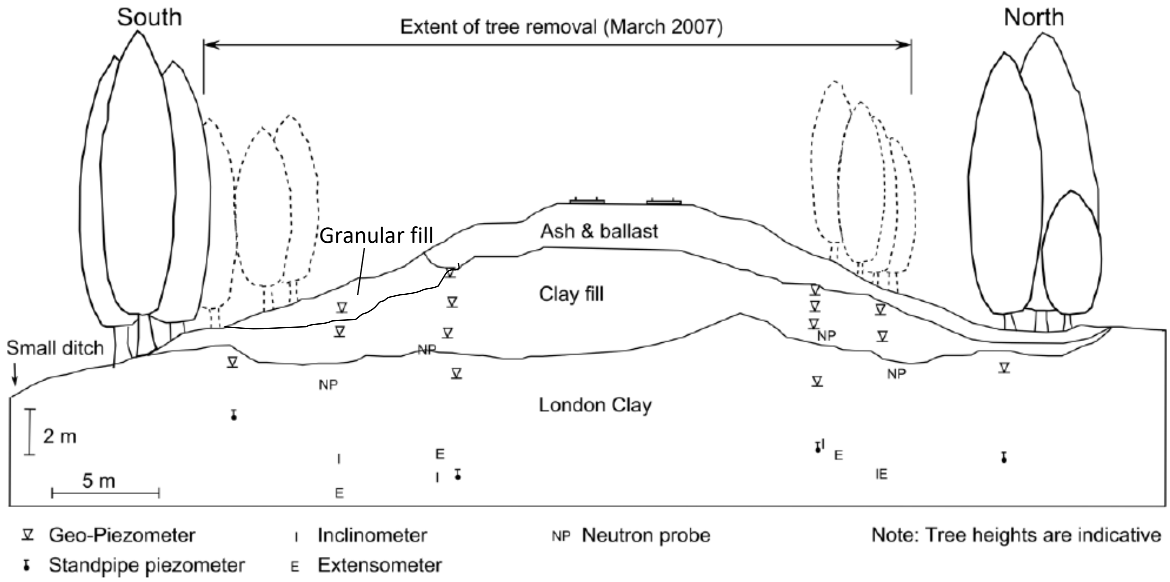

Figure 7.2: Soil stratigraphy of the Magnolia Road embankment (adapted from Smethurst et al., 2012, based on information in Arup Geotechnics, 2007).

7.3 Numerical model of the Magnolia Road embankment in the saturated soil modelling framework

7.3.1 Introduction

Considering that the Magnolia Road embankment is reasonably symmetric about the centre, only half of the geometry (the North side of the embankment) was discretised in the 2D plane strain numerical model. The adopted cross-section of the problem geometry is illustrated in Figure 7.3(a). While both the ash and clay fill layers in Figure 7.2 were shown to be continuous to the base of the embankment slope, a simplified soil stratigraphy was adopted for the numerical model, where both ash and clay fill layers were modelled as horizontal, with thicknesses of 1.55m and 2.65m respectively. This simplification was judged to be acceptable as the main focus of the investigation was on the embankment-foundation interface where a slip surface was found to be developing at the site. The ballast was also modelled as a separate material, with a thickness of 1.4m above the ash.

The geometry was discretised with eight-noded quadrilateral solid elements, as shown in Figure 7.3(b), comprising two displacement degrees of freedoms at each node. All analyses were hydro-mechanically coupled, adopting additional pore pressure degrees of freedom at corner nodes of consolidating materials (unweathered and weathered London Clay, London Clay fill and ash). The finite element mesh was refined near the surface boundaries to accommodate the root depths of the different vegetation types growing on the embankment slopes and the surrounding terrain, as recommended by Nyambayo and Potts (2010).

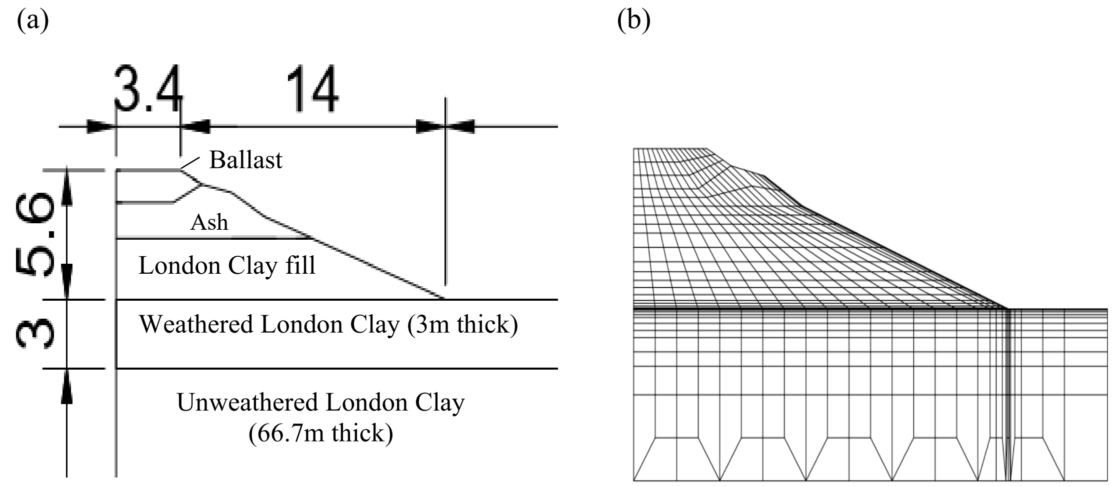

Figure 7.3: (a) Problem geometry and soil stratigraphy of the Magnolia Road embankment; (b) Finite element mesh of the embankment. (All dimensions are in metres).

A saturated numerical model of the Magnolia Road embankment was developed, following the modelling approach established with ICFEP for the modelling of infrastructure embankments and embankment dams (Dounias, 1987; Potts et al., 1990; Kovacevic, 1994; Kovacevic et al., 1997; Potts & Zdravkovic, 2001). In these studies the embankment fill and the stiff clay foundation were modelled with a strain softening Mohr-Coulomb model (Potts & Zdravkovic, 1999) coupled with a nonlinear small strain stiffness overlay model (Jardine et al., 1986). The seasonally varied atmospheric conditions were simulated as a prescribed pore pressure boundary condition on embankment slopes, specified with an appropriate magnitude of suction, according to measurements of seasonal pore water pressures in infrastructure embankments and slopes reported by Walbancke (1976) and Vaughan (1994). A similar modelling approach was adopted subsequently by O'Brien at al. (2004) using the software FLAC.

A more realistic modelling approach for the simulation of atmospheric conditions and effects of vegetation was developed in ICFEP in studies of natural pyroclastic slopes (Pirone, 2009) and infrastructure slopes in London Clay (Tsiampousi et al., 2017). Instead of prescribing a constant pore pressure (suction) along the slope boundary, the advanced precipitation boundary condition (Smith, 2003; Smith et al., 2008) was employed to simulate realistic seasonal rainfall and runoff, while the advanced vegetation boundary condition (Nyambayo, 2003; Nyambayo & Potts, 2010), which uses a root-water uptake model, was employed to simulate realistic seasonal evapotranspiration.

Consequently, the saturated numerical model presented here combined the advanced modelling of soil-atmosphere interaction boundary conditions with the nonlinear strain-softening Mohr-Coulomb modelling of the embankment and foundation soil. This analysis was envisaged to serve as a benchmark for assessing the benefits of developing subsequently an unsaturated numerical model for earthfill embankments.

7.3.2 Soil characterisation

Strength and stiffness

The mechanical behaviour of deeper unweathered London Clay was simulated with a nonlinear Mohr-Coulomb constitutive model, with model parameters adopted from previous studies of Kovacevic at al. (2007) and Tsiampousi et al. (2017). The surface layer of weathered London

Clay, immediately underneath the embankment, was simulated with a nonlinear strain-softening Mohr-Coulomb model, with strength parameters (cohesion, c', angle of shearing resistance, ϕ', and angle of dilation, ψ) assumed to degrade linearly from their peak to residual values, with an increasing deviatoric plastic strain, E_d^p, from 2.5% at peak to 20% at residual (Figure 7.4). The values adopted here were based upon the values adopted by O'Brien (2004), with some slight differences in the post-peak strength parameters. The model strength parameters are summarised in Table 7.1.

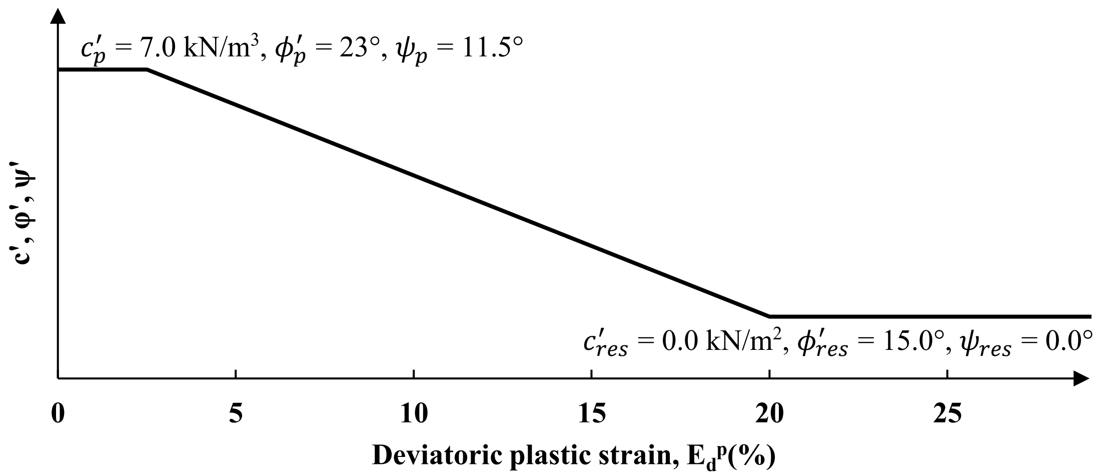

Figure 7.4: Strain-softening Mohr-Coulomb model for weathered London Clay.

Both variants of the Mohr-Coulomb model were applied in combination with the Imperial College Generalised Small Strain Stiffness model (ICG3S, Taborda et al., 2016), which was necessary for assessing the serviceability of the embankment. The small strain stiffness model was calibrated against the tangent shear, G_{tan}, and bulk, K_{tan}, stiffness curves employed by O'Brien et al. (2004), Figure 7.5, in the analyses of similar earthfill embankments along the Central and Metropolitan lines on the London Underground Network. The ICG3S model enables smooth stiffness degradation throughout the small strain range, compared to the model adopted in O'Brien et al. (2004) which has cut-off plateaus at very small and at intermediate strains. Expressions for the stress and strain dependency of the two ICG3S stiffness components are given in Equation 7.1 and Equation 7.2, while the model parameters are summarised in Table 7.2. A continuous degradation approach was assumed, where stiffness of a material continuously decreases with strain, independent of shearing direction.

Table 7.1: Strength and stiffness model parameters.

	Ballast	Ash	London Clay fill	Weathered London Clay	Unweathered London Clay
Bulk unit weight, γ (kN/m³)	18.0	11.0	18.1	19.1	19.1
Cohesion, c'(kN/m³)	2.0	2.0	5.0	see Figure 7.4	7.0
Angle of shearing resistance, φ' (°)	40.0	35.0	22.9	see Figure 7.4	23.0
Angle of dilation, ψ (°)	0.0	0.0	0.0	see Figure 7.4	0.0
Young's Modulus, E (kN/m²)	30000	30000	see Table 7.2	see Table 7.2	see Table 7.2
Poisson's ratio, μ	0.2	0.3	NA	NA	NA

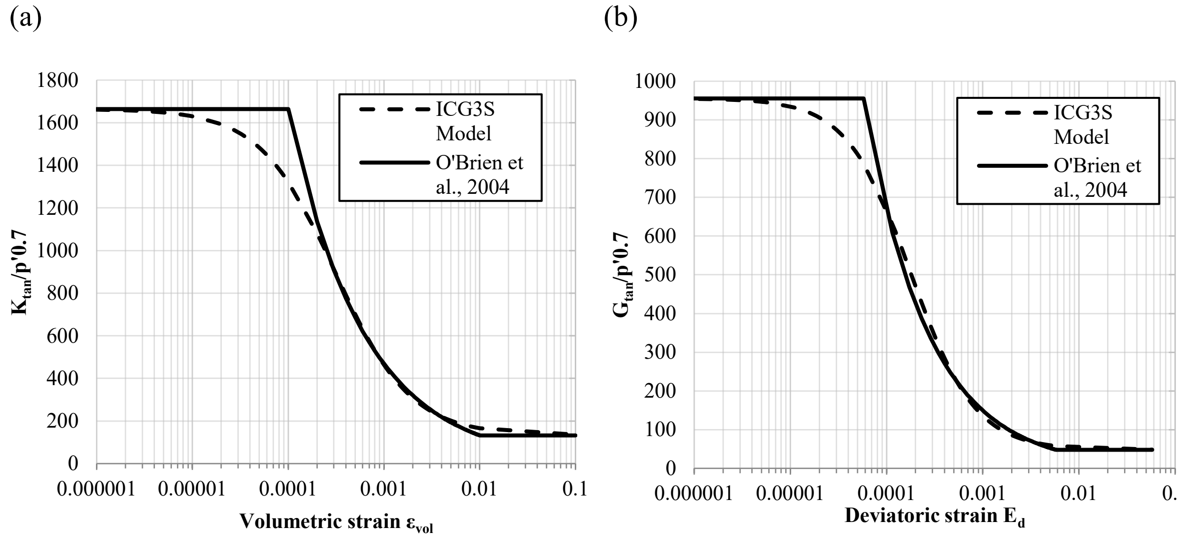

Figure 7.5: Small strain tangent stiffness adopted for modelling (a) bulk stiffness against volumetric strain and (b) shear stiffness against deviatoric strain, for intact London clay and clay fill.

$$G_{tan} = G_0 \cdot \left(\frac{p'}{p'_{ref}}\right)^{m_G} \cdot \left(R_{G,min} + \frac{\left(1 - R_{G,min}\right)}{1 + \left(\frac{\left|E_d - E_{d,r}\right|}{n_G \cdot a}\right)^b}\right) \geq G_{min} \tag{7.1}$$

$$K_{tan} = K_0 \cdot \left(\frac{p'}{p'_{ref}}\right)^{m_K} \cdot \left(R_{K,min} + \frac{(1 - R_{K,min})}{1 + \left(\frac{|\varepsilon_{vol} - \varepsilon_{vol,r}|}{n_K \cdot r}\right)^{s}} \right) \geq K_{min} \tag{7.2}$$

Table 7.2: ICG3S model parameters for intact London clay and clay fill

G_0 (kPa)	K_0 (kPa)	G_{min} (kPa)	K_{min} (kPa)	m_G	m_k	a_0	r_0	$R_{G,min}$	$R_{k,min}$	s_0
955	1665	2000	3000	0.7	0.7	0.000181	0.0003	0.05	0.079	1.1

In the above table G_0 is the reference shear modulus, K_0 the reference bulk modulus, G_{min} the minimum shear modulus, K_{min} the minimum bulk modulus, m_G the parameter controlling the nonlinearity between G_{tan} and p' (mean effective stress), m_k the parameter controlling the nonlinearity between K_{tan} and p', a_0 the degradation parameter for G_{tan}, r_0 the degradation parameter for K_{tan}, $R_{g,min}$ the minimum normalized tangent shear modulus, $R_{k,min}$ the minimum normalized tangent bulk modulus, and s_0 the parameter controlling the nonlinearity of K_{tan} degradation.

Although London Clay fill involves material that has been excavated, compacted and consolidated, laboratory tests conducted by O'Brien et al. (2004) showed that there was little difference in strength between the London Clay fill and undisturbed London Clay. Thus the similar constitutive model used for the unweathered London Clay was employed for the London Clay fill, with model parameters adopted from O'Brien et al. (2004) and shown in Table 7.1. The same small strain stiffness used for the foundation soil (Table 7.2) was also adopted for the London Clay fill. A linear-elastic Mohr-Coulomb model was used for both the ballast and ash, with the model parameters adopted from the Geotechnical Interpretative Report (Arup Geotechnics, 2007) and summarised in Table 7.1.

Permeability

Apart from ballast, which was treated as a drained material, all other soil types in this numerical model were assumed as consolidating, thus requiring a definition of a permeability model in addition to the mechanical model. Table 7.3 tabulates the isotropic permeability values adopted for each soil type.

Table 7.3: Isotropic base permeabilities of consolidating soils

	Ash	**London Clay fill**	**Weathered London Clay**	**Unweathered London Clay**
Permeability, k_0 (m/s)	4×10^{-5}	3.7×10^{-8}	4.3×10^{-9}	3.7×10^{-10}

The ash layer was assumed to have a constant isotropic permeability, $k_0 = 4 \times 10^{-5}$ m/s. The permeability of unweathered London Clay was assumed dependent on the mean effective stress, p', according to the variable permeability model expressed in Equation 7.3 (Vaughan, 1994; Potts & Zdravkovic, 1999) and supported by data from Hight et al. (2003) collected at various sites in the London Basin. This model has been extensively applied to the modelling of London Clay permeability in a number of studies involving slopes and deep excavations (eg Kovacevic et al., 2007; Zdravkovic et al., 2005). The base permeability at $p' = 0$ was estimated as $k_0 = 3.7 \times 10^{-10}$ m/s from field measurements reported in Smethurst et al. (2012) for the cut slope at Newbury and further corroborated with standpipe piezometer equilibration data by Dixon & Bromhead (1999). The model parameter $a = 0.007$ m^2/kN was calibrated in Kovacevic et al. (2007) on data from Hight et al. (2003), controlling the reduction of permeability with increasing p'.

$$k_{sat} = k_0 \mathrm{e}^{ap'} \tag{7.3}$$

The average base permeability of weathered London Clay was estimated at $k_0 = 4.3 \times 10^{-9}$ m/s, from the same field data in Smethurst et al. (2012), and further corroborated with Dixon et al. (2019). As suctions would develop in this layer due to evapotranspiration from the plants and from evaporation from the ground surface, it was likely that desiccation cracks would appear in the superficial soil, in particular in the summer months when mobilised suctions were at highest values, thus increasing the bulk permeability of this layer. The variable permeability model adopted here (Nyambayo, 2003; Nyambayo & Potts, 2010) allowed the base permeability to increase with tensile principal stress according to Equation 7.4, to a maximum permeability of $k_{max} = 3.7 \times 10^{-8}$ m/s. This variation is depicted in Figure 7.6, with limiting tensile total stresses set at $\sigma_{T1} = 0.0$ and $\sigma_{T2} = 100.0$ kPa.

$$\log k = \log k_{sat} + \frac{\sigma_T - \sigma_{T1}}{\sigma_{T2} - \sigma_{T1}} \log\left(\frac{k_{max}}{k_{sat}}\right) \tag{7.4}$$

The permeability of the London Clay fill was assumed constant and set at $k_0 = 3.7 \times 10^{-8}\ \mathrm{m/s}$, estimated from the in-situ measurements along London Underground rail embankments, reported in O'Brien et al. (2004).

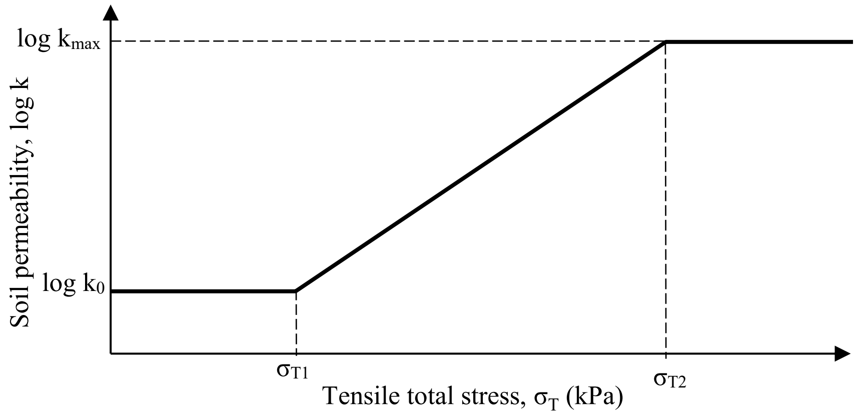

Figure 7.6: Dessication model for permeability, varying with suction.

7.3.3 Construction sequence

At the start of the analysis, all embankment elements were deactivated to first model the greenfield conditions. A bulk unit weight of 19.1 kN/m^3 was employed for both weathered and unweathered London Clay above and below the ground water table. The ground water table was initialised at 1m below ground surface and the pore water pressure profile was hydrostatic, with suctions of 9.81 kN/m^2 at the surface. The coefficient of earth pressure at rest, K_0, was initialised to be 2.1 at the surface and decreasing linearly to 0.6 at 15m below ground surface, similar to that implemented by Nyambayo (2003) and Tsiampousi et al. (2013b; 2017).

Figure 7.7(a) shows the geometry of the modelled domain of the foundation soil and the applied boundary conditions. The horizontal displacements, Δu, and vertical forces, ΔF_y, were prescribed as zero along the two vertical boundaries (with the line of symmetry on the left-hand-side, and a far-field boundary on the right) of the domain, while both horizontal and vertical displacements were fixed along the bottom boundary. As the bottom boundary of the mesh represents the London Clay – Chalk interface, the pore water pressures were not allowed to change throughout the analysis from their initial value at that boundary, given the higher permeability of the Chalk compared to that of London clay. A no flow (impermeable) boundary condition was applied at both vertical boundaries. These boundary conditions were common for all stages of the analysis described below.

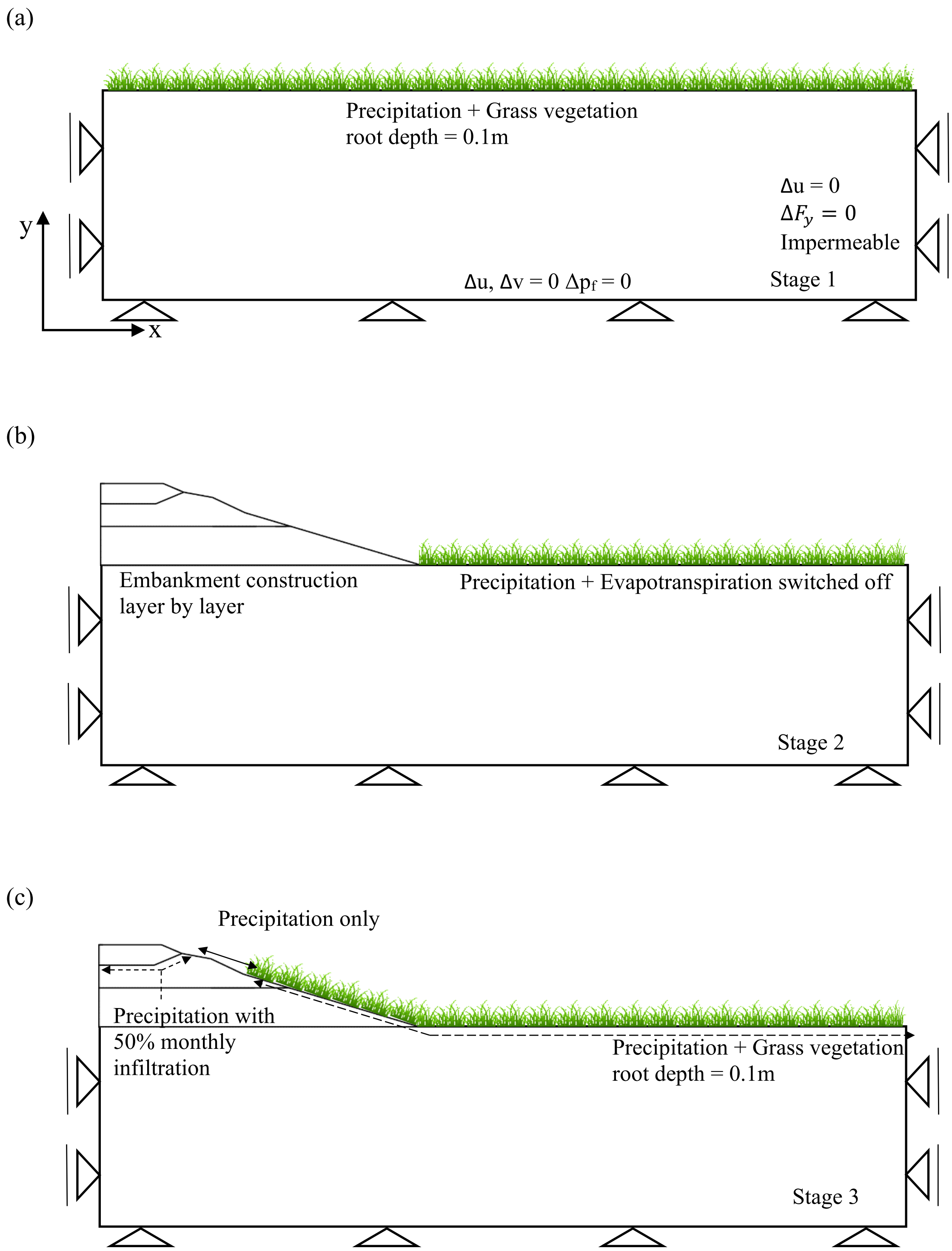

(a)
Precipitation + Grass vegetation
root depth = 0.1m
Δu = 0
$\Delta F_y = 0$
Impermeable
y
Δu, Δv = 0 $\Delta p_f = 0$
Stage 1
x
(b)
Embankment construction
layer by layer
Precipitation + Evapotranspiration switched off
Stage 2
(c)
Precipitation only
Precipitation with
50% monthly
infiltration
Precipitation + Grass vegetation
root depth = 0.1m
Stage 3

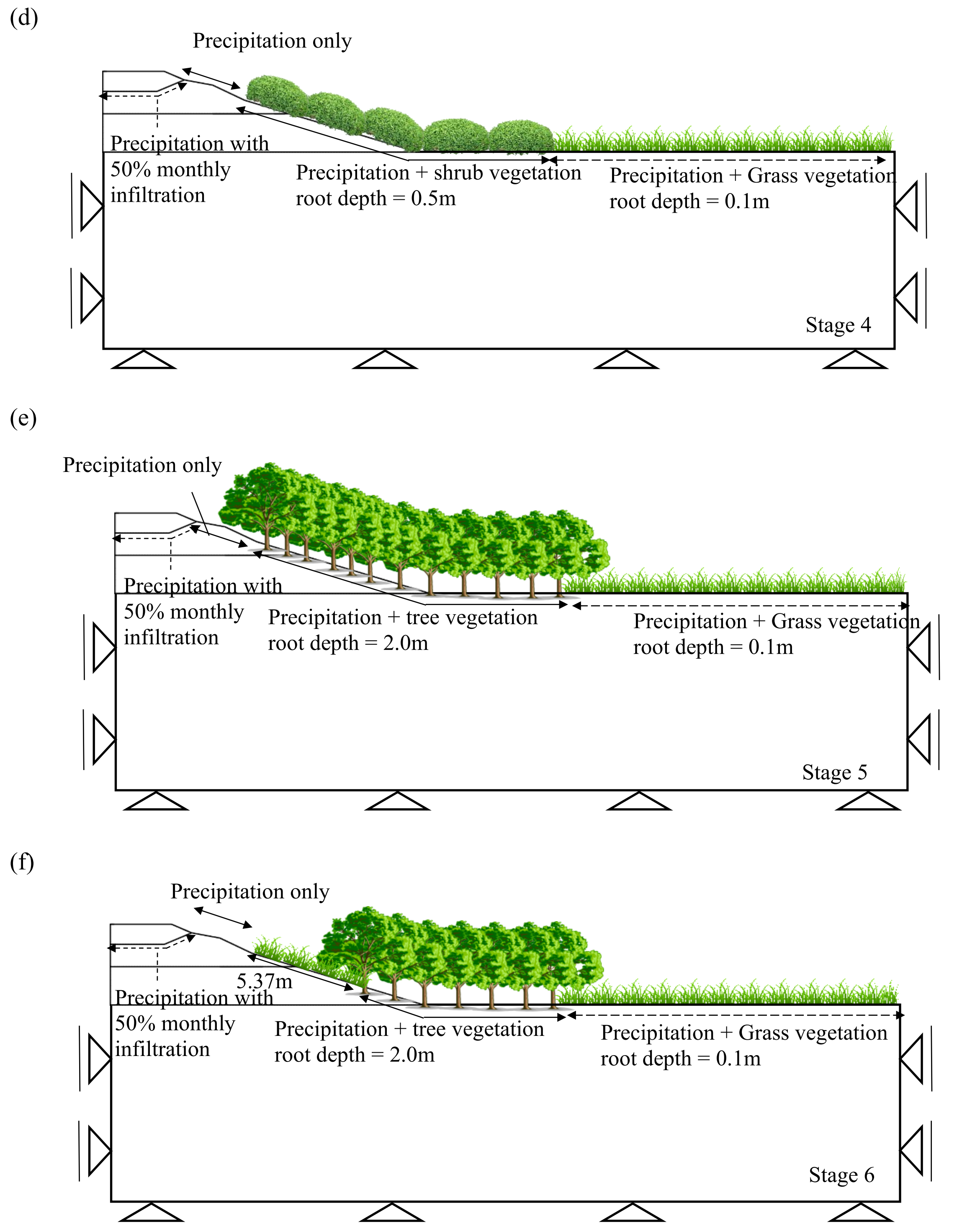

Figure 7.7: Mechanical, hydraulic, vegetation/evapotranspiration and precipitation boundary condition for (a) stage 1: initialisation for grassland (years 1-5); (b) stage 2: embankment construction (year 6); (c) stage 3: low evapotranspiration demand (years 7-10); (d) stage 4: medium evapotranspiration demand (years 11-15); (e) stage 5: high evapotranspiration demand (years 16-25); and (f) stage 6: vegetation removal on slope and maintenance (years 26-35)

Stage 1: Initialisation and seasonal changes for grassland (years 1-5)

In order to establish the seasonal pore pressures and stresses in the foundation soil before the embankment construction, it was necessary to simulate representative annual cycles of evapotranspiration (due to vegetation) and precipitation in greenfield. As the location surrounding the Magnolia Road embankment was mostly agricultural, it was assumed that the site was a grassland prior to the construction of the embankment. The appropriate precipitation and evapotranspiration boundary conditions employed are tabulated in Table 7.4, as derived in Chapter 5, assuming the root depth of the grass of 0.1m. The root depth was kept constant throughout the 5 years as root depth is sensitive to mesh size (Nyambayo and Potts, 2010), thus adopting a transient root depth would require a more refined mesh, resulting in greater numerical cost but no significant benefit to the model accuracy. These boundary conditions were applied over the top surface of the foundation soil domain in Figure 7.7(a). It should be noted, however, that the evapotranspiration boundary condition also affects nodal flow over the depth below the ground surface that corresponds to the vegetation root depth. A typical year in the numerical model starts in April (start of dry season), with each month comprising of 12 increments to reduce numerical instability in particular in the application of the hydraulic boundary conditions.

Table 7.4: Monthly precipitation and evapotranspiration rates for a typical year. Values are given in mm/month

Month	Precipitation	Grass	Shrubs	Trees
April	37.67	7.25	27.90	59.29
May	39.33	8.75	42.88	88.07
June	44.17	9.58	57.37	114.74
July	31.92	11.48	64.10	128.19
August	39.42	8.64	52.75	105.49
September	47.42	5.10	30.99	72.31
October	51.25	2.95	14.74	31.44
November	43.58	1.28	6.41	12.82
December	45.00	0.63	3.13	6.26

January	43.25	0.67	3.35	6.69
February	28.33	1.18	5.88	11.76
March	35.00	2.90	14.53	29.05

As grass evapotranspiration never exceeded precipitation for each month, the pore water pressure and stress regime at site remained constant in the first five years of seasonal cycling, with pore pressure having a hydrostatic profile and the phreatic surface at 1m below ground level. Consequently, the bulk stiffness at this stage would not change due to no volumetric changes with the consistently saturated conditions.

Stage 2: Embankment construction

The embankment construction was simulated at the start of year 6 (April) of the analysis, and was performed within one month, with each layer of the embankment constructed in 10 days. Each layer of the embankment clay fill and ash was constructed with an initial suction of 50kPa, while the ballast was treated as a dry material with no suction. Both vegetation/evapotranspiration and precipitation boundary conditions were deactivated during this stage as it was assumed that the construction was sufficiently fast and that any soil-atmosphere interactions during the construction would be negligible. In addition, the phreatic surface in the foundation soil was also maintained at the same initial elevation during construction, thus enhancing the consolidation process within the foundation soil beneath the embankment and maintaining suctions within the embankment during construction. Along the left vertical boundary, which is the axis of symmetry, the nodes belonging to the newly-constructed embankment were prescribed the same boundary conditions as the nodes below belonging to the foundation soil: $\Delta u = 0$, ΔF_y=0 and no fluid flow across the boundary (i.e. impermeable). These boundary conditions on the embankment remained throughout the rest of the analysis.

Stage 3: Low evapotranspiration demand (years 6-10)

The embankment construction had loaded the foundation soil (London clay) underneath and therefore mobilised some degradation of the small strain shear stiffness as the shear strain increased in London clay, defined by Eq. (7.1) in the ICG3S model. The bulk stiffness of London clay did not change significantly during embankment construction due to its short duration and low permeability of the clay. However, at the start of Stage 3, for the subsequent investigation of the effects of atmospheric and vegetation changes on the slope, the small strain stiffness (both shear and bulk) of the foundation soil was reset to initially high values. Both precipitation and vegetation boundary conditions were resumed, as illustrated in Figure 7.7(c). As the embankment ballast was considered to behave in a drained manner, the precipitation boundary condition was applied along the ballast-ash interface, assuming that only 50% of monthly infiltration would reach this interface through the ballast. Full precipitation was applied along the remaining embankment slope and ground surfaces, as indicated in Figure 7.7(c). During the first year post-embankment construction (year 6), grass was assumed active only on the surface of the foundation soil. From year 7 onwards, grass was assumed to have grown also on the embankment slope. These monthly boundary conditions, as tabulated in Figure 7.4, were applied until the end of year 10 of the analysis, which finished in the month of March (end of wet season).

Stages 4 and 5: Medium and high evapotranspiration demand (years 11-25)

Following from the end of March of year 10, the grass vegetation along the surface of the embankment slope and along the ground surface up to 12.5m from the embankment toe (see Figure 7.7.(d)) was replaced with shrubs to simulate vegetation growth. This was characterised as a medium evapotranspiration demand with 0.5m root depth and was modelled for another five years (up to the end of year 15). Finally, the shrubs were replaced with deciduous trees along the same boundaries (Figure 7.7(e)), characterised as high evapotranspiration demand with their root depth of 2.0m. The analysis was allowed to run for an additional 10 years to model the long-term presence of trees on the side of the embankment. The precipitation boundary condition, with cycles of a representative year, was active throughout this period of 15 years, as indicated in Figure 7.7(e). The end of this period was considered to represent the ‘current’ state of the embankment. Therefore, to verify the numerical model, the predicted displacements and pore water pressures in the embankment in the final year of this stage (April to March of year 25), were compared with those measured on the Magnolia Road embankment between April 2006 and March 2007, before the trees were cleared from the slope.

Stage 6: Vegetation removal and maintenance (years 26-30)

At the end of March of year 25 (March 2007 in real-time) the vegetation on the slope in the numerical analysis was removed, similar in timing to that on the Magnolia Road embankment. Part of the deciduous tree vegetation boundary was replaced with that of grass on a portion of the slope as shown in Figure 7.7(f). The analysis was then allowed to proceed for 5 years (to March 2012) with this change in boundary conditions and the results were compared with field measurements during the first 4 years of this period of post-vegetation removal (April 2008 – March 2011), where field measurements were available. In addition, actual monthly rainfall aggregated up from sub-daily rainfall measured near the site (from Chapter 2) was applied, for a more representative simulation of the atmospheric conditions on site, instead of continuing to apply the rainfall of a typical representative year.

7.3.4 Results and discussion

The embankment behaviour was monitored over the span of 5 years from March 2006 to March 2011 (Geotechnical Observations, 2013). Pore pressures within the embankment were measured using flushable piezometers, while inclinometers and extensometers were used to measure horizontal and vertical displacements (as indicated in Figure 7.2). For the analysed (north) side of the slope the instrumentation was installed in two main vertical sections, one mid-slope of the embankment, and another near the toe of the embankment, as defined in Figure 7.8.

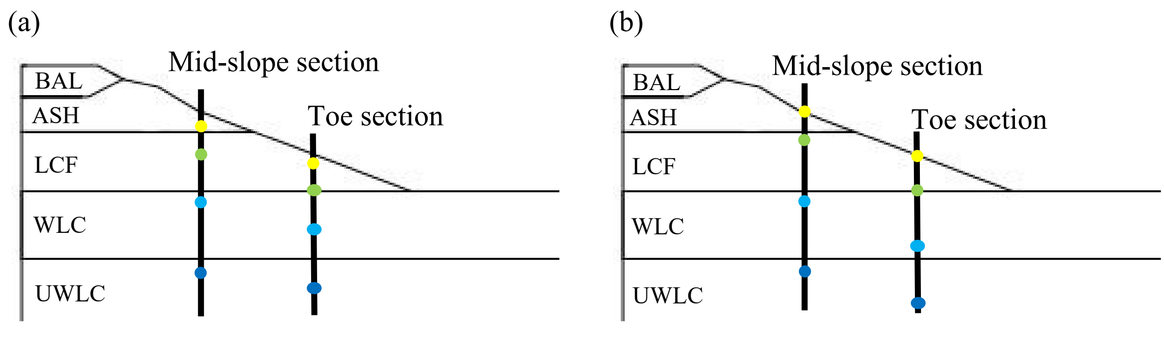

Figure 7.8: (a) Extensometer monitoring points for vertical displacements and (b) inclinometer monitoring points for horizontal displacements for the North slope.

As the mid-slope section passes through the embankment ash and clay layers, vertical (1.5m, 2.5m, 4.1m, and 7.0m below surface) and horizontal (0m, 2.0m, 4.0m, and 7.0m below surface) displacements at 4 different depths, located at each soil stratigraphy in this section, were used to verify the numerical model.

Years after embankment construction (Years 7 – 24)

As the embankment was not monitored throughout its lifecycle before 2006, it was not possible to perform any comparisons between field observations and the numerical results. However, it was still beneficial to assess the evolution of the embankment behaviour and pore water pressure regime with vegetation development in the numerical model throughout the embankment's lifecycle.

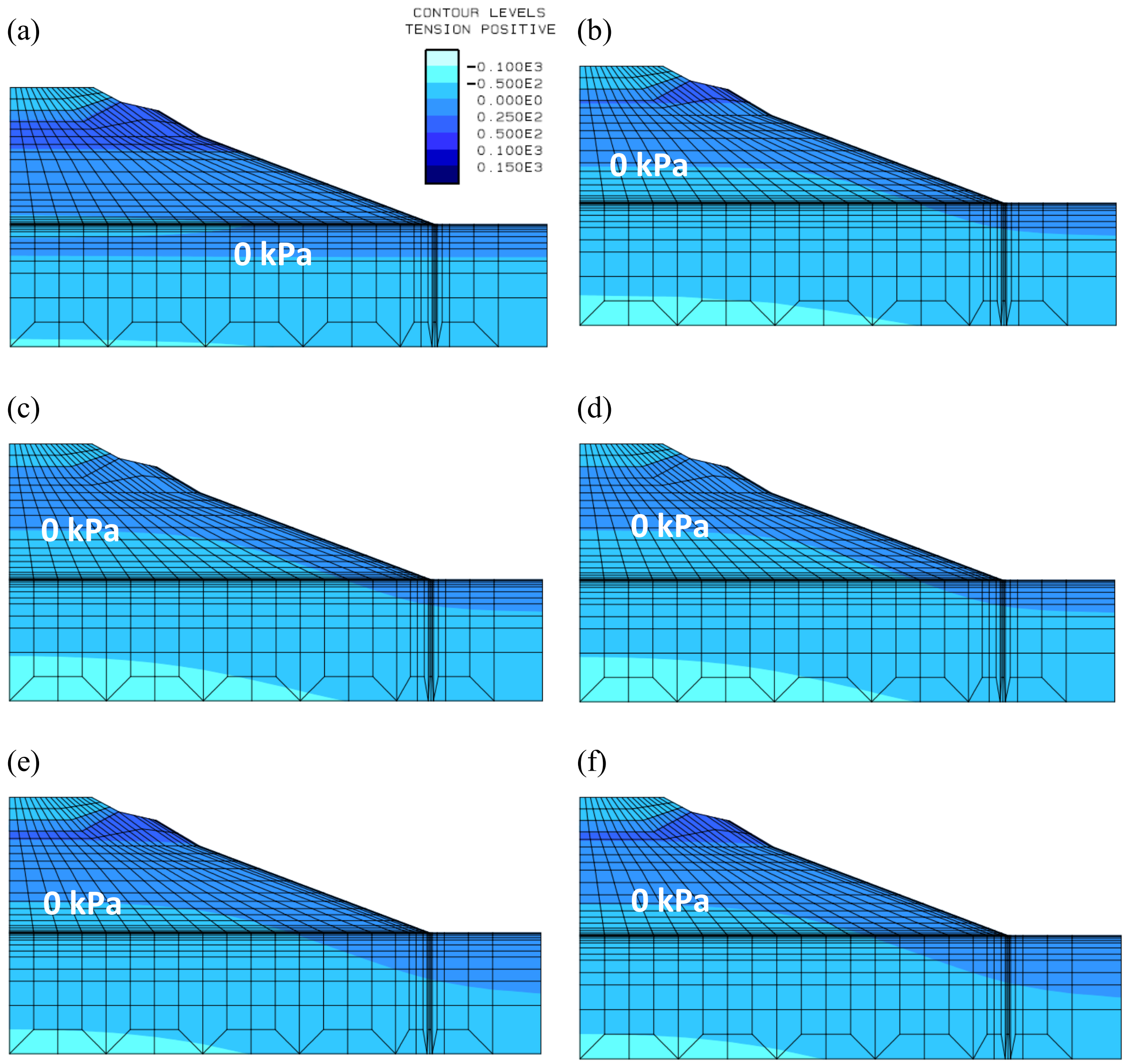

(g)

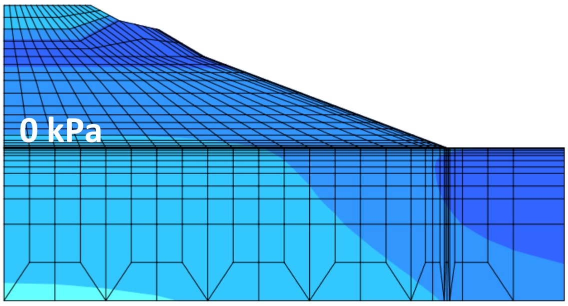

(h)

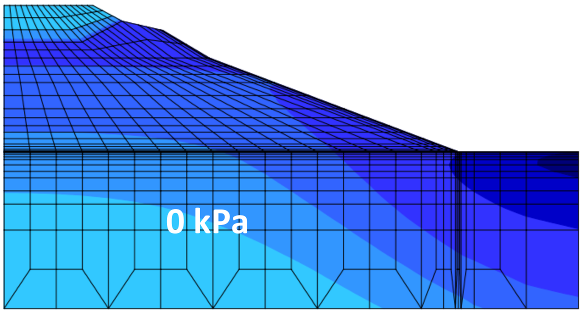

Figure 7.9: Pore water pressure contour plots during embankment lifecycle at (a) end of embankment construction, winter of Year 6; (b) summer of Year 6; (c) winter of Year 10; (d) summer of Year 10; (e) winter of Year 15; (f) summer of Year 15; (g) winter of Year 20; (h) summer of Year 20.

Figure 7.9 (a) and (b) plots the pore water pressure contours at the end of winter (March) and end of summer (September) of year 6, which was after embankment construction. Due to the pore pressure equilibration within the embankment, as atmospheric conditions were not active during construction, the initial suctions within the clay fill and ash decreased from their 50kPa suction prescribed on construction, ultimately reaching a range from 0kPa to 25kPa of suction in the clay fill, and 25kPa to 30kPa of suction in the ash (Figure 7.9(a)). After just 6 months of precipitation on the embankment the suctions within the embankment decreased further to between 0kPa and 25kPa and the phreatic surface rose by around 1.5m at the centre of the embankment (Figure 7.9(b)).

Under the subsequent low evapotranspiration demand years (Y6 – Y10), there was little change to the pore water pressure distribution (Figure 7.9 (c) and (d)). The phreatic surface profile remained at about 2m above ground level at the centre of the embankment, which reduces to 1m below the ground surface at the far-field boundary due to the minimum 10kPa suction adopted for the precipitation boundary condition where excess infiltration was then treated as runoff.

As shrubs started to develop on the embankment, there was higher evapotranspiration demand and this was reflected in the lower phreatic surface in Year 15 (Figure 7.9 (e) and (f)) as compared to the phreatic surfaces in Year 10 (Figure 7.9 (c) and (d)). In addition, the ash layer also developed higher suctions due to its significantly higher permeability of 4×10^{-5} m/s as compared to the clay fill, resulting in a uniform suction across the layer, as compared to the lower permeability clay layers.

Subsequent growth of trees after Year 15 resulted in even greater evapotranspiration demands on the embankment and ground surface, causing further lowering of the phreatic surface to almost the initial ground level during the winter, and 2m below it at the embankment centre during the summer in Year 20 (Figure 7.9 (g) and (h)). In addition, suctions generated during the summer were also not fully dissipated after winter, leading to a gradual build-up of suctions in the embankment after each seasonal cycle.

Year before vegetation removal (Year 25; March 2006 – March 2007)

In the year 2006-2007 before the vegetation removal, piezometers within the embankment measured suctions of up to 80kPa during the drier summer months, while suctions decreased to between 0 kPa and 50kPa during the wetter winter period (Figure 7.10). The seasonal changes in pore water pressure within the embankment, predicted as a result of the applied seasonal precipitation and evapotranspiration changes in the numerical model, are shown in Figure 7.11. Part (a) of the figure shows the pore water pressure contours at the end of September (summer period) of year 25 (Stage 5 of analysis), corresponding to end of September 2006 in reality, while part (b) shows the result at the end of March (winter period) of year 25, corresponding to March 2007 in reality.

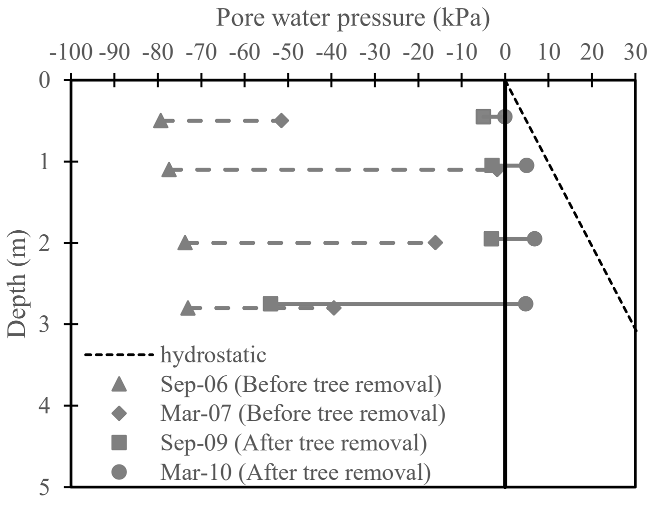

Figure 7.10: Pore suction seasonal variation within the embankment on the North section. Data provided by Geotechnical Observations for Arup Geotechnics, 2007.

While there was less suction within the embankment in the numerical analysis as compared to field measurements at the end of winter, the monitored summer suctions of about 80kPa were well reproduced in the numerical model as shown in Figure 7.11 (a). However, the numerical model was unable to reproduce the extremely depressed phreatic surface (about 13.5m below ground level; Geotechnical Observations, 2013) that was monitored in the foundation. The lowest the phreatic surface reaches in the numerical model is only about 3m to 4m below ground level.

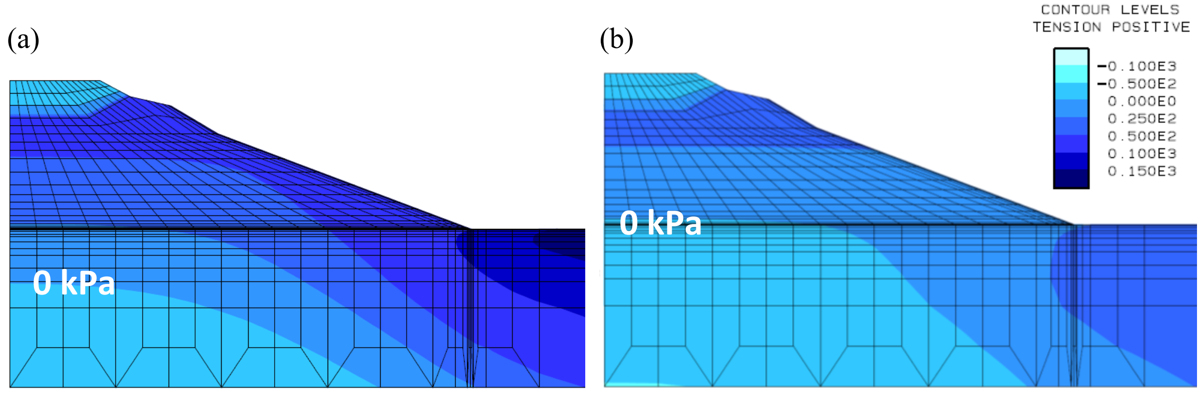

Figure 7.11: Pore water pressure contour plots during (a) end of September/summer and (b) end of March/winter for Year 25 (before vegetation removal). Positive indicates suction. Units in kPa.

The evolution of field displacements for the mid-slope section (see Figure 7.8) is plotted in Figure 7.12 for the year 2006-2007 before the trees were removed, together with displacements predicted from the numerical analysis with the saturated modelling approach (year 25). Figure 7.13 shows vectors of ground movements resulting from seasonal changes between the start of April and end of September of year 25, part (a), and between start of October and end of March of year 25, part (b).

(a)

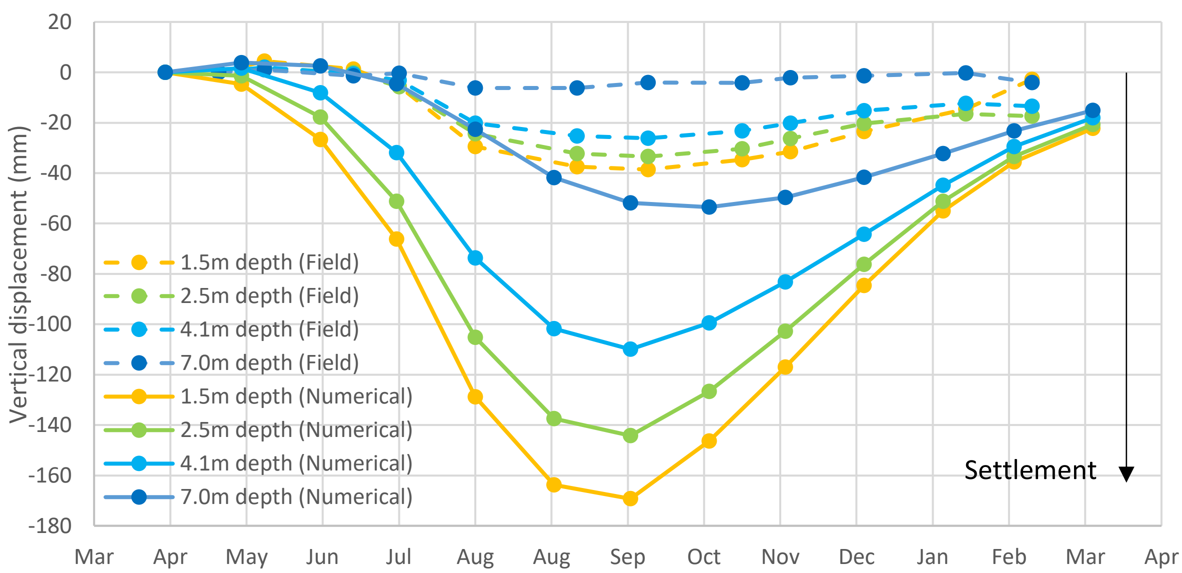

(b)

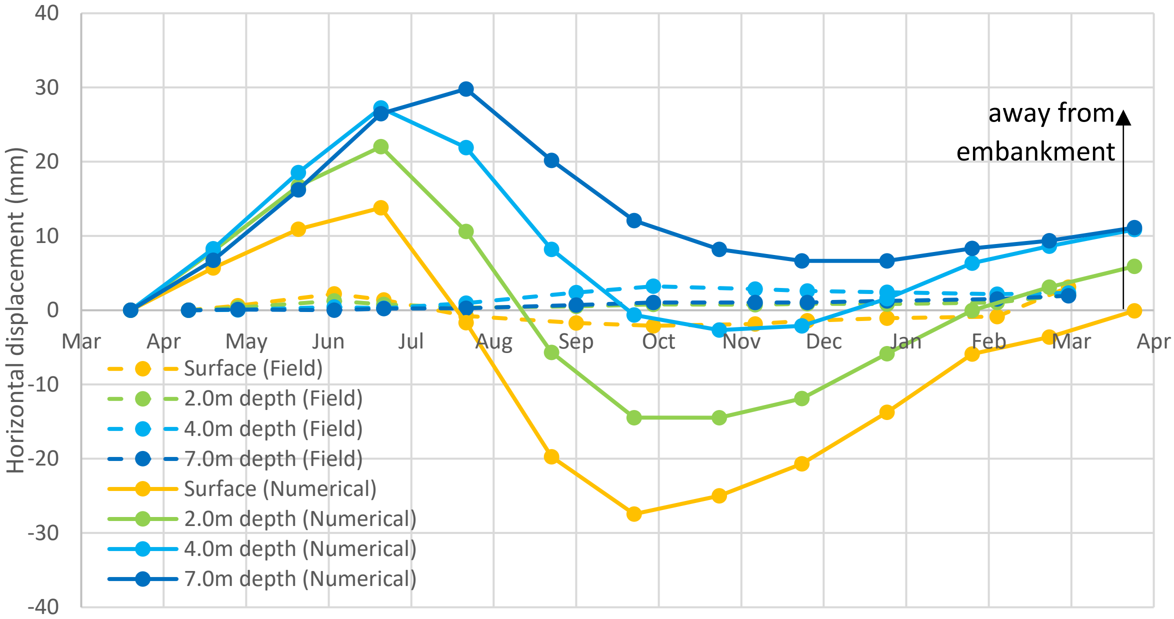

Figure 7.12: Comparison of (a) vertical and (b) horizontal displacements between predictions from the saturated numerical analysis and field monitoring results mid-slope.

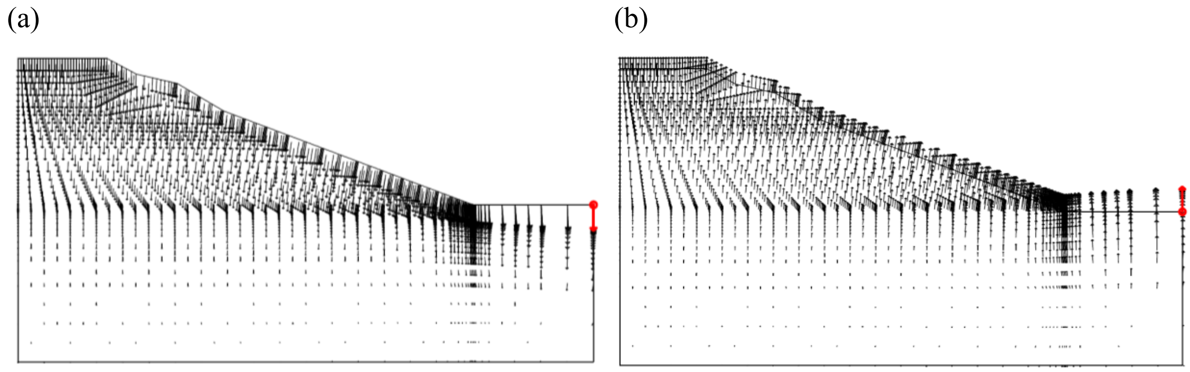

Figure 7.13: Sub-accumulated vectors of displacements for the period of (a) end of March to end of September (vectors of displacement during the summer) and (b) end of September to end of March (vectors of displacement during the winter).

With respect to Figure 7.12 (a) the numerical model predicted correctly the shrinkage (settlement) of the embankment and the foundation soil over the summer months, which was in agreement with increased suctions in this period (Figure 7.11 (a)), while settlements reduced over the winter months due to swelling (heave) as suctions reduced (Figure 7.11 (b)). The vectors of ground movements in Figure 7.13 also showed an overall shrinkage of the embankment in the summer period (part (a)) and swelling in winter (part (b)).

The pattern of the settlement profile in Figure 7.12 (a) was also correctly predicted to mobilise the highest values near the surface of the embankment slope which then reduced at depth. The evolution of settlement values with time at various depths was also in agreement with measured patterns, increasing over the summer and reducing in winter. Similarly, Figure 7.12 (b) shows correctly predicted patterns of the horizontal displacements mid-slope.

However, the magnitudes of the displacements obtained in the numerical model were significantly larger than those measured in the embankment (maximum field settlement of around 40mm during the summer vs. the predicted around 160mm settlement). Similar overestimations were also present in the horizontal displacements, where the predicted maximum of around 30mm compared to around 3mm maximum field horizontal displacements. This overestimation in the numerical model highlighted the weaknesses of using a saturated constitutive model for modelling the compacted embankment clay and is discussed further in Section 7.5.1.

Post vegetation removal (March 2007 – March 2011)

As the vegetation on part of the slope was removed (shown in Figure 7.2 and Figure 7.7(f)), it was observed in the field that the embankment started to swell normally to the slope surface, as residual suctions dissipated due to a net infiltration of water into the soil caused by a much smaller water removal from the soil by evapotranspiration (grass roots compared to tree roots). This swelling behaviour eventually resulted in a slip surface developing at the site between the embankment and the foundation soil.

Figure 7.14 shows snapshots of predicted pore water pressures in the embankment in the first year of post-vegetation removal (Stage 6). The dissipation of residual suctions was reproduced well by the numerical model, as the phreatic surface was shown to rise within the first year after vegetation removal, compared to Figure 7.9. Suctions within the embankment were also much lower and consistent throughout the year, ranging from 0kPa to 25kPa. Suctions near the toe of the embankment, however, remained higher at around 50kPa during the summer and reduced to 25kPa during the winter, due to the remaining presence of trees at the toe.

(a) (b)

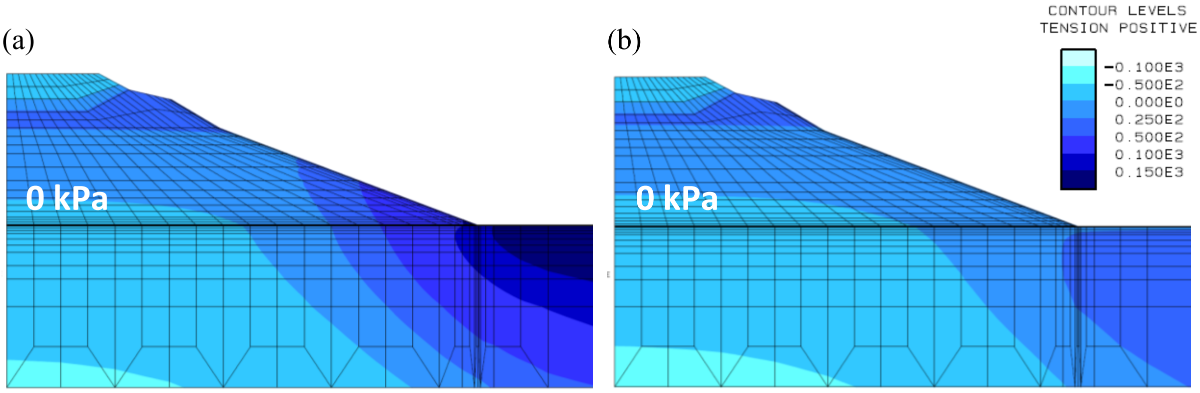

Figure 7.14: Pore water pressure contour plots during (a) 6 months after vegetation removal (end of September 2007) and (b) 1 year after vegetation removal (end of March 2008). Positive indicates suction. Units in kPa.

The evolution of displacements in the same vertical mid-slope section, over the four years post-tree removal from end of March 2007 to end of September 2011, is shown in Figure 7.15. While the measurements in Figure 7.15(a) indicated an overall continuous swelling (heave) of the embankment soil and negligible movements in the foundation soil, the numerical model exhibited seasonal effects of shrinkage over the summer and swelling in the winter, albeit of a lower magnitude compared to the pre-tree removal stage (Figure 7.12). Similarly, the measurements of horizontal movements in the embankment in Figure 7.15(b) were consistent with the overall heave, indicating the direction of the horizontal movement away from the embankment. The numerical model predicted the correct trend over the 4 years, but much larger displacement values and also a seasonal variation.

(a)

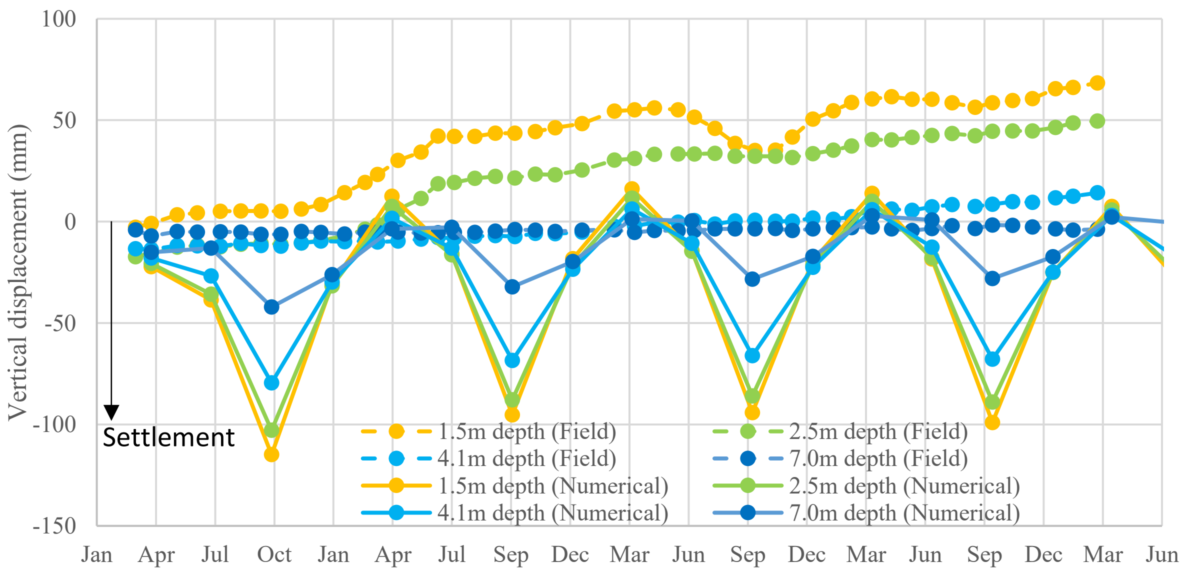

(b)

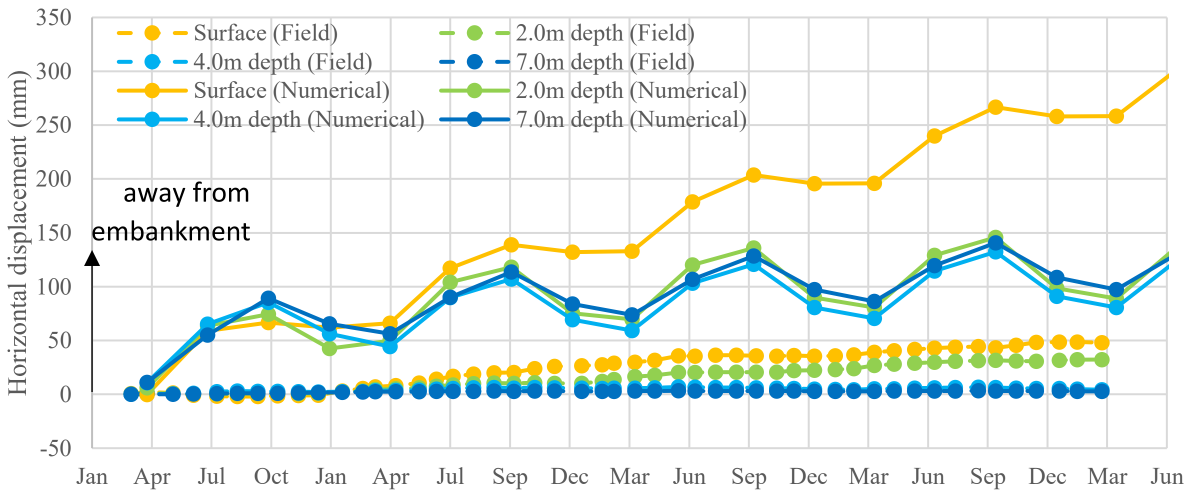

Figure 7.15: Comparison of (a) vertical and (b) horizontal displacements between saturated numerical analysis and field monitoring results mid-slope after vegetation removal.

Considering the above comparisons between the measured and predicted behaviour of the Magnolia Road embankment using the saturated numerical modelling framework, it became clear that this modelling approach was not entirely appropriate for realistic representation of the behaviour of compacted earthfill embankments. While the saturated model was able to broadly predict the correct trends of the embankment response, the magnitudes of movements were grossly overpredicted as a result of large volumetric changes in the embankment clay associated with it being fully saturated. As a result, the modelling approach was in the following changed to simulating the fill material as unsaturated, which, in general, accounted for the presence of both air and water in the pore space and reduced accordingly the overall volumetric changes associated with the water balance in the embankment in relation to the applied atmospheric boundary conditions.

7.4 Numerical model of the Magnolia Road embankment in the unsaturated soil modelling framework

7.4.1 Introduction

Given that earthfill embankments are mostly constructed by clay compaction, the earthfill material is initially unsaturated and the study in Section 7.3 showed that it may not be appropriate to model the behaviour of such a material with a saturated constitutive approach.

Consequently, an unsaturated modelling approach for the Magnolia Road rail embankment was developed and is discussed in this section. With respect to Figure 7.3(a), it is the London Clay fill, weathered London Clay and ash that were modelled as unsaturated; soil layers that experienced high variations of suction in the saturated analysis. The unweathered London Clay remained to be modelled as saturated, using the same modelling approach as in Section 7.3 (i.e. nonlinear strain-softening Mohr-Coulomb model and variable permeability dependent on mean effective stress). Equally, the ballast remained to be treated as drained and simulated with a linear elastic Mohr-Coulomb model. The model parameters for these two materials were the same as summarised in Table 7.1 and Table 7.2.

This section first introduces the mechanical and hydraulic modelling approach that was adopted for the three unsaturated materials. A finite element analysis of the Magnolia Road embankment was then performed, with the construction sequence and boundary conditions as presented in Section 7.3 for the saturated modelling of this case study. The numerical results were then compared with field measurements.

7.4.2 Soil modelling

Mechanical constitutive models

<u>*Soil*</u>

The embankment clay fill and weathered foundation soil were modelled using an unsaturated Imperial College Single Structure Model available in ICFEP (ICSSM; Georgiadis et al. (2005)). The model is an extension of the Barcelona Basic Modelling framework (BBM), first introduced by Alonso et al. (1990). The ICSSM formulation and calibration for London Clay was presented in Chapter 5 and model parameters summarised in Table 5.1.

<u>*Ash*</u>

In addition, the ash material was simulated using an unsaturated Mohr-Coulomb constitutive model available in ICFEP (Smith, 2003). The model formulation enables a bulk modulus, H, to be prescribed that accounts for the effect of the changing matric suction on direct strains in the soil. This is in addition to moduli that control the effect of applied net stress and matric suction on the volumetric water content of the soil.

The initial strength parameters for this model (cohesion, angle of shearing resistance and dilation) were the same as given in Table 7.1 and discussed in the saturated embankment model. The bulk modulus, H, was derived from the void ratio vs. suction data presented in Figure 7.16:

$$H = 3\frac{d(u_a - u_w)}{d\varepsilon_{vol}} \tag{7.5}$$

This data was obtained from the programme of drying and wetting tests performed on embankment ash material by Melgarejo-Corredor (2004). The H modulus of ash calibrated in this way was found to be relatively constant with increasing suction. This was due to the fact that ash was a highly permeable granular material, thus it lost its water content easily at low suctions and remained a dry material at higher suction. Hence its H modulus did not change once it was fully dry, and a value of 25MPa was calibrated from Figure 7.16.

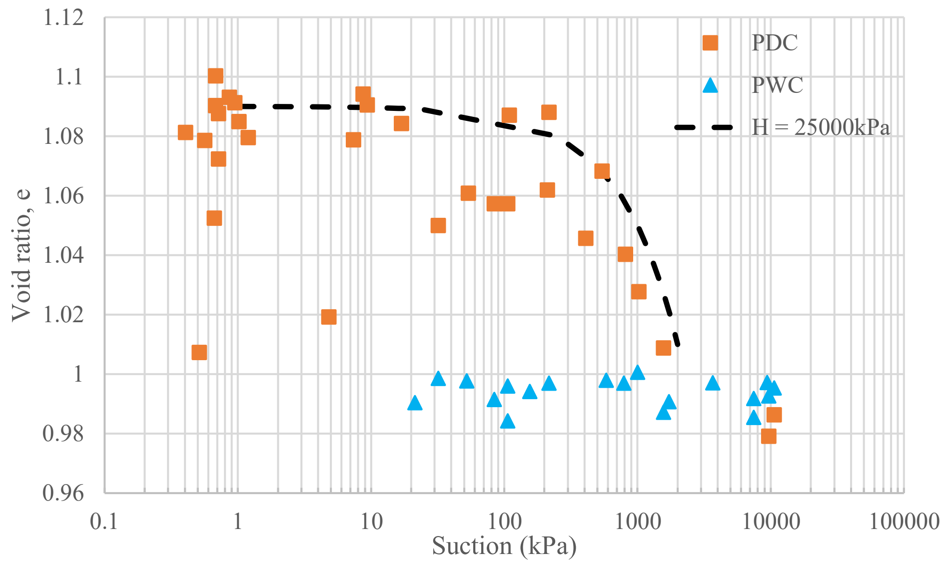

Figure 7.16: Void ratio vs suction for railway ash, with calibration for bulk modulus, H. Laboratory data by Melgarejo-Corredor, 2004. PDC-principal drying curve; PWC-principal wetting curve.

<u>Soil water retention curves (SWRC)</u>

Soil

A hysteretic void ratio-dependent non-linear SWR model (Tsiampousi et al. (2013c)) was employed for the London Clay fill and for the unweathered London Clay, with the following formulation for the primary drying curve:

$$S_r = \frac{1 - \frac{s^*}{s_0^*}}{1 + a_d \cdot s^*} \tag{7.5}$$

where $s^* = (v-1)^{\psi} \cdot (s - s_{air})$ expresses a combined suction which enables this three-dimensional SWR model ($S_r - s_{eq} - v$ space) to be drawn in two dimensions as S_r vs. s^*; v is the specific volume; s_{air} is the air entry value of suction; S_r is the degree of saturation; s_0^* is the void ratio adjusted equivalent suction ($s_{eq} = s - s_{air}$) at $S_r = 0$; ψ is the parameter controlling the effect of specific volume, and a_d is the fitting parameter for the drying curve. The corresponding formulation for the primary wetting curve is:

$$S_r = \frac{1 - \frac{s^*}{s_0^*}}{1 + a_w \cdot s^*} \tag{7.6}$$

where a_w is the fitting parameter for the wetting curve.

To calibrate the above SWR model, sets of experimental data for compacted London Clay were available from the research of Melgarejo Corredor (2004). Specimens of compacted clay were taken from existing London clay embankments and tested both in their intact and reconstituted states. The tests were performed to establish primary drying and wetting curves (PDC and PWC, respectively), as well as primary (P), secondary (S) and tertiary (T) drying/wetting scanning curves (SC) and were plotted in Figure 7.17. The first attempt at calibrating the above SWR model resulted in values of model parameters summarised in Table 7.5 and the primary curves plotted in Figure 7.17 (as suction vs. degree of saturation), with the area between them highlighted in blue. It should be noted that the effect of void ratio / specific volume was not taken into account (i.e. $\psi = 0$).

Table 7.5: Hysteretic SWR model parameters for embankment clay and weathered London Clay

Parameter	Values 1st attempt	Values 2nd attempt
ψ	0	0
s_{air}	5 kPa	20 kPa
s_0^*	1×10^9 kPa	1×10^9 kPa
a_d	2.2×10^{-5}	8×10^{-4}
a_w	8×10^{-4}	3×10^{-3}

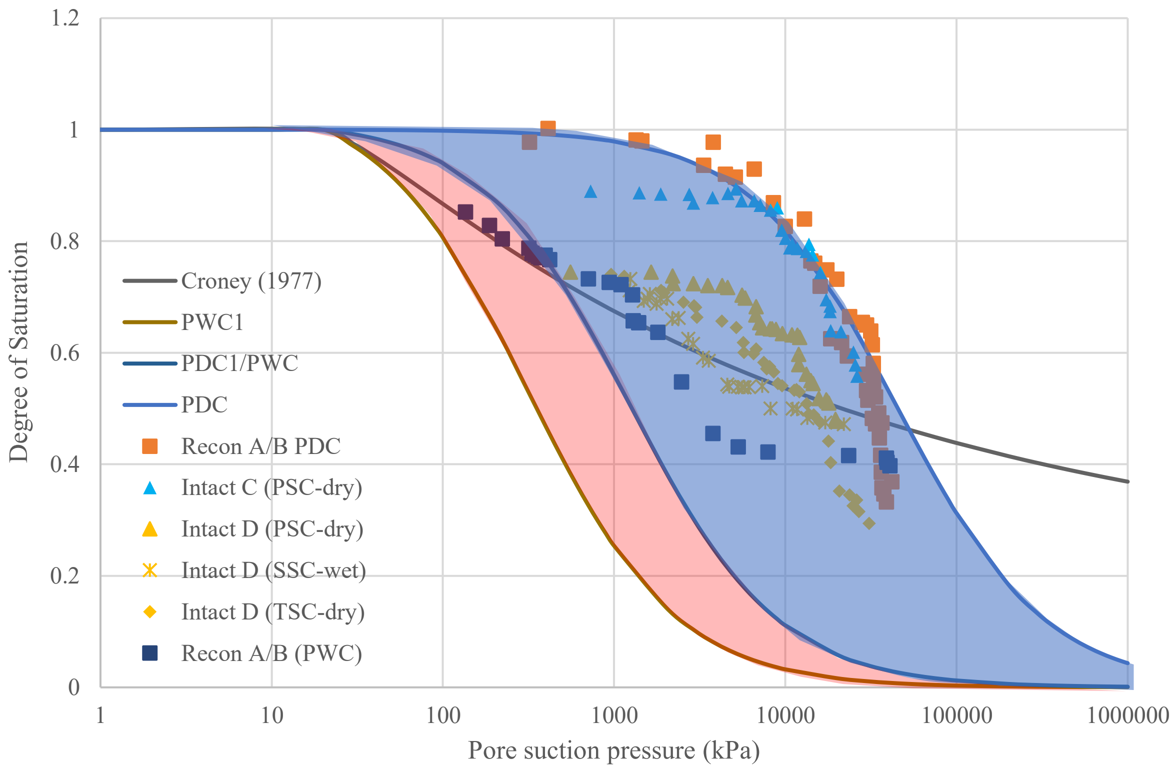

Figure 7.17: Calibration of the hysteretic SWR model for embankment clay. Initial calibration envelope shaded blue, final calibration shaded red. Laboratory data by Melgarejo-Corredor (2004).

A full analysis of the Magnolia Road embankment performed with this SWR model calibration for the clay fill and weath ered London clay showed that the soil remained nearly fully saturated throughout the year, despite the seasonal changes in atmospheric and vegetation boundary conditions. Hence the predictions of ground movements were not dissimilar to those obtained with a fully saturated analysis approach discussed in Section 7.3. The reason for such predictions can be explained by Figure 7.17, which shows that for the range of suctions developed in the analysis and in the field, of up to 200 kPa, the soil mobilised quite a high degree of saturation (above 95%). As field observations at the site indicated reasonably dry soil during the summer (Geotechnical Observations, 2013), the predicted high saturation was not realistic. Therefore, alternative SWRCs were explored.

A hydro-mechanical finite element analysis performed by Briggs et al. (2016) on the same embankment used a monotonic SWRC measured by Croney (1977) in drying tests conducted on London Clay. This curve was plotted in Figure 7.17 together with the Melgarejo-Corredor (2004) wetting and drying test data. It was apparent that the Croney (1977) SWRC was a scanning curve, which agreed well with Melgarejo-Corredor laboratory data on wetted samples, albeit reconstituted. At low suctions of 10kPa to 400kPa, the Croney (1977) SWRC also lies under the PWC of the hysteretic SWR model fitted to Melgarejo-Corredor's data, suggesting that more drying would occur at these suction ranges as compared to the reconstituted laboratory samples (Stirling et al., 2021).

Therefore, for a more accurate representation of the SWR behaviour of compacted London clay at suctions less than 200kPa, a new hysteretic SWR model was fitted (shaded in red) such that the Croney (1977) curve and experimental data approximated a scanning curve at suctions of less than around 200kPa. In doing so, the previous PWC was set as the new PDC, while the new PWC was pushed slightly further to the left. Within the range of measured suctions (up to 200 kPa), the degree of saturation reduced to around 80%. The new SWR model parameters were added to Table 7.5 and adopted in subsequent analyses presented in the current section.

Ash

Considering the available SWR data for the embankment ash, shown in Figure 7.18 (Melgarejo Corredor, 2004), a decision was made to use a monotonic SWR model, of the van-Genuchten (1980) type (Tsiampousi, 2011), given by the following expression:

$$S_r = \left[\frac{1}{1 + \left[\alpha \cdot (v-1)^{\psi} \cdot s_{eq}\right]^n}\right]^m \cdot (1 - S_{ro}) + S_{ro} \tag{7.6}$$

where $s_{eq} = s - s_{air}$ represents equivalent suction in ICFEP's finite element formulation for unsaturated soils, ψ is the parameter controlling the effect of specific volume, S_{ro} is the degree of saturation in long term, α, n and m are fitting parameters. The calibrated model parameters for the embankment ash were tabulated in Table 7.6.

Table 7.6: Monotonic SWR model parameters for railway ash

Parameter	Value
ψ	0
s_{air}	1 kPa
S_{ro}	0.1
α	0.2
n	1.5
m	0.5

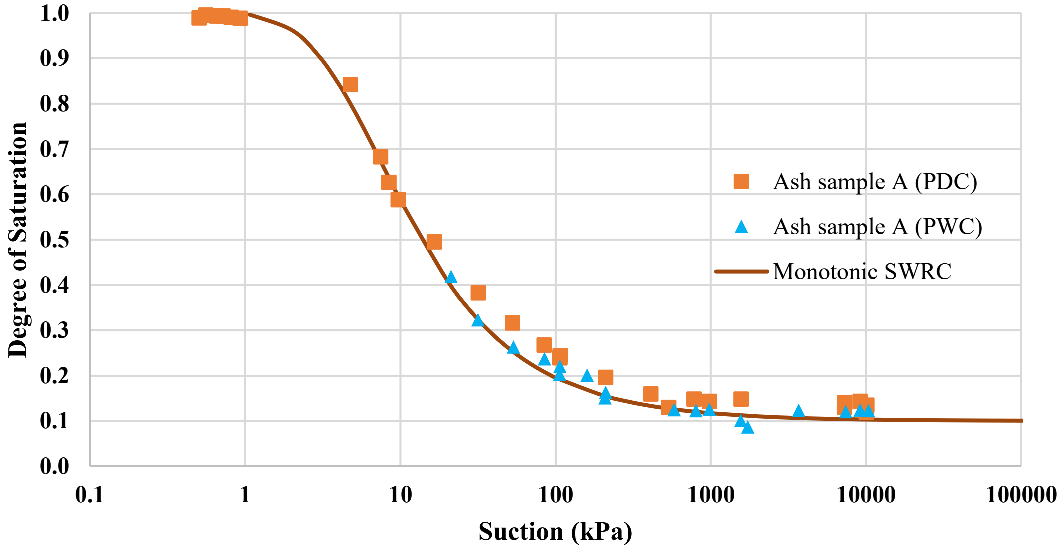

Figure 7.18: Calibration of the monotonic SWR model for railway ash. Laboratory data from Melgarejo-Corredor (2004).

Permeability

The same dessication permeability model used in the saturated analysis (Section 7.3; Equation (7.4)) was employed in the unsaturated analyses to model the increase of bulk permeability due to dessication cracks potentially opening in the ash, clay fill and foundation topsoil (weathered London clay). This modelling approach was further coupled for unsaturated analyses with a desaturation permeability model to account for the reduction of permeability with increasing suction in the intact soil. The formulation of the desaturation model (Potts & Zdravkovic, 1999) is similar to that of the dessication model, but the permeability variation is expressed in terms of equivalent suction, s_{eq}:

$$\log k = \log k_{sat} - \frac{s_{eq} - s_{eq1}}{s_{eq2} - s_{eq1}} \log \left(\frac{k_{sat}}{k_{min}} \right) \tag{7.7}$$

where k_{sat} is the saturated permeability, s_{eq} the current equivalent suctions, s_{eq1} and s_{eq2} are limits of the permeability variation and k_{min} is the minimum permeability reached after the current equivalent suction has reduced to the s_{eq2} limit. For the numerical analyses in this section, the saturated permeabilities for the three soils treated as unsaturated were the same as the permeabilities adopted in the saturated analysis in Section 7.3. The s_{eq1} limit was set equal to the air entry values for each unsaturated material, while the s_{eq2} limit was set uniformly at

100 kPa suction. k_{min} was set to be 75% of the saturated permeability, indicating a permeability drop of 25% at 100kPa of suction for each of the three unsaturated materials.

In the event when both dessication and desaturation are active in the soil element, the numerical algorithm in ICFEP would prioritise dessication over desaturation and permeability would increase accordingly. While the desaturation decrease of permeability is governed by the introduction of air into the soil matrix and reduction of water in the soil (Zhang et al., 2014), the introduction of macro-scale dessication cracks when suction is high would allow fluid to enter easier into the soil matrix, thus increasing the overall permeability of the soil (Albrecht and Benson, 2001).

7.4.3 Construction sequence and boundary conditions

The same stages of the numerical model initiation, embankment construction and soil-plant-atmosphere interaction that were simulated in the saturated modelling approach in Section 7.3, were modelled in the current section for the unsaturated modelling approach. The only difference is that the unsaturated analysis was extended to run from March 2012 to August 2017, continuing to apply actual monthly precipitation recorded at the Rayleigh station. All mechanical and hydraulic boundary conditions were also maintained the same as in the saturated analysis.

7.4.4 Results and discussion of the base case unsaturated analysis

Before vegetation removal (March 2006 – March 2007)

Figure 7.19 shows the predicted pore water pressure variations in the embankment and in the foundation soil at two distinct instances: (a) end of September (summer) of year 25, corresponding to end of September 2006 in reality; (b) end of March (winter) of year 25, corresponding to end of March 2007 in reality. Suctions of up to 125 kPa were calculated in the embankment clay in the summer, reducing to 25 kPa in winter. These magnitudes agreed well with field measurements plotted in Figure 7.7 and were also similar to pore pressure contours predicted by the saturated modelling approach in Figure 7.11.

However, the evolution of displacements in the mid-slope vertical section of the embankment (see Figure 7.8 for its position), predicted during the final year of the pre-vegetation removal

(Figure 7.20), showed magnitudes much closer to field measurements, compared to the same results from the saturated modelling approach (Figure 7.12). The pattern of predicted vertical displacements in Figure 7.20(a) was that of increased settlements in the summer due to ground shrinkage, mobilised by net evapotranspiration, followed by swelling during winter as a result of dominant rainfall infiltration. The predicted horizontal displacements in Figure 7.20(b) also showed swelling (movements away from embankment) in the winter period and shrinkage in the summer period. Both results were also supported by Figure 7.21 which showed vectors of ground movements purely from the summer period March to September 2006 (Figure 7.21(a)) and from the winter period September 2006 to March 2007 (Figure 7.21(b)). The former was a predominant shrinkage of the whole embankment body, while the latter was a predominant swelling. Further discussion on the comparison of results between the saturated and unsaturated analysis is given in Section 7.5.1.

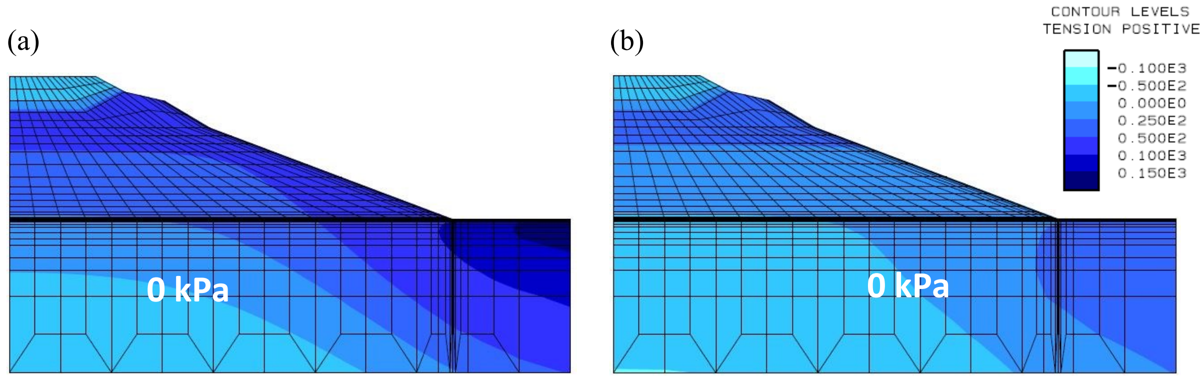

Figure 7.19: Pore water pressure contour plots during (a) end of September/summer and (b) end of March/winter of year 25. Positive indicates suction. Units in kPa.

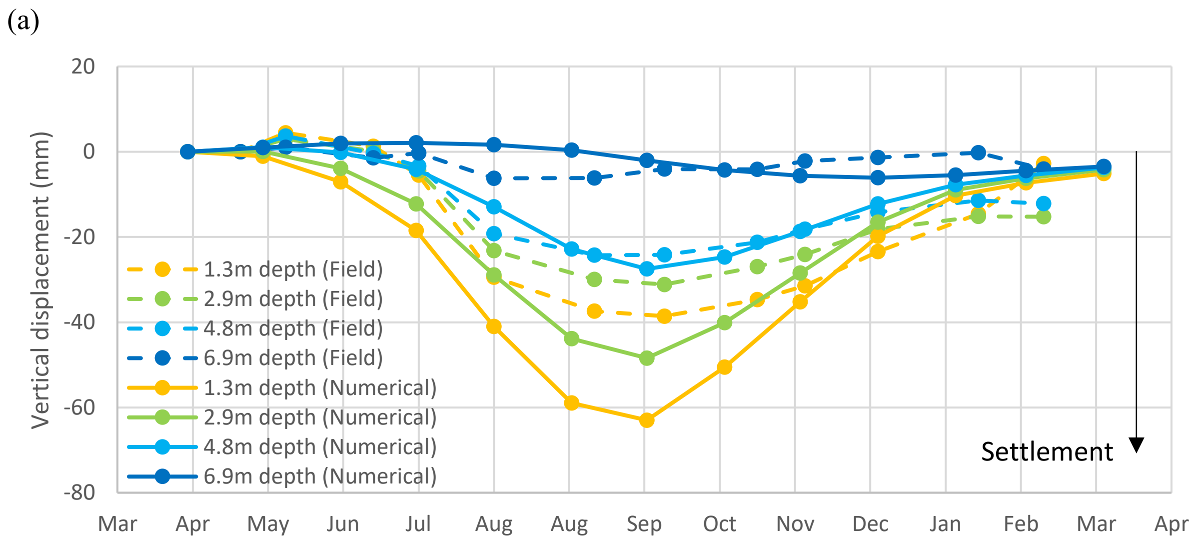

(b)

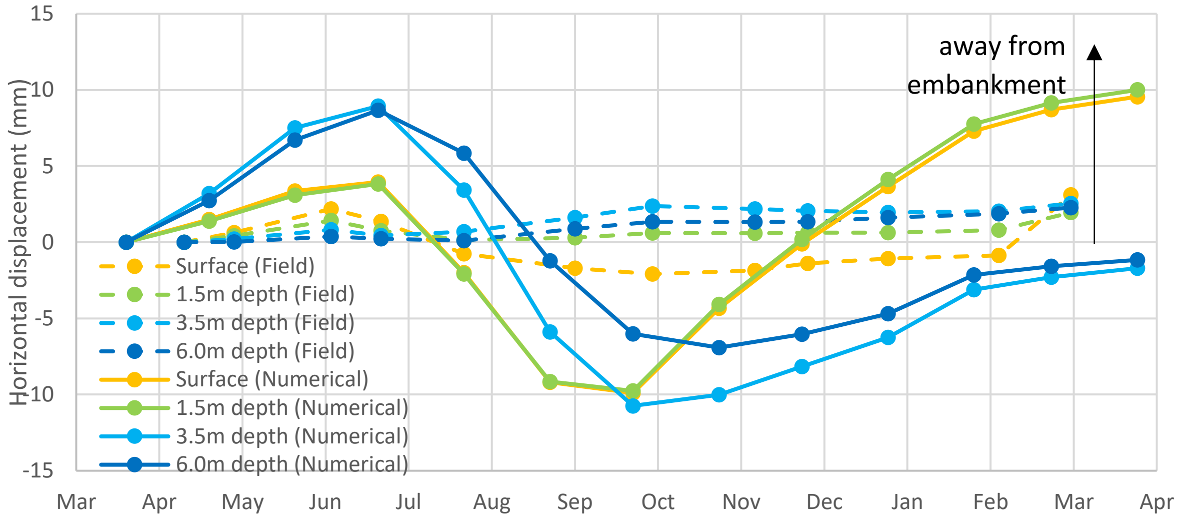

Figure 7.20: Comparison of (a) vertical and (b) horizontal displacements between unsaturated numerical analysis and field monitoring results mid-slope in the final year of pre-vegetation removal (end of March 2006 to end of March 2007).

(a) (b)

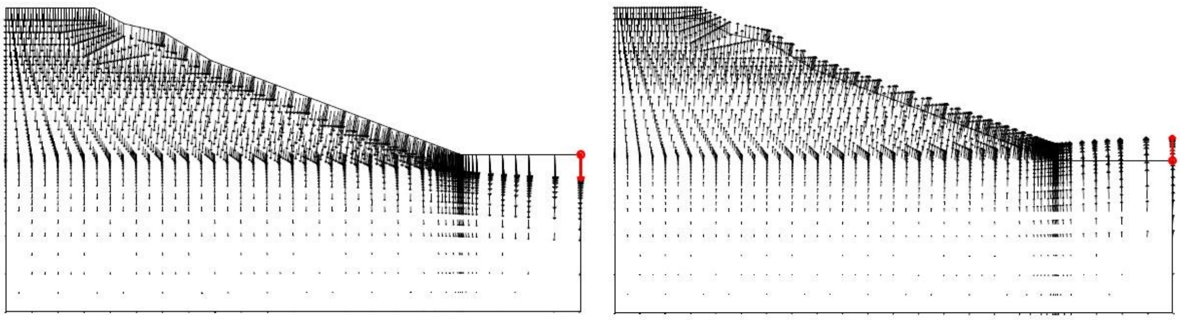

Figure 7.21: Sub-accumulated vectors of displacements for the period of (a) end of March to end of September (summer) and (b) end of September to end of March (winter).

Post vegetation removal (March 2007 – March 2011)

Immediately after vegetation removal at the end of March 2007, suctions within the embankment and foundation soil started to dissipate and the phreatic surface rose, as transpiration through tree roots was no longer active, while precipitation continued as per measured rates shown previously in Figure 5.14. Figure 7.22 is a contour plot of pore pressures 6 months and one year after vegetation removal, where it can be seen that the phreatic surface had risen into the embankment by 1m and 2m respectively and that the embankment was starting to lose its suction, reaching an average suction of 15kPa after 1 year, comparable to the suctions measured in the field after vegetation removal (plotted in Figure 7.10). Trees at the toe of the embankment still ensured that suctions near the toe remained high during the summer, with the main loss in suction occurring predominantly within the embankment body.

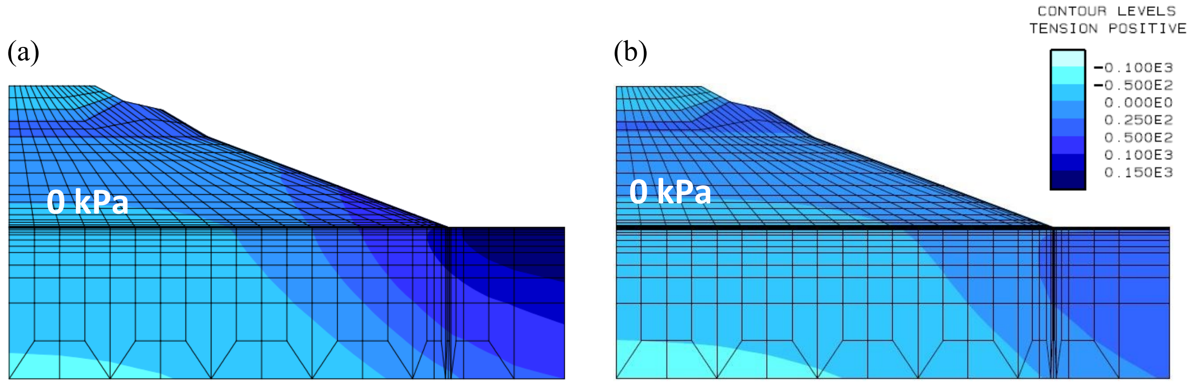

Figure 7.22: Pore water pressure contour plot (a) 6 months (September 2007) and (b) 1 year (March 2008) after vegetation removal. Positive indicates suction. Units in kPa.

The evolution of the predicted vertical and horizontal displacements in the mid-slope section over the period of 4 years post-tree removal is depicted in Figure 7.23, together with field measurements. The agreement between the two, especially the magnitudes of movements, was much more consistent, compared to the predictions from the saturated modelling approach in Figure 7.15. It was noted, however, that the unsaturated numerical model predicted larger than observed movements in the foundation soil, in both the vertical and horizontal directions. The predicted vectors of ground movements (Figure 7.24) over 1 year after trees were removed showed that swelling was similar in the clay fill and in the weathered foundation soil and that no slip surface was formed at the embankment and foundation clay interface, unlike field observations.

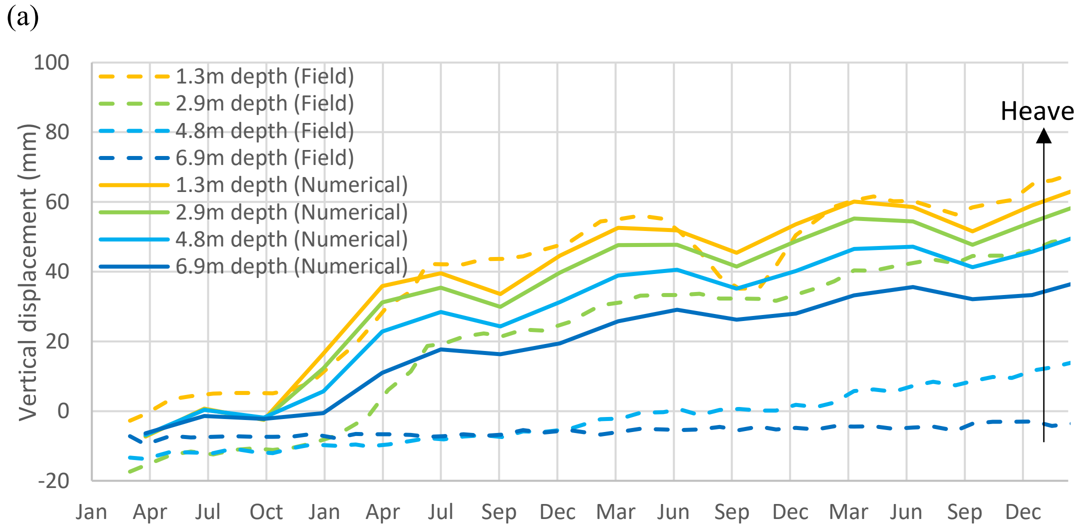

(b)

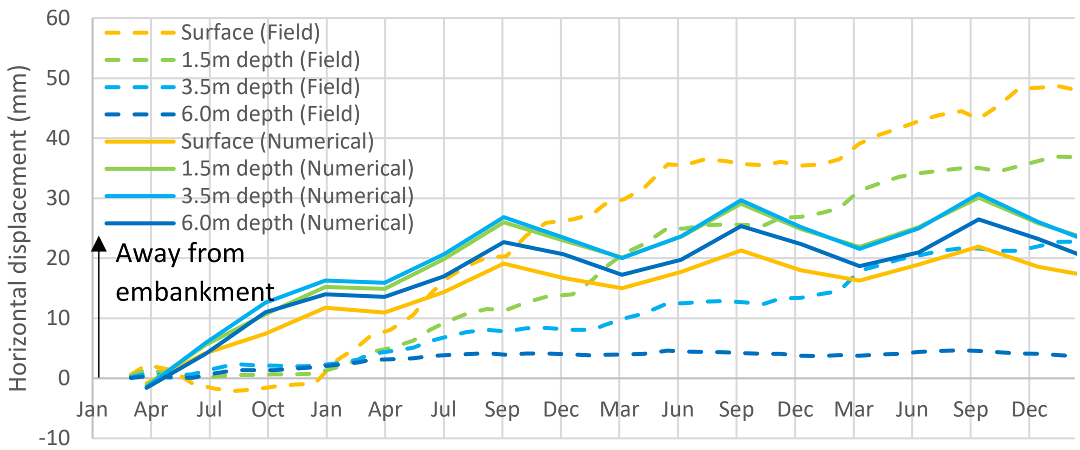

Figure 7.23: Comparison of (a) vertical and (b) horizontal displacements mid-slope, between unsaturated numerical model predictions and field measurements after vegetation removal (end of March 2007 to end of March 2011).

It was thought that the reason for this was rooted in both materials being modelled in the same manner (as unsaturated) and with the same mechanical properties, due to the lack of experimental data to distinguish between the two.

Based on the satisfactory representation of the Magnolia Road embankment using the unsaturated geotechnical modelling approach, this numerical model was extended for further predictive analyses to investigate the effects of climate change, and of the consequent changes in rainfall patterns, on the long-term stability and serviceability of this embankment.

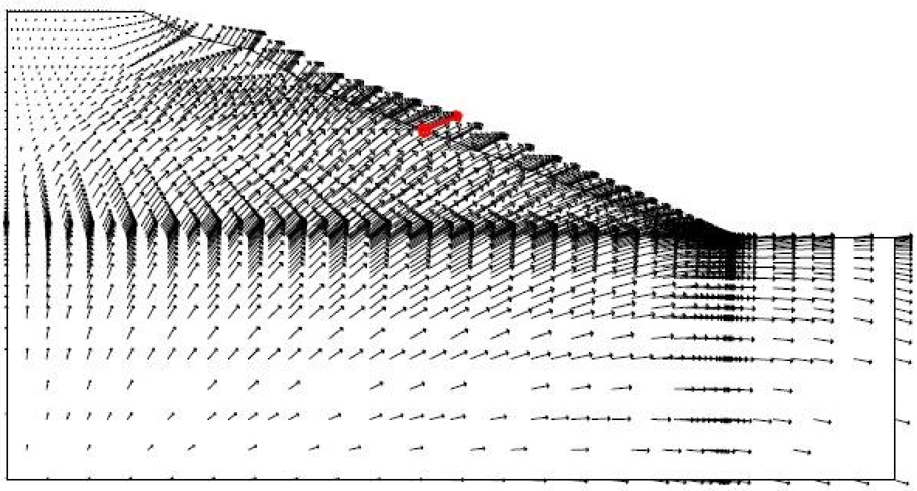

Figure 7.24: Vectors of sub-accumulated displacement over 1 year after vegetation removal (March 2008).

7.5 Projection of future atmospheric conditions

7.5.1 Representative long-term rainfall series

Past end of March 2011, the unsaturated numerical model developed in Section 7.4 was extended by continuing to apply, along the surface boundaries of the embankment and of the foundation soil, the actual rainfall recorded at the nearby Rayleigh station until the end of August 2017. From this point onwards, the subsequent rainfall input in the numerical analysis was derived from the Generalized Linear Model (GLM) in combination with 2018 UK Climate Projection (UKCP18) data, as described in Chapter 3, Section 3.3.4. Multiple simulations of future projected rainfall series were generated using the stochastic GLM model. As it would have been time consuming to perform geotechnical numerical analyses of the embankment using each of the projected rainfall series, the objective was to adopt one representative simulation as input into the numerical analysis of the embankment. To ensure that the chosen rainfall series was representative of all simulated rainfall series, the adopted simulated monthly rainfall (simulation 12) was plotted in Figure 3.7, together with all the simulated rainfall, indicating that the chosen simulation was within the 80% range of all simulations for most of the projected months. The monthly and yearly rainfall series for simulation 12, applied as a boundary condition in the geotechnical analysis, is plotted again here in Figure 7.25 for convenience.

As UKCP18 currently projects climate variables only to year 2080, the predictive geotechnical analysis of the embankment, using projected rainfall, was performed until end of March 2080. All other boundary conditions remained the same as those implemented in the final stage of geotechnical analysis, where trees were partly removed from the embankment slope.

(a)

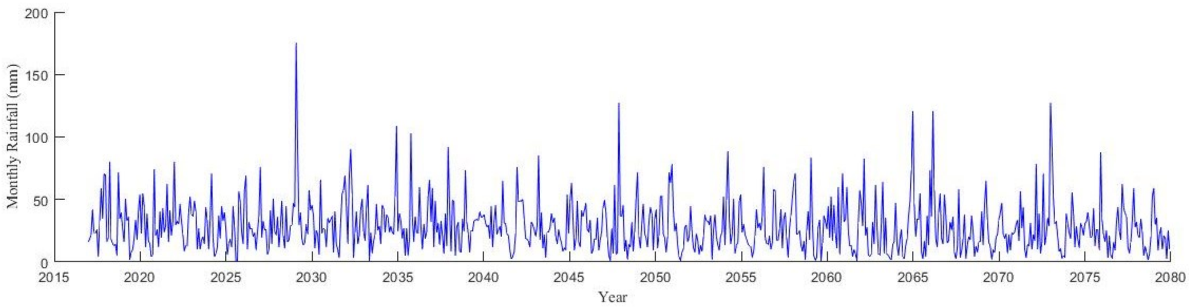

(b)

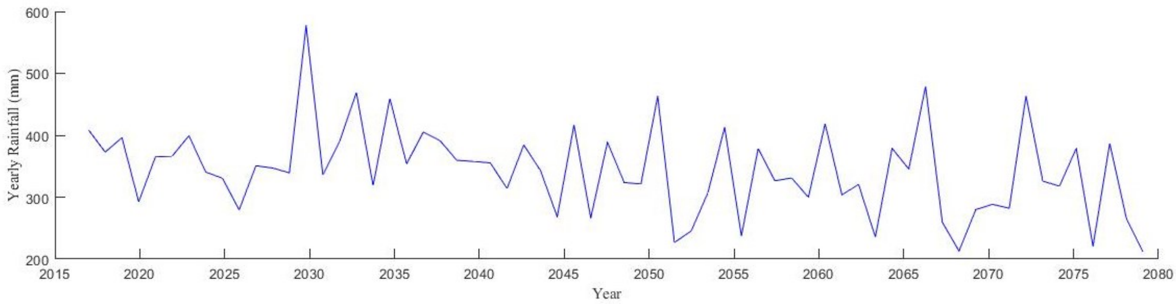

Figure 7.25: (a) Monthly, and (b) yearly rainfall of simulation 12, applied in the lifecycle assessment of the embankment.

7.5.2 Future long-term serviceability and behaviour of the embankment

As temperatures were projected to increase due to anthropogenic climate change, the Rayleigh area of Essex was projected to experience more droughts in the later decades (see Chapter 3). The overall predicted yearly rainfall in Figure 3.7(g) and Figure 7.25(b) shows a clear downward trend of reducing rainfall volume from the year 2017 to 2080, with more dry years in the future. It was therefore expected that numerical predictions would gradually result in higher suctions developing in the embankment. This was confirmed by the results in Figure 7.26, which plot the evolution of the pore water pressure profile in the mid-slope section of the embankment (see Figure 7.8 for the position of this section), across the years from 2007 to 2080 and at two specific times of each year: March, as end of winter, and September, as end of summer. The colours represent successive decades over the modelling period.

The embankment clay fill was predicted to develop a maximum suction of up to 75kPa during the summer, while this was only about 10kPa in 2007, immediately after vegetation removal. In addition, in the 2070-2080 decade, the suctions generated during the summer were not completely dissipated in the foundation soil during the winter. As the clay fill had a higher permeability compared to the foundation soil, it was unable to maintain the summer suctions during winter and behaved hydrostatically instead.

Figure 7.27 plots the evolution of the horizontal displacement profile at the same mid-slope section of the embankment, in a similar manner to the plots in Figure 7.26. The predictions indicated that a slip surface would be forming along the ash – clay fill interface, and a another at the clay fill – foundation soil interface. These slips were initiated in the current decade (2010-2019), as observed on site for the latter interface. They were predicted to progressively develop over the next decade (2020-2029), while the horizontal movements over the subsequent decades were predicted to increase at a much smaller rates, due to the predicted droughts in the long term.

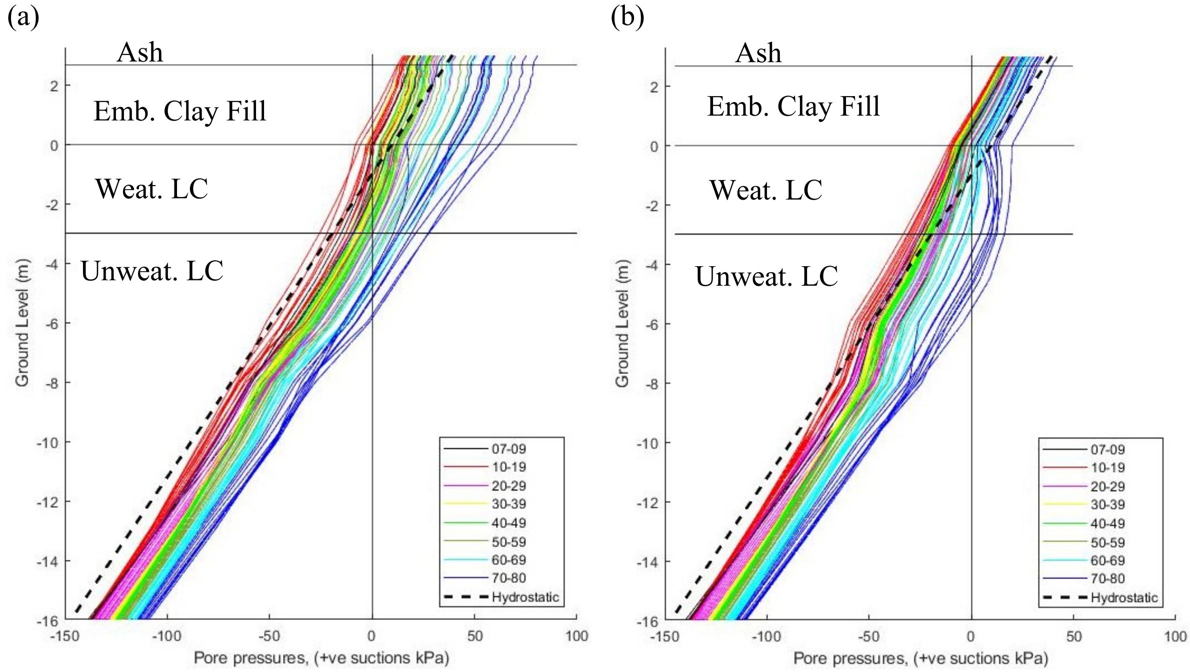

Figure 7.26: Pore water pressure profiles mid-slope of the embankment during (a) end of summer, and (b) end of winter, from 2007 to 2080.

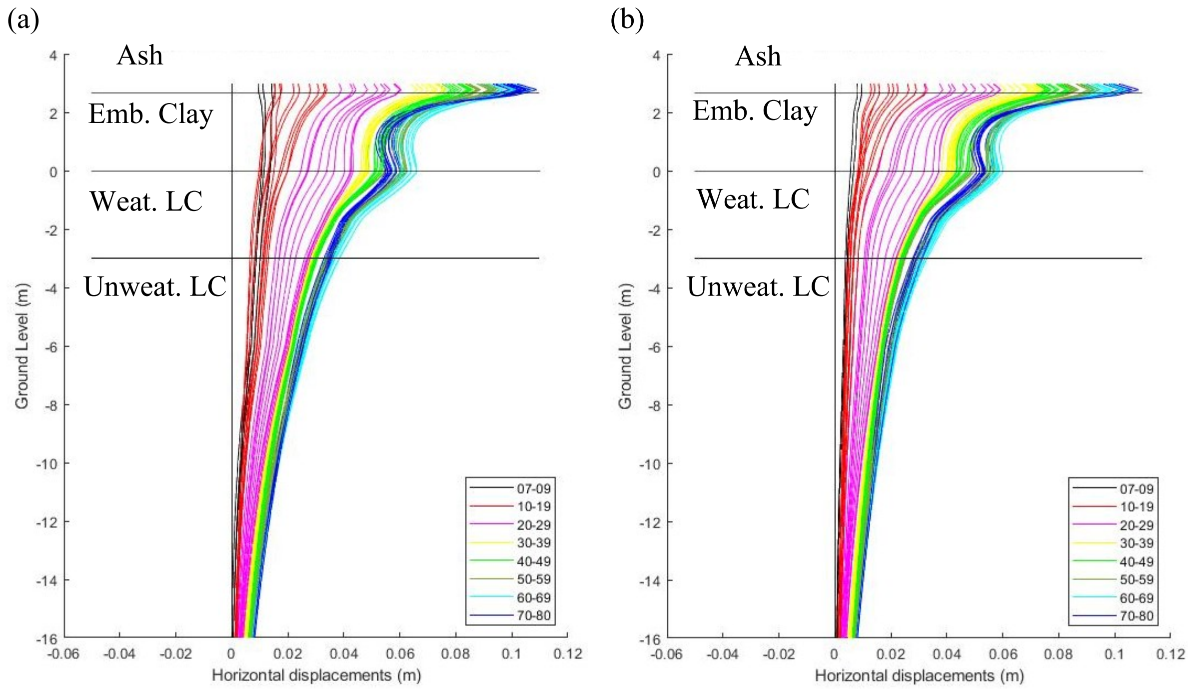

Figure 7.27: Horizontal displacement profiles mid-slope of the embankment during (a) end of summer, and (b) end of winter, from 2007 to 2080.

Figure 7.28 plots the predicted temporal evolution of vertical and horizontal displacements at various elevations in the mid-slope section of the embankment at every 3-monthly intervals, with the surface of the slope at 2.96m above ground level. The development of the ash – clay fill slip surface was much more apparent here from the temporal development of horizontal displacements in Figure 7.28(b), with the growing gap between the elevations of 2.2m (orange) and 1.25m (gold) from the ground surface that originated from year 2014 onwards. The gap grew considerably from 2030 onwards and once again in 2036. Interrogating the applied projected monthly rainfall in those particular time instances (Figure 7.28 (c), based on rainfall data plotted in Figure 7.25(a)), it was clear that the slip surface would deteriorate when there would have been a particularly heavy rainfall in those months, preceded by a period of low rainfall.

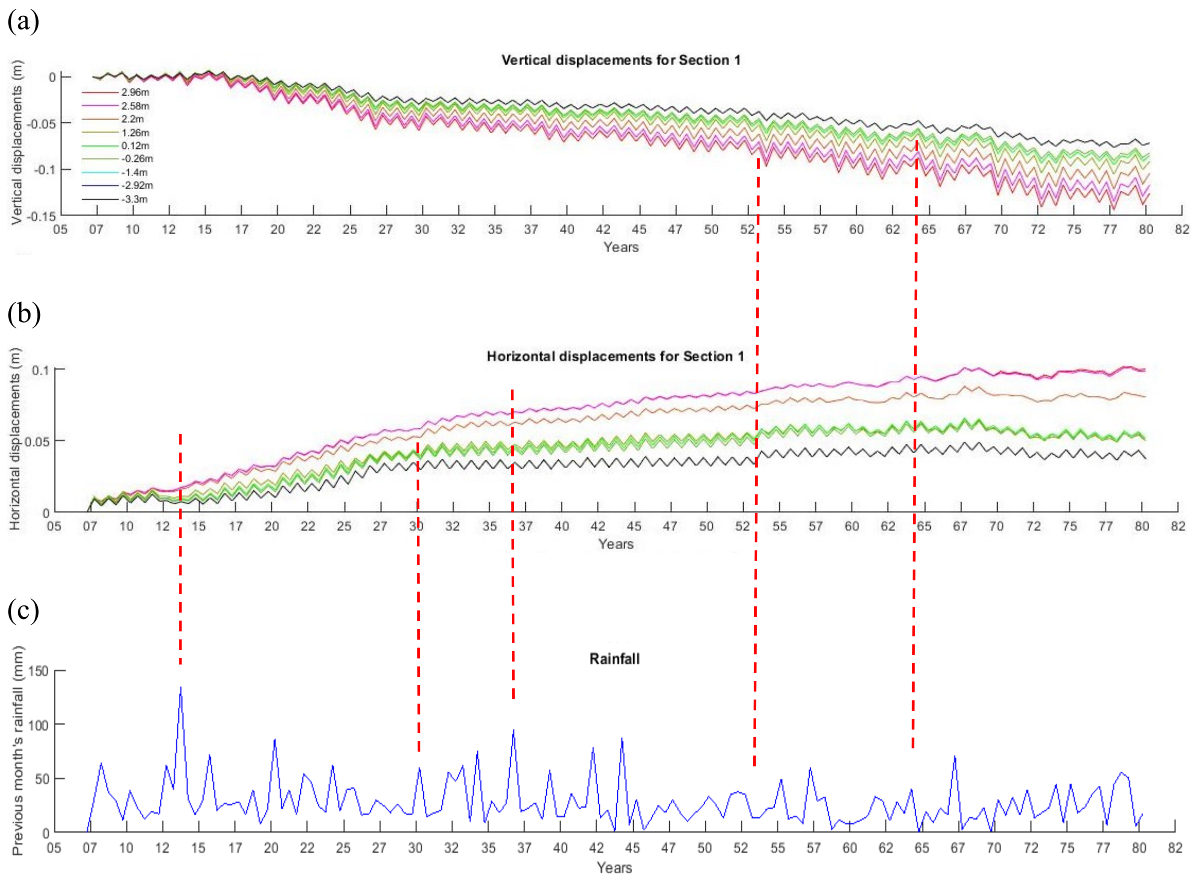

Figure 7.28: Time series of (a) vertical and (b) horizontal displacements mid-slope. The month's rain for each of those data points are plotted in (c).

In addition, a second slip surface, between the embankment clay fill and the foundation soil, as indicated in Figure 7.27, is also shown to form in Figure 7.28 between elevations 0.12m (light green) and -1.4m (light blue, plotted over by black), at the same time as the formation of the ash-clay slip surface but at a smaller relative horizontal displacements.

The vertical displacements, on the other hand, in Figure 7.28(a) showed a steady settlement of the embankments mid-slope, 130mm in total by 2080 in the ash layer (pink) and 50mm in total in the unweathered London clay layer (black). The vertical settlements were a consequence of periods of intense droughts, such as seen in the years 2053 and 2064.

The settlement of the embankment crest was also predicted to increase by up to 180mm by 2080, uniformly across the crest (Figure 7.29(a)) with little differential vertical displacement. This indicated that remedial works would be necessary to maintain the elevation of the track and the service of the railway in the future. The predicted horizontal displacements of the crest (Figure 7.29(b)) were relatively small in comparison to the large horizontal displacements developed at the slip surfaces mid-slope of the embankment, but indicated up to 10 millimetres of lateral spreading in the future between the edge of the crest and the centre of the embankment.

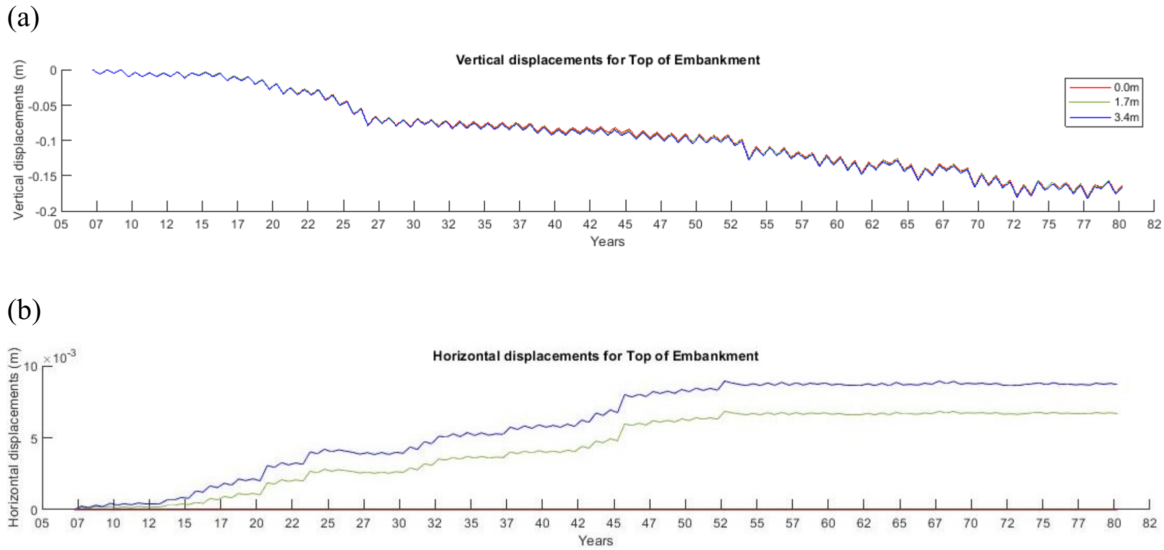

Figure 7.29: Time series of (a) vertical and (b) horizontal displacements along the embankment crest. 0m is at the centre of the embankment, while 3.4m is at the edge of the crest.

7.6 Embankment resilience to storms

7.6.1 Storm events and factors of safety

Due to the computational costs associated with an unsaturated coupled-consolidation analysis and with the long temporal scale of 100 years for a lifecycle analysis, a monthly time resolution was adopted for the rainfall input to perform a lifecycle analysis of the embankment, as outlined in previous sections. The objective was to first establish the general future long-term trends and behaviour of the embankment when subjected to a projected future climate.

As the monthly time resolution is generally too coarse for investigating the effect of individual extreme storm events on the embankment, which could be much shorter in duration, a daily temporal resolution was used in the next step of this study to simulate extreme storm events acting on the embankment. As such, secondary finite element analyses were performed at four critical points in the embankment's lifecycle analysis to assess the resilience of the embankment to extreme storm events at those points.

The four critical moments represented the most extreme antecedent conditions that the embankment would have experienced throughout its lifecycle, namely the driest and wettest winter and summer. Based on pore pressure profiles similar to those plotted in Figure 7.25, it was found that January and August 2014 were the wettest winter and summer respectively, while March and September 2069 were the driest winter and summer.

It was shown in Chapter 4 that the convective storm in August 2014 (95mm) and a winter storm in December 2014 (94mm) were the largest daily rainfall records experienced near the site at Rayleigh. In addition, it was also demonstrated in Chapter 4 that future projected storm events using the GLM and BLRP downscaling stochastic models were about similar to the storms recorded in August and December 2014 events (Figure 4.8(d)). For the purpose of this study a daily maximum value of the measured 95mm was adopted as a storm scenario.

To model the storm in the secondary finite element analyses, six different storm profiles were created, similar to the methodology used in Pirone (2009), aimed at investigating the effect of the antecedent rainfall on embankment's stability. The storm profiles are shown in Table 7.7, where the first five profiles totalled 95mm of rainfall, while the sixth profile totalled 190mm of rainfall over 7 days, split into two separate storms of 95mm each. In total 24 secondary finite element analyses were performed, 6 for each of the four time instances defined above. This means that each secondary analysis started after the appropriate time was reached in the main analysis (i.e. January 2014, August 2014, March 2069 and September 2069) and was conducted over the time period defined in Table 7.7.

The embankment resilience was assessed by calculating the factor of safety (FoS) against failure of the embankment slope before and after the storm, unless the embankment failed as a consequence of the storm. To obtain the FoS at these stages, tertiary finite element analyses were initiated at the appropriate increments of the secondary finite element analyses, but with consolidation switched off which meant that pore water pressures during the FoS analysis were maintained equal to those generated at the final stage of the coupled analysis.

The strength reduction technique developed in ICFEP by Potts and Zdravkovic (2012) and extended to the modelling of unsaturated soils in Tsiampousi et al. (2013b) and Zdravkovic et al. (2014), was used for the calculation of the FoS. In general, the angle of shearing resistance of the soil is gradually reduced by incrementally increasing the material strength factor, F_S:

$$\tan \varphi^{F_S} = \frac{\tan \varphi'}{F_S} \tag{7.8}$$

F_S is increased from 1 until failure is achieved. Failure is defined by a combination of non-convergence in the subsequent analysis increment and development of a full failure mechanism in the embankment, observed by plotting vectors of incremental displacements.

Table 7.7: Extreme storm profiles implemented to assess embankment resilience

	Day (Rainfall in mm/day)						
Runs	1	2	3	4	5	6	7
R1	95	-	-	-	-	-	-
R2	60	35	-	-	-	-	-
R3	30	30	35	-	-	-	-
R4	15	15	15	15	35	-	-
R5	15	15	15	15	15	15	5
R6	60	35	-	-	-	60	35

Table 7.8 tabulates the FoS before and after each storm simulation for all combinations of each antecedent condition and storm profile. It was apparent that when the embankment was in its wettest states, it was unable to take in any additional infiltration of rainwater, which instead ran off (enabled by the employed precipitation boundary condition) as shown with pore water pressure contours in Figure 7.30 with the August 2014 initial state. Thus the FoS throughout each storm scenario remained fairly constant, at around the initial FoS of 1.6. In the R1, R2, R3 and R4 scenarios, there is a short period of several days of no rain after the storm event, allowing some degree of evapotranspiration to occur around the embankment toe, resulting in a slight increase in FoS from 1.6 (Figure 7.30 (b) and (c)).

Figure 7.31 plots the failure mechanisms for the August 2014 initial state and R1 scenario, taken as the incremental displacement vectors at the point of failure for the FoS analyses of those scenarios. As there was little difference in pore pressures within the embankment, the failure mechanisms did not differ by much before and after the R1 storm scenario. This failure mechanism was also similar for the other storm scenarios for the August 2014 antecedent condition.

Table 7.8: Factor of Safety before and after each storm for each antecedent condition.

	Aug-14	Jan-14	Sep-69	Mar-69
	Wettest summer	Wettest winter	Driest summer	Driest winter
Initial	1.60	1.64	2.12	1.68
R1	1.64	1.60	1.82	1.50
R2	1.68	1.66	1.74	1.46
R3	1.68	1.64	1.66	1.38
R4	1.64	1.62	1.66	1.52
R5	1.60	1.64	1.60	1.54
R6	1.58	1.62	-	1.36

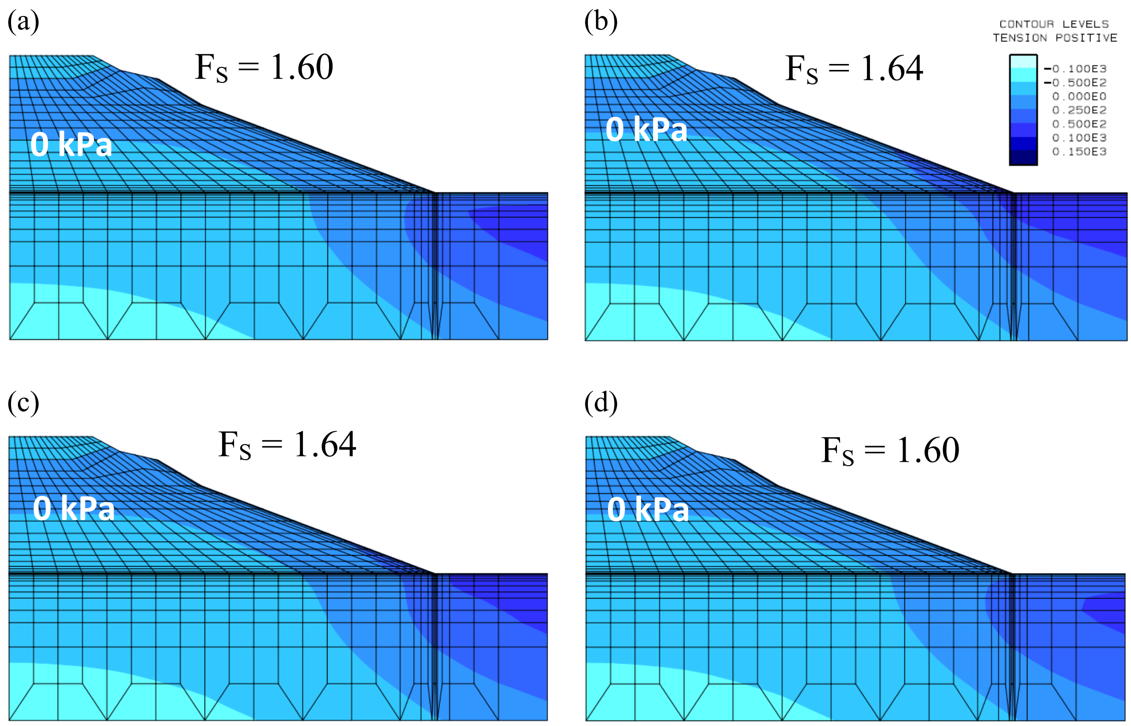

Figure 7.30: Pore water pressure contour plots for August 2014 (a) initial before storm, (b) after the R1 storm event, (c) after the R4 storm event, and (d) after the R5 storm event. Positive indicates suction, units are in kPa.

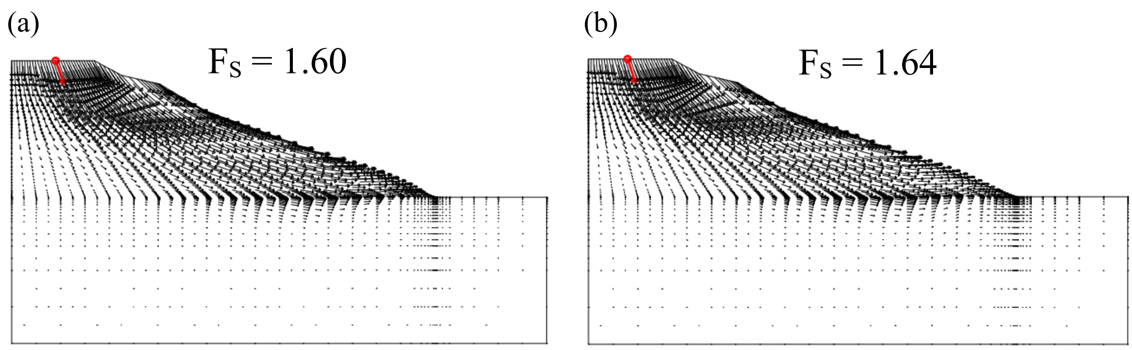

Figure 7.31: Incremental displacement vector plots for August 2014 Factor of Safety analyses (a) initial before storm, and (b) after the R1 storm event.

However, when the embankment was at its driest, the FoS could decrease considerably (Table 7.8) as suction dissipated after a storm event, thus reducing the stability of the embankment. For the driest summer scenario (Sep-69, $F_s = 2.12$), shorter and more intense storm durations such as R1 and R2 did not affect the embankment stability too much, as a proportion of the rain was a runoff instead of infiltration deeper into the embankment. Hence, the drop in FoS was small (see Table 7.8 and Figure 7.32(b)). If the storm was more prolonged, however, there was more time for the rain to infiltrate deeper into the embankment and saturate it. The drop in FoS was therefore more significant, reaching the saturated FoS of 1.6 (Table 7.8 and Figure 7.32(c) and (d)). Due to the high suction remaining in the foundation soil even after the storm events, the predicted slip surfaces for the September 2069 cases plotted in Figure 7.33 were deeper than the saturated cases in Figure 7.31. The R6 analysis had difficulties converging when the second storm hit on day 6 and was an example of the embankment failing during the storm.

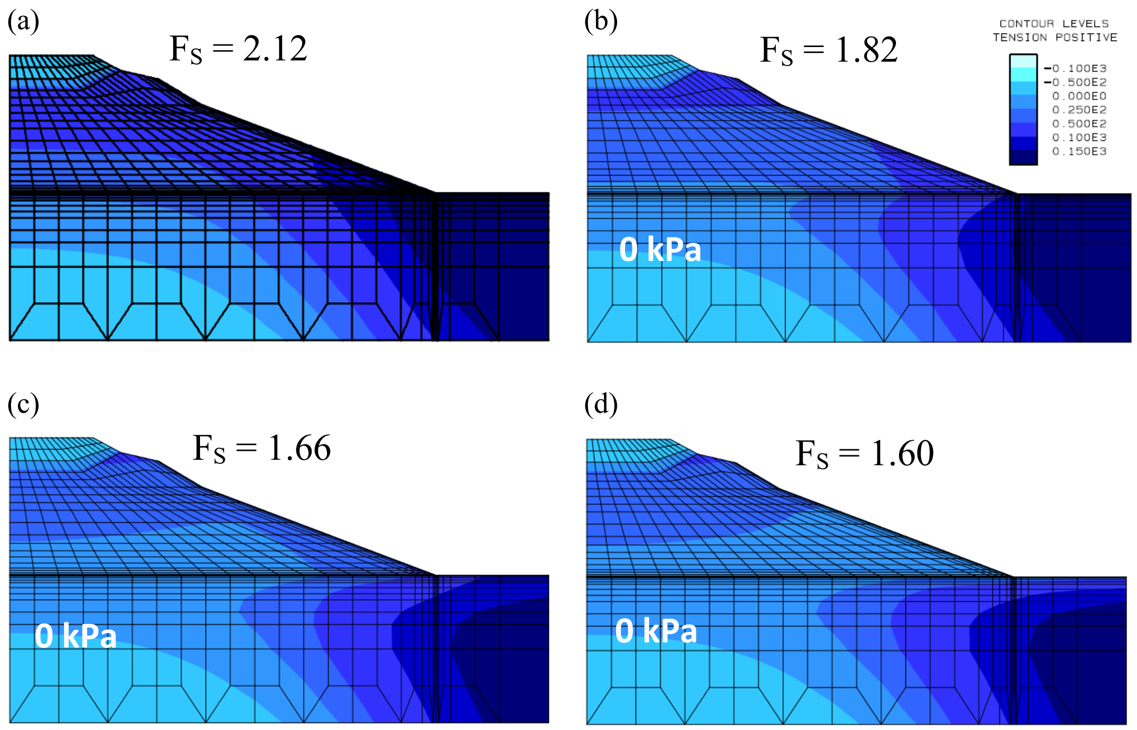

Figure 7.32: Pore water pressure contour plots for September 2069 (a) initial before storm, (b) after the R1 storm event, (c) after the R4 storm event, and (d) after the R5 storm event. Positive indicates suction, units are in kPa.

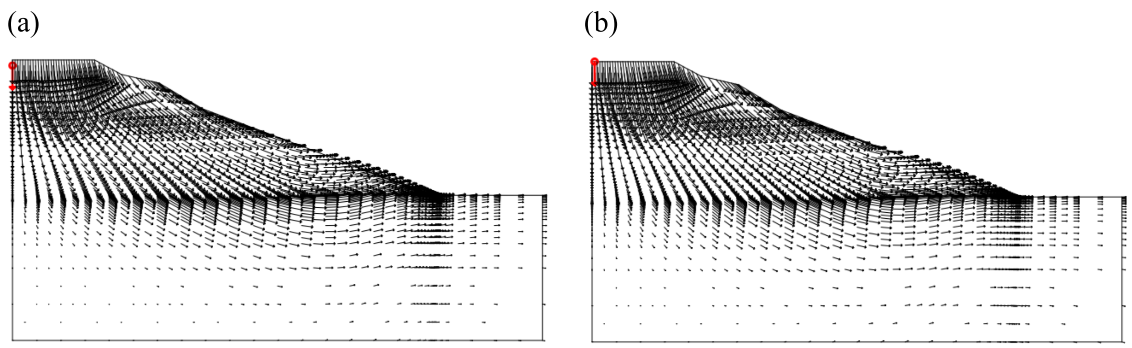

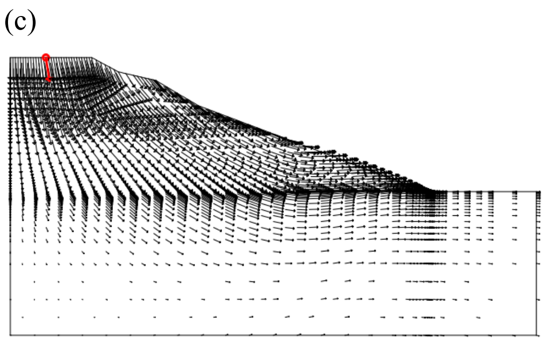

Figure 7.33: Incremental displacement vector plots for September 2069 Factor of Safety analyses (a) initial before storm, (b) after the R1 storm event, (c) after the R4 storm event, and (d) after the R5 storm event.

The most interesting result was from the driest winter (Mar-69) case, where the FoS reduced below the saturated FoS of 1.6 for all storm scenarios (Table 7.8), with the most severe scenario being the R3 and R6 storm profiles. By comparing the pore water pressure contour plots before and after the R3 storm, see Figure 7.34, it was apparent that though suctions of up to 100kPa were still present in the foundation soil, nearly all suction in the embankment had dissipated.

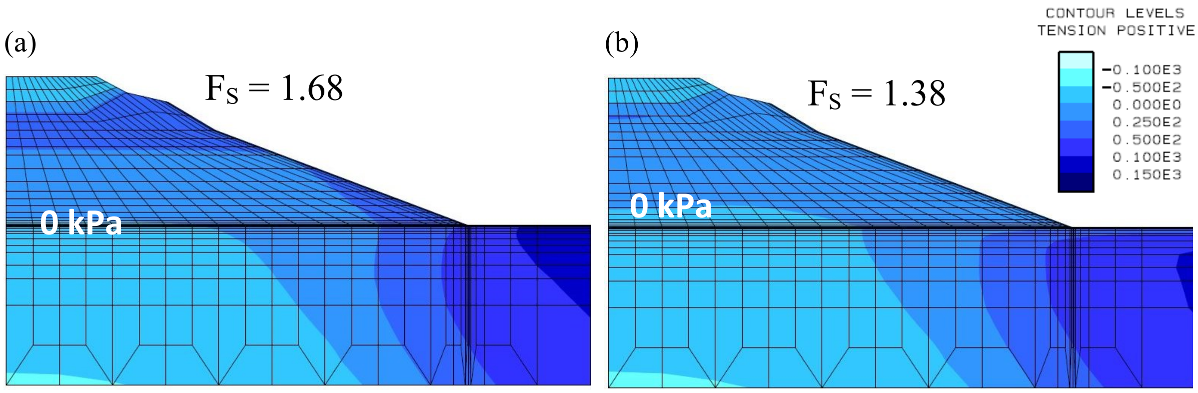

Figure 7.34: Pore water pressure contour plots for March 2069 (a) initial before storm and (b) after the R3 scenario. Positive indicates suction, units are in kPa.

The sudden loss of suctions at these critical areas of the embankment while the foundation soil maintained its suctions may explain the lower than saturated FoS. Figure 7.35 plots the final incremental vectors of displacement of the initial and R3 FoS analysis for March 2069. It is clear from Figure 7.35(b) that two slip surfaces were forming after the R3 storm event: a shallow slip surface close to the surface of the embankment slope, and a deeper slip surface starting from mid-crest before turning at the base of the embankment and following the embankment-foundation boundary to the embankment toe. The loss of suctions on the surface of the embankment facilitated the formation of the first slip surface, while the loss of suction in the ash helped facilitate the formation of the deeper slip surface. This is in contrast to the initial failure mechanism (Figure 7.35 (a)), where the slip surface was more global in nature, encircling nearly the entire embankment, and engaging deeper foundation soil.

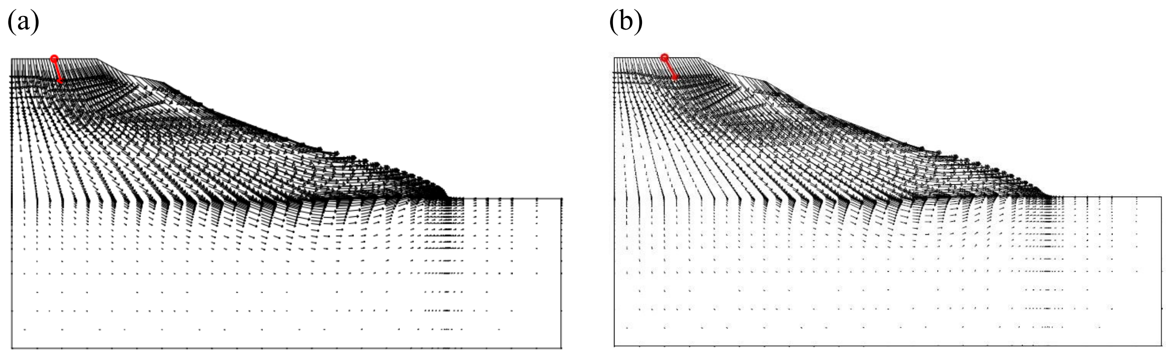

Figure 7.35: Vectors of incremental displacement for the FoS analysis for March 2069 (a) initial before the storm events, and (b) after the R3 scenario.

7.7 General Discussion

7.7.1 Saturated vs unsaturated analyses

Both the saturated and unsaturated analyses were able to model the seasonal behaviour of the embankment, as presented in Section 7.3 and Section 7.4. During the summer, shrinkage of the embankment occurred as water was removed from the soil due to high evapotranspiration rates, while the embankment heaved during the winter as rainfall infiltration exceeded evapotranspiration and suctions within the embankment dissipated.

However, it was clear that the saturated analysis highly overestimated the seasonal displacement changes as compared to the observed field displacements and to the unsaturated analyses results. One reason for this divergence is that a saturated analysis assumes the voids in the soil to be filled with water. Therefore, when water was removed from the soil via the modelled evapotranspiration, this contributed large volumetric strains in the model, giving rise to large displacements in the seasonal wetting – drying cycles. Additionally, the bulk modulus, as represented by the ICG3SM, was assumed to continuously degrade with increasing volumetric strains, until reaching a prescribed minimum value. Hence, a low bulk modulus would also contribute to larger volumetric strains.

Employing an unsaturated modelling framework, which assumes both air and water in the pore space, contributed to a more realistic representation of embankment's response. Air entry into the soil was taken into account and the hydraulic behaviour of the embankment clay and weathered foundation soil was controlled by the Soil Water Retention Model, leading to smaller volumetric changes during the summer as the soil dried out.

7.7.2 Lifecycle analysis methodology

Due to the time scales of a typical embankment's lifecycle (more than 50 year), it is important to choose an adequate temporal resolution for rainfall application, in order to ensure a reasonable balance between accurate representation of atmospheric variation in the numerical model and the associated computational cost (in this case measured by the analysis run-time). Choosing a fine temporal resolution, such as daily, would allow a more accurate implementation of rainfall profiles, but the analysis run-time would be much longer. On the other hand, adopting a yearly temporal resolution would be computationally faster, but it is too coarse to capture seasonal variations in atmospheric conditions and their impact on embankment behaviour.

By performing soil-atmosphere interaction column analysis on the ground profile of this study, it was found that adopting a monthly temporal resolution for the main lifecycle analysis would result in a good balance between numerical stability, accuracy and computational run-time. With a month modelled as 12 equal increments, the soil-atmosphere interaction aspect of the numerical model was sufficiently accurate and stable, as shown in both the saturated and unsaturated analyses of the Magnolia Road embankment, with reasonable computational run-times. This main lifecycle analysis then serves as the foundation to assess embankment resilience at various points throughout the embankment's lifecycle, by adopting a more appropriate finer temporal resolutions in secondary analyses, such as daily or hourly, depending on the storm profiles at the site. The secondary analyses are of much shorter duration as they simulate a few days rather than several decades.

Similar column analyses on the same ground conditions, performed by Lee (2019), showed in Figure 7.36 that by applying actual monthly rainfall obtained from aggregating daily rainfall, instead of the monthly averaged rainfall over 10 years (blue) or 5 years (orange), the numerical model was able to more accurately capture the consequences of natural larger scale weather variations throughout a year (e.g. pore water pressure), such as periods of droughts or heavy rain, which the monthly averaged rainfall is unable to provide. This allows for a fast and accurate approach to simulate antecedent conditions and their influence on the embankment, from which simulations of extreme events can then be performed after the antecedent conditions to assess embankment resilience.

(a)

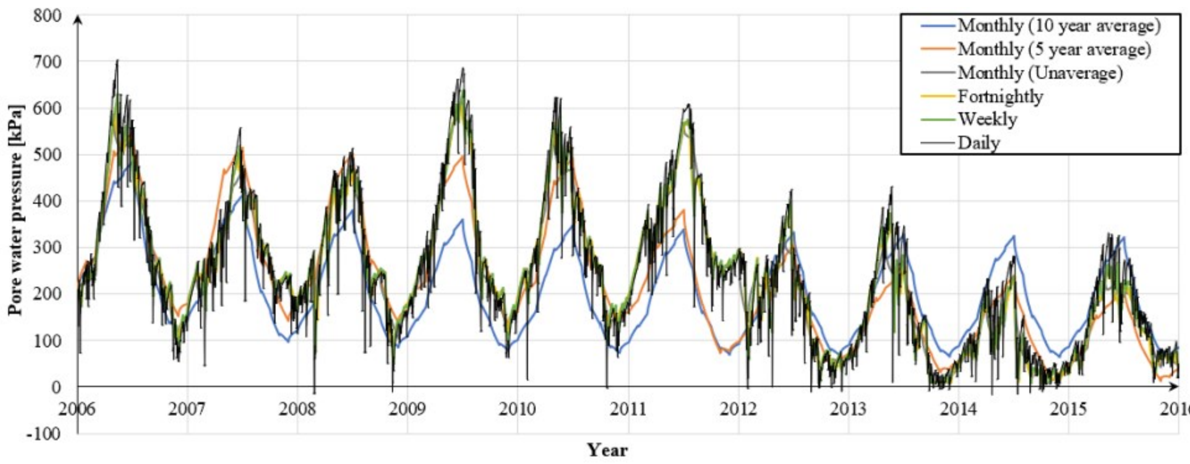

(b)

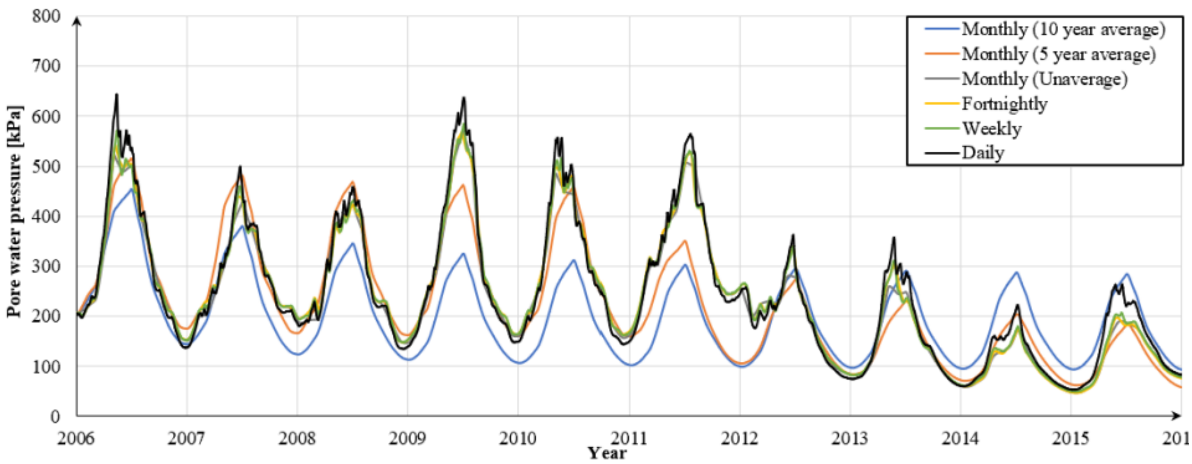

Figure 7.36: Column analysis comparing the effects of various time resolutions of implemented precipitation on the pore pressure evolution on (a) the surface and (b) 3m below ground (Lee, 2019).

7.7.3 Unsaturated soil properties and SWRC

As briefly mentioned in Section 7.4.2, the original calibration of the SWR model, to Melgarejo-Corredor (2004) experimental SWRC for a compacted clay sampled from an embankment, resulted in the model simulating a highly saturated embankment clay fill throughout the year.

A possible reason for the poor performance of the original SWRmodel could be attributed to the double porosity nature of clay fills, where due to the deposition of clay fills as clods or lumps, there is a significant difference in porosity within a clay lump (intra-lump), and the overall matrix of lumps (Hartlen and Ingers, 1981; O'Brien et al., 2004; Robinson et al, 2005). Laboratory drying tests performed on individual clay samples would only be measuring the intra-lump SWRC and not the inter-lump behaviour which is more representative of the soil mass behaviour in soil-atmosphere interaction boundary value problems. However, as the embankment was more than 100 years old, it was questionable whether any clay lumps would have been remoulded into a more homogeneous material via consolidation.

It is also possible for vegetation and roots to directly alter the SWRC of the soil by introducing additional voids into an otherwise homogeneous medium (Ng et al., 2016; Veylon et al., 2015). Veylon et al. (2015) further mentions that if the root system is dense, a cohesive soil can undergo fragmentation and aggregation, forming macro-pores in the soil that increases permeability and reduces the soil's ability to form high matric suction. Experiments by Ni et al. (2018) on sandy decomposed granitic soils showed that vegetation actively lowers the SWRC of a soil. As trees were noted on the embankment slope, it is likely that the embankment clay would have been additionally fragmented into lumps, thus modifying the SWRC of the clay mass to be more granular as compared to the clay's intrinsic SWRC.

7.8 Summary

This chapter explored the Magnolia Road rail embankment case study to develop a numerical modelling approach for infrastructure embankments and a procedure for their lifecycle analysis and assessment under changing climatic conditions.

The work demonstrated that, due to the initially unsaturated state of earthfill embankments, the finite element modelling approach of such embankments should adopt an unsaturated formulation of the governing equations and of constitutive models. The adequacy of such an approach was verified on the Magnolia Road study. Otherwise, it was shown that much larger than measured shrinkage and swelling volumetric deformations during seasonal rainfall and evapotranspiration cycles would be predicted when a fully saturated modelling approach was adopted.

Additionally, a procedure was established for the lifecycle assessment analysis of the stability and serviceability of earth embankments under the changing climate, utilising the rainfall projection methodology developed in Chapter 4. It was shown that the monthly temporal resolution of rainfall application in the numerical model was sufficiently robust for accurate reproduction of deformation patterns in the embankment's lifecycle (over several decades). On the other hand, the effects of specific storm / drought events predicted in the lifecycle analysis, require a finer temporal resolution of rainfall (daily or sub-daily). It was demonstrated that such effects can be derived by secondary numerical analyses from the main lifecycle analysis.

The risk to failure of the Magnolia Road embankment due to changing rainfall patterns was assessed by tertiary finite element analyses that calculated a factor of safety remaining in the embankment slope after application of an extreme storm event (unless the embankment failed during the storm). These analyses demonstrated a significant reduction in the factor of safety if the storm event happened during the driest periods in the embankment lifecycle, but factor of safety did not change significantly if the storm acted during the wettest periods.

The validated unsaturated numerical model of an infrastructure embankment developed in this chapter will be used for the modelling of a flood embankment study in Chapter 8.

Chapter 8: Lifecycle Assessment of a Flood Embankment

8.1 Introduction

This chapter explores the numerical modelling of the lifecycle assessment of a typical flood embankment in the Thames estuary. While the flood embankment modelled in this chapter was not based on a particular case study, as were embankments in Chapters 6 and 7, its construction was loosely based on flood embankments constructed and raised in Dartford, Kent (Marsland, 1973). The adopted embankment geometry followed the recommendations outlined by the Environment Agency (2007) for England and Wales. The fill material was compacted London clay, the same material of the embankment fill in the Magnolia Road case study in Chapter 7. The adopted foundation soil was the same soft clay characterised in Chapter 6 in the case study of a Dartford trial embankment.

A lifecycle analysis involved the embankment construction, followed by the application of cycles of tides and soil-atmosphere boundary conditions of historic, present, and future rainfall (up to year 2080). The modelling of rainfall as a boundary condition was similar to that applied in Chapter 7 and derived for the Rayleigh area of Essex in Chapter 3, while the modelling of tides in monthly increments was assessed in a separate study. The embankment was then assessed for its resilience to overtopping at critical moments of its lifecycle.

Finally, various raising strategies of the embankment were explored, to ensure optimum measures for future-proofing of flood embankments in the light of increasing sea water levels due to climate change, stronger storm surges and potential developments of any additional tidal barriers upstream.

8.2 Base analysis of a flood embankment

8.2.1 Embankment geometry

The flood embankment geometry followed the recommended design geometries outlined by the Environment Agency (2007) for England and Wales and was also similar to those outlined by the US Army Corps of Engineers (USACE, 2008). According to this, it is advisable that both river side and landward side slopes have 1 vertical to 3 horizontal (1V:3H) gradient, with a minimum crest width of 4m. The landward side berm width must also be a minimum of 4m.

A general overview of the adopted flood embankment geometry is presented in Figure 8.1 (a), with the finite element mesh presented in Figures 8.1 (b) and (c). Similar to the trial embankment analysis in Chapter 6, the ground level was set to +3.2mODN. The green component of the embankment in Figure 8.1 comprised the first stage embankment construction over a period of 1 year, with a berm height of 2.5m (+5.7mODN) and an embankment height of 3.1m (+6.3mODN). The embankment base width was 36.4m, with a berm width of 4.2m. This height represented an average flood embankment height at Dartford before 1953. The crest width varied with embankment height, with a minimum width of 4m when the embankment was 5.6m high (+7.8mODN). Both landward and river side slopes had a 1V:3H gradient, in accordance with Environment Agency (2007) design recommendations.

(a)

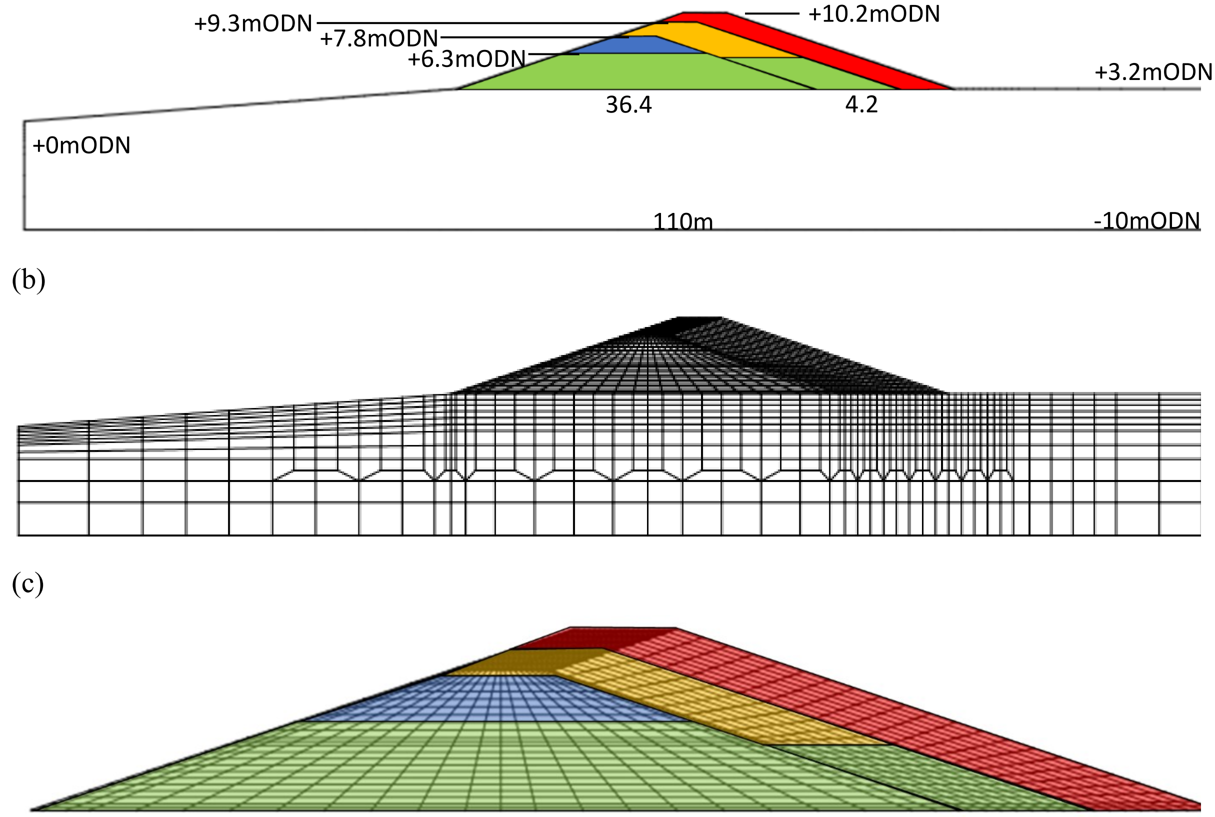

Figure 8.1: (a) Problem geometry of the Thames embankment; (b) Finite element mesh of the embankment and foundation; (c) Finite element mesh of the embankment only, showing the construction stages. (All dimensions are in metres).

The blue component of the embankment in Figure 8.1 represents stage 2 of the embankment construction, where the embankment was raised by a further 1.5m, to an elevation of +7.8mODN, 5 years after stage 1 construction. This was the final embankment height (4.6m) in 1953.

Provisions for further embankment raising were incorporated into the mesh, represented by the yellow and red components of the embankment cross-section, allowing for a maximum embankment height of 6.1m (+9.3mODN) and 7m (+10.2mODN), respectively. The embankment raising strategy revolved around the utilisation of the berm and raising the embankment gradually towards the landward side with minimal increase of the embankment base width to minimise additional land use. These provisions were used when assessing raising strategies for the future. It was expected that the embankment would fail before reaching the maximum height of 7m.

On the riverward side, the ground surface gradually decreased by 3m from +3.2mODN to 0mODN over a distance of 40m, creating a gentle gradient.

8.2.2 Soil properties

Foundation soil

In Chapter 6, a trial flood embankment at Dartford in the Thames estuary was numerically modelled. An extended modified Cam-Clay model was calibrated based on field measurements and laboratory tests of the soft estuarine clay at the site, which was then used to model the foundation soil of the trial flood embankment. Table 6.2 summarised the MCC model parameters from the calibration outlined in Section 6.3, while the undrained shear strength Su, K_0, and OCR initial profiles were plotted in Figure 6.16.

The shear stiffness of the foundation soil was modelled using the Imperial College Generalised Small Strain Stiffness model (ICG3S; Taborda and Zdravkovic, 2012). As outlined in Chapter 6, the small strain stiffness characterisation of the Bothkennar clay was adopted as there were no small strain stiffness measurements available for the soft clay at the site. The calibrated shear stiffness for the foundation soil was plotted in Figure 6.17, with its parameters summarised in Table 6.3.

Based on the pore water pressure comparisons performed in Chapter 6, it was found that an isotropic permeability of 10^{-8} m/s for the foundation soil was a good estimate for the field conditions.

Embankment clay soil

Chapter 7 established the modelling approach for an unsaturated earthfill embankment, which was adopted in the modelling of the flood embankment in this chapter. The mechanical behaviour of embankment clay fills was modelled using an unsaturated Imperial College Single Structure Model available in ICFEP (ICSSM; Georgiadis et al. (2005), with model parameters summarised in Table 5.1.

The hydraulic behaviour of the embankment fill was controlled by a hysteretic void ratio-dependent non-linear soil water retention model (Tsiampousi et al., 2013c) and by a variable permeability model for dessication and desaturation (Potts and Zdravkovic, 1999), as discussed in Chapter 7, with model parameters summarised in Table 7.5.

8.2.3 Boundary conditions

Precipitation and evaporation boundary conditions

In order to optimise numerical calculations, the evapotranspiration boundary condition outlined in Chapter 5 and applied in Chapter 7 was replaced with a simpler evaporation boundary condition. This was done with the assumption that vegetation on the embankment surface that is not affected by the tides consisted of well-trimmed grass, in accordance with design guidelines of most nations such as the UK Environment Agency (Smith et al., 2009), Netherlands (STOWA, 2010) and the US (USACE, 2009). Therefore, it was anticipated that due to the small root depth of grass (previously assumed to be 0.1m in Chapter 7) the transpiration part of the water balance would be small, and that the surface evaporation boundary condition would suffice.

As the precipitation and evaporation boundary condition cannot be applied simultaneously at any node for a given increment, a net water balance (rain – evapotranspiration) was calculated and applied either as precipitation or evaporation boundary condition, depending on whether there was a net infiltration (when rain exceeds evapotranspiration) or evaporation (when evapotranspiration exceeds rain).

The precipitation and evapotranspiration rates used in calculating the monthly water balance were the same as those applied in Chapter 7, with the historic average precipitation and grass evapotranspiration rates derived in Chapter 5 (Tables 5.3 and 5.4), and the future monthly precipitation rates derived in Chapter 3. For the 5 years in between the first and second stage of construction, and the following 30 years after the second stage construction the embankment was subjected to the monthly average water balance of a typical year (taken as the difference between the monthly average rainfall and monthly average grass evapotranspiration rate). At the end of the 30 years, the analysis was assumed to reflect the state of the embankment in 2007.

Following on from that, actual monthly water balance, derived from the difference between rainfall measured at the site in Rayleigh (Chapter 2) and the average monthly grass evapotranspiration, was applied on the embankment surface, landward ground surface and the surface above the tidal range on the seaward side for 14 years from 2007 to 2020. To complete the lifecycle analysis, the embankment was then subjected to 60 years of projected monthly water balance data, derived by taking the difference between the projected monthly rainfall in Chapter 3 (simulation 12, Figure 3.7) and the average monthly grass evapotranspiration rates (Table 5.3), to 2080.

Tidal boundary conditions

A primary difference among the embankments analysed in Chapters 6 and 7 and this flood embankment was the introduction of a cyclical tidal boundary condition on the riverward side. The tidal changes were applied as a combination of 2 boundary conditions: normal stresses on the wetted boundary surface, representing the weight of water, and a hydrostatic pore pressure applied along the same boundary surface.

At the Dartford site, the average tidal range was 5.5m, with low tide at 0mODN and high tide at +5.5mODN (Environment Agency, 2020), cycling twice daily. Because tidal movements occur in hours, a small independent study was performed to identify an adequate approach to represent tidal effects in monthly increments. This was presented in Appendix H, identifying that by splitting a month into 3 isochronous parts, with high tide, low tide and mid-tide modelled for each part respectively, would give sufficiently adequate monthly representation of tidal effects on the embankment.

8.2.4 Initial conditions, construction sequence and lifecycle analysis

The foundation was first initialised as greenfield conditions, similar to the initial conditions adopted in Chapter 6, with the exception that there is now a gentle slope on the seaward side and initial tide level was assumed to be at +2.2mODN (consistent with initial ground water level on the landward far-field boundary).

The embankment was constructed in 2 stages, separated by 5 years of monthly tidal and precipitation / evaporation boundary conditions (Figure 8.2). In the first stage, the embankment was constructed up to +6.3mODN, from the initial ground level of +3.2mODN. During the construction, no atmospheric and tidal boundary conditions were applied, and the phreatic surface at +2.2mODN was maintained, acting as a drain for excess pore pressures and accelerating consolidation within the foundation. The first stage was constructed over 1 year.

Figure 8.2(a) illustrates the geometry of the modelled foundation domain and stage 1 construction, together with the applied mechanical and hydraulic boundary conditions. The horizontal displacements, Δu, and vertical forces, ΔF_y, were prescribed as zero along the two vertical boundaries (with both left and right boundaries represented as far-field boundaries) of the domain. Both horizontal and vertical displacements were fixed along the bottom boundary.

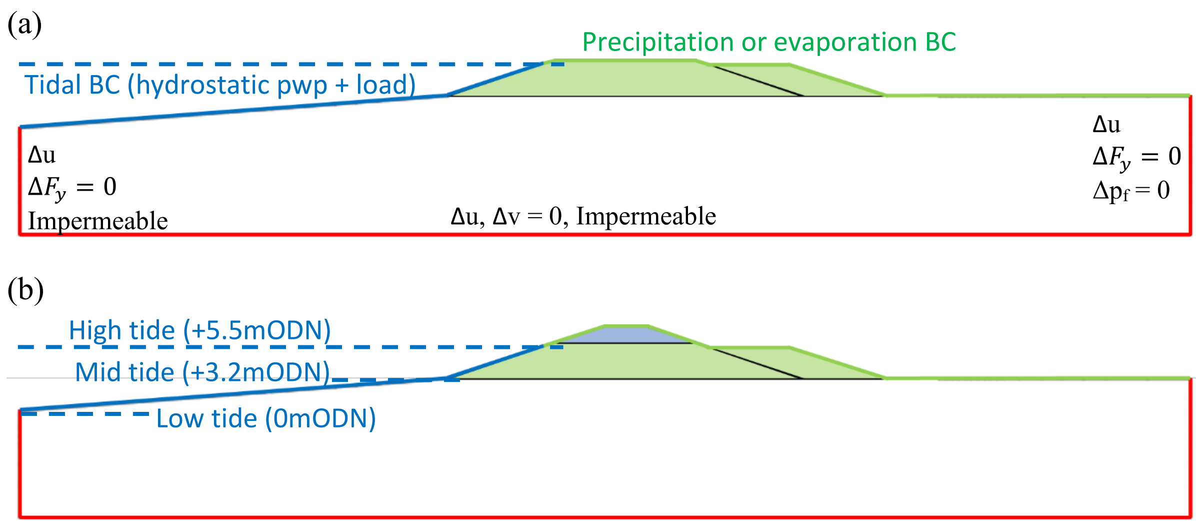

Figure 8.2: Boundary conditions after (a) the first stage construction, and (b) the second stage construction.

A no flow (impermeable) boundary condition was applied on the bottom and left (riverward) boundary, while it was assumed that the landward groundwater would be relatively stable and thus a no change to pore pressure boundary was prescribed on the right (landward) boundary.

Following from stage 1 embankment construction, both monthly tidal and atmospheric boundary conditions were applied for 5 years (Figure 8.2(a)), allowing the foundation soil to consolidate due to dissipation of excess pore water pressures generated during construction. As the average monthly evaporation rates from grass were less than the average monthly precipitation, the water balance was that of continuous precipitation boundary condition applied on the embankment surface. This was to simulate the history of the embankment up to the year 1955.

In the year 1955, the Dartford embankment was raised by 1.5m to +7.8mODN, following from the devastating floods of 1953. This was replicated in the analysis with the second stage. As with the first stage, the tidal and atmospheric boundary conditions were deactivated, and the +2.2mODN phreatic surface was maintained to speed up consolidation in the foundation and maintain suctions within the embankment. Stage 2 was modelled over 1 year.

After stage 2, the embankment was subjected to the monthly tidal and to average water balance of continuous precipitation boundary conditions for another 30 years, approximately simulating the time between the embankment raising and 2007. It was found that within 30 years, excess pore pressures within the foundation soil have dissipated, and its undrained shear strength increased. In addition, due to consistent net positive water balance (when precipitation is greater than evaporation), the pore pressure regime in the embankment and landward side generally remained constant. This would be discussed later in Section 8.2.5. Therefore, to reduce computational demand, only 30 years following from the stage 2 construction was modelled, and not the full 50 years.

From April 2007 onwards, actual monthly water balance was used instead of historic averages. For each month, the precipitation and evaporation rates were checked to identify which was more dominant, and the appropriate boundary condition and rates were applied onto the embankment and landward ground surfaces. This was implemented for the next 14 years to 2020.

After 2020, projected future rainfall up to 2080 was then applied as monthly water balance inputs. Similar to the actual monthly rainfall, precipitation rates were compared with evaporation rates and the appropriate atmospheric boundary condition was applied. Towards the 2080s as the weather was predicted to get drier, there were more months with higher evaporation than precipitation. For the base analysis, no further embankment raising was performed.

8.2.5 Results of lifecycle analysis in current and future climate

Pore water pressure contours

The pore water pressure contours in the embankment and in the foundation soil, at key lifecycle instances, were plotted in Figure 8.3. The stages comprised: initial before construction, immediately after stage 1 construction, 5 years after stage 1 construction (immediately before stage 2 construction), at the end of stage 2 construction, at the end of current conditions in 2020, at the end of summer (September) in 2079 and at the end of winter (March) in 2080.

(a) Greenfield conditions

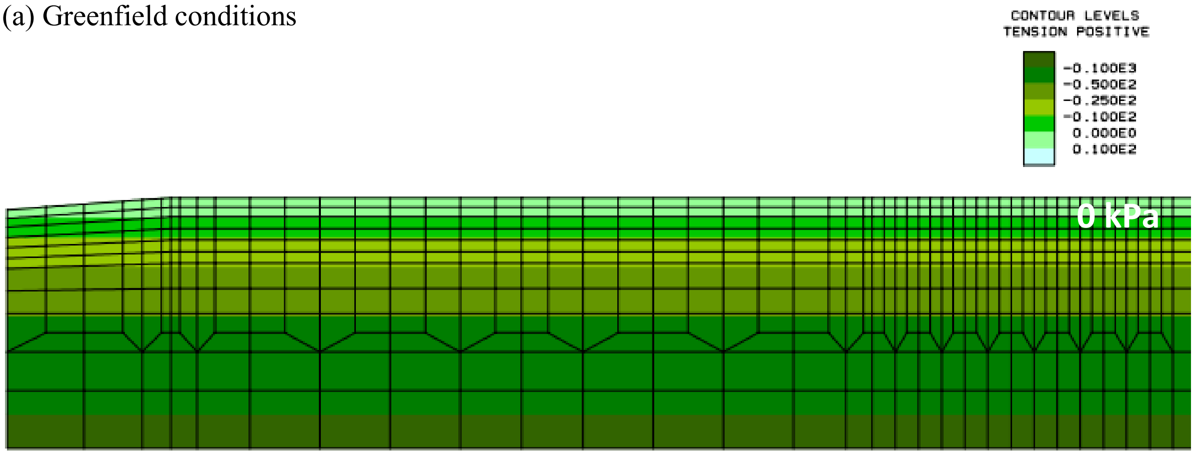

(b) After stage 1 construction

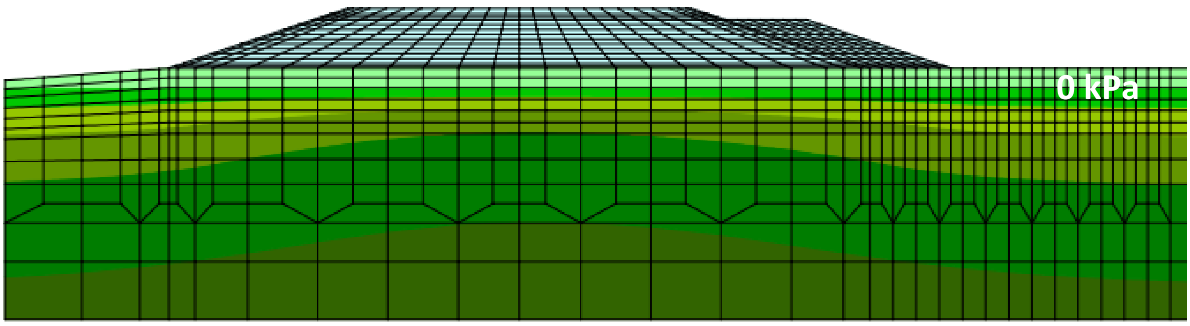

(c) Before stage 2 construction

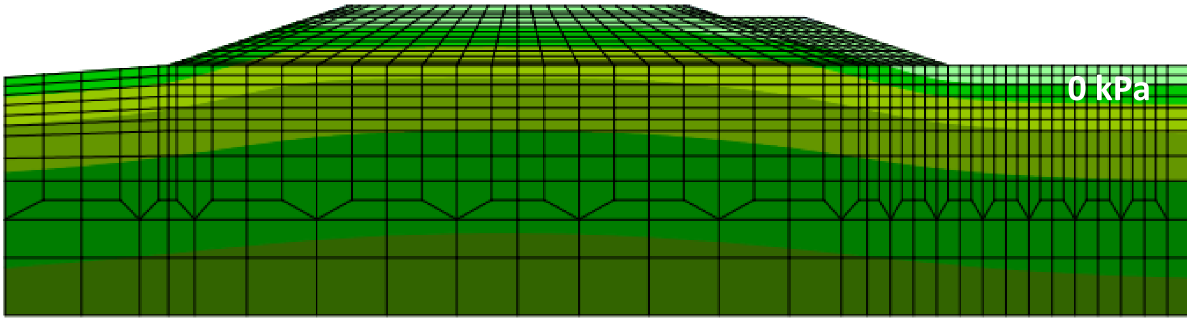

(d) After stage 2 construction

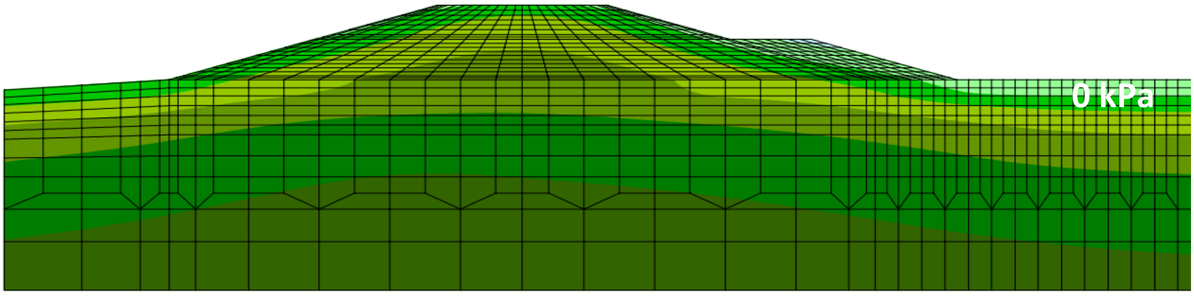

(e) March 2020

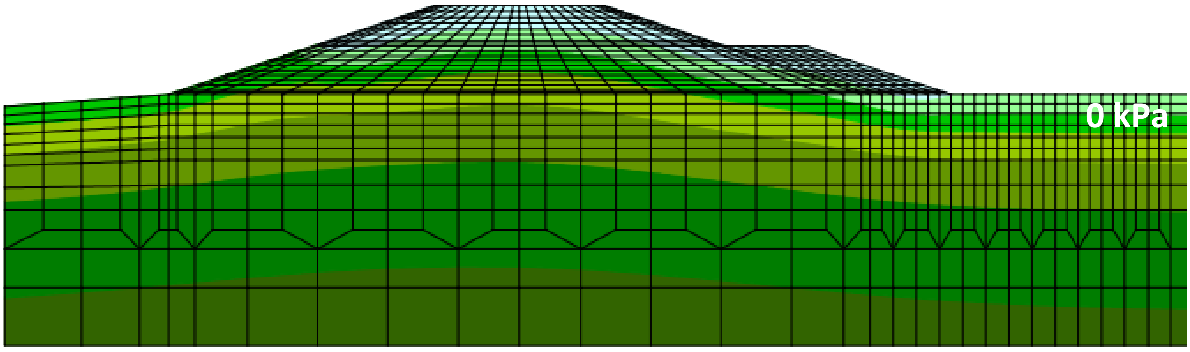

(f) September 2079

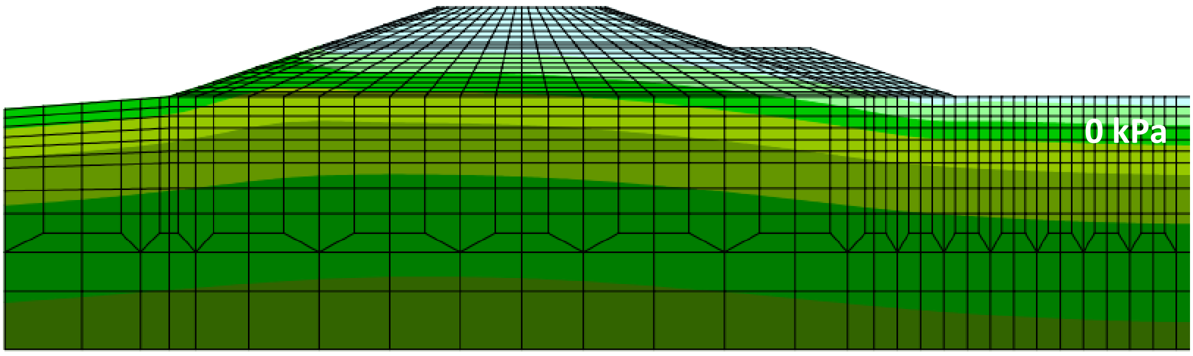

(g) March 2080

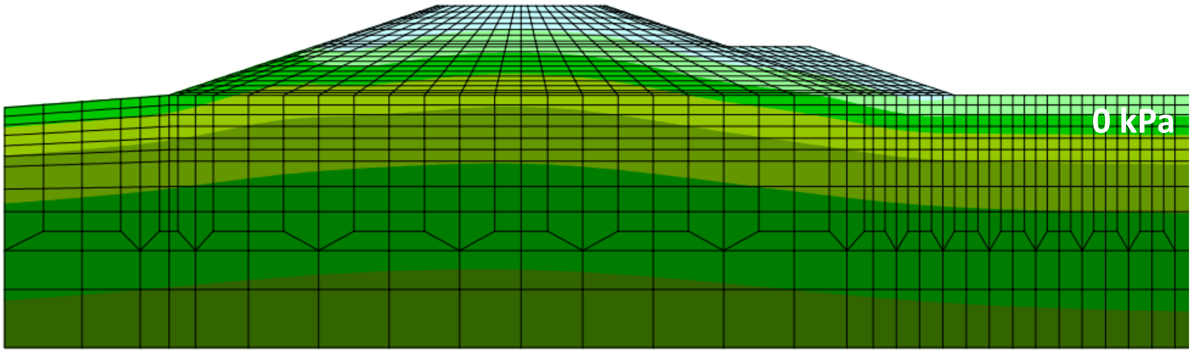

Figure 8.3: Contour plots of pore pressures in the embankment at (a) greenfield conditions, (b) immediately after stage 1 construction, (c) 5 years after stage 1 construction or just before stage 2 construction, (d) immediately after stage 2 construction, raising the embankment to +7.8mODN, (e) March 2020, before projected future rainfall, (f) September 2079, and (g) March 2080.

In addition to the contour plots, the pore water pressure profiles beneath the centre of the embankment and below the berm at various times during winter were plotted in Figures 8.4(a) and (b) respectively, providing a clearer illustration of the evolution of the pore pressures.

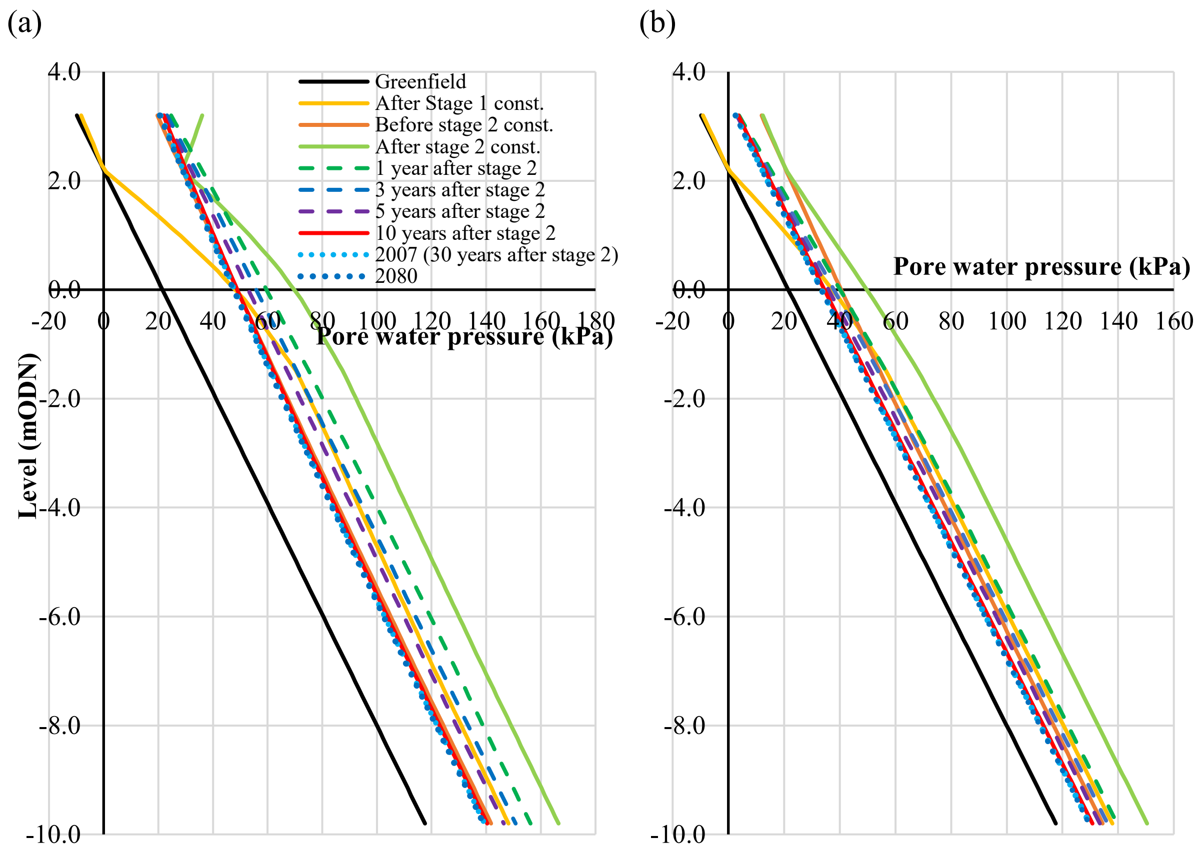

Figure 8.4: Pore water pressure profiles within the foundation soil at (a) below the centre of the embankment, and (b) below the berm. Negative indicates suctions.

Due to the resulting predominantly positive water balance (when precipitation exceeded evaporation) applied on the embankment throughout most of its lifecycle, there were generally small changes to the pore water pressure in the vicinity of the crest and in the landward side of the embankment over time. Within the foundation soil, excess pore water pressures below the embankment and berm were observed immediately after any construction or embankment raising stages (Figures 8.3(b) and (d); Figures 8.4(a) and (b)). The excess pore pressures would eventually dissipate within 10 years after construction, then remaining approximately unchanged over the following years of tides and seasonal variations.

It was only towards the summers of the final predictive decade 2070-2080, where evaporation rates exceeded precipitation, that results showed the generation of additional suctions within the embankment and the lowering of the phreatic surface within the embankment, berm and landward side, as shown in Figure 8.3(f). However, these suction increases were small and seasonal, being depleted over the following winter with more precipitation and the pore pressure regime returning to normal, as seen in Figure 8.3(g).

Utilisation of undrained shear strength

The stability and potential reusability of the flood embankment is largely dependent on the undrained shear strength of the foundation soil. As the dissipation of excess pore water pressures post-construction causes consolidation settlement in the ground and reduction of the void space (void ratio), which in turn increases the undrained shear strength of the foundation soil, it is expected for the embankment to gain stability in the long-term. Figure 8.5 plots the undrained shear strength profiles in triaxial compression, $S_{u,TXC}$, of the foundation clay beneath the embankment centreline and the embankment berm, throughout the embankment's lifecycle. Both Figures 8.5(a) and (b) show that nearly all increase in undrained shear strength occurs approximately in the top 8m of the foundation soil (+3.2mODN to -5mODN), while the undrained shear strength below -5mODN remains constant throughout the embankment's lifecycle. Furthermore, the undrained shear strength increases mostly after the first stage construction, due to the significant changes in the pore water pressure profile from the initial greenfield conditions to post first stage embankment construction illustrated in Figure 8.4.

After the second stage construction, the undrained shear strength beneath the embankment gradually increases over 10 years as consolidation occurs with repeated tidal action. The strength profile then stabilises and remains practically constant until 2080. This increase in strength is lower beneath the berm as compared to the embankment centre, as the raising occurred on the main embankment only and not on the berm.

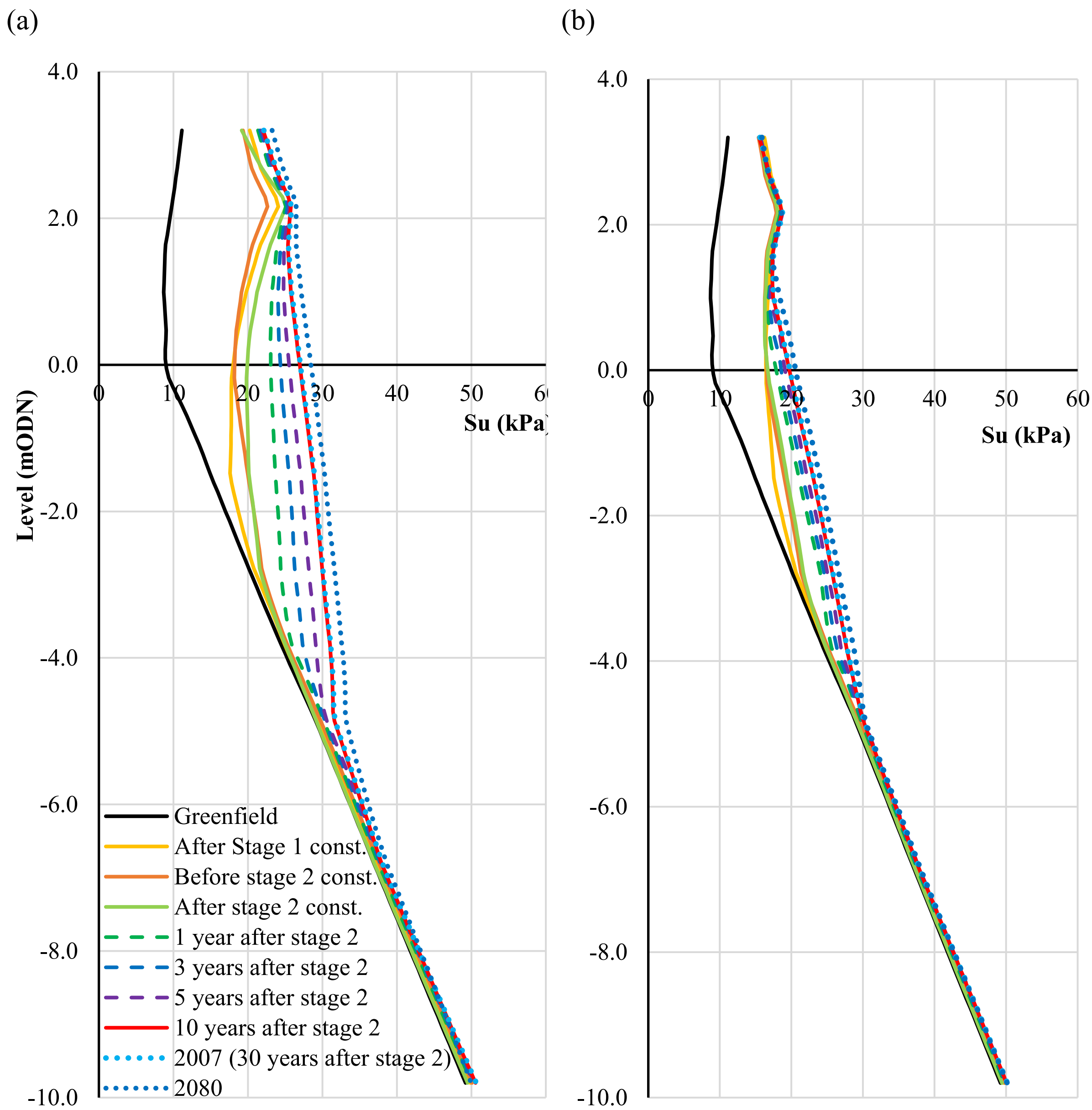

Figure 8.5: Undrained shear strength profiles in triaxial compression, $S_{u,TXC}$, within the foundation soil at (a) below the centre of the embankment, and (b) below the berm.

Displacements

Vectors of displacements for both the embankment and foundation soil at key stages of the lifecycle analysis were plotted in Figure 8.6, with the purpose of checking for any formation of slip surfaces and failures.

The displacements experienced by the embankment after the first stage construction (Figure 8.6(a)), showed that the embankment was mostly settling as the soft clay foundation consolidated over 1 year with the dissipation of excess pore water pressures. This was also more prominent closer to the ground level, as the phreatic surface was kept constant during construction, thus draining excess pore water even faster. Due to the wide base of the embankment and berm, the construction was stable. The maximum settlements predicted at this stage were about 0.8m.

After 5 years of tidal and atmospheric cycling, a further maximum settlement was only 6cm, indicating small remaining pore water pressure dissipation. The displacement mechanism illustrated in Figure 8.6(b) still showed predominant settling, although more concentrated towards the centre of embankment. The raising by an additional 1.5m started to display a preference for slipping toward the riverward direction (Figure 8.6(c)). However, no clear slip surface was formed at this stage. With time the displacement mechanism became again more uniformly distributed over the embankment's and berm's bases and remained stable in the long term.

(a) After first stage construction (maximum total displacement (in red) 0.89m)

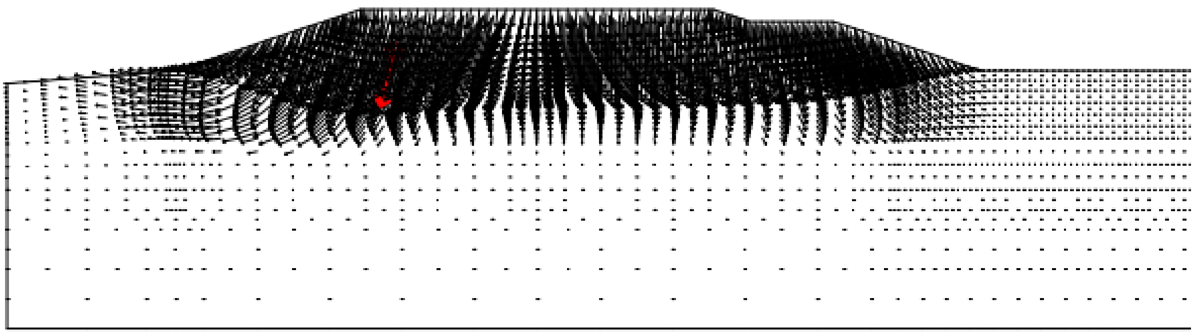

(b) 5 years after first stage construciton (maximum sub-accumulated displacement from (a) in red: 0.20m)

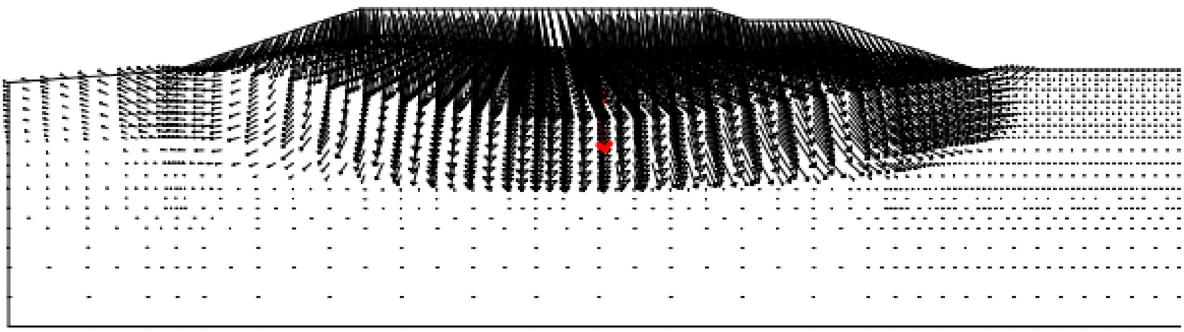

(c) After second stage construction (maximum sub-accumulated displacement from (b) in red: 0.70m)

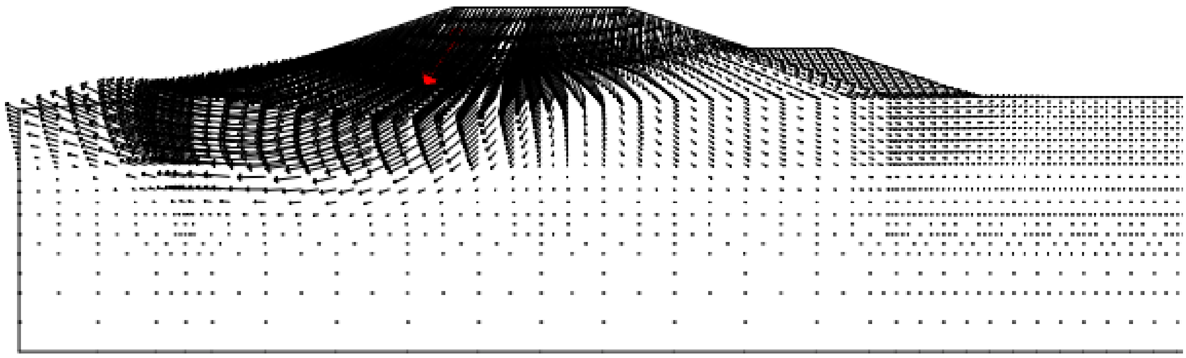

(d) 30 years after second stage construction (March 2007; maximum sub-accumulated displacement from (c) in red: 1.10m)

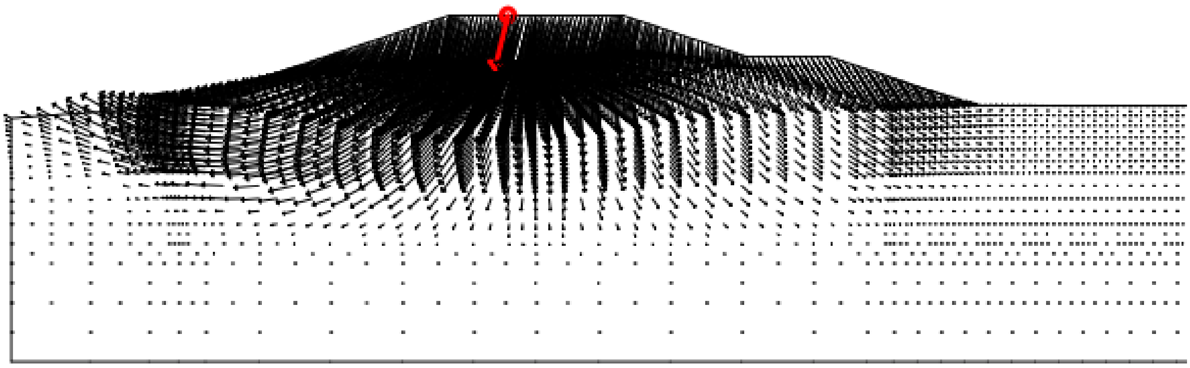

(e) March 2080 (maximum sub-accumulated displacement from (c) in red: 1.16m)

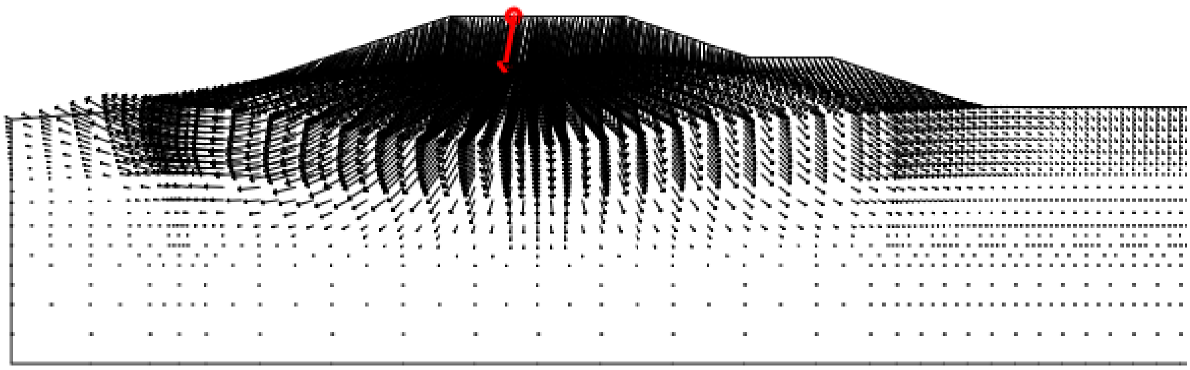

Figure 8.6: Plots of displacement vectors at various points in the embankment's lifecycle. (a) After first stage construction. (b) Sub-accumulated displacements over 5 years of tidal and atmospheric boundary conditions after first stage construction. (c) Sub-accumulated displacements of the second stage construction. (d) Sub-accumulated displacements over 30 years of tidal and atmospheric boundary conditions after second stage construction. (e) Sub-accumulated displacements from the end of second stage construction to 2080.

In addition, displacements along the riverward embankment slope could be compared against actual field measurements taken over several months immediately after the raising of the actual Dartford embankment (Marsland), as presented in Figure 8.7. The heave at points 10 and 11, located around the toe, was reasonably well predicted by the numerical model. The predicted settlements on the slope, at points 7 and 9, were in good agreement with the measurements over the first two months. From mid-June onwards, the field measured settlements started accelerating, which was an indication of failure in the actual embankment. The numerical model was developed not to exhibit such a behaviour and was stable throughout its lifecycle.

(a)

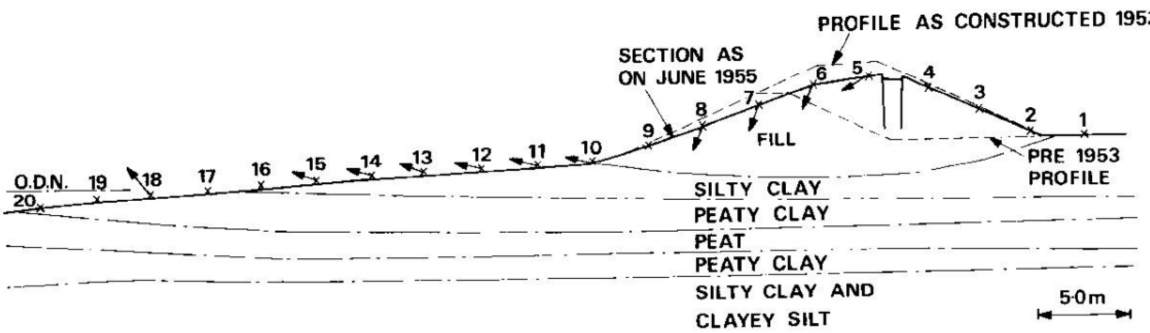

(b)

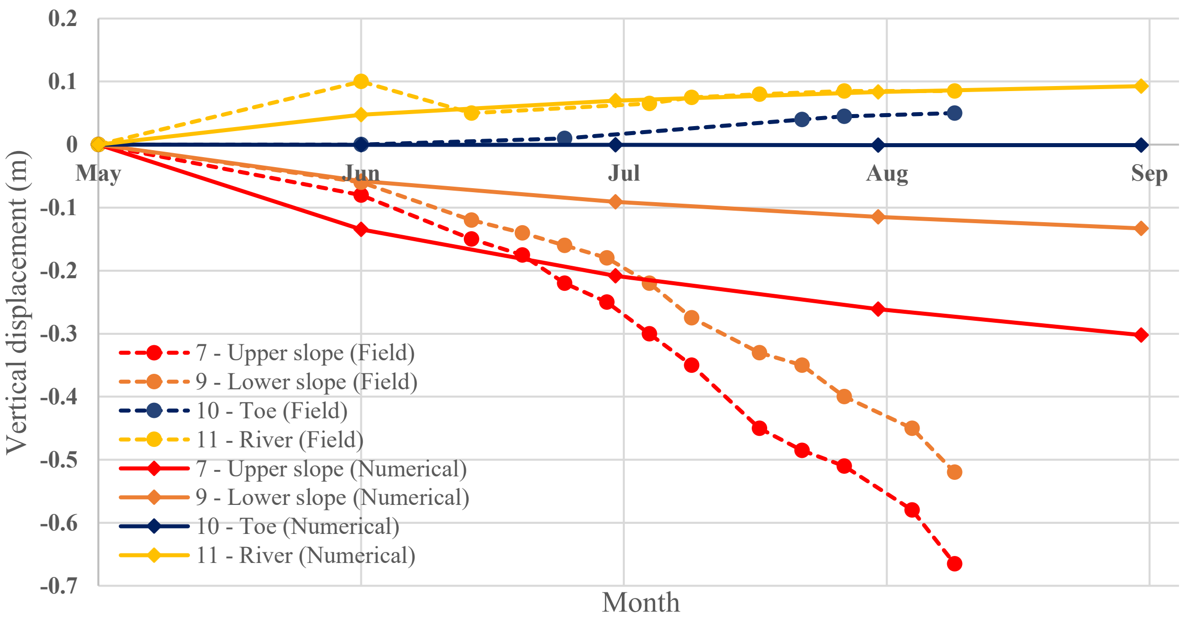

Figure 8.7: (a) Cross section of the displacement monitoring points of Dartford embankment (Marsland, 1973). (b) Comparison between field settlements at Dartford (Marsland, 1973) and numerical analysis of the embankment in 1955.

The numerical displacements after the second stage construction were purely governed by consolidation of the foundation soil, with sub-accumulated settlements from the end of stage 2 construction of up to 1.1m in 2080. Throughout its lifecycle from construction to 2080, the embankment did not exhibit any signs of failure. However, the lifecycle analysis was based on a more macroscale view of the weather, with monthly increments that often smooth out extreme storm peaks. Hence the additional analyses to assess embankment resilience to extreme events and storms.

8.3 Embankment resilience to storms

8.3.1 Storm and overtopping events

The general methodology employed in Chapter 7 to model storm events was repeated in this analysis. Four critical points in the embankment's base lifecycle (with maximum embankment height of +7.8mODN) represented as the wettest winter, driest winter, wettest summer, and driest summer, were chosen as antecedent conditions for the incoming storm event. One difference was that only the most extreme scenario of overtopping was modelled for each of the four antecedent conditions. It was assumed that rainfall, together with a storm surge would cause the river to rise higher than the embankment, causing overtopping. Consequently, a zero pore pressure boundary condition was applied over the crest and landward surface, simulating a thin layer of water over the surface from the overtopping (Figure 8.8).

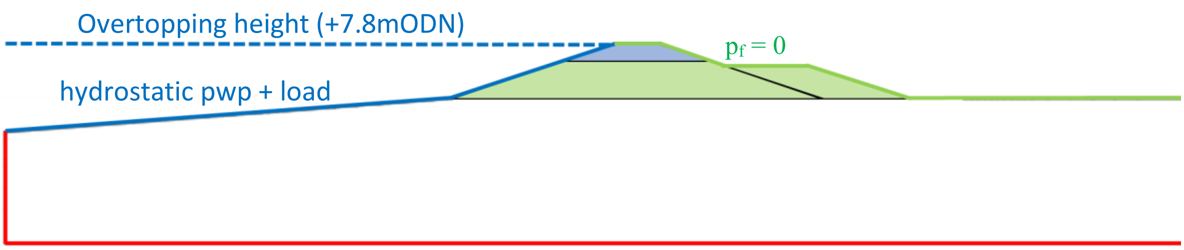

Figure 8.8: Hydraulic boundary conditions applied during the overtopping event.

In this extreme scenario, precipitation was not applied as the surface was covered with a thin layer of water; any additional rainfall in such a case would become a runoff. Hence there was no need for different storm scenarios that were applied in Chapter 7.

8.3.2 Embankment resilience results

The embankment overtopping modelling resulted in similar outcomes for all four antecedent scenarios. Therefore, only one result (the driest winter of March 2069) was presented here.

Figure 8.9 shows the pore water pressure contours in the embankment before and after the overtopping event, indicating that all suctions within the embankment was lost and that the embankment is now fully saturated with the phreatic surface along the crest and landward slopes. The riverward slope had hydrostatic pore pressures from the crest, due to overtopping.

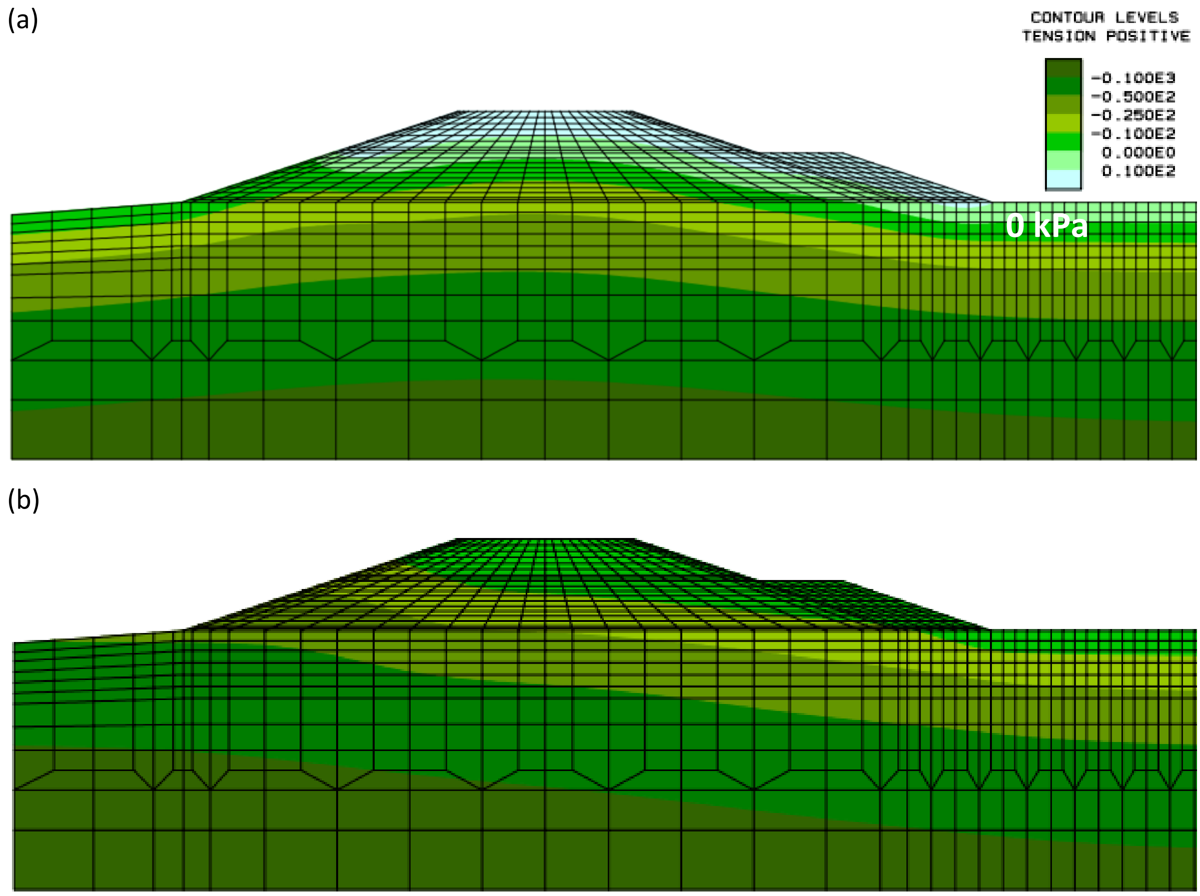

Figure 8.9: Contour plots of pore water pressure of the embankment in March 2069 (a) before and (b) after the overtopping event.

The corresponding vectors of displacements of the embankment at this stage were presented in Figure 8.10. These were sub-accumulated displacements, starting from the beginning of the overtopping event, showing that with the added pressure of water on the embankment, the embankment was pushed towards the landward direction. In addition, dissipation of all suctions and the increase in pore water pressure within the embankment and foundation soil caused the embankment to heave in general.

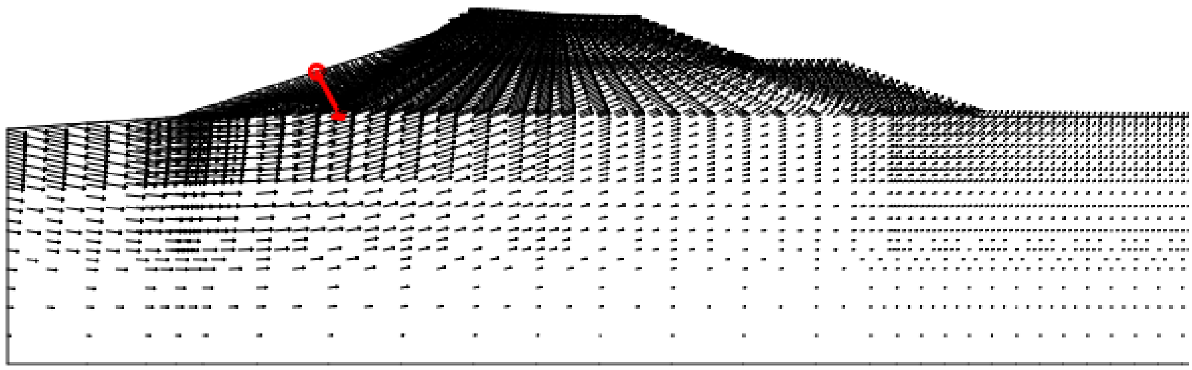

Figure 8.10: Sub-accumulated vectors of displacement of the embankment in March 2069 during the overtopping event. Displacements were sub-accumulated from the start of the storm.

While the stability of the embankment reduced with decreased effective stresses within the soil, no clear slip surfaces was formed in the displacement mechanism in Figure 8.10, suggesting that the embankment remained stable and able to withstand an overtopping scenario. However, it should be noted that no potential erosion from overtopping was modelled, which would adversely affect the embankment and potentially cause failure.

8.4 Embankment raising strategies

8.4.1 Raising strategies

As climate change causes sea levels to rise and the development of more tidal barriers upstream, the design height requirements on flood embankments will increase. Embankment raising is also recommended to avoid overtopping, which is often seen as less desirable due to potential damages the flood may cause inland and on the embankment itself through erosion. Thus, several embankment raising strategies were explored in this analysis.

In all raising scenarios, the embankment was first raised by 0.8m to +8.6mODN by construction of additional layers on the existing embankment and berm as shown in yellow in Figure 8.11(a). This strategy preserved the necessary gradient of 1V:3H of both riverward and landward slopes, while not using additional landward land to raise the embankment.

(a) First raising to +8.6mODN

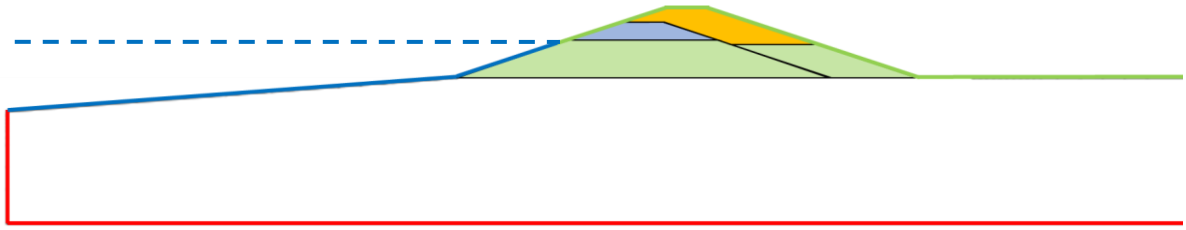

(b) Second raising to a possible maximum of +10.2mODN

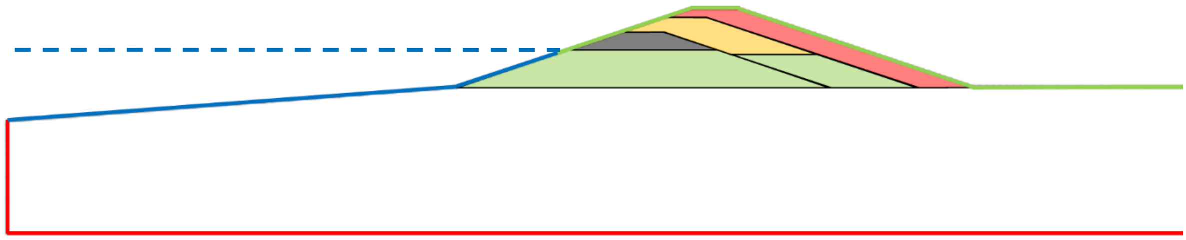

Figure 8.11: Construction sequence and boundary conditions for additional embankment raising for (a) up to +8.6mODN, and (b) up to a maximum of +10.2mODN.

To raise the embankment further, additional land would be necessary to ensure that the crest width remained constant and above the minimum requirement of 4m. This was illustrated in Figure 8.11(b), where the red section represents the additional soil added to raise the embankment higher than +8.6mODN. While the embankment mesh allowed for the embankment to be raised by an additional 1.6m to +10.2mODN, it was expected that the embankment would fail before reaching the maximum height.

Several embankment raising regimes were explored in this numerical model, namely the single stage raising, double stage raising and triple stage raising regimes. In the single stage regime, the embankment in 2007 and in every decade from 2020 to 2080 was raised and the maximum theoretical height achieved before failure was identified.

In the double stage regime, the embankment was first raised by 1m, before being raised again in the next few decades. All possible permutations of the double stage raising were explored, with the final maximum height raised for each scenario identified.

Finally, a triple stage regime was analysed, with the raising performed in 2020, 2050 and 2080. The raising heights for the first two stages were based on results from the double stage regime, where the embankment was raised by 1m in 2020, followed by another 0.5m in 2050. The maximum possible raising height in 2080 was then determined.

8.4.2 Embankment raising results

Embankment raising strategies typically rely on the gradual consolidation of the foundation soil at the site and increase in undrained shear strength, allowing for a higher embankment.

To ensure that the newly raised embankment was stable, the following key indicators were used:

- The maximum incremental vertical settlement must not be higher than the raised height for that given increment.
- There was no clear formation of a slip surface and failure signs.
- Numerical convergence.

If at any point one of the indicators showed failure during the raising, the analysis was stopped and the maximum allowable height was recorded. The indicators adopted here were similar to the indicators adopted for the Factor of Safety analyses in Chapter 7, with the addition of the first indicator involving the maximum incremental vertical settlement.

Table 8.1 presents the 1-stage maximum possible height raised before embankment failure occurred, with the maximum raising height of 1.4m in 2080 and a minimum of 1.2m in 2020. This difference was small and in line with undrained shear strength plots in Figure 8.5. Most of the gain in undrained shear strength after the stage 2 raising of the embankment happened in the subsequent 10 years, with only small further variation up to year 2080.

Table 8.1: One-stage maximum height increase for the flood embankment for each future decade.

Construction Year	Height increase (m)	Embankment Height (mODN)
2020	1.2	9
2030	1.3	9.1
2040	1.3	9.1
2050	1.35	9.15
2060	1.4	9.2
2070	1.4	9.2
2080	1.4	9.2

As it was evident from Table 8.1 that an initial raising of 1m was very much within the capacity of the embankment, a two-stage embankment raising regime was developed. An initial raising of 1m in a set decade was first modelled, followed by finding the maximum possible raising height in the subsequent decades. The results were tabulated in Table 8.2.

Table 8.2: Two-stage maximum height increase for the flood embankment

Initial 1m construction	Second stage construction height in m (total height mODN)					
	2030	2040	2050	2060	2070	2080
2020	0.4 (+9.2)	0.5 (+9.3)	0.6 (+9.4)	0.7 (+9.5)	0.7 (+9.5)	0.8 (+9.6)
2030	/////	0.4 (+9.2)	0.5 (+9.3)	0.6 (+9.4)	0.7 (+9.5)	0.7 (+9.5)
2040	-	/////	0.5 (+9.3)	0.5 (+9.3)	0.5 (+9.3)	0.6 (+9.4)
2050	-	-	/////	0.5 (+9.3)	0.5 (+9.3)	0.6 (+9.4)
2060	-	-	-	/////	0.5 (+9.3)	0.5 (+9.3)
2070	-	-	-	-	/////	0.5 (+9.3)
2080	-	-	-	-	-	/////

Table 8.2 indicated that by splitting the embankment raising into two separate stages, it was possible to achieve a maximum embankment height of +9.6mODN in 2080, if the initial 1m of raising was done in 2020, followed by a 0.8m raise in 2080. This is slightly higher than the 1.6m raised height in 2080 if the raising was performed in one stage, demonstrating the benefits of multi-stage raising.

To take this concept further, a 3-stage raising regime was proposed, in which an initial 1m was first constructed in 2020, followed by 0.5m in 2050, keeping in mind that the maximum possible raising at this point was only 0.6m from the 2-stage analysis (Table 8.2). The third stage was then performed in 2080, and the maximum possible height recorded in Table 8.3.

Table 8.3: Three-stage maximum height increase for the flood embankment

Initial construction	Second stage	Third stage	Total	Final Embankment Height (mODN)
2020	2050	2080		
1m	0.5m	0.3m	1.8m	9.6

It was found that the highest that the embankment could be raised by 2080 was by an additional 1.8m, to a height of +9.6mODN. To achieve that final height, either a two-stage or three-stage raising regime may be adopted.

8.5 Conclusions

This chapter explored the complete lifecycle of a typical flood embankment on the River Thames, by building upon calibration work of the foundation soil in Chapter 6 and embankment clay fill in Chapter 7. The flood embankment was further assessed for its resilience to a changing climate and opportunities for reuse by raising its height for better adaptation to a changing climate and design requirements.

To extend the lifecycle methodology developed in Chapter 7 for flood embankments, a short study into representing semidiurnal tidal cycles in monthly increments showed that this could be done by modelling the high tide, low tide and mid tide cycle for each month.

The flood embankment's lifecycle analysis was performed, with some validation with field monitoring data. In general, the flood embankment showed no risks of failure when assessed against a monthly scale view of the changing climate. The settlement and consolidation of the foundation soil was also noted.

The embankment's resilience to overtopping at various points throughout its lifecycle was then assessed, showing that the embankment in its current and future state is able to withstand an overtopping event should it occur. However, erosion was not considered due to limitations of the numerical model.

The reusability of the embankment was also investigated, by identifying the most optimal strategy in raising the embankment height. A one-stage raising was first performed, demonstrating the benefits of allowing the foundation soil to consolidate and gain strength over time as the embankment could be raised higher. Subsequently, a two-stage raising regime was investigated, and it was found that a maximum height increase of 1.8m is possible if the raising stages were separated with a sufficiently long time in between. Finally, a three-stage raising procedure was performed, but no significant additional benefits were identified as the maximum height increase was still 1.8m.

It is hoped that the results presented in this Chapter will help in the implementation of more lifecycle analyses of earth embankments, which is particularly relevant when assessing the resilience and adaptability of these geotechnical structures in light of a changing climate.

Chapter 9: Conclusions and Further Research

9.1 Main conclusions of the thesis

The primary aim of this research was to establish a lifecycle analysis framework capable of assessing the resilience of flood embankment structures in consideration of climate change. In arriving at the numerical model proposed in this thesis, several critical components to the model were first developed, calibrated and validated separately. These include the projection of future rainfall and storm events, taking into consideration climate change, the calibration of appropriate constitutive models for the soft clay foundation soil and unsaturated behaviour of the embankment clay fill, and the establishment of a lifecycle analysis methodology.

The conclusions for this thesis may be subdivided into two main sections. Section 9.1.1 details the key findings and conclusions of the stochastic rainfall modelling Chapters 2, 3 and 4, while Section 9.1.2 summarises key results from the geotechnical calibration, numerical modelling and lifecycle analyses of earth embankments from Chapters 5, 6, 7 and 8.

9.1.1 Stochastic rainfall modelling

In Chapter 2, rainfall at the case study site of Rayleigh, Essex (close to the Magnolia Road rail embankment) was characterised and several variants of the Bartlett Lewis Rectangular Pulse (BLRP) models were calibrated with the sub-daily rainfall data. Due to the incomplete nature of the observed rainfall data, a weighting system was developed to minimise the influence of missing data on the summary statistic calculations, allowing for a more universal application of this stochastic model that is less dependent on data completeness. It was also found that by implementing the traditional approach in calculating summary statistics, both the variance and skewness would have been underestimated, leading to an underestimation of extremes in the synthetic rainfall generated from the fitted BLRP models. With the implementation of a cumulative approach to summary statistics calculation, this underestimation of extremes was resolved.

The Generalised Linear model (GLM) developed in Chapter 3, together with the European Re-Analysis 5 (ERA5) present climate data, demonstrated that it was possible to link climate variables to rainfall, and generate synthetic daily rainfall series that were statistically similar to the original observed rainfall series. This process was then extended to project future daily rainfall up to the year 2080, using climate projections based on the RCP8.5 scenario from the UK Climate Projections 2018 (UKCP18) project.

Based on the simulated rainfall in Chapter 3, it was predicted that summer rainfall at Rayleigh would decrease by as much as 30% by 2080, compared to current rainfall quantities. In addition, winter rainfall was also projected to occur later in the year, in February, with higher intensities, highlighting the changes to rainfall patterns caused by climate change that were also observed by Blöschl et al. (2017) in the North Sea. To model the effects of this changing weather patterns on the geotechnical modelling, simulation 12 from the GLM simulations was chosen to be the representative projected rainfall for the future.

Chapter 4 highlighted the effectiveness of the adopted downscaling approach in downscaling daily rainfall down to sub-hourly, based on the scaling properties of rainfall statistics, with the model validated using present sub-daily rainfall at Rayleigh. The same approach was subsequently employed in downscaling the projected future rainfall from Chapter 3, to obtain sub-hourly rainfall series for future climates. It was demonstrated that the previous effects of climate change on future rainfall, observed on the daily scale in Chapter 3, were also present at the sub-daily level, with a decrease of rainfall during summer and later rains in winter. Moreover, there was a notable increase in the extreme rainfall envelope in the Gumbel plots of the annual maxima for each decade. Finally, it was found that the maximum daily modelled storms had a magnitude of 95mm, which was chosen as the extreme storm scenario in subsequent resilience studies in the embankment lifecycle analyses.

9.1.2 Geotechnical numerical modelling

In Chapter 5, the Imperial College Single Structure Model (ICSSM, Georgiadis et al., 2005) was successfully calibrated to model the unsaturated behaviour of compacted London Clay, using oedometric experiments on compacted London clay by Monroy (2006) and triaxial experiments on intact London clay by Gasparre (2005). In addition, the monthly average evapotranspiration and precipitation boundary conditions were derived from the records of climate data from 2006 to 2011 in Shoeburyness and daily rainfall from 1971 to 2000 in Greenwich respectively.

Chapter 6 detailed the calibration of the extended Modified Cam Clay (MCC) constitutive model, selected to represent the behaviour of typical soft foundation clays in the Thames estuary, which supported a trial embankment at a site in Dartford (BRE; Marsland and Powell, 1977). The available laboratory and field data were integrated to characterise the behaviour of the soft clay and to initialise the numerical model for the simulation of construction to failure of the trial embankment. The significant scatter in experimental data required careful engineering judgement in deriving model parameters. The results of the hydro-mechanically coupled numerical model developed in ICFEP showed high level of agreement with the field measurements of pore water pressures and movements in the foundation soil, demonstrating consistency in the calibration process of the extended MCC constitutive model and in the fidelity of the simulated construction sequence.

A detailed study of the Magnolia Road rail embankment was performed in Chapter 7. Comparison of saturated and unsaturated modelling frameworks for the embankment fill demonstrated the necessity of representing a compacted clay fill with unsaturated hydro-mechanical constitutive models. The representation of the soil water retention behaviour of the compacted clay was shown to be challenging. The laboratory experiments on samples of compacted clay taken from earthfill embankments, from which the SWRCs were established and used to calibrate the appropriate SWR model, were shown to be inadequate, as they failed to represent the porosity of the fill created by loose compaction of large clay lumps and the impact of vegetation over the long period of time. Consequently, the initialisation of the numerical model in ICFEP required careful consideration of the available experimental data to derive hydro-mechanical model parameters. The numerical methodology to establish the 'current' water balance in the embankment body, due to the embankment-atmosphere interaction since its construction, was developed and its satisfactory accuracy was demonstrated by comparison of numerical predictions with field measurements on the Magnolia Road embankment before vegetation removal. Additionally, the accuracy between numerical results and field measurements post-vegetation removal completed the validation of the numerical model developed for the simulation of infrastructure embankments.

The lifecycle numerical analysis of the Magnolia Road embankment was continued for future projected climates, to assess the embankment behaviour and resilience up to the year 2080. It was found that slip surfaces between the ash and embankment clay fill, and between the embankment and foundation soil would start to develop over time, driven by the sharp exchanges between wet and dry periods. As it was also predicted that the Magnolia Road site would get drier, suctions within the embankment were predicted to increase significantly due to vegetation, causing gradual settlement of the embankment over time. Resilience studies performed during key points of the embankment's lifecycle indicated that the factor of safety could reduce significantly if the storms were to occur during the driest periods in the lifecycle.

Finally, a complete lifecycle analysis of a typical earthfill flood embankment in the Thames estuary was performed in Chapter 8, combining all the concepts developed in the previous chapters. Due to minimal vegetation on such embankments, there were generally little changes in pore water pressures month to month, apart from some small changes caused by the tidal movements. While there were higher suctions predicted in the future due to a drier climate, the embankment showed no risk of failure when assessed from a monthly water balance scale throughout its lifecycle. Resilience studies also showed that the embankment was able to withstand overtopping throughout its lifetime. Reusability and raising studies showed a two-stage staggered raising strategy to be the most optimal safe solution in raising the height of the embankment by up to 1.8m by the year 2080.

9.2 Recommendations for further research

Within the large scope of this research, there are several avenues for improvements and future recommendations that could be applied to the lifecycle analysis.

9.2.1 Stochastic rainfall modelling

The stochastic rainfall modelling methodology adopted in this thesis was developed based on rainfall only at the Rayleigh station. Some application of this stochastic modelling approach was attempted with rain and climate found along the East coast of the UK, stretching from Peterborough to Newcastle (Pagliara, 2020), with the results showing similar conclusions with that of the UKCP18 findings (Lowe et al., 2018). However, this methodology is still untested for other wetter climates that are found towards the West and Northern coasts of the UK, places where weather is generally influenced by the Atlantic. Further research is needed to assess the suitability of this approach in other climates and weather systems.

With the development of more powerful processors and super-computers, the ability to numerically predict sub-daily rainfall for various RCP scenarios is not a too distant future. The recently developed Convective Permitting Model (CPM; Kendon et al., 2019) in conjunction with the UKCP18 by the UK Met Office, is able to produce climate variables and rainfall at 3h time resolution, with a 2.2km grid projection. While several issues with the CPM still need to be resolved (Kendon et al., 2021) before it is ready to be adopted for resilience and lifecycle studies, in time it will most likely serve as the bedrock for all lifecycle assessments of embankments in the UK.

Having said that, stochastic rainfall modelling is still necessary and will most likely be applied alongside CPM. The BLRP models have already shown to be able to check CPM outputs and ensuring consistency (Chen et al., 2020), in addition of being used as a fast rainfall generator to simulate hundreds of rainfall series to observe the extremes. Downscaling methodologies are also needed to downscale the projected rainfall down to the sub-hourly scale.

9.2.2 Soil constitutive modelling

During the geotechnical constitutive model calibrations, several simplifying assumptions were made to reduce computational demands and the total number of parameters for the numerical model. One such major assumption is that creep was not modelled in the soft clay foundation soil of the embankments in Chapters 6 and 8. The adopted extended MCC model was able to reproduce only consolidation in the soil.

Creep behaviour in soft clays, particularly in riverine or estuarine environments, is well known and documented (Nash et al., 1992; Yin, 1999; Sorenson, 2006). A commonly adopted type of constitutive models that can account for both consolidation and creep in the soil are the equivalent time elastic-viscoplastic models (e.g. Yin et al., 2002; Bodas-Freitas et al., 2011), based upon the overstress theory of Perzyna (1963). Application of those creep models in boundary value problems such as footings (Bodas-Freitas et al., 2015) and embankments (Losacco, 2007; Zdravkovic et al. 2019) on soft clays, was shown capable of accurately reproducing the soil deformation and increases in strength over time, the latter being particularly important for the embankment reuse in the context of raising its hight to prevent future overtopping. Adopting such a creep model in the lifecycle analysis would yield more accurate overall results.

There is also a need for further experimental research into the impact of clay lumps and vegetation on the SWRC of earthfill clays, as discussed in Chapter 7. The SWRC of an embankment clay as measured by Melgarejo Corredor (2004) showed a very large envelope of primary drying and wetting curves, which implied that fill was remaining highly saturated (at >85% degree of saturation) at suctions of 200kPa (a typical suction value experienced by vegetated earth embankments during the summer). However, field measurements of moisture content taken in these embankments would suggest a much lower degree of saturation at that level of suction (Marsland, 1968). Research by Ni et al. (2018) in sandy decomposed granite soils showed that vegetation depresses the soil SWRC due to root growth, however, there are no similar studies performed on clayey soils typically used for embankment construction in the UK.

9.2.3 Embankment lifecycle analysis

During the overtopping resilience study of the flood embankment in Chapter 8, the landward slope was assumed not to erode under the moving water. Further research is needed to factor in the numerical modelling of overtopping flows the relationship to eroding. Empirical equations of this process, such as those provided by Vrouwenvelder et al. (2001) may be used to assess erosion risk in the model.

Finally, there is an opportunity to merge the lifecycle analysis framework presented in this thesis with the probabilistic fragility framework discussed in Chapter 5. With a complete lifecycle analysis, snapshots of the state of the embankment at various points in time may be taken and used as a template for subsequent fragility analysis, allowing for the fragility curve to evolve with time along the embankment's lifecycle. This procedure will also provide information on any antecedent weather conditions prior to the selected time period of investigation.

REFERENCES

References on rainfall modelling

Abdellatif, M., Atherton, W., Alkhaddar, R.M. and Osman, Y.Z., 2015. Quantitative assessment of sewer overflow performance with climate change in northwest England. *Hydrological Sciences Journal*, *60*(4), pp.636-650.

Asong, Z.E., Khaliq, M.N. and Wheater, H.S., 2016. Multisite multivariate modeling of daily precipitation and temperature in the Canadian Prairie Provinces using generalized linear models. *Climate Dynamics*, *47*(9), pp.2901-2921.

BBC, 2013. Southend bank holiday business hampered by Essex floods. Viewed 3 June 2021 https://www.bbc.co.uk/news/uk-england-essex-23833072

BBC, 2014. Floods follow intense storms in south-east England. Viewed 3 June 2021 https://www.bbc.co.uk/news/uk-england-28394863

Bengtsson, L., Kanamitsu, M., Kållberg, P. and Uppala, S., 1982. FGGE research activities at ECMWF. Bulletin of the American Meteorological Society, 63(3), pp.277-303.

Beuchat, X., Schaefli, B., Soutter, M. and Mermoud, A., 2011. Toward a robust method for subdaily rainfall downscaling from daily data. Water Resources Research, 47(9).

Blöschl, G., Hall, J., Parajka, J., Perdigão, R.A., Merz, B., Arheimer, B., Aronica, G.T., Bilibashi, A., Bonacci, O., Borga, M. and Čanjevac, I., 2017. Changing climate shifts timing of European floods. Science, 357(6351), pp.588-590.

Bowler, N.E., Arribas, A., Mylne, K.R., Robertson, K.B. and Beare, S.E., 2008. The MOGREPS short-range ensemble prediction system. *Quarterly Journal of the Royal Meteorological Society: A journal of the atmospheric sciences, applied meteorology and physical oceanography*, *134*(632), pp.703-722.

Buytaert, W., Paul, J.D., Ochoa-Tocachi, B.F. and Drenkhan, F., 2019, December. Characterising Extreme Rainfall over the Tropical Andes with a Network of Tipping Bucket Rain Gauges and GPM satellite Data. In *AGU Fall Meeting Abstracts* (Vol. 2019, pp. A24K-01).

Caires, S., 2009. A comparative simulation study of the annual maxima and the peaks-over-threshold methods. *Deltares report 1200264-002 for Rijkswaterstaat, Waterdienst*.

CCIRG, 1991. The Potential Effects of Climate Change in the United Kingdom, Department of the Environment. HMSO, London, p. 124.

CCIRG, 1996. Review of the Potential Effects of Climate Change in the United Kingdom. HMSO, London, p. 247.

Chan, S.C., Kendon, E.J., Roberts, N.M., Fowler, H.J. and Blenkinsop, S., 2016. Downturn in scaling of UK extreme rainfall with temperature for future hottest days. *Nature Geoscience*, *9*(1), pp.24-28.

Chandler, R.E., 2020. Multisite, multivariate weather generation based on generalised linear models. *Environmental Modelling & Software*, *134*, p.104867.

Chandler, R.E. and Wheater, H.S., 2002. Analysis of rainfall variability using generalized linear models: A case study from the west of Ireland. *Water Resources Research*, *38*(10), pp.10-1.

Chen, Y., Paschalis, A. and Onof, C., 2020, May. Evaluating the small-scale space time structure of rainfall in the Convection Permitting Model of UKCP18. In EGU General Assembly Conference Abstracts (p. 8007).

Christierson, B.V., Vidal, J.P. and Wade, S.D., 2012. Using UKCP09 probabilistic climate information for UK water resource planning. Journal of Hydrology, 424, pp.48-67.

Coe, R. and Stern, R.D., 1982. Fitting models to daily rainfall data. *Journal of Applied Meteorology and Climatology*, *21*(7), pp.1024-1031.

Cowpertwait, P.S., 1998. A Poisson-cluster model of rainfall: some high-order moments and extreme values. *Proceedings of the Royal Society of London. Series A: Mathematical, Physical and Engineering Sciences*, *454(1971*), pp.885-898.

Cowpertwait, P., Isham, V. and Onof, C., 2007. Point process models of rainfall: developments for fine-scale structure. *Proceedings of the Royal Society A: Mathematical, Physical and Engineering Sciences*, *463*(2086), pp.2569-2587.

Cowpertwait, P.S.P., Kilsby, C.G. and O'Connell, P.E., 2002. A space-time Neyman-Scott model of rainfall: Empirical analysis of extremes. Water Resources Research, 38(8), pp.6-1.

Cowpertwait, P.S.P., Lockie, T. and Davis, M.D., 2006. A stochastic spatial-temporal disaggregation model for rainfall. Journal of Hydrology (New Zealand), 45(1), pp.1-12.

Cox, D.R. and Hinkley, D.V., 1979. *Theoretical statistics*. CRC Press.

Cox, D.R. and Isham, V., 1994. Stochastic models of precipitation. *Statistics for the Environment*, *2*, pp.3-18.

Cross, D., 2019. *Modelling intense rainfall in a changing climate* (Doctoral dissertation, Imperial College London).

Dale, M., Luck, B., Fowler, H.J., Blenkinsop, S., Gill, E., Bennett, J., Kendon, E. and Chan, S., 2015, October. New climate change rainfall estimates for sustainable drainage. In Proceedings of the Institution of Civil Engineers-Engineering Sustainability (Vol. 170, No. 4, pp. 214-224). Thomas Telford Ltd.

Davison, A.C. and Smith, R.L., 1990. Models for exceedances over high thresholds. *Journal of the Royal Statistical Society: Series B (Methodological)*, *52*(3), pp.393-425.

Dee, D.P., Uppala, S.M., Simmons, A.J., Berrisford, P., Poli, P., Kobayashi, S., Andrae, U., Balmaseda, M.A., Balsamo, G., Bauer, P., Bechtold, P., Beljaars, A.C.M., van de Berg, L., Bidlot, J., Bormann, N., Delsol, C., Dragani, R., Fuentes, M., Geer, A.J., Haimberger, L., Healy, S.B., Hersbach, H., Hólm, E.V., Isaksen, L., Kållberg, P., Köhler, M., Matricardi, M., McNally, A.P., Monge-Sanz, B.M., Morcrette, J.-J., Park, B.-K., Peubey, C., de Rosnay, P., Tavolato, C., Thépaut, J.-N. and Vitart, F. (2011) The ERA-Interim reanalysis: configuration and performance of the data assimilation system. Quarterly Journal of the Royal Meteorological Society, 137, 553–597.

Dupuis, D.J., 1999. Exceedances over high thresholds: A guide to threshold selection. *Extremes*, *1*(3), pp.251-261.

Einfalt, T., Arnbjerg-Nielsen, K., Golz, C., Jensen, N.E., Quirmbach, M., Vaes, G. and Vieux, B., 2004. Towards a roadmap for use of radar rainfall data in urban drainage. *Journal of Hydrology*, *299*(3-4), pp.186-202.

Emmanouil, S., Langousis, A., Nikolopoulos, E.I. and Anagnostou, E.N., 2020. Quantitative assessment of annual maxima, peaks-over-threshold and multifractal parametric approaches in estimating intensity-duration-frequency curves from short rainfall records. *Journal of Hydrology, 589*, p.125151.

Falconer, K., 2004. Fractal geometry: mathematical foundations and applications. John Wiley & Sons.

Feder, J., 1988. The Cluster Fractal Dimension. In Fractals (pp. 31-40). Springer, Boston, MA.

Feyerherm, A.M. and Bark, L.D., 1967. Goodness of fit of a Markov chain model for sequences of wet and dry days. Journal of Applied Meteorology (1962-1982), pp.770-773.

Fisher, R.A. and Tippett, L.H.C., 1928, April. Limiting forms of the frequency distribution of the largest or smallest member of a sample. In *Mathematical proceedings of the Cambridge philosophical society* (Vol. 24, No. 2, pp. 180-190). Cambridge University Press.

Fowler, H.J. and Kilsby, C.G., 2003. A regional frequency analysis of United Kingdom extreme rainfall from 1961 to 2000. *International Journal of Climatology: A Journal of the Royal Meteorological Society*, *23*(11), pp.1313-1334.

Friedman, J.H., 1991. Estimating functions of mixed ordinal and categorical variables using adaptive splines. Stanford Univ CA Lab for Computational Statistics.

Fung, F (2018). How to Bias Correct, UKCP18 Guidance, Met Office

Gabriel, K.R. and Neumann, J., 1962. A Markov chain model for daily rainfall occurrence at Tel Aviv. Quarterly Journal of the Royal Meteorological Society, 88(375), pp.90-95.

Gibson, J.K., Kållberg, P., Uppala, S.M., Hernandez, A., Nomura, A. and Serrano, E. (1999). ECMWF re-analysis project report 1, ERA-15 description (version 2). Technical Report, ECMWF, Reading, UK.

Golding, B., Clark, P. and May, B., 2005. The Boscastle flood: Meteorological analysis of the conditions leading to flooding on 16 August 2004. *Weather*, *60*(8), pp.230-235.

Graham, R.M., Hudson, S.R. and Maturilli, M., 2019. Improved performance of ERA5 in Arctic gateway relative to four global atmospheric reanalyses. Geophysical Research Letters, 46(11), pp.6138-6147.

Gringorten, I.I., 1963. A plotting rule for extreme probability paper. *Journal of Geophysical Research*, *68*(3), pp.813-814.

Gumbel, E.J., 1958. Statistical theory of floods and droughts. *Journal of the Institution of Water Enigneers and Scientists*, (12), pp.157-184.

Gupta, V.K. and Waymire, E., 1990. Multiscaling properties of spatial rainfall and river flow distributions. Journal of Geophysical Research: Atmospheres, 95(D3), pp.1999-2009.

Gupta, V.K. and Waymire, E.C., 1993. A statistical analysis of mesoscale rainfall as a random cascade. Journal of Applied Meteorology and Climatology, 32(2), pp.251-267.

Haan, C.T., Allen, D.M. and Street, J.O., 1976. A Markov chain model of daily rainfall. *Water Resources Research*, *12*(3), pp.443-449.

Hagelin, S., Son, J., Swinbank, R., McCabe, A., Roberts, N. and Tennant, W., 2017. The Met Office convective-scale ensemble, MOGREPS-UK. *Quarterly Journal of the Royal Meteorological Society*, *143*(708), pp.2846-2861.

Hansen, L.P., 1982. Large sample properties of generalized method of moments estimators. *Econometrica: Journal of the Econometric Society*, pp.1029-1054.

Hersbach, H., Bell, B., Berrisford, P., Hirahara, S., Horányi, A., Muñoz-Sabater, J., Nicolas, J., Peubey, C., Radu, R., Schepers, D. and Simmons, A., 2020. The ERA5 global reanalysis. Quarterly Journal of the Royal Meteorological Society, 146(730), pp.1999-2049.

Hosking, J.R., 1990. L-moments: Analysis and estimation of distributions using linear combinations of order statistics. *Journal of the Royal Statistical Society: Series B (Methodological)*, *52*(1), pp.105-124.

Hubert, P., Tessier, Y., Lovejoy, S., Schertzer, D., Schmitt, F., Ladoy, P., Carbonnel, J.P., Violette, S. and Desurosne, I., 1993. Multifractals and extreme rainfall events. *Geophysical Research Letters*, *20*(10), pp.931-934.

Hulme, M. and Dessai, S., 2008. Negotiating future climates for public policy: a critical assessment of the development of climate scenarios for the UK. environmental science & policy, 11(1), pp.54-70.

Hulme, M. and Jenkins, G., 1998. Climate change scenarios for the United Kingdom scientific report 1998.

Hulme, M., Turnpenny, J. and Jenkins, G.J., 2002. Climate change scenarios for the United Kingdom: the UKCIP02 briefing report (p. 15). Norwich, UK: Tyndall Centre for Climate Change Research, School of Environmental Sciences, University of East Anglia.

Hurst, H.E., 1965. Long term storage. An experimental study.

IPCC, 1990. In: Houghton, J.T., Jenkins, G.J., Ephraums, J.J. (Eds.), Climate Change: the IPCC Scientific Assessment. Cambridge University Press, Cambridge, p. 364.

IPCC, 2013: Climate Change 2013: The Physical Science Basis. Contribution of Working Group I to the Fifth Assessment Report of the Intergovernmental Panel on Climate Change [Stocker, T.F., D. Qin, G.-K. Plattner, M. Tignor, S.K. Allen, J. Boschung, A. Nauels, Y. Xia, V. Bex and P.M. Midgley (eds.)]. Cambridge University Press, Cambridge, United Kingdom and New York, NY, USA, 1535 pp.

Jarušková, D. and Hanek, M., 2006. Peaks over threshold method in comparison with block-maxima method for estimating high return levels of several Northern Moravia precipitation and discharges series. *Journal of Hydrology and Hydromechanics*, *54*(4), pp.309-319.

Jenkins, G.J., Murphy, J.M., Sexton, D.M., Lowe, J.A., Jones, P. and Kilsby, C.G., 2010. UK Climate Projections briefing report.

Jenkinson, A.F., 1955. The frequency distribution of the annual maximum (or minimum) values of meteorological elements. *Quarterly Journal of the Royal Meteorological Society*, *81*(348), pp.158-171.

Jones, P.D., Kilsby, C.G., Harpham, C., Glenis, V. and Burton, A., 2009. UK Climate Projections science report: Projections of future daily climate for the UK from the Weather Generator. UK Climate Projections science report.

Kaczmarska, J.M., 2013. *Single-site point process-based rainfall models in a nonstationary climate* (Doctoral dissertation, UCL (University College London)).

Kaczmarska, J., Isham, V. and Onof, C., 2014. Point process models for fine-resolution rainfall. *Hydrological Sciences Journal*, *59*(11), pp.1972-1991.

Katz, R.W., Parlange, M.B. and Naveau, P., 2002. Statistics of extremes in hydrology. *Advances in water resources*, *25*(8-12), pp.1287-1304.

Kavvas, M.L. and Delleur, J.W., 1975. The stochastic and chronologic structure of rainfall sequences--Application to Indiana.

Kavvas, M.L. and Delleur, J.W., 1981. A stochastic cluster model of daily rainfall sequences. *Water Resources Research*, *17*(4), pp.1151-1160.

Kendon, E.J., Ban, N., Roberts, N.M., Fowler, H.J., Roberts, M.J., Chan, S.C., Evans, J.P., Fosser, G. and Wilkinson, J.M., 2017. Do convection-permitting regional climate models improve projections of future precipitation change?. *Bulletin of the American Meteorological Society*, *98*(1), pp.79-93.

Kendon, E.J., Fosser, G., Murphy, J., Chan, S., Clark, R., Harris, G., Lock, A., Lowe, J., Martin, G., Pirret, J. and Roberts, N., 2019. UKCP Convection-permitting model projections: Science report.

Kendon, M. and McCarthy, M., 2015. The UK's wet and stormy winter of 2013/2014. *Weather*, *70*(2), pp.40-47.

Kendon, E.J., Prein, A.F., Senior, C.A. and Stirling, A., 2021. *Challenges and outlook for convection-permitting climate modelling*. Philosophical Transactions of the Royal Society A, 379(2195), p.20190547.

Kendon, E.J., Roberts, N.M., Fowler, H.J., Roberts, M.J., Chan, S.C. and Senior, C.A., 2014. Heavier summer downpours with climate change revealed by weather forecast resolution model. *Nature Climate Change*, *4*(7), pp.570-576.

Kotz, S. and Neumann, J., 1959. Autocorrelation in precipitation amounts. *Journal of Meteorology*, *16*(6), pp.683-685.

Koutsoyiannis, D. and Onof, C., 2001. Rainfall disaggregation using adjusting procedures on a Poisson cluster model. *Journal of Hydrology*, *246*(1-4), pp.109-122.

Langousis, A., Mamalakis, A., Puliga, M. and Deidda, R., 2016. Threshold detection for the generalized Pareto distribution: Review of representative methods and application to the NOAA NCDC daily rainfall database. *Water Resources Research*, *52*(4), pp.2659-2681.

Leadbetter, M.R., Lindgren, G. and Rootzén, H., 2012. *Extremes and related properties of random sequences and processes*. Springer Science & Business Media.

Lewis, E., Fowler, H., Alexander, L., Dunn, R., McClean, F., Barbero, R., Guerreiro, S., Li, X.F. and Blenkinsop, S., 2019. GSDR: a global sub-daily rainfall dataset. *Journal of Climate*, 32(15), pp.4715-4729.

Lovejoy, S. and Mandelbrot, B.B., 1985. Fractal properties of rain, and a fractal model. Tellus A, 37(3), pp.209-232.

Lowe, J.A., Bernie, D., Bett, P., Bricheno, L., Brown, S., Calvert, D., Clark, R., Eagle, K., Edwards, T., Fosser, G. and Fung, F., 2018. UKCP18 science overview report. *Exeter, UK: Met Office Hadley Centre*.

Lu, Y. and Qin, X.S., 2014. Multisite rainfall downscaling and disaggregation in a tropical urban area. Journal of Hydrology, 509, pp.55-65.

Mandelbrot, B.B., 1975. Stochastic models for the Earth's relief, the shape and the fractal dimension of the coastlines, and the number-area rule for islands. Proceedings of the National Academy of Sciences, 72(10), pp.3825-3828.

Mandelbrot, B.B., 1982. The fractal geometry of nature (Vol. 1). New York: WH freeman.

Marani, M., 2003. On the correlation structure of continuous and discrete point rainfall. Water Resources Research, 39(5).

Marani, M., 2005. Non-power-law-scale properties of rainfall in space and time. Water Resources Research, 41(8).

Marani, M. and Zanetti, S., 2007. Downscaling rainfall temporal variability. Water Resources Research, 43(9).

Maraun, D., 2016. Bias correcting climate change simulations-a critical review. Current Climate Change Reports, 2(4), pp.211-220.

Marra, F. and Morin, E., 2018. Autocorrelation structure of convective rainfall in semiarid-arid climate derived from high-resolution X-Band radar estimates. *Atmospheric Research*, *200*, pp.126-138.

Marsh, T.J. and Dale, M., 2002. The UK floods of 2000–2001: a hydrometeorological appraisal. *Water and Environment Journal*, *16*(3), pp.180-188.

Met Office, 2013. Autumn storm, October 2013. [viewed 3 June 2021] https://www.metoffice.gov.uk/binaries/content/assets/metofficegovuk/pdf/weather/learn-about/uk-past-events/interesting/2013/autumn-storm-october-2013---met-office.pdf

Met Office. Eastern England: climate. [viewed 3 June 2021] https://www.metoffice.gov.uk/binaries/content/assets/metofficegovuk/pdf/weather/learn-about/uk-past-events/regional-climates/eastern-england_-climate---met-office.pdf

McCarthy, M., Spillane, S., Walsh, S. and Kendon, M., 2016. The meteorology of the exceptional winter of 2015/2016 across the UK and Ireland. Weather, 71(12), pp.305-313.

Murphy, J.M., Harris, G.R., Sexton, D.M.H., Kendon, E.J., Bett, P.E., Clark, R.T., Eagle, K.E., Fosser, G., Fung, F., Lowe, J.A. and McDonald, R.E., 2018. UKCP18 land projections: Science report.

Nakicenovic, N., Alcamo, J., Davis, G., Vries, B.D., Fenhann, J., Gaffin, S., Gregory, K., Grubler, A., Jung, T.Y., Kram, T. and La Rovere, E.L., 2000. Special report on emissions scenarios.

Nelder, J.A. and Wedderburn, R.W., 1972. Generalized linear models. *Journal of the Royal Statistical Society: Series A (General)*, *135*(3), pp.370-384.

Neyman, J. and Pearson, E.S., 1933. IX. On the problem of the most efficient tests of statistical hypotheses. *Philosophical Transactions of the Royal Society of London. Series A, Containing Papers of a Mathematical or Physical Character*, *231*(694-706), pp.289-337.

Nigam, S. and Ruiz-Barradas, A., 2006. Seasonal hydroclimate variability over North America in global and regional reanalyses and AMIP simulations: Varied representation. Journal of Climate, 19(5), pp.815-837.

Nkuna, T.R. and Odiyo, J.O., 2016. The relationship between temperature and rainfall variability in the Levubu sub-catchment, South Africa. *International Journal of Education and Learning Systems*, *1*.

Onof, C., 1992. *Stochastic modelling of British rainfall using Poisson processes* (Doctoral dissertation, Imperial College London (University of London)).

Onof, C. and Arnbjerg-Nielsen, K., 2009. Quantification of anticipated future changes in high resolution design rainfall for urban areas. *Atmospheric research*, *92*(3), pp.350-363.

Onof, C., Chandler, R.E., Kakou, A., Northrop, P., Wheater, H.S. and Isham, V., 2000. Rainfall modelling using Poisson-cluster processes: a review of developments. *Stochastic Environmental Research and Risk Assessment*, *14*(6), pp.384-411.

Onof, C., Northrop, P., Wheater, H.S. and Isham, V., 1996. Spatiotemporal storm structure and scaling property analysis for modeling. Journal of Geophysical Research: Atmospheres, 101(D21), pp.26415-26425.

Pagliara, S., 2020. *Rainfall modelling for a changing climate*. MSc dissertation, Imperial College London.

Pui, A., Sharma, A., Mehrotra, R., Sivakumar, B. and Jeremiah, E., 2012. A comparison of alternatives for daily to sub-daily rainfall disaggregation. Journal of Hydrology, 470, pp.138-157.

Pulquério, M., Garrett, P., Santos, F.D. and Cruz, M.J., 2015. On using a generalized linear model to downscale daily precipitation for the center of Portugal: an analysis of trends and extremes. *Theoretical and Applied Climatology*, *120*(1), pp.147-158.

R Core Team, 2019. R: A language and environment for statistical computing. R Foundation for Statistical Computing, Vienna, Austria. URL https://www.R-project.org/.

Rodriguez-Iturbe, I., Cox, D.R. and Isham, V., 1987. Some models for rainfall based on stochastic point processes. *Proceedings of the Royal Society of London. A. Mathematical and Physical Sciences*, *410*(1839), pp.269-288.

Rodriguez-Iturbe, I., Cox, D.R. and Isham, V., 1988. A point process model for rainfall: further developments. *Proceedings of the Royal Society of London. A. Mathematical and Physical Sciences*, *417*(1853), pp.283-298.

Rodriguez-Iturbe, I., Gupta, V.K. and Waymire, E., 1984. Scale considerations in the modeling of temporal rainfall. *Water Resources Research*, *20*(11), pp.1611-1619.

Schertzer, D. and Lovejoy, S., 1987. Physical modeling and analysis of rain and clouds by anisotropic scaling multiplicative processes. *Journal of Geophysical Research: Atmospheres*, *92*(D8), pp.9693-9714.

Searcy, J.K. and Hardison, C.H., 1950. Manual of hydrology: Part I, General surface-water techniques. *Geological Survey Water-supply Paper*, *31*.

Segond, M.L., Onof, C. and Wheater, H.S., 2006. Spatial–temporal disaggregation of daily rainfall from a generalized linear model. *Journal of Hydrology*, *331*(3-4), pp.674-689.

Smith, R.L., 2001. Extreme value statistics in meteorology and the environment. *Environmental statistics*, *8*, pp.300-357.

Sonntag, D., 1990. Important new values of the physical constants of 1986, vapour pressure formulations based on the ITS-90, and psychrometer formulae. Zeitschrift für Meteorologie, 40(5), pp.340-344.

Srikanthan, R. and McMahon, T.A., 2001. Stochastic generation of annual, monthly and daily climate data: A review. *Hydrology and Earth System Sciences*, *5*(4), pp.653-670.

Srikanthan, R., Sharma, A. and McMahon, T.A., 2006. Comparison of two nonparametric alternatives for stochastic generation of monthly rainfall. Journal of Hydrologic Engineering, 11(3), pp.222-229.

Stern, R.D. and Coe, R., 1984. A model fitting analysis of daily rainfall data. *Journal of the Royal Statistical Society: Series A (General)*, *147*(1), pp.1-18.

Tessier, Y., Lovejoy, S. and Schertzer, D., 1993. Universal multifractals: Theory and observations for rain and clouds. Journal of Applied Meteorology and Climatology, 32(2), pp.223-250.

Tetzner, D., Thomas, E. and Allen, C., 2019. A validation of ERA5 reanalysis data in the southern Antarctic peninsula—Ellsworth Land region, and its implications for ice Core studies. Geosciences, 9(7), p.289.

Thyer, M. and Kuczera, G., 2000. Modeling long-term persistence in hydroclimatic time series using a hidden state Markov Model. *Water resources research*, *36*(11), pp.3301-3310.

Tsonis, A.A. and Elsner, J.B., 1995. Testing for scaling in natural forms and observables. Journal of Statistical Physics, 81(5), pp.869-880.

Uppala, S.M., Kållberg, P.W., Simmons, A.J., Andrae, U., Bechtold, V.D.C., Fiorino, M., Gibson, J.K., Haseler, J., Hernandez, A., Kelly, G.A. and Li, X., 2005. The ERA-40 re-analysis. Quarterly Journal of the Royal Meteorological Society: A journal of the atmospheric sciences, applied meteorology and physical oceanography, 131(612), pp.2961-3012.

Urraca, R., Huld, T., Gracia-Amillo, A., Martinez-de-Pison, F.J., Kaspar, F. and Sanz-Garcia, A., 2018. Evaluation of global horizontal irradiance estimates from ERA5 and COSMO-REA6 reanalyses using ground and satellite-based data. Solar Energy, 164, pp.339-354.

Van Vuuren, D.P., Edmonds, J., Kainuma, M., Riahi, K., Thomson, A., Hibbard, K., Hurtt, G.C., Kram, T., Krey, V., Lamarque, J.F. and Masui, T., 2011. The representative concentration pathways: an overview. Climatic change, 109(1), pp.5-31.

Vicente-Serrano, S.M. and Beguería-Portugués, S., 2003. Estimating extreme dry-spell risk in the middle Ebro valley (northeastern Spain): a comparative analysis of partial duration series with a general Pareto distribution and annual maxima series with a Gumbel distribution. *International Journal of Climatology: A Journal of the Royal Meteorological Society*, *23*(9), pp.1103-1118.

Wheater, H.S., Chandler, R.E., Onof, C.J., Isham, V.S., Bellone, E., Yang, C., Lekkas, D., Lourmas, G. and Segond, M.L., 2005. Spatial-temporal rainfall modelling for flood risk estimation. *Stochastic Environmental Research and Risk Assessment*, *19*(6), pp.403-416.

Wheater, H.S., Isham, V.S., Cox, D.R., Chandler, R.E., Kakou, A., Northrop, P.J., Oh, L., Onof, C. and Rodriguez-Iturbe, I., 2000a. Spatial-temporal rainfall fields: modelling and statistical aspects. *Hydrology and Earth System Sciences*, *4*(4), pp.581-601.

Wheater, H. S., Isham, V. S., Onof, C., Chandler, R. E., Northrop, P. J., Guiblin, P., Bate, S. M., Cox, D. R., and Koutsoyiannis, D., 2000b. Generation of spatially consistent rainfall data. Report to the Ministry of Agriculture, Fisheries and Food (2 volumes).

Wigley, T.M.L., Jones, P.D. and Kelly, P.M., 1980. Scenario for a warm, high-CO2 world. Nature, 283(5742), pp.17-21.

Yan, Z., Bate, S., Chandler, R.E., Isham, V. and Wheater, H., 2002. An analysis of daily maximum wind speed in northwestern Europe using generalized linear models. *Journal of Climate*, *15*(15), pp.2073-2088.

Yan, Z., Bate, S., Chandler, R.E., Isham, V. and Wheater, H., 2006. Changes in extreme wind speeds in NW Europe simulated by generalized linear models. *Theoretical and Applied Climatology*, *83*(1), pp.121-137.

Yang, C., Chandler, R.E., Isham, V.S. and Wheater, H.S., 2005. Spatial-temporal rainfall simulation using generalized linear models. *Water Resources Research*, *41*(11).

References on geotechnical modelling

Aitchison, G.D., 1968. *Separate roles of site investigation, quantification of soil properties, and selection of operational environment in the determination of foundation design on expansive soils.* In Israel Soc Soil Mechanics & Fdn Eng Asian Conf Soil Mech & Fdn E Proc/Is/.

Albrecht, B.A. and Benson, C.H., 2001. Effect of desiccation on compacted natural clays. Journal of Geotechnical and Geoenvironmental Engineering, 127(1), pp.67-75.

Allen, R.G., Pereira, L.S., Raes, D. and Smith, M., 1998. *Crop evapotranspiration-Guidelines for computing crop water requirements*-FAO Irrigation and drainage paper 56. Fao, Rome, 300(9), p.D05109.

Alonso, E.E., Gens, A. and Josa, A., 1990. *A constitutive model for partially saturated soils*. Géotechnique, 40(3), pp.405-430.

Allsop, W., Kortenhaus, A., Morris, M., Buijs, F.A., Visser, P.J., ter Horst, W.L.A., Hassan, R., Young, M., Van Gelder, P.H.A.J.M., Doorn, N. and Dyer, M., 2008. *Failure mechanisms for flood defence structures.*

Arup Geotechnics. (2007) *Monitoring of London Clay Embankments: Geotechnical Interpretative Report.* Report number: 121286-00/GIR/SSV&SSV/01.

Barber, E.S., 1961. *Notes on secondary consolidation*. In Highway Research Board Proceedings (Vol. 40).

Bishop, A.W., 1955. *The use of the slip circle in the stability analysis of slopes*. Geotechnique, 5(1), pp.7-17.

Bishop, A.W., 1959. *The principle of effective stress*. Teknisk ukeblad, 39, pp.859-863.

Bodas-Freitas, T.M., Potts, D.M. and Zdravkovic, L., 2011. *A time dependent constitutive model for soils with isotach viscosity*. Computers and Geotechnics, 38(6), pp.809-820.

Bodas-Freitas, T.M., Potts, D.M. and Zdravkovic, L., 2015. *Numerical study on the response of two footings at Bothkennar research site.* Géotechnique, 65(3), pp.155-168.

Briggs, K.M., Smethurst, J.A., Powrie, W. and O'Brien, A.S., 2016. *The influence of tree root water uptake on the long term hydrology of a clay fill railway embankment*. Transportation Geotechnics, 9, pp.31-48.

Buijs, F., Simm, J., Wallis, M. and Sayers, P., 2007. *Performance and reliability of flood and coastal defences.* Environment Agency, London.

Burland, J.B., 1964. *Effective stresses in partly saturated soils*. Geotechnique, 14(1), pp.64-68.

Burland, J.B., 1965. *Some Aspects of the Mechanical Behaviour of Party Saturated Soils.* Moisture equilibria and moisture changes in soils beneath covered areas, pp.270-278.

Chalmers, T., 2013. Effect of seasonal changes in pore water pressures on the behaviour of railways embankments in the UK. MSc dissertation, *Imperial College London*.

CIRIA, 2013. *The international levee handbook*. Ciria.

Cooling, L.F and Marsland, A. (1954). Soil Mechanics of Failures in the Sea Defence Banks of Essex and Kent. ICE Conference on the North Sea Floods of 31 January / 1 February 1953.

Cotecchia, F., Pedone, G., Bottiglieri, O., Santaloia, F. and Vitone, C., 2014. *Slope-atmosphere interaction in a tectonized clayey slope: a case study.* Italian Geotechnical Journal, 1(14), pp.34-61.

Croney, D. 1977. *The design and performance of road pavements*. HMSO London.

Cui, Y.J., Delage, P. and Sultan, N., 1995. *An elasto-plastic model for compacted soils*. In PROCEEDINGS OF THE FIRST INTERNATIONAL CONFERENCE ON UNSATURATED SOILS/UNSAT'95/PARIS/FRANCE/6-8 SEPTEMBER 1995. VOLUME 2.

Dexter, A.R., Czyż, E.A. and Richard, G., 2012. Equilibrium, non-equilibrium and residual water: consequences for soil water retention. *Geoderma*, *177*, pp.63-71.

Dixon, N. and Bromhead, E.N., 1999. Depth-dependent permeability in London Clay measured using standpipe piezometer equilibration data. *Géotechnique*, *49*(5), pp.651-660.

Dixon, N., Crosby, C.J., Stirling, R., Hughes, P.N., Smethurst, J., Briggs, K., Hughes, D., Gunn, D., Hobbs, P., Loveridge, F. and Glendinning, S., 2019. In situ measurements of near-surface hydraulic conductivity in engineered clay slopes. *Quarterly Journal of Engineering Geology and Hydrogeology*, *52*(1), pp.123-135.

Dounias, G.T., 1987. Progressive failure in embankment dams. Ph.D. thesis, Imperial College, University of London, UK.

Drucker, D.C., Gibson, R.E. and Henkel, D.J., 1957. *Soil mechanics and work-hardening theories of plasticity*. Transactions of the American Society of Civil Engineers, 122(1), pp.338-346.

Dyer, M., 2004. Performance of flood embankments in England and Wales. In Proceedings of the Institution of Civil Engineers-Water Management (Vol. 157, No. 4, pp. 177-186). Thomas Telford Ltd.

Environment Agency, 2007. Technical design details – embankments, No 110_07, version 1, Environment Agency, Bristol, UK

Eurocode, C.E.N., 2004. *7: Geotechnical Design—Part 1: General Rules. EN1997-1*. Brussels: European Committee for Standardization.

Feddes, R. A., Kowalik, P. J., Zaradny, H., 1978. *Water uptake by plant roots*. In Simulation of Field Water Use and Crop Yield. Eds RA Feddes, PJ Kowalik and H Zaradny. pp 16–30. John Wiley & Sons, Inc., New York.

Fredlund, D.G. and Morgenstern, N.R., 1977. *Stress state variables for unsaturated soils.* Journal of the geotechnical engineering division, 103(5), pp.447-466.

Fredlund, D.G. and Rahardjo, H., 1993. *Soil mechanics for unsaturated soils*. John Wiley & Sons.

Gallipoli, D., Gens, A., Sharma, R. and Vaunat, J., 2003. *An elasto-plastic model for unsaturated soil incorporating the effects of suction and degree of saturation on mechanical behaviour*. Géotechnique, 53(1), pp.123-135.

Gasparre, A., 2005. *Advanced laboratory characterisation of London Clay* (Doctoral thesis, Imperial College London).

Gatmiri, B., Najari, M., 2009. Modeling of Settlement and Induced Matric Suction in Multiphase Porous Media under Root Water Uptake Effect by F.E.M. Communications in Numerical Methods Engineering. doi:10.1002/cnm.1264.

Georgiadis, K., 2003. *Development, implementation and application of partially saturated soil models in finite element analysis* (Doctoral thesis, Imperial College London).

Georgiadis, K., Potts, D.M. and Zdravkovic, L., 2005. *Three-dimensional constitutive model for partially and fully saturated soils*. International Journal of Geomechanics, 5(3), pp.244-255.

Geotechnical Observations. (2013) 07 - 011 Magnolia Road Southend - Raw Data. [Dataset].

Ghiadistri, G.M., 2019. *Constitutive modelling of compacted clays for applications in nuclear waste disposal* (Doctoral thesis, Imperial College London).

Golder, H.Q. and Palmer, D.J., 1955. Investigation of a bank failure at Scrapsgate, Isle of Sheppey, Kent. *Géotechnique*, *5*(1), pp.55-73.

Google. (2021) *Google maps.* [Online] Available from: https://maps.google.co.uk/ [Accessed 12/01/2021].

Grammatikopoulou, A., Zdravkovic, L. and Potts, D.M., 2007. *The effect of the yield and plastic potential deviatoric surfaces on the failure height of an embankment.* Géotechnique, 57(10), pp.795-806.

Greenwood, J.R., Norris, J.E. and Wint, J., 2004. *Assessing the contribution of vegetation to slope stability*. Proceedings of the Institution of Civil Engineers-Geotechnical Engineering, 157(4), pp.199-207.

Hartlen, J. and Ingers, C., 1981, “Land Reclamation Using FineGrained Dredged Material,” Proceedings of the 10th International Conference on Soil Mechanics and Foundation Engineering, Balkema, Rotterdam, Vol. 1, pp. 145–148.

Hemmati S., 2009, Etude de l'interaction Sol-Végétation-Atmosphère avec une approche couplée Thermo-Hydro-Mécanique, PhD thesis, Ecole Nationale des Ponts et Chaussées, France.

Hight, D.W., McMillan, F., Powell, J.J.M., Jardine, R.J. and Allenou, C.P., 2003. Some characteristics of London clay. *Characterisation and engineering properties of natural soils*, *2*, pp.851-946.

Hight, D.W., Paul, M.A., Barras, B.F., Powell, J.J.M., Nash, D.F.T., Smith, P.R., Jardine, R.J. and Edwards, D.H., 2003. The characterisation of the Bothkennar clay. *Characterisation & Engineering Properties of Natural Soils*, *1*, pp.543-597.

Jardine, R.J., Potts, D.M., Fourie, A.B. and Burland, J.B., 1986. Studies of the influence of non-linear stress–strain characteristics in soil–structure interaction. *Geotechnique*, *36*(3), pp.377-396.

Janbu, N., 1973. *Slope stability computations–Embankment–Dam Engineering*, Casagrande Volume. John Wiley and Sons, New York, pp.47-86.

Jennings, J.E.B. and Burland, J.B., 1962. *Limitations to the use of effective stresses in partly saturated soils*. Géotechnique, 12(2), pp.125-144.

Jommi, C., 2000. *Remarks on the constitutive modelling of unsaturated soils*. In Experimental evidence and theoretical approaches in unsaturated soils (pp. 147-162). CRC Press.

Josa, A., Balmaceda, A., Gens, A. and Alonso, E.E., 1992. *An elastoplastic model for partially saturated soils exhibiting a maximum of collapse*. In 3rd international conference on computational plasticity, Barcelona (Vol. 1, pp. 815-826).

Kovacevic, N., 1994. *Numerical analyses of rockfill dams, cut slopes and road embankments.* Ph.D. thesis, Imperial College, University of London, UK.

Kovacevic, N., 1997. Assessing the safety of old embankment dams by observing and analysing movement during reservoir operation. In *Inter. Conf. on Large Dams* (pp. 551-566).

Kovacevic, N., Hight, D.W. and Potts, D.M., 2007. Predicting the stand-up time of temporary London Clay slopes at Terminal 5, Heathrow Airport. *Géotechnique*, *57*(1), pp.63-74.

Kovacevic, N., Potts, D.M. and Vaughan, P.R., 2008. Recent advances in the numerical modelling of embankment dams. In *Ensuring reservoir safety into the future: Proceedings of the 15th Conference of the British Dam Society at the University of Warwick from 10–13 September 2008* (pp. 164-176). Thomas Telford Publishing.

Ladd, C.C. and Edgers, L., 1972. Consolidated-Undrained Direct-Simple Shear Tests on Saturated Clays. Massachusetts Institute of Technology Cambridge Soil Mechanics Division.

Ladd, C.C., Foott, R., Ishihara, K., Schlosser, F. and Poulos, H.G., 1977. Stress-deformation and strength characteristics. ICSMFE 9, Tokyo, July 1977. In *Proceedings* (Vol. 2, pp. 421-494).

Lade, P.V. and Duncan, J.M., 1975. Elastoplastic stress-strain theory for cohesionless soil. *Journal of the Geotechnical Engineering Division*, *101*(10), pp.1037-1053.

Lagioia, R., Puzrin, A.M. and Potts, D.M., 1996. *A new versatile expression for yield and plastic potential surfaces*. Computers and Geotechnics, 19(3), pp.171-191.

Lambe, T.W., 1964. *Methods of estimating settlement*. Journal of the Soil Mechanics and Foundations Division, 90(5), pp.43-67.

Lee, J. S., 2019. Assessment of modelling procedure for climate change-induced rainfall events. MEng dissertation, *Imperial College London*.

Leroueil, S., Leart, P., Hight, D.W. and Powell, J.J.M., 1992. Hydraulic conductivity of a recent estuarine silty clay at Bothkennar. *Geotechnique*, *42*(2), pp.275-288.

Little, A.L. and Price, V.E., 1958. *The use of an electronic computer for slope stability analysis*. Geotechnique, 8(3), pp.113-116.

Lo, K.Y., 1961. *Secondary compression of clays.* Journal of the Soil Mechanics and Foundations Division, 87(4), pp.61-88.

Losacco N., 2007. *Raising of embankments on soft clay.* MSc dissertation. Imperial College London.

Marsland, A., 1957. The design and construction of earthen flood banks. *J. Inst. Water Eng*, *11*(3), pp.236-258.

Marsland, A., 1968. The shrinkage and fissuring of clay in flood banks. Building Research Station internal note.

Marsland, A., 1973, October. Instrumentation of flood defense banks along the river Thames. In *This paper was originally published in Proceeding of the British Geotechnical Society Symposium on Field Instrumentation, held May 30-June 1, 1973 at the Institution Of Electrical Engineers, London.*.

Marsland, A., 1974. Investigation for proposed flood defence banks along the South Bank of the River Thames between the River Darenth (Longreach) and Greenhithe. *Building Research Establishment (BRE).*

Marsland A. and Powell J. M., 1977. The behaviour of a trial bank constructed to failure on soft alluvium of the River Thames. *Proc. Int. Symp. on Soft Clay*, Bangkok, 505-525.

Marsland, A., 1986. The flood plain deposits of the Lower Thames. *Quarterly Journal of Engineering Geology and Hydrogeology*, *19*(3), pp.223-247.

Matsuoka, H. and Nakai, T., 1974. *Stress-deformation and strength characteristics of soil under three different principal stresses.* In Proceedings of the Japan Society of Civil Engineers (Vol. 1974, No. 232, pp. 59-70). Japan Society of Civil Engineers.

Melgarejo-Corredor, ML, 2004. Laboratory and numerical investigations of soil retention curves. PhD thesis, *Imperial College London*.

Mesri, G., 1973. *Coefficient of secondary compression.* Journal of the soil mechanics and foundations division, 99(1), pp.123-137.

Met Office (2012): Met Office Integrated Data Archive System (MIDAS) Land and Marine Surface Stations Data (1853-current). NCAS British Atmospheric Data Centre, 7/6/2017.

Meyer, J.L., Gebeault, V.A. and Youngner, V.B., 1985. *Irrigation of turfgrass below replacement of evapotranspiration as a means of water conservation: Determining crop coefficient of turfgrasses.* In Proceedings of the 5th international turfgrass research conference, Avignon, July 1-5, 1985 (pp. 357-364).

Monroy, R., 2006. *The influence of load and suction changes on the volumetric behaviour of compacted London Clay* (Doctoral thesis, Imperial College London (University of London)).

Monroy, R., Zdravkovic, L. and Ridley, A., 2010. *Evolution of microstructure in compacted London Clay during wetting and loading.* Géotechnique, 60(2), pp.105-119.

Monroy, R., Zdravkovic, L. and Ridley, A.M., 2015. *Mechanical behaviour of unsaturated expansive clay under K0 conditions*. Engineering Geology, 197, pp.112-131.

Monteith, J.L., 1965. *Evaporation and environment*. In Symposia of the society for experimental biology (Vol. 19, pp. 205-234). Cambridge University Press (CUP) Cambridge.

Morgenstern, N.U. and Price, V.E., 1965. *The analysis of the stability of general slip surfaces*. Geotechnique, 15(1), pp.79-93.

Nash, D.F.T., Sills, G.C. and Davison, L.R., 1992. One-dimensional consolidation testing of soft clay from Bothkennar. *Géotechnique*, *42*(2), pp.241-256.

Ng, C.W.W., Ni, J.J., Leung, A.K. and Wang, Z.J., 2016. A new and simple water retention model for root-permeated soils. *Géotechnique Letters*, *6*(1), pp.106-111.

Ng, C.W., Wang, B. and Tung, Y.K., 2001. *Three-dimensional numerical investigations of groundwater responses in an unsaturated slope subjected to various rainfall patterns*. Canadian Geotechnical Journal, 38(5), pp.1049-1062.

Ni, J.J., Leung, A.K. and Ng, C.W.W., 2018. *Modelling soil suction changes due to mixed species planting*. Ecological Engineering, 117, pp.1-17.

Nyambayo, V. P., Potts, D.M., and Addenbrooke, T.I., 2004. *"The Influence Of Permeability On The Stability Of Embankments Experiencing Seasonal Cyclic Pore Water Pressure Changes."* In Advances in geotechnical engineering: The Skempton conference: Proceedings of a three day conference on advances in geotechnical engineering, organised by the Institution of Civil Engineers and held at the Royal Geographical Society, London, UK, on 29–31 March 2004, pp. 898-910. Thomas Telford Publishing, 2004.

Nyambayo, V.P. and Potts, D.M., 2010. *Numerical simulation of evapotranspiration using a root water uptake model*. Computers and Geotechnics, 37(1-2), pp.175-186.

O'Brien, A., 2013. *The assessment of old railway embankments–time for a change?*. In Partial Saturation in Compacted Soils: Géotechnique Symposium in Print 2011 (pp. 19-32).

O'Brien, A. S., E. A. Ellis, and D. Russell. *"Old railway embankment clay fill–laboratory experiments, numerical modelling and field behaviour*." In Advances in geotechnical engineering: The Skempton conference: Proceedings of a three day conference on advances in geotechnical engineering, organised by the Institution of Civil Engineers and held at the Royal Geographical Society, London, UK, on 29–31 March 2004, pp. 911-921. Thomas Telford Publishing, 2004.

Ordnance Survey. (2010) old-maps.co.uk. [Online] Available from: http://www.old-maps.co.uk/index.html [Accessed 10/09/2017].

Penman, H.L., 1948. *Natural evaporation from open water, bare soil and grass.* Proceedings of the Royal Society of London. Series A. Mathematical and Physical Sciences, 193(1032), pp.120-145.

Perzyna, P., 1963. *The constitutive equations for rate sensitive plastic materials.* Quarterly of applied mathematics, 20(4), pp.321-332.

Pirone, M., 2009. Analysis of slope failure mechanism in unsaturated pyroclastic soils, based on testing site monitoring PhD thesis. *University of Naples, Federico II, Naples, Italy*.

Potts, D.M., Dounias, G.T. and Vaughan, P.R., 1990. Finite element analysis of progressive failure of Carsington embankment, Géotechnique, 40, 79–101.

Potts, D.M., Zdravkovic, L., 1999. *Finite element analysis in geotechnical engineering: Theory*. Thomas Telford, London.

Potts, D.M., Zdravković, L., Addenbrooke, T.I., Higgins, K.G. and Kovačević, N., 2001. *Finite element analysis in geotechnical engineering: application* (Vol. 2). London: Thomas Telford.

Powell, J.M. and Uglow, I., 1987. Effect of tidal loading on groundwater and stability of flood banks. In *European conference on soil mechanics and foundation engineering. 9* (pp. 317-322).

Prasad, R., 1988. *A linear root water uptake mode*l. Journal of Hydrology, 99(3-4), pp.297-306.

Richards, L.A., 1931. *Capillary conduction of liquids through porous mediums*. Physics, 1(5), pp.318-333.

Richards, L.A. and Weaver, L.R., 1943. Fifteen-atmosphere percentage as related to the permanent wilting percentage. *Soil Science*, *56*(5), pp.331-340.

Robinson, R.G., Tan, T.S., Dasari, G.R., Leung, C.F. and Vijayakumar, A., 2005. Experimental study of the behavior of a lumpy fill of soft clay. *International Journal of Geomechanics*, *5*(2), pp.125-137.

Roscoe, K. and Burland, J.B., 1968. On the generalized stress-strain behaviour of wet clay. *Engineering Plasticity*, pp.535-609.

Roscoe, K.H., Schofield, A. and Wroth, A.P., 1958. *On the yielding of soils*. Geotechnique, 8(1), pp.22-53.

Roscoe, K.H., Schofield, A. and Thurairajah, A., 1963. *Yielding of clays in states wetter than critical*. Geotechnique, 13(3), pp.211-240.

Schofield, A.N. and Wroth, P., 1968. *Critical state soil mechanics* (Vol. 310). London: McGraw-hill.

Shinozuka, M., Feng, M.Q., Lee, J. and Naganuma, T., 2000. *Statistical analysis of fragility curves*. Journal of engineering mechanics, 126(12), pp.1224-1231.

Skempton, A.W. and Bjerrum, L., 1957. *A contribution to the settlement analysis of foundations on clay*. Geotechnique, 7(4), pp.168-178.

Smethurst, J.A., Briggs, K.M., Powrie, W., Ridley, A. and Butcher, D.J.E., 2015. Mechanical and hydrological impacts of tree removal on a clay fill railway embankment. *Géotechnique*, *65*(11), pp.869-882.

Smethurst, J.A., Clarke, D. and Powrie, W., 2012. Factors controlling the seasonal variation in soil water content and pore water pressures within a lightly vegetated clay slope. *Géotechnique*, *62*(5), pp.429-446.

Smith, K., Hinchsliffe, K., Harding, M., 2009. Flood embankment vegetation management trials – final report, Science report SC030228/SR1, Environment Agency, Bristol.

Smith, P.G.C. 2003. *Numerical analysis of infiltration into partially saturated soil slopes*. Ph.D. thesis, Imperial College, University of London, UK.

Smith, P.G.C., Potts, D.M. and Addenbrooke, T.I., 2008. A precipitation boundary condition for finite element analysis. In *Proceedings of the 1st European Conference on Unsaturated Soils* (Vol. 773, p. 778).

Sorenson, K.K., 2006. *Influence of viscosity and ageing on the behaviour of clays.* Ph.D thesis. University of London.

Stirling, R.A., Toll, D.G., Glendinning, S., Helm, P.R., Yildiz, A., Hughes, P.N. and Asquith, J.D., 2021. Weather-driven deterioration processes affecting the performance of embankment slopes. *Géotechnique*, *71*(11), pp.957-969.

Taborda, D.M.G. and Zdravkovic, L., 2012. Application of a Hill-Climbing technique to the formulation of a new cyclic nonlinear elastic constitutive model. *Computers and Geotechnics*, *43*, pp.80-91.

Taborda, D. M. G., Potts, D. M. & Zdravkovic´, L. 2016. On the assessment of energy dissipated through hysteresis in finite element analysis. *Computers and Geotechnics, 71*, pp.180–194.

Tarantino, A., 2007. *A possible critical state framework for unsaturated compacted soils*. Géotechnique, 57(4), pp.385-389.

Tommasi, P., Boldini, D., Caldarini, G. and Coli, N., 2013. *Influence of infiltration on the periodic re-activation of slow movements in an overconsolidated clay slope*. Canadian Geotechnical Journal, 50(1), pp.54-67.

Tsaparas, I., Rahardjo, H., Toll, D.G. and Leong, E.C., 2002. *Controlling parameters for rainfall-induced landslides*. Computers and geotechnics, 29(1), pp.1-27.

Tsiampousi, A., 2011. *Numerical analysis of slopes in unsaturated soils (*Doctoral thesis, Imperial College London).

Tsiampousi, A., Zdravković, L. and Potts, D.M., 2013a. A new Hvorslev surface for critical state type unsaturated and saturated constitutive models. *Computers and Geotechnics*, *48*, pp.156-166.

Tsiampousi, A., Zdravković, L. and Potts, D.M., 2013b. Variation with time of the factor of safety of slopes excavated in unsaturated soils. *Computers and Geotechnics*, *48*, pp.167-178.

Tsiampousi, A., Zdravković, L. and Potts, D.M., 2013c. A three-dimensional hysteretic soil-water retention curve. *Géotechnique*, *63*(2), pp.155-164.

Tsiampousi, A., Zdravkovic, L. and Potts, D.M., 2017. *Numerical study of the effect of soil–atmosphere interaction on the stability and serviceability of cut slopes in London clay*. Canadian Geotechnical Journal, 54(3), pp.405-418.

UNISDR, 2015. The human cost of natural disasters: A global perspective.

USACE, 1999. *Risk-based analysis in geotechnical engineering for support of planning studies.* ETL, (1110-2-556).

USACE Sacremento District, 2008. Geotechnical levee practice, standard operating procedures, REFP10L0, US Army Corps of Engineers, Washington DC, USA.

Van Eekelen, H.A.M., 1980. Isotropic yield surfaces in three dimensions for use in soil mechanics. *International Journal for Numerical and Analytical Methods in Geomechanics*, *4*(1), pp.89-101.

Van Genuchten, M.T., 1980. A closed-form equation for predicting the hydraulic conductivity of unsaturated soils. *Soil science society of America journal*, *44*(5), pp.892-898.

Vaughan, P.R., 1994. Assumption, prediction and reality in geotechnical engineering. *Géotechnique*, *44*(4), pp.573-609.

Veylon, G., Ghestem, M., Stokes, A. and Bernard, A., 2015. Quantification of mechanical and hydric components of soil reinforcement by plant roots. *Canadian Geotechnical Journal*, *52*(11), pp.1839-1849.

Vrouwenvelder, A.C.W.M., Steenbergen, H.M.G.M. and Slijkhuis, K.A.H., 2001. *Theoretical manual of PC-Ring, Part A: descriptions of failure modes*.

Walbancke, H.J., 1976. Pore pressure in clay embankments and cuttings', PhD thesis, Imperial College, University of London.

Wang, Z.F., Li, J.H. and Zhang, L.M., 2011. *Influence of cracks on the stability of a cracked soil slope*. In Proc., 5th Asia-Pacisif Conf. on Unsaturated Soils (AP-UNSAT 2011) (pp. 721-728).

Wheeler, S.J., Sharma, R.S. and Buisson, M.S.R., 2003. *Coupling of hydraulic hysteresis and stress–strain behaviour in unsaturated soils*. Géotechnique, 53(1), pp.41-54.

Wheeler, S.J. and Sivakumar, V., 1995. *An elasto-plastic critical state framework for unsaturated soil*. Géotechnique, 45(1), pp.35-53.

Wiecheteck, L.H., Giarola, N.F., de Lima, R.P., Tormena, C.A., Torres, L.C. and de Paula, A.L., 2020. Comparing the classical permanent wilting point concept of soil (− 15,000 hPa) to biological wilting of wheat and barley plants under contrasting soil textures. *Agricultural Water Management*, *230*, p.105965.

Wilson, G. W., Fredlund, D. G., and Barbour, S. L. (1994). "Coupled soil-atmosphere modelling for soil evaporation." Canadian Geotechnical Journal, 31(2), 151-161.

Yin, J.H., 1999. *Non-linear creep of soils in oedometer tests*. Geotechnique, 49(5), pp.699-707.

Yin, J.H., Zhu, J.G. and Graham, J., 2002. *A new elastic viscoplastic model for time-dependent behaviour of normally and overconsolidated clays: theory and verification.* Canadian Geotechnical Journal, 39(1), pp.157-173.

Zdravkovic, L., Potts, D.M. & Bodas Freitas, T.M. (2019). *Extending the life of existing infrastructure.* In Proceedings of the XVII ECSMGE-2019 Geotechnical Engineering foundation of the future. Reykjavik Iceland: Icelandic Geotechnical Society. doi:10.32075/17ECSMGE-2019-1104

Zdravkovic, L., Potts, D.M. and St John, H.D., 2011. *Modelling of a 3D excavation in finite element analysis*. In Stiff Sedimentary Clays: Genesis and Engineering Behaviour: Géotechnique Symposium in Print 2007 (pp. 319-335). Thomas Telford Ltd.

Zdravković, L., Taborda, D.M., Potts, D.M., Abadias, D., Burd, H.J., Byrne, B.W., Gavin, K.G., Houlsby, G.T., Jardine, R.J., Martin, C.M. and McAdam, R.A., 2020. *Finite-element modelling of laterally loaded piles in a stiff glacial clay till at Cowden. Géotechnique*, *70*(11), pp.999-1013.

Zhang, F., Fredlund, D.G., Wilson, G.W. and Sedgwick, A., 2014, December. *Determination of the permeability function for drying oil sands tailings undergoing volume change and desaturation*. In Proceedings of the 4th International Oil Sands Tailings Conference, Banff, AB 2014.

APPENDIX

Appendix A: Monthly summary statistics for Rayleigh

Table A.1: Monthly summary statistics for Rayleigh (standard methodology).

	Jan	Feb	Mar	Apr	May	June	July	Aug	Sep	Oct	Nov	Dec
Mean 1h (mm/h)	0.0791	0.0675	0.0434	0.0436	0.0559	0.0537	0.0735	0.0663	0.0424	0.0758	0.0777	0.0678
CoeffVar 0.25h	5.72	5.63	7.02	10.69	11.27	10.63	10.88	10.10	11.09	6.78	6.13	6.03
CoeffVar 1h	4.53	4.46	5.35	7.23	7.44	7.69	7.63	7.19	7.39	5.08	4.83	4.75
CoeffVar 6h	2.98	2.99	3.30	4.13	4.36	4.01	4.43	3.94	4.80	3.26	3.05	3.26
CoeffVar 24h	1.65	1.84	1.99	2.31	2.52	2.30	2.43	2.31	2.86	1.97	1.90	1.91
Skewness 0.25h	10.24	8.99	12.03	16.17	15.89	19.31	22.20	16.91	18.09	13.83	11.33	10.53
Skewness 1h	7.67	6.99	8.54	10.47	10.19	12.40	13.06	10.53	10.58	8.82	7.67	7.33
Skewness 6h	4.45	4.18	4.61	5.26	5.90	5.47	6.32	5.60	6.50	4.87	4.17	4.68
Skewness 24h	2.12	2.07	2.43	2.56	2.89	2.81	2.82	2.78	3.26	2.60	2.23	2.38
Ac 0.25h	0.557	0.537	0.508	0.423	0.520	0.506	0.401	0.514	0.503	0.532	0.552	0.547
Ac 1h	0.476	0.546	0.444	0.401	0.454	0.352	0.266	0.378	0.430	0.453	0.480	0.521
Ac 6h	0.160	0.215	0.292	0.177	0.250	0.161	0.181	0.220	0.217	0.245	0.266	0.218
Ac 24h	0.095	0.087	0.200	0.173	0.022	0.041	0.046	-0.004	0.029	0.076	0.122	0.006
Pwet 0.25h	0.06	0.06	0.04	0.03	0.04	0.03	0.04	0.03	0.03	0.05	0.06	0.05
Pwet 1h	0.11	0.11	0.07	0.07	0.07	0.06	0.08	0.07	0.05	0.10	0.11	0.10
Pwet 6h	0.30	0.27	0.22	0.17	0.17	0.15	0.20	0.19	0.16	0.28	0.29	0.26
Pwet 24h	0.65	0.59	0.50	0.40	0.36	0.36	0.43	0.45	0.36	0.60	0.63	0.60

Table A.2: Monthly summary statistics for Rayleigh (cumulative approach)

	Jan	Feb	Mar	Apr	May	June	July	Aug	Sep	Oct	Nov	Dec
Mean 1h (mm/h)	0.0791	0.0671	0.0434	0.0436	0.0559	0.0537	0.0735	0.0663	0.0424	0.0758	0.0777	0.0678
CoeffVar 0.25h	5.64	5.45	6.88	7.94	7.32	9.04	10.80	8.14	10.38	7.07	5.89	5.84
CoeffVar 1h	4.58	4.40	5.28	6.05	5.71	6.88	8.07	6.40	7.43	5.41	4.70	4.63
CoeffVar 6h	3.14	3.08	3.25	3.82	3.75	4.08	4.40	4.07	4.89	3.56	3.05	3.16
CoeffVar 24h	1.83	1.89	1.98	2.28	2.30	2.39	2.64	2.39	3.17	2.08	1.83	1.91
Skewness 0.25h	11.82	11.90	15.53	17.89	15.23	20.98	27.98	16.51	28.09	24.29	11.79	11.62
Skewness 1h	8.72	8.38	10.01	13.89	9.81	12.38	24.82	11.03	13.16	14.46	8.07	8.33
Skewness 6h	6.11	4.66	4.78	6.84	5.93	6.52	8.47	7.44	8.99	8.17	4.87	5.37
Skewness 24h	3.20	2.40	3.05	4.19	3.09	3.51	4.27	3.91	5.54	3.87	2.71	3.10
Ac 0.25h	0.60	0.56	0.50	0.48	0.55	0.51	0.43	0.54	0.49	0.52	0.55	0.57
Ac 1h	0.53	0.53	0.41	0.41	0.50	0.48	0.25	0.42	0.45	0.47	0.50	0.53
Ac 6h	0.17	0.25	0.33	0.36	0.28	0.28	0.15	0.23	0.29	0.22	0.25	0.28
Ac 24h	0.20	0.10	0.22	0.39	0.11	0.25	-0.02	0.07	0.07	0.22	0.15	0.13
Pwet 0.25h	0.06	0.05	0.04	0.03	0.04	0.03	0.04	0.03	0.03	0.05	0.06	0.05
Pwet 1h	0.11	0.11	0.07	0.07	0.07	0.06	0.08	0.07	0.05	0.10	0.11	0.10
Pwet 6h	0.30	0.27	0.22	0.17	0.17	0.15	0.20	0.19	0.16	0.28	0.29	0.26
Pwet 24h	0.65	0.59	0.49	0.40	0.36	0.36	0.43	0.46	0.36	0.60	0.63	0.60

Appendix B: Fitting Equations for BLRP models

B.1: BLRP (Rodriguez-Iturbe et al., 1987; Cowpertwait, 1998)

$\mu_C = 1 + \frac{\beta}{\gamma}$

$\rho = \frac{\lambda}{\eta}$

$f_1 = \frac{E(X^2)}{\mu_x^2}$

$f_2 = \frac{E(X^3)}{\mu_x^3}$

Mean:

$$E(Y_i^h) = h\rho\mu_C\mu_x$$

Variance:

$$var(Y_i^h) = 2\rho\mu_C\left\{E(X^2) + \frac{\beta\mu_x^2}{\gamma}\right\}\frac{h}{\eta} + 2\rho\mu_C\mu_x^2\beta\eta\left\{\frac{1 - e^{-\gamma h}}{\gamma^2(\gamma^2 - \eta^2)}\right\}$$
$$- 2\rho\mu_C\left\{E(X^2) + \frac{\beta\gamma\mu_x^2}{(\gamma^2 - \eta^2)}\right\}\frac{(1 - e^{-\eta h})}{\eta^2}$$

Covariance at lag k ≥ 1:

$$cov(Y_i^h, Y_{i+k}^h) = \rho\mu_C\left\{E(X^2) + \frac{\beta\gamma\mu_x^2}{(\gamma^2-\eta^2)}\right\}\frac{(1-e^{-\eta h})^2 e^{-\eta(k-1)h}}{\eta^2} - \rho\mu_C\mu_x^2\beta\eta\left\{\frac{(1-e^{-\gamma h})^2 e^{-\gamma(k-1)h}}{\gamma^2(\gamma^2-\eta^2)}\right\}$$

Third Central Moment:

$$E\left[\left(Y_i^h - E(Y_i^h)\right)^3\right] = \frac{\lambda\mu_C\mu_x^3\sum_{k=1}^{8}P_k(\phi,\kappa,\eta,f_1,f_2)}{(1+2\phi+\phi^2)(\phi^4 - 2\phi^3 - 3\phi^2 + 8\phi - 4)\phi^3}$$

where

$$
\begin{aligned}
P_1(\phi,\kappa,\eta,f_1,f_2) \\
&= 6\eta^{-4}e^{-\eta h}\phi^2[\phi\kappa^2(2\phi^4-7\phi^2-3\phi+2)+2\phi f_2(\phi^6-6\phi^4+9\phi^2-4) \\
&+\kappa f_1(4\phi^6-22\phi^4-\phi^3+25\phi^2+4\phi-4)]
\end{aligned}
$$

$$P_2(\phi,\kappa,\eta,f_1,f_2)=6\eta^{-3}e^{-\eta h}\phi^3 h[f_2(\phi^6-6\phi^4+9\phi^2-4)+\phi\kappa f_1(\phi^2-1)(\phi^2-4)]$$

$$
\begin{aligned}
P_3(\phi,\kappa,\eta,f_1,f_2) \\
&= 6\eta^{-4}e^{-\eta\phi h}\kappa[f_1(-\phi^5+\phi^4+6\phi^3-4\phi^2-8\phi) \\
&+\kappa(\phi^5-3\phi^4+2\phi^3+14\phi^2-8)]
\end{aligned}
$$

$$P_4(\phi,\kappa,\eta,f_1,f_2)=6\eta^{-3}e^{-\eta\phi h}h\kappa^2[\phi^3(5-\phi^2)-4\phi]$$

$$
\begin{aligned}
P_5(\phi,\kappa,\eta,f_1,f_2) \\
&= \eta^{-4}[-12\phi^3 f_2(\phi^6-6\phi^4+9\phi^2-4) \\
&+\kappa^2(-9\phi^7+39\phi^5+18\phi^4-12\phi^3-84\phi^2+48) \\
&-3\phi\kappa f_1(7\phi^7-39\phi^5-2\phi^4+46\phi^3+12\phi^2-8\phi-16)]
\end{aligned}
$$

$$P_6(\phi,\kappa,\eta,f_1,f_2)=\eta^{-3}[(6h\phi^3 f_2+12h\phi^2\kappa f_1+6h\phi\kappa^2)(\phi^6-6\phi^4+9\phi^2-4)]$$

$$P_7(\phi,\kappa,\eta,f_1,f_2)=3\eta^{-4}e^{-2\eta h}\phi^4(1-\phi^2)[\phi\kappa^2+\kappa f_1(\phi^2-4)]$$

$$P_8(\phi,\kappa,\eta,f_1,f_2)=6\eta^{-4}e^{-(1+\phi)\eta h}\kappa\phi^2(\phi-2)(\phi-1)[f_1(\phi+2)-\phi\kappa]$$

B.2: BLRPR (Rodriguez-Iturbe et al., 1988; Cowpertwait, 1998)

$\mu_C = 1 + \frac{\kappa}{\phi}$

$f_1 = \frac{E(X^2)}{\mu_x^2}$

$f_2 = \frac{E(X^3)}{\mu_x^3}$

$$T(k,u,l) = \frac{\nu^\alpha}{(\nu+u)^{\alpha-k}} \frac{\Gamma(\alpha - k, l(\nu + u))}{\Gamma(\alpha)}$$

Mean:

$$E(Y_i^h) = \frac{h\lambda\nu\mu_C\mu_x}{\alpha - 1}$$

Variance:

$$var(Y_i^h) = 2\lambda\mu_C\mu_x^2 \left[\left(f_1 + \frac{\kappa}{\phi}\right) hT(2,0,0) + \left(\frac{\kappa(1-\phi^3)}{\phi^2(\phi^2-1)} - f_1\right) T(3,0,0) - \frac{\kappa}{\phi^2(\phi^2-1)} T(3,\phi h,0) + \left(f_1 + \frac{\kappa\phi}{\phi^2-1}\right) T(3,h,0)\right] \; for\ \alpha > 3$$

$$var(Y_i^h) \approx 2\lambda\mu_C\mu_x^2 \left[\frac{\nu^\alpha h^2 \eta_0^{\alpha-1}}{2(\alpha-1)\Gamma(\alpha)} \left(\frac{\kappa}{\phi+1} + f_1\right) + \left(f_1 + \frac{\kappa}{\phi}\right) hT(2,0,\eta_0) + \left(\frac{\kappa(1-\phi^3)}{\phi^2(\phi^2-1)} - f_1\right) T(3,0,\eta_0) - \frac{\kappa}{\phi^2(\phi^2-1)} T(3,\phi h,\eta_0) + \left(f_1 + \frac{\kappa\phi}{\phi^2-1}\right) T(3,h,\eta_0)\right] \; for\ 1 < \alpha \le 3$$

$$var(Y_i^h) = \infty \; for\ \alpha \le 1$$

Covariance at lag k ≥ 1:

$$cov(k,h) = \lambda\mu_C\mu_x^2\Bigg[\left(f_1 + \frac{\kappa\phi}{\phi^2-1}\right)[T(3,(k-1)h,0) - 2T(3,kh,0) + T(3,(k+1)h,0)]$$
$$- \left(\frac{\kappa}{\phi^2(\phi^2-1)}\right)[T(3,\phi(k-1)h,0) - 2T(3,\phi kh,0)$$
$$+ T(3,\phi(k+1)h,0)]\Bigg] \; for\ \alpha > 3$$

$$cov(k,h) \approx \lambda\mu_C\mu_x^2\Bigg[\frac{\nu^\alpha h^2\eta_0^{\alpha-1}}{(\alpha-1)\Gamma(\alpha)}\left(\frac{\kappa}{\phi+1} + f_1\right)$$
$$+ \left(f_1 + \frac{\kappa\phi}{\phi^2-1}\right)[T(3,(k-1)h,\eta_0) - 2T(3,kh,\eta_0) + T(3,(k+1)h,\eta_0)]$$
$$- \left(\frac{\kappa}{\phi^2(\phi^2-1)}\right)[T(3,\phi(k-1)h,\eta_0) - 2T(3,\phi kh,\eta_0)$$
$$+ T(3,\phi(k+1)h,\eta_0)]\Bigg] \; for\ 1 < \alpha \le 3$$

$$cov(k,h) = \infty \; for\ \alpha \le 1$$

Third central moment:

$$E\left[\left(Y_i^h - E(Y_i^h)\right)^3\right] = \frac{\lambda\mu_C\mu_x^3\sum_{k=1}^{8} Q_k(\phi,\kappa,f_1,f_2,0)}{(1+2\phi+\phi^2)(\phi^4-2\phi^3-3\phi^2+8\phi-4)\phi^3} \; for\ \alpha > 4$$

$$E\left[\left(Y_i^h - E(Y_i^h)\right)^3\right]$$
$$\approx \frac{\lambda\mu_C\mu_x^3}{(1+2\phi+\phi^2)(\phi^4-2\phi^3-3\phi^2+8\phi-4)\phi^3}\Bigg[\frac{\nu^\alpha h^3\eta_0^{\alpha-1}}{(\alpha-1)\Gamma(\alpha)}\big(2\kappa^2(\phi^7$$
$$- 3\phi^6 + \phi^5 + 3\phi^4 - 2\phi^3) + f_2(\phi^9 - 6\phi^7 + 9\phi^5 - 4\phi^3)$$
$$+ 3\kappa f_1(\phi^8 - \phi^7 - 5\phi^6 + 5\phi^5 + 4\phi^4 - 4\phi^3)\big)$$
$$+ \sum_{k=1}^{8} Q_k(\phi,\kappa,f_1,f_2,\eta_0)\Bigg] \; for\ 1 < \alpha \le 4$$

$$E\left[\left(Y_i^h - E(Y_i^h)\right)^3\right] = \infty \; for\ \alpha \le 1$$

where

$$Q_1(\phi,\kappa,f_1,f_2,l)$$
$$= 6T(4,h,l)\phi^2[\phi\kappa^2(2\phi^4 - 7\phi^2 - 3\phi + 2) + 2\phi f_2(\phi^6 - 6\phi^4 + 9\phi^2 - 4)$$
$$+ \kappa f_1(4\phi^6 - 22\phi^4 - \phi^3 + 25\phi^2 + 4\phi - 4)]$$

$$Q_2(\phi,\kappa,f_1,f_2,l) = 6T(3,h,l)\phi^3 h[f_2(\phi^6 - 6\phi^4 + 9\phi^2 - 4) + \phi\kappa f_1(\phi^2 - 1)(\phi^2 - 4)]$$

$$Q_3(\phi,\kappa,f_1,f_2,l)$$
$$= 6T(4,\phi h,l)\kappa[f_1(-\phi^5 + \phi^4 + 6\phi^3 - 4\phi^2 - 8\phi)$$
$$+ \kappa(\phi^5 - 3\phi^4 + 2\phi^3 + 14\phi^2 - 8)]$$

$$Q_4(\phi,\kappa,f_1,f_2,l) = 6T(3,\phi h,l)h\kappa^2[\phi^3(5 - \phi^2) - 4\phi]$$

$$Q_5(\phi,\kappa,f_1,f_2,l)$$
$$= T(4,0,l)[-12\phi^3 f_2(\phi^6 - 6\phi^4 + 9\phi^2 - 4)$$
$$+ \kappa^2(-9\phi^7 + 39\phi^5 + 18\phi^4 - 12\phi^3 - 84\phi^2 + 48)$$
$$- 3\phi\kappa f_1(7\phi^7 - 39\phi^5 - 2\phi^4 + 46\phi^3 + 12\phi^2 - 8\phi - 16)]$$

$$Q_6(\phi,\kappa,f_1,f_2,l) = T(3,0,l)[(6h\phi^3 f_2 + 12h\phi^2\kappa f_1 + 6h\phi\kappa^2)(\phi^6 - 6\phi^4 + 9\phi^2 - 4)]$$

$$Q_7(\phi,\kappa,\eta,f_1,f_2) = 3T(4,2h,l)\phi^4(1 - \phi^2)[\phi\kappa^2 + \kappa f_1(\phi^2 - 4)]$$

$$Q_8(\phi,\kappa,\eta,f_1,f_2) = 6T(4,(1+\phi)h,l)\kappa\phi^2(\phi - 2)(\phi - 1)[f_1(\phi + 2) - \phi\kappa]$$

B.3: BLRPRx (Kaczmarska et al., 2014)

$\mu_C = 1 + \frac{\kappa}{\phi}$

$f_1 = \frac{E(X^2)}{\mu_x^2}$

$f_2 = \frac{E(X^3)}{\mu_x^3}$

$$T(k,u,l) = \frac{\nu^\alpha}{(\nu+u)^{\alpha-k}} \frac{\Gamma(\alpha - k, l(\nu+u))}{\Gamma(\alpha)}$$

Mean:

$E(Y_i^h) = \lambda h \iota \mu_C$

Variance:

$$var(Y_i^h) = 2\lambda\mu_C\iota^2 \left[\left(f_1 + \frac{\kappa}{\phi}\right) h + \left(\frac{\kappa(1-\phi^3)}{\phi^2(\phi^2-1)} - f_1\right) T(1,0,0) - \frac{\kappa}{\phi^2(\phi^2-1)} T(1,\phi h,0) + \left(f_1 + \frac{\kappa\phi}{\phi^2-1}\right) T(1,h,0) \right] \; for\ \alpha > 1$$

$$var(Y_i^h) \approx 2\lambda\mu_C\iota^2 \left[\frac{\nu^\alpha h^2 \eta_0^{\alpha+1}}{2(\alpha+1)\Gamma(\alpha)} \left(\frac{\kappa}{\phi+1} + f_1\right) + \left(f_1 + \frac{\kappa}{\phi}\right) hT(0,0,\eta_0) + \left(\frac{\kappa(1-\phi^3)}{\phi^2(\phi^2-1)} - f_1\right) T(1,0,\eta_0) - \frac{\kappa}{\phi^2(\phi^2-1)} T(1,\phi h,\eta_0) + \left(f_1 + \frac{\kappa\phi}{\phi^2-1}\right) T(1,h,\eta_0) \right] \; for -1 < \alpha \leq 1$$

Covariance at lag k ≥ 1:

$$cov(k,h) = \lambda\mu_C \iota^2 \Bigg[\left(f_1 + \frac{\kappa\phi}{\phi^2 - 1}\right)[T(1,(k-1)h,0) - 2T(1,kh,0) + T(1,(k+1)h,0)]$$
$$- \left(\frac{\kappa}{\phi^2(\phi^2 - 1)}\right)[T(1,\phi(k-1)h,0) - 2T(1,\phi kh,0)$$
$$+ T(1,\phi(k+1)h,0)]\Bigg] \; for\; \alpha > 1$$

$$cov(k,h) \approx \lambda\mu_C \iota^2 \Bigg[\frac{\nu^\alpha h^2 \eta_0^{\alpha+1}}{(\alpha+1)\Gamma(\alpha)}\left(\frac{\kappa}{\phi + 1} + f_1\right)$$
$$+ \left(f_1 + \frac{\kappa\phi}{\phi^2 - 1}\right)[T(1,(k-1)h,\eta_0) - 2T(1,kh,\eta_0) + T(1,(k+1)h,\eta_0)]$$
$$- \left(\frac{\kappa}{\phi^2(\phi^2 - 1)}\right)[T(1,\phi(k-1)h,\eta_0) - 2T(1,\phi kh,\eta_0)$$
$$+ T(1,\phi(k+1)h,\eta_0)]\Bigg] \; for -1 < \alpha \le 1$$

Third central moment:

$$E\left[\left(Y_i^h - E(Y_i^h)\right)^3\right] = \frac{\lambda\mu_C \iota^3 \sum_{k=1}^{8} R_k(\phi,\kappa,f_1,f_2,0)}{(1+2\phi+\phi^2)(\phi^4 - 2\phi^3 - 3\phi^2 + 8\phi - 4)\phi^3} \; for\; \alpha > 1$$

$$E\left[\left(Y_i^h - E(Y_i^h)\right)^3\right]$$
$$\approx \frac{\lambda\mu_C \iota^3}{(1+2\phi+\phi^2)(\phi^4 - 2\phi^3 - 3\phi^2 + 8\phi - 4)\phi^3}\Bigg[\frac{\nu^\alpha h^3 \eta_0^{\alpha+2}}{(\alpha+2)\Gamma(\alpha)}\big(2\kappa^2(\phi^7$$
$$- 3\phi^6 + \phi^5 + 3\phi^4 - 2\phi^3) + f_2(\phi^9 - 6\phi^7 + 9\phi^5 - 4\phi^3)$$
$$+ 3\kappa f_1(\phi^8 - \phi^7 - 5\phi^6 + 5\phi^5 + 4\phi^4 - 4\phi^3)\big)$$
$$+ \sum_{k=1}^{8} R_k(\phi,\kappa,f_1,f_2,\eta_0)\Bigg] \; for -2 < \alpha \le 1$$

where

$$R_1(\phi,\kappa,f_1,f_2,l)$$
$$= 6T(1,h,l)\phi^2[\phi\kappa^2(2\phi^4 - 7\phi^2 - 3\phi + 2) + 2\phi f_2(\phi^6 - 6\phi^4 + 9\phi^2 - 4)$$
$$+ \kappa f_1(4\phi^6 - 22\phi^4 - \phi^3 + 25\phi^2 + 4\phi - 4)]$$

$$R_2(\phi,\kappa,f_1,f_2,l) = 6T(0,h,l)\phi^3 h[f_2(\phi^6 - 6\phi^4 + 9\phi^2 - 4) + \phi\kappa f_1(\phi^2 - 1)(\phi^2 - 4)]$$

$$R_3(\phi,\kappa,f_1,f_2,l)$$
$$= 6T(1,\phi h,l)\kappa[f_1(-\phi^5+\phi^4+6\phi^3-4\phi^2-8\phi)$$
$$+\kappa(\phi^5-3\phi^4+2\phi^3+14\phi^2-8)]$$

$$R_4(\phi,\kappa,f_1,f_2,l) = 6T(0,\phi h,l)h\kappa^2[\phi^3(5-\phi^2)-4\phi]$$

$$R_5(\phi,\kappa,f_1,f_2,l)$$
$$= T(1,0,l)[-12\phi^3 f_2(\phi^6-6\phi^4+9\phi^2-4)$$
$$+\kappa^2(-9\phi^7+39\phi^5+18\phi^4-12\phi^3-84\phi^2+48)$$
$$-3\phi\kappa f_1(7\phi^7-39\phi^5-2\phi^4+46\phi^3+12\phi^2-8\phi-16)]$$

$$R_6(\phi,\kappa,f_1,f_2,l) = T(0,0,l)[(6h\phi^3 f_2+12h\phi^2\kappa f_1+6h\phi\kappa^2)(\phi^6-6\phi^4+9\phi^2-4)]$$

$$R_7(\phi,\kappa,\eta,f_1,f_2) = 3T(1,2h,l)\phi^4(1-\phi^2)[\phi\kappa^2+\kappa f_1(\phi^2-4)]$$

$$R_8(\phi,\kappa,\eta,f_1,f_2) = 6T(1,(1+\phi)h,l)\kappa\phi^2(\phi-2)(\phi-1)[f_1(\phi+2)-\phi\kappa]$$

Appendix C: BLRP models simulation fits

C.1: BLRPR fitting (standard methodology)

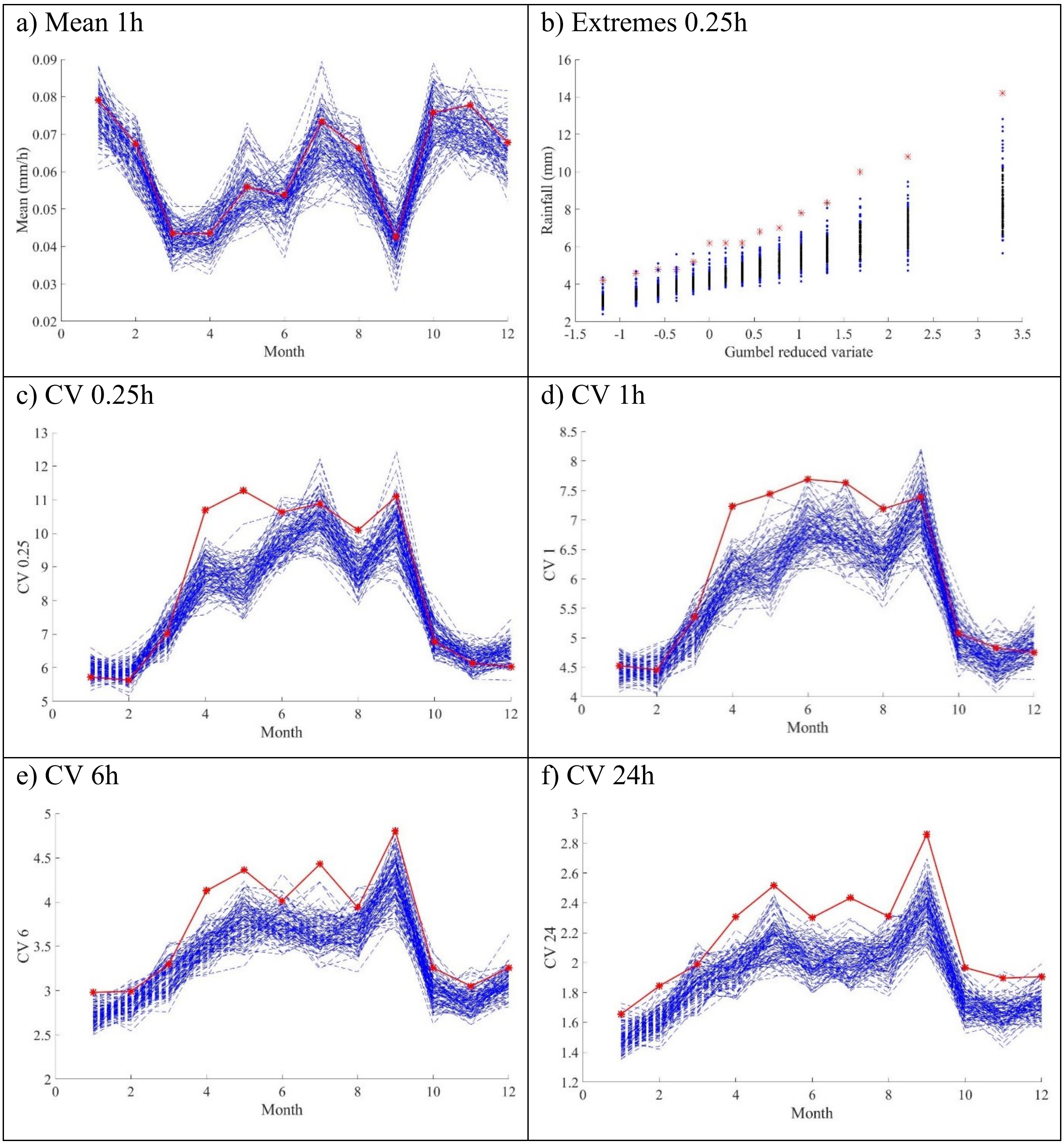

g) Skewness 0.25h

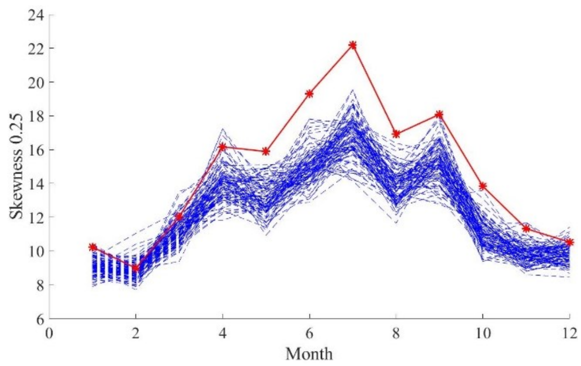

h) Skewness 1h

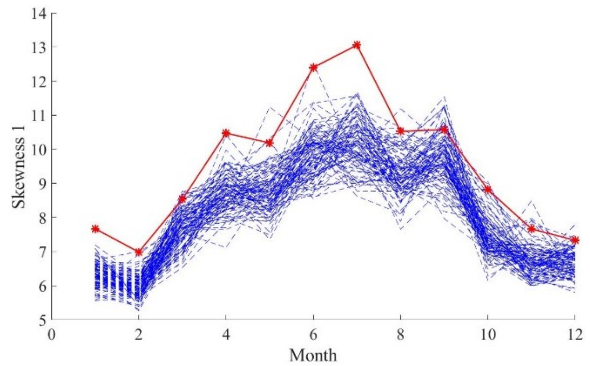

i) Skewness 6h

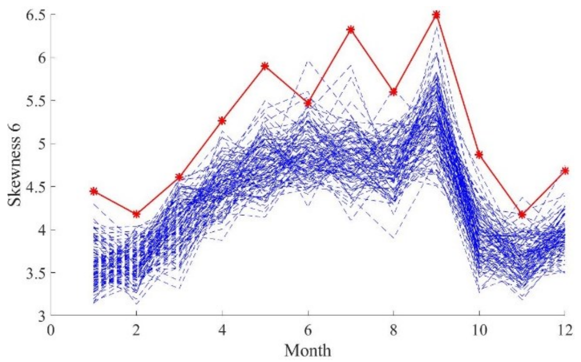

j) Skewness 24h

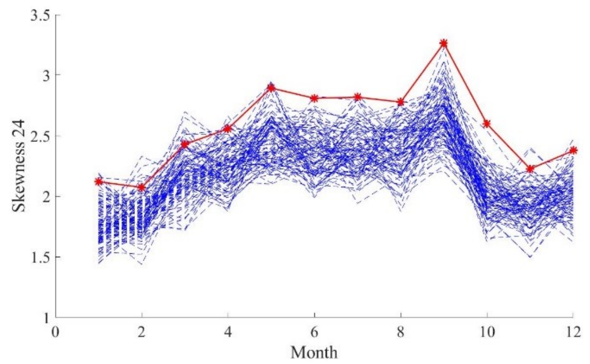

k) AC 0.25h

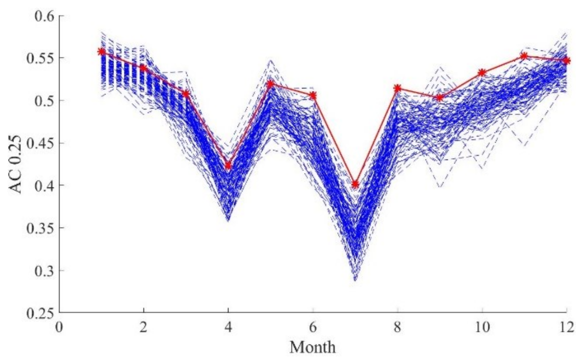

l) AC 1h

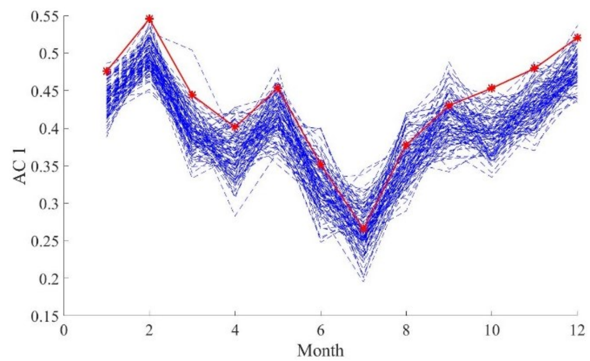

m) AC 6h

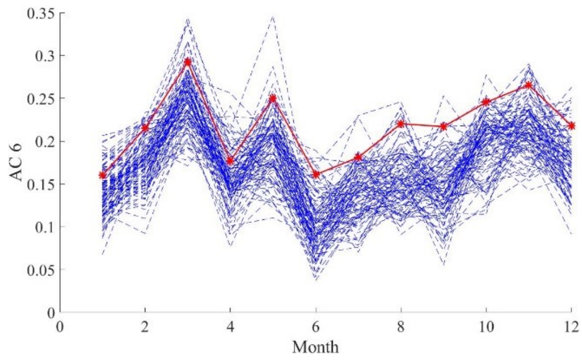

n) AC 24h

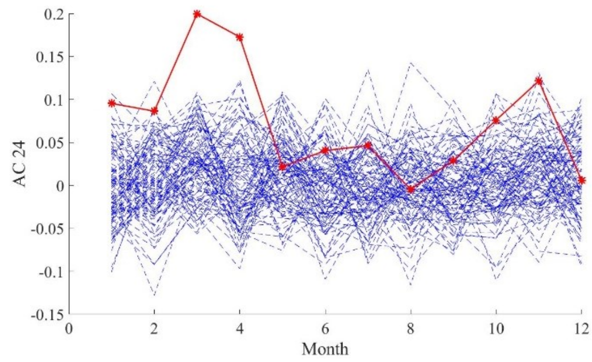

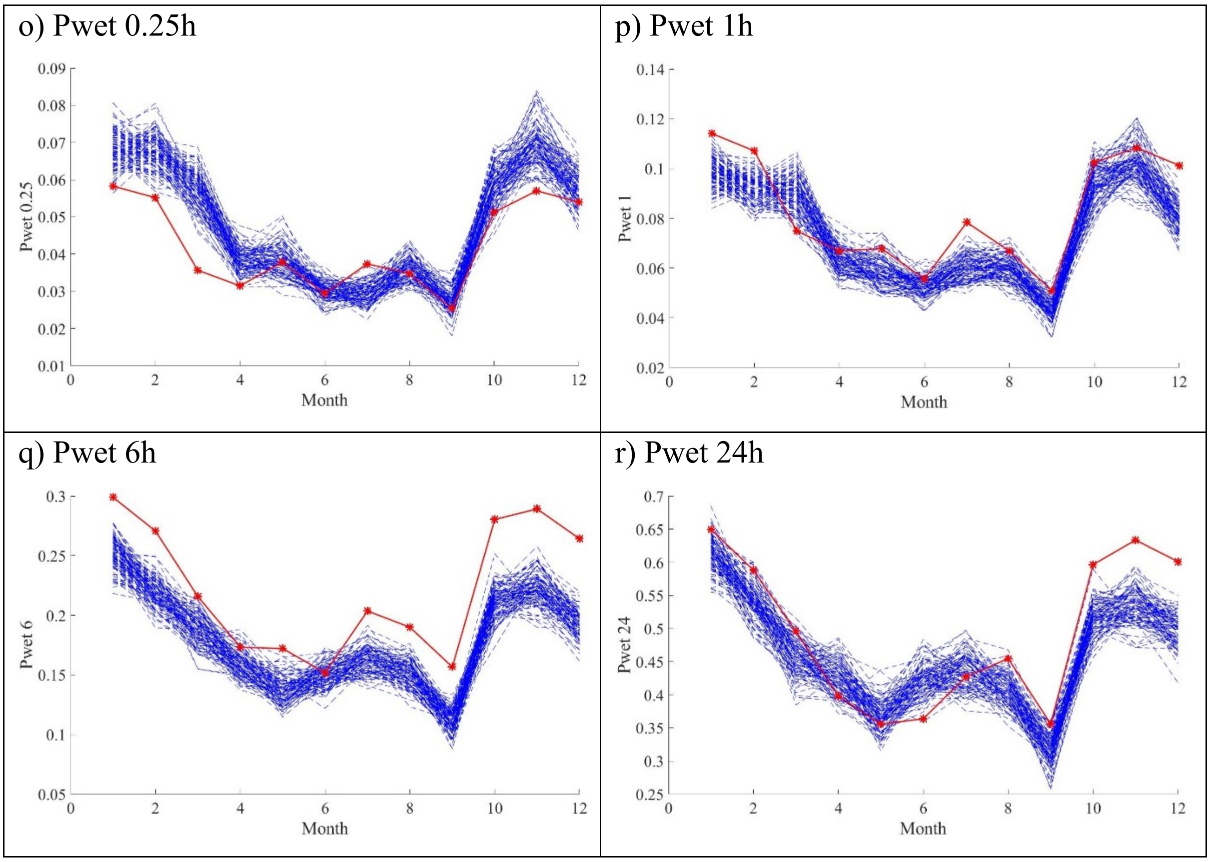
o) Pwet 0.25h
Pwet 0.25
Month
p) Pwet 1h
Pwet 1
Month
q) Pwet 6h
Pwet 6
Month
r) Pwet 24h
Pwet 24
Month

C.2: BLRPRx fitting (standard methodology)

a) Mean 1h

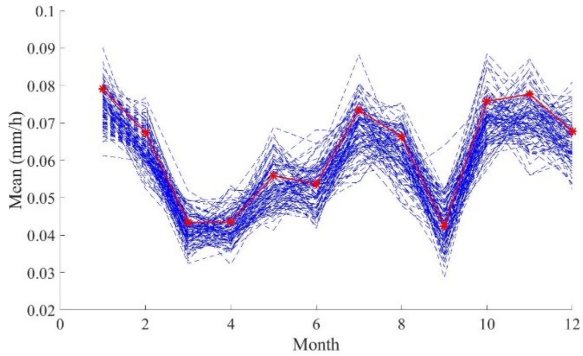

b) Extremes 0.25h

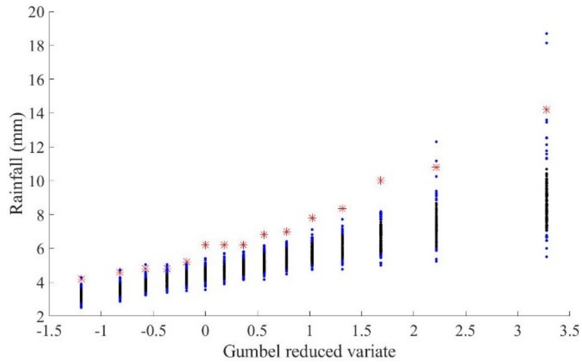

c) CV 0.25h

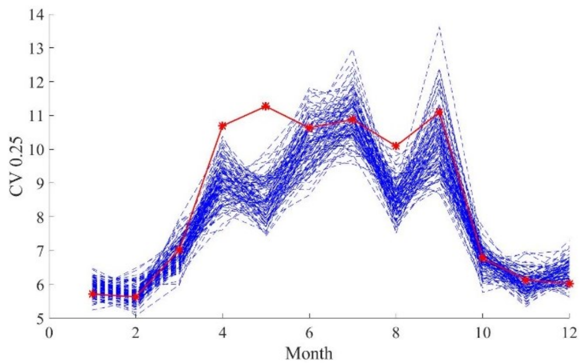

d) CV 1h

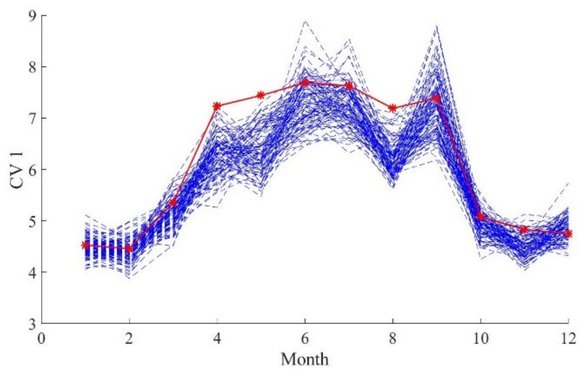

e) CV 6h

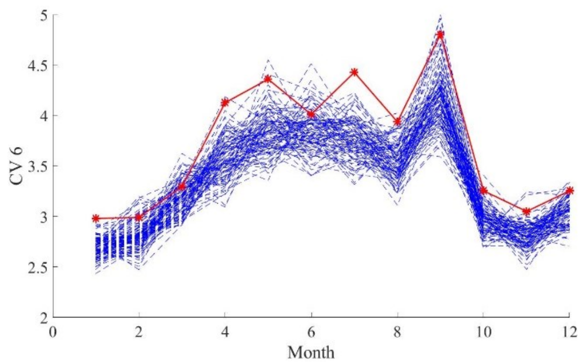

f) CV 24h

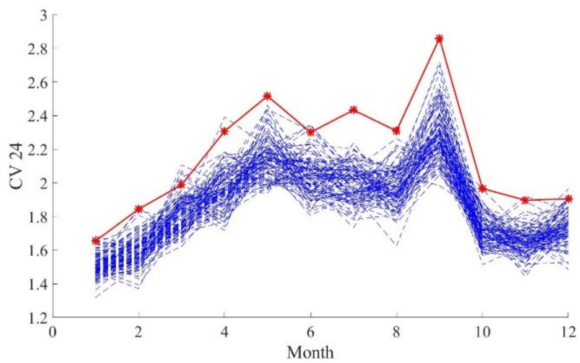

g) Skewness 0.25h

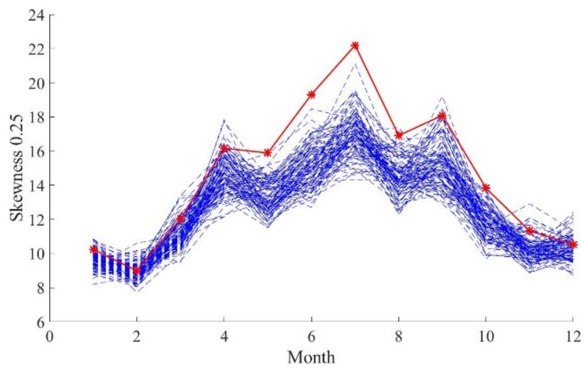

h) Skewness 1h

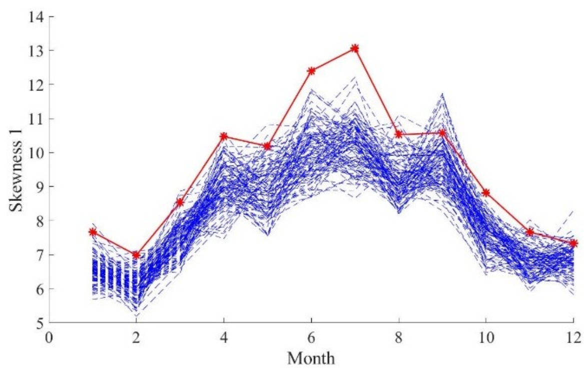

i) Skewness 6h

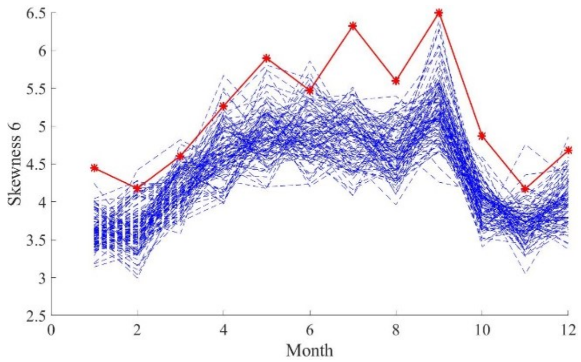

j) Skewness 24h

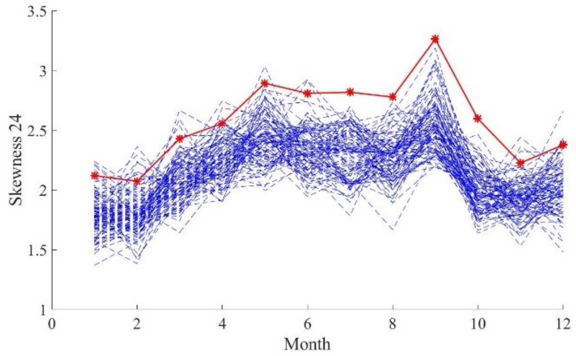

k) AC 0.25h

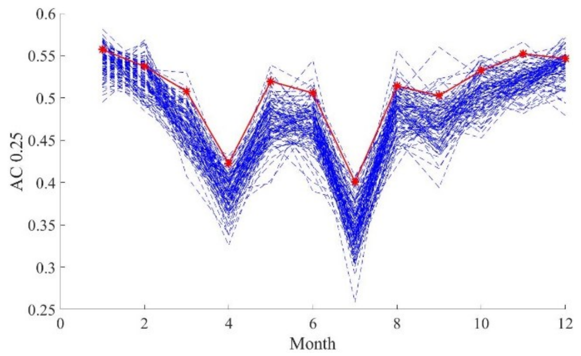

l) AC 1h

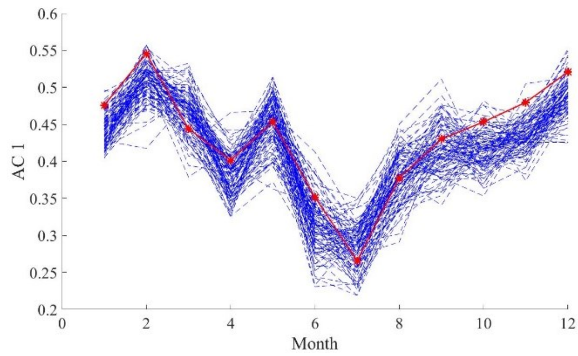

m) AC 6h

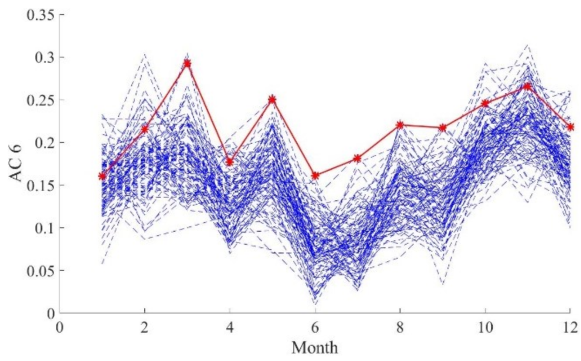

n) AC 24h

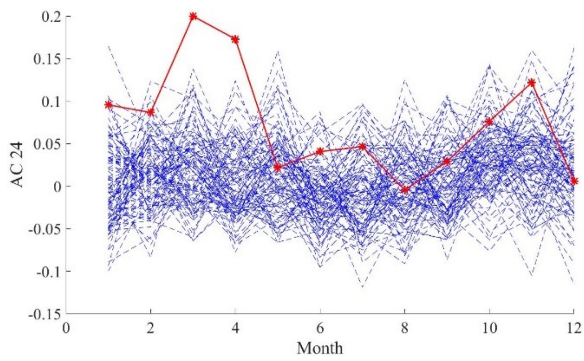

o) Pwet 0.25h

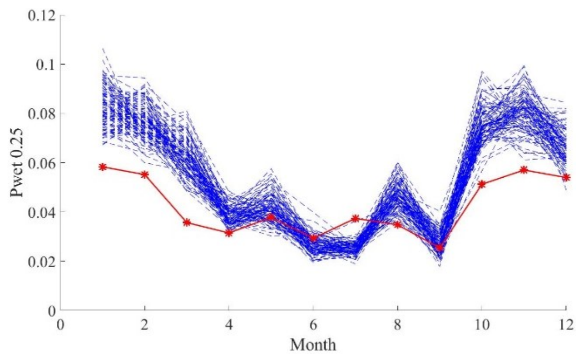

p) Pwet 1h

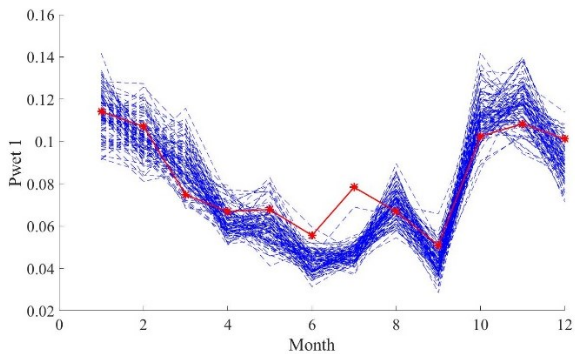

q) Pwet 6h

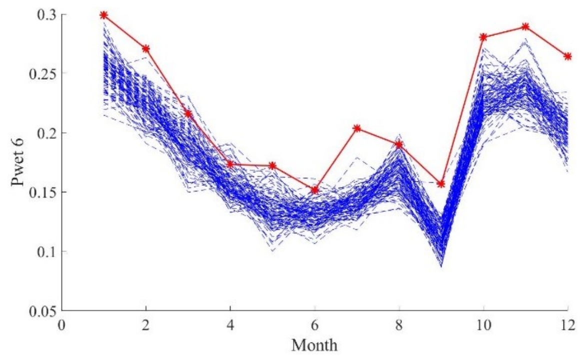

r) Pwet 24h

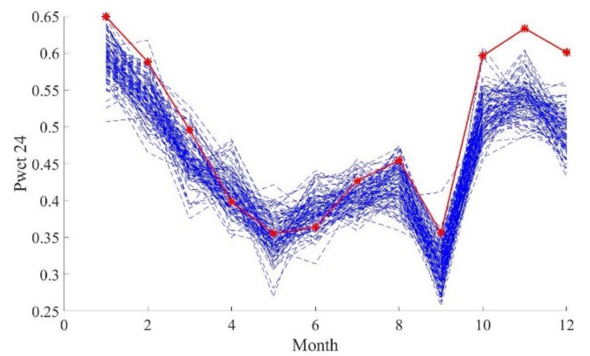

C.3: BLRP fitting (cumulative approach)

a) Mean 1h

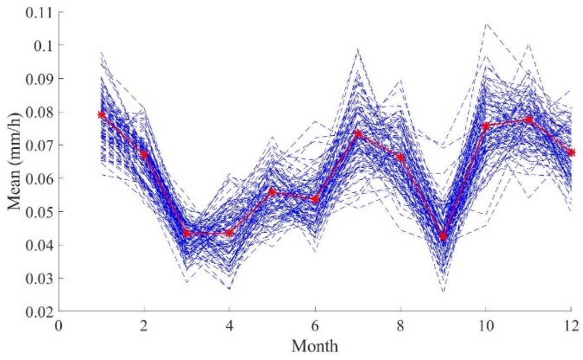

b) Extremes 0.25h

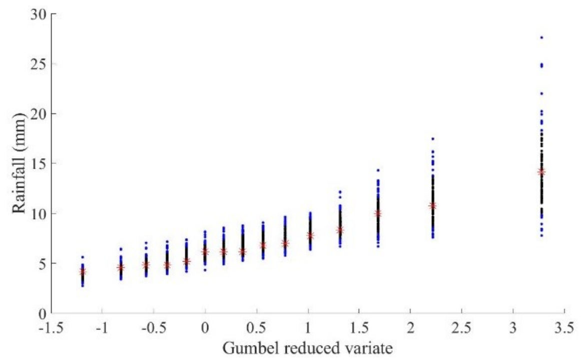

c) CV 0.25h

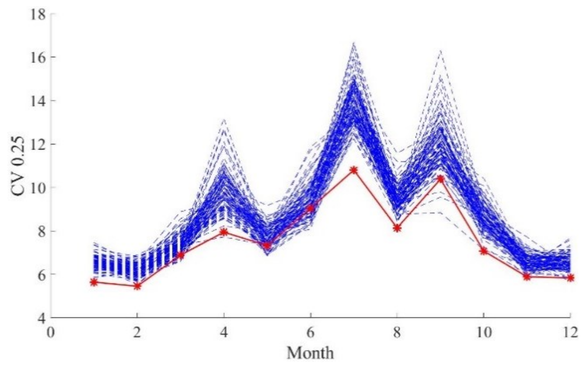

d) CV 1h

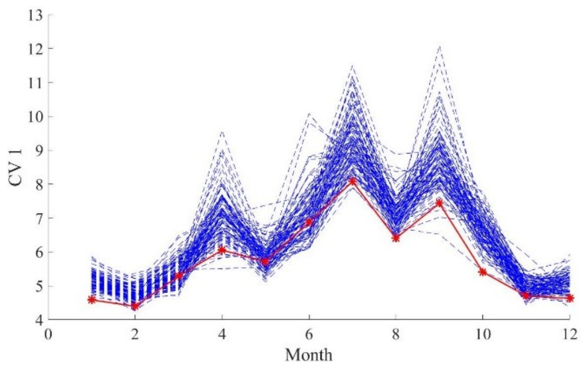

e) CV 6h

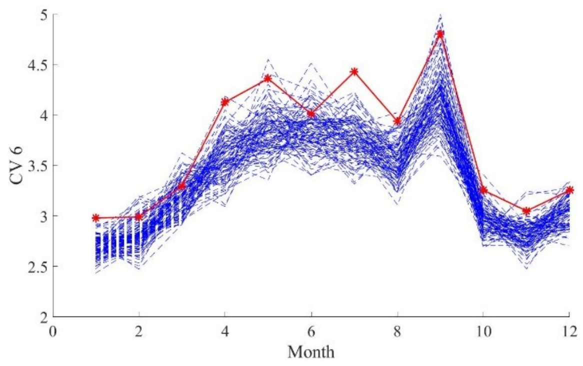

f) CV 24h

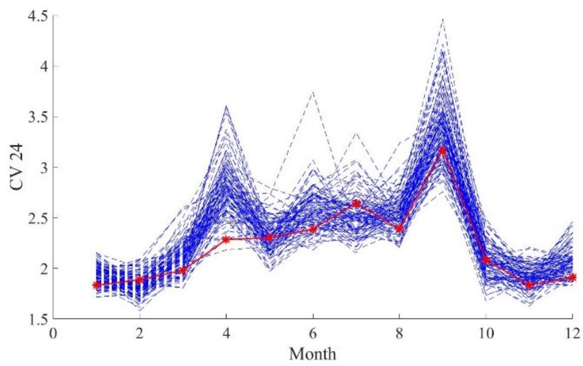

g) Skewness 0.25h

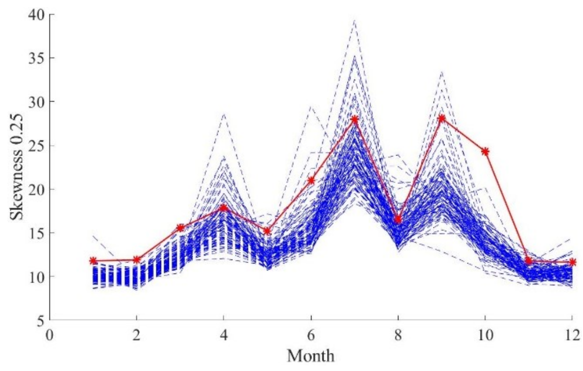

h) Skewness 1h

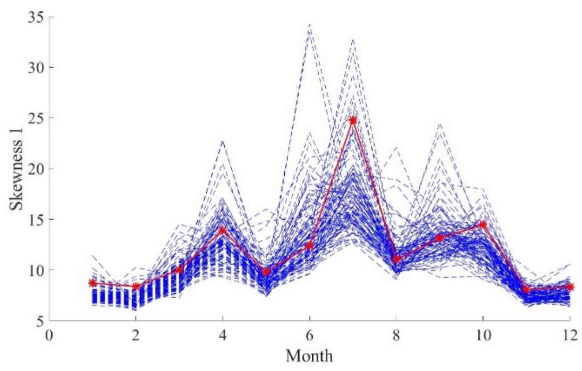

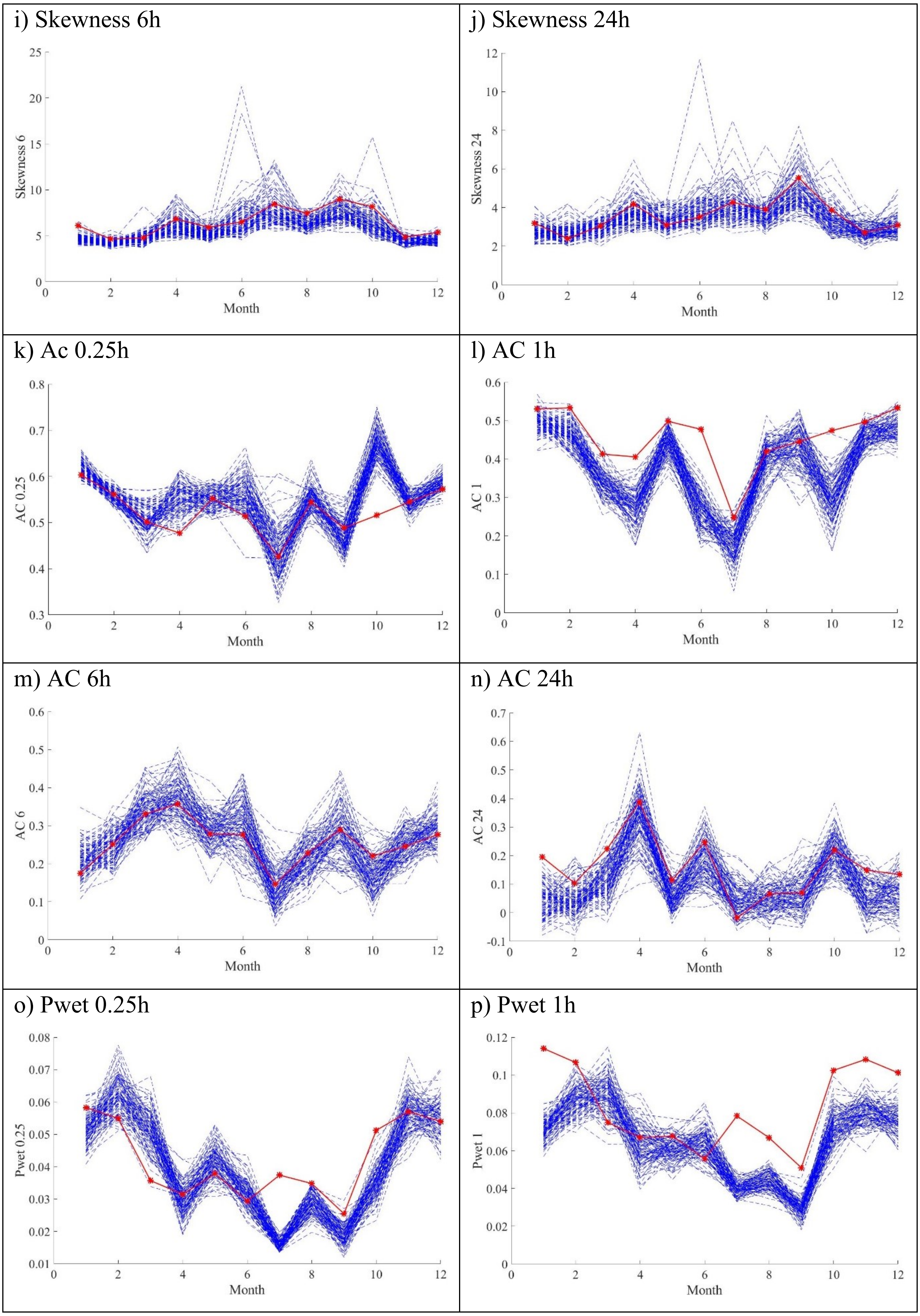
i) Skewness 6h
Skewness 6
Month
j) Skewness 24h
Skewness 24
Month
k) Ac 0.25h
AC 0.25
Month
l) AC 1h
AC 1
Month
m) AC 6h
AC 6
Month
n) AC 24h
AC 24
Month
o) Pwet 0.25h
Pwet 0.25
Month
p) Pwet 1h
Pwet 1
Month

q) Pwet 6h

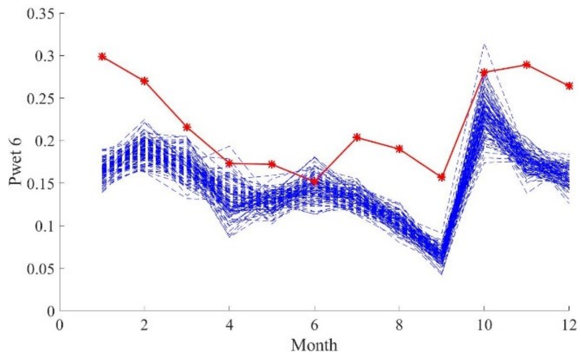

r) Pwet 24h

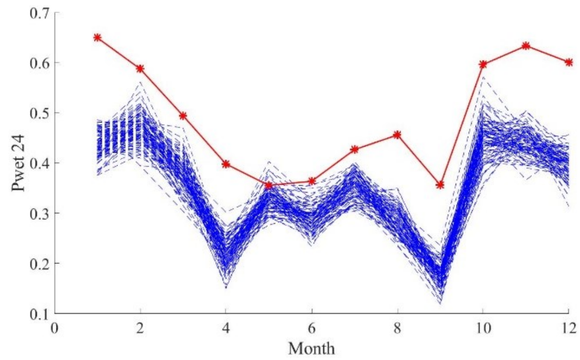

C.4: BLRPR fitting (cumulative approach)

a) Mean 1h

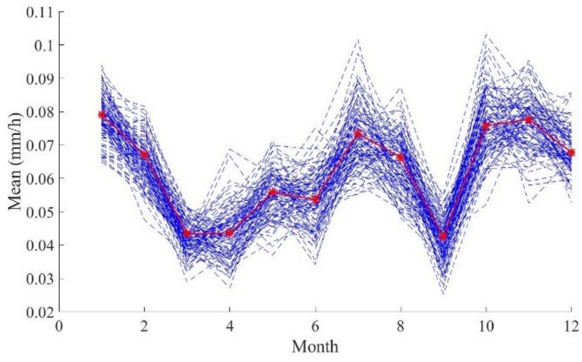

b) Extremes 0.25h

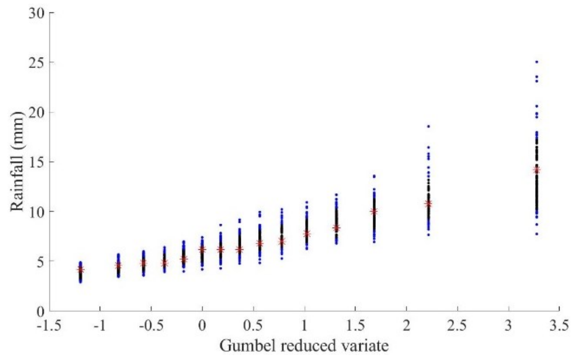

c) CV 0.25h

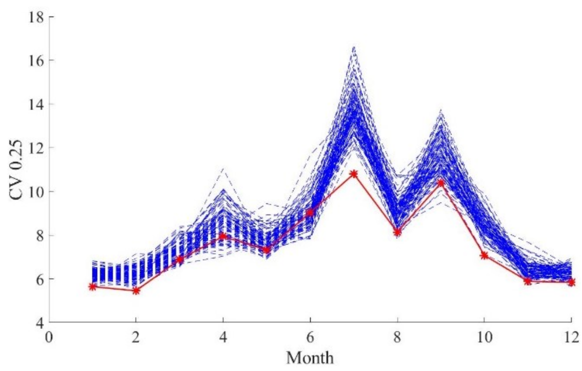

d) CV 1h

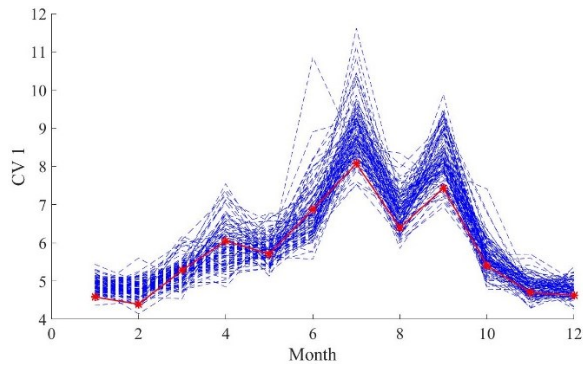

e) CV 6h

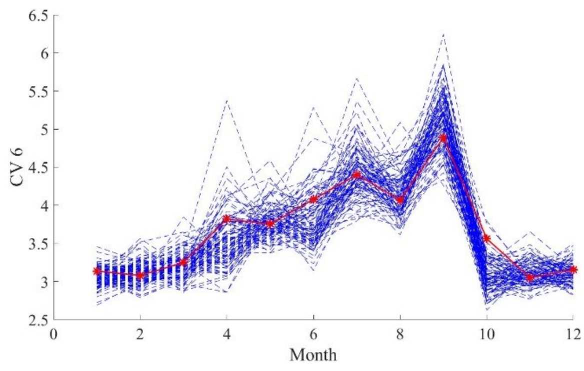

f) CV 24h

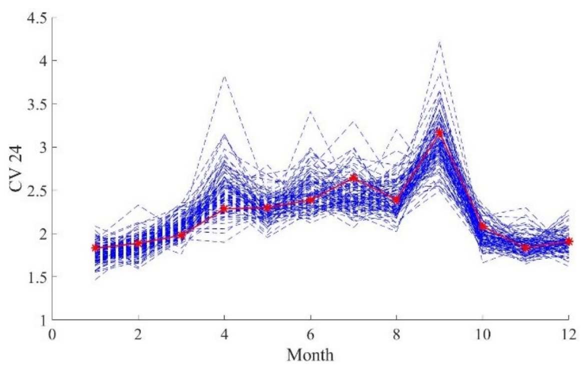

g) Skewness 0.25h

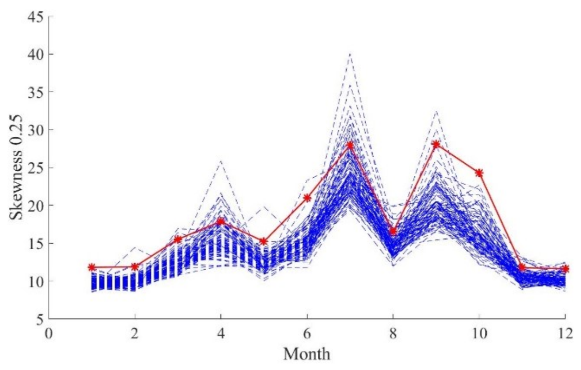

h) Skewness 1h

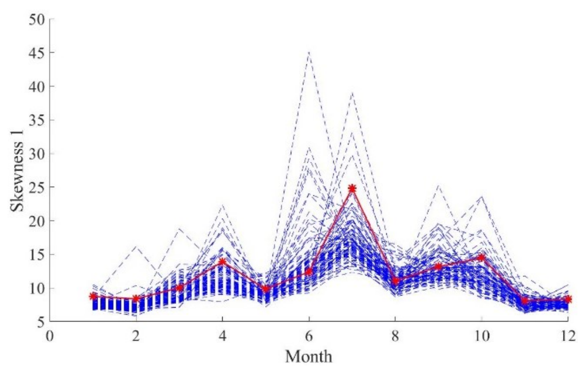

i) Skewness 6h

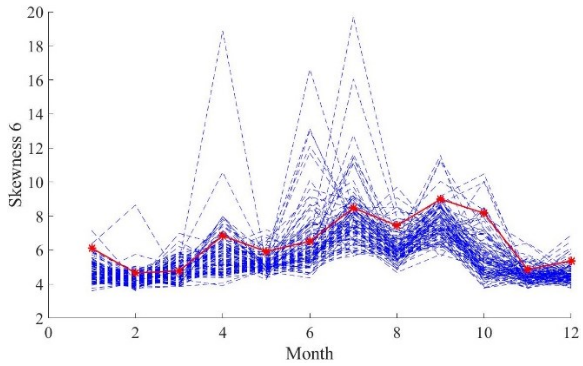

j) Skewness 24h

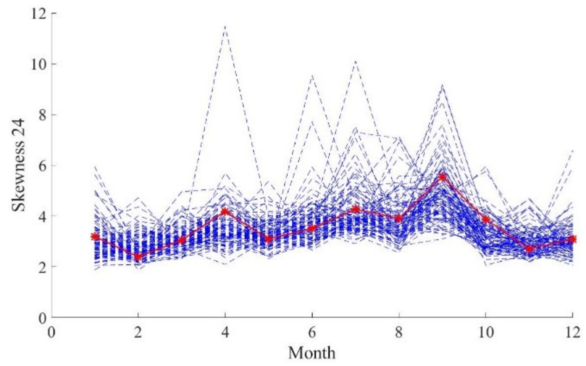

k) AC 0.25h

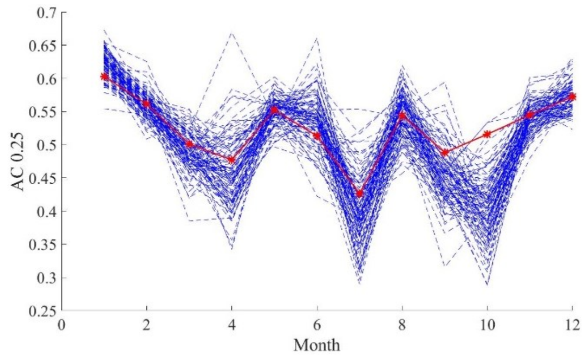

l) AC 1h

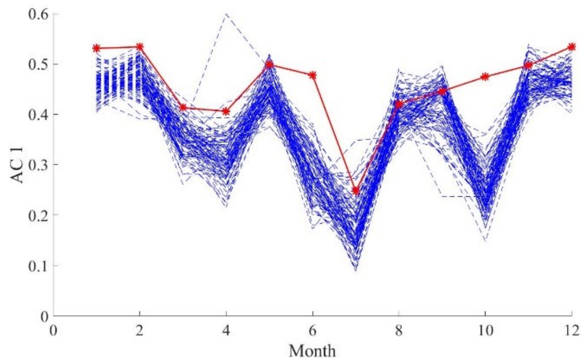

m) AC 6h

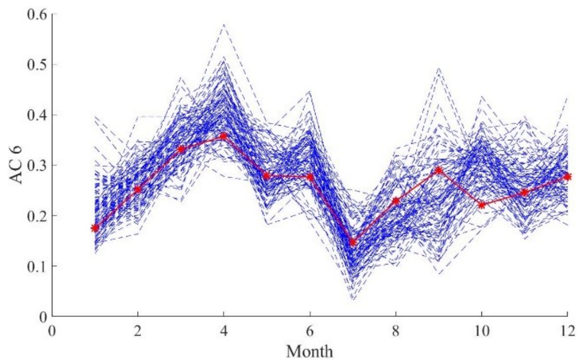

n) AC 24h

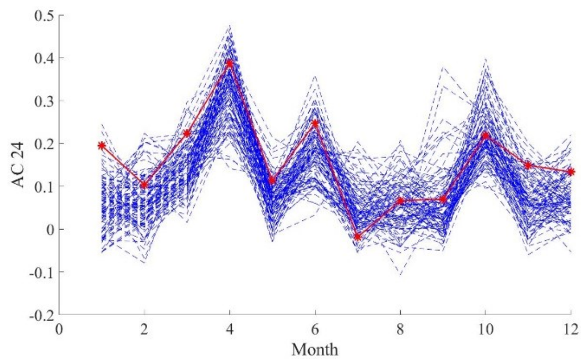

o) Pwet 0.25h

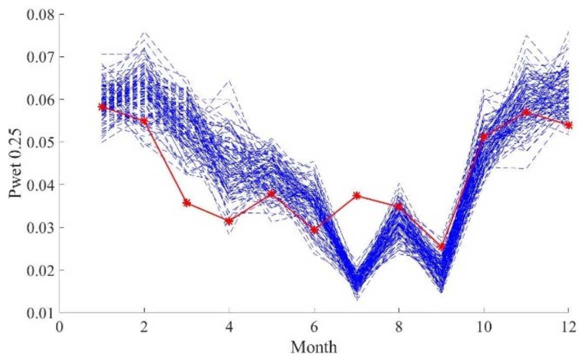

p) Pwet 1h

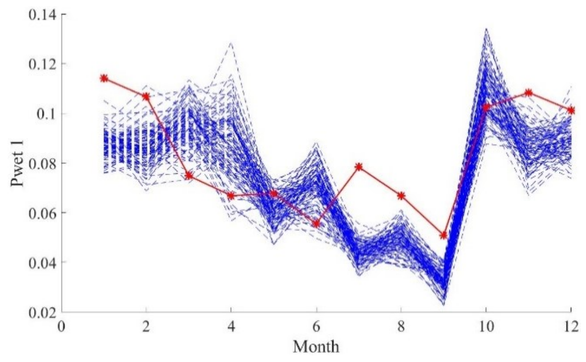

q) Pwet 6h

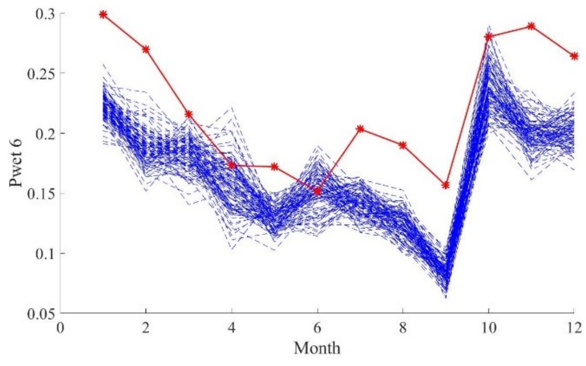

r) Pwet 24h

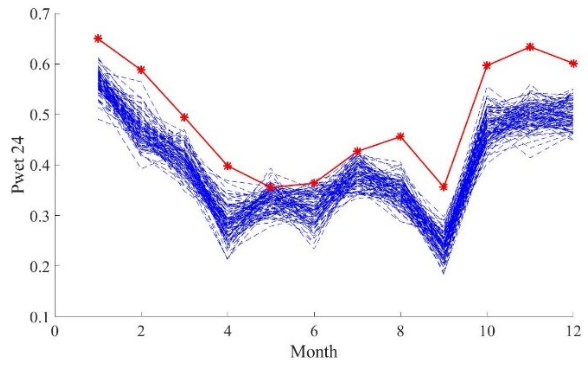

C.5: BLRPRx fitting (cumulative approach)

a) Mean 1h

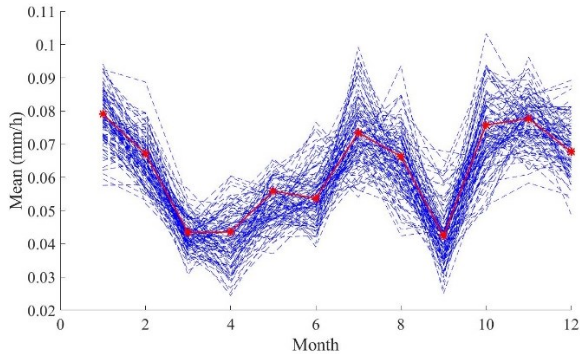

b) Extremes 0.25h

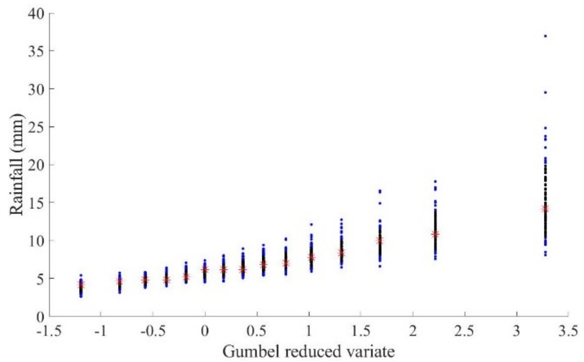

c) CV 0.25h

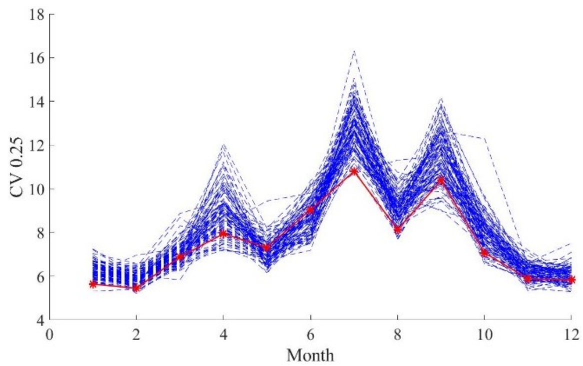

d) CV 1h

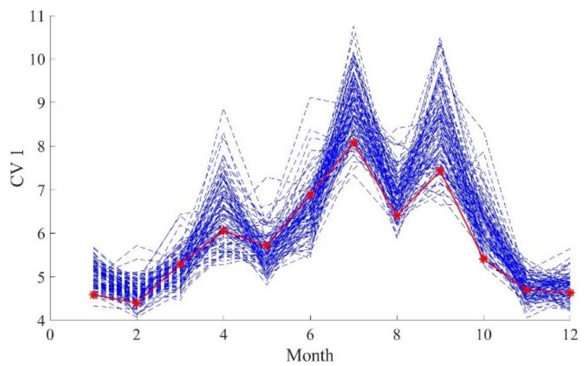

e) CV 6h

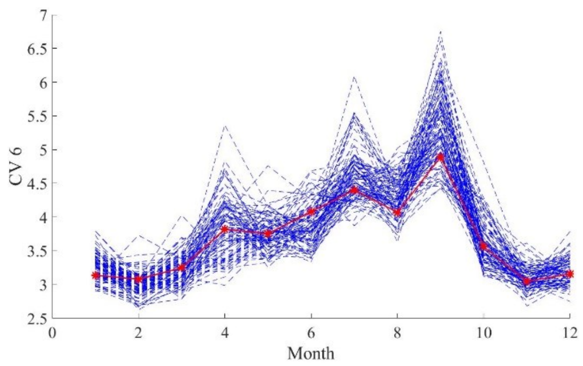

f) CV 24h

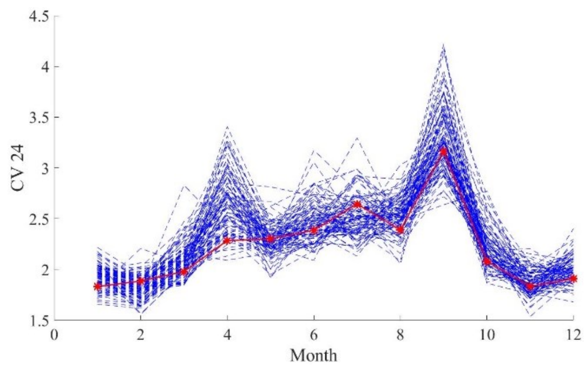

g) Skewness 0.25h

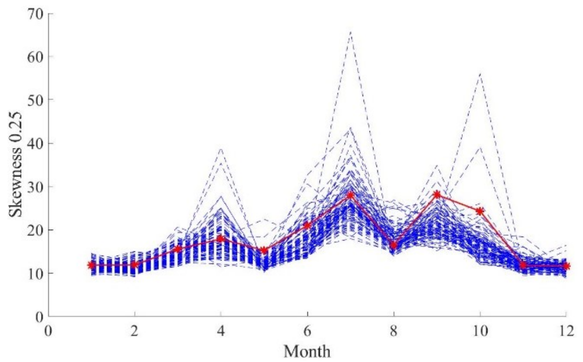

h) Skewness 1h

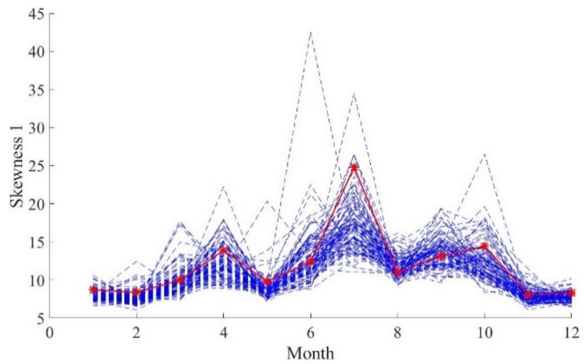

i) Skewness 6h

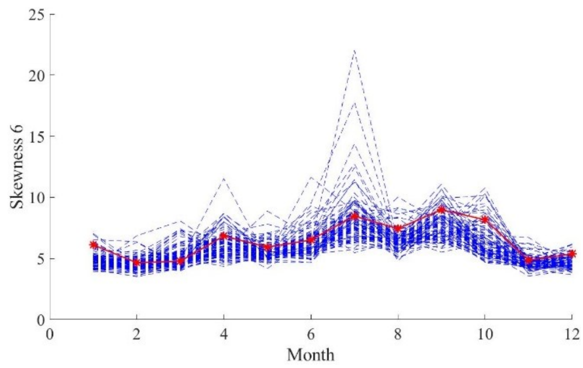

j) Skewness 24h

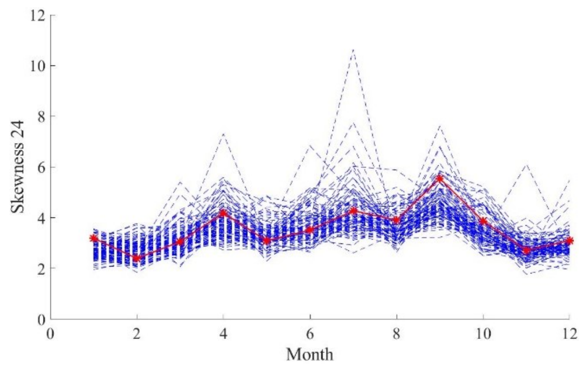

k) AC 0.25h

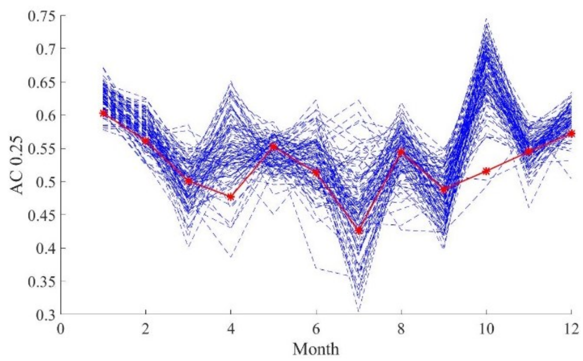

l) AC 1h

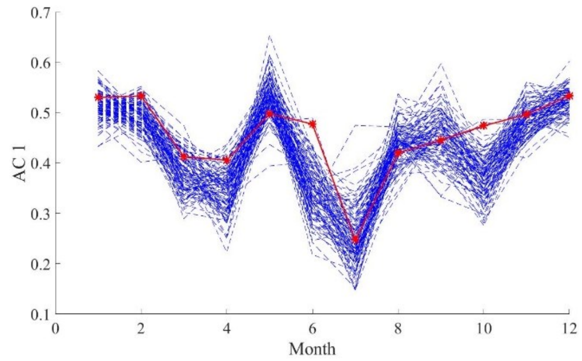

m) AC 6h

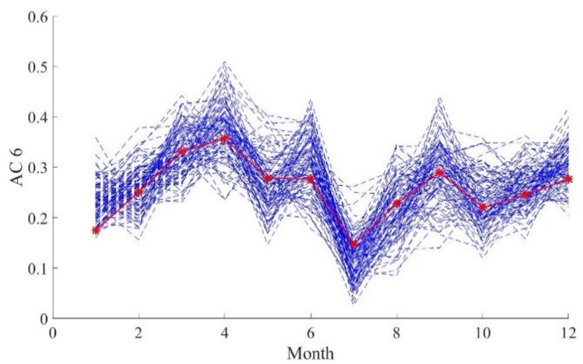

n) AC 24h

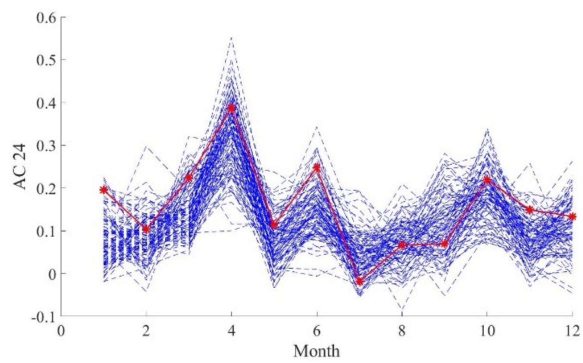

o) Pwet 0.25h

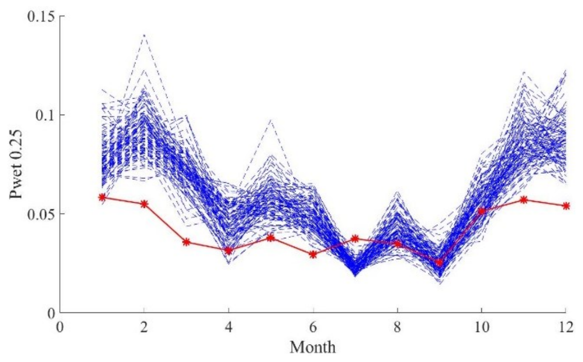

p) Pwet 1h

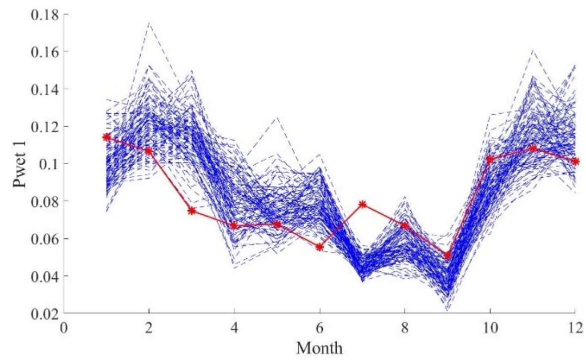

q) Pwet 6h

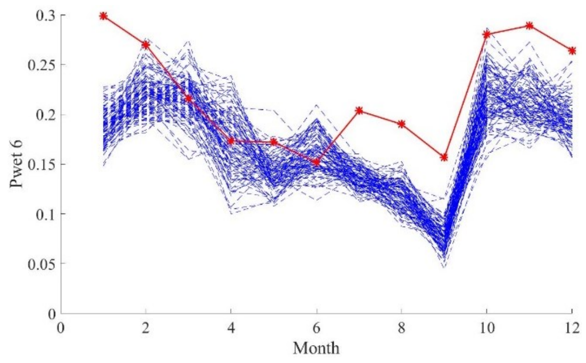

r) Pwet 24h

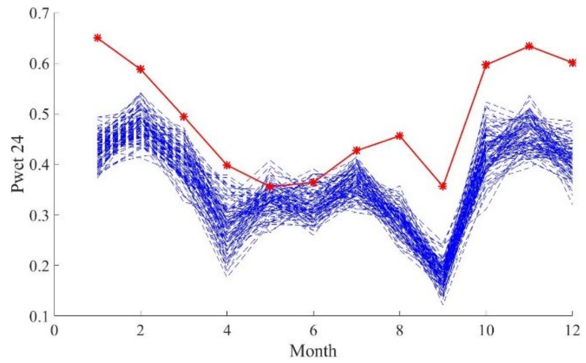

Appendix D: Monthly summary statistics of GLM simulations

D.1: Box and whisker plot for 24h coefficient of variation for each month in each decade for the simulated projected rainfall based on UKCP18 (2020 – 2080).

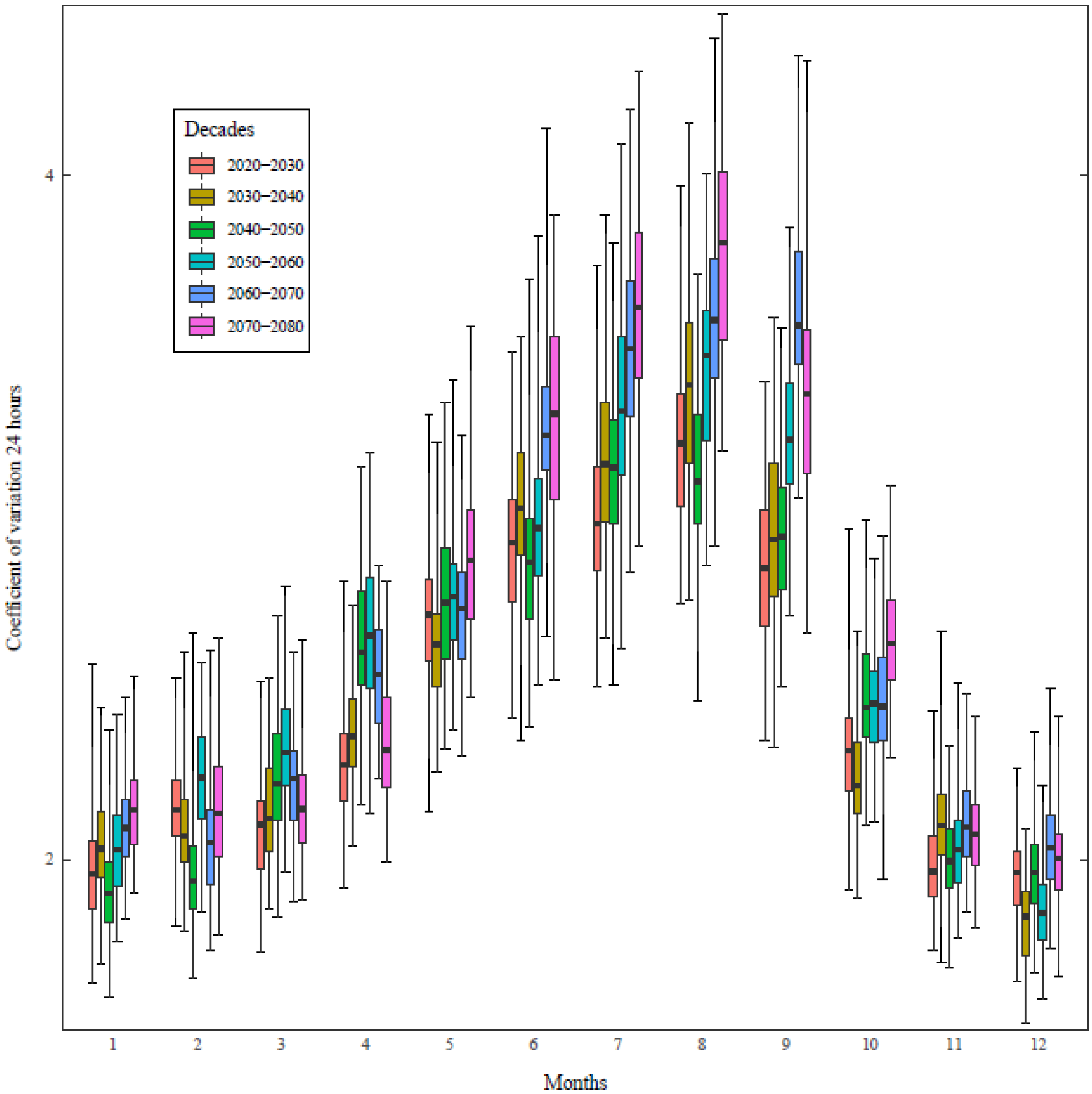

D.2: Box and whisker plot for 24h skewness for each month in each decade for the simulated projected rainfall based on UKCP18 (2020 – 2080).

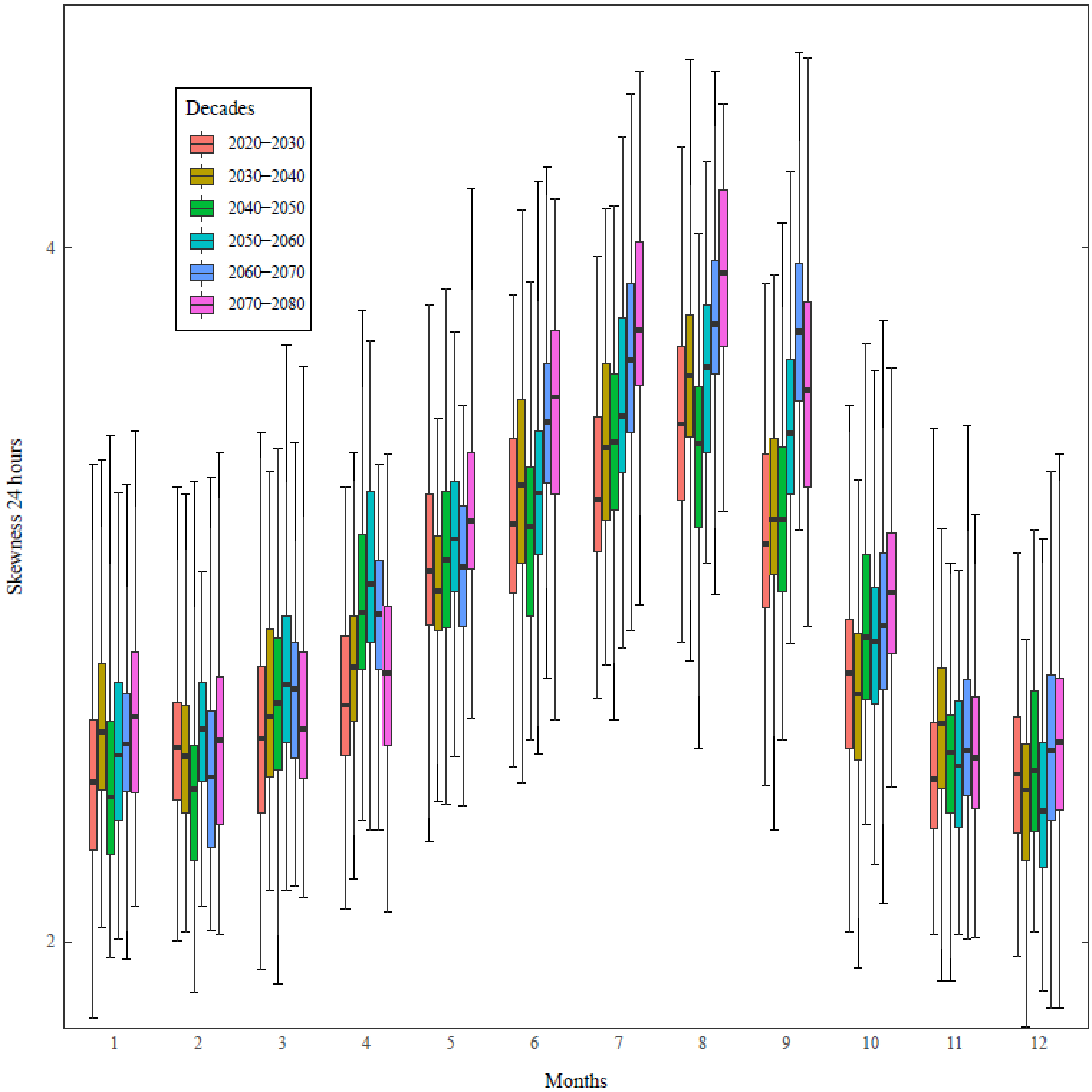

D.3: Box and whisker plot for 24h lag-1 autocorrelation for each month in each decade for the simulated projected rainfall based on UKCP18 (2020 – 2080).

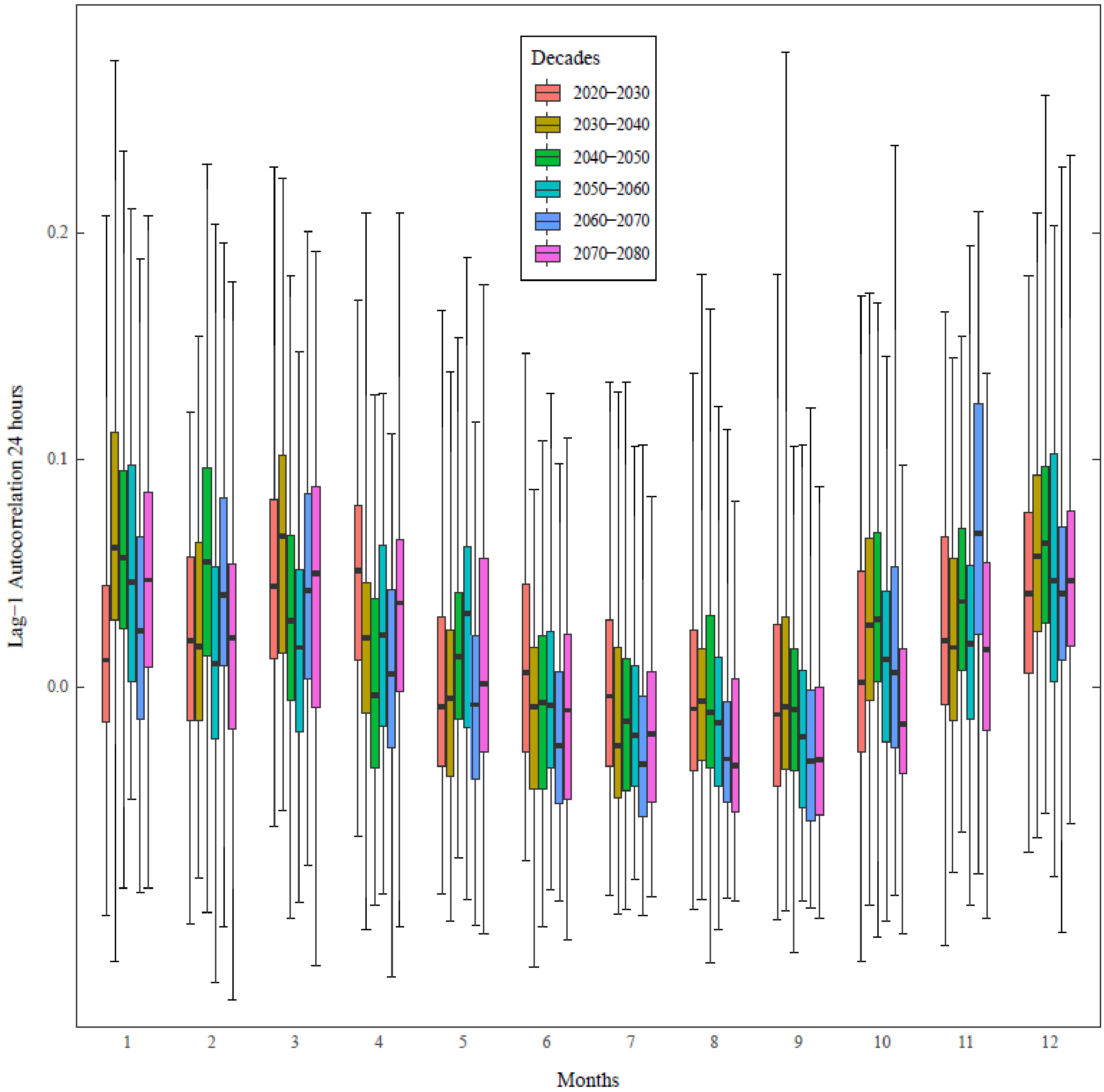

D.4: Box and whisker plot for 24h percentage wet for each month in each decade for the simulated projected rainfall based on UKCP18 (2020 – 2080).

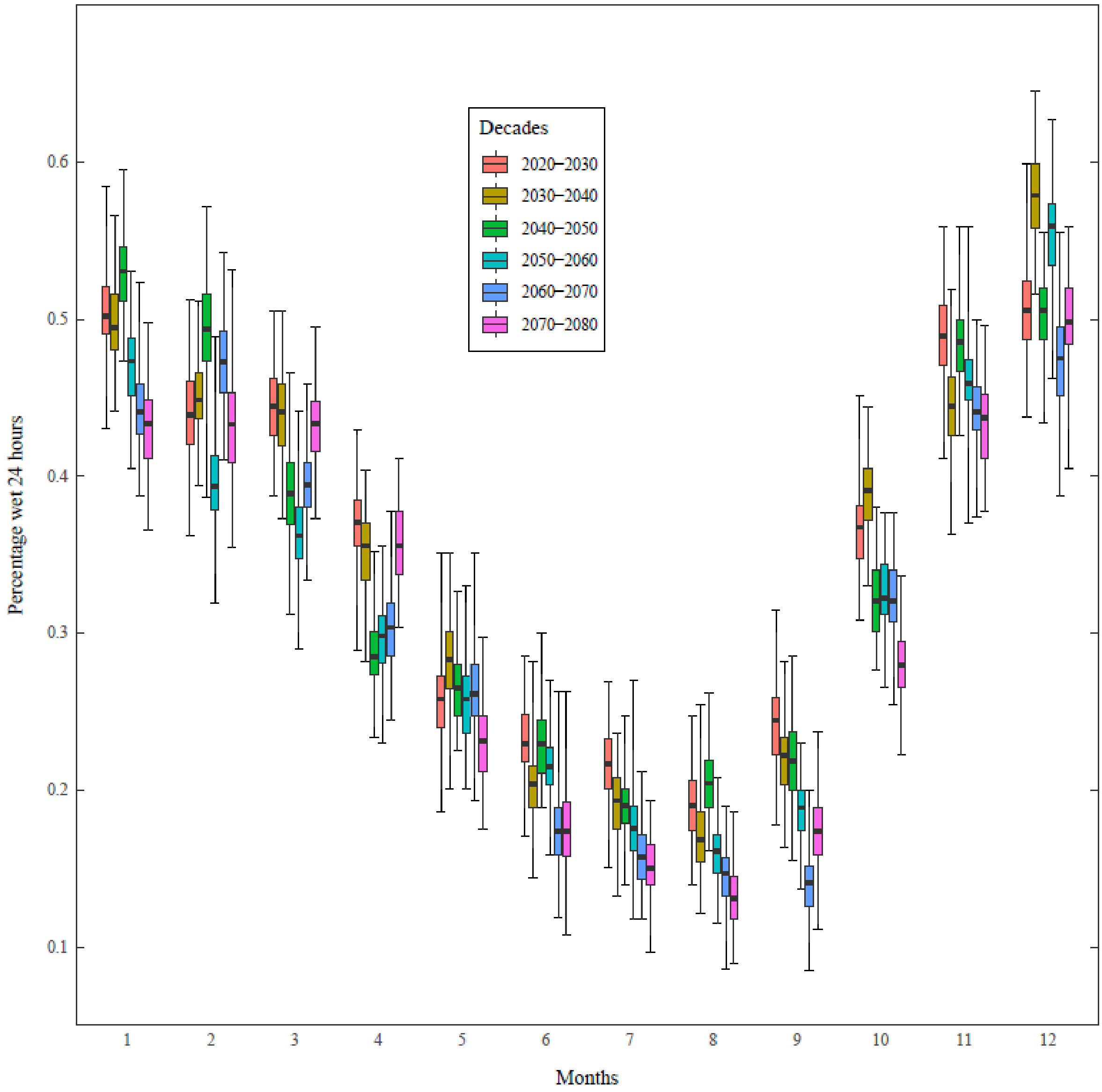

Appendix E: BLRPRx parameters from downscaling validation analysis

E.1: BLRPRx parameters obtained from the downscaling validation analysis

Month		Jan	Feb	Mar	Apr	May	Jun	Jul	Aug	Sep	Oct	Nov	Dec
BLRPRx	λ	0.108	0.028	0.018	0.007	0.022	0.014	0.029	0.012	0.018	0.077	0.023	0.017
	ι	0.70	0.23	0.33	0.20	0.15	0.50	2.45	0.69	2.38	0.94	0.26	0.33
	α	2.00	4.62	2.00	2.40	3.97	2.00	100	2.00	100	2.00	4.33	2.00
	$\frac{\alpha}{\nu}$	7.58	12.84	8.80	5.58	100	12.82	100	10.03	100	8.54	9.21	8.10
	κ	0.141	0.223	0.100	0.518	0.154	0.151	0.103	0.100	0.145	0.100	0.319	0.236
	ϕ	0.092	0.028	0.017	0.020	0.011	0.023	0.048	0.017	0.042	0.010	0.029	0.022

Appendix F: Monthly summary statistics from downscaled GLM simulations

F.1: Box and whisker plot for 0.25h mean for each month in each decade for the downscaled rainfall based on UKCP18 RCP8.5 scenario (2020 – 2080).

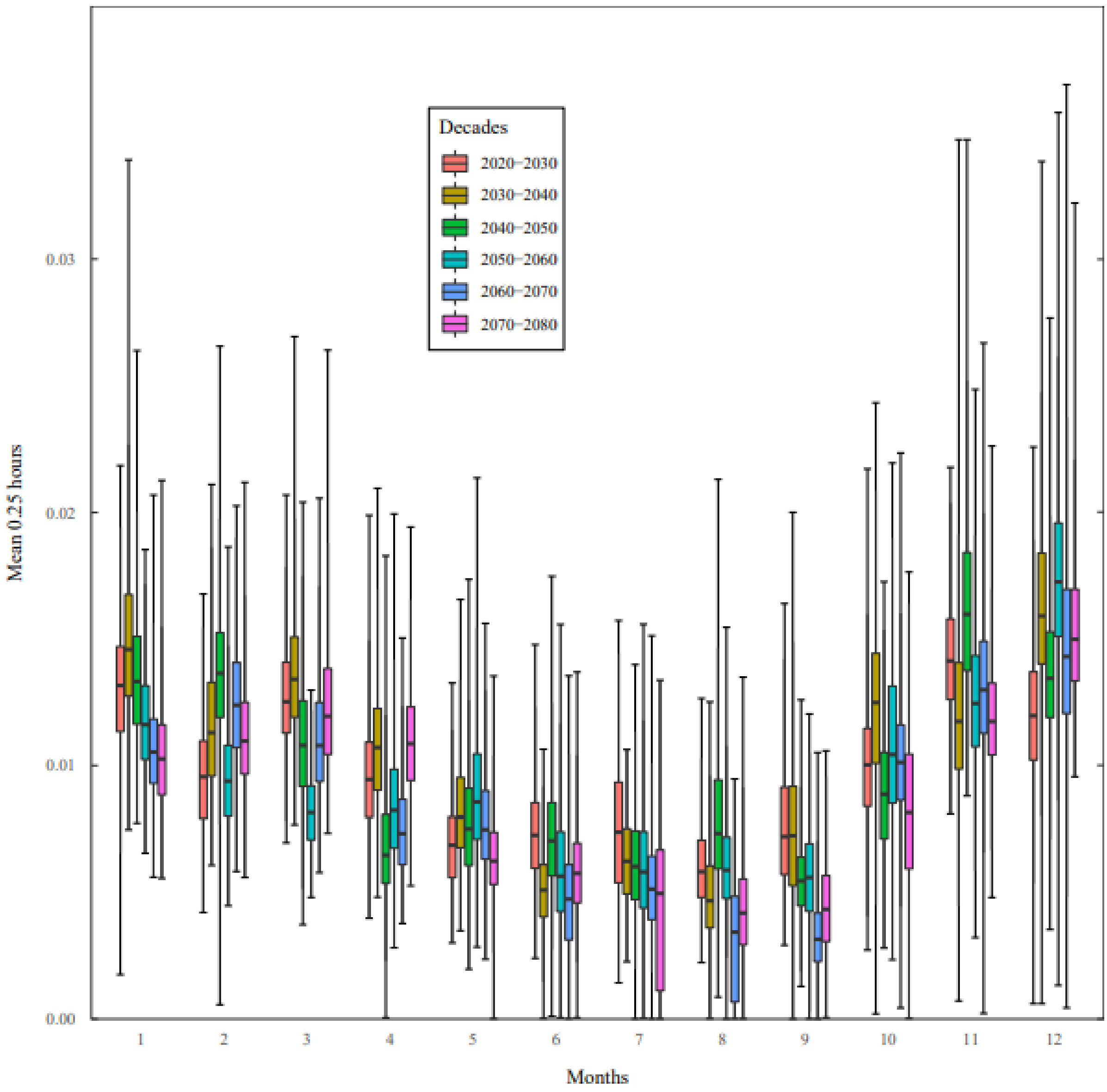

F.2: Box and whisker plot for 1h mean for each month in each decade for the downscaled rainfall based on UKCP18 RCP8.5 scenario (2020 – 2080).

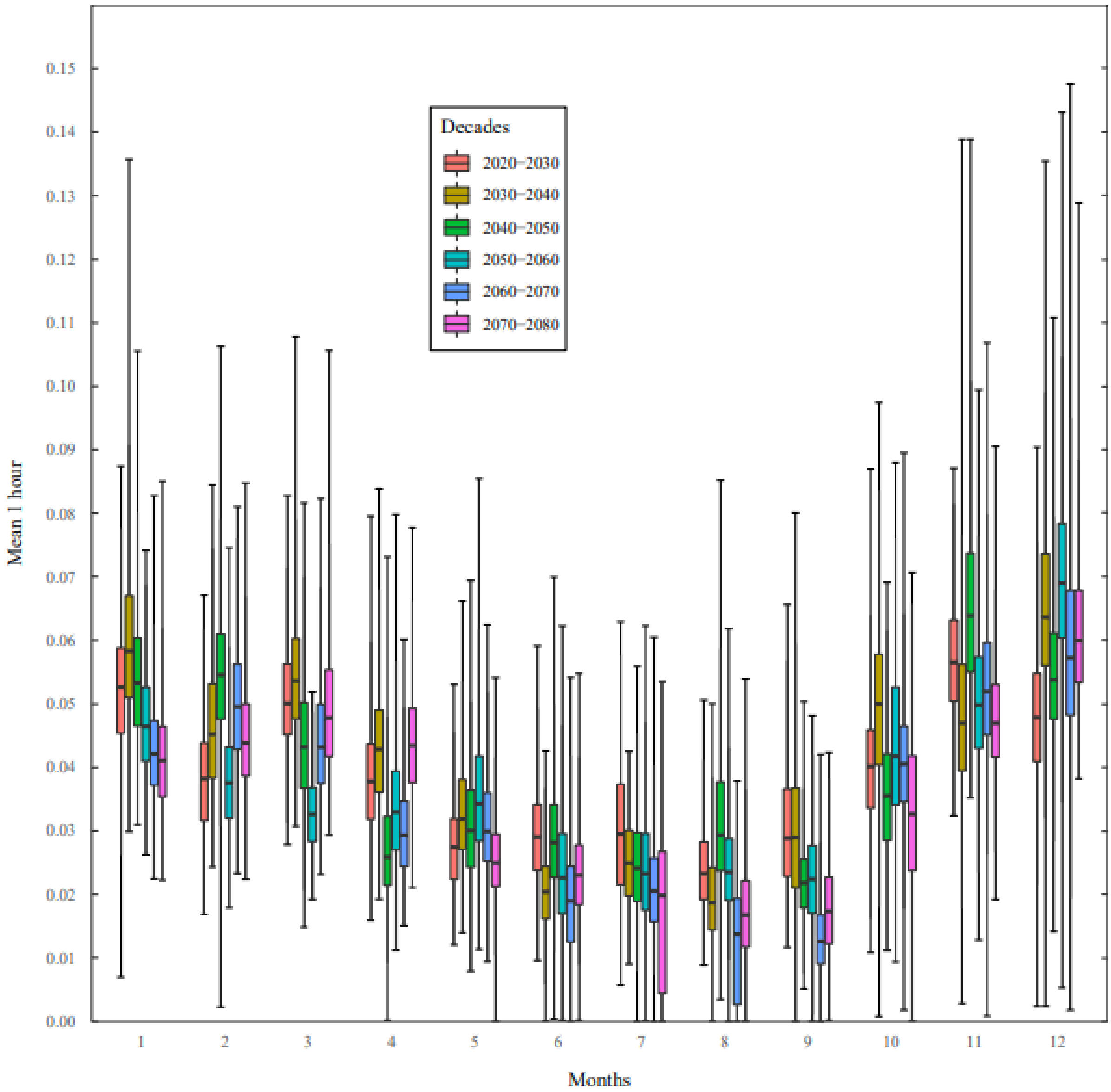

F.3: Box and whisker plot for 6h mean for each month in each decade for the downscaled rainfall based on UKCP18 RCP8.5 scenario (2020 – 2080).

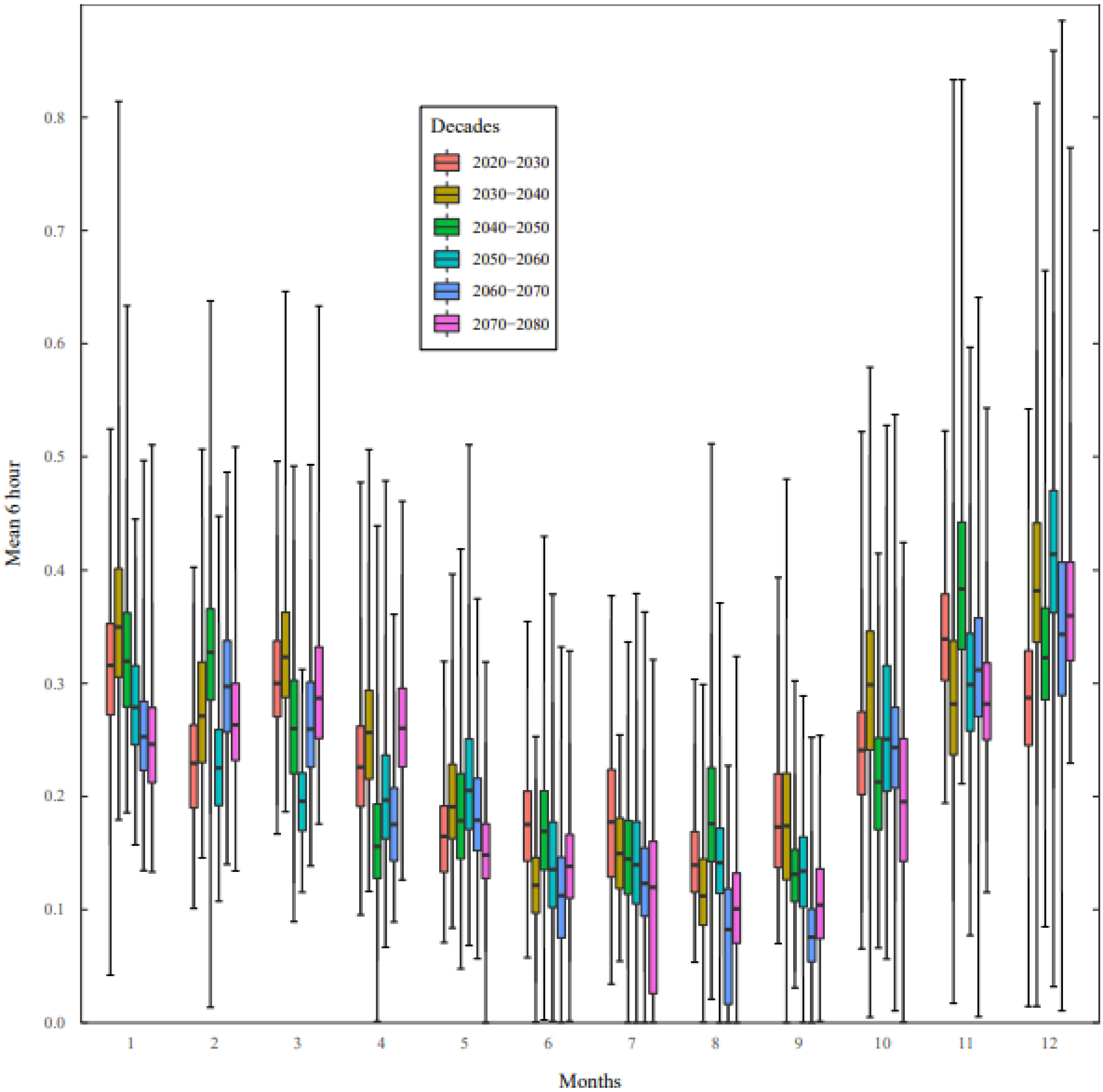

F.4: Box and whisker plot for 24h mean for each month in each decade for the downscaled rainfall based on UKCP18 RCP8.5 scenario (2020 – 2080).

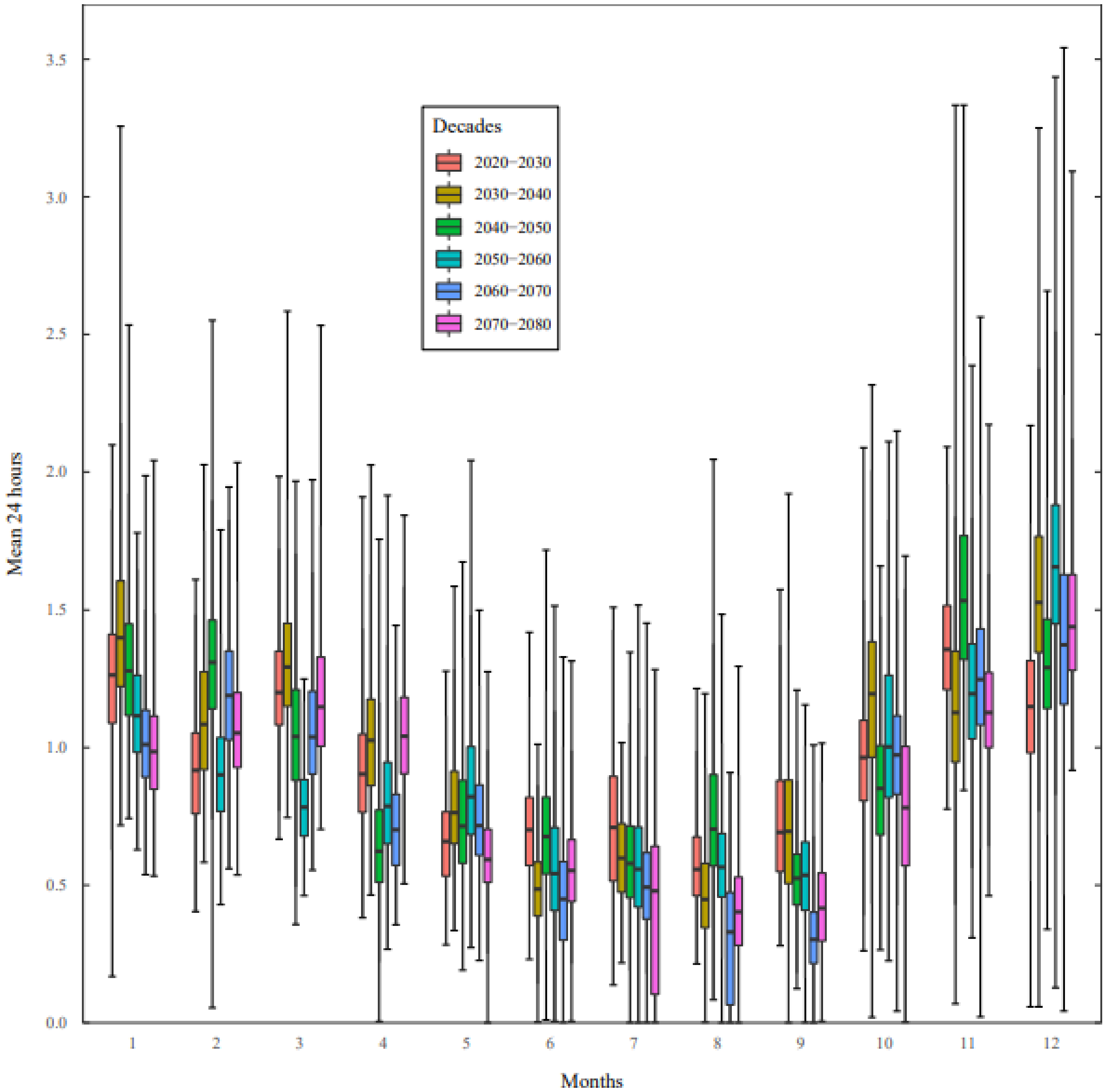

F.5: Box and whisker plot for 0.25h coefficient of variation for each month in each decade for the downscaled rainfall based on UKCP18 RCP8.5 scenario (2020 – 2080).

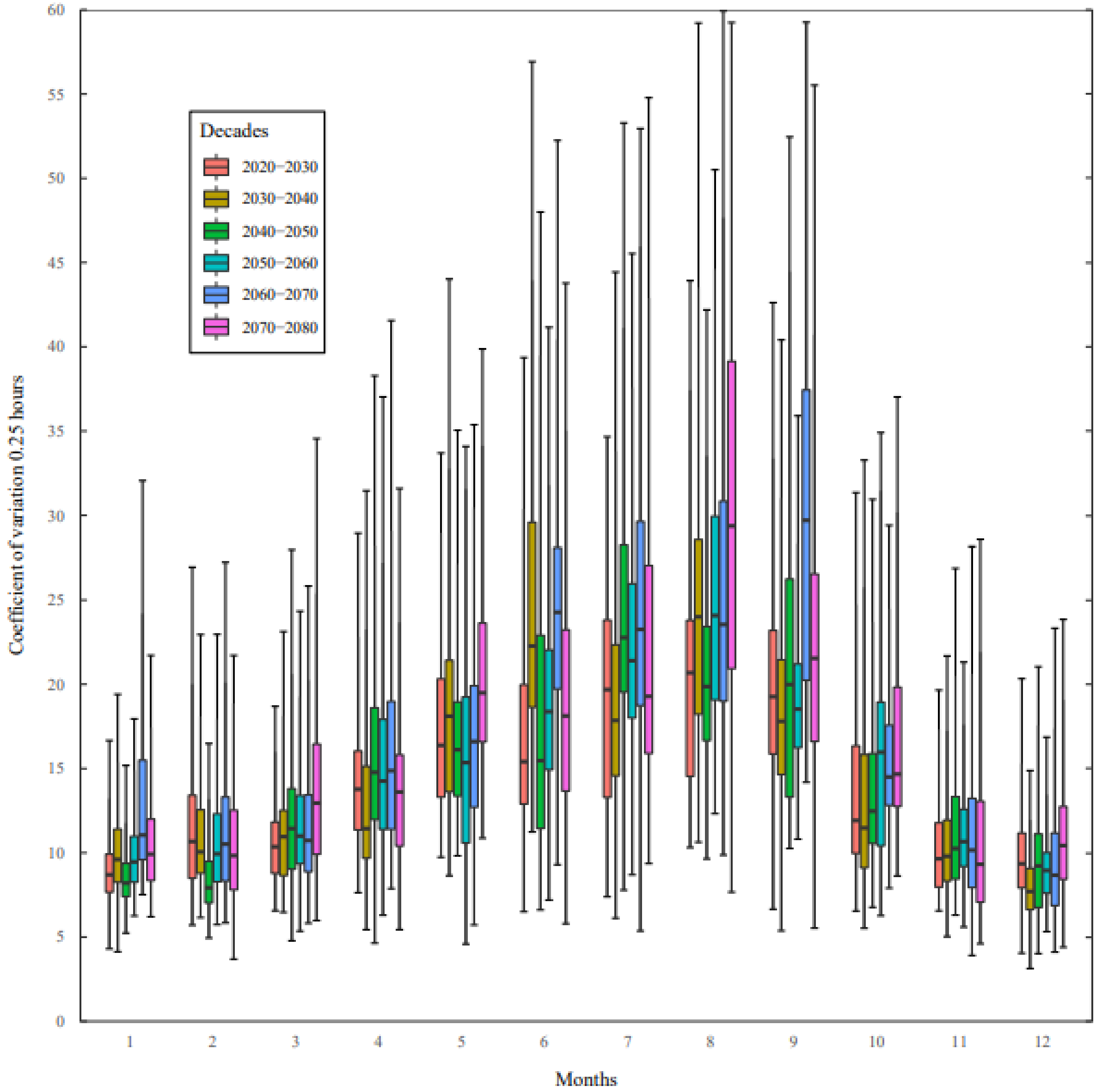

F.6: Box and whisker plot for 1h coefficient of variation for each month in each decade for the downscaled rainfall based on UKCP18 RCP8.5 scenario (2020 – 2080).

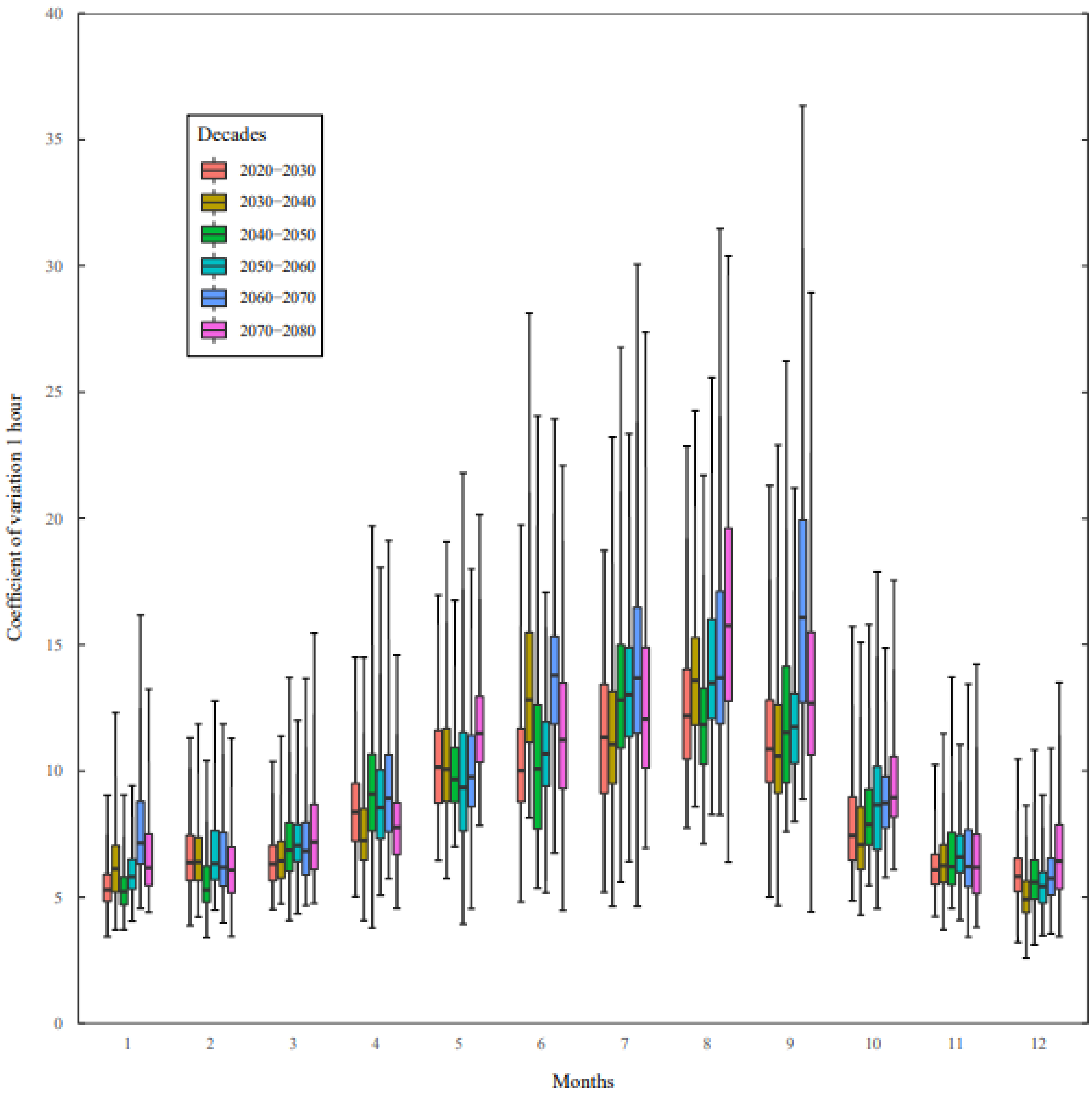

F.7: Box and whisker plot for 6h coefficient of variation for each month in each decade for the downscaled rainfall based on UKCP18 RCP8.5 scenario (2020 – 2080).

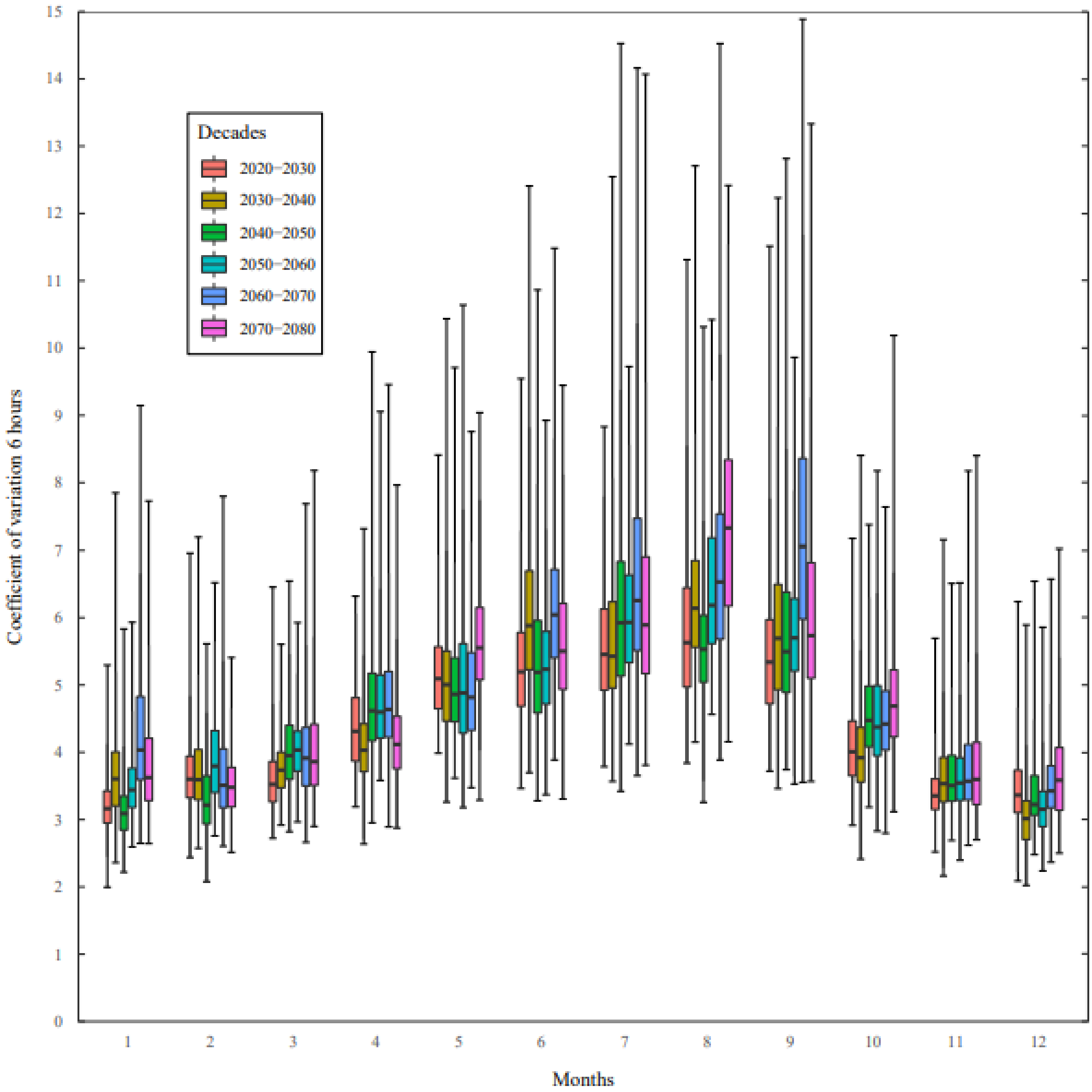

F.8: Box and whisker plot for 24h coefficient of variation for each month in each decade for the downscaled rainfall based on UKCP18 RCP8.5 scenario (2020 – 2080).

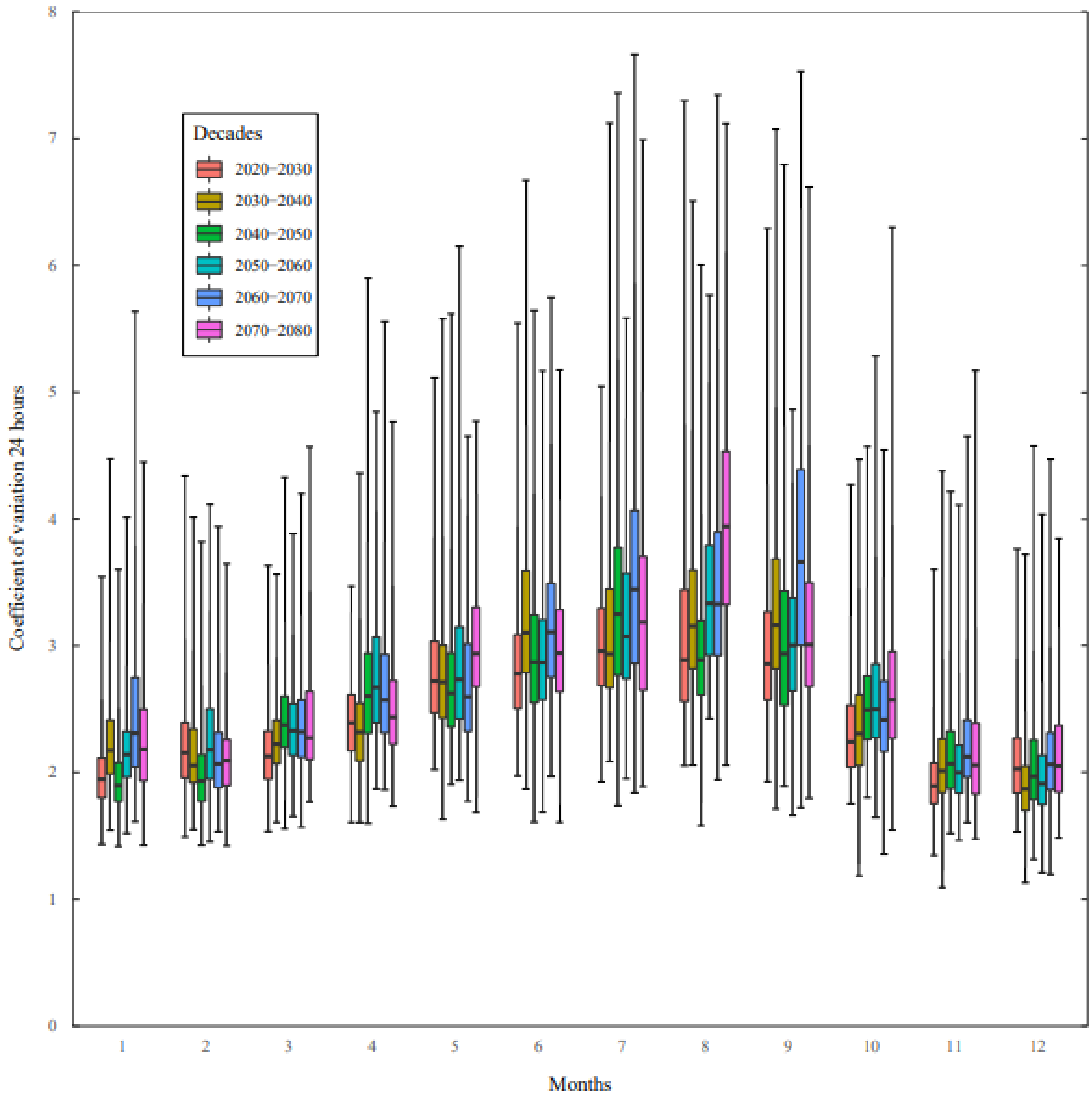

F.9: Box and whisker plot for 0.25h skewness for each month in each decade for the downscaled rainfall based on UKCP18 RCP8.5 scenario (2020 – 2080).

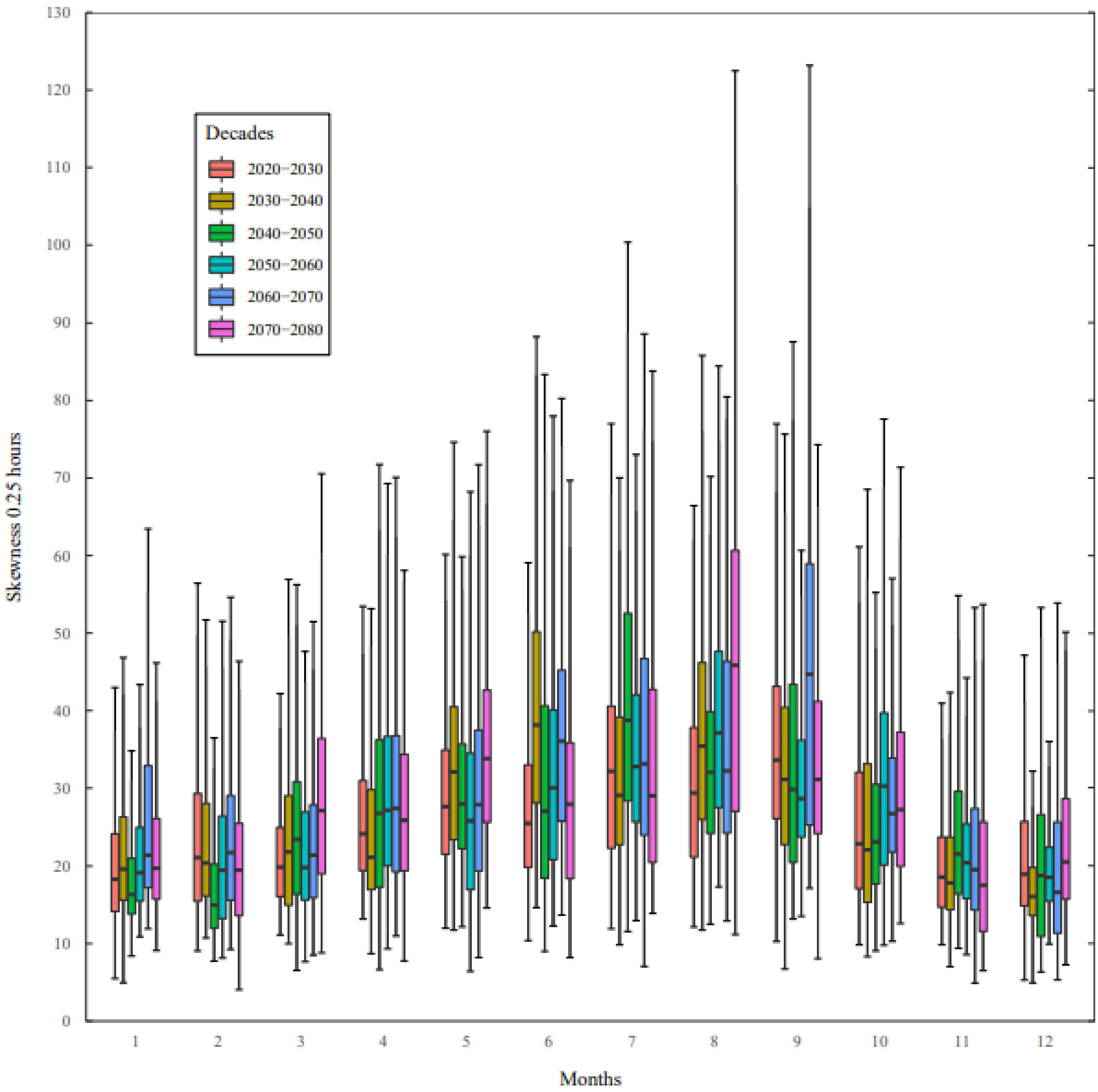

F.10: Box and whisker plot for 1h skewness for each month in each decade for the downscaled rainfall based on UKCP18 RCP8.5 scenario (2020 – 2080).

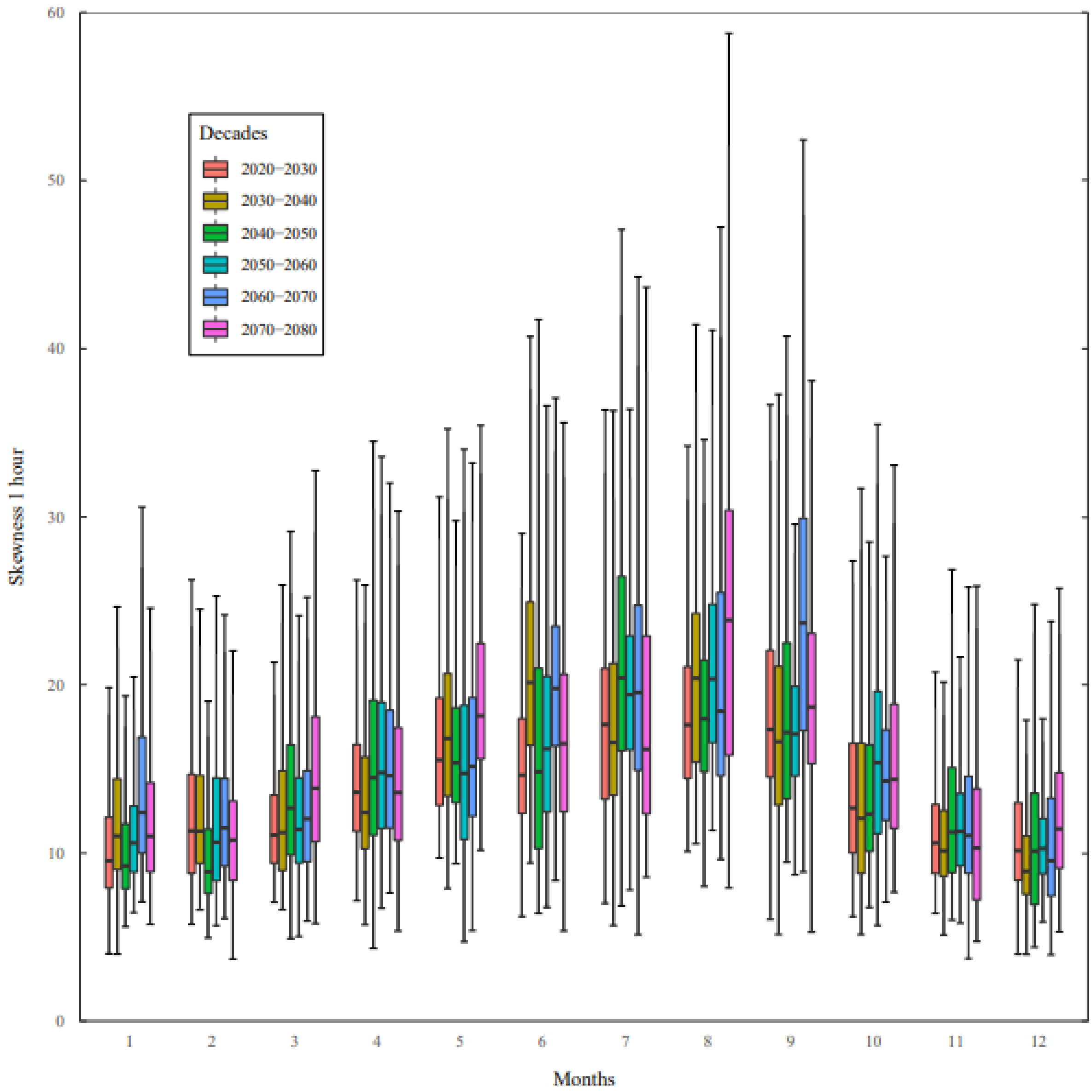

F.11: Box and whisker plot for 6h skewness for each month in each decade for the downscaled rainfall based on UKCP18 RCP8.5 scenario (2020 – 2080).

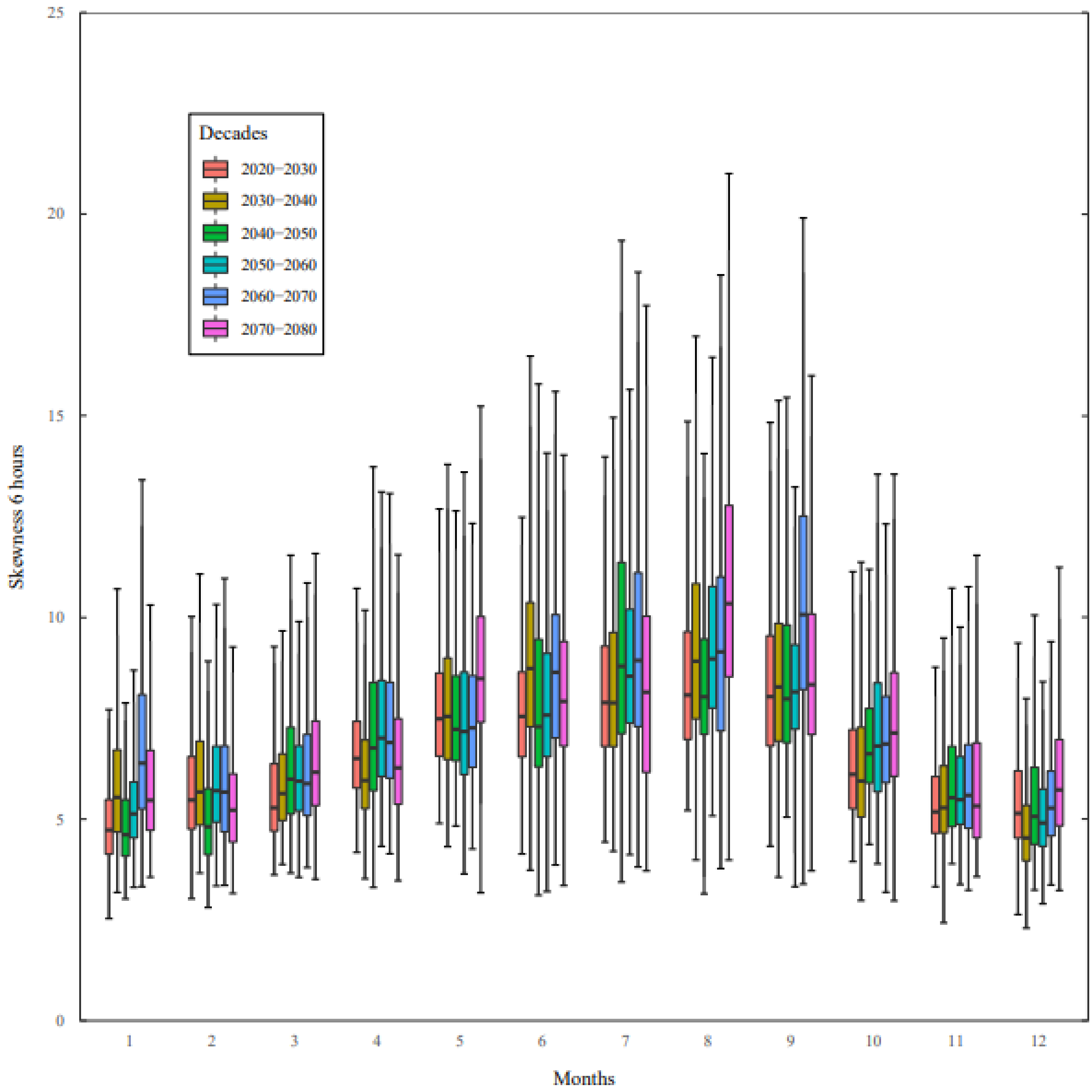

F.12: Box and whisker plot for 24h skewness for each month in each decade for the downscaled rainfall based on UKCP18 RCP8.5 scenario (2020 – 2080).

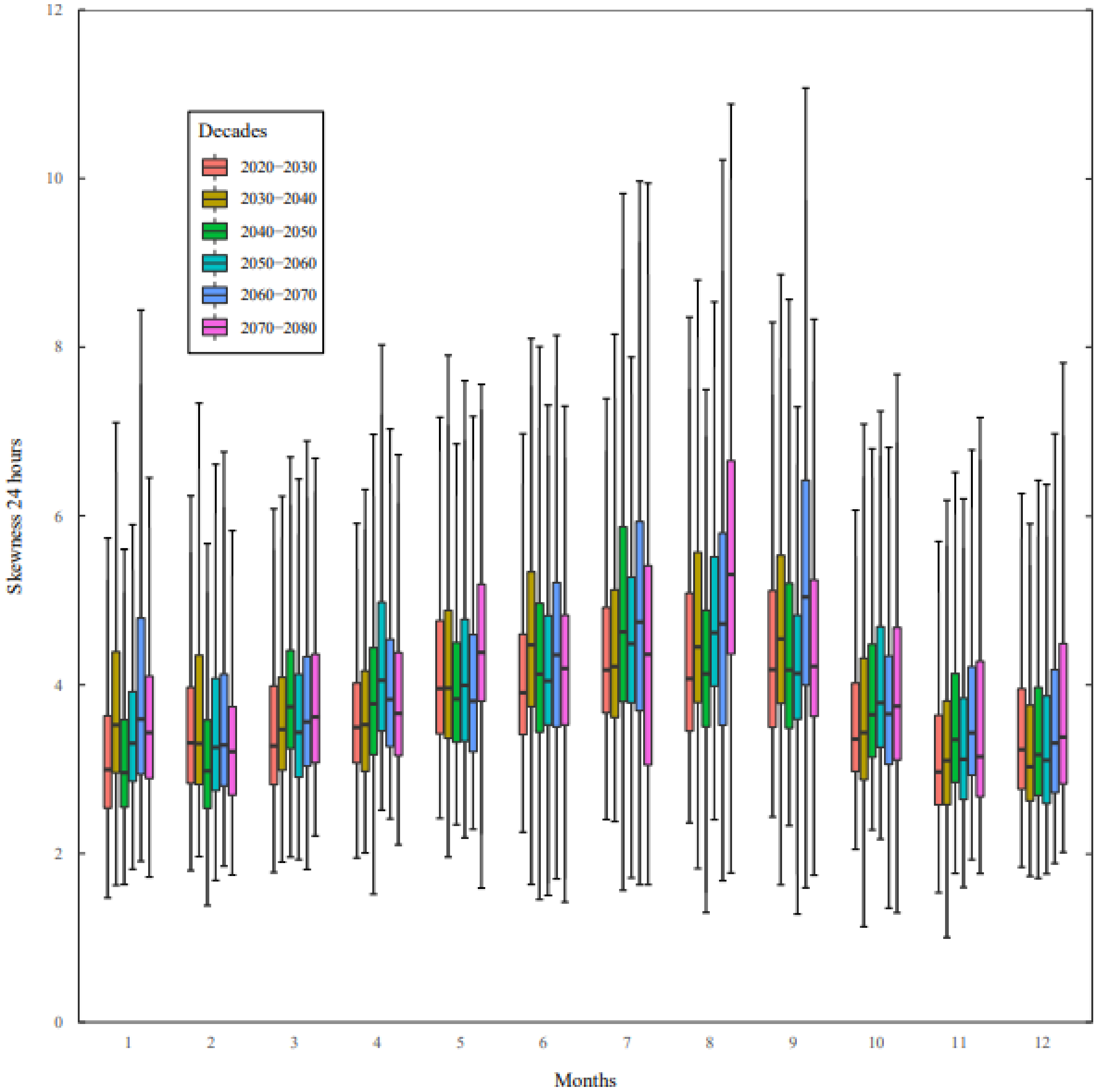

F.13: Box and whisker plot for 0.25h lag-1 autocorrelation for each month in each decade for the downscaled rainfall based on UKCP18 RCP8.5 scenario (2020 – 2080).

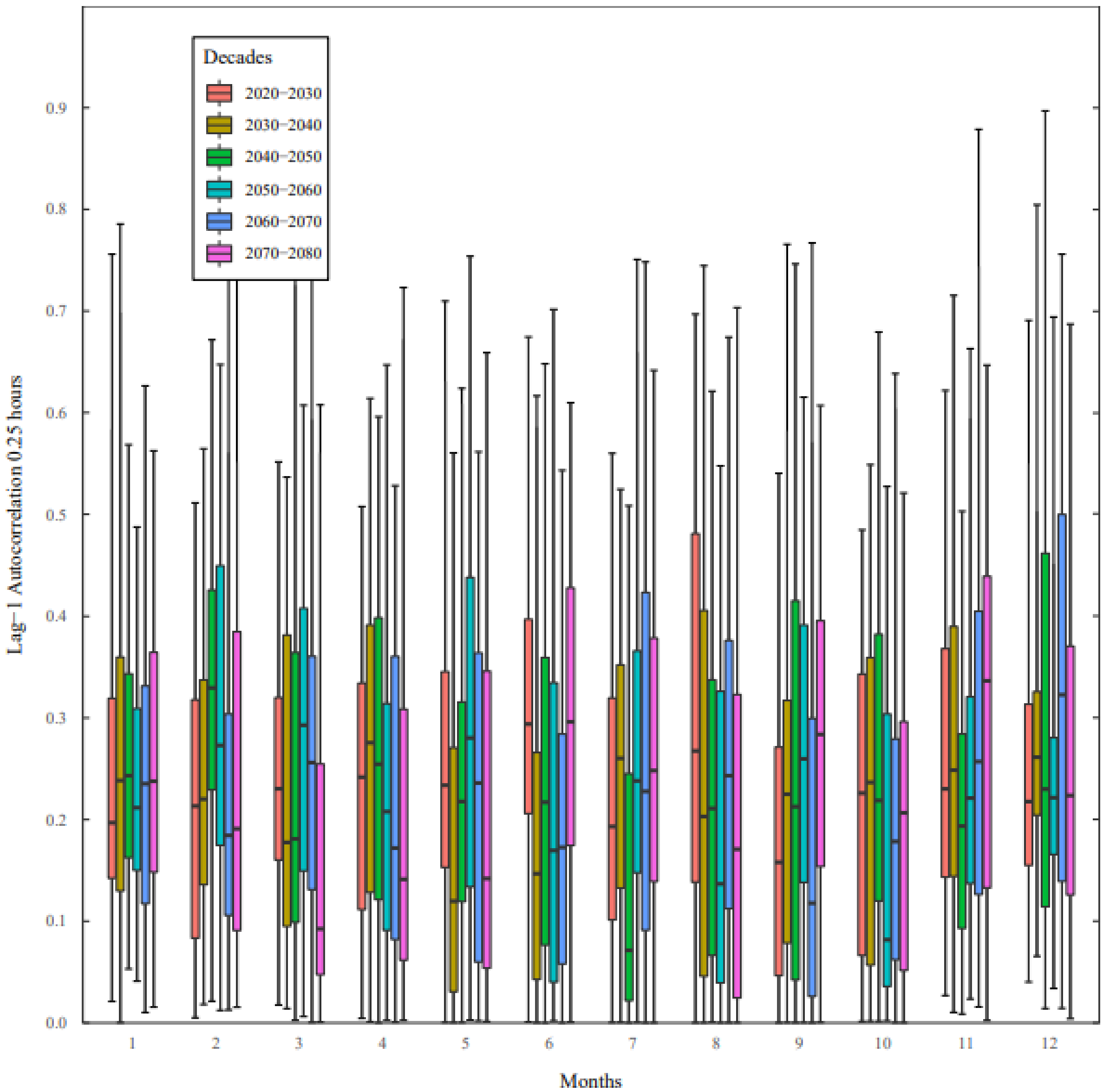

F.14: Box and whisker plot for 1h lag-1 autocorrelation for each month in each decade for the downscaled rainfall based on UKCP18 RCP8.5 scenario (2020 – 2080).

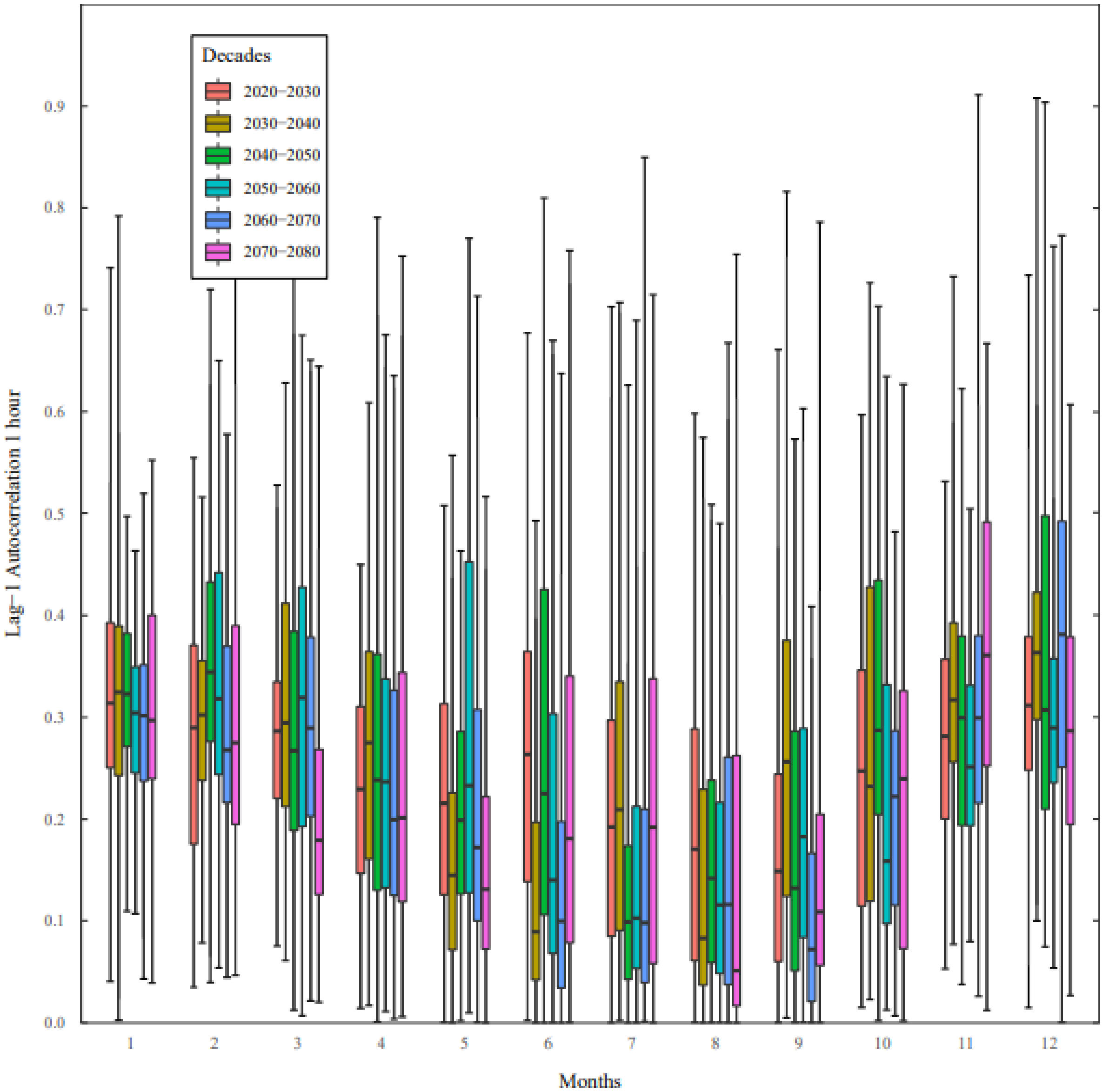

F.15: Box and whisker plot for 6h lag-1 autocorrelation for each month in each decade for downscaled rainfall based on UKCP18 RCP8.5 scenario (2020 – 2080).

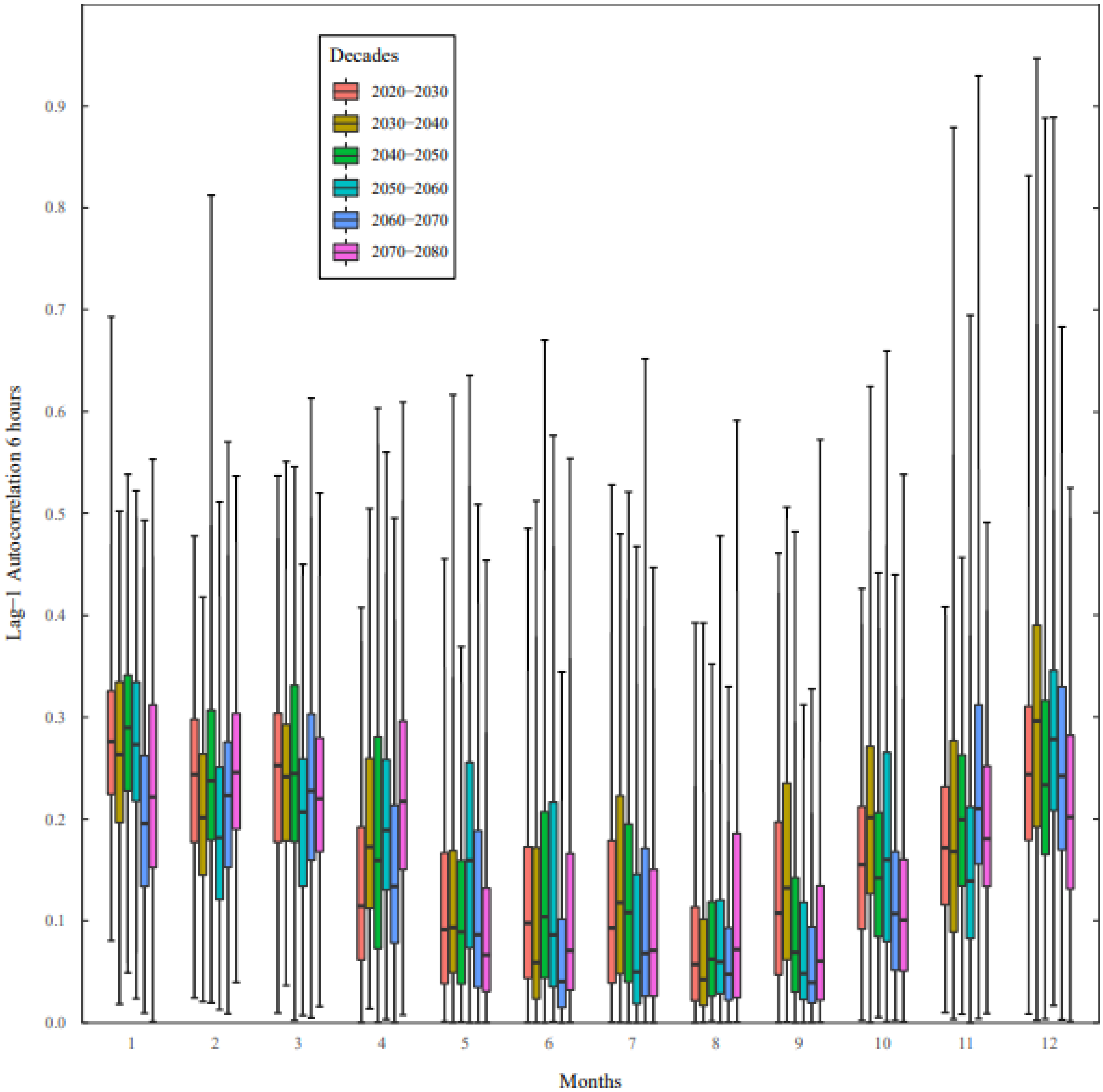

F.16: Box and whisker plot for 24h lag-1 autocorrelation for each month in each decade for the downscaled rainfall based on UKCP18 RCP8.5 scenario (2020 – 2080).

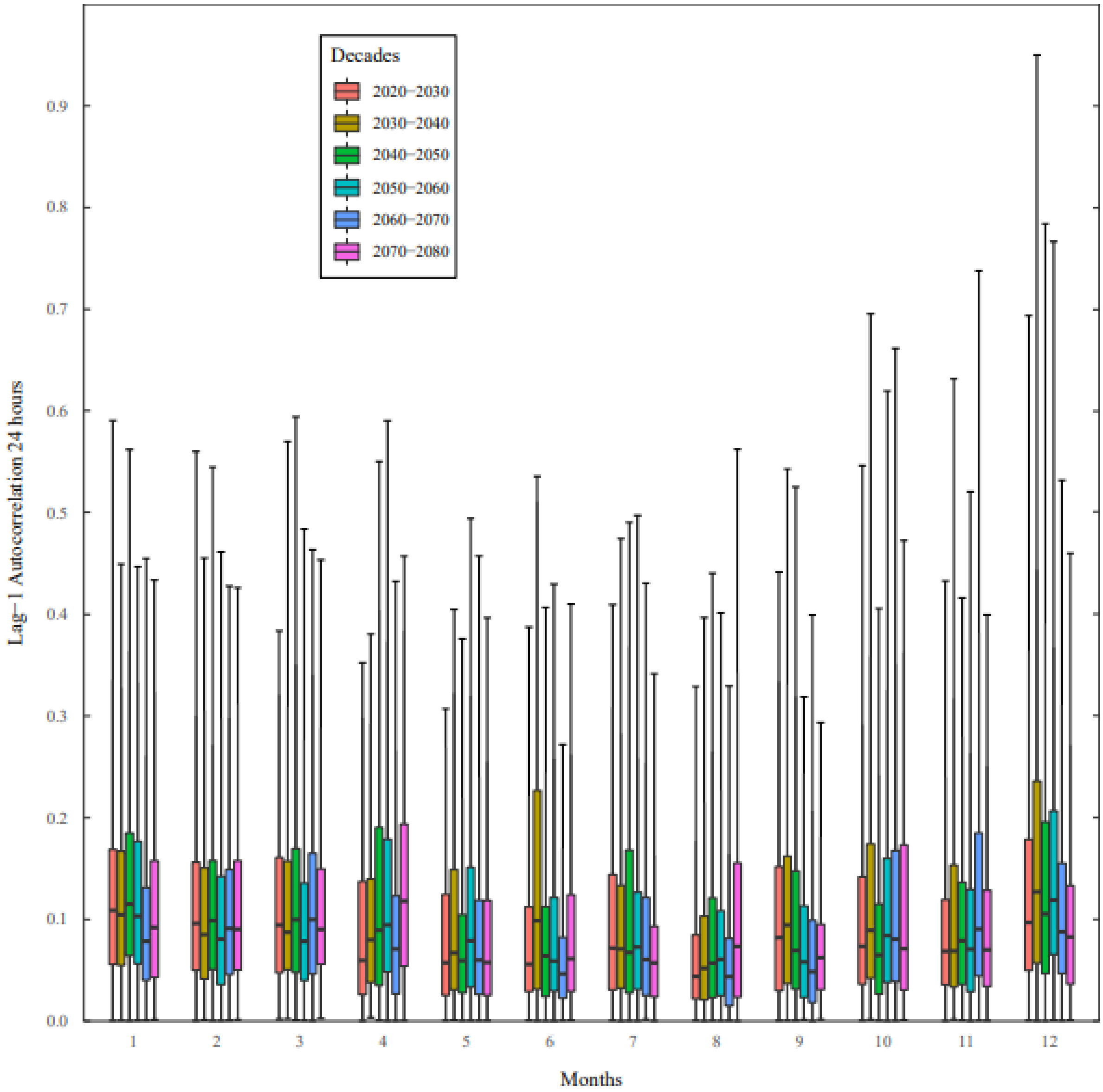

F.17: Box and whisker plot for 0.25h percentage wet for each month in each decade for the downscaled rainfall based on UKCP18 RCP8.5 scenario (2020 – 2080).

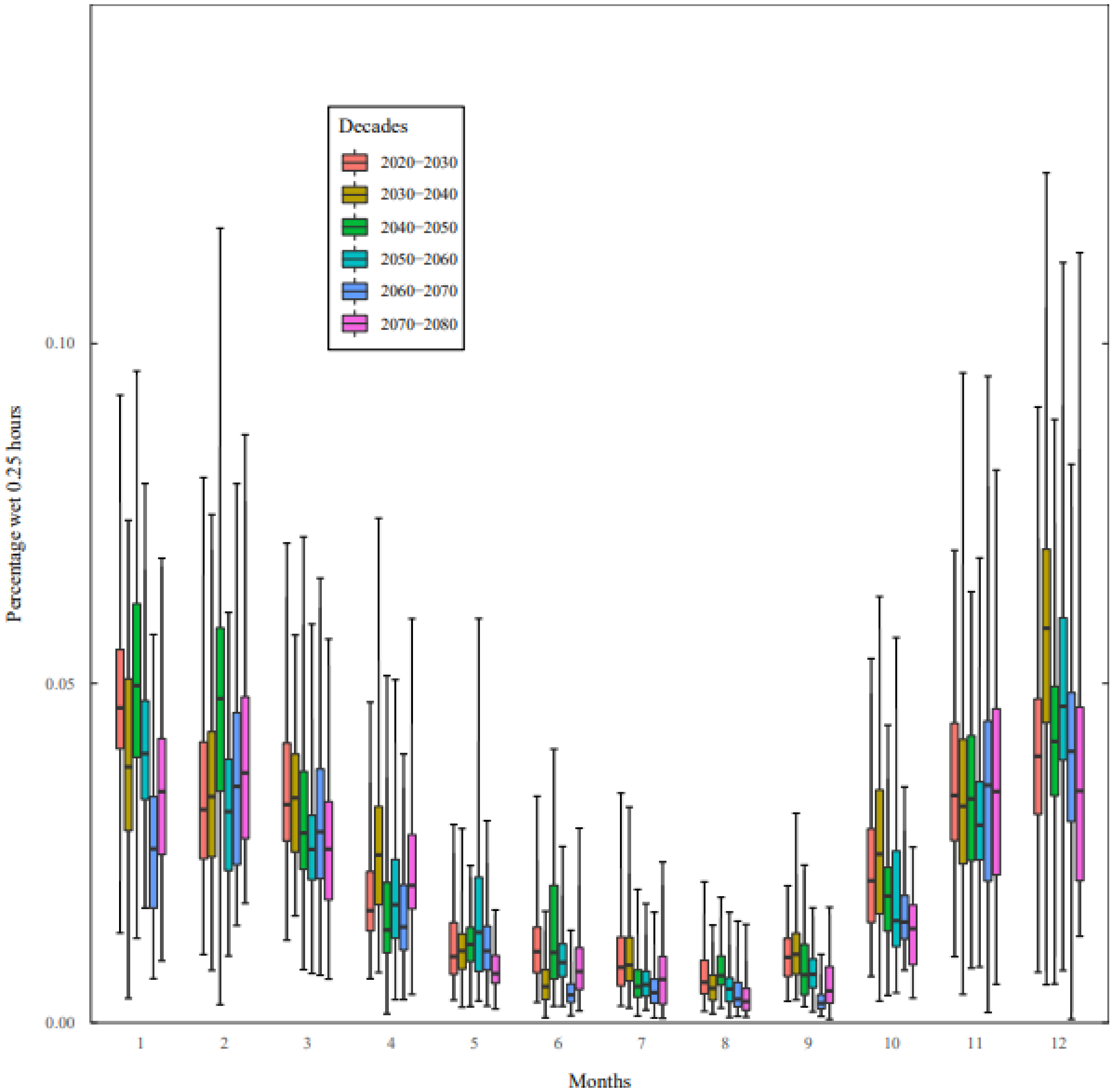

F.18: Box and whisker plot for 1h percentage wet for each month in each decade for the downscaled rainfall based on UKCP18 RCP8.5 scenario (2020 – 2080).

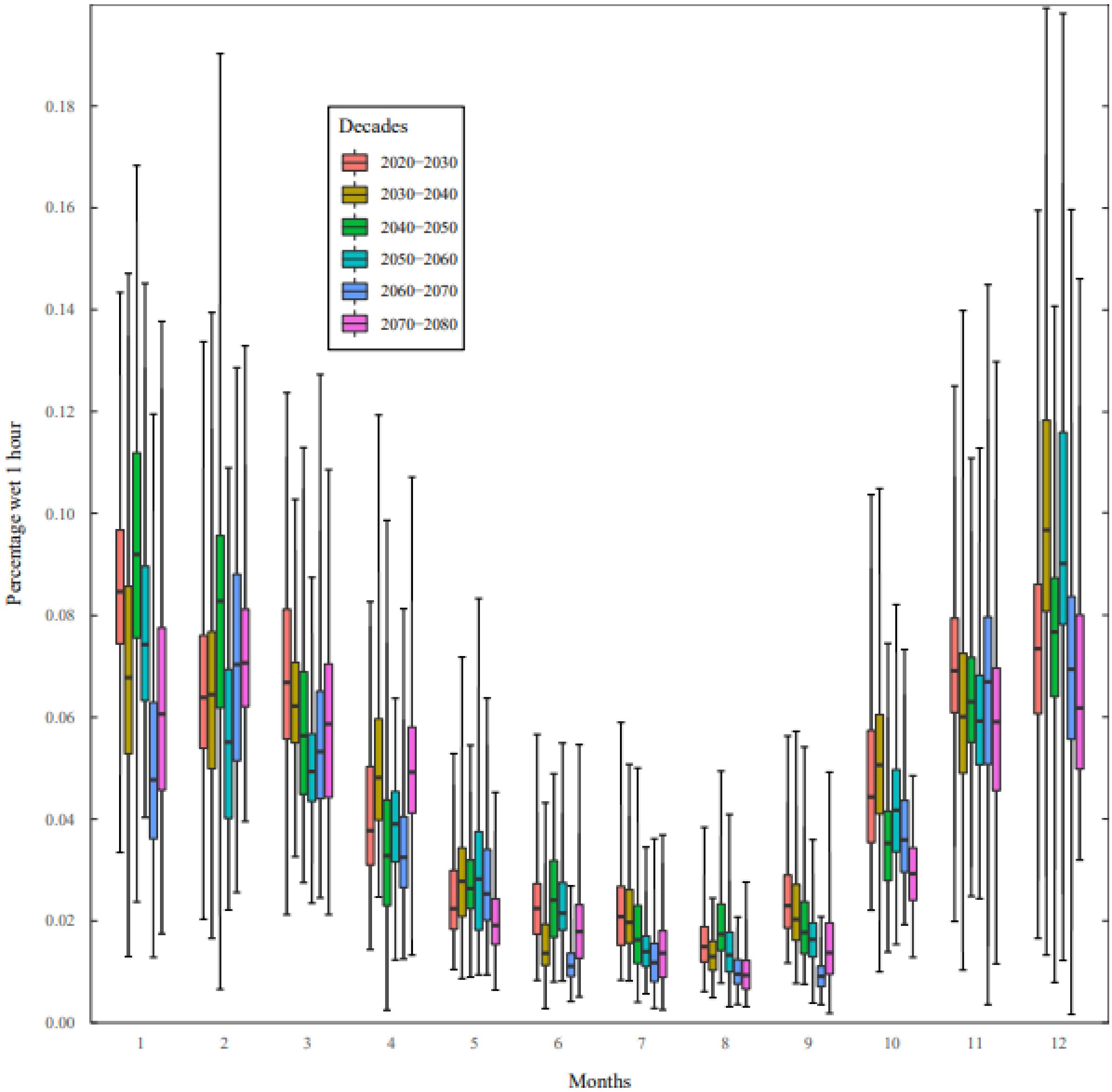

F.19: Box and whisker plot for 6h percentage wet for each month in each decade for the downscaled rainfall based on UKCP18 RCP8.5 scenario (2020 – 2080).

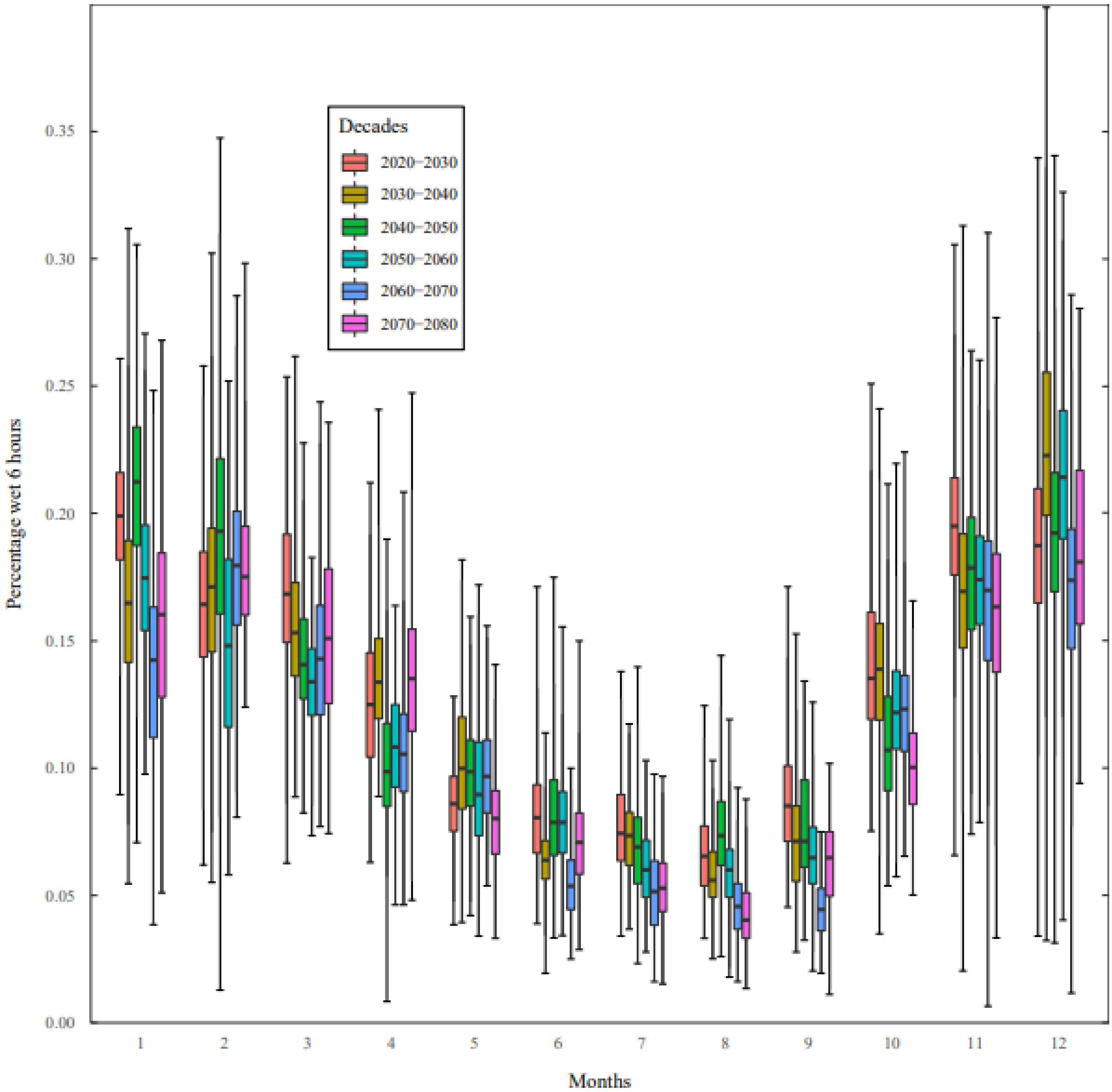

F.20: Box and whisker plot for 24h percentage wet for each month in each decade for the downscaled rainfall based on UKCP18 RCP8.5 scenario (2020 – 2080).

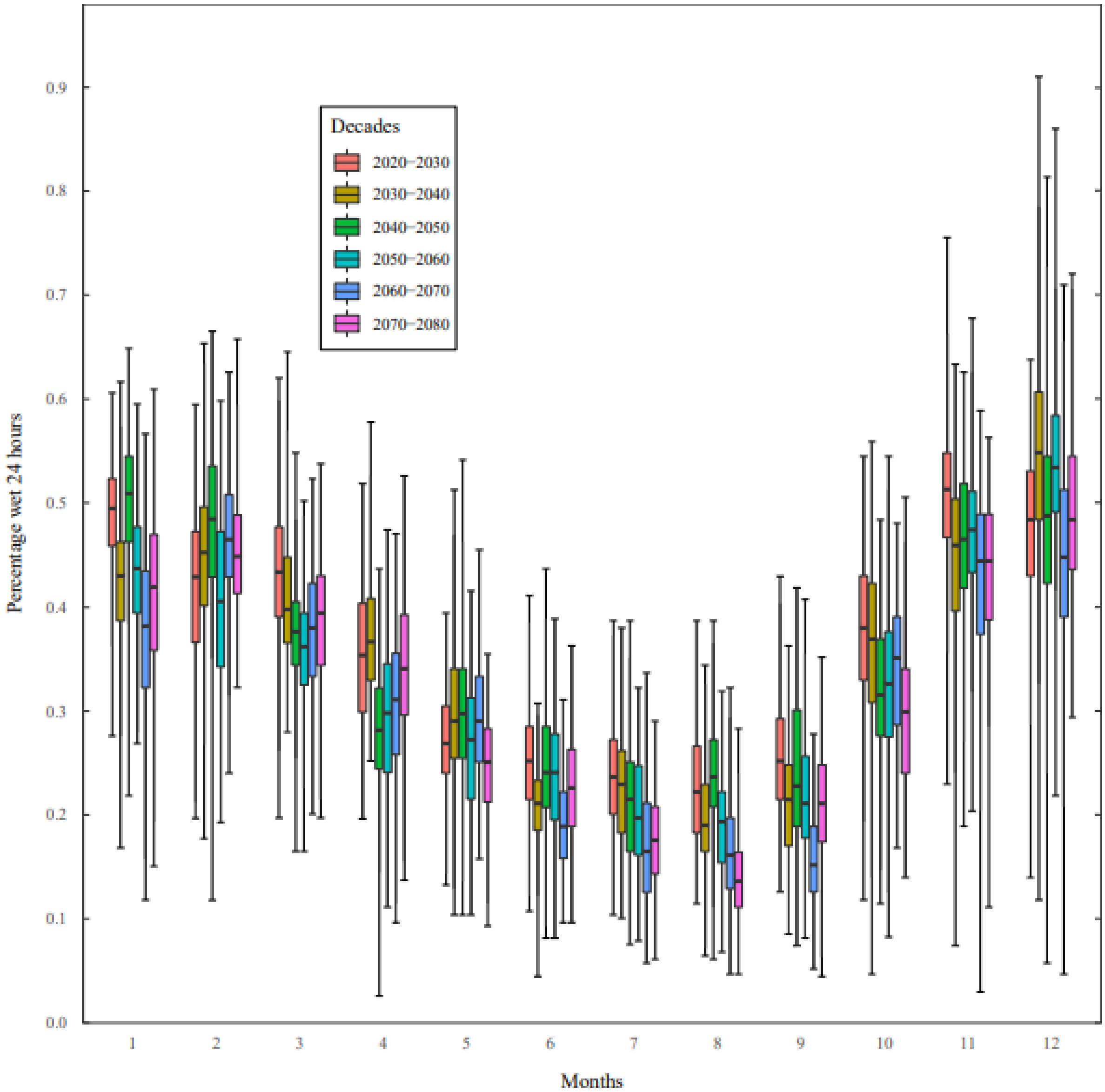

Appendix G: Key nodes from the Dartford analysis

G.1: Nodes on the side berms at which the predicted evolution of horizontal displacements was compared against field measurements in Figure 6.20.

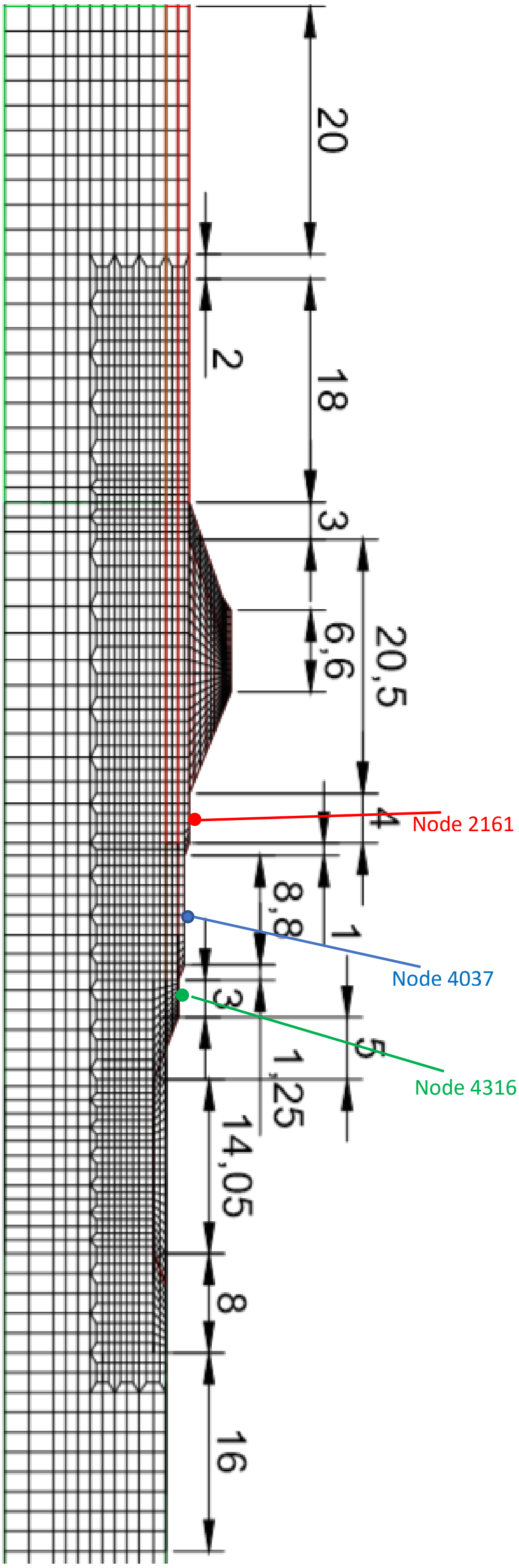

Appendix H: Tidal boundary condition

In Chapter 7, the selection of a monthly time increment was discussed and found to be the most optimal in the lifecycle analysis. The decision was based on numerical analyses of various time resolutions by Lee (2019), showing that by using monthly actual rainfall, the lifecycle analysis was able to reproduce the general seasonal behaviour of the embankment that was obtained from the daily time increment analysis.

As the embankment analysed by Lee (2019) was a rail embankment, only precipitation and evapotranspiration from vegetation was explored. In a flood embankment however, the presence of semidiurnal tidal cycles and their immediate influence on pore pressures within the embankment required further investigation to identify the most optimum approach in reproducing tidal cycles and their effects in monthly increments.

For this investigation, a control analysis was conducted of the embankment, constructed to the first stage elevation of +6.3mODN, subjected to semidiurnal tidal cycles in hourly increments for one month. The pore pressures and displacements from this analysis were used for comparisons with those from the monthly time resolution analyses to assess the suitability of each monthly tidal representation in replicating the semidiurnal control analysis. For the monthly time resolution analyses, one tidal cycle involved a third of the time in high tide, followed by a third of the time in low tide and ending with a third of the time in tide at the mean river level. The total number of tidal cycles per month were varied (1, 2 and 4) to identify the most optimum number in matching the semidiurnal analysis.

Figure H.1(a) shows the pore water pressure contours at the end of the first stage embankment construction, with the embankment in suction during construction within the unsaturated London Clay fill. In addition, excess pore pressures were generated at the base of the embankment, predominantly in the deeper foundation clay as the initial phreatic surface was kept constant.

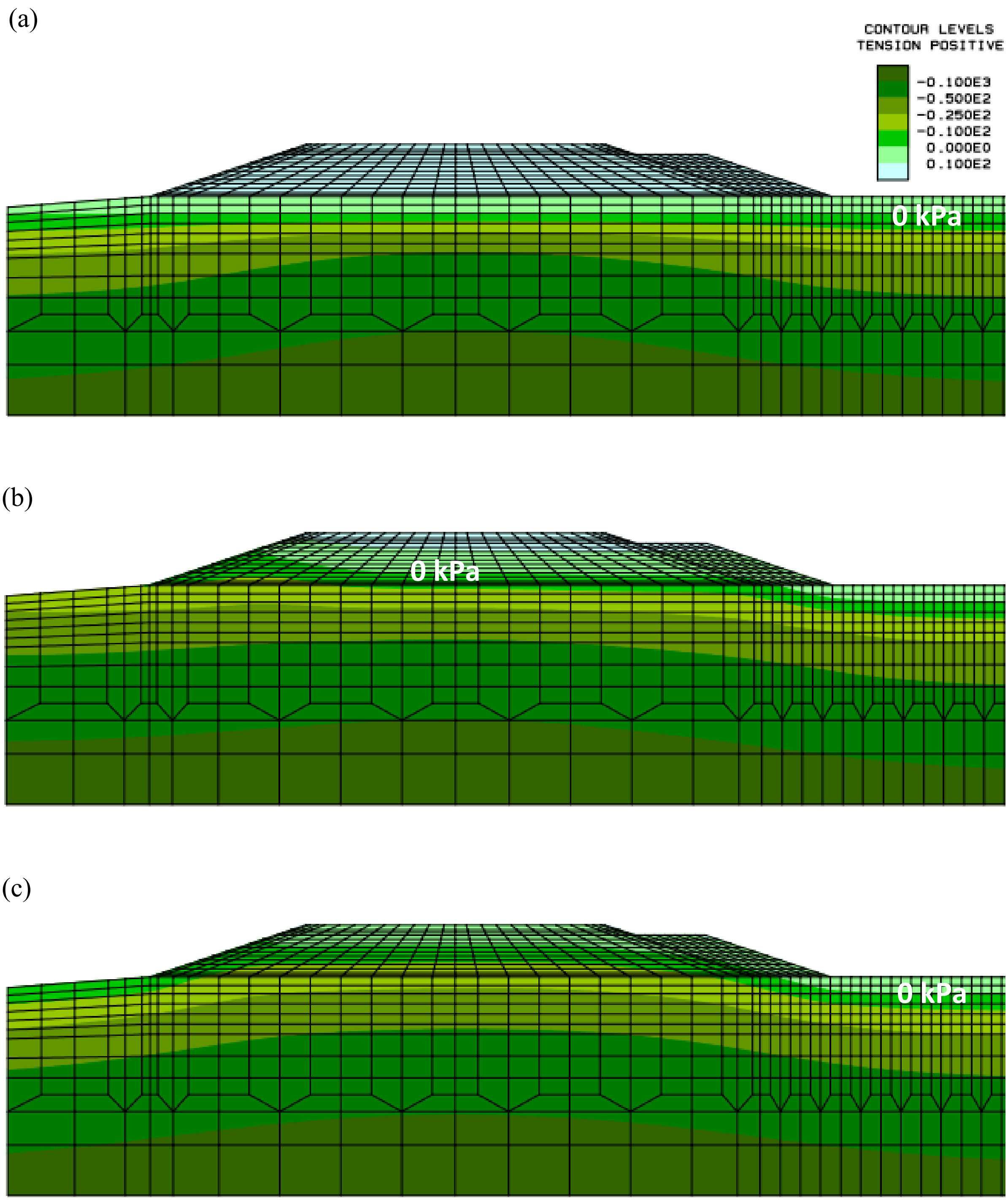
(a)
CONTOUR LEVELS
TENSION POSITIVE
-0.100E3
-0.500E2
-0.250E2
-0.100E2
0.000E0
0.100E2
0 kPa
(b)
0 kPa
(c)
0 kPa

(d)

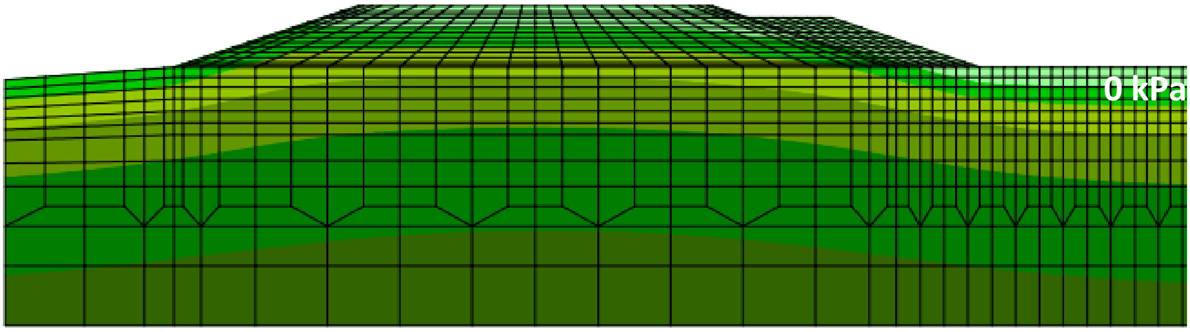

Figure H.1: Contour plots of pore water pressure of the embankment at (a) immediately after embankment construction, (b) 10.5 days of tidal cycles after embankment construction for the control case in high tide, (c) 1 month of tidal cycle after embankment construction for the control case in mid-tide, and (d) 1 month of tidal cycle after embankment construction for the 1-cycle case in mid-tide. Suctions are positive.

The suctions within the embankment were lost progressively over the month with the introduction of the precipitation and tidal boundary conditions (Figures H.1(b) and (c)). With infiltration from rain, the phreatic surface gradually rose within the embankment, eventually reaching up to 1m below the surface of the crest at the end of the month (Figure H.1(d)).

On the riverward slope with the now active tidal boundary condition, the phreatic surface was heavily influenced by the tides, with a high tide establishing a higher phreatic surface on the riverward slope. Deeper within the foundation, it is evident that the tides do have an effect in generating high pore pressures within the foundation directly beneath the riverward side of the embankment, which dissipates as the tide drops (Figures H.1(b) and (c)). The excess pore pressures generated in foundation due to the embankment construction is still present, clearly visible when it is mid-tide (Figure H.1(c)).

In terms of pore water pressure contours, there wasn't any visible difference when increasing the number of tidal cycles in the monthly time resolution, hence only the 1-cycle case was plotted in Figure H.1(d). This was also found to be similar to the control case, indicating a good reproduction at the end of the month in terms of pore water pressure behaviour in the monthly time resolution increments.

In addition to pore water pressure contours, displacement vectors at the end of the month were also compared between the various analyses to assess the suitability of the monthly tidal cycles in replicating the semidiurnal tides over the month. These are plotted in Figure H.2, with the maximum displacement for each also noted and identified in red.

(a) Maximum displacement of 23.4mm

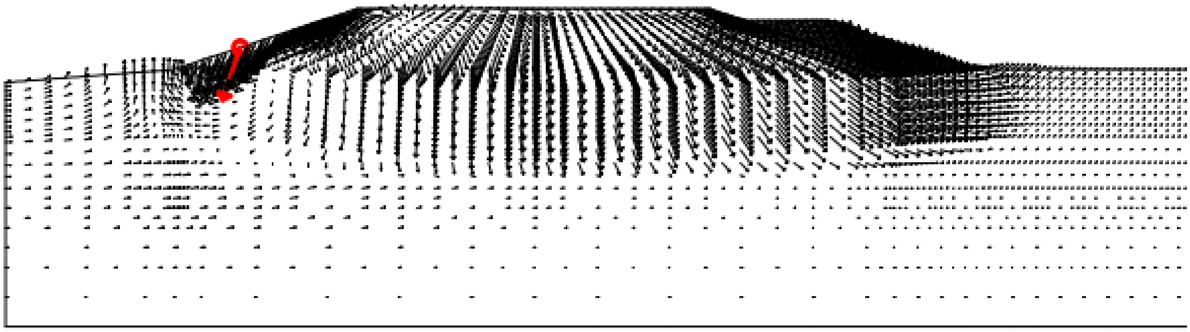

(b) Maximum displacement of 20.7mm

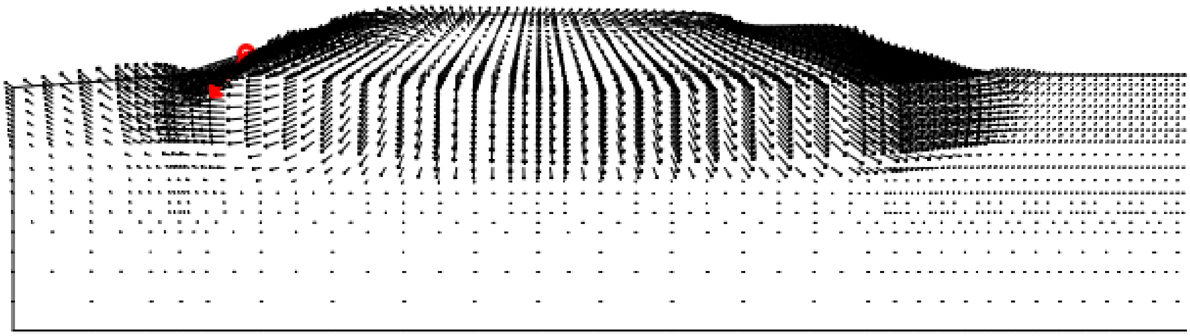

(c) Maximum displacement of 21.5mm

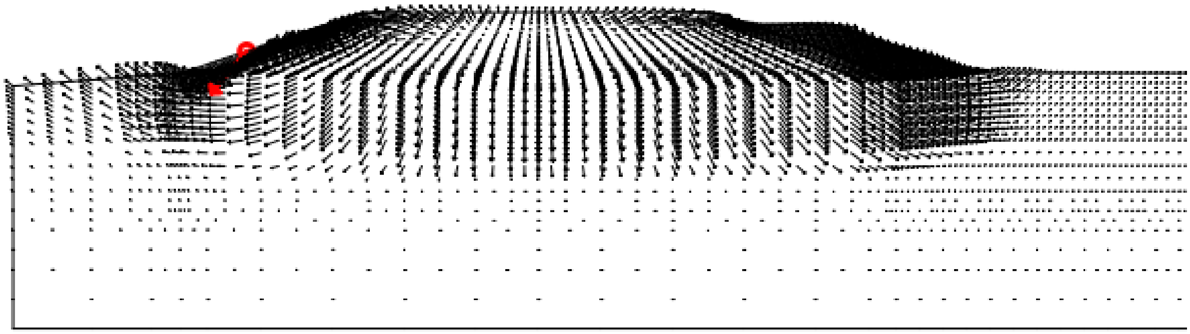

(d) Maximum displacement of 22.2mm

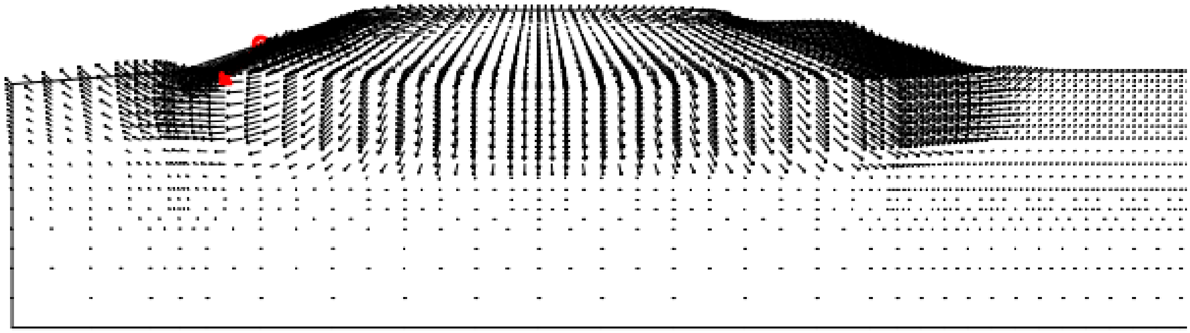

Figure H.2: Plots of displacement vectors, sub-accumulated from the end of embankment construction to 1 month after construction. (a) Control analysis. (b) 1-cycle analysis. (c) 2-cycle analysis. (d) 4-cycle analysis.

All analyses produced similar displacement vectors after one month, with the embankment settling and the maximum displacement found on the riverward slope of the embankment. The only difference among the analyses was the value of the maximum displacement, in which the control analysis had the largest maximum displacement of 23.4mm, while the 1-cycle in a month produced 20.7mm. With increasing tidal cycles, the maximum displacement also increased.

Based on this evidence, it was concluded that adopting the monthly 1-cycle strategy was sufficient in replicating the semidiurnal tidal cycles over a month for the subsequent lifecycle analysis, both in terms of pore water pressures and displacements. While increasing the total number of cycles per month may improve the maximum displacements modelled, the improvements gained for doubling the amount of computational work from 1-cycle to 2-cycle per month is small (a gain of only 0.8mm), thus it was judged that 1-cycle was sufficient in representing the tidal behaviour over a month.